UNIWERSYTET
MIKOŁAJA KOPERNIKA
W TORUNIU
Wydział Chemii

Rozprawa doktorska

mgr Barbara Kubiak

Wybrane kompleksy tytanu(IV) i rutenu(III): synteza oraz fotoindukowana aktywność katalityczna i biologiczna

Promotor: **dr hab. Piotr Piszczek, prof. UMK**

Wydział Chemii Uniwersytetu Mikołaja Kopernika w Toruniu

Promotor pomocniczy: **dr hab. Aleksandra Radtke, prof. UMK**

Wydział Chemii Uniwersytetu Mikołaja Kopernika w Toruniu

Toruń 2025



NARODOWE CENTRUM NAUKI

Niniejsza praca powstała w wyniku realizacji projektu badawczego OPUS-19 o nr 2020/37/B/ST4/01082 finansowanego ze środków Narodowego Centrum Nauki

Podziękowania

Pragnę wyrazić serdeczne podziękowania moim Promotorom, ***dr hab. Piotrowi Piszczkowi, prof. UMK oraz dr hab. Aleksandrze Radtke, prof. UMK****, za ich nieocenioną pomoc, wsparcie i cenne wskazówki, które towarzyszyły mi przez cały okres przygotowywania rozprawy doktorskiej.*

Składam również podziękowania ***prof. dr hab. Patrycji Golińskiej*** *oraz* ***dr Tadeuszowi Muziołowi*** *za cierpliwość oraz przekazaną wiedzę.*

Chciałabym podziękować także ***Pracownikom i Koleżankom*** *z Katedry Chemii Nieorganicznej i Koordynacyjnej, za stworzenie przyjaznej atmosfery podczas realizacji doktoratu.*

Jestem niezmiernie wdzięczna moim ***Przyjaciółkom: Wioli, Paulinie i Kasi*** *oraz* ***Siostrom: Marcie i Kasi****, za Ich nieocenione wsparcie i obecność przez cały czas trwania mojej drogi doktorskiej. Dziękuję za to, że zawsze byłyście przy mnie, w chwilach radości i w momentach trudniejszych, niosąc ze sobą poczucie bezpieczeństwa i otuchy.*

Chciałabym złożyć szczególne podziękowania moim ***Rodzicom****, których miłość, wsparcie i nieustanna wiara we mnie były dla mnie fundamentem na każdym etapie drogi doktorskiej. To dzięki Wam nauczyłam się, jak dążyć do swoich celów, nie poddając się w obliczu przeciwności losu. Wasze wsparcie było dla mnie niezastąpione.*

Dziękuję mojemu partnerowi ***Henrykowi*** *za wspólne pokonywanie trudności i motywację, która pozwoliła mi zrealizować ten projekt. Twoje wsparcie było dla mnie nieocenione.*

Spis treści

Wykaz skrótów stosowanych w pracy 5

Abstract 9

1. Wprowadzenie 11

1.2. Kompleksy okso-tytanu(IV) 13

1.2.1. Przykłady najczęściej otrzymywanych struktur TOCs 14

1.2.1. a) $\{Ti_3O\}$ 15

1.2.1. b) $\{Ti_4O_2\}$ 16

1.2.1. c) $\{Ti_4O_4\}$ 16

1.2.1. d) $\{Ti_6O_4\}$ 16

1.2.1. e) $\{Ti_6O_6\}$ 17

1.2.2. Stabilność struktur TOCs 18

1.3. Kompleksy okso-tytanu(IV) jako fotokatalizatory 19

1.4. Kompleksy rutenu jako fotokatalizatory 22

1.5. Aktywność przeciwdrobnoustrojowa związków tytanu 24

2. Cel rozprawy doktorskiej 28

3. Układ pracy 30

4. Streszczenie zbioru artykułów wchodzących w skład rozprawy 31

P1. *Oxo-Titanium(IV) Complex/Polymer Composites—Synthesis, Spectroscopic Characterization and Antimicrobial Activity Test.* 31

P2. *Photocatalytic and Antimicrobial Activity of Titanium(IV)-Oxo Clusters of Different Core Structure* 35

P3. *The Composites of PCL and Tetranuclear Titanium(IV) – Oxo Complexes as Materials Exhibiting the Photocatalytic and the Antimicrobial Activity.* 40

P4. *Structural Characterization and Bioactivity of a Titanium(IV) – Oxo Complex Stabilized by Mandelate Ligands.* 44

P5. *Investigation of Titanium(IV) – Oxo Complexes Stabilized with α-Hydroxy Carboxylate Ligands: Structural Analysis and DFT Studies.* 47

P6. *Analysis of Photocatalytic Properties of Poly(Methyl Methacrylate) Composites with Titanium(IV) and Ruthenium(III) Complexes* 53

5. Podsumowanie 59

6. Literatura 63

7. Dorobek naukowy kandydata na doktora 71

Załączniki 75

Wykaz skrótów stosowanych w pracy

A – powinowactwo elektronowe (*ang. electron affinity*)

BTB – błękit bromotymolowy (*ang. bromothymol blue*)

CV – fiolet krystaliczny (*ang. crystal violet*)

dc – stopień kondensacji *(ang. degree of condensation*)

DFT – teoria funkcjonałów gęstości (*ang. density functional theory*)

DMF – N,N-dimetyloformamid (*ang. N,N-Dimethylformamide*)

DNA – kwas deoksyrybonukleinowy (*ang. deoxyribonucleic acid*)

DRIFT – spektroskopia rozproszonego odbicia w zakresie podczerwieni z transformatą Fouriera (ang. *diffuse reflectance infrared Fourier transform spectroscopy*)

ds - stopień podstawienia *(ang. degree of substitiution*)

DSC – skaningowa kalorymetria różnicowa (ang. *differential scanning calorimetry)*

E - moduł sprężystości - moduł Younga (ang. *elastic modulus*)

E. coli – pałeczka okrężnicy (*łac. Escherichia coli*)

EDTA - kwas etylenodiaminotetraoctowy (ang. *ethylenediaminetetraacetic acid*)

EPR - spektroskopia elektronowego rezonansu paramagnetycznego *(ang. electron paramagnetic resonance spectroscopy)*

ESI – MS – spektrometria mas z jonizacją przez elektrorozpylanie (*ang. electrospray ionization-mass spectrometry*)

FY – detektor wydajności fluorescencji (*ang. fluorescence yield detector*)

HOMO – najwyższy obsadzony orbital molekularny (ang. *highest occupied molecular orbital*)

IR – spektroskopia w podczerwieni (*ang. infrared spectroscopy*)

LMCT – przeniesienie ładunku z liganda do metalu (*ang. ligand – metal charge transfer*)

LSPR – powierzchniowy rezonans plazmonowy (ang. Localized surface plasmon resonance)

LUMO – najniższy nieobsadzony orbital molekularny (ang. *lowest unoccupied molecular orbital)*

LZO – lotne związki organiczne (*ang. volatile organic compounds*)

MB – błękit metylenowy (*ang. methylene blue*)

MBC – minimalne stężenie bakteriobójcze (*ang. minimal biocidal concentration*)

MCCT – przeniesienie ładunku z metalu do rdzenia (*ang. metal – core chargé transfer*)

MEP – elektrostatyczny potencjał molekularny (*ang. molecular electrostatic potential*)

MIC – minimalne stężenie hamujące (*ang. minimal inhibitory concentration*)

MLCT – przeniesieniu ładunku z metalu do liganda (*ang. metal – ligand chargé transfer*)

MTT - test cytotoksyczności wykorzystujący bromek 3-(4,5-dimetylotiazol-2-ylo)-2,5-difenylotetrazoliowy

PCL – poli(ε-kaprolakton) (*ang. poly(e-caprolactone*))

PMMA – poli(metakrylan metylu) (*ang. poly(methyl methacrylate))*

R – współczynnik redukcji (*ang. reduction index*)

RFT – reaktywne formy tlenu (*ang. reactive oxygen species*)

RhB – rodamina B (*ang. rhodamine B*)

S. aureus – gronkowiec złocisty (*łac. Staphylococcus aureus*)

SEM - skaningowa mikroskopia elektronowa (ang. *scanning electron microscopy*)

SEM/EDX – skaningowa mikroskopia elektronowa sprzężona z energo-dyspersyjną mikrosondą elektronową (ang. *scanning electron microscopy equipped with an energy dispersive X-ray spectrometer*)

TEY – detektor całkowitej wydajności elektronów (*ang. total electron yield detector*)

Tg – temperatura zeszklenia (*ang. glass transition*)

TGA – analiza termograwimetryczna (*ang. termogravimetric analysis*)

THF – tetrahydrofuran (*ang. tetrahydrofurane*)

TOCs – kompleksy okso-tytanu(IV) (*ang. titanium(IV) – oxo clusters)*

UV – promieniowanie ultrafioletowe (*ang. ultraviolet light*)

UV – Vis DRS – spektroskopia w ultrafiolecie i świetle widzialnym rozproszonego odbicia (*ang. ultraviolet – visible diffuse reflectance spectroscopy*)

Vis – promieniowanie widzialne (*ang. visible light*)

WHO – Światowa Organizacja Zdrowia (*ang. Worlds Health Organization*)

XANES – spektroskopia bliskiej krawędzi absorpcji promieni rentgenowskich (*ang. X-ray absorption near edge structure*)

Streszczenie

Opracowanie nowych metod oczyszczania wody oraz przeciwdziałanie narastającej oporności mikroorganizmów na antybiotyki to istotne wyzwania współczesnej nauki. Główne źródła zanieczyszczeń wody obejmują działalność przemysłową i rolniczą, które przyczyniają się do obecności substancji takich jak farmaceutyki, pestycydy, barwniki oraz metale ciężkie. Te zanieczyszczenia stanowią poważne zagrożenie zarówno dla zdrowia ludzi, jak i dla fauny zamieszkującej skażone środowiska. Jednocześnie, według raportów WHO, problem oporności mikroorganizmów na antybiotyki narasta, głównie z powodu nadmiernego stosowania antybiotyków w medycynie i rolnictwie.

W odpowiedzi na te wyzwania swoje badania skoncentrowałam na syntezie oraz charakterystyce kompleksów okso-tytanu(IV) (TOCs), a także analizie ich właściwości fotokatalitycznych i biologicznych, indukowanych promieniowaniem ultrafioletowym i widzialnym. Badania obejmowały również ocenę potencjału aplikacyjnego TOCs jako aktywnych składników powłok kompozytowych, w których wspomniane kompleksy rozproszone były w matrycy polimerowej. W ramach przeprowadzonych syntez uzyskałam kompleksy o zróżnicowanej strukturze rdzenia $\{Ti_aO_b\}$, stabilizowane ligandami karboksylanowymi, takimi jak 4-hydroksybenzoesan, 4-aminobenzoesan i 9-fluoreno-karboksylan, oraz α-hydroksykarboksylanowymi, w tym migdałowym i 9-hydroksy-9-fluorenokarboksylanowym. Dodatkowo dokonałam oceny aktywności fotokatalitycznej kompleksów rutenu(III), co jest zagadnieniem stosunkowo słabo zbadanym. Uzyskane wyniki porównałam z danymi dotyczącymi TOCs, co pozwoliło lepiej zrozumieć mechanizmy ich działania.

Aktywność fotokatalityczną i biologiczną TOCs badałam biorąc pod uwagę wpływ rodzaju liganda stabilizującego oraz struktury rdzenia tytan-tlen na kompleks wprowadzony do matrycy z polimetakrylanu metylu (PMMA + TOCs) [**P1**, **P2**]. Oceniałam także wpływ ligandów w kompleksach o rdzeniu $\{Ti_4O_2\}$, stabilizowanych 4-aminobenzoesanem lub 9-fluorenokarboksylanem, po ich wprowadzeniu do matrycy z poli(kaprolaktonu) (PCL) [**P3**]. Kolejnym etapem była synteza i charakterystyka strukturalna TOCs o rdzeniach $\{Ti_4O\}$, $\{Ti_6O_4\}$ i $\{Ti_8O_2\}$, stabilizowanych ligandami α-hydroksykarboksylanowymi, takimi jak 9-hydroksy-9-fluorenokarboksylan oraz migdałowy [**P4**, **P5**]. Oceniłam również aktywność fotokatalityczną oraz zdolność adsorpcyjną kompozytów PMMA + TOCs stabilizowanych

ligandami α-hydroksykarboksylanowymi i otrzymane wyniki porównałam z kompozytami PMMA + Ru(III) [**P6**].

Podsumowując, w ramach przeprowadzonych badań uzyskałam osiem nowych okso-kompleksów tytanu(IV), które zostały poddane charakterystyce strukturalnej i spektroskopowej. Badania aktywności fotokatalitycznej przeprowadzono dla siedmiu nowych oraz trzech wcześniej zsyntetyzowanych okso-kompleksów Ti(IV), jak również dla dwóch znanych kompleksów Ru(III). Aktywność przeciwdrobnoustrojową analizowano dla pięciu nowych i trzech znanych wcześniej okso-kompleksów Ti(IV).

Abstract

Developing new methods for water purification and combating the growing resistance of microorganisms to antibiotics are crucial challenges in modern science. The main sources of water pollution include industrial and agricultural activities, which contribute to the presence of substances such as pharmaceuticals, pesticides, dyes, and heavy metals. These pollutants pose a significant threat to both human health and the fauna living in contaminated environments. At the same time, according to WHO reports, the problem of antibiotic resistance in microorganisms is increasing, primarily due to the excessive use of antibiotics in medicine and agriculture.

In response to these challenges, my research focused on the synthesis and characterization of oxo-titanium(IV) complexes (TOCs), as well as an analysis of their photocatalytic and biological properties induced by ultraviolet and visible radiation. The research also included an evaluation of the application potential of TOCs as active components in composite coatings, in which these complexes were dispersed within a polymer matrix. During the synthesis, I isolated complexes with varied core structures $\{Ti_aO_b\}$, stabilized by carboxylate ligands such as 4-hydroxybenzoate, 4-aminobenzoate, and 9-fluorene-carboxylate, as well as α-hydroxy-carboxylate ligands, including almond and 9-hydroxy-9-fluorenecarboxylate. Additionally, I conducted studies on the photocatalytic activity of ruthenium(III) complexes, a relatively underexplored scientific area. The results were compared with data on TOCs, which allowed for a better understanding of their mechanisms of action.

I studied the photocatalytic and biological activity of TOCs in terms of the effect of the stabilizing ligand type and the titanium-oxygen core structure in composite systems (PMMA + TOCs) [**P1**, **P2**]. I also assessed the impact of the ligand in complexes with the $\{Ti_4O_2\}$ core, stabilized by 4-aminobenzoate or 9-fluorene-carboxylate ligands, after incorporation into a poly(caprolactone) (PCL) matrix [**P3**]. The next step involved synthesizing and structurally characterizing TOCs with $\{Ti_4O\}$, $\{Ti_6O_4\}$, and $\{Ti_8O_2\}$ cores, stabilized by α-hydroxycarboxylate ligands such as 9-hydroxy-9-fluorenecarboxylate and almond [**P4**, **P5**]. I also compared the photocatalytic activity and adsorption capacity of PMMA + TOCs composites stabilized by α-hydroxycarboxylate ligands and compared them with PMMA + Ru(III) composites [**P6**].

In summary, my research resulted in the synthesis of eight new oxo-titanium(IV) complexes, which were subjected to structural and spectroscopic characterization. Photocatalytic activity was tested for seven new and three previously synthesized Ti(IV) oxo-complexes, as well as two known Ru(III) complexes. Antimicrobial activity was analysed for five new and three previously known Ti(IV) oxo-complexes.

1. Wprowadzenie

Synteza i analiza właściwości związków chemicznych charakteryzujących się aktywnością fotokatalityczną stanowią podstawę dwóch ważnych wyzwań współczesnej nauki, jakimi są: (1) przeciwdziałanie degradacji środowiska, ze szczególnym uwzględnieniem ochrony zasobów wody pitnej, oraz (2) poszukiwanie nowych środków przeciwdrobnoustrojowych w odpowiedzi na narastającą oporność mikroorganizmów na antybiotyki i dotychczas stosowane preparaty [1–6]. Fotokataliza stanowi obiecujące rozwiązanie obu tych zagadnień. Modyfikacja strukturalna fotokatalizatorów pozwala na optymalne wykorzystania określonego zakresu promieniowania widzialnego, które indukuje ich aktywność i dostosowanie tej aktywności do określonych potrzeb [7–9].

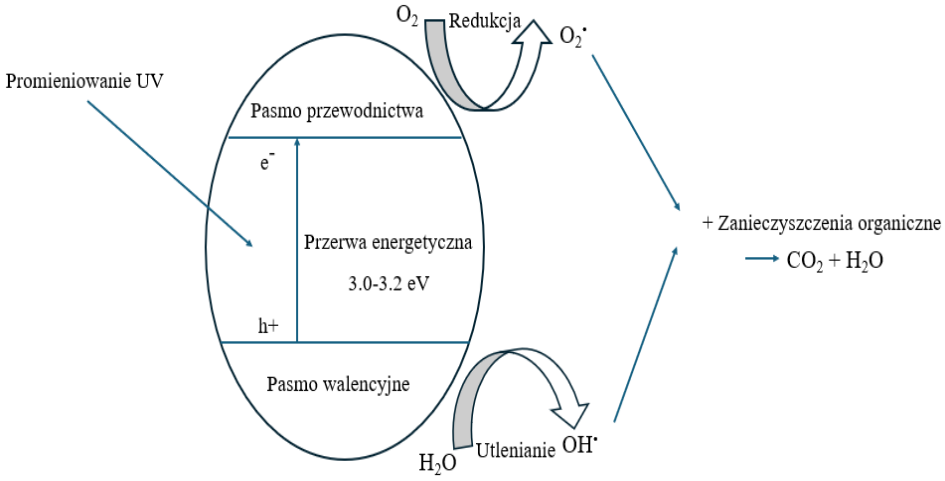
Przeprowadzone przeze mnie badania wpisują się w przedstawiony wyżej nurt badań. Ich innowacyjność polega na tym, że dotyczą aktywności fotokatalitycznej kompleksów okso-Ti(IV) (TOCs), a także mikrobiologicznej. Najwięcej czasu poświęciłam badaniu związków z grupy TOCs. W trakcie swoich badań zainteresowałam się również aktywnością fotokatalityczną kompleksów Ru(III), która zaczyna być intensywniej analizowana w ostatnich latach.

1.1. Fotokatalityczna aktywność związków tytanu(IV)

Do grupy fotokatalizatorów zaliczamy substancje, które ułatwiają lub inicjują reakcje chemiczne poprzez pochłanianie energii świetlnej, najczęściej w zakresie UV lub światła widzialnego. Absorbowana przez fotokatalizator energia aktywuje reakcje chemiczne w sposób, który nie wystąpiłby w normalnych warunkach [10]. Ditlenek tytanu (TiO_2) jest fotokatalizatorem intensywnie badanym i wykorzystywanym w różnych technologiach, np. w celu redukcji zanieczyszczeń powietrza i wody [11,12], samooczyszczania powierzchni [13], produkcji wodoru w wyniku rozkładu wody [14], czy w dezaktywacji mikroorganizmów [15].

Aby lepiej zrozumieć możliwości aplikacyjne ditlenku tytanu jako fotokatalizatora, konieczne jest poznanie mechanizmu jego działania (Rysunek 1). W wyniku absorpcji fotonów o energii równej lub większej od wartości przerwy energetycznej (w przypadku TiO_2 jest to zakres 3.0-3.2 eV), dochodzi do przeniesienia elektronów (e^-) z pasma walencyjnego do pasma przewodnictwa, i powstania w paśmie walencyjnym dodatnio naładowanych dziur (h^+). Para elektron-dziura bierze udział w reakcjach redoks z wodą lub tlenem, które mają kontakt z powierzchnią cząstek ditlenku tytanu. W rezultacie procesów redoks generowane są

reaktywne formy tlenu (RFT). Dziura powstała w paśmie walencyjnym (h^+) uczestniczy w procesach utleniania cząsteczek wody lub jonu OH^- do rodnika hydroksylowego (OH•), natomiast elektron (e^-) redukuje tlen do rodnika ponadtlenkowego (O_2•), który następnie zostaje przekształcony do rodnika hydroksylowego (OH•). Generowanie RFT prowadzi do procesów degradacji zanieczyszczeń, których produktami są woda i ditlenek węgla [16–19].



Rysunek 1. Mechanizm działania fotokatalitycznego TiO_2. Opracowanie własne na podstawie literatury [20].

Jak już wspomniałam TiO_2 jest szeroko stosowny jako fotokatalizator, np. do oczyszczania powietrza z lotnych związków organicznych (LZO), które powstają w rezultacie spalania paliw kopalnych oraz obecności kwaśnych deszczy lub smogu [11,13,21,22]. Ditlenek tytanu stosowany jest również do oczyszczania wody, w której znajdują się rozmaite niepożądane substancje takie jak: barwniki, pestycydy, pozostałości leków [12,23]. Należy również zauważyć, że aktywność fotokatalityczna TiO_2 w zakresie UV została wykorzystana w procesach wytwarzania wodoru w wyniku rozszczepienia wody pod wpływem światła [14].

Ograniczeniem szerszego zastosowania ditleneku tytanu (pomimo jego wielu zalet) jest jego zdolność absorpcji promieniowania elektromagnetycznego tylko w zakresie ultrafioletu (UV), co wynika z szerokiej przerwy energetycznej (anataz 3.20 eV, rutyl 3.02 eV). Powoduje to, że TiO_2 tylko częściowo wykorzystuje światło słoneczne, w którym promieniowanie UV stanowi jedynie 5%. Dlatego istotne znaczenie mają badania nad modyfikacją materiałów bazujących na ditlenku tytanu w celu obniżenia przerwy energetycznej lub otrzymywaniu zupełnie nowych związków, które absorbują promieniowanie elektromagnetyczne w zakresie widzialnym.

1.2. Kompleksy okso-tytanu(IV)

Jednym z proponowanych rozwiązań mających na celu wykorzystanie zakresu widzialnego promieniowania elektromagnetycznego do procesów fotokatalitycznych jest zastosowanie wielordzeniowych kompleksów okso-tytanu(IV) (TOCs), które były głównym przedmiotem moich badań. Kompleksy te wyróżniają się różnorodnością tworzonych struktur, a także interesującymi właściwościami optycznymi, fotokatalitycznymi oraz reaktywnością. Do tej grupy związków należą kompleksy o wzorze sumarycznym $[Ti_aO_b(OR)_xL_y]$, gdzie $a \geq 2$, $b = 2a - x/2 - y/2$, $x \geq 1$, $y \geq 1$. Rdzeń tych związków tworzą układy typu $\{Ti_aO_b\}$, które są stabilizowane przez ligandy alkoholanowe (OR) oraz ligandy (L), którymi mogą być grupy karboksylanowe, fosfonianowe, fosfinianowe, sulfonianowe, β-diketonianowe lub β-ketoestrowe [24,25]. Aby lepiej zrozumieć wpływ struktury wielordzeniowych okso-kompleksów tytanu na ich właściwości i aktywność fotokatalityczną, należy przeanalizować, które czynniki strukturalne mogą mieć na nie bezpośredni wpływ. Ze względu na fakt, że kompleksy o rdzeniu stabilizowanym ligandami alkoholanowymi i karboksylanowymi stanowią liczną grupę związków [26], w swoich badaniach skoncentrowałam się właśnie na nich.

Substratami niezbędnymi do syntezy tych związków są alkoholan tytanu(IV) oraz kwas karboksylowy, a proces przebiega w warunkach bezwodnych. Mechanizm reakcji zakłada hydrolizę *in situ*, która polega na wytwarzaniu wody podczas reakcji estryfikacji, bez dostarczania jej z zewnątrz. Proces tworzenia okso – kompleksu obejmuje sekwencję trzech równocześnie zachodzących etapów reakcji (Równania 1-3) [27]. W pierwszym z nich jedna lub kilka grup alkoholanowych alkoholanu Ti(IV) zostaje podstawiona przez ligandy karboksylanowe. Ważnym produktem tego etapu jest utworzenie cząsteczki alkoholu (1). Etap drugi polega na wspomnianej reakcji estryfikacji (2). W procesie tym bierze udział cząsteczka alkoholu, która powstała w etapie pierwszym oraz nieprzereagowany kwas karboksylowy. W ostatnim etapie zachodzą procesy hydrolizy i kondensacji prowadzące do utworzenia wielordzeniowego kompleksu okso-Ti(IV) (3) o wzorze $Ti_aO_b(OR)_c(OOCR')_{4a-2b-c}$ [27].

$$Ti(OR)_4 + R'COOH \longrightarrow [Ti(OR)_3(OOCR')]_n + ROH \quad (1)$$

$$ROH + R'COOH \longrightarrow R'COOR + H_2O \quad (2)$$

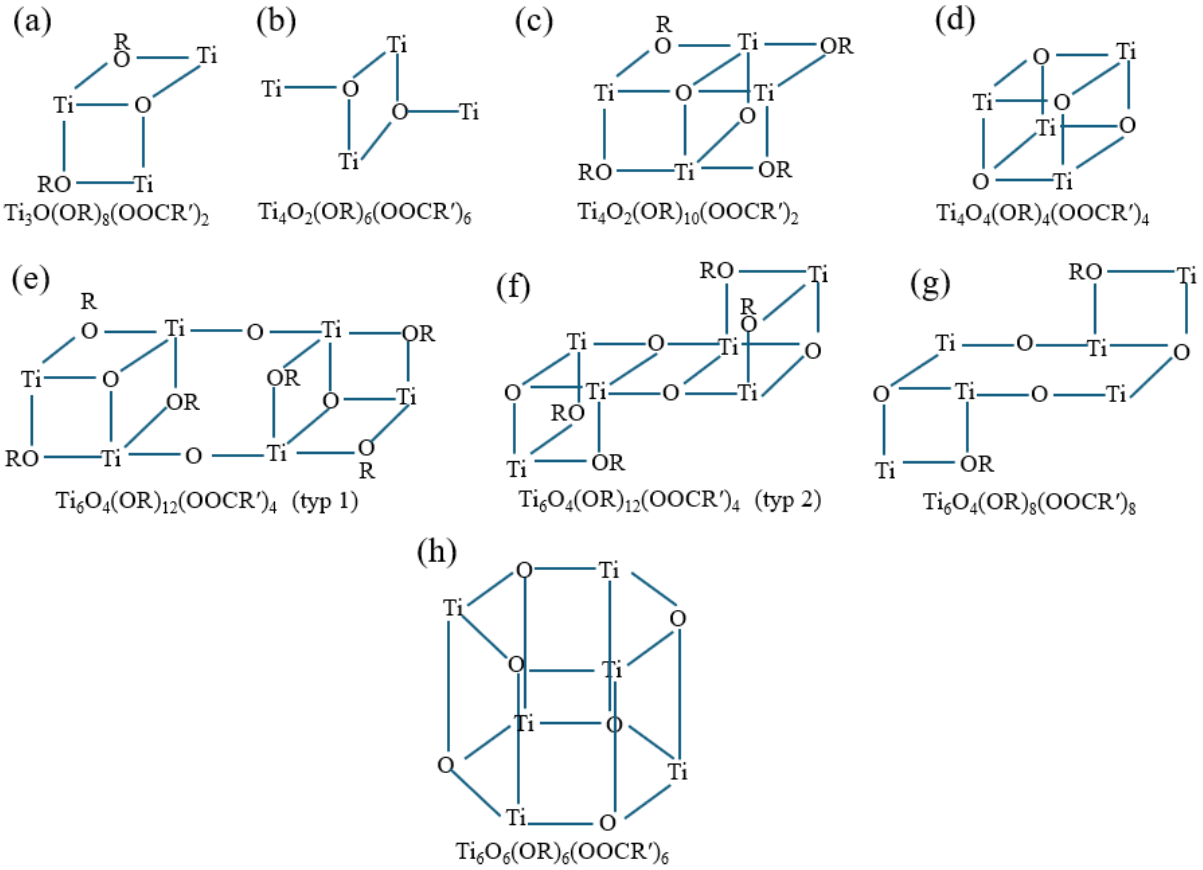
$$Ti(OR)_{4-n}(OOCR')_n + H_2O \longrightarrow Ti_aO_b(OR)_c(OOCR')_{4a-2b-c} + ROH \quad (3)$$

Rodzaj alkoholanu i kwasu karboksylowego, stosunek molowy alkoholanu tytanu(IV) do kwasu, rodzaj rozpuszczalnika oraz temperatura to główne czynniki wpływające na strukturę i właściwości tworzonych kompleksów okso-tytanu(IV) [27,28]. Spośród tych czynników kluczowe znaczenie ma rodzaj zastosowanego kwasu karboksylowego, który bezpośrednio wpływa na stabilność struktury rdzenia $\{Ti_aO_b\}$, właściwości fizykochemiczne oraz fotokatalityczne okso – kompleksu. Rodzaj kwasu determinuje liczbę tworzonych mostków tlenowych w rdzeniu oraz wpływa na geometrię i stabilność kompleksu, a także decyduje o topologii połączeń. Analiza danych literaturowych wskazuje, że małe ligandy, takie jak octan lub propionian, mają tendencję do szybkiej estryfikacji i tworzenia mniejszych, zwartych rdzeni [29,30]. Z kolei zastosowanie bardziej rozbudowanych ligandów, takich jak p-nitrobenzoesan lub metakrylan, spowalnia proces estryfikacji, prowadząc do powstania bardziej złożonych struktur. Karboksylany mogą pełnić rolę ligandów monodentnych, mostkujących lub chelatujących, co wpływa na reaktywność i stabilność okso – kompleksu. Rdzenie stabilizowane przez chelaty uznawane są za bardziej stabilne, ponieważ zapobiegają hydrolizie i utrzymują integralność tworzonych struktur [31,32].

Kolejnym ważnym czynnikiem jest stosunek molowy alkoholanu tytanu(IV) do kwasu karboksylowego (Ti:O), który wpływa na strukturę tworzącego się rdzenia, jego geometrię, a także decyduje o właściwościach otrzymanego związku. Gdy ilość użytego kwasu jest mała, wówczas w reakcji estryfikacji powstaje mniejsza ilość wody, ponieważ większość kwasu karboksylowego jest zużywana do podstawienia grup alkoholanowych. Otrzymany okso – kompleks charakteryzuje się wysokim stopniem kondensacji (*dc*) Ti:O oraz dużą liczbą ligandów alkoholanowych. Z drugiej strony użycie dużej ilości kwasu karboksylowego powoduje, że więcej wody może się wytworzyć podczas estryfikacji a *dc* rdzenia otrzymanej struktury jest mniejszy. Przykładem potwierdzającym tę zależność są reakcje $Ti(O^iPr)_4$ z 1 lub 2 molami kwasu mrówkowego, które doprowadziły do otrzymania klastrów odpowiednio $[Ti_4O_2(O^iPr)_{10}(OOCH)_2]$ i $[Ti_6O_6(O^iPr)_6\ (OOCH)_6]$ [33].

1.2.1. Przykłady najczęściej otrzymywanych struktur TOCs

Dotychczasowe badania wykazały, że wielordzeniowe kompleksy okso-Ti(IV) charakteryzują się rozmaitością struktur, w których rdzenie $\{Ti_aO_b\}$mogą być tworzone przez atomy tytanu w ilości od 2 do 52. W tej części rozprawy przedstawiłam informacje o strukturach TOCs (Rysunek 2), które miały istotne znaczenie dla mojej pracy.



Rysunek 2. Rdzenie znanych klastrów $Ti_aO_b(OR)_c(OOCR')_{4a-2b-c}$ otrzymanych w wyniku reakcji $Ti(OR)_4$ z kwasami karboksylowymi. Opracowanie na podstawie literatury [27].

1.2.1. a) {Ti_3O}

Rdzeń {Ti_3O} jest zaliczany do tzw. jednostek podstawowych, które często służą do budowania bardziej skomplikowanych struktur (Rysunek 2 (a)). Przykładem jest kompleks $[Ti_3O(OR)_8(OOCR')_2]$, którego rdzeń tworzy mostek μ_3-O [34–36]. W tej grupie kompleksów można wyróżnić:

1. Układy, w których ligandy karboksylanowe łączą różne krawędzie rdzenia; jeden z karboksylanów znajduje się w płaszczyźnie trójkąta {Ti_3O} a drugi jest prostopadły do tej płaszczyzny. Sprawia to, że każdy z atomów tytanu ma inną sferę koordynacyjną [34–38].
2. Układy, w których najdłuższa krawędź trójkąta {Ti_3O} jest mostkowana przez oba ligandy karboksylanowe. Pojawiający się w tej strukturze tytan pięciokoordynacyjny nie jest połączony z żadnym ligandem karboksylanowym [39].

1.2.1. b) $\{Ti_4O_2\}$

W rdzeniu kompleksu o wzorze ogólnym $[Ti_4O_2(OR)_6(OOCR')_6]$ oktaedry jonów centralnych (TiO_6) połączone są za pomocą mostków μ_3-O, tworząc strukturę w kształcie litery ‘’T’’ (Rysunek 2 (b)). W tym przypadku ligandy alkoholanowe są głównie terminalne, natomiast ligandy karboksylanowe mostkują atomy tytanu, łącząc wierzchołki tych oktaedrów. Powyższe struktury są bardziej otwarte w porównaniu ze związkami o wzorze ogólnym $[Ti_4O_2(OR)_{10}(OOCR')_2]$, co wynika z luźniejszego upakowania oraz tworzenia otwartych przestrzeni w strukturze, za sprawą większej ilości ligandów karboksylanowych [28,40,41]. Natomiast rdzeń układu $[Ti_4O_2(OR)_{10}(OOCR')_2]$ tworzą cztery atomy tytanu, które połączone są mostkiem μ_4-O, oraz mostkiem μ-O, co prowadzi do utworzenia zniekształconego czworościanu (Rysunek 2 (c)). Rdzeń jest stabilizowany ligandami alkoholanowymi, które mogą być mostkujące lub terminalne, przy czym ligandy mostkujące łączą atomy tytanu przez uwspólnianie krawędzi oktaedrów. Ligandy karboksylanowe mają charakter mostkujący [33,42–45].

1.2.1. c) $\{Ti_4O_4\}$

Rdzeń okso – kompleksów o wzorze ogólnym $[Ti_4O_4(OR)_4(OOCR')_4]$ zbudowany jest z czterech oktaedrycznie otoczonych atomów tytanu, które tworzą strukturę sześcianu (Rysunek 2 (d)). Jest to najbardziej zwarta struktura spośród klastrów zawierających cztery atomy tytanu i może tworzyć się w trakcie procesów przemian strukturalnych układów np. $[Ti_6O_6(OR)_6(OOCR')_6]$. W tego typu związkach ligandy alkoholanowe zawsze są terminalne, a ligandy karboksylanowe mostkujące [44,46–48].

1.2.1. d) $\{Ti_6O_4\}$

Układy zawierające rdzenie $\{Ti_6O_4\}$ stanowią najbardziej strukturalnie zróżnicowaną grupę TOCs. Ich wzór ogólny to: $[Ti_6O_4(OR)_{16-x}(O_2CR')_x]$, gdzie wartość x zależy od stopnia podstawienia (*ds*), czyli stosunku alkoholanu do kwasu. Wraz ze zmianą *ds*, wartość x przyjmuje wartości odpowiednio: x = 2, 4, 6, 8. Odpowiednie związki otrzymywano dla *ds* wynoszącego: 0.33, 0.67, 1.0, 1.33, co prowadziło do powstania związków o wzorach ogólnych: $[Ti_6O_4(OR)_{14}(O_2CR')_2]$, $[Ti_6O_4(OR)_{12}(O_2CR')_4]$, $[Ti_6O_4(OR)_{10}(O_2CR')_6]$, $[Ti_6O_4(OR)_8(O_2CR')_8]$ [49–53]. Badając struktury tych kompleksów należy zwrócić uwagę na $[Ti_6O_4(OR)_{12}(O_2CR')_4]$, dla którego możliwe są dwa typy struktur rdzeni przedstawione na

Rysunkach 2 (e) i (f). Składają się one z dwóch podjednostek typu $[Ti_3O_2(OR)_6(O_2CR')_2]$, połączonych mostkującymi anionami tlenu. Ligandy karboksylanowe mostkują atomy tytanu znajdujące się w obszarze tylko tej samej podjednostki. Obie struktury są centrosymetryczne tworząc:

1. Układ typu (1) (Rysunek 2 (e)):
   Obie podjednostki $[Ti_3O_2(OR)_6(O_2CR')_2]$ połączone są przez dwa mostki (μ-O) [51,54–56].
2. Układ typu (2) (Rysunek 2 (f)):
   Obie podjednostki $[Ti_3O_2(OR)_6(O_2CR')_2]$ uwspólniają krawędź, a wszystkie atomy tlenu tworzą mostki typu (μ_3-O) [47,54].

Jednak najczęściej tworzone są związki o wzorze ogólnym $[Ti_6O_4(OR)_8(O_2CR')_8]$, w którym cztery mostkujące ligandy karboksylanowe oraz dwa mostki typu (μ-O) łączą dwie podjednostki $\{Ti_3(\mu_3\text{-O})(\mu\text{-OR})\}$. Pozostałe cztery grupy karboksylanowe spinają jony Ti(IV) w podjednostkach (Rysunek 2 (g)) [53,57–61].
Syntezując ten rodzaj kompleksów należy zwrócić szczególną uwagę na precyzyjną kontrolę stopnia podstawienia (*ds*) oraz rodzaj ligandów, co pozwala na uzyskanie złożonych, ale dobrze zdefiniowanych układów.

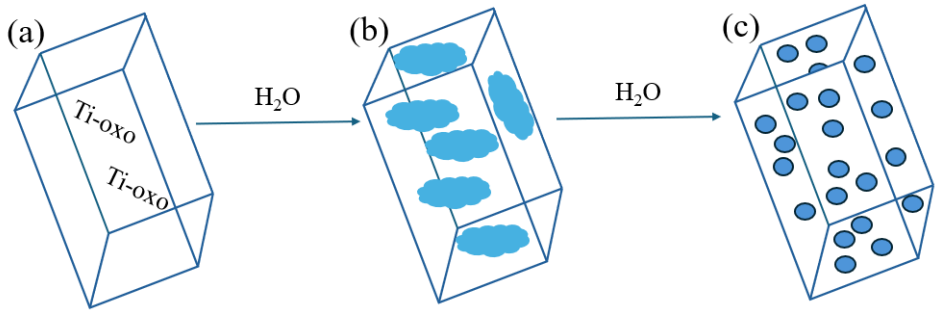
1.2.1. e) $\{Ti_6O_6\}$

Klastry o wzorze $Ti_6O_6(OR)_6(O_2CR')_6$ podobnie jak $Ti_4O_4(OR)_4(O_2CR')_4$ charakteryzują się stopniem kondensacji (*dc*) równym 1. W literaturze można znaleźć wiele przykładów tego typu struktur, co potwierdza, że są one niezwykle liczną grupą. Rdzeń ma postać zniekształconego graniastosłupa sześciokątnego, w którym atomy tytanu i tlenu są naprzemiennie ułożone a każdy z anionów tlenu jest mostkiem typu (μ_3-O) (Rysunek 2 (h)). Wszystkie ligandy alkoholanowe są terminalne a trzy z nich są ustawione prostopadle do każdej płaszczyzny $\{Ti_3O_3\}$, natomiast atomy tytanu na każdej ścianie pryzmatu są mostkowane przez ligandy karboksylanowe [62–68].

Jak już wspomniałam, omówione wyżej rodzaje struktur okso – kompleksów miały istotne znaczenie dla mojej pracy. Należy jednak pamiętać, że zmieniając stosunek alkoholanu do tytanu można otrzymać dużo bardziej rozbudowane struktury rdzeni w TOCs, np. $\{Ti_8O_8\}$ [69], $Ti_{12}O_{12}\}$ [64], $\{Ti_{32}O_{16}\}$ [70], $\{Ti_{44}O_{62}\}$ [44], czy też $\{Ti_{52}O_{74}\}$ [52].

1.2.2. Stabilność struktur TOCs

Wielordzeniowe kompleksy okso-tytanu(IV) uznawane są za struktury łatwo ulegające procesom hydrolizy. Ustalono, że rdzeń $\{Ti_aO_b\}$, który stabilizowany jest jedynie ligandami alkoholanowymi pierwotnie zachowuje swoją strukturę (Rysunek 3 (a)), ale pod wpływem działania środowiska wodnego dochodzi do kurczenia się klastrów i utworzenia amorficznych agregatów (Rysunek 3 (b)). Następnie, w wyniku dalszego zagęszczania powstają nanocząstki ditlenku tytanu (Rysunek 3 (c)) [71]. Ta cecha będzie szczególnie ceniona w przypadku, gdy chcemy uzyskać materiał, który posłuży jako prekursor do otrzymywania ditlenku tytanu. Natomiast w przypadku, gdy taki związek chcemy wykorzystać jako fotokatalizator lub środek przeciwdrobnoustrojowy, ważne jest, aby struktura związku nie zmieniała się. W celu poprawy stabilności okso – kompleksu wprowadza się dodatkowe ligandy takie jak karboksylany, fosfoniany, kaliksareny [24,72,73]. Kluczowe znaczenie ma rodzaj liganda oraz sposób jego koordynacji. Kompleksy otrzymane przy pomocy ligandów organicznych są dużo bardziej odporne na hydrolizę, za sprawą możliwości utworzenia pierścieni chelatowych oraz efektów sterycznych [74].



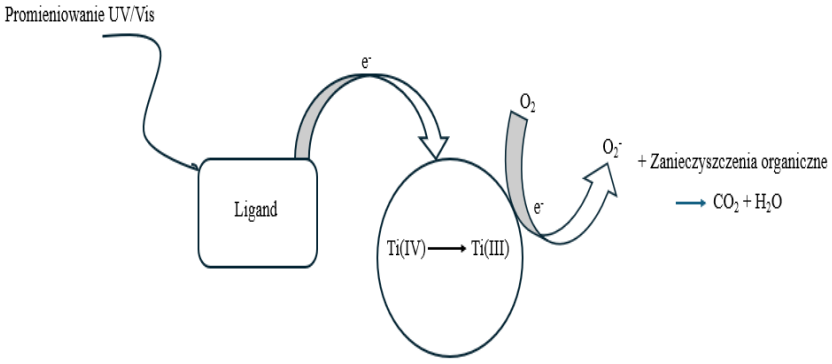
Rysunek 3. Schemat przebiegu hydrolizy okso – kompleksów tytanu. (a) struktura nie zmienia się, (b) kurczenie się TOCs pod wpływem wody, (c) powstanie struktury amorficznej. Opracowanie własne na podstawie literatury [75].

Zhang et al. otrzymali związek o rdzeniu $\{Ti_{44}O_{62}\}$, który mimo swych rozmiarów charakteryzuje się wyjątkową stabilnością, co zawdzięcza dokładnemu ekranowaniu rdzenia przez karboksylany, ponieważ struktura ta nie zawiera ligandów alkoholanowych [44]. Natomiast kompleks o rdzeniu $\{Ti_{42}O_{60}\}$ uzyskany przez Gao et al. budową przypomina fulleren, ale jest niestabilny, zapewne za sprawą dużej ilości ligandów alkoholanowych, ponieważ zawiera ich aż 42 [76]. Hou et al. postanowili porównać stabilność związków zawierających rdzenie $\{Ti_8O_5\}$, stabilizowane ligandami katecholowymi i alkoholanowymi

oraz związki o rdzeniach $\{Ti_{16}O_8\}$, które były stabilizowane tylko ligandami katecholu. Badania prowadzono w środowisku wielu rozpuszczalników (dichlorometanu, chloroformu, acetonitrylu, izopropanolu, toluenu) oraz w roztworach o szerokim zakresie pH. Okazało się, że klaster $\{Ti_{16}O_8\}$ charakteryzuje się największą stabilnością, co zawdzięcza 20 ligandom katecholowym, które ekranują rdzeń przed niekorzystnymi czynnikami (rozpuszczalniki organiczne, pH). Natomiast klaster $\{Ti_8O_5\}$ nie jest tak efektywny za sprawą ligandów alkoholanowych, które niedostatecznie chronią rdzeń [71].

1.3. Kompleksy okso-tytanu(IV) jako fotokatalizatory

Zainteresowanie kompleksami okso-Ti(IV) wynika z faktu, że modyfikując strukturę tych związków możemy kontrolować ich aktywność fotokatalityczną [53,77]. Należy zauważyć, że mechanizm aktywności fotokatalitycznej powyższej grupy związków tytanu jest inny niż w przypadku wspomnianego wcześniej ditlenku tytanu, który jest półprzewodnikiem. Opiera się on na mechanizmie przeniesienia ładunku z liganda do metalu (LMCT). Absorpcja promieniowania z zakresu UV lub widzialnego powoduje przeniesienie elektronu z najwyższego obsadzonego orbitalu molekularnego (HOMO), który zlokalizowany jest na ligandzie (tlenie) do najniższego nieobsadzonego orbitalu molekularnego (LUMO), który znajduje się na atomie tytanu. W trakcie tego procesu zachodzi redukcja Ti(IV) do Ti(III), a uwolniony elektron reaguje z tlenem, który znajduje się w środowisku reakcji, co prowadzi do generowania reaktywnych form tlenu (Rysunek 4) [78,79].



Rysunek 4. Mechanizm fotokatalityczny okso – kompleksów tytanu. Opracowanie własne na podstawie literatury [80].

A zatem modyfikując strukturę okso – kompleksu (strukturę rdzenia oraz rodzaj liganda stabilizującego) możemy kontrolować przebieg procesów fotokatalitycznych. Na temat

wpływu struktury rdzenia $\{Ti_aO_b\}$ nie ma zbyt wiele doniesień, chociaż literatura dostarcza informacji mogących usystematyzować wiedzę w tym temacie. Liu et al. otrzymali okso – kompleksy o rdzeniach: $\{Ti_6O_2\}$, $\{Ti_9O_6\}$, $\{Ti_{11}O_{11}\}$, $\{Ti_{19}O_{18}\}$ tworzących układy amino-polialkoholowe [81]. Z przeprowadzonych badań wynika, że najlepszą aktywność wykazywały kompleksy o rdzeniu $\{Ti_{19}O_{18}\}$ [81]. Stwierdzono, że większa liczba mostków tlenowych sprawia, że transfer elektronów między atomami tytanu jest ułatwiony. Wówczas reakcje redoks na powierzchni kompleksu mogą zachodzić szybciej, a degradacja zanieczyszczeń takich jak barwniki jest bardziej efektywna [82]. Potwierdzają to również badania przeprowadzone przez Li et al., którzy ustalili, że fotoaktywność okso – kompleksów tytanu można uszeregować następująco: $\{Ti_{16}O_8\} > \{Ti_7O_4\} > \{Ti_4O_2\}$ [73,83]. Spośród struktur o rdzeniach $\{Ti_6O_4\}$, $\{Ti_6O_6\}$, $\{Ti_{18}O_{25}\}$ stabilizowanych cykloheks-3-en-1-karboksylanem i badanych pod kątem aktywności w reakcjach wydzielania wodoru, najbardziej efektywne okazały się związki zawierające rdzenie $\{Ti_6O_4\}$ oraz $\{Ti_{18}O_{25}\}$. Wynikało to z różnic w ich strukturze oraz sposobie koordynacji ligandów [56]. Kolejnym przykładem jest funkcjonalizowanie struktury TOCs ligandami ferrocenu [84]. W układzie o rdzeniu $\{Ti_6O_4\}$ stabilizowanym ligandami trifluorooctanowymi oraz fenylofosfonianowymi w wyniku przejść O→Ti absorbowane jest tylko promieniowanie z zakresu UV, natomiast struktury o rdzeniach $\{Ti_6O_2\}$ i $\{Ti_8O_4\}$, stabilizowane ferrocenem są zdolne do absorpcji promieniowania z zakresu widzialnego. Aktywność fotokatalityczna kompleksów zawierających powyższe rdzenie była badana w kontekście możliwości przekształcenia dwutlenku węgla do kwasu mrówkowego pod wpływem światła widzialnego. Dla każdego związku efektywność wynosiła odpowiednio 4.03 $\{Ti_6O_4\}$, 17.03 ($Ti_6O_2\}$ i 35.00 $\{Ti_8O_4\}$ μmol [84].

Innym sposobem zwiększenia aktywności fotokatalitycznej TOCs jest wprowadzenie dodatkowego metalu, co skutkuje utworzeniem rdzenia heterometalicznego. Wang et al. przygotowali trzy związki o rdzeniach: $\{Ti_4Co_2O_2\}$, $\{Ti_5Cu_4O_6\}$ i $\{Ti_{12}Cd_5O_{18}\}$. Według ich badań, dodatek kobaltu powoduje uzyskanie najlepszej aktywności fotokatalitycznej, a sam mechanizm tego procesu różni się w porównaniu z klasycznymi TOCs. Jest to spowodowane mieszanymi przejściami przenoszenia ładunku, obejmującymi zarówno O→Ti, jak i MCCT (przeniesienie ładunku z metalu do rdzenia) [85].

Najlepiej zbadaną metodą umożliwiającą kontrolowanie aktywności fotokatalitycznej TOCs jest zastosowanie odpowiedniego liganda stabilizującego (np. liganda karboksylanowego), który pozwala na regulację wielkości przerwy energetycznej HOMO-

LUMO. W tym przypadku kontrolujemy ilość energii niezbędnej do przeniesienia elektronu, a w konsekwencji – wygenerowania RFT. Dotychczasowe badania potwierdziły, że rodzaj grupy karboksylanowej ma bezpośredni wpływ na zmniejszenie wielkości przerwy HOMO-LUMO okso – kompleksów, czemu towarzyszyło przesunięcie maksimum absorpcji w kierunku światła widzialnego. Janek et al. [35,42] zauważyli, że klastry o rdzeniach $\{Ti_3O\}$ i $\{Ti_4O_2\}$ stabilizowane ligandami 9-fluorenokarboksylanowymi wpływały na zmniejszenie wielkości przerwy energetycznej HOMO-LUMO, w porównaniu do struktur stabilizowanych ligandami 3-chlorobenzoesanowymi oraz 3-nitrobenzoesanowymi. Skutkowało to najefektywniejszą degradacją błękitu metylenowego (MB) podczas naświetlania promieniowaniem UV-Vis. Zagadnieniem tym szerzej zajęli się Liu et al. badając wpływ ligandów karboksylanowych, fosfonianowych i sulfonianowych (w syntezie TOCs zastosowano kwas octowy, kwas propanowy, kwas piwalowy, kwas bromooctowy, kwas trifluorooctowy, kwas 2-naftalenokarboksylowy, kwas 4-bromo-benzenokarboksylowy, kwas pentafluorobenzoesowy, kwas m-nitrobenzoesowy, kwas p-toluenosulfonowy, kwas fenylofosfonowy) na wielkość przerwy energetycznej HOMO-LUMO oraz aktywność fotokatalityczną [72]. Modyfikacja stabilnego klastra o rdzeniu $\{Ti_6O_4\}$ pozwoliła na efektywne wykorzystanie jego aktywnych miejsc, bez zmiany struktury. Badania wykazały, że najmniejszą wartość przerwy HOMO-LUMO (3.21 eV) zaobserwowano w przypadku stabilizacji rdzenia ligandami m-nitrobenzoesanowymi, w porównaniu do najwyższej wartości (3.70 eV), gdzie modyfikatorem był kwas octowy [72]. Włączając się w ten kierunek prac, Kim et al. badali efekty modyfikacji ligandów benzoesowych przez grupy aminowe oraz halogenowe, które stabilizowały klastry o rdzeniach $\{Ti_6O_6\}$. Badanie procesów fotokatalitycznego rozkładu błękitu metylenowego (MB) oraz rodaminy B (RhB) wykazało, że najlepszą aktywność wykazywały okso kompleksy stabilizowane drugorzędowymi grupami aminowymi [86]. Yu et al. otrzymali sześć struktur, których rdzeń składał się z sześciu atomów tytanu i był stabilizowany ligandami zdolnymi do modyfikacji właściwości optycznych kompleksu (2-hydroksypirydyną, salicyloaldoksymem i katecholem). Przeprowadzone testy potwierdziły, że rodzaj zastosowanego liganda oraz ich liczba powodują przesunięcie absorpcji w kierunku światła widzialnego oraz zmniejszenie wielkości przerwy HOMO-LUMO z 3.41 eV do 1.98 eV. Tak wąska przerwa energetyczna wydaje się być bardzo obiecująca w kontekście rozkładu barwników lub produkcji wodoru pod wpływem światła widzialnego [87]. Często stosowanym ligandem był katechol, który choć nie jest chromoforem, to z powodzeniem jest stosowany do stabilizowania rdzeni TOCs [43]. Zastosowanie katecholu, jego pochodnych a także ligandów karboksylanowych umożliwia redukcję przerwy energetycznej z 2.09 eV do

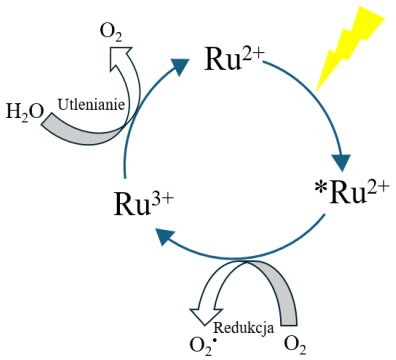
1.51 eV. Obecność grupy metoksylowej lub alkilowej w strukturze katecholu wpływa na jej znaczne zmniejszenie [88]. Interesującym sposobem poprawy właściwości optycznych oraz aktywności fotokatalitycznej okso – kompleksów o rdzeniu $\{Ti_4O_2\}$ było zastosowanie ligandów kaliks[8]arenu [89]. Wprowadzenie ligandów O lub N donorowych (izopropanol, kwas piwalowy, acetonitryl, kwas propionowy, kwas octowy, DMF) w celu modyfikacji górnej i dolnej powierzchni rdzenia $\{Ti_4O_2\}$ powoduje, że krawędź absorpcji przesuwała się do zakresu 600 – 700 nm. Badanie aktywności fotokatalitycznej tych związków wykazało, że najlepsze wyniki otrzymano w wyniku modyfikacji rdzenia ligandami karboksylowymi [89]. Do podobnych wniosków doszli He et al. oraz Kumar et al. którzy wykazali, że kaliksareny oraz tiakaliks[4]aren powodują redukcję przerwy HOMO-LUMO, więc ułatwiają transfer elektronów. W przypadku tiakaliks[4]arenu efekt ten jest dodatkowo wzmacniany przez utworzone mostki siarczkowe. W rezultacie zwiększona jest aktywność fotokatalityczna w postaci produkcji wodoru lub utleniania siarczków, która zachodzi pod wpływem naświetlania promieniowaniem widzialnym lub UV/Vis [77,90,91]. Inny kierunek zaprezentowali Liu et al., którzy badali wpływ ligandów 9-antracenokarboksylanowych oraz ferrocenowych, a także obu wyżej wymienionych ligandów na właściwości fotoelektrokatalityczne TOCs. Uzyskane wyniki wykazały, że okso – kompleksy mieszane osiągały najlepsze rezultaty w kontekście degradacji 4-chlorofenolu pod wpływem naświetlania lampą ksenonową, wspomaganej elektrochemicznie. Wynika to z większej liczby centrów aktywnych w tej strukturze, w porównaniu do struktur stabilizowanych jednym rodzajem ligandów. Wówczas możliwe jest wygenerowanie większej ilości RFT. Drugą przyczyną jest synergistyczny efekt ligandów. Ligandy ferrocenowe powodują zwiększenie przewodnictwa elektronowego, a ligandy octanowe odpowiadają za ułatwienie dostępności miejsc aktywnych dla cząsteczek 4-chlorofenolu [92].

1.4. Kompleksy rutenu jako fotokatalizatory

Biorąc udział w projekcie OPUS-19, nr 2020/37/B/ST4/01082, w którym badałam kompleksy rutenu(III) zwróciłam uwagę, na efekt odbarwiania roztworu błękitu metylenowego (MB) w trakcie oświetlania próbek światłem dziennym, co sugerowało, że związki te mogą być aktywne w zakresie światła widzialnego. Analizując doniesienia literaturowe zwróciłam uwagę na informacje dotyczące modyfikacji ditlenku tytanu kompleksami rutenu, w celu poprawy właściwości fotokatalitycznych i przesunięcia absorpcji w kierunku światła widzialnego [93–

96]. Dlatego zdecydowałam się zbadać aktywność fotokatalityczną wybranych kompleksów Ru(III) i porównać do badanych wcześniej okso-kompleksów Ti(IV).

Dotychczasowe doniesienia wskazują, że jako fotokatalizatory stosowane są głównie kompleksy tris(bipirydyny) rutenu(II). Wynika to z faktu, że związki te charakteryzują się długim okresem życia w stanie wzbudzonym oraz wysoką absorpcją światła. Mechanizm aktywności fotokatalitycznej kompleksów rutenu zgodnie z literaturą opiera się na przeniesieniu ładunku z metalu do liganda (MLCT) pod wpływem ekspozycji na światło, co powoduje wzbudzenie kompleksu [RuII]*. Wzbudzony kompleks może działać jako utleniacz lub jako reduktor, w zależności od obecności akceptorów lub donorów elektronów w środowisku reaktywnym (Rysunek 5) [97].



Rysunek 5. Mechanizm fotokatalityczny kompleksów rutenu(II). Opracowanie własne na podstawie literatury [97].

Efektywność fotokatalityczna kompleksów rutenu zależy od: (a) stabilności kompleksów oraz (b) obecności takich ligandów jak: bipirydynowe, pyrazynowe lub fenantrolinowe [98–101]. Przeprowadzane badania wykazały, że błękit bromotymolowy (BTB) najlepiej rozkładany jest przez kompleks rutenu(II) z ligandem fenantroliny w otoczeniu silnie alkalicznym (pH ok. 12).

Jak już wspomniałam, niewiele jest doniesień, które opisywałyby aktywność kompleksów rutenu(III). Dopiero w ostatnich latach pojawiły się doniesienia o możliwości zastosowania również kompleksów Ru(III), jako fotokatalizatorów. Przykładem jest praca Dhanaraj et al. [102], w której badano kompleksy Ru(III) stabilizowane 4-aminoantipiryną. Stwierdzono, że związki RuL^1Cl_2, RuL^2Cl_2, RuL^3Cl_2, RuL^4Cl_2 i RuL^5Cl_2 naświetlane promieniowaniem UV odbarwiają roztwory błękitu metylenowego odpowiednio w 69,7, 70,0, 78,5, 80,7 i 87,3%. Autorzy tej pracy proponują mechanizm zakładający, że kompleksy Ru(III) wytwarzały rodniki hydroksylowe podczas reakcji [102]:

$$[RuLCl_2] + \nu_{UV} \rightarrow [RuLCl_2]^* + {}^3O_2 \rightarrow OH^\bullet$$

Przyjęto, że generowane rodniki $OH^\bullet$ w kolejnym etapie tego procesu prowadziły do zmiany barwy roztworu MB.

$$OH^\bullet + MB \rightarrow \text{Produkty utlenienia}$$

Gao et al. [103] wykazali, że dirdzeniowe kompleksy [{(Me$_3$tacn)RuIII}$_2$(κ_2-S$_2$COR)(κ_2 -S$_2$C = O)(μ-S$_2$)]PF$_6$ (R = Me, Et, ^{n}Pr, ^{i}Pr) naświetlane światłem widzialnym wykazywały aktywność fotokatalityczną w procesach wytwarzania wodoru poprzez rozszczepienie cząsteczek wody wobec metanolu. Autorzy sugerują, że układ Ru···Ru zwiększa absorpcję światła, co ułatwia tworzenie aktywnego pośredniego produktu Ru–H i sprzyja wytwarzaniu wodoru [103]. Pomyślne wyniki badań nad zastosowaniem fotokatalizatora Ru···Rh w procesie redukcji CO_2 opisali Ghosh et al. [104]. Badany układ fotokatalityczny składał się z kompleksu $[Rh(BL)(Cp^*)Cl]^+$ jako katalizatora i kompleksu $[Ru(dmb)_2(BL)]^{2+}$ jako fotosensybilizatora (Cp* = 1,2,3,4,5-pentametylocyklopentadienyl, BL = 1,2-bis(4′-metylo[2,2′-bipirydyno]-4-ylo)etan, dmb = 4,4′-dimetylo-2,2′-bipirydyna). Autorzy tej pracy wykazali, że mieszany układ obu kompleksów monordzeniowych wytwarzał fotokatalitycznie H_2 jako główny produkt.

Kompleksy rutenu(III) wykazują znaczną aktywność fotokatalityczną w redukcji jonów wodorowęglanowych (HCO_3^-) do mrówczanów ($HCOO^-$), co zostało opisane w pracy Chatterjee i van Edik'a [105]. W badaniach tych zastosowano kompleks $[RuIII(edta)(H_2O)]^-$ zaadsorbowany na powierzchni TiO_2 modyfikowanego niemetalami (C-TiO_2, N-TiO_2, S-TiO_2). Mechanizm reakcji obejmuje absorpcję światła przez półprzewodnik, transfer elektronów do kompleksu rutenu oraz redukcję skoordynowanego jonu wodorowęglanowego do mrówczanu. W tym przypadku kompleks RuIII(edta)(H_2O), pełni rolę pośrednika w transferze elektronów.

$$[RuIII(edta)(HCO_3)]^{2-} + e^- \rightarrow [RuIII(edta)(HCO_2)]^- + OH^-$$

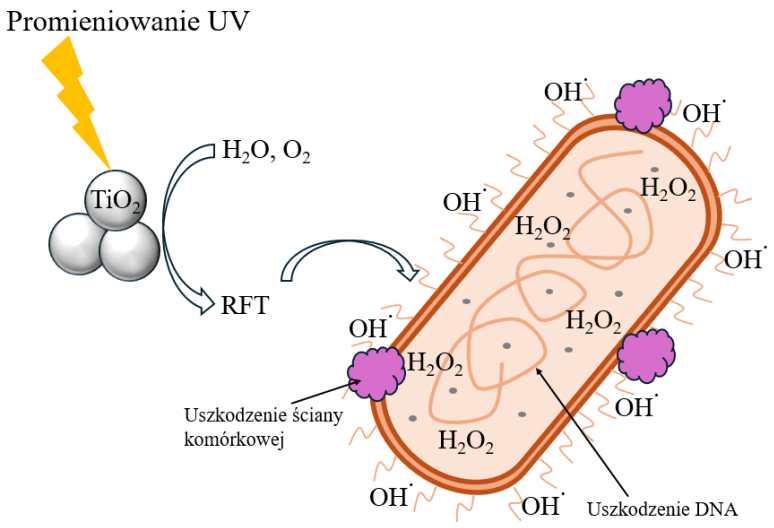
Biorąc pod uwagę wyniki tych badań zdecydowałam się na włączenie do swoich prac nad aktywnością fotokatalityczną tytanu(IV) także wybranych kompleksów Ru(III).

1.5. Aktywność przeciwdrobnoustrojowa związków tytanu

Zagrożenie dla naszego zdrowia i życia ze strony drobnoustrojów powoduje, że efektywna walka z nimi wymaga poszukiwania nowych czynników pozwalających na ich

zwalczanie oraz poznania podstawowych mechanizmów działania mikrobiobójczego. W ostatnich latach szczególne zainteresowanie budzą tlenki metali, a zwłaszcza ditlenek tytanu, który z powodzeniem znajduje zastosowanie do zwalczania bakterii oraz grzybów [15,106,107].

Aktywność przeciwdrobnoustrojowa ditlenku tytanu została odkryta przez Mutsunaga et al. w 1985 roku, którzy zauważyli, że platyna pokryta TiO_2, pod wpływem promieniowania UV, powoduje zmniejszenie liczebności bakterii *Lactobacillus acidophilus*, *Saccharomyces cerevisiae* i *Escherichia coli* [108]. Za sprawą wcześniejszych prac Hondy i Fujishimy wiedziano, że przyczyną redukcji ilości drobnoustrojów są mechanizmy generowania reaktywnych form tlenu (RFT) [109]. RFT docierając do ściany komórkowej powodują zaburzenie jej integralności przez uszkodzenie dwuwarstwy lipidowej. Ściana traci funkcję ochronną a RFT mają prostą drogę do dostania się do wnętrza komórki. Tam powodują uszkodzenia DNA oraz denaturację białek. W efekcie, komórka nie jest zdolna do przeżycia, dochodzi do nekrozy lub apoptozy (Rysunek 6) [110]. W przypadku TiO_2 jego silna aktywność przeciwdrobnoustrojowa będzie ograniczona do zakresu UV, co wynika z szerokiej przerwy energetycznej (3.0-3.2 eV) i aktywności fotokatalitycznej w tym zakresie.



Rysunek 6. Mechanizm działania przeciwdrobnoustrojowego ditlenku tytanu. Opracowanie własne na podstawie literatury [111].

Podjęto i nadal podejmuje się wiele prób poprawy tej właściwości, tak aby ditlenek tytanu mógł być czynnikiem przeciwdrobnoustrojowym również w zakresie światła widzialnego. Najpopularniejszym sposobem jest domieszkowanie TiO_2 takimi metalami jak miedź, nikiel,

srebro, platyna czy też wanad. Zastosowanie miedzi okazało się bardzo skuteczne w stosunku do bakterii Gram-dodatnich i Gram-ujemnych. Przy czym bakterie Gram-dodatnie są bardziej podatne na działanie tego czynnika, co wynika z faktu, że miedź łatwo koordynuje z białkami powierzchniowymi i ułatwia wniknięcie RFT do wnętrza komórki [112,113]. Dodatek niklu również szybciej unieszkodliwia bakterie Gram-dodatnie, które w porównaniu do bakterii Gram-ujemnych, posiadają grubszą warstwę peptydoglikanu, jednak to bakterie Gram-ujemne otoczone są błoną zewnętrzną, co stanowi dodatkową barierę wymagającą większej ilości RFT [114,115]. Utworzenie kompozytów Ag-TiO_2 powoduje zwiększoną aktywność przeciwdrobnoustrojową wobec *E. coli*, w porównaniu do czystego TiO_2 a wytworzenie kompozytów mieszanych Cu/Ag-TiO_2, dodatkowo potęguje ten efekt [116]. Nanocząstki Pt lub Ag poszerzają zakres działania ditlenku tytanu na zakres widzialny. Zjawisko powierzchniowego rezonansu plazmonowego (LSPR) sprawia, że elektrony na powierzchni metalu, pod wpływem światła o określonej długości fali zaczynają drgać, tworząc rezonans. Skutkuje to powstaniem silnego pola elektromagnetycznego wokół kompozytu metal szlachetny – TiO_2 i w efekcie możliwe jest pochłanianie również promieniowania widzialnego. Zwiększa to zakres działania związku, poprawiając właściwości przeciwdrobnoustrojowe [117,118]. Domieszkowanie wanadem (V) skutecznie hamuje adhezję *S. aureus* i *E. coli* przez generowanie większej ilości RFT w świetle widzialnym, w porównaniu do samego TiO_2 [119].

Niemetale takie jak azot, węgiel, fluor, czy też bor również stosowane są do modyfikacji przerwy energetycznej TiO_2 w celu poprawy właściwości przeciwdrobnoustrojowych. Mukherjee et al. wykazali, że dodatek azotu oraz fluoru powoduje zahamowanie kiełkowania zarodników grzybów *Fusarium oxysporum* pod wpływem światła widzialnego [120]. Zastosowanie boru spowodowało, że naświetlanie materiałów w obecności bakterii prowadzi do śmierci komórek Gram-dodatnich (*S. aureus* i *Streptococcus pyogenes*) oraz Gram-ujemnych (*Acinetobacter baumannii* i *E. coli*) a także do inaktywacji bakterii Gram-dodatnich (*S. aureus* i *Pseudomonas aeruginosa*) [121,122]. Koli et al. udowodnili również, że otrzymanie kompozytów na bazie ditlenku tytanu, boru oraz nanorurek węgla (B-TiO_2-CNT) zwiększa fotokatalityczną aktywność przeciwdrobnoustrojową wobec *E. coli* [123].

Svensson et al. zwrócili uwagę na możliwość wykorzystania kompleksów okso-Ti(IV) o rdzeniu $\{Ti_4O_2\}$, stabilizowanych przez ligandy triklosanowe, jako środka przeciwbakteryjnego przeciwko szczepom *S. aureus*. Prace te skupiły się jednak na badaniu właściwości hydrolizowanego kompleksu, który może być stosowany w aplikacjach

dostarczania przeciwbakteryjnego triklosanu do określonych obszarów naszego ciała [124]. Luo et al. dokonali modyfikacji rdzenia kompleksu Ti(IV) wprowadzając atomy srebra i otrzymując rdzenie {Ag_9Ti_4} stabilizowane przez ligandy salicylanowe. Udowodnili oni skuteczność bakteriostatyczną tego typu związków przeciwko szczepom *S. aureus* (94.51%) i *E. coli* (95.42%). Natomiast efekt mikrobiobójczy uzyskano przez utworzenie hydrożelu {Ag_9Ti_4-żel} (99,6% wobec *S. aureus* i 99,95% wobec *E. coli)*. Autorzy sugerują, że wzrost aktywności przeciwdrobnoustrojowej badanych układów jest wynikiem synergicznego działania klastra {Ag_9Ti_4} i polidopaminy, która została dodana jako środek sieciujący w procesach tworzenia hydrożelu [125].

Opierając się na wynikach badań aktywności fotokatalitycznej kompleksów okso-tytanu(IV) oraz możliwości przesunięcia zakresu absorpcji w kierunku światła widzialnego wydaje się, że mogą one być również dobrym czynnikiem przeciwdrobnoustrojowym. Co postanowiłam zbadać w trakcie swoich prac.

2. Cel rozprawy doktorskiej

Celem rozprawy doktorskiej było opracowanie syntezy nowych kompleksów okso-tytanu(IV) (TOCs) wykazujących aktywność fotokatalityczą i przeciwdrobnoustrojową, zdolnych do działania w świetle widzialnym. Rosnąca potrzeba poszukiwania innowacyjnych metod oczyszczania wody oraz skutecznych środków przeciwdrobnodustrojowych spowodowała, że badania skoncentrowały się na syntezie oraz ocenie właściwości kompozytów zawierających kompleksy okso-tytanu(IV). Ponadto celem pracy było określenie aktywności fotokatalitycznej wybranych kompleksów rutenu(III).

Realizacja głównego celu badawczego wymagała przeprowadzenia badań w następujących etapach:

1. **Opracowanie metod syntezy TOCs oraz ich charakterystyka strukturalna** — opracowanie metody otrzymywania nowych kompleksów TOCs z odpowiednich alkoholanów tytanu(IV) oraz kwasów karboksylowych. Uzyskanie wysokiej jakości kryształów, umożliwiających dokładną analizę strukturalną metodą dyfrakcji rentgenowskiej i spektroskopii. Zbadanie właściwości fizykochemicznych wyizolowanych związków.

2. **Synteza wybranych kompleksów rutenu(III)** o znanej strukturze, ich charakterystyka spektroskopowa i określenie właściwości fizykochemicznych.

3. **Wytworzenie kompozytów** poprzez wprowadzenie wyizolowanych związków kompleksowych Ti(IV) i Ru(III) do matrycy polimerowej w celu uzyskania materiałów (np. powłokowych) o działaniu fotokatalitycznym i przeciwdrobnoustrojowym.

4. **Ocena aktywności fotokatalitycznej** — analiza aktywności fotokatalitycznej badanej grupy związków kompleksowych oraz uzyskanych układów kompozytowych, naświetlanych promieniowaniem UV oraz światłem widzialnym.

5. **Ocena aktywności przeciwdrobnoustrojowej** — analiza aktywności przeciwdrobnoustrojowej TOCs oraz uzyskanych układów kompozytowych.

Nowatorski charakter tej pracy wynikał z oceny aktywności fotokatalitycznej oraz przeciwdrobnoustrojowych kompleksów okso-tytanu(IV) osadzonych w matrycy polimerowej (polimer + TOCs). Wyniki tych badań otwierają nowe możliwości zastosowania takich układów w technologii oczyszczania wody oraz w projektowaniu materiałów samoczyszczących. Istotnym aspektem pracy była również analiza aktywności fotokatalitycznej kompleksów rutenu(III) w kompozytach polimerowych (polimer + Ru(III)).

3. Układ pracy

Rozprawa jest przeglądem sześciu prac, które opublikowałam w czasopismach o zasięgu międzynarodowym:

[**P1**] P. Piszczek*, **B. Kubiak,** P. Golińska, A. Radtke*, Oxo-Titanium(IV) Complex/Polymer Composites—Synthesis, Spectroscopic Characterization and Antimicrobial Activity Test. *IJMS* **2020**, *21*, 9663, doi:10.3390/ijms21249663. IF_{2020}= 5.923, PM=140

[**P2**] **B. Kubiak*,** P. Piszczek*, A. Radtke, T. Muzioł, G. Wrzeszcz, P. Golińska, Photocatalytic and Antimicrobial Activity of Titanium(IV)-Oxo Clusters of Different Core Structure. *Crystals* **2023**, *13*, 998, doi:10.3390/cryst13070998. IF_{2023}= 2.700, PM=70

[**P3**] **B. Kubiak,** A. Radtke*, A. Topolski, G. Wrzeszcz, P. Golińska, E. Kaszkowiak, M. Sobota, J. Włodarczyk, M. Stojko, P. Piszczek*, The Composites of PCL and Tetranuclear Titanium(IV) – Oxo Complexes as Materials Exhibiting the Photocatalytic and the Antimicrobial Activity. *IJMS* **2021**, *22*, 7021, doi:10.3390/ijms22137021. IF_{2021}= 6.208, PM=140

[**P4**] **B. Kubiak*, T.** Muzioł, G. Wrzeszcz, A. Radtke, P. Golińska, T. Jędrzejewski, S. Wrotek, P. Piszczek*, Structural Characterization and Bioactivity of a Titanium(IV) – Oxo Complex Stabilized by Mandelate Ligands. *Molecules* **2024**, *29*, 1736, doi:10.3390/molecules29081736. IF_{2023}= 4.200, PM=140

[**P5**] **B. Kubiak***, T. M. Muzioł, M. Jabłoński, A. Radtke, P. Piszczek*, Investigation of Titanium(IV) – Oxo Complexes Stabilized with α-Hydroxy Carboxylate Ligands: Structural Analysis and DFT Studies. *Dalton Trans.* **2024**, 53, 14457-14468, doi:10.1039/D4DT01710B. IF_{2023}= 3.500, PM=140

[**P6**] **B. Kubiak*,** A. Topolski, A. Radtke*, T. Muzioł, O. Impert, A. Katafias, R. van Eldik, P. Piszczek, Analysis of Photocatalytic Properties of Poly(Methyl Methacrylate) Composites with Titanium(IV) and Ruthenium(III) Complexes. *Applied Sciences*, **2025**, 15(4), 1679, doi: 10.3390/app15041679. IF_{2023}= 2.500, PM=100

Ponadto w rozprawie zaprezentowałam i przeanalizowałam wyniki badań, które mają istotne znaczenie dla tematyki pracy. Badania te zostały już przeprowadzone lub są nadal w toku, jednak ich wyniki nie zostały dotychczas opublikowane.

4. Streszczenie zbioru artykułów wchodzących w skład rozprawy

P1. *Oxo-Titanium(IV) Complex/Polymer Composites—Synthesis, Spectroscopic Characterization and Antimicrobial Activity Test.*

P. Piszczek*, **B. Kubiak,** P. Golińska, A. Radtke*, *IJMS* **2020**, *21*, 9663.

W niniejszej pracy dokonałam oceny wpływu rodzaju liganda karboksylanowego na aktywność fotokatalityczną i przeciwdrobnoustrojową kompleksów okso-tytanu(IV). Badania przeprowadzono stosując kompozyty uzyskane poprzez wprowadzenie TOCs do matrycy polimerowej. Praca wpisuje się w nurt badań nad modyfikacją okso kompleksów w celu przesunięcia absorpcji promieniowania elektromagnetycznego w kierunku światła widzialnego, co powinno zwiększyć ich skuteczność zarówno w procesach fotodegradacji barwników, jak i w działaniu przeciwbakteryjnym.

Kompleksy zawierające rdzenie $\{Ti_3O\}$ i $\{Ti_4O_2\}$ otrzymano w wyniku reakcji izobutanolanu Ti(IV) lub izopropanolanu Ti(IV) z kwasem 4-aminobenzoesowym lub kwasem 4-hydroksybenzoesowym w temperaturze pokojowej, atmosferze gazu obojętnego i w stosunku molowym alkoholan-kwas wynoszącym 4:1. Wyizolowane związki o wzorach ogólnych $[Ti_3O(O^iPr)_8(O_2CC_6H_4NH_2)_2]$ (**1**), $[Ti_3O(O^iPr)_8(O_2CC_6H_4OH)_2]$ (**2**), $[Ti_4O_2(O^iBu)_{10}(O_2C\text{-}C_6H_4NH_2)_2]$ (**3**), $[Ti_4O_2(O^iBu)_{10}(O_2CC_6H_4OH)_2]$ (**4**) scharakteryzowano spektroskopowo. Analiza widm IR oraz Ramana związków (**1**)-(**4**) wykazała obecność skoordynowanych ligandów karboksylanowych, alkoholanowych oraz mostków tlenowych tworzących rdzenie $\{Ti_aO_b\}$. Interpretacja widm spektrometrii mas z jonizacją przez elektro-rozpylanie (ESI – MS), udowodniła obecność jonów fragmentacyjnych zawierających rdzenie $\{Ti_3O\}$ oraz $\{Ti_4O_2\}$, co potwierdziło strukturę otrzymanych TOCs. Zarejestrowane widma UV-Vis DRS pozwoliły ustalić, że kompleksy trirdzeniowe wykazywały maksimum absorpcji przy 400 nm (**1**) oraz 360 nm (**2**), natomiast kompleksy tetrardzeniowe odpowiednio przy 405 nm (**3**) i 390 nm (**4**). Wartości przerwy energetycznej HOMO-LUMO (ΔE), na którą bezpośredni wpływ ma rodzaj stabilizujących grup karboksylanowych wynosiły odpowiednio 2,0 eV dla (**1**) i 2,15 eV dla (**3**), tj. okso – kompleksów stabilizowanych ligandami 4-aminobenzoesanu. Natomiast wyższe wartości ΔE wynoszące odpowiednio 2,38 eV (**2**) i 2,25 eV (**4**) posiadały związki stabilizowane ligandami 4-hydroksybenzoesanu.

Otrzymane związki (TOCs) wprowadzono do matrycy z poli(metakrylanu metylu) (PMMA), wytwarzając w ten sposób układy kompozytowe (PMMA + TOCs). W publikacji (**P1**) opisano właściwości folii kompozytowych zawierających 20% wagowych badanego związku (PMMA + TOCs 20% wag.). Dyspersję ziaren kontrolowano za pomocą analizy obrazów uzyskanych ze skaningowego mikroskopu elektronowego (SEM). Wyniki tych badań wykazały, że kompozyty PMMA + TOCs 20 wt.% zawierały ziarna kompleksów (**1**), (**2**) oraz (**4**) o średnicach od 100 do 300 μm. Z kolei kompozyt PMMA + (**3**) 20 wt.% zawierał ziarna o znacznie mniejszych średnicach (3–5 μm), które miały zdolność do tworzenia większych agregatów. Analiza map Ramana potwierdziła obecność badanych kompleksów w wytwarzanych foliach kompozytowych, ponadto brak zmian w ich strukturze po wprowadzeniu do matrycy PMMA.

Właściwości termiczne otrzymanych kompozytów określono stosując analizę termograwimetryczną (TGA) oraz skaningową kalorymetrię różnicową (DSC). Stabilność termiczna była badana w zakresie temperatur 30 – 500^{o}C w atmosferze obojętnej. Badania wykazały, że próbki tracą niewielką ilość masy (10 – 15%) poniżej 280^{o}C, co wynika z odparowania resztek rozpuszczalnika potrzebnego do wytworzenia kompozytu. Przemiana termiczna, której towarzyszy większa utrata masy (70 – 85%) została zarejestrowana między 280^{o}C a 450^{o}C i jest wynikiem termicznego rozkładu badanych próbek. Temperatura zeszklenia (T_g) czystego PMMA wynosi 99.6^{o}C a temperatura topnienia 368.6^{o}C. Wprowadzenie TOCs (**1**)–(**3**) do matrycy polimerowej spowodowało podwyższenie temperatury topnienia, natomiast w przypadku próbki PMMA + (**4**) była ona niższa i wynosiła 364.5^{o}C.

Aktywność fotokatalityczną badanej grupy kompozytów określano zgodnie z normą ISO 10678:2010, analizując procesy odbarwiania roztworu błękitu metylenowego (MB) lub rodaminy B (RhB), pod wpływem promieniowania UV oraz światła widzialnego przez 180 minut. Na podstawie uzyskanych wyników stwierdzono, że najlepsze właściwości fotokatalityczne w świetle UV wykazywały kompozyty wzbogacone przez okso – kompleksy o rdzeniu $\{Ti_4O_2\}$. W świetle widzialnym najwyższą efektywność osiągnął kompozyt zawierający TOCs o rdzeniu $\{Ti_4O_2\}$ i stabilizowany ligandami 4-hydroksybenzoesanu.

W ostatniej części artykułu skupiono się na określeniu aktywności przeciwdrobnoustrojowej układów kompozytowych PMMA + TOCs 20% wag. (TOCs = (**1**)-(**4**)). Badania prowadzono w odniesieniu do bakterii Gram-dodatnich (*S. aureus* ATCC 6538 i *S. aureus* ATCC 25923), Gram-ujemnych (*E. coli* ATCC 8739 i *E. coli* ATCC 25922) oraz

grzybów *Candida albicans* (Tabela 1). Próbki wszystkich układów kompozytowych wykazywały aktywność przeciwdrobnoustrojową wobec wszystkich badanych bakterii (R = 2,5–6,0). Dodatkowo, kompozyty zawierające związki (**2**)–(**4**) charakteryzowały się wysoką aktywnością mikrobiobójczą wobec komórek grzybów *C. albicans*.

Badanie aktywności przeciwdrobnoustrojowej przeprowadzono również dla kompozytów zawierających 1, 2, 5 i 10% wag. kompleksów stabilizowanych ligandami 4-hydroksybenzoesanu ((**2**) i (**4**)). Uzyskane wyniki nie zostały uwzględnione w artykule **P1**, ponieważ przeprowadzono je już po jego napisaniu, jednak ze względu na ich istotność przedstawiono je w niniejszej części rozprawy (Tabela 1).

Tabela 1. Aktywność przeciwdrobnoustrojowa kompozytów (PMMA + TOCs) po 24-godzinnej inkubacji. R ≥ 2 determinuje aktywność przeciwdrobnoustrojową.

Nr	Próbki	Mikroorganizmy				
		E. coli ATCC 8739	*E. coli* ATCC 25922	*S. aureus* ATCC 6538	*S. aureus* ATCC 25923	*C. albicans* ATCC 10231
1	PMMA	0	0	0	0	0
2	PMMA + (**1**) 20% wag.	2.5	3.3	6.0	6.0	1.7
3	PMMA + (**2**) 20 % wag.	6.0	6.0	6.0	6.0	6.0
4	PMMA + (**3**) 20% wag.	6.0	6.0	6.0	6.0	6.0
5	PMMA + (4) 20% wag.	6.0	6.0	6.0	6.0	6.0
6	PMMA + (**2**) 1% wag.	1.7	1.1	0.9	0.2	0
7	PMMA + (**2**) 2% wag.	2.1	1.2	0.7	2.6	0
8	PMMA + (**2**) 5% wag.	2.4	2.2	5.8	6.0	0
9	PMMA + (**2**) 10% wag.	4.5	5.9	5.8	6.0	0
10	PMMA + (**4**) 1% wag.	1.6	1.6	1.5	1.2	0
11	PMMA + (**4**) 2% wag.	1.2	2.0	1.6	1.8	0
12	PMMA + (**4**) 5% wag.	3.5	3.8	5.8	6.0	0
13	PMMA + (**4**) 10% wag.	5.9	5.9	5.8	6.0	0

Efekt biobójczy wobec *E. coli* ATCC 8739 oraz *S. aureus* ATCC 25923 obserwowano przy użyciu 2% dodatku kompleksu (**2**) oraz przy 1% dodatku kompleksu (**4**) wobec *E. coli* ATCC 25922. Natomiast 5% dodatek każdego z kompleksów wywołuje efekt mikrobiobójczy wobec

wszystkich bakterii. Badane folie nie wykazują aktywności wobec *C. albicans*. Postulowanym mechanizmem odpowiedzialnym za aktywność przeciwdrobnoustrojową kompozytów jest generowanie reaktywnych form tlenu (RFT) pod wpływem promieniowania UV lub światła widzialnego.

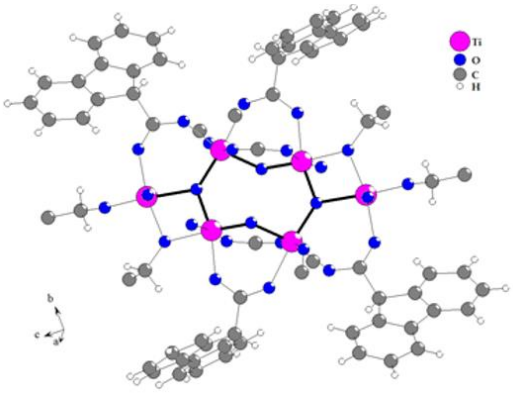
Podsumowując, przeprowadzone badania doprowadziły do wyizolowania okso – kompleksów zawierających rdzenie $\{Ti_3O\}$ oraz $\{Ti_4O_2\}$, stabilizowanych ligandami 4-aminobenzoesanu lub 4-hydroksybenzoesanu. Strukturę tych związków potwierdzono za pomocą spektroskopii IR i Ramana oraz spektrometrii ESI-MS. Aktywność fotokatalityczna wytworzonych kompozytów z 20% wagowym dodatkiem TOCs była głównie uzależniona od rodzaju ligandu stabilizującego. Zwrócono również uwagę na możliwość wpływu struktury rdzenia $\{Ti_aO_b\}$ okso na wyżej wymienioną aktywność. Badania aktywności przeciwdrobnoustrojowej kompozytów wzbogaconych o 20% masowy dodatek TOCs wykazały, że materiały te w większości wykazują działanie mikrobiobójcze wobec wszystkich zastosowanych drobnoustrojów. Przy niższych stężeniach (1% wag.) najbardziej obiecujący okazał się kompozyt PMMA + (**4**).

P2. *Photocatalytic and Antimicrobial Activity of Titanium(IV)-Oxo Clusters of Different Core Structure*

B. Kubiak*, P. Piszczek*, A. Radtke, T. Muzioł, G. Wrzeszcz, P. Golińska*, Crystals* **2023**, *13*, 998.

Jednym ze sposobów kontrolowania aktywności fotokatalitycznej kompleksów okso-tytanu(IV) może być modyfikacja struktury rdzenia $\{Ti_aO_b\}$. W niniejszej pracy starałam się określić wpływ struktury rdzenia w związkach: $[Ti_6O_4(O^jBu)_8(O_2C_{13}H_9)_8] \cdot 2(CH_3)_2CO$ (**1**), $[Ti_6O_6(O^jBu)_6(O_2C_{13}H_9)_6]$ (**2**), (**3**), $[Ti_3O(O^jPr)_8(O_2C_{13}H_9)_2]$ (**4**), $[Ti_4O_2(O^jBu)_{10}(O_2C_{13}H_9)_2]$ (**5**), stabilizowanych ligandami 9-fluorenokarboksylanu oraz alkoholanu na ich właściwości fotokatalityczne i przeciwdrobnoustrojowe.

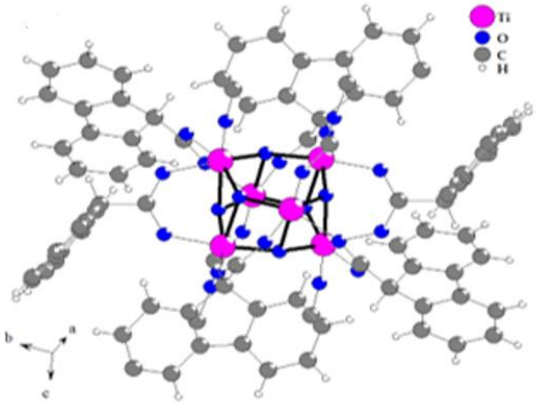
Związki o wzorach ogólnych: $[Ti_6O_4(O^iBu)_8(O_2C_{13}H_9)_8] \cdot 2(CH_3)_2CO$ (**1**) oraz dwie polimorficzne formy $[Ti_6O_6(O^iBu)_6(O_2C_{13}H_9)_6]$ (**2**) i (**3**) zostały otrzymane w wyniku reakcji izobutanolanu tytanu(IV) z kwasem 9-fluorenokarboksylowym w stosunku molowym 1:1, przy zastosowaniu acetonu jako rozpuszczalnika, w atmosferze obojętnej. Struktury zostały rozwiązane przy pomocy dyfrakcji rentgenowskiej pojedynczego kryształu. Rdzeń (**1**) składa się z dwóch jednostek $\{Ti_3\text{-}(\mu_3\text{-}O)\}$ (Rysunek 7). Każda z nich stabilizowana była przez dwa karboksylany i jeden mostek alkoholanowy. Jednostki te połączone były ze sobą za pomocą dwóch mostków (μ-O) i czterech mostków karboksylowych. Dodatkowo, rdzeń stabilizowany był sześcioma terminalnymi ligandami alkoholanowymi.



Rysunek 7. Struktura kompleksu $[Ti_6O_4(O^iBu)_8(O_2C_{13}H_9)_8] \cdot 2\ (CH_3)_2CO$ (**1**) [P2].

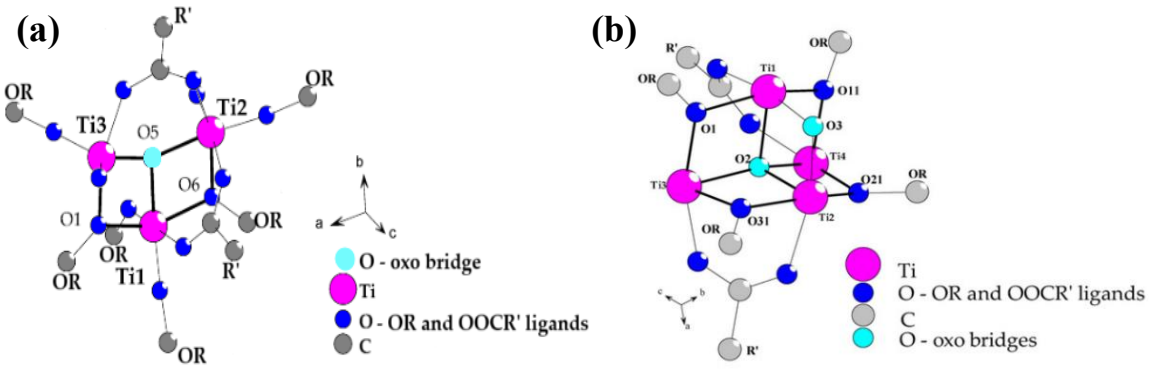
Struktura związku (**2**) i (**3**) jest podobna do wcześniej otrzymanych heksardzeniowych TOCs (Rysunek 8). Rdzeń utworzony jest z dwóch sześciokątów $\{Ti_3O_3\}$ połączonych sześcioma ligandami karboksylanowymi. Każdy z atomów tytanu koordynowany jest przez trzy mostkujące atomy tlenu (μ_3-O), dwa atomy tlenu z karboksylanów oraz jeden atom tlenu

z terminalnego liganda alkoholanowego. Kompleks (**2**) krystalizuje w układzie jednoskośnym a w sieci krystalicznej charakteryzuje się gęstym upakowaniem. Natomiast związek (**3**) tworzy analogiczny rodzaj struktury rdzenia, jednak krystalizuje w układzie tetragonalnym, a w jego sieci krystalicznej można zauważyć wolne przestrzenie wskazujące na luźniejsze upakowanie.



Rysunek 8. Struktura kompleksu $[Ti_6O_6(O^iBu)_6(O_2C_{13}H_9)_6]$ (**2**) i (**3**) [P2].

Synteza i struktury związków (**4**) i (**5**) (Rysunek 9) zostały opisane we wcześniejszych publikacjach [35,42].



Rysunek 9. Struktura kompleksu: a) $[Ti_3O(O^jPr)_8(O_2C_{13}H_9)_2]$ (**4**) [35] i b) $[Ti_4O_2(O^jBu)_{10}$-$(O_2C_{13}H_9)_2]$ (**5**) [35,42].

Kompozyty PMMA + TOCs zostały utworzone w celu ochrony związków przed ewentualnymi procesami hydrolizy, na co zwracali uwagę recenzenci naszych wcześniejszych publikacji. Materiały kompozytowe otrzymano przez dyspersję 10 lub 20% wag. TOCs (**1**), (**2**), (**4**), (**5**) w matrycy PMMA. Mikroskopia SEM pozwoliła ustalić, że rozmiar ziaren (**2**), (**4**), (**5**) wynosi od 30 do 70 µm, natomiast w przypadku związku (**1**) rozmiar jest mniejszy i wynosi od 3 do 15 µm. Obecność kompleksów (**1**) i (**2**) w kompozytach potwierdzono przy pomocy

techniki SEM EDX a rejestracja map Ramana wykazała, że 20% dodatek TOCs wskazuje na możliwy efekt agregacji, w przeciwieństwie do 10% dodatku, gdzie związek jest dobrze rozdrobniony i zdyspergowany. Analiza właściwości termicznych kompozytów zawierających związek (**1**) lub (**2**) wykazała, że materiały te charakteryzują się rozkładem dwuetapowym, a dodatek kompleksu nie miał większego wpływu na zmianę temperatury rozkładu.

Zarejestrowano również widma UV-Vis DRS kompleksów (**1**) oraz (**2**) i wyznaczono ich przerwy energetyczne HOMO-LUMO (ΔE). Wartości te są bardzo zbliżone dla obu związków i wynoszą odpowiednio: 2.98 i 2.99 eV. Maksimum absorpcji (λ_{max}) wynosi 326 nm a krawędź absorpcji rozciąga się do 395 – 400 nm. Dla porównania zarejestrowano również widma wcześniej otrzymanych klastrów (**4**) i (**5**). Analiza tych danych wykazała, że λ_{max} wynosi 380 i 395 nm, podczas gdy ΔE= 2,17 i 2,55 eV odpowiednio dla (**4**) i (**5**).

Badanie aktywności fotokatalitycznej przeprowadzono wyłącznie wobec próbek kompozytów zawierających 20% dodatek kompleksów (**1**), (**2**), (**4**) i (**5**). Proces opierał się na dekoloryzacji błękitu metylenowego (MB) pod wpływem naświetlania promieniowaniem UV lub Vis, w obecności kompozytów. Zaobserwowano, że odbarwienie MB przebiega szybciej pod wpływem światła UV, natomiast najbardziej aktywnym materiałem, zarówno pod wpływem promieniowania UV jak i Vis, jest kompozyt zawierający związek (**2**).

Aktywność fotokatalityczną badanych kompozytów powiązano z efektem generowania reaktywnych form tlenu (RFT) w trakcie naświetlania próbek promieniowaniem UV-Vis. Dla potwierdzenia ich tworzenia zarejestrowane zostały widma EPR otrzymanych materiałów. Widmo próbki PMMA + (**1**) oraz PMMA + (**5**) potwierdziło generowanie anionów O_2^- i O^-, a także jonów Ti(III). W przypadku PMMA + (**2**) pojawiają się sygnały przypisywane O^- oraz Ti(III), natomiast nie można wykluczyć obecności O_2^-, jednak ich ilość na powierzchni próbki jest prawdopodobnie znacznie niższa. Dla materiału PMMA + (**4**) zaobserwowano sygnały od O_2^- i O^- oraz sygnał Ti(III), jednak były one bardzo słabe i szybko traciły intensywność.

Badanie aktywności przeciwdrobnoustrojowej wykazało, że kompozyty są bardziej efektywne wobec bakterii Gram-dodatnich (R = 5.3 – 5.4) niż wobec bakterii Gram-ujemnych (R = 1.3 – 3.2). Próbki PMMA + (**2**) 20% wag. oraz PMMA + (**4**) 20% wag. charakteryzują się aktywnością bakteriostatyczną i bakteriobójczą wobec szczepów *E. coli* (R = 1.3 – 3.2), natomiast materiały PMMA + (**1**) 20% wag. oraz PMMA + (**5**) 20% wag. wykazywały aktywność biobójczą (R = 2.0 – 3.2) wobec tych szczepów. Żadna z folii nie okazała się biobójcza wobec grzybów *C. albicans*. Postulowanym mechanizmem działania

przeciwdrobnoustrojowego jest interakcja RFT z komórkami mikroorganizmów, co prowadzi do peroksydacji lipidów, utleniania aminokwasów w białkach, uszkodzenia kwasów nukleinowych, skutkując zaburzeniem normalnego funkcjonowania drobnoustrojów. Próbki PMMA + (**1**) oraz PMMA + (**5**) generowały oba rodzaje anionów tlenowych (O_2^- oraz O^-), potwierdzając kluczową rolę reaktywnych form tlenu (RFT) w działaniu przeciwbakteryjnym. Z kolei układ PMMA + (**2**), który generował tylko formy O^- , wykazywał słabszą aktywność wobec szczepów *E. coli* w porównaniu do PMMA + (**1**).

Ocenę cytotoksyczności kompozytu zawierającego 20% wag. (**5**), przeprowadzono w oparciu o normę PN-ISO 10993-5:2009 z użyciem linii komórkowej mysich fibroblastów L929 w warunkach *in vitro*. Średnia przeżywalność fibroblastów po kontakcie z kompozytem wyniosła 77,20%, a zatem nie wykazuje on działania cytotoksycznego (Tabela 2).

Tabela 2. Średnia przeżywalność komórek po inkubacji z materiałem PMMA + (**5**) 20% wag.

Dla 100% ekstraktu	**% przeżywalności**
Powtórzenie 1	74,88
Powtórzenie 2	73,26
Powtórzenie 3	83,48
Średnia	**77,20**

Badanie działania drażniącego i uczulającego na skórę przeprowadzono zgodnie z normą PN-EN ISO 10993-10:2015-02. Do przeprowadzenia badania wykorzystano kawie domowe (świnki morskie), na ich skórę nałożono materiał badany oraz materiał kontrolny negatywny. Zmiany zachodzące na skórze zwierząt oceniano wg skali Magnussona-Kligmana. Zgodnie z tą skalą, kompozyt zawierający 20% wag. (**5**) nie wykazuje działania uczulającego (Tabela 3).

Tabela 3. Sposób obliczeń wskaźnika uczulenia i przeciętnej skali uczulenia dla próbki PMMA + (**5**) 20 wt.% oraz kontroli negatywnej.

Grupa	**Liczba zwierząt**	**Przeciętna skala uczulenia**		**Wskaźnik uczulenia [%]**	
		Po 24h	**Po 48h**	**Po 24h**	**Po 48h**
Materiał badany	10	0,0	0,0	0,0	0,0
Kontrola negatywna	5	0,0	0,0	0,0	0,0

Reasumując, badania zawarte w artykule pozwoliły ustalić wpływ struktury rdzenia $\{Ti_aO_b\}$, stabilizowanego ligandami 9-fluorenokarboksylanu, na aktywność fotokatalityczną oraz przeciwdrobnoustrojową TOCs. Analiza widm UV – Vis DRS wskazuje, że absorpcja sześciojądrowych struktur ($\{Ti_6O_4\}$ oraz $\{Ti_6O_6\}$) ma tendencję do przesuwania się w kierunku zakresu UV, w porównaniu do kompleksów składających się z prostych jednostek ($\{Ti_3O\}$ oraz $\{Ti_4O_2\}$), gdzie przesunięcie następuje w kierunku zakresu widzialnego. Aktywność fotokatalityczna kompozytów PMMA + TOCs była wyższa w zakresie UV niż Vis. Materiały zawierające kompleksy z rdzeniami o gęstej strukturze, takie jak $\{Ti_6O_6\}$ (**2**) oraz $\{Ti_4O_2\}$ (**5**), wykazywały wyższą aktywność w porównaniu z układami o płaskim rdzeniu, a mianowicie $\{Ti_3O\}$ (**4**) i $\{Ti_6O_4\}$ (**1**). Wszystkie badane próbki wykazywały aktywność przeciwbakteryjną wobec szczepów bakterii Gram-dodatnich, natomiast aktywność wobec szczepów Gram-ujemnych można uszeregować następująco: $\{Ti_3O\}$ (**4**) <$\{Ti_6O_6\}$ (**2**) <$\{Ti_4O_2\}$ (**5**) <$\{Ti_6O_4\}$ (**1**). Wysoką aktywność związków o rdzeniach $\{Ti_4O_2\}$ oraz $\{Ti_6O_4\}$ powiązano z faktem, że w trakcie naświetlania powierzchni tych kompozytów promieniowaniem UV oraz Vis generowane były RFT, które zidentyfikowano jako aniony O_2^- jak i O^-.

P3. *The Composites of PCL and Tetranuclear Titanium(IV) – Oxo Complexes as Materials Exhibiting the Photocatalytic and the Antimicrobial Activity.*

B. Kubiak, A. Radtke*, A. Topolski, G. Wrzeszcz, P. Golińska, E. Kaszkowiak, M. Sobota, J. Włodarczyk, M. Stojko, P. Piszczek*, *IJMS* **2021**, *22*, 7021.

Z medycznego punktu widzenia, korzystne jest otrzymywanie kompozytów biodegradowalnych, które zdolne są do uwalniania środków przeciwdrobnoustrojowych. Jednym z bardziej znanych polimerów, które pełnią funkcję matrycy dla składników aktywnych jest poli(ε-kaprolakton) (PCL), od lat z powodzeniem stosowany do produkcji wyrobów medycznych, np. stentów, cewników oraz wkładek wewnątrzmacicznych. W pracy **P1** przedstawiono wyniki badań aktywności przeciwdrobnoustrojowej kompozytów, których matrycę stanowiło PMMA, tj. polimer, który nie jest biodegradowalny. Z tego powodu zdecydowałam się sprawdzić jak zastosowanie matrycy PCL wpływa na aktywność fotokatalityczną i przeciwdrobnoustrojową TOCs o rdzeniu $\{Ti_4O_2\}$.

W niniejszej pracy przedstawiono wyniki badań dotyczących materiałów kompozytowych, które zostały otrzymane przez wprowadzenie do matrycy PCL, 5 lub 20% wag. TOCs, o wzorze ogólnym $[Ti_4O_2(O^iBu)_{10}(O_2CR')_2]$ (R' = $PhNH_2$ (**1**) oraz $C_{13}H_9$ (**2**)). Struktury tych kompleksów zostały opublikowane wcześniej [42]. Próbki zostały wyprodukowane przy użyciu urządzeń do przetwórstwa tworzyw sztucznych składających się z wytłaczarki dwuślimakowej i pneumatycznej miniwtryskarki. Prace te prowadzono przy współpracy z dr hab. Michałem Sobotą z Centrum Materiałów Polimerowych i Węglowych Polskiej Akademii Nauk.

Analiza widm IR rejestrowanych techniką dyfuzyjnego rozproszenia (DRIFT) oraz widm Ramana pozwoliła na potwierdzenie struktury obu związków przed otrzymaniem kompozytów. Analiza obrazów SEM gotowych kształtek PCL + TOCs, wykazała stosunkowo jednorodne rozmieszczenie ziaren w próbkach zawierających 5% wag. kompleksów. Przeważały ziarna o średnicy od 3 do 15 μm, jednak stwierdzono również obecność większych ziaren (30–90 μm). W przypadku zwiększenia stężenia TOCs do 20% wag. widać, że rozmieszczenie ziaren jest równomierne i mają one wielkość ok. 20–70 μm. Rejestracja widm Ramana kompozytów potwierdziła obecność oraz stabilność struktur związków (**1**) i (**2**). Powyższa informacja była ważna, gdyż otrzymanie materiałów kompozytowych wymagało podgrzania mieszaniny składników do około 70°C, co mogło zmienić strukturę kompleksów. Sygnały przypisane do Ti, C, O w widmach SEM EDX potwierdzały również występowanie ziaren TOCs w matrycy PCL, natomiast sygnały pochodzące od Ti nie były obecne w czystym polimerze.

Wpływ dodatku kompleksów (**1**) i (**2**) na właściwości termiczne PCL został określony przy pomocy analizy termograwimetrycznej (TGA) i różnicowej kalorymetrii skaningowej (DSC). Pomiary przeprowadzone w zakresie temperatur 30–550ºC, w atmosferze azotu wykazały, że rozkład termiczny PCL jest procesem jednoetapowym i zachodzi w zakresie temperatur od 20 do 460ºC. Dla porównania rozkład materiałów na bazie PMMA jest dwuetapowy. Porównanie krzywych DSC czystych polimerów PCL i PMMA oraz ich kompozytów z dodatkiem kompleksów (**1**) i (**2**) wykazało, że różnią się one temperaturą termicznego rozkładu. W przypadku próbki PCL + (**2**) 20% wag. zaobserwowano obniżenie temperatury rozkładu o około 34ºC w porównaniu do czystego PCL. Kompozyty zawierające 5% wag. TOCs w matrycy PCL posiadają temperaturę rozkładu ($T_{d/max}$) nieco niższą (398ºC; 395ºC) niż dla czystego polimeru (402ºC). Analiza DSC kompozytów PMMA + TOCs wykazała, że dodatek kompleksów eliminuje efekt termiczny pojawiający się przy 151ºC, który był obecny w przypadku czystego PMMA. Wzrost temperatury rozkładu kompozytów w porównaniu do czystego PMMA sugeruje poprawę stabilności termicznej tych materiałów.

Próbki PCL oraz kompozytów PCL + (**1**) 20% wag. i PCL + (**2**) 20% wag. zostały poddane statycznej próbie rozciągania w celu określenia wpływu TOCs na wytrzymałość mechaniczną kompozytów. Po wprowadzeniu kompleksów (**1**) i (**2**) do matrycy polimerowej obserwuje się zwiększenie wartości modułu Younga (E) w porównaniu z czystym PCL i wzrost ten był większy w przypadku związku (**1**) w porównaniu do (**2**). Wytrzymałość na rozciąganie i wydłużenie przy zerwaniu zmniejszyły swoje wartości niezależnie od zastosowanego TOCs. W teście ściskania również zaobserwowano wzrost modułu Younga, ale różnice były mniej wyraźne. Rezultaty te pokazują, że nawet przy 20% wag. dodatku TOCs, kompozyty zachowują elastyczność.

Przed przystąpieniem do badania aktywności fotokatalitycznej zarejestrowano widma UV – Vis – DRS kompozytów PCL + TOCs, aby określić w jakim zakresie absorbują promieniowanie. Analiza widm wykazała, że po wprowadzeniu kompleksów do matrycy polimerowej następuje przesunięcie maksimum absorpcji z 236 nm (PCL) do 375 – 400 nm (kompozyty). Zgodnie z tymi danymi, badanie aktywności fotokatalitycznej było prowadzone w obecności światła widzialnego, obserwując odbarwianie roztworu błękitu metylenowego (MB) w czasie 30 godzin. Dla porównania określono także aktywność fotokatalityczną kompozytów PMMA + 20TOC (TOCs = (**1**) lub (**2**)). Z przeprowadzonych badań wynika, że czysty PCL nie wykazuje aktywności fotokatalitycznej, natomiast już 5% dodatek kompleksu poprawia tę właściwość. Zwiększenie zawartości TOC do 20% wag. znacząco poprawiło

aktywność fotokatalityczną badanych materiałów, szczególnie w przypadku systemu PCL + (**2**) 20% wag. (dekoloryzacja wynosiła 87%). Wśród kompozytów PMMA + TOCs, najlepsze rezultaty uzyskano dla próbki PMMA + (**2**) 20% wag. (85%).

Aktywność przeciwdrobnoustrojową badano wobec bakterii Gram-dodatnich (*Staphylococcus aureus*), bakterii Gram-ujemnych (*Escherichia coli)* oraz grzybów *Candida albicans* (Tabela 4). Żaden z kompozytów nie wykazuje działania mikrobiobójczego wobec grzybów, natomiast w przypadku 5% wag. dodatku (**1**) uzyskuje się jedynie efekt bakteriostatyczny, o czym świadczy wartość współczynnika redukcji (R) na poziomie 0.2 – 1.6. Materiał PCL + (**2**) 5%wt. wykazuje działanie bakteriobójcze wobec bakterii Gram-dodatnich i Gram-ujemnych, z wyjątkiem szczepu *Staphylococcus aureus* ATCC 6538. Zwiększenie zawartości TOCs do 20% wag. powoduje, że kompozyty mają charakter bakteriobójczy wobec wszystkich badanych szczepów bakterii.

Tabela 4. Aktywność przeciwdrobnoustrojowa PCL i PCL + nTOCs.

Nr	Próbki	Mikroorganizmy				
		E. coli ATCC 8739	*E. coli* ATCC 25922	*S. aureus* ATCC 6538	*S. aureus* ATCC 25923	*C. albicans* ATCC 10231
1	PCL	0.9	0.9	0.1	0.6	0.0
2	PCL + (**1**) 5% wag.	1.6	0.7	0.2	0.7	0.3
3	PCL + (**2**) 5% wag.	2.0	2.6	1.1	2.3	0.3
4	PCL + (**1**) 20% wag.	2.0	2.0	2.0	2.5	0.7
5	PCL + (**2**) 20% wag.	4.5	3.5	2.0	2.6	0.9

Zarówno aktywność fotokatalityczna jak i przeciwdrobnoustrojowa wynika ze zdolności do generowania RFT. Ich obecność została potwierdzona przy pomocy spektroskopii EPR. W przypadku próbki PCL + (**1**) 20% wag. na powierzchni wykryto aniony O^-, natomiast na powierzchni próbki PCL + (**2**) 20% wag. zarówno O^- jak i O_2^-. Z tego powodu kompozyt zawierający kompleks z ligandami 9-fluorenokarboksylanu jest lepszym fotokatalizatorem i czynnikiem przeciwdrobnoustrojowym.

Podsumowując, utworzenie kompozytów na bazie matrycy PCL poprzez wprowadzenie kompleksów o rdzeniu $\{Ti_4O_2\}$ stabilizowanych ligandami 4-aminobenzoesanu (**1**) oraz 9-fluorenokarboksylanu (**2**), powoduje niewielkie zmiany we właściwościach termicznych

i mechanicznych matrycy polimerowej. Utworzenie kompozytu powoduje przesunięcie maksimum absorpcji w kierunku światła widzialnego, co sugeruje, że tego rodzaju kompozyty powinny być aktywne w zakresie światła widzialnego.

Wyraźnie widoczny był wpływ rodzaju liganda na aktywność fotokatalityczną i przeciwdrobnoustrojową, ponieważ najlepsze rezultaty uzyskano dla kompozytu z dodatkiem kompleksu (**2**), którego rdzeń jest stabilizowany ligandami 9-fluorenokarboksylanu. Wynika to z faktu, że w wyniku ekspozycji na światło, na jego powierzchni generowane są aniony O^{-} oraz O_2^{-}, w przeciwieństwie do próbki PCL + (**1**) 20% wag., na którego powierzchni potwierdzono generowanie jedynie O^{-} .

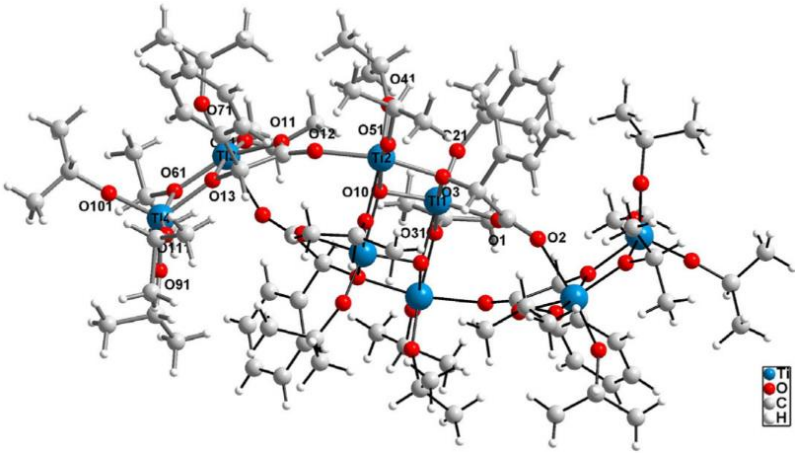
P4. *Structural Characterization and Bioactivity of a Titanium(IV) – Oxo Complex Stabilized by Mandelate Ligands.*

B. Kubiak*, T. Muzioł, G. Wrzeszcz, A. Radtke, P. Golińska, T. Jędrzejewski, S. Wrotek, P. Piszczek*, *Molecules* **2024**, *29*, 1736.

Badania omówione w pracach **P1** – **P3** wykazały, że TOCs, których rdzenie są stabilizowane ligandami karboksylanowymi charakteryzują się obiecującą aktywnością przeciwdrobnoustrojową. Aby wzmocnić właściwości mikrobiobójcze syntetyzowanych TOC, zdecydowałam się włączyć do ich struktury ligandy α-hydroksykarboksylanowe, znane ze swoich właściwości przeciwbakteryjnych i przeciwzapalnych. α-hydroksykwasy mają więcej możliwości koordynacji z Ti(IV), co skutkuje powstawaniem również bardziej stabilnych strukturalnie układów w porównaniu do związków stabilizowanych grupami karboksylowymi.

Artykuł **P4** przedstawia wyniki badań dotyczących kompleksu o wzorze ogólnym $[Ti_8O_2(O^iPr)_{20}(man)_4]$ (**1**) (man = ligand migdałowy), który otrzymano w wyniku reakcji izopropanolanu tytanu(IV) i kwasu migdałowego ($HOOCCH(OH)C_6H_5$) w stosunku molowym 4:1, z zastosowaniem THF jako rozpuszczalnika. Analiza danych dyfrakcji rentgenowskiej pojedynczego kryształu wykazała, że struktura tego związku składa się z jednostki centralnej $\{Ti_4O_2\}$, do której, za pomocą ligandów migdałowych, przyłączone są dwa dimery $\{Ti_2\}$ (Rysunek 10). Rdzeń $\{Ti_4O_2\}$ kompleksu stabilizowany jest przez mostki (μ_3-O), aniony izopropionianowe oraz grupy hydroksylowe z anionu kwasu migdałowego. Anion tlenowy tworzy jedno krótkie i dwa długie wiązania, co wyróżnia tę topologię od wcześniej opisanych rdzeni $\{Ti_4O_2\}$ [42]. Kationy Ti1, Ti2 i Ti3 znajdują się w otoczeniu oktaedrycznym, podczas gdy zewnętrzny kation Ti4 jest pięciokoordynacyjny i tworzy silnie zniekształconą bipiramidę trygonalną. Ligandy migdałowe tworzą mostki i pierścienie chelatowe, prowadząc do wzmożonej koncentracji gęstości elektronowej w powyższych pierścieniach.

Analiza widm IR oraz dyfraktogramów proszkowych zarejestrowanych przed i po zanurzeniu w wodzie na 72h pozwoliła na ustalenie stabilności związku (**1**). Dyfraktogramy potwierdziły brak transformacji w kierunku krystalicznego TiO_2 czy innych form krystalicznych, natomiast widma IR nie wykazały żadnych zmian w intensywności i pozycjach pasm w badanych zakresach, co wskazuje na odporność próbki na proces hydrolizy.



Rysunek 10. Struktura $[Ti_8(\mu_3\text{-}O)_2(\mu\text{-}O^iPr)_4(O^iPr)_{16}(man)_4]$ (**1**). Jednostkę asymetryczną przedstawiono za pomocą wiązań pokazanych w kolorze szarym, a atomy symetrycznie zależne poprzez operację inwersji pokazano na czarno [**P4**].

Kolejnym etapem było wytworzenie materiałów kompozytowych PMMA + (**1**), które zawierały: 2, 5, 10 i 20% wag. TOCs. Procedura była taka sama jak w pracach **P1** i **P2**. Obecność związku w matrycy polimerowej potwierdzono za pomocą metody SEM EDX. Dodatkowo, aby zbadać ewentualne zmiany strukturalne spowodowane wytworzeniem kompozytu, porównano widma Ramana kompleksu (**1**), czystego PMMA oraz próbki PMMA + (**1**) 20% wag. Otrzymane wyniki potwierdziły, że struktura związku pozostaje niezmieniona po wprowadzeniu go do matrycy.

Naświetlenie proszku (**1**) i kompozytów, promieniowaniem widzialnym, powoduje generowanie RFT na powierzchni próbek, co zostało potwierdzone przy pomocy spektroskopii EPR. Intensywność sygnałów rośnie wraz ze wzrostem ilości kompleksu w matrycy polimerowej. Zidentyfikowano obecność anionów O^- i O_2^- na powierzchni materiałów kompozytowych, natomiast O_2^- jest generowany na powierzchni proszku (**1**).

Ocenie aktywności przeciwdrobnoustrojowej został poddany zarówno sproszkowany kompleks, jak i próbki kompozytów. Badanie to wykonano wobec bakterii *Staphylococcus aureus* i *Escherichia coli*, a także grzybów *Candida albicans*. Zgodnie z normą ISO 22196:2011, zawiesiny wykazują efekt mikrobiobójczy, gdy wartość współczynnika redukcji (R) wynosi ≥ 3. Uzyskane rezultaty wskazują, że kompleks (**1**) wykazuje działanie bakteriobójcze już w stężeniu 2% (w/v) (*E. coli* (R = 6.0) i *S. aureus* (R = 4.2 – 5.4)), natomiast działanie grzybobójcze w 20% (w/v). Kompozyty wykazały silną aktywność wobec *E. coli* (R = 2.0 – 4.9) i *S. aureus* (R = 4.7 – 5.1) we wszystkich testowanych stężeniach TOCs (2% wag., 5% wag., 10% wag., 20% wag.). Nie wykazują jednak działania grzybobójczego. Wyjaśnienie

właściwości biobójczych związku (**1**) i jego kompozytów PMMA + (**1**) wymaga uwzględnienia dwóch czynników: (i) zdolności fotokatalitycznych kompleksu oraz (ii) czynników strukturalnych, w szczególności tworzenia pierścieni chelatowych. RFT generowane na powierzchni proszku oraz kompozytów prowadzą do indukowania stresu oksydacyjnego a w rezultacie upośledzenia lipidów, białek i kwasów nukleinowych, co ostatecznie prowadzi do śmierci mikroorganizmu. Natomiast zgodnie z teorią chelatacji Tweedy'ego i koncepcją Overtone'a, koordynacja zmniejsza polarność jonów metali. Zwiększona delokalizacja π-elektronów w pierścieniu chelatowym zwiększa lipofilowy charakter związku. Sprzyja to rozpuszczalności kompleksu w lipidach, prowadząc do nieodwracalnego uszkodzenia błony i funkcji komórki.

Cytotoksyczność kompozytów zawierających związek (**1**) badano za pomocą testów MTT wobec linii komórkowej fibroblastów mysich L929. Materiał uznaje się za niecytotoksyczny, jeśli żywotność komórek jest większa niż 70%. Testy wykazały, że poziom żywotności komórek zmierzony dla referencyjnych próbek PMMA był porównywalny z wartościami otrzymanymi dla próbek zawierających kompleks (**1**) we wszystkich badanych stężeniach. Co ważne, wyniki te wykazały również, że wraz ze wzrostem czasu inkubacji na wszystkich badanych próbkach namnażało się więcej fibroblastów L929. Te obserwacje potwierdziła również analiza obrazów SEM po procesie hodowli. Wydłużony kształt komórek obserwowany po 24h inkubacji wskazuje na prawidłową adhezję. Po 72h liczba wypustek cytoplazmatycznych wzrosła, a ich obecność odgrywa kluczową rolę w migracji, proliferacji i tworzeniu połączeń międzykomórkowych.

Podsumowując, reakcja izopropanolanu tytanu(IV) z kwasem migdałowym prowadziła do otrzymania stabilnego związku $[Ti_8O_2(O^iPr)_{20}(man)_4]$ (**1**). Zarówno czysty proszek (**1**) jak i kompozyty uzyskane przez wprowadzenie związku do matrycy polimerowej charakteryzują się aktywnością przeciwbakteryjną wobec szczepów Gram-dodatnich i Gram-ujemnych. Wysoką aktywność przeciwdrobnoustrojową kompleksu (**1**) przypisuje się synergicznemu efektowi generowaniu RFT oraz obecności pierścienia chelatowego. Materiały PMMA + (**1**) okazały się nietoksyczne dla fibroblastów L929, co potwierdza ich potencjał jako powłok antybakteryjnych do zastosowań w miejscach publicznych lub szpitalach, zmniejszając ryzyko zakażeń bakteryjnych.

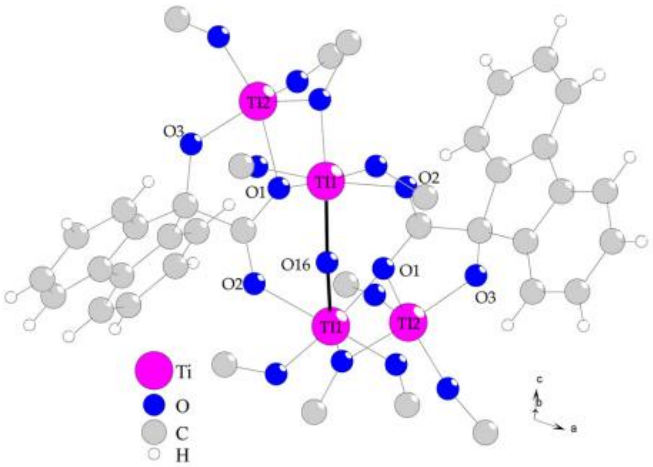
P5. *Investigation of Titanium(IV) – Oxo Complexes Stabilized with α-Hydroxy Carboxylate Ligands: Structural Analysis and DFT Studies.*

B. Kubiak*, T. M. Muzioł, M. Jabłoński, A. Radtke, P. Piszczek*, *Dalton Trans.* **2024**, 53, 14457-14468.

Kontynuując badania nad syntezą TOCs z wykorzystaniem kwasów α-hydroksy-karboksylowych przeprowadziłam badania nad reakcjami izopropanolanu tytanu(IV) z kwasem 9-hydroksy-9-fluorenokarboksylowym, a otrzymane wyniki przedstawiłam w artykule **P5**. W pracy tej przedstawiłam wyniki badań nad strukturą dwóch okso – kompleksów, ich stabilnością, a także potencjalną reaktywnością, która została oszacowana za pomocą teorii funkcjonału gęstości (DFT).

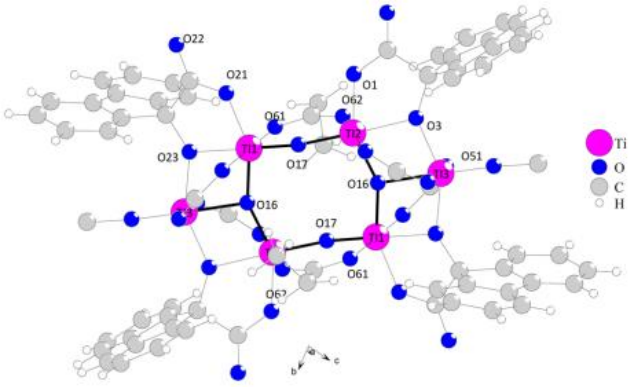
Kompleks (**1**) o wzorze ogólnym $[Ti_4O(O^iPr)_{10}(O_3C_{14}H_8)_2]$ (Rysunek 11) został otrzymany w wyniku reakcji izopropanolanu tytanu(IV) z kwasem 9-hydroksy-9-fluorenokarboksylowym w stosunku molowym 4:1, stosując mieszaninę tetrahydrofuran/izopropanol (THF/HO^iPr) (1:1) jako rozpuszczalnik. Reakcja była prowadzona w temperaturze pokojowej i w komorze rękawicowej. Związek krystalizował w jednoskośnej grupie przestrzennej C2/c. Na uwagę zasługuje unikalna architektura rdzenia {Ti_4-O} wyizolowanego związku, którego centralną część tworzył mostek Ti-O-Ti. Wcześniejsze badania kompleksów tworzących podobny typ rdzenia wskazały na tworzenie się układu, w którym cztery kationy Ti(IV) połączone były z czterokrotnym mostkiem tlenowym (μ_4−O) tworząc {Ti_4-(μ_4-O)}. Innym sposobem uzyskania rdzenia {Ti_4-O} jest wykorzystanie trzech kationów Ti(IV), które połączone są mostkiem (μ_3−O), natomiast czwarty jon Ti(IV) jest przyłączony poprzez ligand fosfonianowy. Taka struktura charakteryzuje się większą asymetrią w porównaniu do rdzenia, w którym występuje mostek (μ_4−O). Natomiast w otrzymanym przeze mnie związku (**1**), rdzeń tworzą cztery atomy Ti(IV), z których dwa (Ti1) połączone są za pomocą mostka μ-O a pozostałe dwa (Ti2) są wiązane poprzez ligandy α-hydroksykarboksylanowe (Rysunek 11). Kationy Ti1 tworzą otoczenie oktaedryczne, złożone z trzech atomów tlenu pochodzących od anionów izopropylanowych (dwóch terminalnych i jednego mostkowego), dwóch atomów tlenu, ligandów 9-hydroksy-9-fluorenokarboksylowych i atomu tlenu anionu okso. Natomiast pięciokoordynacyjne kationy Ti2 znajdowały się w otoczeniu piramidy kwadratowej, której sfera koordynacyjna składała się z trzech atomów tlenu, anionów izopropylanowych (dwóch terminalnych i jednego mostkującego) oraz dwóch atomów tlenu pochodzących od ligandów α-hydroksykarboksylanowych. Kationy Ti1 i Ti2 były połączone asymetrycznymi mostkami

izopropylanowymi i ligandami 9-hydroksy-9-fluorenokarboksylowymi, podczas gdy centralne kationy Ti1 były połączone grupami karboksylowymi dwóch anionów α-hydroksykwasów i jedynego anionu okso (Rysunek 11).



Rysunek 11. Struktura $[Ti_4O(O^iPr)_{10}(O_3C_{14}H_8)_2]$ (**1**) [P5].

Okso kompleks (**2**) o wzorze ogólnym $[Ti_6O_4(O^iPr)_2(O_3C_{14}H_8)_4(O_2CEt)_6]$ został otrzymany w wyniku reakcji izopropanolanu tytanu(IV), kwasu 9-hydroksy-9-fluorenokarboksylowego oraz kwasu propionowego stosując THF jako rozpuszczalnik. Stosunek molowy alkoholanu do kwasów organicznych wynosił 1:1.2. Reakcja była prowadzona w temperaturze 70°C, w komorze rękawicowej. Kompleks ten krystalizował w trójskośnej grupie przestrzennej P-1. Rdzeń kompleksu został utworzony przez sześć kationów tytanu(IV) ułożonych w dwa niemal współpłaszczyznowe trójkąty ($Ti_3(\mu_3\text{-}O)$). W każdym z nich, trzy kationy tytanu(IV) są połączone mostkiem μ_3-O, a dodatkowo stabilizowane ligandami 9-hydroksy-9-fluorenokarboksylowymi i propionianowymi. Oba trójkąty $\{Ti_3O\}$ są połączone dwoma mostkami μ-okso i dwoma anionami propionianowymi. Należy zauważyć, że w tej strukturze ligandy 9-OH-9-fluorenokarboksylanu tworzą pierścień chelatowy, ale jedna grupa karbonylowa w każdym ligandzie karboksylanowym pozostaje nieskoordynowana i może być wystawiona na działanie rozpuszczalnika (Rysunek 12).



Rysunek 12. Struktura $[Ti_6O_4(O^iPr)_2(O_3C_{14}H_8)_4(O_2CEt)_6]$ (**2**) [P5].

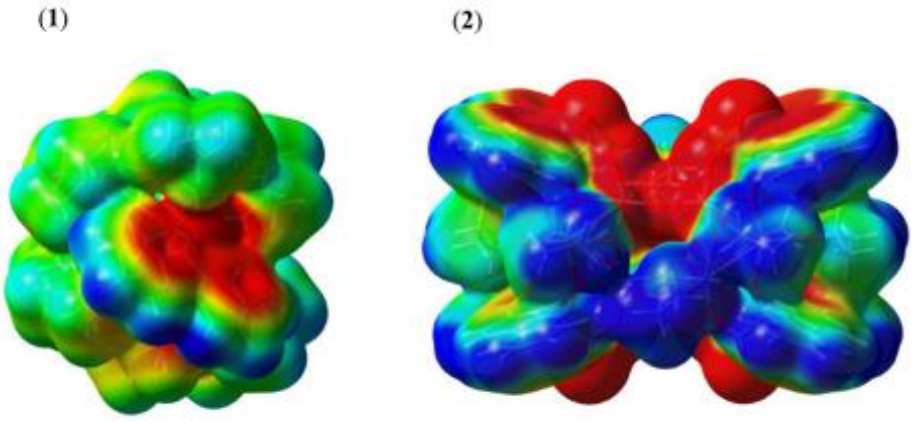
W dalszej części pracy przedyskutowałam widma zarejestrowane stosując metody spektroskopii IR oraz Ramana. Obecność mostków karboksylowych skoordynowanych z atomami Ti(IV) w strukturze (**1**) potwierdzają pasma pochodzące od asymetrycznych i symetrycznych drgań rozciągających grup –COO, pojawiające się odpowiedni w zakresie 1600-1640 cm^{-1} i ok. 1449 cm^{-1}. Obecność dwóch różnych ligandów karboksylanowych (9-OH-9-fluorenokarboksylanowych i propionianowych) w strukturze kompleksu (**2**) powoduje pojawienie się dwóch różnych pasm pochodzących od asymetrycznych drgań rozciągających grup –COO. Pasma te pojawiały się odpowiednio przy 1711 i 1510 cm^{-1}. Przypisanie pasm drgań dla mostka Ti–O–Ti było trudne ze względu na nakładanie się tych pasm z pasmami grup funkcyjnych ligandów organicznych poniżej 1000 cm^{-1} w widmach IR i Ramana. Zastosowanie metoy DFT pozwoliło przewidzieć położenie pasm pochodzących od drgań normalnych mostków Ti–O–Ti zarówno w rdzeniach $\{Ti_4O\}$ (**1**), jak i $\{Ti_6O_4\}$ (**2**). Przeprowadzone obliczenia sugerują, że drgania rozciągające mostów Ti–O–Ti mogą pojawiać się odpowiednio przy 740 i 795 cm^{-1} oraz 538 i 434 cm^{-1} w widmach IR i Ramana (**1**) i (**2**).

Analiza widm UV–Vis–DRS obu związków wykazała, że maksima absorpcji pojawiają się przy 306 nm (**1**) oraz przy 330 i 395 nm (**2**). Wynik ten jest jakościowo zgodny z obliczeniami DFT, gdzie λ_{max} wynoszą 283 nm dla (**1**) i 420 nm dla (**2**). Wyznaczone wartości przerwy HOMO–LUMO wynosiły 2,96 eV dla (**1**) i 2,39 eV dla (**2**). Teoretyczne wartości przerwy HOMO–LUMO są większe od eksperymentalnych (4,31 eV dla (**1**) i 3,21 eV dla (**2**)), ale zachowana jest tendencja wskazująca na to, że przerwa w przypadku (**2**) jest zdecydowanie mniejsza.

Zarejestrowanie dyfraktogramów XRD obu związków przed i po 72h kontaktu z wodą, potwierdziło, że struktury obu związków są stabilne, tj. nie ulegają procesom hydrolizy. Nie

wykryto żadnej istotnej transformacji w kierunku krystalicznego TiO_2, form amorficznych lub innych form krystalicznych związanych z przegrupowaniem sfer koordynacyjnych tytanu i zmianą topologii.

Obliczenia teoretyczne wykazały, że w obu związkach orbitale HOMO są zlokalizowane na fragmentach aromatycznych, z kolei orbitale LUMO są zdominowane przez *d*-orbitale atomów tytanu. Wygenerowanie map elektrostatycznego potencjału molekularnego (MEP) oraz obliczeń ładunków atomowych Hirshfelda pozwoliło na porównanie rozkładu ładunków w obu strukturach. Zgodnie z mapami MEP, w związku (**1**) ujemny potencjał rozciąga się na pierścienie fluorenu i sąsiadujących atomów, natomiast w przypadku związku (**2**) obszar ujemny obejmuje mostki zawierające tlen oraz nieskoordynowane grupy C=O (Rysunek 13). Z kolei, dodatni obszar obejmuje prawie całą cząsteczkę związku (**2**). Analiza ładunków atomowych pokazała, że najbardziej ujemny ładunek, w przypadku obu struktur, zlokalizowany jest na mostkowych atomach tlenu. Dodatkowo, w przypadku struktury (**2**), wartości te są wyższe niż na atomach tlenu z grup karbonylowych. Wyznaczone wskaźniki reaktywności wskazują, że kompleks (**2**) jest zdecydowanie bardziej reaktywny niż kompleks (**1**). Wartość powinowactwa elektronowego (A) wskazuje, że związek (**2**) chętniej akceptuje elektrony niż związek (**1**) (odpowiednio 2,19 eV i 0,76 eV). Potwierdza to również wyższa wartość indeksu elektrofilowości ω dla systemu (**2**) (2,20 eV w porównaniu do 1,21 eV dla systemu (**1**)), co lepiej opisuje jego właściwości elektrofilowe. Dodatkowo, niższa twardość chemiczna systemu (**2**) (4,85 eV) w porównaniu do systemu (**1**) (6,30 eV) sugeruje, że system (**2**) jest bardziej podatny na zmiany struktury elektronowej, co czyni go bardziej reaktywnym.



Rysunek 13. Mapy potencjału elektrostatycznego (od −0,02 (czerwony) do +0,02 (ciemnoniebieski)) układów (**1**) i (**2**) [P5].

Podsumowując, omawiana praca dostarczyła nowych informacji o syntezie TOCs, których rdzeń jest stabilizowany ligandami α-hydroksykarboksylanowymi. W strukturze obu związków powstają pierścienie chelatowe, które mogą mieć istotne znaczenie z punktu widzenia aktywności przeciwdrobnoustrojowej tych związków. W przypadku kompleksu (**2**), aktywność ta może być dodatkowo wspomagana przez nieskoordynowane grupy C=O, gdzie zwiększona gęstość elektronowa występuje na tlenach z grup karboksylowych. Sugerowana większa reaktywność okso – kompleksu (**2**) została potwierdzona obliczeniami DFT.

Dla otrzymanych związków (**1**) i (**2**) wykonałam również wstępne badania aktywności przeciwdrobnoustrojowej, które przedstawiłam w niniejszej rozprawie (Tabela 5). Badania te były prowadzone we współpracy z prof. Patrycją Golińską z Wydziału Nauk Biologicznych i Weterynaryjnych Uniwersytetu Mikołaja Kopernika w Toruniu. Szczegółowe badania są prowadzone także przez dr Oleksandrę Pryshchepę z zespołu dr hab. Pawła Pomastowskiego, prof. UMK w Interdyscyplinarnym Centrum Nowoczesnych Technologii UMK i po ich zakończeniu zostaną opublikowane.

Aktywność przeciwdrobnoustrojową związków (**1**) i (**2**) oraz kwasu 9-hydroksy-9-fluorenokarboksylowego oceniono na podstawie minimalnego stężenia hamującego (MIC) i minimalnego stężenia bakteriobójczego wobec bakterii Gram-dodatnich, Gram-ujemnych oraz grzybów. Szczepy *S. aureus* były bardziej wrażliwe na kwas 9-hydroksy-9-fluorenokarboksylowy (MIC = 0,125% i 0,5%, MBC = 0,5%) niż *E. coli* (MIC = MBC = 0,5%) i *C. albicans* (MIC = MBC = 1%). Kompleks (**1**) nie wykazywał żadnej aktywności w badanych stężeniach, natomiast wartości MIC (0.0625%) kompleksu (**2**) w stosunku do bakterii Gram-dodatnich były zdecydowanie niższe niż w badaniu kwasu 9-hydroksy-9-fluorenokarboksylowego. W przypadku bakterii Gram-ujemnych oraz drożdży *C. albicans* zaobserwowano jedynie efekt hamujący. Zauważyć można, że dodatek kwasu propionowego do syntezy związku (**2**) znacząco wpływał na polepszenie właściwości przeciwbakteryjnych. Przeprowadzenie obliczeń teoretycznych okazało się być bardzo pomocne w opisaniu mechanizmu działania przeciwdrobnoustrojowego badanych związków. Zgodnie z tymi obliczeniami, zmniejszenie przerwy HOMO-LUMO (4.31 eV dla (**1**) i 3.21 eV dla (**2**)) zwiększa reaktywność kompleksów. Związek (**2**), którego miękkość chemiczna (0.21 eV^{-1}) jest większa, posiada również większą aktywność mikrobiologiczną niż (**1**), co zostało potwierdzone badaniami eksperymentalnymi. Według teorii chelatacji Tweedy'ego, koordynacja powoduje zmniejszenie polarności jonów metalu i zwiększa rozpuszczalność kompleksu w lipidach. Rezultatem jest zakłócenie funkcji błony komórkowej. Zgodnie z MEP,

największa gęstość elektronowa zlokalizowana jest na pierścieniach chelatowych a dodatkowo, w przypadku związku (**2**) jest ona większa ze względu na obecność wolnych par elektronowych grup C=O. Duża gęstość elektronowa jest kluczowa z mikrobiologicznego punktu widzenia, ponieważ odpowiada za chelatowanie kationów obecnych w błonie zewnętrznej bakterii Gram-ujemnych, powodując jej destabilizację. Ściana komórkowa bakterii Gram-dodatnich posiada obfitą porowatą warstwę peptydoglikanu o średniej wielkości porów około 30 nm. Uważam, że przez te pory TOCs mogą dotrzeć do błony komórkowej i spowodować jej zniszczenie poprzez interakcję z lipidami błony komórkowej. Natomiast ściana komórkowa drożdży zawiera pory o średnicy około 5,8 nm a pod nią błonę lipidową. Najpopularniejszym mechanizmem działania przeciwgrzybiczego związków jest dotarcie do błony lipidowej i zaburzenie jej integralności poprzez zahamowanie syntezy ergosterolu. Uważam, że ten mechanizm będzie odpowiedni również dla związku (**2**), ponieważ jego średnica nie jest większa niż 3 nm.

Tabela 5. Aktywność przeciwdrobnoustrojowa TOCs (**1**) i (**2**); minimalne stężenie hamujące (MIC) i minimalne stężenie bakteriobójcze (MBC) w %.

		Mikroorganizmy				
Próbki		*E. coli* ATCC 25922	*E. coli* ATCC 8739	*S. aureus* ATCC 25923	*S. aureus* ATCC 6538	*C. albicans* ATCC 10231
Kwas	MIC	0.5%	0.5%	0.125%	0.5%	1.0%
9-hydroksy-9-fluoreno-karboksylowy	MBC	0.5%	0.5%	0.5%	0.5%	1.0%
(**1**)	MIC	none	none	none	none	none
	MBC	none	none	none	none	none
(**2**)	MIC	0.5%	1.0%	0.0625%	0.0625%	1.0%
	MBC	none	none	0.25%	0.5%	none

P6. *Analysis of Photocatalytic Properties of Poly(Methyl Methacrylate) Composites with Titanium(IV) and Ruthenium(III) Complexes*

B. Kubiak*, A. Topolski, A. Radtke*, T. Muzioł, O. Impert, A. Katafias, R. van Eldik, P. Piszczek, *Applied Sciences,* **2025**, *15,* 1679

Rozwój technologii stawia przed nami coraz większe wymagania dotyczące skutecznych metod oczyszczania wody i powietrza. Tradycyjne rozwiązania, takie jak adsorpcja czy filtracja, choć skuteczne, są jednocześnie bardzo energochłonne. Fotokataliza, zwłaszcza w zakresie światła widzialnego, oraz wykorzystanie fotokatalizatorów, takich jak ditlenek tytanu (TiO_2), oferują obiecującą alternatywę. Jednak TiO_2 efektywnie absorbuje jedynie promieniowanie UV, które stanowi niewielki procent światła słonecznego, co ogranicza jego szerokie zastosowanie. W artykule **P6** przedstawiono wyniki badań nad kompozytami zdolnymi do absorpcji światła widzialnego, co może znacząco zwiększyć skuteczność w usuwaniu zanieczyszczeń.

Przedmiotem badań były materiały kompozytowe na bazie poli(metakrylanu metylu) (PMMA) i kompleksów tytanu(IV), których rdzeń stabilizowany był ligandami α-hydrokarboksylanowymi (PMMA + (**1**) – (**3**)), a także kompleksów rutenu(III), zawierających ligandy EDTA lub pikolinianu (PMMA + (**4**), (**5**)). Syntezę i strukturę związków tytanu opisano w pracach **P4** i **P5**, natomiast kompleksów rutenu(III) w artykułach [126,127]. Zawartość związków w matrycy polimerowej wynosiła: 2, 5, 10 i 20% wag. Procedura wytwarzania kompozytów była podobna do opisanej w pracach **P1**, **P2** i **P4**.

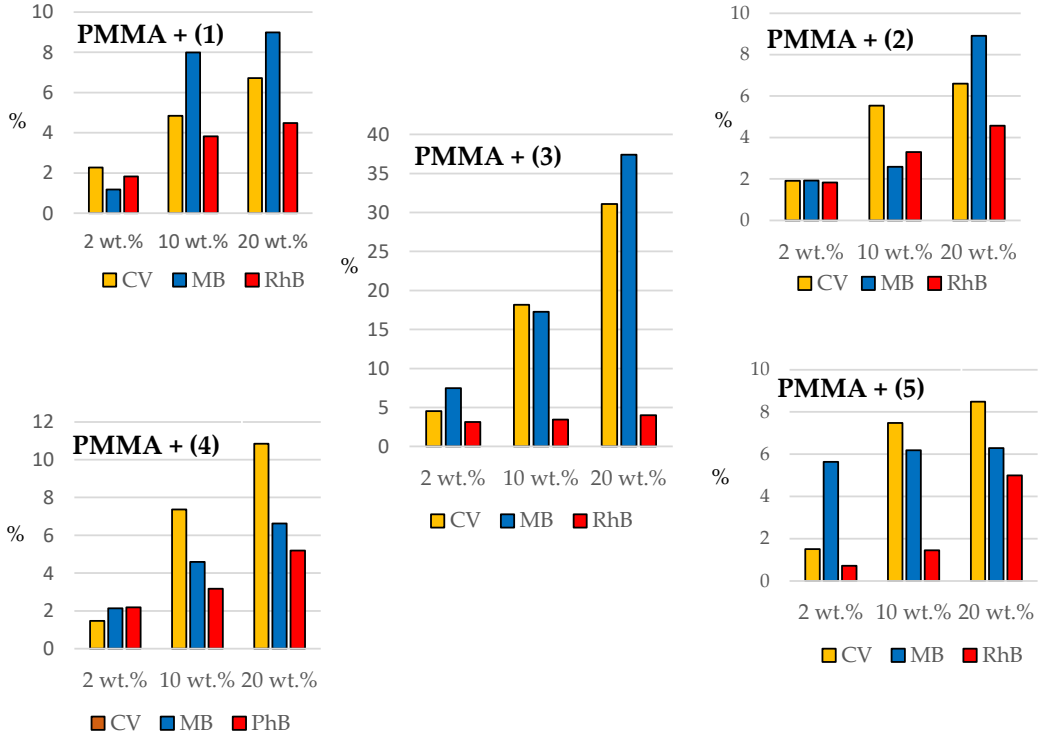
Zastosowanie metody UV–Vis–DRS pozwoliło wyznaczyć przerwy HOMO – LUMO związków (**1**) – (**5**). W przypadku TOCs przerwy HOMO-LUMO wynosiły odpowiednio 3,12 eV (**1**), 2,96 eV (**2**) i 2,39 eV (**3**). Z kolei dla kompleksów rutenu(III) wynosi odpowiednio 2,75 eV (**4**) i 2,78 eV (**5**). Wyznaczone na podstawie zarejestrowanych widm maksima absorpcji (λ_{max}) wynosiły odpowiednio 308 nm (**1**), 306 nm (**2**), 330 nm, 395 nm (**3**) oraz 334 nm zarówno dla (**4**), jak i (**5**). Parametr ten wyznaczono także dla kompozytów. Materiały zawierające związek (**1**) wykazują dwa maksima w zakresie UV, natomiast dodatek 20% wag. powoduje pojawienie się szerokiego pasma pomiędzy 200 a 450 nm. W widmach kompleksów (**2**) i (**3**) obserwowano przesunięcie krawędzi absorpcji do 480 i 500 nm. Wprowadzenie związków rutenu do matrycy polimerowej, sprawia, że krawędź absorpcji przesuwa się do 400 – 450 nm, w porównaniu do widma czystego PMMA, a w przypadku próbki PMMA + (5) 20% wag., nawet do 550 nm.

Analiza obrazów SEM pozwoliła ustalić rozmiar i sposób rozproszenia nano-mikroproszków związków (**1**) – (**5**) w matrycy PMMA. Obecność kompleksów po wprowadzeniu do polimeru, potwierdzono przy pomocy techniki SEM – EDX, która wykazała występowanie pików pochodzących od tytanu lub rutenu. Rejestracja map Ramana pozwoliła ustalić, że struktury kompleksów nie zmieniają się po wprowadzeniu do matrycy polimerowej.

Badanie struktury elektronowej związków tytanu, w tym ich krawędzi L, było prowadzone metodą XANES, przy użyciu dwóch trybów detekcji: TEY (penetracja próbki na głębokość kilkudziesięciu nm) i FY (penetracja próbki na głębokość kilkuset nm). Z zarejestrowanych widm wynika, że struktury klastrów tytanu są stabilne w matrycy polimerowej. Przesunięcia energetyczne po wprowadzeniu do PMMA wynosiły do 0.3 eV, to wskazuje, że matryca ma niewielki wpływ strukturę TOCs. W przypadku proszków, zaobserwowano dodatkowe cechy, które przypisano przejściom wzbronionym dipolowym, które zlokalizowane są w zakresie przedkrawędziowym (~456,4 i 457,3 eV). Przejścia te są typowe dla wielu związków Ti(IV), np. TiO_2, ale nie obserwuje się ich w widmach kompozytów, zarejestrowanych w trybie FY. Widma kompozytów z 20% dodatkiem TOCs posiadały bardzo dużo szumów i wymagały wygładzenia, jednak ich główne cechy, takie jak intensywniejsze pasma krawędzi L_2 oraz ich pozycje, pozostały widoczne. Rozszczepienie pola krystalicznego, czyli różnica między poziomami t_{2g} i e_g przy krawędziach L_3 i L_2, były prawie identyczne dla proszków i kompozytów, z wartościami między 2.3 eV a 3.1 eV. Oznacza to, że struktura elektronowa kompleksów tytanu nie uległa zmianie po przygotowaniu kompozytów. Co więcej, dane te zgadzają się z danymi ustalonymi metodą Kubelka-Munka i obliczeniami teoretycznymi, wynoszącymi odpowiednio 3,12, 2,96 i 2,39 eV dla (**1**), (**2**) i (**3**).

Zdolności adsorpcyjne otrzymanych kompozytów były badane w ciemności, wobec trzech barwników kationowych (błękit metylenowy (MB), rodamina B (RhB) i fiolet krystaliczny (CV)) (Tabela 6, Rysunek 14). W ten sposób sprawdzany był potencjał tych próbek do zastosowania w usuwaniu zanieczyszczeń organicznych z wody. Kompleksy okso-Ti(IV) wykazywały lepszą adsorpcję MB w porównaniu z innymi barwnikami, podczas gdy kompleksy Ru(III) skuteczniej adsorbowały CV. Oba typy kompleksów wykazywały niską adsorpcję RhB. Ilość zaadsorbowanego barwnika zależy od struktury barwnika i gęstości elektronowej adsorbentów. Cząsteczki MB i CV są mniejsze niż RhB, co pozwala większej liczbie z nich na interakcję z TOC lub kompleksami Ru. Obszary o dużej gęstości elektronów będą przyciągać cząsteczki barwnika, ponieważ azot jest na ogół skłonny do interakcji z bogatymi w elektrony grupami powierzchniowymi. Ilość zaadsorbowanego barwnika

wzrastała wraz ze wzrostem stężenia kompleksu. Kompozyt wzbogacony o kompleks (**3**) wykazywał najwyższą adsorpcję, podczas gdy adsorpcja barwnika przez kompozyty zawierające pozostałe kompleksy była stosunkowo podobna, pozostając poniżej 11% nawet przy 20% wag. zawartości kompleksu.

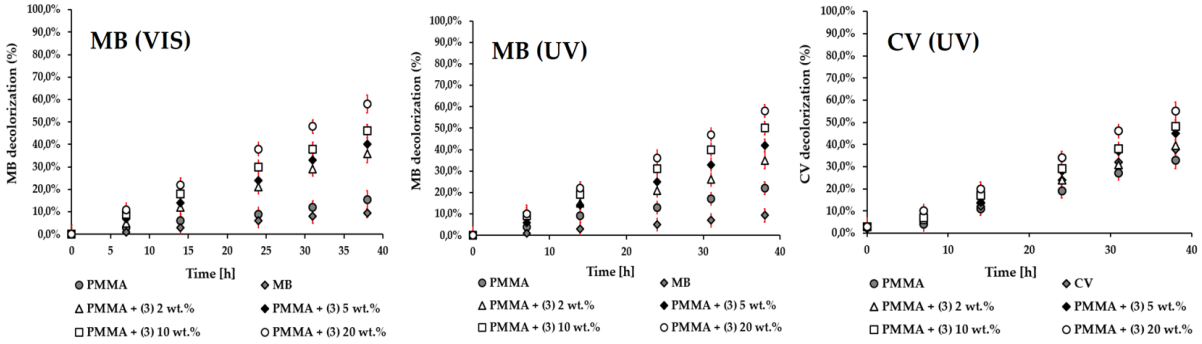


Rysunek 14. Procentowa redukcja stężenia barwników przez kompozyty PMMA z kompleksami (**1**) – (**5**).

Aktywność fotokatalityczną badanych kompozytów, zawierających 2, 5, 10 oraz 20 wt.% kompleksów (**1**)–(**5**), oceniano poprzez analizę dekoloryzacji próbek roztworu MB lub CV poddanych naświetlaniu światłem UV i/lub widzialnym (Vis). Przed przeprowadzeniem eksperymentów fotokatalitycznych próbki zostały umieszczone w roztworze barwnika, aby umożliwić nasycenie miejsc aktywnych. Krok ten zapewnił osiągnięcie równowagi adsorpcji przed napromieniowaniem, minimalizując wpływ początkowych efektów adsorpcji na pomiary fotokatalityczne. W rezultacie aktywność fotokatalityczna odzwierciedla przede wszystkim proces degradacji, a nie zwykłą adsorpcję. Takie podejście pozwoliło nam lepiej ocenić skuteczność testowanych kompozytów w generowaniu reaktywnych form odpowiedzialnych za fotokatalizę. Proces rozkładu MB pod wpływem światła monitoruje się spektrofotometrycznie, ponieważ niebieski, utleniony MB reaguje z reaktywnymi formami tlenu, głównie z $^{\bullet}OH$ generowanymi na powierzchni fotokatalizatora, tworząc bezbarwne

produkty pośrednie. Dekoloryzacja wynika z pęknięcia centralnego pierścienia aromatycznego, a dalszy rozkład prowadzi do powstania CO_2, H_2O i innych jonów nieorganicznych. Fotodegradacja CV przebiega analogicznie. Wolny elektron powstały podczas naświetlania reaguje z cząsteczkami wody na powierzchni kompozytu, generując różne reaktywne formy tlenu (RFT). Kluczową rolę odgrywa tutaj rodnik hydroksylowy, który fragmentuje cząsteczkę CV do bezbarwnych produktów, prowadząc ostatecznie do powstania prostych związków nieorganicznych. Pierwszymi etapami rozkładu CV są procesy N-demetylacji i degradacji oksydacyjnej.

Do identyfikacji RFT generowanych na powierzchni badanych materiałów użyto spektroskopii EPR, co pomogło zrozumieć ich mechanizm fotokatalityczny. Wyniki wskazują, że najbardziej efektywnym materiałem jest kompozyt PMMA + (**2**) – jego widmo EPR wykazuje najsilniejsze sygnały oraz najmniejszy poziom zakłóceń, co sugeruje wydajny transfer ładunku. Kompozyty zawierające kompleksy tytanu charakteryzują się występowaniem sygnałów odpowiadających anionom O^-, O_2^- oraz kationowi Ti^{3+}, których obecność jest kluczowa dla procesu fotokatalitycznego. Natomiast w kompleksach Ru(III) ujawniono jedynie sygnały Ru(III), co sugeruje, że fotokataliza odbywa się przez redukcję Ru(III) do diamagnetycznego Ru(II) i bezpośredni transfer elektronów. Wyniki potwierdzają, że kompozyty na bazie tytanu działają głównie poprzez generowanie RFT, podczas gdy materiały rutenowe wykorzystują mechanizmy bezpośredniego transferu elektronów. Analiza otrzymanych wyników wykazała, że najlepsze rezultaty osiągnięto w przypadku redukcji MB przez próbki kompozytów PMMA + (**2**), pod wpływem promieniowania UV. W zależności od stężenia kompleksu, udało się zredukować stężenie barwnika na poziomie 45.3% do 73.1%, natomiast dla czystego PMMA, jedynie 17.4%. W przypadku roztworu CV, próbki PMMA + (**2**) osiągnęły odbarwienie na poziomie od 51.1% do 70.9% (Tabela 6). Związki (**1**) i (**2**) wykazują mniejszą aktywność pod wpływem promieniowania widzialnego, natomiast związek (**3**) osiąga wówczas wydajność zbliżoną do tej uzyskanej pod wpływem promieniowania UV (Rysunek 15).



Rysunek 15. Zmiany procentowego odbarwienia barwnika w funkcji czasu – dla MB (VIS i UV) i CV (UV) uzyskane przy zastosowaniu kompozytu PMMA + (**3**).

Próbki zawierające kompleksy rutenu(III) (**4**) i (**5**), są bardziej fotokatalitycznie aktywne w świetle widzialnym, jednak 2% wag. dodatek nie jest wystarczający do redukcji stężenia CV (Tabela 6). Zwiększenie stężenia kompleksu w matrycy polimerowej, skutkuje zwiększeniem wydajności fotokatalitycznej. Testowane kompozyty można sklasyfikować według ich profilu aktywności w następujący sposób: (i) kompozyty aktywne głównie w zakresie UV, wzbogacone o kompleksy (**1**) i (**2**); (ii) kompozyty aktywne w świetle widzialnym, zawierające kompleksy (**4**) i (**5**); oraz (iii) kompozyt wykazujący aktywność zarówno w zakresie UV, jak i widzialnym, zawierający kompleks (**3**).

Tabela 6. Tabela porównująca właściwości kompozytów PMMA z kompleksami Ti(IV) i Ru(III) (przedstawione dane odnoszą się do kompozytów zawierających 2% wag. i 20% wag. badanych kompleksów).

Kompozyt	**Maksymalna adsorpcja barwnika (%)**	**Aktywność fotokatalityczna (MB, UV/Vis) (%)**	**Intensywność sygnału EPR**	**Aktywacja światłem**
PMMA + (**1**)	2.27 – 8.99 % (MB)	38-69% (UV), 27-55% (Vis)	Umiarkowany (O_2^-, O^-, Ti^{3+})	UV
PMMA + (**2**)	1.92 – 8.91 % (MB)	45-73% (UV), 34-64% (Vis)	Silny (O_2^-, O^-, Ti^{3+})	UV
PMMA + (**3**)	7.48 – 37.40 % (MB)	35-58% (UV), 36-59% (Vis)	Umiarkowany (O^-, O_2^-, Ti^{3+})	UV + Vis
PMMA + (**4**)	1.47 – 10.84 % (CV)	19-33% (UV), 18-45% (Vis)	Słaby (Ru^{3+})	Vis
PMMA + (**5**)	1.51 – 8.48 % (CV)	17-32% (UV), 16-41% (Vis)	Słaby (Ru^{3+})	Vis

Przeprowadzone badania, których wyniki przedstawiono w pracy **P6**, przyczyniają się do uporządkowania wiedzy na temat właściwości adsorpcyjnych i aktywności fotokatalitycznej kompozytów, w których jako napełniaczy zastosowano kompleksy okso-Ti(IV) stabilizowane

ligandami α-hydroksykarboksylanowymi ((**1**)–(**3**)) oraz kompleksy Ru(III) ((**4**) i (**5**)). Badania spektroskopowe potwierdziły, że utworzenie powyższych materiałów nie powoduje zmian w strukturach badanych związków. Kompozyty na bazie Ti(IV) wykazały lepszą aktywność fotokatalityczną ze względu na zdolność Ti(IV) do generowania reaktywnych form tlenu (RFT), które są niezbędne do wydajnej fotokatalizy. Natomiast kompleksy na bazie Ru(III) opierają swoje działanie na cyklu redoks pomiędzy Ru(III) i Ru(II), co w moim przypadku skutkowało ich niższą aktywnością fotokatalityczną.

Rodzaj liganda stabilizującego ma kluczowe znaczenie dla zdolności absorpcji światła i aktywności fotokatalitycznej. Ligandy takie jak migdałowy lub 9-hydroksy-9-fluorenokarboksylowy poszerzają przerwę energetyczną HOMO–LUMO i wzmacniają aktywność w świetle UV. Natomiast ligandy 9-hydroksy-9-fluorenokarboksylowy i propionowy, EDTA czy pikolinianowy zmniejszają tę przerwę i rozszerzają zakres aktywności na światło widzialne.

W podsumowaniu autorzy sugerują, że wytworzone materiały kompozytowe mogą w przyszłości zostać zastosowane, jako powłoki samoczyszczące np. na klawiatury lub ekrany dotykowe udostępniane w przestrzeni publicznej.

5. Podsumowanie

W ramach zrealizowanej pracy doktorskiej zsyntezowano nowe kompleksy okso-tytanu(IV) stabilizowane ligandami karboksylanowymi. Kompleksy te wykazują aktywność fotokatalityczną oraz przeciwdrobnoustrojową. Przeprowadzone eksperymenty umożliwiły dokładniejsze zrozumienie ich właściwości, zwłaszcza w przypadku zastosowania α-hydroksykarboksylanów jako ligandów stabilizujących. Dodatkowo zbadano fotokatalityczne właściwości kompleksów rutenu(III), które dotychczas nie były szczegółowo analizowane.

Badania koncentrowały się na syntezie nowych kompleksów okso-tytanu(IV), powstających w reakcjach alkoholanów tytanu(IV) z kwasami karboksylowymi (**P1**–**P3**) oraz α-hydroksy-karboksylowymi (**P4**, **P5**). Stosując ligandy karboksylanowe jako stabilizatory rdzenia $\{Ti_aO_b\}$, wyizolowano kryształy kompleksów o strukturach $\{Ti_3O\}$, $\{Ti_4O_2\}$, $\{Ti_6O_4\}$ i $\{Ti_6O_6\}$. Chociaż podobne struktury rdzeni zostały już wcześniej opisywane, celem moich badań było uzyskanie kompleksów stabilizowanych ligandami 4-hydroksy-benzoesanu i 9-fluorenokarboksylanu, które dotychczas nie zostały otrzymane ani scharakteryzowane. Zastosowanie kwasów α-hydroksykarboksylowych w syntezie pozwoliło uzyskać związki krystaliczne o nowych strukturach rdzeni $\{Ti_aO_b\}$. Dzięki obecności grupy hydroksylowej i karboksylowej ligandy te mogły tworzyć dodatkowe wiązania z centralnymi jonami tytanu, zwiększając stabilność struktur. W kompleksach opisanych w pracach **P4** i **P5** zaobserwowano tworzenie pierścieni chelatowych. W przypadku kompleksu $[Ti_6O_4(O^iPr)_2(O_3C_{14}H_8)_4(O_2CEt)_6]$ jedna z grup karbonylowych (C=O) w każdym ligandzie α-hydroksykarboksylanowym pozostaje nieskoordynowana, co może wpływać na właściwości tego układu. Widma XRD wykazały, że struktury tych związków były stabilne po 72 godzinach kontaktu z wodą, co świadczy o ich odporności na hydrolizę.

Synteza kompleksów rutenu(III) obejmowała związki o już scharakteryzowanych strukturach, takie jak $K[Ru^{III}(Hedta)Cl]\cdot{}_2H_2O$ i $[Ru(pic)_3]\cdot H_2O$. W tym przypadku głównym celem była ocena ich właściwości fizykochemicznych oraz aktywności katalitycznej indukowanej światłem.

Prace nad syntezą kompleksów tytanu(IV) i rutenu(III) zostały rozszerzone o ich zastosowanie w wytwarzaniu materiałów kompozytowych (**P1**–**P4**, **P6**). Kompozyty te były tworzone poprzez wprowadzenie kompleksów do matrycy polimerowej, takiej jak polimetakrylan metylu (PMMA) lub poli(ε-kaprolakton) (PCL). Kluczowym etapem było

sprawdzenie, czy metody wytwarzania kompozytów, takie jak zastosowanie łaźni ultradźwiękowej, wytłaczarki dwuślimakowej czy miniwtryskarki pneumatycznej, nie wpływały na strukturę kompleksów. Badania z wykorzystaniem mikroskopu Ramana i metody XANES potwierdziły, że struktura kompleksów (TOCs) pozostawała nienaruszona w trakcie procesów technologicznych.

Tworzenie kompozytów miało istotne znaczenie aplikacyjne, ponieważ celem było zbadanie możliwości wytwarzania materiałów, które mogłyby służyć jako powłoki o właściwościach fotokatalitycznych i przeciwdrobnoustrojowych. Mogłyby one znaleźć zastosowanie jako samoczyszczące warstwy na powierzchniach, takich jak ekrany dotykowe czy klawiatury używane w miejscach publicznych. Dodatkowo wprowadzenie kompleksów Ti(IV) i Ru(III) do matrycy polimerowej zapewniało ich ochronę przed działaniem czynników zewnętrznych takich jak woda, zapobiegając procesom hydrolizy czy rozpuszczania. Ochrona ta okazała się szczególnie istotna w przypadku wrażliwych kompleksów rutenu(III).

W kolejnym etapie moich badań skupiłam się na określeniu aktywności fotokatalitycznej kompozytów zawierających kompleksy okso-Ti(IV) (**P1**–**P3** i **P6**) oraz Ru(III) (**P6**). W artykule **P1** udowodniłam, że zarówno funkcjonalizacja liganda karboksylowego, jak i struktura rdzenia kompleksu wpływają na szybkość degradacji barwnika. Zwróciłam szczególną uwagę na rolę rdzenia kompleksu, ponieważ układy zawierające klastry o rdzeniu $\{Ti_4O_2\}$ wykazywały większą efektywność fotokatalityczną niż te o rdzeniu $\{Ti_3O\}$. W pracy **P2** przeanalizowałam dokładniej wpływ rdzenia okso-kompleksu na aktywność fotokatalityczną TOCs. Okazało się, że zarówno w świetle UV, jak i widzialnym, najlepszą efektywność wykazywał kompozyt zawierający związek o rdzeniu $\{Ti_6O_6\}$. Wynika to z jego gęstej struktury oraz zdolności do generowania reaktywnych form tlenu.

W artykule **P3** potwierdzono, jak istotne jest generowanie RFT w kontekście aktywności fotokatalitycznej. Próbki, na powierzchni których wykryto aniony O^- i O^{2-}, wykazywały wyższą aktywność fotokatalityczną niż te, w których obecny był tylko anion O^-. W tej pracy udowodniłam również, że kompleksy okso-Ti(IV) wprowadzone do matrycy z poli(ε-kaprolaktonu) (PCL) wykazują aktywność fotokatalityczną na poziomie porównywalnym z kompozytami bazującymi na polimetakrylanie metylu (PMMA).

Wprowadzenie do struktury TOCs ligandów α-hydroksykarboksylanowych (**P6**) nie wpłynęło na poprawę ich aktywności fotokatalitycznej w zakresie światła widzialnego, a większa liczba ligandów alkoholanowych sprzyjała aktywności w świetle UV. Dopiero ich częściowe zastąpienie ligandami propionianowymi ($[Ti_6O_4(O^iPr)_2(O_3C_{14}H_8)_4\ (O_2CEt)_6]$) spowodowało przesunięcie maksimum absorpcji w stronę światła widzialnego, co pozwoliło uzyskać niemal

równą aktywność zarówno w UV, jak i w świetle widzialnym. W pracy **P6** udowodniono, że oba zsyntetyzowane kompleksy rutenu(III) wykazują aktywność fotokatalityczną w zakresie światła widzialnego. Jednak porównanie ich aktywności z kompleksami okso-Ti(IV) wykazuje, że lepszymi fotokatalizatorami są te ostatnie. Prawdopodobnie wynika to z faktu, że kompleksy na bazie Ru(III), w odróżnieniu od kompleksów Ti(IV), opierają się na cyklu redoks pomiędzy Ru(III) i Ru(II), a nie na generowaniu RFT, co skutkuje niższą aktywnością fotokatalityczną.

Ważnym kierunkiem moich badań było określenie aktywności przeciwdrobnoustrojowej TOCs. Z prac **P1** – **P4** wynika, że bakterie Gram – dodatnie są najbardziej wrażliwe na działanie kompozytów zawierających TOCs a grzyby *C.albicans* są najbardziej oporne. Przyczyn można doszukiwać się w różnicach w budowie ściany komórkowej między bakteriami a grzybami. Ściana *C. albicans* jest najbardziej sztywna i stanowi największą barierę dla RFT, które są podstawą działania kompozytów zawierających TOCs. W pracy **P2** najlepsze rezultaty uzyskały próbki, które zawierają kompleksy o rdzeniach $\{Ti_6O_4\}$ lub $\{Ti_4O_2\}$ stabilizowane ligandami 9-fluorenokarboksylanowymi. Wynika to z rodzaju i ilości RFT generowanych na powierzchni próbek, w porównaniu z pozostałymi materiałami. W artykule **P3** określono także wpływ liganda na aktywność przeciwdrobnoustrojową TOCs o rdzeniu $\{Ti_4O_2\}$. Lepsze rezultaty uzyskano, gdy rdzeń był stabilizowany ligandami 9-fluorenokarboksylanowymi, w porównaniu do ligandów 4-aminobenzoesanowymi. Dotychczasowe badania mechanizmu działania przeciwdrobnoustrojowego kompleksów, w których rdzeń stabilizowany jest ligandami α-hydroksykarboksylanowymi, wskazują, że kluczowe dla tej aktywności są dwa czynniki: (i) właściwości fotokatalityczne okso – kompleksu, w tym jego zdolność do generowania reaktywnych form tlenu, oraz (ii) czynniki strukturalne, szczególnie obecność pierścieni chelatowych, które mogą wpływać na stabilność i bioaktywność tych związków (**P4**, **P5**). Zwiększona aktywność związku $[Ti_6O_4(O^iPr)_2(O_3C_{14}H_8)_4(O_2CEt)_6]$ została potwierdzona obliczeniami DFT i wynika z obecności obszarów bardziej elektroujemnych niż w przypadku struktury zawierającej rdzenie $\{Ti_4O\}$ i stabilizowanej wyłącznie ligandami 9-hydroksy-9-fluorenokarboksylowymi.

Wyniki badań poszerzają wiedzę o zastosowaniu kompleksów tytanu(IV) i rutenu(III) jako fotokatalizatorów. ze szczególnym uwzględnieniem aktywności przeciwdrobnoustrojowej okso-tytanu(IV). Skupiono się na aktywności przeciwdrobnoustrojowej kompleksów okso-tytanu(IV), analizując wpływ liganda stabilizującego i struktury rdzenia $\{Ti_aO_b\}$. Otrzymane wyniki wskazują na potencjał kompozytów z nano- i mikroproszkami TOCs do tworzenia samoczyszczących powierzchni. W dalszych badaniach należy zwrócić większą uwagę na

fotokatalityczną aktywność kompleksów rutenu(III) w zakresie światła widzialnego, co może mieć znaczenie dla dalszego wykorzystania związków tego metalu.

6. Literatura

1. Yan, X.; Feng, J.; Li, P.; Li, J.; Ren, B.; Gao, S.; Cao, R. Fast and Efficient Removal of Mercury Ions Using Zirconium-Based Metal–Organic Framework Filter Membranes. *Inorganic Chemistry Communications* **2021**, *131*, 108796, doi:10.1016/j.inoche.2021.108796.
2. Al-Tohamy, R.; Ali, S.S.; Li, F.; Okasha, K.M.; Mahmoud, Y.A.-G.; Elsamahy, T.; Jiao, H.; Fu, Y.; Sun, J. A Critical Review on the Treatment of Dye-Containing Wastewater: Ecotoxicological and Health Concerns of Textile Dyes and Possible Remediation Approaches for Environmental Safety. *Ecotoxicology and Environmental Safety* **2022**, *231*, 113160, doi:10.1016/j.ecoenv.2021.113160.
3. Olisah, C.; Adams, J.B.; Rubidge, G. The State of Persistent Organic Pollutants in South African Estuaries: A Review of Environmental Exposure and Sources. *Ecotoxicology and Environmental Safety* **2021**, *219*, 112316, doi:10.1016/j.ecoenv.2021.112316.
4. Larsson, D.G.J.; Flach, C.-F. Antibiotic Resistance in the Environment. *Nat Rev Microbiol* **2022**, *20*, 257–269, doi:10.1038/s41579-021-00649-x.
5. Urban-Chmiel, R.; Marek, A.; Stępień-Pyśniak, D.; Wieczorek, K.; Dec, M.; Nowaczek, A.; Osek, J. Antibiotic Resistance in Bacteria—A Review. *Antibiotics* **2022**, *11*, 1079, doi:10.3390/antibiotics11081079.
6. Chinemerem Nwobodo, D.; Ugwu, M.C.; Oliseloke Anie, C.; Al-Ouqaili, M.T.S.; Chinedu Ikem, J.; Victor Chigozie, U.; Saki, M. Antibiotic Resistance: The Challenges and Some Emerging Strategies for Tackling a Global Menace. *Clinical Laboratory Analysis* **2022**, *36*, e24655, doi:10.1002/jcla.24655.
7. He, X.; Yang, D.-P.; Zhang, X.; Liu, M.; Kang, Z.; Lin, C.; Jia, N.; Luque, R. Waste Eggshell Membrane-Templated CuO-ZnO Nanocomposites with Enhanced Adsorption, Catalysis and Antibacterial Properties for Water Purification. *Chemical Engineering Journal* **2019**, *369*, 621–633, doi:10.1016/j.cej.2019.03.047.
8. Xiao, M.; Wang, Z.; Lyu, M.; Luo, B.; Wang, S.; Liu, G.; Cheng, H.; Wang, L. Hollow Nanostructures for Photocatalysis: Advantages and Challenges. *Advanced Materials* **2019**, *31*, 1801369, doi:10.1002/adma.201801369.
9. Saravanan, R.; Gracia, F.; Stephen, A. Basic Principles, Mechanism, and Challenges of Photocatalysis. In *Nanocomposites for Visible Light-induced Photocatalysis*; Khan, M.M., Pradhan, D., Sohn, Y., Eds.; Springer Series on Polymer and Composite Materials; Springer International Publishing: Cham, 2017; pp. 19–40 ISBN 978-3-319-62445-7.
10. Wu, J.; Zheng, W.; Chen, Y. Definition of Photocatalysis: Current Understanding and Perspectives. *Current Opinion in Green and Sustainable Chemistry* **2022**, *33*, 100580, doi:10.1016/j.cogsc.2021.100580.
11. Zhao, J.; Yang, X. Photocatalytic Oxidation for Indoor Air Purification: A Literature Review. *Building and Environment* **2003**, *38*, 645–654, doi:10.1016/S0360-1323(02)00212-3.
12. Byrne, C.; Subramanian, G.; Pillai, S.C. Recent Advances in Photocatalysis for Environmental Applications. *Journal of Environmental Chemical Engineering* **2018**, *6*, 3531–3555, doi:10.1016/j.jece.2017.07.080.
13. Chen, J.; Poon, C. Photocatalytic Construction and Building Materials: From Fundamentals to Applications. *Building and Environment* **2009**, *44*, 1899–1906, doi:10.1016/j.buildenv.2009.01.002.
14. Do, H.H.; Nguyen, D.L.T.; Nguyen, X.C.; Le, T.-H.; Nguyen, T.P.; Trinh, Q.T.; Ahn, S.H.; Vo, D.-V.N.; Kim, S.Y.; Le, Q.V. Recent Progress in TiO2-Based Photocatalysts for Hydrogen Evolution Reaction: A Review. *Arabian Journal of Chemistry* **2020**, *13*, 3653–3671, doi:10.1016/j.arabjc.2019.12.012.
15. Nasiri Sovari, S.; Zobi, F. Recent Studies on the Antimicrobial Activity of Transition Metal Complexes of Groups 6–12. *Chemistry* **2020**, *2*, 418–452, doi:10.3390/chemistry2020026.
16. Grätzel, M. Photoelectrochemical Cells. *Nature* **2001**, *414*, 338–344, doi:10.1038/35104607.
17. Haider, A.J.; Al– Anbari, R.H.; Kadhim, G.R.; Salame, C.T. Exploring Potential Environmental Applications of TiO2 Nanoparticles. *Energy Procedia* **2017**, *119*, 332–345, doi:10.1016/j.egypro.2017.07.117.

18. Linsebigler, A.L.; Lu, G.; Yates, J.T. Photocatalysis on TiO2 Surfaces: Principles, Mechanisms, and Selected Results. *Chem. Rev.* **1995**, *95*, 735–758, doi:10.1021/cr00035a013.
19. Haider, A.J.; Jameel, Z.N.; Al-Hussaini, I.H.M. Review on: Titanium Dioxide Applications. *Energy Procedia* **2019**, *157*, 17–29, doi:10.1016/j.egypro.2018.11.159.
20. Sujatha, G.; Shanthakumar, S.; Chiampo, F. UV Light-Irradiated Photocatalytic Degradation of Coffee Processing Wastewater Using TiO2 as a Catalyst. *Environments* **2020**, *7*, 47, doi:10.3390/environments7060047.
21. Ballari, M.M.; Brouwers, H.J.H. Full Scale Demonstration of Air-Purifying Pavement. *Journal of Hazardous Materials* **2013**, *254–255*, 406–414, doi:10.1016/j.jhazmat.2013.02.012.
22. Fujishima, A.; Rao, T.N.; Tryk, D.A. Titanium Dioxide Photocatalysis. *Journal of Photochemistry and Photobiology C: Photochemistry Reviews* **2000**, *1*, 1–21, doi:10.1016/S1389-5567(00)00002-2.
23. Armaković, S.J.; Savanović, M.M.; Armaković, S. Titanium Dioxide as the Most Used Photocatalyst for Water Purification: An Overview. *Catalysts* **2022**, *13*, 26, doi:10.3390/catal13010026.
24. Radtke, A.; Piszczek, P.; Muzioł, T.; Wojtczak, A. The Structural Conversion of Multinuclear Titanium(IV) μ-Oxo-Complexes. *Inorg. Chem.* **2014**, *53*, 10803–10810, doi:10.1021/ic5002545.
25. Czakler, M.; Artner, C.; Schubert, U. Influence of the Phosphonate Ligand on the Structure of Phosphonate-Substituted Titanium Oxo Clusters. *Eur. J. Inorg. Chem.* **2013**, *2013*, 5790–5796, doi:10.1002/ejic.201300859.
26. Schubert, U. Titanium-Oxo Clusters with Bi- and Tridentate Organic Ligands: Gradual Evolution of the Structures from Small to Big. *Chem. Eur. J.* **2021**, *27*, 11239–11256, doi:10.1002/chem.202101287.
27. Schubert, U. Chemical Modification of Titanium Alkoxides for Sol–Gel Processing. *J. Mater. Chem.* **2005**, *15*, 3701, doi:10.1039/b504269k.
28. Moraru, B.; Hüsing, N.; Kickelbick, G.; Schubert, U.; Fratzl, P.; Peterlik, H. Inorganic−Organic Hybrid Polymers by Polymerization of Methacrylate- or Acrylate-Substituted Oxotitanium Clusters with Methyl Methacrylate or Methacrylic Acid. *Chem. Mater.* **2002**, *14*, 2732–2740, doi:10.1021/cm021113f.
29. Hwu, J.R.; Hsu, C.-Y.; Jain, M.L. Efficient Photolytic Esterification of Carboxylic Acids with Alcohols in Perhalogenated Methane. *Tetrahedron Letters* **2004**, *45*, 5151–5154, doi:10.1016/j.tetlet.2004.04.155.
30. Newman, M.S. Some Observations Concerning Steric Factors. *J. Am. Chem. Soc.* **1950**, *72*, 4783–4786, doi:10.1021/ja01166a123.
31. Rozes, L.; Sanchez, C. Titanium Oxo-Clusters: Precursors for a Lego-like Construction of Nanostructured Hybrid Materials. *Chem. Soc. Rev.* **2011**, *40*, 1006, doi:10.1039/c0cs00137f.
32. Czakler, M.; Artner, C.; Schubert, U. Titanium Oxo/Alkoxo Clusters with Both Phosphonate and Methacrylate Ligands. *Monatshefte für Chemie - Chemical Monthly* **2015**, *146*, 1249–1256, doi:10.1007/s00706-015-1444-5.
33. Boyle, T.J.; Alam, T.M.; Tafoya, C.J.; Scott, B.L. Formic Acid Modified $Ti(OCHMe_2)_4$. Syntheses, Characterization, and X-Ray Structures of $Ti_4(\mu_4\text{-}O)(\mu\text{-}O)(OFc)_2(\mu\text{-}OR)_4(OR)_6$ and $Ti_6(\mu_3\text{-}O)_6(OFc)_6(OR)_6$ (OFc = O_2CH; OR = $OCHMe_2$). *Inorg. Chem.* **1998**, *37*, 5588–5594, doi:10.1021/ic980601f.
34. Senouci, A.; Yaakoub, M.; Huguenard, C.; Henry, M. Molecular Templating Using Titanium(Iv)(Oxo)Alkoxides and Titanium(Iv)(Oxo)Aryloxides. *J. Mater. Chem.* **2004**, *14*, 3215, doi:10.1039/b406696k.
35. Janek, M.; Muzioł, T.M.; Piszczek, P. Trinuclear Oxo-Titanium Clusters: Synthesis, Structure, and Photocatalytic Activity. *Materials* **2019**, *12*, 3195, doi:10.3390/ma12193195.
36. Hou, J.-L.; Weng, Y.-G.; Liu, P.-Y.; Cui, L.-N.; Zhu, Q.-Y.; Dai, J. Effects of the Ligand Structures on the Photoelectric Activities, a Model Study Based on Titanium–Oxo Clusters Anchored with S-Heterocyclic Ligands. *Inorg. Chem.* **2019**, *58*, 2736–2743, doi:10.1021/acs.inorgchem.8b03310.
37. Boyle, T.J.; Tyner, R.P.; Alam, T.M.; Scott, B.L.; Ziller, J.W.; Potter, B.G. Implications for the Thin-Film Densification of TiO_2 from Carboxylic Acid-Modified Titanium Alkoxides.

Syntheses, Characterizations, X-Ray Structures of $Ti_3(\mu_3\text{-}O)(O_2CH)_2(ONep)_8$, $Ti_3(\mu_3\text{-}O)(O_2CMe)_2(ONep)_8$, $Ti_6(\mu_3\text{-}O)_6(O_2CCHMe_2)_6(ONep)_6$, $[Ti(\mu\text{-}O_2CCMe_3)(ONep)_3]_2$, and $Ti_3(\mu_3\text{-}O)(O_2CCH_2CMe_3)_2(ONep)_8$ (ONep = OCH_2CMe_3)[1]. *J. Am. Chem. Soc.* **1999**, *121*, 12104–12112, doi:10.1021/ja992521w.

38. Mijatovic, I.; Kickelbick, G.; Puchberger, M.; Schubert, U. Preservation of the Cluster Core upon Formation of Ti3O(OPri)8(Benzoate)2 from Ti3O(OR)10. *New J. Chem.* **2003**, *27*, 3–5, doi:10.1039/b208255a.
39. Zou, D.-H.; Cui, L.-N.; Liu, P.-Y.; Yang, S.; Zhu, Q.-Y.; Dai, J. Molecular Model of Dye Sensitized Titanium Oxides Based on Aryl-Amine Dye Anchored Titanium Oxo Clusters. *Inorg. Chem.* **2019**, *58*, 9246–9252, doi:10.1021/acs.inorgchem.9b00945.
40. Bailey, A.; Shang, M.; Fehlner, T.P. Synthesis and Characterization of a Novel Asymmetric Ferrocene Alkoxycarboxylate of Titanium, $Ti_4O_2(O^iPr)_6\{(\eta^5\text{-}O_2CC_5H_4)Fe(\eta^5\text{-}C_5H_5)\}_6$. *Inorg. Chem.* **2000**, *39*, 4374–4376, doi:10.1021/ic000790d.
41. Cui, Y.; Zou, G.-D.; Li, H.-M.; Fan, Y. Syntheses, Structures and Photoelectrochemical Properties of Phosphite-Stabilized Titanium-Oxo Clusters Containing 2,2′-Biphenolato Ligands. *Inorganic Chemistry Communications* **2018**, *97*, 176–179, doi:10.1016/j.inoche.2018.09.034.
42. Janek, M.; Radtke, A.; Muzioł, T.; Jerzykiewicz, M.; Piszczek, P. Tetranuclear Oxo-Titanium Clusters with Different Carboxylate Aromatic Ligands: Optical Properties, DFT Calculations, and Photoactivity. *Materials* **2018**, *11*, 1661, doi:10.3390/ma11091661.
43. Benedict, J.B.; Coppens, P. The Crystalline Nanocluster Phase as a Medium for Structural and Spectroscopic Studies of Light Absorption of Photosensitizer Dyes on Semiconductor Surfaces. *J. Am. Chem. Soc.* **2010**, *132*, 2938–2944, doi:10.1021/ja909600w.
44. Gao, M.; Zhang, L.; Zhang, J. Acid-Controlled Synthesis of Carboxylate-Stabilized Ti_{44} -Oxo Clusters: Scaling up Preparation, Exchangeable Protecting Ligands, and Photophysical Properties. *Chemistry A European J* **2019**, *25*, 10450–10455, doi:10.1002/chem.201901671.
45. Janek, M.; Muzioł, T.M.; Piszczek, P. The Structure and Photocatalytic Activity of the Tetranuclear Titanium(IV) Oxo-Complex with 4-Aminobenzoate Ligands. *Polyhedron* **2018**, *141*, 110–117, doi:10.1016/j.poly.2017.11.028.
46. Radtke, A.; Piszczek, P.; Muzioł, T.; Wojtczak, A. The Structural Conversion of Multinuclear Titanium(IV) μ-Oxo-Complexes. *Inorg. Chem.* **2014**, *53*, 10803–10810, doi:10.1021/ic5002545.
47. Lei, X.; Shang, M.; Fehlner, T.P. Clusters as Ligands. 5. Tricobalt Cluster Alkoxycarboxylates of Titanium and Zirconium Exhibiting Novel Structures and Properties. *Organometallics* **1997**, *16*, 5289–5301, doi:10.1021/om970837b.
48. Guerrero, G.; Mehring, M.; Mutin, P.H.; Dahan, F.; Vioux, A. Syntheses and Single-Crystal Structures of Novel Soluble Phosphonato- and Phosphinato-Bridged Titanium Oxo Alkoxides. *J. Chem. Soc., Dalton Trans.* **1999**, 1537–1538, doi:10.1039/a902407g.
49. Mijatovic, I; Kickelbick, G; Schubert, U Rearrangement of a Titanium Alkoxide Cluster upon Substitution of the Alkoxide Groups by Carboxylate Ligands − Synthesis of [Ti6O4(OEt)14(OOCPh)2] from [Ti7O4(OEt)20]. *European Journal of Inorganic Chemistry,* **2001**, *2001*, 1933–1935.
50. Yang, S.; Su, H.-C.; Hou, J.-L.; Luo, W.; Zou, D.-H.; Zhu, Q.-Y.; Dai, J. The Effects of Transition-Metal Doping and Chromophore Anchoring on the Photocurrent Response of Titanium-Oxo-Clusters. *Dalton Trans.* **2017**, *46*, 9639–9645, doi:10.1039/C7DT01603D.
51. Boyle, T.J.; Schwartz, R.W. An Investigation of Group (IV) Alkoxides as Property Controlling Reagents in the Synthesis of Ceramic Materials. *Comments on Inorganic Chemistry* **1994**, *16*, 243–278, doi:10.1080/02603599408035772.
52. Fang, W.-H.; Zhang, L.; Zhang, J. A 3.6 Nm Ti_{52} –Oxo Nanocluster with Precise Atomic Structure. *J. Am. Chem. Soc.* **2016**, *138*, 7480–7483, doi:10.1021/jacs.6b03489.
53. Lin, Y.; Zhu, Y.-F.; Chen, Z.-H.; Liu, F.-H.; Zhao, L.; Su, Z.-M. Synthesis, Structure, and Photocatalytic Hydrogen of Three Environmentally Friendly Titanium Oxo-Clusters. *Inorganic Chemistry Communications* **2014**, *40*, 22–25, doi:10.1016/j.inoche.2013.11.023.

54. Lei, X.; Shang, M.; Fehlner, T.P. Utilization of a Cobalt Carbonyl Cluster Carboxylic Acid in the Isolation of Novel Titanium(IV) Oxo Alkoxy Carboxylates. *Organometallics* **1996**, *15*, 3779–3781, doi:10.1021/om960326+.
55. Steunou, N.; Robert, F.; Boubekeur, K.; Ribot, F.; Sanchez, C. Synthesis through an in Situ Esterification Process and Characterization of Oxo Isopropoxo Titanium Clusters. *Inorganica Chimica Acta* **1998**, *279*, 144–151, doi:10.1016/S0020-1693(98)00109-1.
56. Gao, M.-Y.; Chen, S.; Hu, L.-X.; Zhang, L.; Zhang, J. Synthesis and Photocatalytic H_2 Evolution Properties of Four Titanium-Oxo-Clusters Based on a Cyclohex-3-Ene-1-Carboxylate Ligand. *Dalton Trans.* **2017**, *46*, 10630–10634, doi:10.1039/C7DT00627F.
57. Gautier-Luneau, I.; Mosset, A.; Galy, J. Structural Characterization of a Hexanuclear Titanium Acetate Complex, $Ti_6(\mu_3-O)_2(\mu_2-O)_2(\mu_2-OC_2H_5)_2\text{-}\mu\text{-}CH_3COO)_8(OC_2H_5)_6$, Built up of Two Trinuclear, Oxo-Centered, Units. *Zeitschrift für Kristallographie* **1987**, *180*, 83–95, doi:10.1524/zkri.1987.180.1-4.83.
58. Laaziz, I.; Larbot, A.; Guizard, C.; Durand, J.; Cot, L.; Joffre, J. Structure de Ti6(CH3COO)8(OiPr)8O4. *Acta Crystallogr C Cryst Struct Commun* **1990**, *46*, 2332–2334, doi:10.1107/S0108270190003134.
59. Heinz, P.; Puchberger, M.; Bendova, M.; Baumann, S.O.; Schubert, U. Clusters for Alkyne-Azide Click Reactions. *Dalton Trans.* **2010**, *39*, 7640, doi:10.1039/c0dt00618a.
60. Gao, Y.; Kogler, F.R.; Peterlik, H.; Schubert, U. Ring-Opening Metathesis Polymerizations with Norbornene Carboxylate-Substituted Metal Oxo Clusters. *J. Mater. Chem.* **2006**, *16*, 3268, doi:10.1039/b518277h.
61. Schubert, U.; Arpac, E.; Glaubitt, W.; Helmerich, A.; Chau, C. Primary Hydrolysis Products of Methacrylate-Modified Titanium and Zirconium Alkoxides. *Chem. Mater.* **1992**, *4*, 291–295, doi:10.1021/cm00020a014.
62. Papiernik, R.; Hubert-Pfalzgraf, L.G.; Vaissermann, J.; Goncalves, M.C.H.B. Synthesis and Characterization of New Titanium Hexanuclear Oxo Carboxylato Alkoxides. Molecular Structure of [Ti6(M3-O)6(μ-O2CC6H4OPh)6(OEt)6]. *J. Chem. Soc., Dalton Trans.* **1998**, 2285–2288, doi:10.1039/a803266a.
63. Sui, R.; Charpentier, P.A.; Rizkalla, A.S.; Jennings, M.C. Hexakis(μ-Acetato-$\kappa^2 O, O'$)Hexaisopropoxyhexa-μ_3-Oxo-Hexatitanium. *Acta Crystallogr E Struct Rep Online* **2006**, *62*, m373–m375, doi:10.1107/S1600536806002492.
64. Seisenbaeva, G.A.; Ilina, E.; Håkansson, S.; Kessler, V.G. A New Concept for Titanium Oxo-Alkoxo-Carboxylates' Encapsulated Biocompatible Time Temperature Food Indicators Based on Arising, Not Fading Color. *J Sol-Gel Sci Technol* **2010**, *55*, 1–8, doi:10.1007/s10971-010-2195-8.
65. Fang, W.-H.; Zhang, L.; Zhang, J. Synthetic Investigation, Structural Analysis and Photocatalytic Study of a Carboxylate–Phosphonate Bridged Ti_{18}-Oxo Cluster. *Dalton Trans.* **2017**, *46*, 803–807, doi:10.1039/C6DT04474C.
66. Hou, J.-L.; Luo, W.; Guo, Y.; Zhang, P.; Yang, S.; Zhu, Q.-Y.; Dai, J. Titanium Oxo Cluster with Six Peripheral Ferrocene Units and Its Photocurrent Response Properties for Saccharides. *Inorg. Chem.* **2017**, *56*, 6451–6458, doi:10.1021/acs.inorgchem.7b00522.
67. Piszczek, P.; Grodzicki, A.; Richert, M.; Wojtczak, A. Structural and Thermal Stability Studies of Ti(IV) Hexanuclear Oxo Trimethylacetato Isopropoxide Complex. *Inorganica Chimica Acta* **2004**, *357*, 2769–2775, doi:10.1016/j.ica.2004.02.022.
68. Hong, K.; Bak, W.; Chun, H. Robust Molecular Crystals of Titanium(IV)-Oxo-Carboxylate Clusters Showing Water Stability and CO_2 Sorption Capability. *Inorg. Chem.* **2014**, *53*, 7288–7293, doi:10.1021/ic500629y.
69. Chaumont, C.; Huen, E.; Huguenard, C.; Mobian, P.; Henry, M. Toward Colored Reticular Titanium-Based Hybrid Networks: Evaluation of the Reactivity of the [Ti8O8(OOCCH2But)16] Wheel with Phenol, Resorcinol and Catechol. *Polyhedron* **2013**, *57*, 70–76, doi:10.1016/j.poly.2013.04.021.
70. Zhao, C.; Han, Y.; Dai, S.; Chen, X.; Yan, J.; Zhang, W.; Su, H.; Lin, S.; Tang, Z.; Teo, B.K.; et al. Microporous Cyclic Titanium-Oxo Clusters with Labile Surface Ligands. *Angew Chem Int Ed* **2017**, *56*, 16252–16256, doi:10.1002/anie.201709096.

71. Hou, J.; Huang, N.; Acharya, D.; Liu, Y.; Zhu, J.; Teng, J.; Wang, Z.; Qu, K.; Zhang, X.; Sun, D. All-Catecholate-Stabilized Black Titanium-Oxo Clusters for Efficient Photothermal Conversion. *Chem. Sci.* **2024**, *15*, 2655–2664, doi:10.1039/D3SC05617A.
72. Liu, J.-X.; Gao, M.-Y.; Fang, W.-H.; Zhang, L.; Zhang, J. Bandgap Engineering of Titanium-Oxo Clusters: Labile Surface Sites Used for Ligand Substitution and Metal Incorporation. *Angew. Chem. Int. Ed.* **2016**, *55*, 5160–5165, doi:10.1002/anie.201510455.
73. Li, N.; Liu, J.-J.; Sun, J.-W.; Dong, B.-X.; Dong, L.-Z.; Yao, S.-J.; Xin, Z.; Li, S.-L.; Lan, Y.-Q. Calix[8]Arene-Constructed Stable Polyoxo-Titanium Clusters for Efficient CO_2 Photoreduction. *Green Chem.* **2020**, *22*, 5325–5332, doi:10.1039/D0GC01497D.
74. Hoebbel, D.; Reinert, T.; Schmidt, H.; Arpac, E. [No Title Found]. *Journal of Sol-Gel Science and Technology* **1997**, *10*, 115–126, doi:10.1023/A:1018305811088.
75. Svensson, F.G.; Daniel, G.; Tai, C.-W.; Seisenbaeva, G.A.; Kessler, V.G. Titanium Phosphonate Oxo-Alkoxide "Clusters": Solution Stability and Facile Hydrolytic Transformation into Nano Titania. *RSC Adv.* **2020**, *10*, 6873–6883, doi:10.1039/C9RA10691J.
76. Gao, M.-Y.; Wang, F.; Gu, Z.-G.; Zhang, D.-X.; Zhang, L.; Zhang, J. Fullerene-like Polyoxotitanium Cage with High Solution Stability. *J. Am. Chem. Soc.* **2016**, *138*, 2556–2559, doi:10.1021/jacs.6b00613.
77. Wang, C.; Wang, S.-J.; Kong, F.-G. Calixarene-Protected Titanium-Oxo Clusters and Their Photocurrent Responses and Photocatalytic Performances. *Inorg. Chem.* **2021**, *60*, 5034–5041, doi:10.1021/acs.inorgchem.1c00063.
78. Bui, H.T.; Park, H.Y.; Alvarez, P.J.J.; Lee, J.; Kim, W.; Kim, E.-J. Visible-Light Activation of a Dissolved Organic Matter–TiO_2 Complex Mediated *via* Ligand-to-Metal Charge Transfer. *Environ. Sci. Technol.* **2022**, *56*, 10829–10837, doi:10.1021/acs.est.2c02975.
79. Wang, D.; Zhao, P.; Yang, J.; Xu, G.; Yang, H.; Shi, Z.; Hu, Q.; Dong, B.; Guo, Z. Photocatalytic Degradation of Organic Dye and Phytohormone by a Cu(II) Complex Powder Catalyst with Added H2O2. *Colloids and Surfaces A: Physicochemical and Engineering Aspects* **2020**, *603*, 125147, doi:10.1016/j.colsurfa.2020.125147.
80. Zhang, G.; Kim, C.; Choi, W. Poly(4-Vinylphenol) as a New Stable and Metal-Free Sensitizer of Titania for Visible Light Photocatalysis through Ligand-to-Metal Charge Transfer Process. *Catalysis Today* **2017**, *281*, 109–116, doi:10.1016/j.cattod.2016.06.048.
81. Liu, X.-X.; Chen, S.; Fang, W.-H.; Zhang, L.; Zhang, J. Amino-Polyalcohol-Solvothermal Synthesis of Titanium-Oxo Clusters: From Ti_6 to Ti_{19} with Structural Diversity. *Inorg. Chem.* **2019**, *58*, 7267–7273, doi:10.1021/acs.inorgchem.9b00293.
82. Wu, Y.-Y.; Lu, X.-W.; Qi, M.; Su, H.-C.; Zhao, X.-W.; Zhu, Q.-Y.; Dai, J. Titanium–Oxo Cluster with 9-Anthracenecarboxylate Antennae: A Fluorescent and Photocurrent Transfer Material. *Inorg. Chem.* **2014**, *53*, 7233–7240, doi:10.1021/ic500390j.
83. Li, N.; Lin, J.-M.; Li, R.-H.; Shi, J.-W.; Dong, L.-Z.; Liu, J.; He, J.; Lan, Y.-Q. Calix[4]Arene-Functionalized Titanium-Oxo Compounds for Perceiving Differences in Catalytic Reactivity Between Mono- and Multimetallic Sites. *J. Am. Chem. Soc.* **2023**, *145*, 16098–16108, doi:10.1021/jacs.3c04480.
84. Liu, J.-J.; Li, N.; Sun, J.-W.; Liu, J.; Dong, L.-Z.; Yao, S.-J.; Zhang, L.; Xin, Z.-F.; Shi, J.-W.; Wang, J.-X.; et al. Ferrocene-Functionalized Polyoxo-Titanium Cluster for CO_2 Photoreduction. *ACS Catal.* **2021**, *11*, 4510–4519, doi:10.1021/acscatal.0c04495.
85. Wang, C.; Liu, C.; Li, L.-J.; Sun, Z.-M. Synthesis, Crystal Structures, and Photochemical Properties of a Family of Heterometallic Titanium Oxo Clusters. *Inorg. Chem.* **2019**, *58*, 6312–6319, doi:10.1021/acs.inorgchem.9b00508.
86. Kim, S.; Sarkar, D.; Kim, Y.; Park, M.H.; Yoon, M.; Kim, Y.; Kim, M. Synthesis of Functionalized Titanium-Carboxylate Molecular Clusters and Their Catalytic Activity. *Journal of Industrial and Engineering Chemistry* **2017**, *53*, 171–176, doi:10.1016/j.jiec.2017.04.022.
87. Yu, Y.-Z.; Zhang, Y.-R.; Geng, C.-H.; Sun, L.; Guo, Y.; Feng, Y.-R.; Wang, Y.-X.; Zhang, X.-M. Precise and Wide-Ranged Band-Gap Tuning of Ti_6 -Core-Based Titanium Oxo Clusters by the Type and Number of Chromophore Ligands. *Inorg. Chem.* **2019**, *58*, 16785–16791, doi:10.1021/acs.inorgchem.9b02951.

88. Gao, M.-Y.; Wang, Z.; Li, Q.-H.; Li, D.; Sun, Y.; Andaloussi, Y.H.; Ma, C.; Deng, C.; Zhang, J.; Zhang, L. Black Titanium-Oxo Clusters with Ultralow Band Gaps and Enhanced Nonlinear Optical Performance. *J. Am. Chem. Soc.* **2022**, *144*, 8153–8161, doi:10.1021/jacs.2c00765.
89. Yang, X.-X.; Yu, W.-D.; Yi, X.-Y.; Liu, C. Accurate Regulating of Visible-Light Absorption in Polyoxotitanate–Calix[8]Arene Systems by Ligand Modification. *Inorg. Chem.* **2020**, *59*, 7512–7519, doi:10.1021/acs.inorgchem.0c00330.
90. Wang, X.; Yu, Y.; Wang, Z.; Zheng, J.; Bi, Y.; Zheng, Z. Thiacalix[4]Arene-Protected Titanium–Oxo Clusters: Influence of Ligand Conformation and Ti–S Coordination on the Visible-Light Photocatalytic Hydrogen Production. *Inorg. Chem.* **2020**, *59*, 7150–7157, doi:10.1021/acs.inorgchem.0c00615.
91. Dai, L.-F.; Liu, X.-R.; Tian, Y.-Q.; Yi, X.-Y.; Liu, C. Auxiliary Carboxylate-Induced Assembly of Calix[6]Arene-Polyoxotitanate Hybrid Systems with Photocatalytic Activity in the Oxidation of Sulfides. *Inorg. Chem.* **2023**, *62*, 6047–6054, doi:10.1021/acs.inorgchem.2c04528.
92. Liu, J.-J.; Sun, S.-N.; Liu, J.; Kuang, Y.; Shi, J.-W.; Dong, L.-Z.; Li, N.; Lu, J.-N.; Lin, J.-M.; Li, S.-L.; et al. Achieving High-Efficient Photoelectrocatalytic Degradation of 4-Chlorophenol via Functional Reformation of Titanium-Oxo Clusters. *J. Am. Chem. Soc.* **2023**, *145*, 6112–6122, doi:10.1021/jacs.2c11509.
93. Bossmann, S.H.; Wörner, M.; Pokhrel, M.R.; Baumeister, B.; Göb, S.; Braun, A.M. Ruthenium(II)-Tris-Bipyridine/Titanium Dioxide Codoped Zeolite Y Photocatalyst: Performance Optimization Using 2,4-Xylidine (1-Amino-2,4-Dimethyl-Benzene). *Separation and Purification Technology* **2009**, *67*, 201–207, doi:10.1016/j.seppur.2009.03.015.
94. Gajardo, F.; Leiva, A.M.; Loeb, B.; Delgadillo, A.; Stromberg, J.R.; Meyer, G.J. Interfacial Electron Transfer on TiO2 Sensitized with an Axially Anchored Trans Tetradentate Ru(II) Compound. *Inorganica Chimica Acta* **2008**, *361*, 613–619, doi:10.1016/j.ica.2007.03.062.
95. Ni, J.-S.; Hung, C.-Y.; Liu, K.-Y.; Chang, Y.-H.; Ho, K.-C.; Lin, K.-F. Effects of Tethering Alkyl Chains for Amphiphilic Ruthenium Complex Dyes on Their Adsorption to Titanium Oxide and Photovoltaic Properties. *Journal of Colloid and Interface Science* **2012**, *386*, 359–365, doi:10.1016/j.jcis.2012.07.019.
96. Sastre, F.; Bouizi, Y.; Fornés, V.; Garcia, H. Visible-Light Hydrogen Generation Using as Photocatalysts Layered Titanates Incorporating in the Intergallery Space Ruthenium Tris(Bipyridyl) and Methyl Viologen. *Journal of Colloid and Interface Science* **2010**, *346*, 172–177, doi:10.1016/j.jcis.2010.02.056.
97. Prier, C.K.; Rankic, D.A.; MacMillan, D.W.C. Visible Light Photoredox Catalysis with Transition Metal Complexes: Applications in Organic Synthesis. *Chem. Rev.* **2013**, *113*, 5322–5363, doi:10.1021/cr300503r.
98. Xue, L.-X.; Meng, T.-T.; Yang, W.; Wang, K.-Z. Recent Advances in Ruthenium Complex-Based Light-Driven Water Oxidation Catalysts. *Journal of Photochemistry and Photobiology B: Biology* **2015**, *152*, 95–105, doi:10.1016/j.jphotobiol.2015.07.005.
99. Aghazada, S.; Nazeeruddin, M.K. Ruthenium Complexes as Sensitizers in Dye-Sensitized Solar Cells. *Inorganics* **2018**, *6*, 52, doi:10.3390/inorganics6020052.
100. Wun Fui, M.-L.; Siew San, T.; Kassim, M.B.; Minggu, L.J.; Kim Hang Ng Photocatalytic Degradation of Bromothylmol Blue by Novel Ruthenium(II) Complex. In Proceedings of the 3rd IET International Conference on Clean Energy and Technology (CEAT) 2014; Institution of Engineering and Technology: Kuching, Malaysia, 2014; p. 13 (5 .)-13 (5 .).
101. Singha, K.; Laha, P.; Chandra, F.; Dehury, N.; Koner, A.L.; Patra, S. Long-Lived Polypyridyl Based Mononuclear Ruthenium Complexes: Synthesis, Structure, and Azo Dye Decomposition. *Inorg. Chem.* **2017**, *56*, 6489–6498, doi:10.1021/acs.inorgchem.7b00536.
102. C. Justin Dhanaraj, C.J.D.; S. S. Salin Raj, S.S.S.R. Synthesis, Structural Elucidation and Photocatalytic Studies of Some 4-Aminoantipyrine Based Ruthenium (III) Complexes. *J. Environ. Nanotechnol.* **2019**, *8*, 21–22, doi:10.13074/jent.2019.12.194382.
103. Gao, Y.; Qian, B.-F.; Wang, J.-L.; Jia, A.-Q.; Mei, Q.; Zhang, Q.-F. μ-Disulfido Complexes of Ruthenium(III) 1,1′-Dithiolate [{(Me3tacn)Ru}2(K2-S2COR)(K2-S2C = O)(μ-S2)]PF6 (Me3tacn = 1,4,7-Trimethyl-1,4,7-Triazacyclononane; R = Alkyl). *Inorganica Chimica Acta* **2023**, *548*, 121374, doi:10.1016/j.ica.2022.121374.

104. Ghosh, D.; Takeda, H.; Fabry, D.C.; Tamaki, Y.; Ishitani, O. Supramolecular Photocatalyst with a Rh(III)-Complex Catalyst Unit for CO_2 Reduction. *ACS Sustainable Chem. Eng.* **2019**, *7*, 2648–2657, doi:10.1021/acssuschemeng.8b05728.
105. Chatterjee, D.; Edik, R.V. Prospect of Ru^{III} (Edta) in Catalysis of Bicarbonate Reduction. *CCAT* **2020**, *9*, 23–31, doi:10.2174/2211544708666190902124817.
106. Garza-Cervantes, J.A.; Chávez-Reyes, A.; Castillo, E.C.; García-Rivas, G.; Antonio Ortega-Rivera, O.; Salinas, E.; Ortiz-Martínez, M.; Gómez-Flores, S.L.; Peña-Martínez, J.A.; Pepi-Molina, A.; et al. Synergistic Antimicrobial Effects of Silver/Transition-Metal Combinatorial Treatments. *Sci Rep* **2017**, *7*, 903, doi:10.1038/s41598-017-01017-7.
107. Pervaiz, M.; Sadiq, S.; Sadiq, A.; Younas, U.; Ashraf, A.; Saeed, Z.; Zuber, M.; Adnan, A. Azo-Schiff Base Derivatives of Transition Metal Complexes as Antimicrobial Agents. *Coordination Chemistry Reviews* **2021**, *447*, 214128, doi:10.1016/j.ccr.2021.214128.
108. Matsunaga, T.; Tomoda, R.; Nakajima, T.; Wake, H. Photoelectrochemical Sterilization of Microbial Cells by Semiconductor Powders. *FEMS Microbiology Letters* **1985**, *29*, 211–214, doi:10.1111/j.1574-6968.1985.tb00864.x.
109. Fujishima, A.; Honda, K. Electrochemical Photolysis of Water at a Semiconductor Electrode. *Nature* **1972**, *238*, 37–38, doi:10.1038/238037a0.
110. Javed, R.; Ain, N.U.; Gul, A.; Arslan Ahmad, M.; Guo, W.; Ao, Q.; Tian, S. Diverse Biotechnological Applications of Multifunctional Titanium Dioxide Nanoparticles: An Up-to-date Review. *IET Nanobiotechnology* **2022**, *16*, 171–189, doi:10.1049/nbt2.12085.
111. Jiang, S.; Lin, K.; Cai, M. ZnO Nanomaterials: Current Advancements in Antibacterial Mechanisms and Applications. *Front. Chem.* **2020**, *8*, 580, doi:10.3389/fchem.2020.00580.
112. Karunakaran, C.; Abiramasundari, G.; Gomathisankar, P.; Manikandan, G.; Anandi, V. Cu-Doped TiO2 Nanoparticles for Photocatalytic Disinfection of Bacteria under Visible Light. *Journal of Colloid and Interface Science* **2010**, *352*, 68–74, doi:10.1016/j.jcis.2010.08.012.
113. Yadav, H.M.; Otari, S.V.; Koli, V.B.; Mali, S.S.; Hong, C.K.; Pawar, S.H.; Delekar, S.D. Preparation and Characterization of Copper-Doped Anatase TiO2 Nanoparticles with Visible Light Photocatalytic Antibacterial Activity. *Journal of Photochemistry and Photobiology A: Chemistry* **2014**, *280*, 32–38, doi:10.1016/j.jphotochem.2014.02.006.
114. Yadav, H.M.; Otari, S.V.; Bohara, R.A.; Mali, S.S.; Pawar, S.H.; Delekar, S.D. Synthesis and Visible Light Photocatalytic Antibacterial Activity of Nickel-Doped TiO2 Nanoparticles against Gram-Positive and Gram-Negative Bacteria. *Journal of Photochemistry and Photobiology A: Chemistry* **2014**, *294*, 130–136, doi:10.1016/j.jphotochem.2014.07.024.
115. Foster, H.A.; Ditta, I.B.; Varghese, S.; Steele, A. Photocatalytic Disinfection Using Titanium Dioxide: Spectrum and Mechanism of Antimicrobial Activity. *Appl Microbiol Biotechnol* **2011**, *90*, 1847–1868, doi:10.1007/s00253-011-3213-7.
116. Wysocka, I.; Kowalska, E.; Ryl, J.; Nowaczyk, G.; Zielińska-Jurek, A. Morphology, Photocatalytic and Antimicrobial Properties of TiO2 Modified with Mono- and Bimetallic Copper, Platinum and Silver Nanoparticles. *Nanomaterials* **2019**, *9*, 1129, doi:10.3390/nano9081129.
117. Moon, K.-S.; Choi, E.-J.; Bae, J.-M.; Park, Y.-B.; Oh, S. Visible Light-Enhanced Antibacterial and Osteogenic Functionality of Au and Pt Nanoparticles Deposited on TiO2 Nanotubes. *Materials* **2020**, *13*, 3721, doi:10.3390/ma13173721.
118. Yoo, S.M.; Rawal, S.B.; Lee, J.E.; Kim, J.; Ryu, H.-Y.; Park, D.-W.; Lee, W.I. Size-Dependence of Plasmonic Au Nanoparticles in Photocatalytic Behavior of Au/TiO 2 and Au@SiO 2 /TiO 2. *Applied Catalysis A: General* **2015**, *499*, 47–54, doi:10.1016/j.apcata.2015.04.003.
119. Abdulagatov, I.M.; Ragimov, R.M.; Khamidov, M.A.; Maksumova, A.M.; Abdullaeva, N.M. ALD Coated Polypropylene Hernia Meshes for Prevention of Mesh-Related Post-Surgery Complications: An Experimental Study in Animals. *Biomed. Mater.* **2022**, *17*, 015006, doi:10.1088/1748-605X/ac361e.
120. Mukherjee, K.; Acharya, K.; Biswas, A.; Jana, N.R. TiO_2 Nanoparticles Co-Doped with Nitrogen and Fluorine as Visible-Light-Activated Antifungal Agents. *ACS Appl. Nano Mater.* **2020**, *3*, 2016–2025, doi:10.1021/acsanm.0c00108.
121. Wong, M.-S.; Sun, M.-T.; Sun, D.-S.; Chang, H.-H. Visible-Light-Responsive Antibacterial Property of Boron-Doped Titania Films. *Catalysts* **2020**, *10*, 1349, doi:10.3390/catal10111349.

122. Sopchenski, L.; Cogo, S.; Dias-Ntipanyj, M.F.; Elifio-Espósito, S.; Popat, K.C.; Soares, P. Bioactive and Antibacterial Boron Doped TiO2 Coating Obtained by PEO. *Applied Surface Science* **2018**, *458*, 49–58, doi:10.1016/j.apsusc.2018.07.049.
123. Koli, V.B.; Ke, S.-C.; Dodamani, A.G.; Deshmukh, S.P.; Kim, J.-S. Boron-Doped TiO2-CNT Nanocomposites with Improved Photocatalytic Efficiency toward Photodegradation of Toluene Gas and Photo-Inactivation of Escherichia Coli. *Catalysts* **2020**, *10*, 632, doi:10.3390/catal10060632.
124. Svensson, F.G.; Seisenbaeva, G.A.; Kessler, V.G. Mixed-Ligand Titanium "Oxo Clusters": Structural Insights into the Formation and Binding of Organic Molecules and Transformation into Oxide Nanostructures on Hydrolysis and Thermolysis. *Eur. J. Inorg. Chem.* **2017**, *2017*, 4117–4122, doi:10.1002/ejic.201700775.
125. Luo, W.; Hu, B.; Zhang, H.-L.; Li, C.; Shi, Y.; Li, X.; Jin, L. Antibacterial, Photothermal and Stable Ag-Titanium-Oxo-Clusters Hydrogel Designed for Wound Healing. *Materials & Design* **2023**, *226*, 111674, doi:10.1016/j.matdes.2023.111674.
126. Diamantis, A.A.; Dubrawski, J.V. Preparation and Structure of Ethylenediaminetetraacetate Complexes of Ruthenium(II) with Dinitrogen, Carbon Monoxide, and Other .Pi.-Acceptor Ligands. *Inorg. Chem.* **1981**, *20*, 1142–1150, doi:10.1021/ic50218a037.
127. Impert, O.; Katafias, A.; Kita, P.; Wrzeszcz, G.; Fenska, J.; Lente, G.; Fábián, I. Base Hydrolysis of Mer-Trispicolinatoruthenium(III): Kinetics and Mechanism. *Transition Met Chem* **2011**, *36*, 761–766, doi:10.1007/s11243-011-9530-y.

7. Dorobek naukowy kandydata na doktora

Edukacja

1. 10/2019–02/2025 – Uniwersytet Mikołaja Kopernika w Toruniu, Szkoła Doktorska Nauk Ścisłych i Przyrodniczych, Studia doktoranckie z dziedziny nauk chemicznych
2. 10/2017–06/2019 – Uniwersytet Mikołaja Kopernika w Toruniu, Wydział Chemii, Katedra Chemii Nieorganicznej i Koordynacyjnej, Magister chemii kryminalistycznej
3. 10/2016–10/2018 – Uniwersytet Mikołaja Kopernika w Toruniu, Wydział Chemii, Katedra Chemii Materiałów, Adsorpcjii Katalizy, Magister chemii kosmetycznej
4. 10/2013–07/2016 – Uniwersytet Mikołaja Kopernika w Toruniu, Wydział Chemii, Katedra Chemii Materiałów, Adsorpcjii Katalizy, Licencjat chemii kosmetycznej

Doświadczenie zawodowe

1. 12/2023 – 01/2025 – Instytut Technik Węglowych Sp. z o.o. w Toruniu, specjalista ds. B + R
2. 06/2023 – 03/2024 – Lumidatis Sp. z o.o. w Toruniu, chemik
3. 11/2022 – 01/2023 – Nanoseen Sp. z o.o. w Gdyni, pracownik działu B + R

Staże i praktyki

1. 07/2019 – 09/2019 – Oceanic S.A. w Trąbkach Małych, stażysta
2. 07/2017 – Polski Koncern Naftowy Orlen w Płocku, praktykant
3. 07/2015 – Zespół Elektrowni Pątnów – Adamów – Konin w Koninie, praktykant

Szkolenia

1. 07/2021 – Training School COST Action BIONECA CA16122, 4th Course “From biomaterials and tissue engineering to characterization”, Loreto, Italy
2. 05/2021 – szkolenie „Angielski w badaniach klinicznych” organizowane przez firmę Soft Communication, Warszawa, Polska
3. 04/2021 – szkolenie „Monitorowanie badań klinicznych” organizowane przez firmę Education For Business & Science, Warszawa, Polska
4. 04/2021 – szkolenie „Podstawy Pharmacovigilance” organizowane przez firmę Soft Communication, Warszawa, Polska
5. 03/2021 – szkolenie „Certyfikat GCP – Dobra Praktyka Kliniczna” organizowane przez firmę Soft Communication, Warszawa, Polska
6. 03/2021 – szkolenie „Odkryj swoją przyszłość w Przemyśle Farmaceutycznym” organizowane przez firmę Education For Business & Science, Warszawa, Polska
7. 02/2021 – szkolenie „Rejestracja produktów z pogranicza” organizowane przez firmę Education For Business & Science, Warszawa, Polska
8. 05/2017 - szkolenie „Walidacja metod fizykochemicznych” organizowane przez firmę isoQRS, Toruń, Polska

Publikacje w czasopismach z listy filadelfijskiej

1. **B. Kubiak*,** A. Topolski, A. Radtke*, T. Muzioł, O. Impert, A. Katafias, R. van Eldik, P. Piszczek, Analysis of Photocatalytic Properties of Poly(Methyl Methacrylate) Composites with Titanium(IV) and Ruthenium(III) Complexes, *Applied Sciences*, **2025**, 15, 1679; doi.: 10.3390/app15041679., IF_{2023}= 2.500, PM=100
2. **B. Kubiak***, T. M. Muzioł, M. Jabłoński, A. Radtke, P. Piszczek*, Investigation of Titanium(IV) – Oxo Complexes Stabilized with α-Hydroxy Carboxylate Ligands: Structural Analysis and DFT Studies. *Dalton Trans.* **2024**, 53, 14457-14468, doi:10.1039/D4DT01710B. IF_{2023}= 3.500, PM=140
3. **B. Kubiak*,** T. Muzioł, G. Wrzeszcz, A. Radtke, P. Golińska, T. Jędrzejewski, S. Wrotek, P. Piszczek*, Structural Characterization and Bioactivity of a Titanium(IV) – Oxo Complex Stabilized by Mandelate Ligands. *Molecules* **2024**, *29*, 1736, doi:10.3390/molecules29081736. IF_{2023}= 4.200, PM=140
4. **B. Kubiak*,** P. Piszczek*, A. Radtke, T. Muzioł, G. Wrzeszcz, P. Golińska, Photocatalytic and Antimicrobial Activity of Titanium(IV)-Oxo Clusters of Different Core Structure. *Crystals* **2023**, *13*, 998, doi:10.3390/cryst13070998. IF_{2023}= 2.700, PM=70
5. **B. Kubiak,** A. Radtke*, A. Topolski, G. Wrzeszcz, P. Golińska, E. Kaszkowiak, M. Sobota, J. Włodarczyk, M. Stojko, P. Piszczek*, The Composites of PCL and Tetranuclear Titanium(IV) – Oxo Complexes as Materials Exhibiting the Photocatalytic and the Antimicrobial Activity. *IJMS* **2021**, *22*, 7021, doi:10.3390/ijms22137021. IF_{2021}= 6.208, PM=140
6. P. Piszczek*, **B. Kubiak,** P. Golińska, A. Radtke*, Oxo-Titanium(IV) Complex/Polymer Composites—Synthesis, Spectroscopic Characterization and Antimicrobial Activity Test. *IJMS* **2020**, *21*, 9663, doi:10.3390/ijms21249663. IF_{2020}= 5.923, PM=140

Udział w konferencjach krajowych oraz międzynarodowych – prezentacje ustne

1. **B. Kubiak**, P. Piszczek, A. Radtke, P. Golińska. *Comparison of photocatalytic and antimicrobial properties of composites made of polymer and titanium(iv) oxo – complexes with $\{Ti_6O_6\}$ and $\{Ti_6O_4\}$ core*, Biomaterials in Medicine and Veterinary Medicine,13-16 October 2022, Rytro, Poland
2. **B. Kubiak**, P. Piszczek, A. Radtke. *Titanium(IV) oxo – complexes with $\{Ti_4O_2\}$ core, their photocatalytic and antimicrobial properties*, Future Materials 2021, 29-30 July 2021, Vancouver, Canada (online)
3. **B. Kubiak**, P. Piszczek. *Ocena aktywności fotokatalitycznej i mikrobiologicznej materiałów kompozytowych wytwarzanych przez dyspersję wielordzeniowych okso – kompleksów tytanu(IV) w matrycy PMMA*, III Ogólnopolska Konferencja Naukowa „Biopolimery – źródło nowych materiałów", 20 maja 2021, Lublin, Polska

Udział w konferencjach krajowych oraz międzynarodowych – postery

1. **B. Kubiak**, P. Piszczek, A. Radtke, T. Muzioł, G. Wrzeszcz, A. Topolski, P. Golińska, T. Jędrzejewski. *Titanium(IV) oxo – complexes with α-hydroxycarboxylate ligands:*

their structure and antimicrobial properties, 33rd Annual Conference on Biomaterials in Medicine and Veterinary Medicine, 10 – 13 October 2024, Rytro, Poland

2. **B. Kubiak**, A. Radtke, P. Piszczek, P. Golińska, T. Jędrzejewski. *Porównanie aktywności fotokatalitycznej i biologicznej kompleksów okso – tytanu(IV) (TOCs) o rdzeniach {Ti_4O} oraz {Ti_6O_4},* V Interdyscyplinarna Konferencja Nano(&)BioMateriały – od teorii do aplikacji, Toruń, 14 – 16 czerwca 2023, Toruń, Polska
3. **B. Kubiak**, P. Piszczek, A. Radtke. *Photocatalytic and microbial activity of titanium(IV) oxo – complexes in PCL matrix composites*, Chemistry for Beauty and Health, 12 – 14 May 2021, Toruń, Poland
4. **B. Kubiak**, P. Piszczek, A. Radtke. *Photocatalytic and microbial activity of titanium(IV) oxo-complexes in PMMA matrix composites*, The 9th Intercollegiate Biotechnology Symposium "Symbioza", 21 – 23 May 2021, Warsaw, Poland
5. **B. Kubiak**, P. Piszczek , A. Radtke, P. Golińska. *Porównanie aktywności mikrobiologicznej i fotokatalitycznej materiałów kompozytowych na bazie polikaprolaktonu (PCL) i okso – kompleksów tytanu(IV) (TOCs) o rdzeniu {Ti_4O_2},* IV Ogólnopolskie Forum Chemii Nieorganicznej, 7 – 9 września 2021, Toruń, Polska
6. **B. Kubiak**, P. Piszczek. *Ocena aktywności mikrobiologicznej i fotokatalitycznej materiałów kompozytowych na bazie polikaprolaktonu (PCL) i okso-kompleksów tytanu(IV) (TOCs) o rdzeniu {Ti_4O_2},* Kopernikańskie Seminarium Doktoranckie, 20 – 22 września 2021, Toruń, Polska
7. **B. Kubiak**, P. Piszczek, A. Radtke. *Titanium(IV) oxo-complexes as photocatalytic and antimicrobial agents,* International Workshop on Functional Nanostructured Materials – "*FuNaM-3*", 12 – 14 October 2021, Kraków, Poland
8. **B. Kubiak**, P. Piszczek. *Aktywność fotokatalityczna i mikrobiologiczna okso-kompleksów tytanu(IV) otrzymanych na drodze reakcji alkoholanów z kwasami karboksylowymi*, Kopernikańskie Seminarium Doktoranckie, 07 Września 2020, Toruń, Polska
9. **B. Kubiak**, P. Piszczek. *Porównanie aktywności mikrobiologicznej okso – kompleksów tytanu(IV) o rdzeniu {Ti_3O} oraz {Ti_4O_2},* IX Kopernikańskie Sympozjum Studentów Nauk Przyrodniczych, 18 – 20 września 2020, Toruń, Polska

Współautorstwo

1. P. Piszczek, **B. Kubiak**, T. Muzioł, A. Radtke, P. Golińska, T. Jędrzejewski, S. Wrotek. *Investigating the bioactivity of composite films incorporating polymer enriched with titanium(IV) – oxo complexes*, 32nd Annual Conference on Biomaterials in Medicine and Veterinary Medicine, 12 – 15 October 2023, Rytro, Poland
2. M. Leżańska, **B. Kubiak**, A. Pacuła. *Charakterystyka fizykochemiczna i elektrochemiczna węgli aktywnych otrzymanych w wyniku modyfikacji chemicznej drewna wierzby wiciowej kwasem fosforowym(V),* 64 Zjazd Naukowy PTChem, 11 – 16 września 2022, Lublin, Polska

3. P. Piszczek, **B. Kubiak**, A. Radtke, J. Śmigiel, T. Muzioł, G. Wrzeszcz. *The (polymer/titanium(IV) – oxo clusters) composite films as the biomaterials of antimicrobial and photocatalytic activity*, Biomaterials in Medicine and Veterinary Medicine,13 – 16 October 2022, Rytro, Poland
4. P. Piszczek, **B. Kubiak**, A. Radtke, P. Golińska, P. Dobrzyński, M. Sobota. *Okso – kompleksy tytanu(IV), jako nowy czynnik przeciwdrobnoustrojowy*, IV Ogólnopolskie Forum Chemii Nieorganicznej, 7 – 9 września 2021, Toruń, Polska
5. P. Piszczek, **B. Kubiak**, A. Radtke, P. Golińska, M. Sobota. *Multinuclear Titanium(IV) – Oxo Complexes as The Novelty Antimicrobial Agents*, 30th Conference on Biomaterials in Medicine and Veterinary Medicine, 14 – 17 October 2021, Rytro, Poland

Zgłoszenia patentowe

1. B. Kubiak, P. Piszczek, A. Radtke, pt.: „Zastosowanie tetra-μ3-okso-μ-okso-deka-μ-2,2-dimetylopropioniano-di-μ-9-fluorenotytanu (IV) do wytwarzania kompozytów polimerowych". 31. 10. 2022; P. 442700.

Udział w projektach badawczych

1. 10/2023 – 09/2024 – grant NCN, OPUS, nr 2020/37/B/ST4/01082, *„Mechanistic clarification of the interaction of nanoparticles and nanoscale coordination compounds at the interface of multiphase chemical and medicinal related processes"* (wykonawca)
2. 10/2020 – 10/2021 – grant Inkubator Innowacyjności UMK_4.0, nr MNISW/2020/331/DIR *„Ocena właściwości mechanicznych i aktywności biologicznej powłok kompozytowych wytwarzanych na podłożach aluminiowych i stalowych" (wykonawca)*
3. 05/2020 – 05/2021 – grant Grants4NCUStudents, Inicjatywa Doskonałości, Uczelnia Badawcza, *„Estimation of photocatalytic and microbiological properties of Titanium(IV) Oxo-Complexes"* (kierownik projektu)
4. 03/2021 – 11/2021 – Grant Młodych dla uczestników Studiów Doktoranckich oraz młodych pracowników Wydziału Chemii, Uniwersytet Mikołaja Kopernika w Toruniu. Realizacja projektu pt. *„ Badanie właściwości fotokatalitycznych i mikrobiologicznych materiałów kompozytowych na bazie wielordzeniowych okso-kompleksów tytanu(IV)"*(kierownik projektu)
5. 03/2020 – 11/2020 – Grant Młodych dla uczestników Studiów Doktoranckich oraz młodych pracowników Wydziału Chemii, Uniwersytet Mikołaja Kopernika w Toruniu. Realizacja projektu pt. *„ Badanie właściwości bioaktywnych materiałów kompozytowych na bazie wielordzeniowych okso-kompleksów tytanu(IV)"*(kierownik projektu)

Dorobek organizacyjny

1. 09/2021 – Współorganizacja IV Ogólnopolskiego Forum Chemii Nieorganicznej, Uniwersytet Mikołaja Kopernika, Toruń
2. 01/2021 – Współorganizacja II Sympozjum „*Biomateriały w medycynie i kosmetologii*", Uniwersytet Mikołaja Kopernika, Toruń
3. 01/2020 – Współorganizacja I Sympozjum „*Biomateriały w medycynie i kosmetologii*", Uniwersytet Mikołaja Kopernika, Toruń

Załączniki

Artykuły

P1. *Oxo-Titanium(IV) Complex/Polymer Composites—Synthesis, Spectroscopic Characterization and Antimicrobial Activity Test.*

International Journal of
Molecular Sciences

MDPI

Article

Oxo-Titanium(IV) Complex/Polymer Composites—Synthesis, Spectroscopic Characterization and Antimicrobial Activity Test

Piotr Piszczek [1,*], Barbara Kubiak [1], Patrycja Golińska [2] and Aleksandra Radtke [1,*]

[1] Faculty of Chemistry, Nicolaus Copernicus University in Toruń, Gagarina 7, 87-100 Toruń, Poland; basiak0809@gmail.com
[2] Faculty of Biological and Veterinary Sciences, Nicolaus Copernicus University in Toruń, Lwowska 1, 87-100 Toruń, Poland; golinska@umk.pl
* Correspondence: piszczek@umk.pl (P.P.); aradtke@umk.pl (A.R.); Tel.: +48-607-883-357 (P.P.); +48-600-321-294 (A.R.)

Received: 2 November 2020; Accepted: 15 December 2020; Published: 18 December 2020



Abstract: The emergence of a large number of bacterial strains resistant to many drugs or disinfectants currently used contributed to the search of new, more effective antimicrobial agents. In the presented paper, we assessed the microbiocidal activity of tri- and tetranuclear oxo-titanium(IV) complexes (TOCs), which were dispersed in the poly(methyl methacrylate) (PMMA) matrix. The TOCs were synthesized in reaction to $Ti(OR)_4$ (R = ^{i}Pr, ^{i}Bu) and HO_2CR' (R' = 4-$PhNH_2$ and 4-PhOH) in a 4:1 molar ratio at room temperature and in Ar atmosphere. The structure of isolated oxo-complexes was confirmed by IR and Raman spectroscopy and mass spectrometry. The antimicrobial activity of the produced composites (PMMA + TOCs) was estimated against Gram-positive (*Staphylococcus aureus* ATCC 6538 and *S. aureus* ATCC 25923) and Gram-negative (*Escherichia coli* ATCC 8739 and *E. coli* ATCC 25922) bacteria and yeasts of *Candida albicans* ATCC 10231. All produced composites showed biocidal activity against the bacteria. Composites containing $\{Ti_4O_2\}$ cores and the $\{Ti_3O\}$ core stabilized by the 4-hydroxybenzoic ligand showed also high activity against yeasts. The results of investigations carried out suggest that produced (PMMA + TOCs) composites, due to their microbiocidal activity, could find an application in the elimination of microbial contaminations in various fields of our lives.

Keywords: antimicrobial activity; oxo-titanium(IV) complexes; polymer-inorganic composites; physicochemical properties; thermal properties

1. Introduction

The unique physical and chemical properties of materials based on titanium dioxide, i.e., photocatalytic activity, hydrophilicity, or strong absorption of UV radiation, contribute to their wide-application inter alia in various fields of chemical, cosmetics, biomedical, pharmaceutical, and disinfecting applications [1–5]. The photocatalytic activity of TiO_2 nanoparticles or nanocoatings, associated with the electron transfer between the valence band and the conduction one (the O2*p*-Ti3*d* charge transfer transition), which can take place in the presence of photons of wavelengths smaller than 350 nm (this corresponds to ca. 5% of the daylight), is of particular importance [3,4,6]. The above-mentioned phenomenon initiates the oxidation and reduction reactions, which proceed on the surface of TiO_2 nanoparticles/nanocoatings and lead to the formation of the reactive oxygen species (ROS) responsible for the antimicrobial activity of these materials, among others [3]. Aiming to extend the absorption range of TiO_2 in daylight, attention was paid to the oxo-titanium(IV) complexes (TOCs), which contain $\{Ti_aO_b\}$ cores of different architectures in their structures and their potential

use as antimicrobial and photocatalytic active substrates [7–11]. These compounds are studied for the possibility of their use for the photoinduced degradation of organic dyes or water splitting [8,12]. In the case of TOCs, the electron transfer takes place also between the 2*p* electron shell of the oxygen atom and the 3*d* shell of the titanium atom; however, the presence of ligands, which stabilize the oxo-titanium(IV) complex cluster, act as photosensitizers, and in this way, the radiation can be absorbed in a wider range [13,14]. By placing the ligands in the coordination sphere (e.g., carboxylate ligands (-O_2CR')), the orbitals HOMO-LUMO of ligands and the {Ti_aO_b} core can be mixed. As a result, the distance for electrons to move is smaller. The charge transfer from the ligands to the cluster core is possible due to its low-energy absorption band [15,16]. The photocatalytic activity of the oxo-titanium(IV) complexes, of the different {Ti_aO_b} core architectures and possessing various carboxylic ligands, was most often assessed based on the photodegradation processes of organic dye aqueous solutions, such as methylene orange (MO), methylene blue (MB), and rhodamine B (RB) [16–19]. The samples, during the photocatalytic experiments were mostly irradiated by UV light in the range 315–400 nm; however, also, visible light was used. Kim et al. studied the oxo-Ti(IV) complexes with the {Ti_6O_6} core, and stabilized by such carboxylate ligands as 4-aminobenzoic, 4-amino-2-fluoro-benzoic, 4-amino-2-chloro-benzoic, 4-amino-3-chloro-benzoic, and 5-dichlorobenzoic acids, the anions were especially interesting. They showed a direct dependence of oxo-complex photocatalytic activity versus the way of -O_2CR' group functionalization. This effect is closely related to the change in the distance between HOMO and LUMO orbitals in the tested compounds [19]. The results of our earlier studies on the photocatalytic activity of oxo-clusters with {Ti_3O} and {Ti_4O_2} cores also exhibited a significant influence in the way carboxylate ligands functionalize [20–22]. According to these works, the oxo-Ti(IV) complexes stabilized by 9-fluorenecarboxylate and 4-aminobenzonate ligands revealed the best photocatalytic properties in the photodegradation of the methylene blue (MB) solution [20,21].

An interesting issue that may be related to the photocatalytic activity of oxo-Ti(IV) complexes are their antimicrobial properties. Nowadays, searching for new antimicrobial materials results from the necessity of their wide use in everyday life and from their importance in the public health system. Analyzing the literature data, we turned our attention on the antibacterial activity of compounds that contain metal-oxo cores, e.g., oxo-iron(III) complexes [23] or polyoxometalates [24], in their structures. The antibacterial assay of the $(Fe_3O(PhCO_2)_6(MeOH)_3)(NO_3)(MeOH)_2$ cluster showed a significant growth inhibition of *Bacillus cereus* MTCC 1272, *Staphylococcus epidermidis* MTCC 3086, and *Salmonella typhimurium* MTCC 98 but not of *Escherichia coli* MTCC 723 [23]. The results of studies on the antibacterial properties of polyoxometalates against *Moraxella catarrhalis* seem to be particularly interesting. It has been revealed that microbiocidal activity of these types of compounds mainly depends on their composition; metal-oxide anion core shape and size; and the type of the central metal in MO_6 unit (M = Mo, V, and W) [24]. Antimicrobial properties have been found in the mixed ligand titanium dioxide complex, which was produced from TiO_2 nanoparticles and 8-hydroxyquinoline and glycine as the ligands [25]. This complex showed good antifungal activity against *Alternaria alternata*, *Rhizoctania solani*, *Helminthosporium oryzae*, *Fusarium oxysporum*, *Curvularia lunata*, and *Aspergillus niger*, as well as antibacterial activity against *Salmonella*, *E. coli*, *S. epidermis*, and *Enterococcus faecalis*. However, this compound did not show biocidal activity against *Aspergillus fumigatus*, *Aspergillus terreus*, *Trichoderma viride*, and *Cladosporium herbarium* [25]. The investigations of Kaushal et al. revealed the promising biological activities of titanium complexes synthesized by reacting to $TiCl_4$ with Schiff bases (SBs) [26,27]. The synthesized complexes were tested for their antimicrobial activity against pathogenic bacterial strains i.e., *B. cereus* MTCC 6728, *Micrococcus luteus* MTCC 1809, *S. aureus* MTCC 3160, *S. epidermidis* MTCC 3086, *Aeromonas hydrophila* MTCC 1739, *Aclaligenes faecalis* MTCC 126, *Shigella sonnei* MTCC 2957, *Klebsiella pneumoniae* MTCC 3384, *Pseudomonas aeruginosa* MTCC 1035, and *S. typhimurium* MTCC 1253. The $(TiCl_2(SB)_2)$ complexes showed higher antimicrobial activity than their parent Schiff bases [27]. The analysis of the literature reports have shown that the antimicrobial activity of multinuclear oxo-titanium(IV) complexes have not been fully explored so far. Attention should be drawn to the results of the study by Svensson et al., which revealed the antibacterial activity of the oxo-complexes that

consisted of $\{Ti_4O_2\}$ cores stabilized by two triclosan ligands against *S. aureus* [28]. However, in this case, the antibacterial activity of the hydrolyzed form of synthesized complex was studied by the authors.

It should be noted that all the above-mentioned antimicrobial agents can be used in liquid form, which distinguishes them from TOCs systems, which are discussed in the presented paper. The studied compounds (TOCs) containing $\{Ti_3O\}$ and $\{Ti_4O_2\}$ cores due to their hydrophobic natures and their resistance to hydrolysis processes [20–22] were dispersed in a poly(methyl methacrylate) (PMMA) matrix (i.e., films (PMMA + TOCs) were produced). The aim of our investigations was the synthesis of a (PMMA + TOCs) composite characterized by very high surface antimicrobial activity. PMMA is an important material, which, due to sufficient mechanical properties and minimal inflammatory response, is used in different fields of our lives—inter alia, in dentistry [29]. An important direction of the research related to the use of PMMA-based materials is their modification aimed to improving their antimicrobial activity. This effect can be achieved by the addition of inorganic agents such as silver nanoparticles, titanium dioxide, a mixture of titanium dioxide and silicon dioxide nanoparticles, and anion powder (Na_2SiO_3) [29–34]. In this paper, the results of the modification of the PMMA films by the introduction of TOC micro-grains are discussed. The influence of TOC structures on the physicochemical properties and photocatalytic and microbicidal activity of the PMMA + TOC systems was assessed.

2. Results

Studied oxo-complexes (TOCs) were isolated from a the reaction mixture of appropriate titanium alkoxides and organic acids (4:1 alkoxide: acid molar ratio) at room temperature (RT) and at an inert gas atmosphere (Ar, Schlenk line), according to earlier described procedures (Table 1) [20–22]. 4-aminobenzoic acid (HOOC-4-$PhNH_2$) and 4-hydroxobenzoic acid (HOOC-4-PhOH) were used in these reactions. The type of the titanium alkoxide (OR; R = ^{i}Pr and ^{i}Bu) is the factor that directly influences the $\{Ti_aO_b\}$ core architecture.

Table 1. The compositions of the reaction mixtures. THF: tetrahydrofuran.

4:1 Molar Ratio		Isolated	
$Ti(OR)_4$	HOOCR′	Solid Product	Solvent
$Ti(O^iPr)_4$	HOOC-4-$PhNH_2$	(1)	THF/^{i}PrOH
$Ti(O^iPr)_4$	HOOC-4-PhOH	(2)	THF/^{i}PrOH
$Ti(O^iBu)_4$	HOOC-4-$PhNH_2$	(3)	Toluene
$Ti(O^iBu)_4$	HOOC-4-PhOH	(4)	THF/^{i}BuOH

Unfortunately, the weak quality of the formed crystals that caused the structure of isolated solid reaction products were determined based on the analysis of IR, Raman spectra (Figures 1 and 2 and Table 2), and mass spectrometry ones (Table 3).

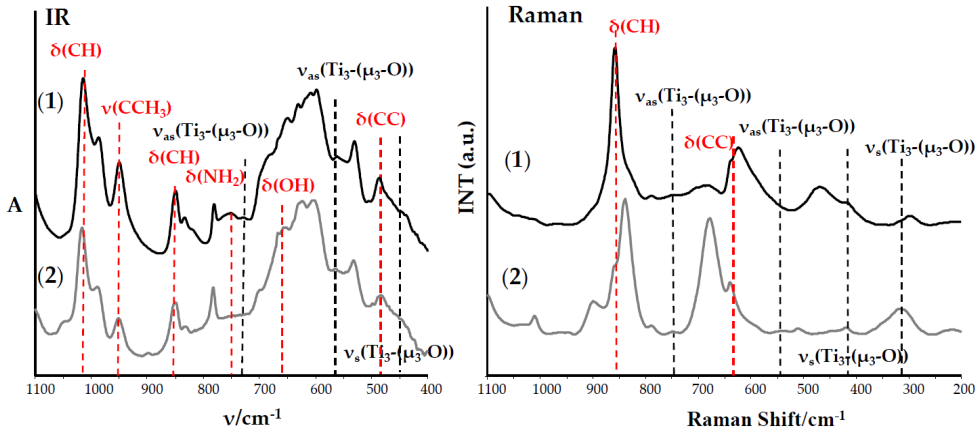


Figure 1. IR and Raman spectra of the (**1**) and (**2**) complexes.

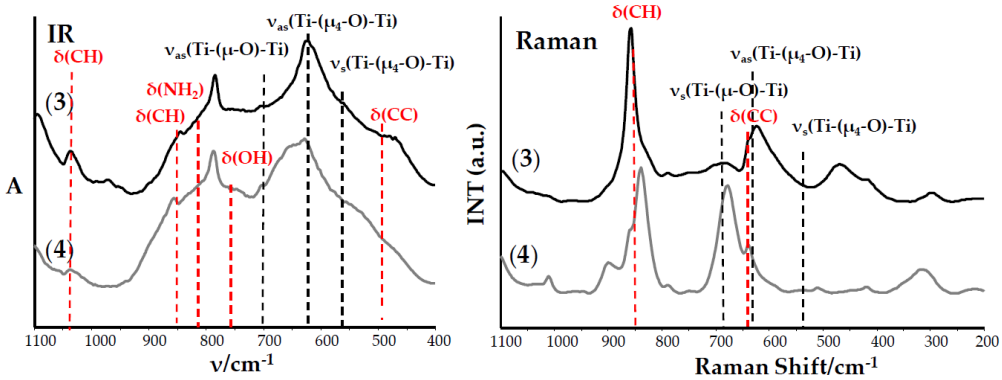


Figure 2. IR and Raman spectra of the (**3**) and (**4**) complexes.

The vibrational spectra analysis of the (**1**)–(**4**) compounds (Table 2) confirmed the presence of the coordinated carboxylate ligands 1514–1536 cm^{-1} ν_{as}(COO)) containing 1,4-substituted Ph groups 780–784 cm^{-1} (ν(CH), IR spectra) functionalized by NH_2 or OH groups (3100–3500 cm^{-1}) and, also, alkoxide groups 1014–1036 cm^{-1} and 948–988 cm^{-1} (ν(Ti-OR)) in their structures. The identification of normal vibrations bands, which descended from titanium-oxide bridge modes, was the spectral proof of the formed $\{Ti_aO_b\}$ core type. For this purpose, the results of our previous DFT calculations were used [20–22]. The medium bands at 483 and 483 cm^{-1} in the IR spectra of (**1**) and (**2**) and weak and very weak bands, which were found at 719–728 cm^{-1}, 539–564 cm^{-1}, and 342–419 cm^{-1} in the IR and Raman spectra of these compounds, were attributed to vibrations of $\{Ti_3\text{-}(\mu_3\text{-}O)\}$ cores (Figure 1 and Table 2).

Table 2. Results of the vibrational spectra studies of the (**1**)–(**3**) complexes (the band intensity: strong (s), middle (m), weak (w), very weak (vw).

	(1)		(2)		(3)		(4)	
Modes	**IR**	**R**	**IR**	**R**	**IR**	**R**	**IR**	**R**
ν(OH) ν(NH_2)	3200–3450	3162 (w)	3300–3500		3200–3450	3175 (w)	3300–3500	
ν(CC) (Ph)	1622 (m) 1601 (m)	1603 (s)	1622 (m) 1603 (m)	1595 (s)	1621 (m) 1603 (m)	1602 (s)	1622 (m) 1603 (m)	1594 (s)
δ(NH_2)	1587 (m)				1589 (m)			
ν_{as}(COO)	1533 (m) 1516 (m)	1524 (m)	1536 (m) 1516 (m)	1519 (w)	1523 (m)	1524 (m)	1536 (m) 1510 (w)	1518 (w)
ν_s(COO)	1462 (w)	1436 (m)	1464 (w)	1450 (w)	1497 (m)	1459 (w)	1498 (m)	1445 (w)
δ(NH_2)	1362 (m)	1306 (m)			1299 (m)	1300 (m)		
ν(C-O) + δ(CC)	1014 (s)		1016 (m)		1036 (m)		1016 (m)	
ν(Ti-OR) + ν(CC) + δ(CH)	986 (m) 949 (m)	856 (m)	988 (m) 951 (m)	838 (m)	971 (m) 948 (w)	856 (m)	988 (m) 951 (w)	838 (m)
ν(CH) 1,4-Ph	780 (m)		782 (m)		784 (s)		782 (m)	
ν(Ti_3-(μ_3-O)	750 (w) 728 (w)	747 (vw) 719 (w)	755 (vw) 727 (vw)	748 (vw)				
ν(Ti_2-(μ-O)					703 (m)	690 (vw)	702 (m)	687 (vw)
ν(Ti_4-(μ_4-O)					639 (m)	623 (w)	634 (m)	610 (vw)
δ(CCC)	683 (w) 666 (m) 622 (m)	622 (m) 605 (w)	701 (w) 638 (m) 629 (w)	678 (m) 638 (w)				
ν(Ti_3-(μ_3-O)	561 (w)		564 (w)	539 (vw)				
ν(Ti_4-(μ_4-O)			532 (w)	510 (w)	532 (m)	548 (vw)	556 (m)	536 (vw)
ν(Ti_3-(μ_3-O)	486 (m)	417 (w)	483 (m)	419 (w)				
ν(Ti_3-(μ_3-O)		342 (vw)		350 (vw)				

Analysis of the electrospray ionization-mass spectrometry (ESI-MS) spectra of (**1**) and (**2**) confirm the presence of peaks, which can be assigned to the fragmentation ions containing {Ti_3-(μ_3-O)} cores (Table 3). Considering these data, we can state that the trinuclear oxo-Ti(IV) complexes, i.e., [$Ti_3O(O^iPr)_8(O_2C$-4-$PhNH_2)_2$] (**1**) and [$Ti_3O(O^iPr)_8(O_2C$-4-$PhOH)_2$] (**2**) were isolated from the 4:1 reaction mixture of $Ti(O^iPr)_4$ and HO_2CR'; R′ = 4-$PhNH_2$ and 4-PhOH using the tetrahydrofuran (THF)/Pr^iOH (1:1 mixture) as a solvent. The bands, which were detected at 702 and 703 cm^{-1} and 687 and 690 cm^{-1} in the IR and Raman spectra of (**3**) and (**4**), were attributed to stretching modes of Ti_4(μ_4-O) bridges, whereas bands at 634–639 cm^{-1} and 532–556 cm^{-1} (IR) and 687–690 cm^{-1} and 536–548 cm^{-1} (Raman) were assigned to vibrations of Ti_4-(μ-O) bridges of {Ti_4O_2} cores (Figure 2 and Table 2). Additionally, in these cases, the presence of peaks attributed to fragmentation ions containing {Ti_4O_2} cores in MS spectra of (**3**) and (**4**) confirms the tetranuclear structures of these complexes (Table 2). The results obtained indicate the isolation of the tetranuclear Ti(IV) oxo-complexes [$Ti_4O_2(O^iBu)_{10}(O_2C$-4-$PhNH_2)_2$] (**3**) and [$Ti_4O_2(O^iBu)_{10}(O_2C$-4-$PhOH)_2$] (**4**) from the mother liquor composed of a 4:1 mixture of $Ti(O^iBu)_4$ and the above-mentioned organic acids and a 1:1 mixture of THF and Bu^iOH as a solvent.

Table 3. The results of electrospray ionization-mass spectrometry (ESI-MS) spectra studies of the (**1**)–(**4**) complexes. TOCs: tetranuclear oxo-titanium(IV) complexes.

TOCs	*m/z*	Fragmentation Ion	Intensity (%)
[$Ti_3O(O^iPr)_8(O_2C$-4-$PhNH_2)_2$] (**1**)	768	$(Ti_3O(O^iPr)_8(O_2C$-4-$PhNH_2))^+$	8
	550	$(Ti_3O(O^iPr)_2(O_2C$-4-$PhNH_2))^+$	36
[$Ti_3O(O^iPr)_8(O_2C$-4-$PhOH)_2$] (**2**)	847	$(Ti_3O(O^iPr)_7(O_2C$-4-$PhOH)_2)^+$	26
	769	$(Ti_3O(O^iPr)_8(O_2C$-4-$PhOH))^+$	90
[$Ti_4O_2(O^iBu)_{10}(O_2C$-4-$PhNH_2)_2$] (**3**)	1080	$(Ti_4O_2(O^iBu)_8(O_2C$-4-$PhNH_2)_2)^+$	5
	881	$(Ti_4O_2(O^iBu)_9)^+$	5
[$Ti_4O_2(O^iBu)_{10}(O_2C$-4-$PhOH)_2$] (**4**)	1229	$(Ti_4O_2(O^iBu)_{10}(O_2CPhOH)_2) + H^+$	8
	945	$(Ti_4O_2(O^iBu)_8(O_2CPhOH))^+$	10

2.1. UV–Vis Diffuse Reflectance Spectra (UV-Vis-DRS) of the (1)–(4) Oxo-Complexes and HOMO-LUMO Gap Determination

UV-Vis-DRS spectra of the (**1**)–(**4**) oxo-complexes were registered at room temperature using magnesium oxide as a standard reference (Figure 3). The HOMO-LUMO gap values were determined basing on the Kubelka-Munk (K-M) function versus light energy, i.e., K = f($h\nu$), where $K = (1-R)^2/2R$ and R is the reflectance, which was used for the optical band gap determination (Figure 3). According to these data, trinuclear oxo-complexes (**1**) and (**2**) exhibit absorption on the border of the UV and Vis range, λ_{max} = 400 nm for (**1**) and λ_{max} = 360 nm for (**2**), and with a sharp absorption edge at ca. 520 nm and 480 nm for complexes (**1**) and (**2**), respectively (Figure 3a). The wide absorption bands with maxima at 405 nm and 390 nm and with the same sharp absorption edge at 500 nm were found in the spectra of (**3**) and (**4**), respectively (Figure 3b). The determined HOMO-LUMO energy gap values (ΔE) revealed significant differences between the oxo-complexes with a different type of stabilized carboxylate groups. The lowest ΔE values were found for (**1**), ΔE = 2.0 eV, and (**3**), ΔE = 2.15 eV, i.e., oxo-complexes containing -O_2C-4-$PhNH_2$ ligands. The HOMO-LUMO energy gap values of complexes that contain the -O_2C-4-PhOH groups in their structures were the highest and were equal to ΔE = 2.38 eV for (**2**) and ΔE = 2.25 eV for (**4**) (Figure 3).

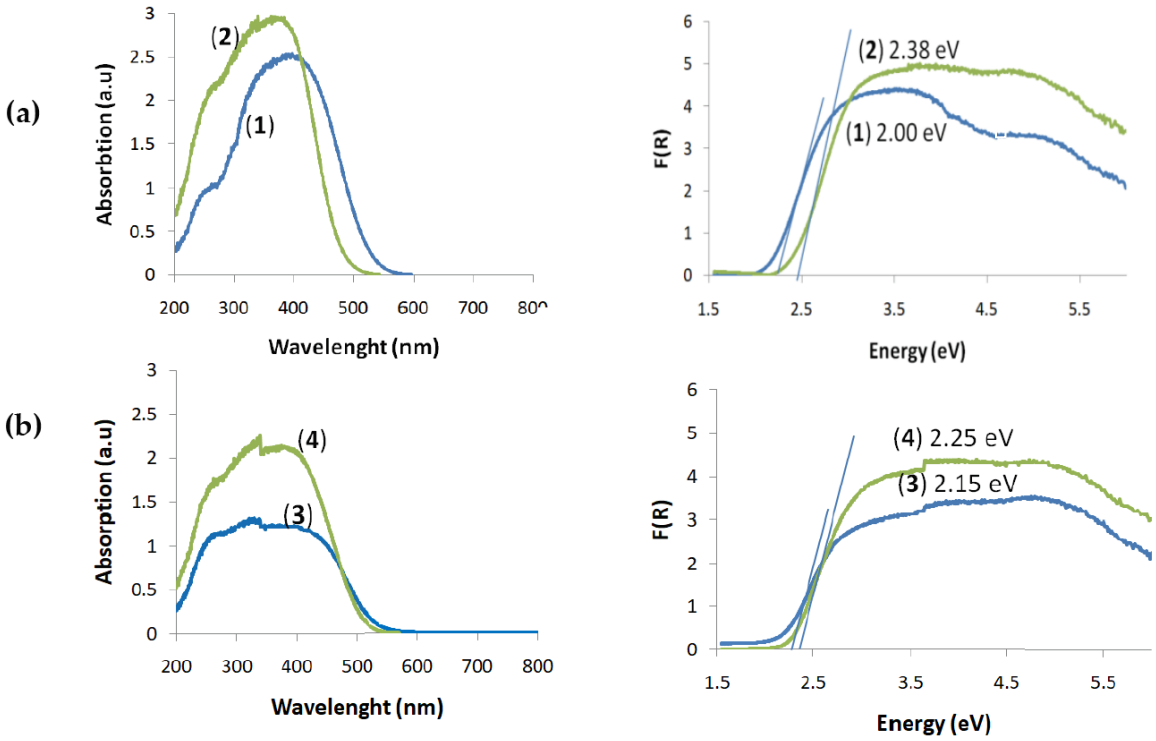


Figure 3. Solid-state UV-Vis-diffuse reflectance spectra (DRS) of the (**1**)–(**4**) micro-grains (the left side) and Kubelka-Munk function versus light energy plot for the HOMO-LUMO gap determination (the right side): (**a**) $[Ti_3O(O^iPr)_8(O_2CC_6H_4NH_2)_2]$ (**1**) and $[Ti_3O(O^iPr)_8(O_2CC_6H_4OH)_2]$ (**2**) and (**b**) $[Ti_4O_2(O^iBu)_{10}(O_2CC_6H_4NH_2)_2]$ (**3**) and $[Ti_4O_2(O^iBu)_{10}(O_2CC_6H_4OH)_2]$ (**4**).

2.2. (PMMA + TOC) Composites

The photocatalytic properties of the (**1**)–(**4**) titanium(IV) oxo-complexes (TOCs) and their antimicrobial activity were estimated using (PMMA + TOC) composite foils produced by the dispersion of 20 wt.% TOC micro-grains in the PMMA matrix [21,22]. SEM images, presented in Figure 4, show that composite foils (PMMA + (**1**), (**2**), and (**4**)) contain the dispersed TOC grains of diameters 100–300 μm. In the case of (PMMA + (**3**)), fine grains (of diameters 3–5 μm) of the oxo-complex that may form larger aggregates are dispersed in the polymer matrix. The registration of Raman microscopy maps allowed to investigate the TOC grain presence and distribution in the PMMA matrix (Figure 5).

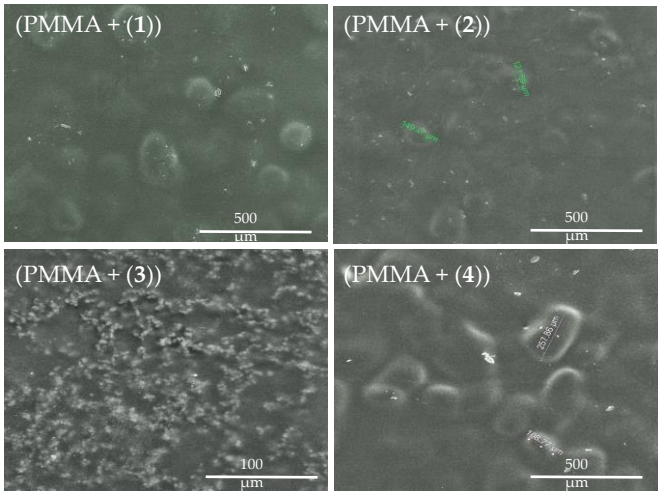


Figure 4. SEM images of poly(methyl methacrylate) (PMMA) + TOCs and TOCs= (**1**)–(**4**) composites dispersed in the PMMA matrix.

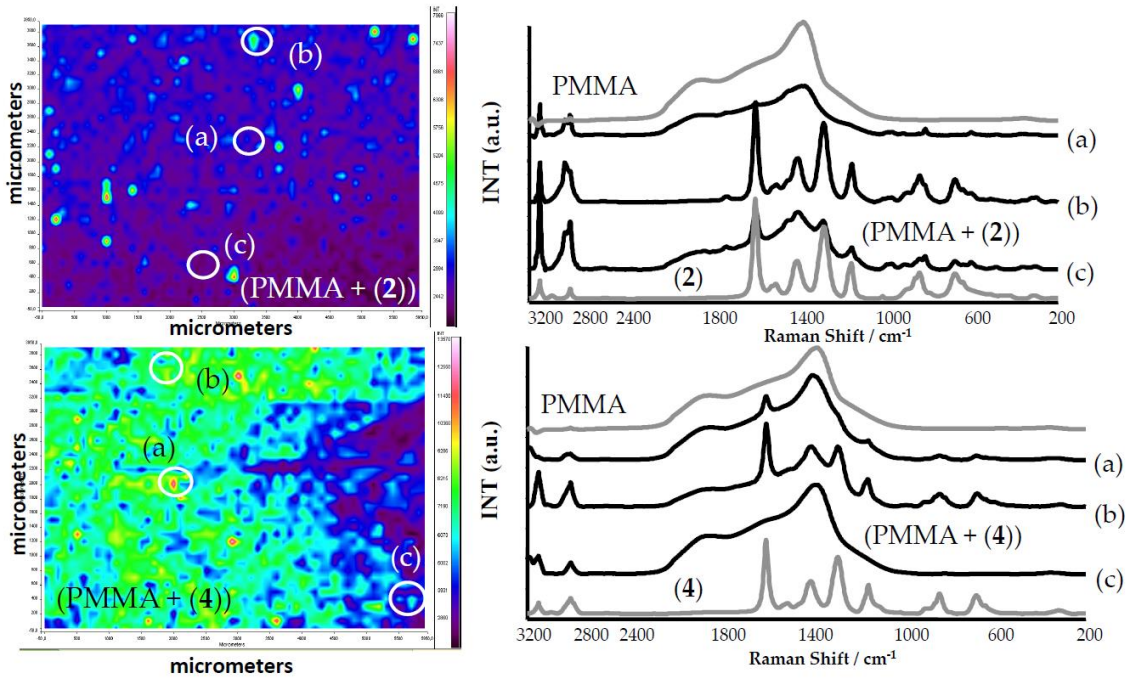


Figure 5. Raman microscopy maps, registered for PMMA + TOC composites (TOCs (**2**) and (**4**)). The Raman spectra, in selected points (a)–(c) on the surface of PMMA + TOCs, are presented alongside.

An analysis of the Raman spectra of composite foils proved the presence of tri- and tetranuclear titanium(IV) oxo-complexes of the earlier determined structure. The use of an ultrasonic bath for the dispersion of TOC grains in the polymer solution allowed the appropriate uniform distribution of the fine grains of TOCs throughout the entire polymer volume (Figure 5). However, probably, the solvent evaporation led to the formation of larger TOC grains and places dominated by the polymer.

2.3. Thermal Analysis of PMMA/TOC Composites

The use of thermogravimetric analysis (TGA) and differential scanning calorimetry (DSC) allowed the thermal characterization of (PMMA + TOCs) composites and the PMMA matrix in the temperature range 30–500 °C at inert atmosphere. The results of these investigations are presented in Table 4 and Figure 6. The analysis of the TGA data of all studied samples revealed a slight weight loss (10–15%), which occurred below 280 °C (I Stage), and the major one (70–85%) between 280 and 450 °C (II Stage). Considering the previous investigations, Stage I can be attributed to the loss of the residual solvent and/or monomer, while Stage II was due the samples' thermal decomposition [35,36].

Table 4. Thermal parameters received from thermogravimetric analysis (TGA) and differential scanning calorimetry (DSC) of the poly(methyl methacrylate) (PMMA) and (PMMA + TOCs) composites (T_g = glass transition temperature, T = evaporation temperature of an unreacted monomer, T_m = melting temperature. T_{max} = temperature in the thermal transition maximum, Δm = thermal transition weight loss).

	DSC			TGA		
Composite	**T_g/°C**	**T/°C**	**T_m/°C**	**Stage I T_{max}/°C/Δm/%**	**Stage II T_{max}/°C/Δm/%**	**Solid Residue at 450 °C (%)**
PMMA	99.6	150.8	368.6	194.9/12	365.1/85	3
(PMMA+(1))	100.6	-	370.4	188.2/12	367.8/70	18
(PMMA+(2))	101.2	-	375.7	183.9/11	365.4/74	15
(PMMA+(3))	99.0	-	377.8	159.9/15	372.7/76	9
(PMMA+(4))	115.2	-	364.5	171.0/10	374.0/79	11

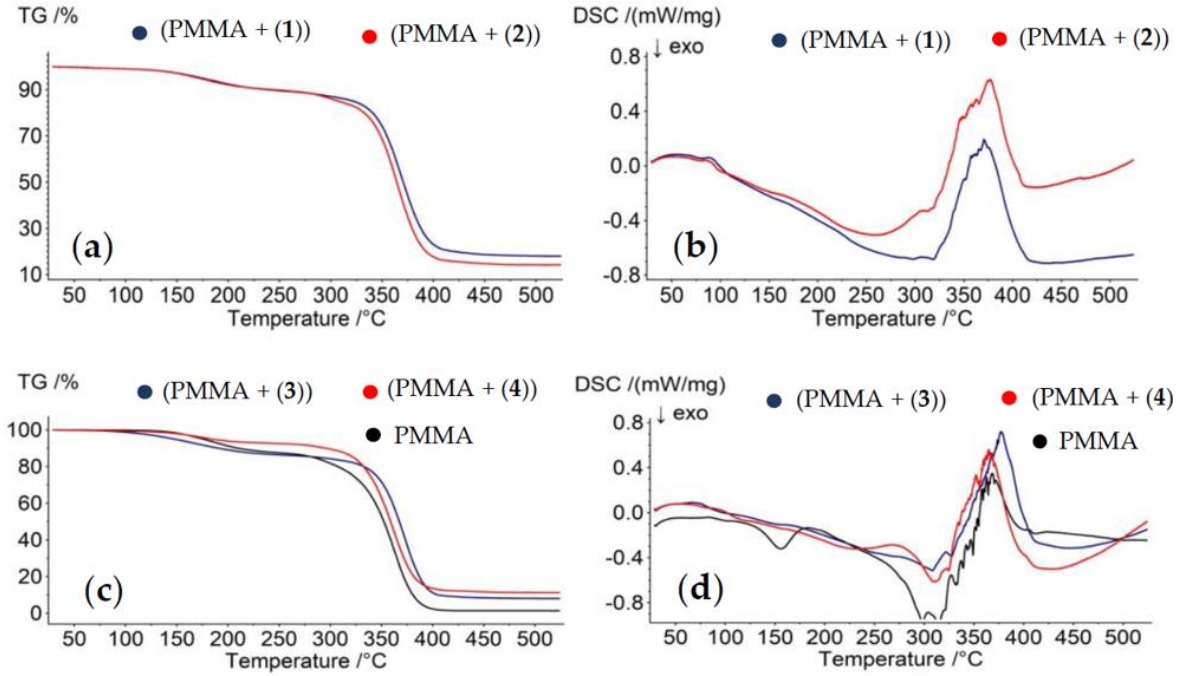


Figure 6. Thermogravimetric curves (TGA) (**a**,**c**) and the differential scanning calorimetry curves of (DSC) (**b**,**d**) of the produced composite materials (PMMA + (**1**)–(**4**)) and PMMA.

An analysis of the DSC thermograms exhibits that the PMMA matrix has a glass transition temperature (T_g) at 99.6 °C, while the exothermic region at 150.8 °C (T), according to previous reports, can be assigned to the evaporation of an unreacted monomer [37] (Figure 6d). The latter effect in the DSC curves of (PMMA + (**1**)–(**4**)) samples was not observed. The endothermic peak at 368.6 °C, which was found on the PMMA DSC thermogram, can be assigned to the PMMA melting temperature (T_m). In the case of composite films enriched with (**1**), (**2**), and (**3**) oxo-complexes, the strong endothermic peaks appear at 370.4 °C, 375.7 °C, and 377.8 °C; this is above the T_m of the pure PMMA matrix. The exception is (PMMA + (**4**)), for which the T_m was registered at about 364.5 °C.

*2.4. Estimation of Photocatalytic Activity of the (**1**)–(**4**) Oxo-Complexes*

The photocatalytic activity of the (PA + TOCs) systems, with TOCs (**1**)–(**4**), was estimated on the basis of the photodecolorization process of the methylene blue (MB) solution irradiated in the UVA range, according to the ISO 10678:2010 procedure [38,39]. The changes of MB concentrations versus irradiation times for the studied (PMMA + TOCs) composites and the reaction observed rate constants are presented in Figure 7 and Table 5. According to these data, the (PMMA + (**3**)) and (PMMA + (**4**)) composites exhibit the best photocatalytic activity. Simultaneously, in the case of the (PMMA + (**1**)) and (PMMA (**2**)) samples, the very weak photocatalytic activity that was noticed ((PMMA + (**1**)) has activity similar to the pure PMMA (difference in absorbance during 180-min measurements, $\Delta A_{180} = 0.011$). The calculated values of ΔA_{180} are presented in Table 5. Moreover, the photodegradation of Rhodamine B of the above-mentioned composite films was carried out under VIS light, and the obtained results are presented in Figure 7 and in Table 5 [40].

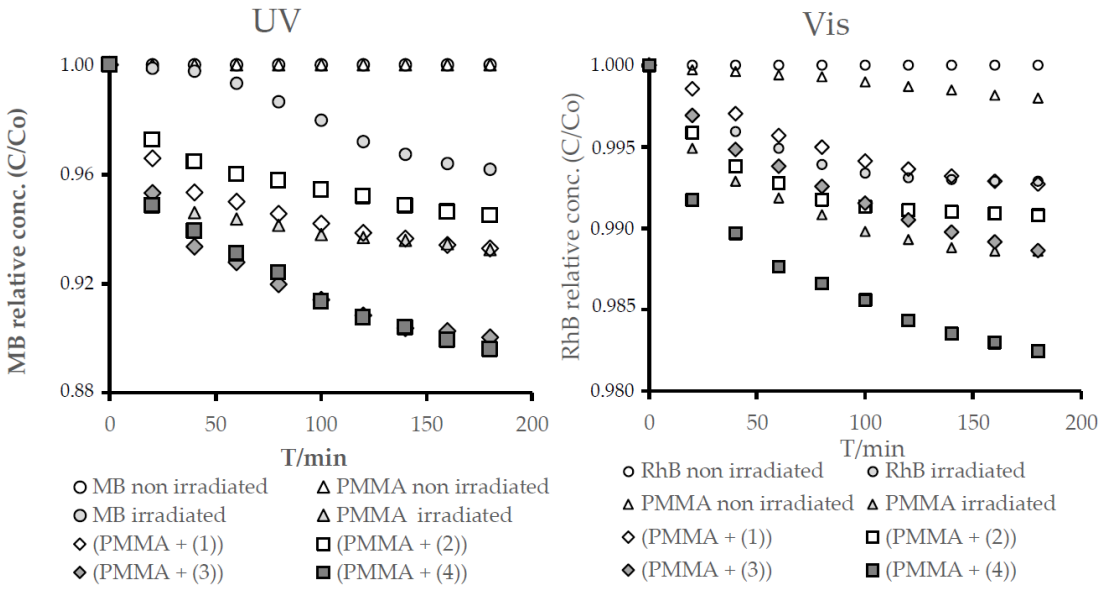


Figure 7. Changes in the concentrations of the methylene blue (MB) and Rhodamine B (RhB) solutions as a function of time for the respective composite materials irradiated with UV and Vis light.

Table 5. Organic dye decolorization percentages and ΔA_{180} parameters for the studied reactions in relation to the composites.

Composite	MB Decolorization [a] (%)	ΔA_{180}	ΔA_{180} in Reference to PMMA
PMMA+(1)	6.70	0.067	–0.001
PMMA+(2)	5.50	0.055	–0.013
PMMA+(3)	9.97	0.100	0.032
PMMA+(4)	10.42	0.104	0.036
PMMA(irradiated)	6.76	0.068	-
Composite	**RhB Decolorization [b] (%)**	**ΔA_{180}**	**ΔA_{180} in Reference to PMMA**
PMMA+(1)	0.73	0.007	–0.004
PMMA+(2)	0.92	0.009	–0.002
PMMA+(3)	1.14	0.011	0
PMMA+(4)	1.75	0.018	0.007
PMMA(irradiated)	1.14	0.011	-

[a] Methylene blue (MB) decolorization at the end of the measurements (t = 180 min). [b] Rhodamine B (RhB) decolorization at the end of the measurements (t = 180 min).

2.5. Antimicrobial Activity of (PMMA + TOCs) Composites

The results of the (PMMA + (**1**)–(**4**)) antimicrobial activity tests against Gram-positive (*S. aureus* ATCC 6538 and *S. aureus* ATCC 25923) and Gram-negative (*E. coli* ATCC 8739 and *E. coli* ATCC 25922) bacteria and yeasts of *Candida albicans* ATCC 10231 of (PMMA + TOCs) composites, where TOCs (**1**)–(**4**) are presented in Table 6. According to these data, all of the (PMMA + TOCs) composites showed high antimicrobial activity against all tested bacteria (*R* between 2.5–6.0). In case of tests performed on the yeasts of *C. albicans* biocidal activity, $R \geq 2$ or 99% was found for PMMA (**2**)–(**4**)—namely, the complex containing the $\{Ti_3O\}$ core and stabilized by the 4-hydroxybenzoic ligand, as well as for complexes with $\{Ti_4O_2\}$ cores but not for PMMA (**1**), which is a complex with a $\{Ti_3O\}$ core and stabilized by the $-O_2C$-4-$PhNH_2$ ligand.

Table 6. Antimicrobial activity of the (PMMA +TOCs) systems (*R* = biocidal rate (%), *R*% = reduction percentage).

Microorganisms	PMMA+ (1)		PMMA+ (2)		PMMA+ (3)		PMMA+(4)	
	R	***R*%**	***R***	***R*%**	***R***	***R*%**	***R***	***R*%**
E. coli ATCC 8739	2.5	99.6	6.0	>99.99	6.0	>99.99	6.0	>99.99
E. coli ATCC 25922	3.3	99.95	6.0	>99.99	6.0	>99.99	6.0	>99.99
S. aureus ATCC 6538	6.0	>99.99	6.0	>99.99	6.0	>99.99	6.0	>99.99
S. aureus ATCC 25923	6.0	>99.99	6.0	>99.99	6.0	>99.99	6.0	>99.99
C. albicans ATCC 10231	1.7	85.0	6.0	>99.99	6.0	>99.99	6.0	>99.99

$R \geq 2$ is a biocidal effect when the microbial growth is reduced at least 100 times (99.0%).

3. Discussion

The multinuclear oxo-titanium(IV) complex applicability as a potentially new group of agents with antimicrobial properties was assessed based on carried out investigations. Considering the results of previous works, the oxo-clusters forming the small $\{Ti_aO_b\}$ core structures (i.e., $\{Ti_4O_2\}$ and $\{Ti_3O\}$), and stabilized by $-O_2C$-4-PhR′ (R′ = $-NH_2$, -OH) ligands have been chosen to further microbiological experiments [20–23]. The complexes were isolated as micro-grain powders from the reaction mixtures of appropriate titanium alkoxides and organic acids (4:1 molar ratio) at room temperature and in inert atmosphere. The structure of the isolated compounds such as $(Ti_3O(O^iPr)_8(O_2C$-4-PhR′$)_2)$ (R′ = $-NH_2$ (**1**), -OH (**2**)), $(Ti_4O_2(O^iBu)_{10}(O_2C$-4-PhR′$)_2)$ (R′ = $-NH_2$ (**3**), and -OH (**4**)) were determined as a result of IR, Raman, and ESI-MS spectra analyses. Studies of UV-Vis-DRS spectra revealed that the absorption maximum of the (**1**)–(**4**) compounds is shifted towards the visible range, i.e., 360–405 nm, with a sharp absorption edge between 480–520 nm (Figure 3). The results of the previous investigations proved that the $\{Ti_aO_b\}$ cores were absorbed in the UV range, which is due to the O2*p*-Ti3*d* charge transfer transition [41]. The shifting of the absorption to the visible range, which was registered in the spectra of the (**1**)–(**4**) compounds, can be explained by the ligand-to-core charge transfer (LCCT) from the $-O_2CR'$ (R′ = 4-PhNH$_2$ or 4-PhOH) ligands to the tri- or tetranuclear titanium-oxo cores. A similar effect was discussed by Cui et al. for a group of multinuclear Ti(IV)-oxo complexes stabilized by 4-chlorosalicylate ligands [42]. The designated values of the HOMO-LUMO gap energy for the studied oxo-complexes changes in the row (**1**) < (**3**) < (**4**) < (**2**) (Figure 3). The analysis of these data confirms that the type of carboxylate ligand, which stabilizes the $\{Ti_aO_b\}$ skeleton, is the main factor allowed to effectively control the HOMO-LUMO energy gap of multinuclear oxo-complexes. This effect was highlighted during earlier studies of Ti(IV)-oxo clusters of similar core structures and significant different carboxylate ligands [13,14,21,22,41,42]. The influence of the $\{Ti_aO_b\}$ cluster core size on the HOMO-LUMO energy gap (E_g) is definitely more negligible, e.g., the results of Cui et al.'s investigations revealed that, for the $\{Ti_4O\}$, $\{Ti_{11}O_9\}$, and $\{Ti_{14}O_{12}\}$ clusters stabilized by O^{i}Pr and 4-chlorosilicylate ligands, the E_g values were 3.0, 2.8, and 2.9 eV, i.e., they differed from each other by 0.1 and 0.2 eV [42]. In the case of the studied $\{Ti_3O\}$ ((**1**) and (**2**)) and $\{Ti_4O_2\}$ ((**3**) and (**4**)) clusters, these differences amounted to 0.13 and 0.15 eV, respectively (Figure 3).

The research carried out led to the isolation of micro-grained powders of TOCs containing $\{Ti_3O\}$ ((**1**) and (**2**)) and $\{Ti_4O_2\}$ ((**3**) and (**4**)} cores, in which the absorption maximum was shifted towards the UVA-Vis range in comparison to TiO_2 (UV, λ_{max} = 300–350 nm [43]). The type of the carboxylate ligand, which stabilizes the $\{Ti_aO_b\}$ core, influences the HOMO-LUMO gap values (ΔE), i.e., ΔE (**1**) and (**2**) < ΔE (**3**) and (**4**).

Due to the hydrophobic characters of studied powders, their photocatalytic and microbiocidal activity were estimated using (PMMA + TOCs) composite films of 0.25–0.50-μm thickness. The analysis of the SEM images proved that the uniform dispersion of TOC fine grains (3–5 μm) in the PMMA matrix was found only in the (PMMA + (**3**)) composite, while, in the cases of (PMMA + TOCs and TOC = (**1**), (**2**), and (**4**)) composites, the studied materials contained the dispersed, larger (100–300 μm) TOC grains (Figure 4). The nonuniform distribution of TOCs in composite films revealed the analysis of Raman microscopy maps of the (PMMA + (**2**) and (**4**)) films (Figure 5). The large grains of TOCs

are separated from each other by the pure polymer sites and by the areas that are formed by fine grains dispersed in PMMA matrices. The thermal characterization of (PMMA + (**1**)–(**4**)) showed a lack of significant differences between their thermal properties and the PMMA matrix. However, higher thermal decomposition temperatures of composite films versus the pure polymer indicate that the Ti(IV)-oxo complex addition to the PMMA matrix improves its thermal stability. A similar effect was observed for the PMMA matrix containing 20% $BaTiO_3$ [37]. While analyzing the data presented in Table 3, attention should be paid to the differences in the thermal stability of (PMMA + TOCs) composites resulting from the type of added oxo-cluster. The dispersion of trinuclear oxo-complexes in the PMMA matrix slightly improves the thermal stability of the composite in comparison to the pure polymer, i.e., 0.3–2.7 °C, while this difference is clearer and was found to be 7.6–8.9 °C for the tetranuclear ones (Table 4).

For the reason that studied oxo-complexes can be a potential source of the reactive oxygen species (ROS), before the antimicrobial tests, their photocatalytic activity was determined. Luo et al. [18] and Lv et al. [44] demonstrated the promising photocatalytic activity of the oxo-Ti(IV) clusters dispersed in solutions of MO (methyl orange) and MB. Considering the potential application of TOCs (i.e., (**1**)–(**4**)) clusters, as an antimicrobial agent introduced to the polymer matrix (e.g., PMMA), the photocatalytic activity assessment was made for their (PMMA + (**1**)–(**4**)) composites. Our earlier studies drew our attention to the good photocatalytic activity of ($Ti_4O_2(O^iPr)_{10}(O_2C\text{-}4\text{-}PhNH_2)_2$), which the 20 wt.% addition to the polystyrene (PS) matrix or PMMA was one, clearly improved the photodecolorization effect of methylene blue (MB) solution [21,22]. Additionally, trinuclear systems exhibited good photocatalytic activity, which, in the case of ($Ti_3O(O^iBu)_8(O_2CR')_2$), (R′ = $-C_{13}H_9$, -3-$PhNO_2$) was proven to be better than for the appropriate tetranuclear oxo-Ti(IV) systems [22]. In the case of the (PMMA + (**1**)–(**4**)) films, the best photocatalytic activity revealed the (PMMA + (**4**)) system irradiated with UVA and Visible light for the MB solution and RhB one, respectively. The PMMA film containing uniformly dispersed fine grains of (**3**) showed slightly weaker activity also in the UVA-Vis range. Cui et al. drew attention to the importance of the size of the oxo-cluster and the related specific surface area [42]. In our case, the cluster size was similar, while the sizes of the grains dispersed in the PMMA matrix were different (Figure 4), which can be associated with the influence of the grain surfaces on their photocatalytic activity. It is interesting that a decrease the of Ti_3O core size of the oxo-clusters influences the significant decrease of the (PMMA + TOCs) composites (where the TOC (**1**) and (**2**)) have photocatalytic activity, especially in Vis range, and practically no significant changes in UV activity.

The (PMMA + TOCs) systems were sterilized with the use of UVC light, which, according to our UV–Vis-DRS measurements, did not activate the studied samples. In the next stage, the samples were irradiated with natural indoor light directly before inoculation with microorganisms. Considering the results of our earlier works regarding the photocatalytic activity of the (polymer + TOCs) systems [21,22], we assumed that the antimicrobial mechanism of the action of the TOCs could be similar to that of the TiO_2-assisted ultraviolet treatment (TUV). TUV is a well-known technique used in water disinfection [45,46] or the food industry [47] for the inactivation of microorganisms. The degree of photoinduced deactivation of the microorganisms depends on various treatment parameters, the nature of the microorganisms, and environmental conditions [45,48]. The mechanisms for the bactericidal action of TiO_2 photocatalysis are associated with the generation of reactive oxygen species (ROSs), such as superoxide radical anion ($O_2^{-}\cdot$), hydrogen peroxide (H_2O_2), and hydroxyl radical (OH·), which cause oxidative damage to living organisms [47,49]. Many authors suggested that the cell membrane is the primary site of ROS attack [50–52]. This attack of the cell membrane by ROS induce lipid peroxidation. The cell membrane damage directly leads to the leakage of minerals, proteins, and genetic materials, which is the root cause of cell death [51]. Apart from the cytoplasmic membrane, the supercoiled plasmid DNA, genomic DNA, and internal organelles are destructed when the bacteria are exposed to TUV [47]. Similar mechanisms of PMMA coated with TiO_2 action against *E. coli* and *S. aureus* were suggested by Su et al. [49]. Moreover, they claimed that a further oxidative attack of internal cellular components accelerates the cell death and, ultimately, results in the decrease of

the survival ratio of both tested bacterial strains, namely *S. aureus* and *E. coli* BL21. Furthermore, Pan et al. [53] evaluated the antibacterial properties of nano-trititanate ($H_2Ti_3O_7$ nanomaterial) against *E. coli* MC1061 and observed that the bactericidal capabilities of these nano-trititanates were more significant compared to nano-TiO_2, both with and without exposure to UV light. Various nano-titanates activated with UV light inhibited the bacterial growth in the range of 11.9–57.1%, while these nonirradiated in the range of 25.7–94.7%. The dependence between the photocatalytic properties and antimicrobial activity was also noticed for studied foils of (PMMA + TOCs) composites, containing the 20 wt.% of (**1**)–(**4**) TOCs. The weakest biocidal activity was observed for the (PMMA + (**1**)), which simultaneously showed the worst photocatalytic properties, even irradiated by the light in the UVA-Vis range. The photocatalytic activity of the (PMMA + (**2**)–(**4**)) films was higher, which can explain the strong inhibition of microorganism growth (>99.99%) on their surfaces. It should be noted that the biocidal activity of the (PMMA + TOC) composite films was assessed for 20 wt.% of TOC micro-grain contents due to our earlier studies of (polymer + (**3**)) composite photocatalytic activity (polymer PS and PMMA) [22]. Although ROS generation is the main proposed mechanism of antimicrobial activity of titanium nanomaterials or titanium nanomaterial-containing complexes, the other mechanism of action should be also considered. It is well-known that some nanomaterials, especially metal-based ones, exhibit strong inhibitory effects towards a broad spectrum of bacterial strains. It is claimed that the biocidal effect of these materials, including titanium oxide nanoparticles, results from the "electromagnetic" attraction between the microbe and metal oxide nanoparticles, as microorganisms carry a negative charge while metal oxides carry a positive charge [54]. Overall, metal-based nanoparticles may interact with the sulfur-containing proteins present in the cell envelopes causing irreversible changes in the cell wall structure, resulting in its disruption and affecting the permeability of the cell membrane by altering transport activity through the plasma [55] or disrupting the ATP production [56]. Nanoparticles can further penetrate inside the microbial cells and interact with ribosomes and biomolecules such as proteins, lipids, and DNA, which may alter translation, replication, and other processes in microbial cells. Moreover, the ion release, as a secondary oxidation process, contributes to the biocidal properties of nanomaterials. Metal ions also affect the losses in the ability to replicate DNA, translation process in ribosomes, and protein activities [57–59]. They can affect membrane transport and the release of potassium (K^+) ions from the microbial cells. The increase of membrane permeability caused by both nanomaterials and released ions may lead to the leakage of cellular contents, including ions, proteins, reducing sugars, and, sometimes, cellular energy reservoirs (ATP) [58,60–62]. It should, however, be noted that the above-mentioned mechanism can be the result of the direct contact between the nanoparticles and bacterial cell. In the discussed case, the TOC micro-grains were surrounded by the polymer matrix, thus limiting their mutual contact. Therefore, the received results suggested that a mechanism based on the ROS formation seems to be the most probable.

In further investigations, the lowest but still highly active content of TOCs as an antimicrobial agent in the polymer matrix should be determined. Moreover, the possible cytotoxicity of studied (PMMA + TOCs) composites should be assessed, which is extremely important in the case of the potential biomedical applications of these systems. The antimicrobial activity of nanomaterials prevents bacterial adhesion and biofilm formation. This activity is especially important for medical applications of nanomaterials or nanomaterial-containing composites. Biofilms protect the underlying microbes from antibiotics and host defense mechanisms and, thus, may lead to serious infections. Moreover, the antimicrobial properties of nanomaterials may be used to prevent microbial contaminations that cause food spoilage, the spread of foodborne diseases, and bio-fouling of materials [29,63].

4. Materials and Methods

4.1. Materials

Titanium(IV) isopropoxide (Aldrich, St. Louis, MO, USA), titanium(IV) isobutoxide (Aldrich, St. Louis, MO, USA), 4-aminobenzoic acid (Aldrich, St. Louis, MO, USA), and 4-hydroxybenzoic

acid (Aldrich, St. Louis, MO, USA) were purchased commercially and were used without further purification. All solvents used in the synthesis, i.e., tetrahydrofuran (THF), isobutanol (HO^iBu), and isopropanol (HO^iPr) were distilled before their use and stored in argon atmosphere. The processes of Ti(IV) oxo-complexes synthesis were carried out using the standard Schlenk technique in the inert gas atmosphere (Ar) and at room temperature (RT).

4.2. Synthesis of Ti(IV) Oxo-Complexes (TOCs) and (PMMA +TOCs) Composites

The synthesis of $[Ti_3O(O^iPr)_8(O_2CC_6H_4NH_2)_2]$ (**1**): 0.12 g of 4-aminobenzoic acid (0.875 mmol) was added to the solution of 1-mL titanium(IV) isopropoxide (3.5 mmol) in 2 mL of THF/Pr^iOH (1:1), leading to a clear yellow solution. The solution was left for crystallization. The yield based on acid: 68% (0.31 g). Anal. Calc. for $C_{38}H_{68}O_{13}Ti_3N_2$: C, 50.44; H, 7.52; N, 3.10; Ti, 15.93. Found: C, 50.38; H, 7.48; N, 2.99; Ti, 15.96.

The synthesis of $[Ti_3O(O^iPr)_8(O_2CC_6H_4OH)_2]$ (**2**): 0.12 g of 4-hydroxybenzoic acid (0.875 mmol) was added to the solution of 1-mL titanium(IV) isopropoxide (3.5 mmol) in 2 mL of THF/Pr^iOH (1:1), leading to a clear yellow solution. The solution was left for crystallization. The yield based on acid: 74% (0.33 g). Anal. Calc. for $C_{38}H_{66}O_{15}Ti_3$: C, 50.33; H, 7.28; Ti, 15.89. Found: C, 50.81; H, 7.22; Ti, 15.80.

The synthesis of $[Ti_4O_2(O^iBu)_{10}(O_2CC_6H_4NH_2)_2]$ (**3**): complex was synthesized, as reported [21]. 0.12 g of 4-aminobenzoic acid (0.875 mmol) was added to the solution of 1.19-mL titanium(IV) isobutoxide (3.5 mmol) in 2 mL of toluene, leading to a clear yellow solution. The solution was left for crystallization. The yield based on acid: 41% (0.22 g). Anal. Calc. for $C_{54}H_{102}O_{14}Ti_4N_2$: C, 52.86; H, 8.38; N, 2.28; Ti, 15.61. Found: C, 53.14; H, 7.83; N, 2.05; Ti, 15.56.

The synthesis of $[Ti_4O_2(O^iBu)_{10}(O_2CC_6H_4OH)_2]$ (**4**): 0.12 g of 4-hydroxybenzoic acid (0.875 mmol) was added to the solution of 1.19-mL titanium(IV) isobutoxide (3.5 mmol) in 2 mL of THF/Bu^iOH (1:1), leading to a clear yellow solution. The solution was left for crystallization. The yield based on acid: 63% (0.30 g). Anal. Calc. for $C_{54}H_{100}O_{18}Ti_4$: C, 52.77; H, 8.14; Ti, 15.64. Found: C, 51.36; H, 7.92; Ti, 16.01.

The polymer foils containing 20 wt.% of synthesized Ti(IV)oxo-clusters (TOCs) were prepared by an addition of the solution of the TOC solution (ca. 0.25 g of (**1**)–(**4**) TOCs were dispersed in 1 cm^3 of THF) to the poly(methyl methacrylate) (PMMA) solution (1.0 g of PMMA dissolved in 5 cm^3 of THF). The resulting mixtures were stirred in an ultrasonic bath for 120 min; in the next step, they were poured into a glass Petri dish and left for the evaporation of the solvent at RT. The composite foil thickness ca. 50 μm were characterized by Raman and IR spectroscopy and scanning electron microscopy.

4.3. Analytical Procedures

The structures of the isolated solid reaction products (crystals and powders) were confirmed using vibrational spectroscopy methods, i.e., IR spectrophotometry (Perkin Elmer Spectrum 2000 FTIR spectrophotometer (400–4000 cm^{-1} range, KBr pellets)) and Raman spectroscopy (RamanMicro 200 spectrometer (PerkinElmer, Waltham, MA, USA)). Raman spectra were registered using a laser with the wavelength 785 nm, with a maximum power of 350 mW, in the range 200–3200 cm^{-1}, using a 20 × 0.40/FN22 objective lens and an exposure time of 15 s each time. Elemental analyses were performed on an Elemental Analyser vario Macro CHN Elemental Analyser vario Macro CHN Elementar Analysen Systeme GmbH (Elementar, Hanau, Germany). The mass spectra were recorded using the ESI-MS method using a QToFSynapt G2 Si (Waters Corporation, Mundelein, IL, USA) spectrometer. The main measurement parameters: capillary voltage: 2.5–3 kV, source temperature: 110 °C, sampling cone voltage 20–50 V, source offset 40–60 V, desolvation temperature 250–350 °C, cone gas flow: 50.0 dm^3/h, and desolation gas flow: 798.0–900 dm^3/h. The produced PMMA + TOCs foil surfaces were studied using a scanning electron microscope with field emission (SEM, Quanta 3D FEG, Houston, TX, USA). Composite materials underwent thermal treatment (Bruker Optik, Ettingen, Germany) in the range 20–500 °C, with the heating speed of 5 °C/min in the atmosphere of nitrogen.

4.4. HOMO-LUMO Gap Determination

The HOMO-LUMO gap energy values of isolated (**1**)–(**4**) complexes were determined by using diffuse reflectance UV-Vis spectra (UV-VIS-DRS), which were registered between 200 and 800 nm. Jasco V-750 spectrophotometer was used (JASCO Deutschland GmbH, Pfungstadt, Germany). The recorded spectra were evaluated in terms of energy band gap values via Spectra Manager TM CFR software.

4.5. The Photocatalytic Activity Evaluation of (PMMA + TOCs) Composites

The photocatalytic activity of PMMA + TOCs foils (TOCs = (**1**)–(**4**)) was studied by monitoring the degradation processes of MB aqueous solution according to ISO 10678:2010 procedure and, also, Rhodamine B (RhB) solution [38–40]. Foil samples of sizes 10 × 10 mm were preconditioned by exposure to UVA or Vis light for 30 h. In the next step, foils were placed in quartz cuvettes with both dye solutions (V = 3.5 cm^3 and C = 2.0×10^{-5} M). After 12 h in the dark, the solutions were replaced by the appropriate test of MB and RhB solutions (for both: V = 3.5 cm^3 and C = 1.0×10^{-5} M). The prepared samples were exposed to UVA irradiation (18-W lamp, 340–410-nm range, with a maximum at 365 nm) and Vis light (77-W tungsten halogen lamp, range of 350–2200 nm). All cuvettes were covered with quartz glass panes during irradiation. MB absorbance at 660 nm and RhB absorbance at 554 nm were registered (Metertech SP-830 PLUS, Metertech, Inc., Taipei, Taiwan) after 0, 20, 40, 60, 80, 100, 120, 140, 160, and 180 min of irradiation. Percentage of MB decolorization was calculated using the equation

$$\% \text{ dye decolorization} = ((C_0 - C_t)/C_0) \times 100 = ((A_0 - A_t)/A_0) \times 100 \quad (1)$$

where C_0 is an initial concentration of dye, C_t is a dye concentration at a given time t, and A_0 and A_t are absorbances at 0 and t times [38,64].

The rate of both photodegradation processes was estimated by a simple calculation of a difference in absorbance during 180-min measurements (ΔA_{180}). Such kind of calculation is a result of a low degradation degree of dyes.

4.6. The Evaluation of Antimicrobial Properties of (PMMA + TOCs) Systems

Antimicrobial activity of PMMA + TOCs (TOCs = (**1**)–(**4**)) composite foils (30 × 30 × 0.05 mm) was studied against Gram-positive (*S. aureus* ATCC 6538 and *S. aureus* ATCC 25923) and Gram-negative (*E. coli* ATCC 8739 and *E. coli* ATCC 25922) bacteria and yeasts of *Candida albicans* ATCC 10231 using method according to the ISO 22196:2011 standard [65]. All strains were purchased from the American Type Culture Collection (Manassas, VA, USA). PMMA +TOC specimens were sterilized using a UVC lamp for 30 min in the laminar hood (Bioquell, Hampshire, UK) and placed in sterile Petri plates. The earlier investigations revealed that the absorption maximum of the (PMMA + TOCs) samples was found at the UVA-Vis border, which enabled the use of UVC radiation in order for their sterilization. Microbial suspension ($1.0–1.8 \times 10^6$ colony-forming units (cfu) $cm^3/^{-1}$) prepared in sterile deionized water was placed on the surfaces of the appropriate PMMA + TOCs samples and covered with sterile foil films (polypropylene; PP) and incubated for 24 h at 37 °C in a humid atmosphere. The PP film was then removed and microbial suspension collected into a 2-cm^3 centrifuge tube. Subsequently, serial ten-fold dilutions of each sample were prepared. Aliquots (100 µL) of each dilution were aseptically spread over the surface of Tryptic Soy Agar (TSA, Becton Dickinson, Sparks Glencoe, MD, USA) or Sabouraud Dextrose Agar (SDA, Becton Dickinson) in Petri plates for the bacteria and fungi, respectively. Inoculated samples were incubated at 37 °C for 24 h. Assays were performed in triplicate. After incubation, colony-forming units (cfu) were counted on the agar plates. Control was PMMA inoculated with the test microorganism.

The antimicrobial activity was calculated using Formula (2), according to the ISO 22196:2011 standard [65]:

$$R = U_t - A_t \quad (2)$$

where U_t is the average of the common logarithm of the number of viable bacteria in cells/cm^2 recovered from the untreated test specimens (PMMA) after 24 h, and A_t is the average of the common logarithm of the number of viable bacteria in cells/cm^2 recovered from the treated test specimens (PMMA + TOCs) after 24 h. $R \geq 2$ determines the biocidal activity

The percentage reduction (R%) of the bacterial or fungal growth was calculated using Formula (3):

$$R\% = ((B - A)/\mathrm{B}) \times 100 \quad (3)$$

where R is the biocidal rate (%), B—the average number of microorganisms on unmodified PMMA in T_0, and A—the average number of microorganisms on the surfaces of the studied (PMMA + TOCs) composites after 24 h. The 100-times reduction of the number of colonies determines at least 99% of the reduction of microbial growth (biocidal activity).

5. Conclusions

The work carried out led to the production of oxo-titanium(IV) complexes (TOCs), i.e., ($Ti_3O(O^iPr)_8(O_2C$-4-PhR′$)_2$) (**1**) and (**2**) and ($Ti_4O_2(O^iBu)_{10}(O_2C$-4-PhR′) (**3**) and (**4**) (R′ = -NH_2 and -OH), which structures were confirmed by IR, Raman spectroscopy, and ESI-MS spectrometry. The dispersion of 20 wt.% of TOCs (**1**)–(**4**) in the PMMA matrix allowed the formation of (PMMA + TOCs) composite films for which the thermal and photocatalytic properties and biocidal activity were estimated. The obtained results suggest that ($Ti_4O_2(O^iBu)_{10}(O_2C$-4-PhOH$)_2$) (**4**) can be used for the production of composites (polymer + TOC), which, in the form of films, coatings, or resin additives, can be used as a bactericidal agent in various areas of our lives. It should be noted that the potential use of materials based on PMMA with the addition of TOCs in dentistry would require medical experiments carried out in accordance with the procedures specified by Isola et al. [66,67].

Author Contributions: Conceptualization, P.P.; methodology, P.P., B.K., P.G., and A.R.; formal analysis, P.P., B.K., P.G., and A.R.; investigation, B.K. and P.G.; data curation, P.P. and B.K.; writing—original draft preparation, P.P.; writing—review and editing, P.P. and A.R.; and supervision, P.P. and A.R. All authors have read and agreed to the published version of the manuscript.

Funding: This research received no external funding.

Conflicts of Interest: The authors declare no conflict of interest.

References

1. Hashimoto, K.; Irie, H.; Fujishima, A. TiO_2 Photocatalysis: A Historical Overview and Future Prospects. *Jpn. J. Appl. Phys.* **2005**, *44*, 8269–8285. [CrossRef]
2. Chen, X.; Mao, S.S. Titanium Dioxide Nanomaterials: Synthesis, Properties, Modifications, and Applications. *Chem. Rev.* **2007**, *107*, 2891–2959. [CrossRef] [PubMed]
3. Carp, O.; Huisman, C.L.; Reller, A. Photoinduced Reactivity of Titanium Dioxide. *Prog. Solid State Chem.* **2004**, *32*, 33–177. [CrossRef]
4. Fujishima, A.; Zhang, X.X.; Tryk, D.A. TiO_2 photocatalysis and related surface phenomena. *Surf. Sci. Rep.* **2008**, *63*, 515–558. [CrossRef]
5. Benedict, J.B.; Coppens, P. The Crystalline Nanocluster Phase as a Medium for Structural and Spectroscopic Studies of Light Absorption of Photosensitizer Dyes on Semiconductor Surfaces. *J. Am. Chem. Soc.* **2010**, *132*, 2938–2944. [CrossRef] [PubMed]
6. Li, N.; Matthews, P.D.; Luo, H.-K.; Wright, D.S. Novel properties and potential applications of functional ligand-modified polyoxotitanate cages. *Chem. Commun.* **2016**, *52*, 11180–11190. [CrossRef]
7. Assi, H.; Mouchaham, G.; Steunou, N.; Devic, T.; Serre, C. Titanium coordination compounds: From discrete metal complexes to metal–organic frameworks. *Chem. Soc. Rev.* **2017**, *46*, 3431–3452. [CrossRef]
8. Benedict, J.B.; Freindorf, R.; Trzop, E.; Cogswell, J. Large Polyoxotitanate Clusters: Well-Defined Models for Pure-Phase TiO_2Structures and Surfaces. *J. Am. Chem. Soc.* **2010**, *132*, 13669–13671. [CrossRef]
9. Coppens, P.; Chen, Y.; Trzop, E. Crystallography and Properties of Polyoxotitanate Nanoclusters. *Chem. Rev.* **2014**, *114*, 9645–9661. [CrossRef]

10. Rozes, L.; Sanchez, C. Titanium oxo-clusters: Precursors for a Lego-like construction of nanostructured hybrid materials. *Chem. Soc. Rev.* **2011**, *40*, 1006–1030. [CrossRef]
11. Su, H.-C.; Wu, Y.-Y.; Hou, J.-L.; Zhang, G.-L.; Zhu, Q.-Y.; Dai, J. Dye molecule bonded titanium alkoxide: A possible new type of dye for sensitized solar cells. *Chem. Commun.* **2016**, *52*, 4072–4075. [CrossRef] [PubMed]
12. Zou, D.-H.; Cui, L.-N.; Liu, P.-Y.; Yang, S.; Zhu, Q.-Y.; Dai, J. Triphenylamine derived titanium oxo clusters: An approach to effective organic–inorganic hybrid dyes for photoactive electrodes. *Chem. Commun.* **2018**, *54*, 9933–9936. [CrossRef] [PubMed]
13. Fan, Y.; Zhang, Y.; Zou, H.-M.; Li, H.-M.; Cui, Y.; Jing, Q.-S.; Lu, H.-T. Modulating the band gap and photoelectrochemical activity of dicarboxylate-stabilized titanium-oxo clusters. *Inorg. C. Acta* **2018**, *482*, 16–22. [CrossRef]
14. Macyk, W.; Szaciłowski, K.; Stochel, G.; Buchalska, M.; Kuncewicz, J.; Łabuz, P. Titanium(IV) complexes as direct TiO_2 photosensitizers. *Coord. Chem. Rev.* **2010**, *254*, 2687–2701. [CrossRef]
15. Hong, Z.-F.; Xu, S.-H.; Yan, Z.-H.; Lu, D.-F.; Kong, X.-J.; Long, L.-S.; Zheng, L.-S. A Large Titanium Oxo Cluster Featuring a Well-Defined Structural Unit of Rutile. *Cryst. Growth Des.* **2018**, *18*, 4864–4868. [CrossRef]
16. Su, M.K.; Wu, Y.; Tan, W.; Wang, D.; Yuan, M.H. A monomeric bowl-like pyrogallol[4]arene Ti12 coordination complex. *Chem. Commun.* **2017**, *53*, 9598–9601. [CrossRef]
17. Wu, Y.-Y.; Luo, W.; Wang, Y.-H.; Pu, Y.-Y.; Zhang, X.; You, L.-S.; Dai, J. Titanium–oxo–Clusters with Dicarboxylates: Single-Crystal Structure and Photochromic Effect. *Inorg. Chem.* **2012**, *51*, 8982–8988. [CrossRef]
18. Luo, W.; Ge, G. Two Titanium-oxo-Clusters with Malonateand Succinate Ligands: Single-Crystal Structuresand Catalytic Property. *J. Clust. Sci.* **2016**, *27*, 635–643. [CrossRef]
19. Kim, S.; Sarkar, D.; Kim, Y.; Park, M.H.; Yoon, M.; Kim, Y.; Kim, M. Synthesis of functionalized titanium-carboxylate molecular clusters and their catalytic activity. *J. Ind. Eng. Chem.* **2017**, *53*, 171–176. [CrossRef]
20. Janek, M.; Muzioł, T.M.; Piszczek, P. Trinuclear Oxo-Titanium Clusters: Synthesis, Structure, and Photocatalytic Activity. *Materials* **2019**, *12*, 3195. [CrossRef]
21. Janek, M.; Radtke, A.; Muzioł, T.M.; Jerzykiewicz, M.; Piszczek, P. Tetranuclear Oxo-Titanium Clusters with Different Carboxylate Aromatic Ligands: Optical Properties, DFT Calculations, and Photoactivity. *Materials* **2018**, *11*, 1661. [CrossRef] [PubMed]
22. Janek, M.; Muzioł, T.; Piszczek, P. The structure and photocatalytic activity of the tetranuclear titanium(IV) oxo-complex with 4-aminobenzoate ligands. *Polyhedron* **2018**, *141*, 110–117. [CrossRef]
23. Pathak, S.; Jana, B.; Mandal, M.; Mandal, V.; Ghorai, T.K. Antimicrobial activity study of a μ_3-oxo bridged $[Fe_3O(PhCO_2)_6(MeOH)_3](NO_3)(MeOH)_2]$ cluster. *J. Mol. Struct.* **2017**, *1147*, 480–486. [CrossRef]
24. Gumerova1, N.I.; Al-Sayed, E.; Lukáš Krivosudský, L.; Čipčić-Paljetak, H.; Verbanac, D.; Rompel, A. Antibacterial Activity of Polyoxometalates Against Moraxella catarrhalis. *Front. Chem.* **2018**, *6*, 336. [CrossRef]
25. Kumar, S.; Bhanjana, G.; Kumar, R.; Dilbaghi, N. Synthesis, Characterization and Antimicrobial Activity of Nano Titanium(IV) Mixed Ligand Complex. *Mater. Focus* **2013**, *2*, 475–481. [CrossRef]
26. Kaushal, R.; Kumar, N.; Thakur, A.; Nehra, K.; Awasthi, P.; Kaushal, R.; Arora, S. Synthesis, Spectral Characterization, Antibacterial and Anticancer Activity of some Titanium Complexes. *Anticancer Agents Med. Chem* **2018**, *18*, 739–746. [CrossRef] [PubMed]
27. Kaushal, R.; Thakur, S. Syntheses and Biological screening of Schiff base complexes of Titanium(IV). *Chem. Eng. Trans.* **2013**, *32*, 1801–1806. [CrossRef]
28. Svensson, F.G.; Seisenbaeva, G.A.; Kessler, V.G. Mixed-Ligand Titanium "Oxo Clusters": Structural Insights into the Formation and Binding of Organic Molecules and Transformation into Oxide Nanostructures on Hydrolysis and Thermolysis. *Eur. J. Inorg. Chem.* **2017**, *35*, 4117–4122. [CrossRef]
29. Zafar, M.S. Prosthodontic Applications of PolymethylMethacrylate (PMMA): An Update. *Polymers* **2020**, *12*, 2299. [CrossRef]
30. Liu, M.; Zhang, X.; Zhang, J.; Zheng, Q.; Liu, B. Study on Antibacterial Property of PMMA Denture Base Materials with Negative Ion Powder. *Mater. Sci. Eng.* **2018**, *301*, 012034. [CrossRef]
31. Chen, R.; Han, Z.; Huang, Z.; Karki, J.; Wang, C.; Zhu, B.; Zhang, X. Antibacterial activity, cytotoxicity and mechanical behaviour of nano-enhanced denture base resin with different kinds of inorganic antibacterial agents. *Dent. Mol. J.* **2017**. [CrossRef] [PubMed]

32. Sadagar, A.; Khalil, S.; Kassaee, M.Z.; Shahroudi, A.S.; Pourakbari, B.; Bahador, A. Antimicrobial properties of poly(methyl methacrylate) acrylic resins incorporated with silicon dioxide and titanium dioxide nanoparticles on cariogenic bacteria. *J. Orthod. Sci.* **2016**, *5*, 7–13. [CrossRef]
33. De Mori, A.; Di Grgorio, E.; Kao, A.P.; Tozzi, G.; Barbu, E.; Sanghani-Kerai, A.; Draheim, R.R.; Rolado, M. Antibacterial PMMA Composite Cments with Tunable Thermal and Mechanical Properties. *ACS Omega* **2019**, *4*, 19664–19675. [CrossRef] [PubMed]
34. Kumar, M.; Arun, S.; Upadhyaya, P.; Pugazhenthi, G. Properties of PMMA/clay nanocomposites prepared using various compatibilizer. *Int. J. Mech. Mat. Eng.* **2015**, *10*, 7. [CrossRef]
35. Gałka, P.; Kowalonek, J.; Kaczmarek, H. Thermogravimetric analysis of thermal stability of poly(methylmethacrylate) films modified with photoinitiators. *J. Therm. Anal. Calorim.* **2014**, *115*, 1387–1394. [CrossRef]
36. Lu, P.; Huang, Q.; Mukherjee, A.; Hsieh, Y.-L. Effects of polymer matrices to the formation of silicon carbide (SiC) nanoporous fibers and nanowires under carbothermal reduction. *J. Mater. Chem.* **2011**, *21*, 1005–1012. [CrossRef]
37. Elshereksi, N.W.; Mohamd, S.H.; Arifin, A.; Ishak, Z.A.M. Thermal Characterization of Poly(Methyl Methacrylate) Filled with Barium Titanate as Denture Base Material. *J. Phys. Sci.* **2014**, *25*, 15–27.
38. ISO 10678:2010(E) Standards. Fine Ceramics (Advanced Ceramics, Advanced Technical Ceramics)—Determination of Photocatalytic Activity of Surfaces in an Aqueous Medium by Degradation of Methylene Blue. Available online: https://www.iso.org/standard/46019.html (accessed on 10 June 2020).
39. Ehlert, M.; Radtke, A.; Topolski, A.; Śmigiel, J.; Piszczek, P. The Photocatalytic Activity of Titania Coatings Produced by Electrochemical and Chemical Oxidation of Ti6Al4V Substrate, Estimated According to ISO 10678:2010. *Materials* **2020**, *13*, 2649. [CrossRef]
40. Patrick, W.; Dietmar, S. Photodegradation of rhodamine B In aqueous solution via SiO_2@TiO_2 nanosphares. *J. Photochem. Photobiol. A Chem.* **2007**, *185*, 19–25. [CrossRef]
41. Liu, J.-X.; Gao, M.-Y.; Fang, W.-H.; Zhang, L.; Zhang, J. Bandgap Engineering of Titanium-Oxo Clusters: Labile Surface Sites Used for Ligand Substitution and Metal Incorporation. *AngewandeChemie* **2016**, *128*, 5246–5251. [CrossRef]
42. Cui, Y.; Zou, G.-D.; Li, H.-M.; Huang, Y.; Fan, Y. 4-Chlorocalicylate-stabilized titanium-oxo clusters with structures mediated by tetrazole and their photophysical properties. *Polyhedron* **2019**, *157*, 177–182. [CrossRef]
43. Habibi, S.; Jamshidi, M. Sol–gel synthesis of carbon-doped TiO_2 nanoparticles based on microcrystalline cellulose for efficient photocatalytic degradation of methylene blue under visible light. *J. Environ. Technol.* **2020**, *41*, 3233–3247. [CrossRef] [PubMed]
44. Lv, H.-T.; Li, H.-M.; Zou, G.-D.; Cui, Y.; Huang, Y.; Fan, Y. Tioanium-oxo clusters functionalized with cateholate-tye ligands: Modulating the optical properties through charge-transfer transition. *Dalton Trans.* **2018**, *47*, 8158–8163. [CrossRef] [PubMed]
45. Kim, S.; Ghafoor, K.; Lee, J.; Feng, M.; Hong, J.; Lee, D.; Park, J. Bacterial inactivation in water, DNA strand breaking, and membrane damage induced by ultraviolet assisted titanium dioxide photocatalysis. *Water Res.* **2013**, *47*, 4403–4411. [CrossRef]
46. Wu, M.J.; Bak, T.; O'Doherty, P.J.; Moffitt, M.C.; Nowotny, J.; Bailey, T.D.; Kersaitis, C. Photocatalysis of titanium dioxide for water disinfection: Challenges and future perspectives. *Int. J. Photogramm.* **2014**, 973484. [CrossRef]
47. Ramesh, T.; Nayak, B.; Amirbahman, A.; Tripp, C.P.; Mukhopadhyay, S. Application of ultraviolet light assisted titanium dioxide photocatalysis for food safety: A review. *Innov. Food Sci. Emerg. Technol.* **2016**, *38*, 105–115. [CrossRef]
48. Maness, P.; Smolinski, S.; Blake, D.M.; Huang, Z.; Wolfrum, E.J.; Jacoby, W.A. Bactericidal activity of photocatalytic TiO_2 reaction: Toward an understanding of its killing mechanism. *Appl. Environ. Microbiol.* **1999**, *65*, 4094–4098. [CrossRef]
49. Su, W.; Wang, S.; Wang, X.; Fu, X.; Weng, J. Plasma pre-treatment and TiO_2 coating of PMMA for the improvement of antibacterial properties. *Surf. Coat. Technol.* **2010**, *205*, 465–469. [CrossRef]
50. Lin, H.; Xu, Z.; Wang, X.; Long, J.; Su, W.; Fu, X.; Lin, Q. Photocatalytic and antibacterial properties of medical-grade PVC material coated with TiO_2 film. *J. BiomedMater. Res. B Appl. Biomater.* **2008**, *87*, 425–431. [CrossRef]

51. Yu, J.C.; Ho, W.; Lin, J.; Yip, H.; Wong, P.K. Photocatalytic activity, antibacterial effect, and photoinduced hydrophilicity of TiO_2 films coated on a stainless steel substrate. *Environ. Sci. Technol.* **2003**, *37*, 2296–2301. [CrossRef]
52. Huang, Z.; Maness, P.C.; Blake, D.M.; Wolfrum, E.J.; Smolinski, S.L.; Jacoby, W.A. Bactericidalmode of titaniumdioxidephotocatalysis. *J. Photochem. Photobiol. A Chem.* **2000**, *130*, 163–170. [CrossRef]
53. Pan, R.; Liu, Y.; Chen, W.; Dawson, G.; Wang, X.; Li, W.; Dong, B.; Zhu, Y. The toxicity evaluation of nano-trititanate with bactericidal properties in vitro. *Nanotoxicology* **2012**, *6*, 327–337. [CrossRef]
54. Jesline, A.; John, N.P.; Narayanan, P.M.; Vani, C.; Murugan, S. Antimicrobial activity of zinc and titanium dioxide nanoparticles against biofilm-producing methicillin-resistant. *Staphylococcus aureus. Appl. Nanosci.* **2015**, *5*, 157–162. [CrossRef]
55. Ghosh, S.; Patil, S.; Ahire, M.; Kitture, R.; Kale, S.; Pardesi, K. Synthesis of silver nanoparticles using *Dioscoreabulbifera* tuberextract and evaluation of its synergistic potential in combination with antimicrobial agents. *Int. J. Nanomed.* **2012**, *7*, 483–496. [CrossRef]
56. Inbaneson, S.J.; Ravikumar, S.; Manikandan, N. Antibacterial potential of silver nanoparticles against isolated urinary tract infectious bacterial pathogens. *Appl. Nanosci.* **2011**, *1*, 231–236. [CrossRef]
57. Morones, J.R.; Elechiguerra, J.L.; Camacho, A.; Ramirez, J.T. The bactericidal effect of silver nanoparticles. *Nanotechnology* **2005**, *16*, 2346–2353. [CrossRef]
58. Chauhan, R.; Kumar, A.; Abraham, J. A biological approach to the synthesis of silver nanoparticles with *Streptomyces* sp. JAR1 and its antimicrobial activity. *Sci. Pharm.* **2013**, *81*, 607–621. [CrossRef]
59. Jung, W.K.; Koo, H.C.; Kim, K.W.; Shin, S.; Kim, S.H.; Park, Y.H. Antibacterial activity and mechanism of action of the silver ion in *Staphylococcus aureus* and *Escherichia coli*. *Appl. Environ. Microbiol.* **2008**, *74*, 2171–2178. [CrossRef]
60. Lok, C.N.; Ho, C.M.; Chen, R.; He, Q.Y.; Yu, W.Y.; Sun, H. Proteomic analysis of the mode of antibacterial action of silver nanoparticles. *J. Proteome Res.* **2006**, *5*, 916–924. [CrossRef]
61. Kim, S.H.; Lee, H.S.; Ryu, D.S.; Choi, S.J.; Lee, D.S. Antibacterial activity of silver-nanoparticles against *Staphylococcus aureus* and *Escherichia coli*. *Korean J. Microbiol. Biotechnol.* **2011**, *39*, 77–85.
62. Li, J.; Rong, K.; Zhao, H.; Li, F.; Lu, Z.; Chen, R. Highly selective antibacterial activities of silver nanoparticles against *Bacillus subtilis*. *J. Nanosci. Nanotechnol.* **2013**, *13*, 6806–6813. [CrossRef] [PubMed]
63. Bajpaia, V.K.; Kamleb, M.; Shuklaa, S.; Mahatoc, D.K.; Chandrad, P.; Hwange, S.K.; Kumarb, P.; Huhe, Y.S.; Han, Y.-K. Prospects of using nanotechnology for food preservation, safety, and security. *J. Food Drug Anal.* **2018**, *26*, 1201–1214. [CrossRef] [PubMed]
64. Xu, H.; Ouyang, S.; Liu, L.; Reunchan, P.; Umezawa, N.; Ye, J. Recent advances in TiO_2-based photocatalysis. *J. Mat. Chem. A.* **2014**, *2*, 12642–12661. [CrossRef]
65. ISO 22196:2011 Standards. Measurement of Antibacterial Activity on Plastics and Other Non-Porous Surfaces. Available online: https://www.kieferusa.com/wp-content/uploads/2019/07/MRSA-ISO-22196.pdf (accessed on 3 June 2019).
66. Isola, G.; Alibrandi, A.; Currò, M.; Matarese, M.; Ricc, A.S.; Matarese, G.; Ientile, R.; Kocher, T. Evaluation of salivary and serum ADMA levels in patients with periodontal and cardiovascular disease as subclinical marker of cardiovascular risk. *J. Periodontol.* **2020**, *91*, 1076–1084. [CrossRef]
67. Isola, G.; Polizzi, A.; Patini, R.; Ferlito, S.; Alibrandi, A.; Palazzo, G. Association among serum and salivary A. actinomycetemcomitans specific immunoglobulin antibodies and periodontitis. *BMC Oral Health* **2020**, *20*, 283. [CrossRef]

Publisher's Note: MDPI stays neutral with regard to jurisdictional claims in published maps and institutional affiliations.

© 2020 by the authors. Licensee MDPI, Basel, Switzerland. This article is an open access article distributed under the terms and conditions of the Creative Commons Attribution (CC BY) license (http://creativecommons.org/licenses/by/4.0/).

P2. *Photocatalytic and Antimicrobial Activity of Titanium(IV)-Oxo Clusters of Different Core Structure*

crystals

MDPI

Article

Photocatalytic and Antimicrobial Activity of Titanium(IV)-Oxo Clusters of Different Core Structure

Barbara Kubiak [1,*], Piotr Piszczek [1,*], Aleksandra Radtke [1], Tadeusz Muzioł [1], Grzegorz Wrzeszcz [1] and Patrycja Golińska [2]

[1] Department of Inorganic and Coordination Chemistry, Faculty of Chemistry, Nicolaus Copernicus University in Toruń, Gagarina 7, 87-100 Toruń, Poland; aradtke@umk.pl (A.R.); tadeuszmuziol@wp.pl (T.M.); wrzeszcz@umk.pl (G.W.)

[2] Department of Microbiology, Faculty of Biological and Veterinary Sciences, Nicolaus Copernicus University in Toruń, Lwowska 1, 87-100 Toruń, Poland; golinska@umk.pl

* Correspondence: basiak0809@gmail.com (B.K.); piszczek@umk.pl (P.P.)

Abstract: The purpose of this paper is to assess the relationship between the core architecture of titanium(IV)-oxo complexes (TOCs) known as $\{Ti_aO_b\}$ and their photocatalytic and antimicrobial activity. The following TOCs: $[Ti_6O_4(O^iBu)_8(O_2C_{13}H_9)_8] \cdot 2(CH_3)_2CO$ (**1**), $[Ti_6O_6(O^iBu)_6(O_2C_{13}H_9)_6]$ (**2**), $[Ti_6O_6(O^iBu)_6(O_2C_{13}H_9)_6]$ (**3**), $[Ti_3O(O^iPr)_8(O_2C_{13}H_9)_2]$ (**4**), and $[Ti_4O_2(O^iBu)_{10}(O_2C_{13}H_9)_2]$ (**5**), where $-O^2C^{13}H^9$represents 9-fluorene-carboxylate ligands, werestudied to investigate thiseffect. The structures of (**1**)–(**5**) were confirmed using single-crystal X-ray diffraction and spectroscopic methods. Since TOCs can be sensitive to hydrolysis processes, their photocatalytic and antimicrobial activity was evaluated after dispersing them in a polymer matrix, which acted as a protective agent against the aquatic environment. The results revealed that the photocatalytic activity of the studied TOCs follows the trend (**2**) > (**5**) > (**4**) > (**1**) in both the UV and visible ranges. All studied oxo complexes exhibited strong antibacterial activity against Gram-positive strains and weaker activity against Gram-negative strains. The proposed mechanism of the antimicrobial activity of TOCs assumes that this effect is associated with the generation of reactive oxygen species (ROS) on the surface of composite samples. Samples of PMMA + (**1**) 10 wt.% and PMMA + (**5**) 20 wt.%, in which both O^- and O_2^- paramagnetic species were observed in the electron paramagnetic spectroscopy (EPR) spectra, demonstrated the highest antimicrobial activity.

Keywords: titanium(IV)-oxo clusters; titanium-oxo core structure; spectral characterization; photocatalytic properties; antimicrobial activity

check for updates

Citation: Kubiak, B.; Piszczek, P.; Radtke, A.; Muzioł, T.; Wrzeszcz, G.; Golińska, P. Photocatalytic and Antimicrobial Activity of Titanium(IV)-Oxo Clusters of Different Core Structure. *Crystals* **2023**, *13*, 998. https://doi.org/10.3390/cryst13070998

Academic Editors: Karolina Siedliska, Kamila Komędera and Raffaello Mazzaro

Received: 29 May 2023
Revised: 19 June 2023
Accepted: 20 June 2023
Published: 22 June 2023

Copyright: © 2023 by the authors. Licensee MDPI, Basel, Switzerland. This article is an open access article distributed under the terms and conditions of the Creative Commons Attribution (CC BY) license (https://creativecommons.org/licenses/by/4.0/).

1. Introduction

A significant part of the research on new materials that improve the quality of our life involves materials based on titanium dioxide. These materials have diverse applications, including water treatment [1], photocatalysis [2,3], sun protection [4], self-cleaning surfaces [5], pharmaceutical and food industries [6,7], and the production of biocompatible and antibacterial implants [8,9]. An important direction for the application of TiO_2-based materials, which exhibit photocatalytic properties, is their use in antibiotic elimination technologies [10]. The main requirement is extensive use of antibiotics, primarily in agriculture but also in medicine, which poses a huge threat to our environment. Therefore, it is important to develop new photocatalysts that are environmentally friendly, cost-effective to produce, and characterized by high activity in the photodecomposition of antibiotics [11,12]. However, TiO_2-based materials face limitations in their practical use as photocatalysts due to their wide bandgap, which primarily requires ultraviolet excitation. Moreover, the recombination of electrons and light-induced holes easily occurs, reducing the photocatalytic activity of titania particles. Therefore, the main aim of these investigations is the development and production of a photocatalyst whose activity is shifted toward visible light.

To address this challenge, attention has turned to multinuclear oxo-titanium(IV) complexes (TOCs) with a core composed of $\{Ti_aO_b\}$ skeletons [13–15]. The advantage of these compounds is the ability to control their physicochemical, photocatalytic, and biological properties via changes in the core size and architecture of $\{Ti_aO_b\}$, as well as the functionalization of carboxylate groups as stabilizing ligands [16–20]. From the perspective of TOC synthesis, the type of alkoxide groups, solvent, and temperature are also important factors [19–21]. Investigations on clusters with $\{Ti_4O\}$ and $\{Ti_4O_2\}$ cores, stabilized by 4-tert-butylcatechol and N, N-diethylformamide ligands, used in the photo-induced direct degradation of methylene blue (MB) in visible light, are good examples of this [21]. The study shows that after 2.5 h, 98% degradation of MB concentration is observed, whereas, in the case of TiO_2, only 15% degradation is observed at the same time. The better photocatalytic activity of TOCs is due to the narrowed band gap compared to TiO_2 and the wide absorption band [21]. Functionalization of poly-oxo-titanate clusters with 1,1-ferrocene dicarboxylic acid ligands resulted in obtaining TOCs with $\{Ti_8O_4\}$ and $\{Ti_6O_2\}$ cores. The ligands cause an increase in the absorption maximum into the visible range and increase the electron transfer in 1,1-ferrocene dicarboxylic acid and Ti-oxo skeletons [22]. Moreover, obtaining sub-clusters with $\{Ti_4O\}$ and $\{Ti_6O_4\}$ cores exhibit a better ability to degrade MB than each of the clusters used separately [23,24]. It should be noted that another way to increase the photocatalytic activity of titanium-based materials is to introduce an extra atom into the $\{Ti_aO_b\}$ core. The research of Wang et al. on clusters with the core $\{Ti_4Co_2O_4\}$, $\{Ti_5Cu_4O_6\}$, $\{Ti_{12}Cd_5O_{18}\}$ is an example [25].

The limited knowledge related to the bactericidal activity of TOCs is one of the factors that justify research on their use as antimicrobial agents. Swenson et al. pointed out the possibility of using TOCs as an antibacterial agent against *Staphylococcus aureus* for $\{Ti_4O_2\}$ clusters stabilized by triclosan ligands [26]. However, these works focused on studying the antibacterial properties of the hydrolyzed complex, which may be used for drug delivery applications. When studying the use of transition metal oxides (e.g., TiO_2, CuO, ZnO, Fe_2O_3) as antimicrobial agents, it was noted that after activation with light at a specific wavelength, reactive oxygen species (ROS) are generated on their surface [27–30]. According to these investigations, the formed ROS are responsible for microbial cell death (e.g., *Escherichia coli* (*E. coli*), *Staphylococcus aureus* (*S. aureus*), *Rhizopus stolonifer*, *Rhizopus oryzae*) [29]. Therefore, in our work, we decided to test this antimicrobial effect in the case of TOCs. The main issue that needed to be addressed was the protection of the oxo complex grains against potential hydrolysis processes [31,32]. For this reason, we chose to disperse TOCs grains in a polymer matrix (e.g., poly(methyl methacrylate) (PMMA)) [31,32]. The results of our earlier investigations of composites enriched with TOCs, containing the $\{Ti_4O_2\}$ cores and stabilized by 4-aminobenzoic, 4-hydroxybenzoic, and 9-fluorene-carboxylate acid ligands, demonstrated their strong antimicrobial activity at levels of 85–99% against Gram-positive and Gram-negative bacteria [31,32]. Analysis of this data revealed that the highest activity was observed for TOCs stabilized by 9-fluorene-carboxylate ligands ($O_2C_{13}H_9$) Początekformularza [32].

The presented paper focuses on the comparative analysis of the photocatalytic and antimicrobial activities of Ti(IV)-oxo complexes. These complexes contain $\{Ti_6O_6\}$, $\{Ti_6O_4\}$, $\{Ti_4O_2\}$, and $\{Ti_3O\}$ skeletons, and their structures were confirmed using X-ray single crystal diffraction. The stability of these oxo clusters was achieved through the use of a 9-fluorene-carboxylate ligand, along with $-O^iBu$ and $-O^iPr$ (only for $\{Ti_3O\}$) ones. This systematic approach allows us to examine how the structure of the $\{Ti_aO_b\}$ core influences the properties of these complexes. Notably, our research contributes novelty by assessing the impact of the core structure on the antimicrobial activity exhibited by the synthesized oxo complexes.

2. Materials and Methods

2.1. General ProcedureandReagents

Titanium(IV) isobutoxide (Aldrich, St. Louis, MO, USA), titanium(IV) isopropoxide (Aldrich, St. Louis, MO, USA), 9-fluorene-carboxylic acid (TCI, Tokyo, Japan) were purchased commercially and were used without further purification. All solvents used in our experiments were dried, distilled before use, and stored in an argon atmosphere. The processes of Ti(IV) oxo-complexes syntheses were carried out using the standard Schlenk technique in the inert gas atmosphere (Ar) and at room temperature (RT).

2.2. Analytical Procedures

The structures of the isolated solid reaction products (crystals) were confirmed using vibrational spectroscopy methods, i.e., IR spectrophotometry (Perkin Elmer Spectrum 2000 FTIR spectrophotometer (400–4000 cm^{-1} range, KBr pellets)) and Raman microscopy (RamanMicro 200 spectrometer (PerkinElmer, Waltham, MA, USA)). Elemental analyses were performed on Elemental AnalyserVario Macro CHN (Elementar Analysensysteme GmbH, Langenselbold, Germany). Titanium content was gravimetrically determined as TiO_2, according to a method described by Meth-Chon et al. [33]. Raman spectra were registered using a laser with the wavelength 785 nm, with a maximum power of 350 mW, in the range 200–3200 cm^{-1}, using a 20 × 0.40/FN22 objective lens and an exposure time of 15 s each time. The diffuse reflectance UV-Vis (UV-VIS-DRS) spectra registered between 200 and 800 nm were used for the maximum absorption determination. The Jasco V-750 spectrophotometer was used in above mentioned works (JASCO Deutschland GmbH, Pfungstadt, Germany). The produced PMMA + TOCs film surfaces morphology was studied using a scanning electron microscope with field emission (SEM, Quanta 3D FEG, Houston, TX, USA).

*2.3. Synthesis of $[Ti_6O_4(O^iBu)_8(O_2C_{13}H_9)_8] \cdot 2(CH_3)_2CO$ (**1**), $[Ti_6O_6(OiBu)_6(O_2C_{13}H_9)_6]$ (**2**), and $[Ti_6O_6(O^iBu)_6(O_2C_{13}H_9)_6]$ (**3**)*

A total of 0.184 g of 9-fluorene-carboxylic acid (0.875 mmol) was added to the solution of 0.3 g of titanium(IV) isobutoxide (0.875 mmol) in 2 mL of acetone, leading to a clear violet solution. The solution was left for crystallization. After 6–7 days, the mixture of crystals was formed, and the general yield basing on acid: (**1**) 15% (0.05 g), (**2**) 21% (0.07 g), (**3**) 5% (0.01 g). Using the optical microscope, the crystals of different shapes were separated and isolated from the reaction mixture. Elemental composition was determined for samples, and structures were solved by single-crystal X-ray diffraction.

Anal. Calc. for $\mathbf{C_{116}H_{138}O_{26}Ti_6}$ (**1**): C, 62.31; H, 6.18; Ti, 12.89. Found: C, 62.14; H, 6.13; Ti, 12.56.^{13}C NMR (solid state, 295 K, δ[ppm]): 19.7 (CH_3), 31.3 (CH), 52.2, 53.4, 55.4, 56.8, 59.6, 73.6, 74.6 (CH_2), 119.6, 120.7, 127.5, 141.5 (C(Ph)),175.4, 177.6, 178.7 (COO).

Anal. Calc. for $\mathbf{C_{102}H_{108}O_{24}Ti_6}$ (**2**): C, 62.32; H, 5.49; Ti,14.60. Found: C, 62.17; H, 5.86;Ti, 14.64. ^{13}C NMR (solid state, 295 K, δ[ppm]): 19.6 (CH_3), 30.6 (CH), 53.7, 54.6, 73.7 (CH_2), 121.3, 128.5, 140.7 (C(Ph)), 176.4, 177.9, 179.7 (COO).

Anal. Calc. for $\mathbf{C_{102}H_{108}O_{24}Ti_6}$ (**3**): C, 62.32; H, 5.49; Ti,14.60. Found: C, 62.23; H, 5.76;Ti, 14.75. ^{13}C NMR (solid state, 295 K, δ[ppm]): 19.6 (CH_3), 30.6 (CH), 73.7 (CH_2), 54.6, 121.3, 128.5, 140.7 (C(Ph)), 176.4, 177.9, 179.7 (COO).

*2.4. Synthesis of $[Ti_3O(O^iPr)_8(O_2C_{13}H_9)_2]$ (**4**)*

The complex was synthesized, as reported [34]. 0.184 g of 9-fluorene-carboxylic acid (0.875 mmol) was added to the solution of 1 mL of titanium(IV) isopropoxide (3.5 mmol) in 2 mL of acetone, leading to a clear yellow solution. The solution was left for crystallization (3–4 days). The yield basing on acid: 62% (0.36 g).

Anal. Calc. for $\mathbf{C_{50}H_{74}O_{13}Ti_3}$ (**4**): C, 58.49; H, 7.21; Ti,14.04. Found: C, 58.54; H, 7.13; Ti, 13.95. ^{13}C NMR (solid state, 295 K, δ[ppm]): 14.0, 19.5 (CH_3), 30.9, 35.1 (CH), 55.4, 77.8 (CH_2), 119.2, 127.6, 141.6 (C(Ph)), 179.6 (COO).

*2.5. Synthesis of [$Ti_4O_2(O^iBu)_{10}(O_2C_{13}H_9)_2$] (**5**)*

The complex was synthesized, as reported [35]. 0.184 g of 9-fluorene-carboxylic acid (0.875 mmol) was added to the solution of 1.19 g of titanium(IV) isobutoxide (3.5 mmol) in 2 mL of acetone, leading to a clear yellow solution. The solution was left for crystallization. The yield basing on acid: 78% (0.39 g).

Anal. Calc. for $\mathbf{C_{68}H_{108}O_{16}Ti_4}$ (**5**): C, 59.28; H, 7.93; Ti, 13.94. Found: C, 58.17; H, 7.86; Ti, 13.64. ^{13}C NMR (solid state, 295 K, δ[ppm]): 14.2, 19.3 (CH_3), 34.8 (CH), 55.1, 77.3 (CH_2), 119.3, 127.4, 141.9 (C(Ph)), 178.8 (COO).

2.6. Single Crystal X-ray Diffraction Measurements

The diffraction data of (**1**)–(**3**) were collected at 100 K on Rigaku XtaLAB Synergy (Dualflex) diffractometer with HyPix detector and monochromatedCuKα X-ray source (λ = 1.54184 Å). The data were processed, and the numerical absorption correction was applied using CrysAlis Pro [36]. The structures were solved by direct methods and refined with full-matrix least-squares procedure on F^2 (SHELX-97 [37]. Heavy atoms were refined with anisotropic displacement parameters, whereas hydrogen atoms were assigned at calculated positions with thermal displacement parameters fixed to a value of 20% or 50% higher than those of the corresponding carbon atoms. We also observed positional disorder for some isobutanolate anions (O66 and O86 in (**1**), O71 and O81 in (**2**) and (**3**)). For the stability of the refinement process, several geometrical (DFIX) and thermal parameters (ISOR) restraints were applied for the disordered isobutanolates and acetone molecules. Additionally, EADP constraints were used for disordered Bu^iO^- anions. All figures were prepared in DIAMOND [38] and ORTEP-3 [39].

2.7. Preparation of PMMA + TOCs Composite Films

The composite films containing 10 or 20 wt.% of synthesized Ti(IV)-oxo clusters (TOCs) were prepared by a dispersion of the TOCs (ca. 0.12 or 0.25 g of (**1**), (**2**), (**4**), and (**5**) TOCs dispersed in 1 cm^3 of THF) in the poly(methyl methacrylate) (PMMA) solution (1.0 g of PMMA dissolved in 5 cm^3 of THF). The mixtures were stirred in an ultrasonic bath for 120 min; in the next step, they were poured into a glass Petri dish and left for the evaporation of the solvent at RT (glove box). The composite film thickness ca. 50 µm was characterized by Raman and IR spectroscopy and scanning electron microscopy. Due to the low synthesis efficiency of (**3**), the crystals of this oxo cluster were not used in our subsequent experiments. The received foils, after thorough drying in a vacuum, were cut into pieces of 1 × 1 cm for photocatalytic experiments and 3 × 3 cm for microbiological tests.

2.8. The Photocatalytic Activity Evaluation of PMMA + TOCs Composite Films

The photocatalytic activity of PMMA + TOCs foils (TOCs = (**1**), (**2**), (**4**), (**5**)) was estimated by monitoring the concentration changes of MB aqueous solution. Foil samples (10 × 10 mm) were preconditioned by exposure to UVA or Vis light (the range of radiation used to irradiate the samples were selected based on the analysis of their UV-VIS-DRS spectra) and after 28 h placed in quartz cuvettes with dye solution (V = 3.5 cm^3 and C = 2.0 × 10^{-5} M). After 12 h in the dark, the solution was replaced by MB solution (C = 1.0 × 10^{-5} M). The prepared samples were exposed to UVA irradiation (18-W lamp, 340–395-nm range) and Vis light (range of 395–420 nm). MB absorbance at 664 nm was registered (Metertech SP-830 PLUS, Metertech, Inc., Taipei, Taiwan) every 2 h during 18 h (UV range) and 24 h (Vis range) of irradiation. The percentage of MB decolorization was calculated using the equation:

$$\%\ \text{MB decolorization} = \frac{(C_0 - C_t)}{C_0} \times 100$$

where C_0 is an initial concentration of dye, and C_t is a dye concentration at a given time t [40].

2.9. EPR Studies

Electron paramagnetic resonance (EPR) spectroscopy was employed to confirm the formation of reactive oxygen species on the surface of the investigated composite samples. The measurements were conducted using an X-band EPR SE/X-2541M spectrometer (Radi-open, Poznań, Poland) with a 100 kHz modulation. The microwave frequency was monitored using a frequency meter, while the magnetic field was measured using an automatic NMR-type JTM-147 magnetometer (Radiopan, Poznań, Poland). The measurement conditions were as follows: microwave frequency of approximately 9.33 GHz, microwave power ranging from 6 to 58 mW, modulation amplitude between 0.2 and 1 mT, sweep ranging from 10 to 50 mT, sweep time from 1 to 8 min, time constant from 0.03 to 0.3 s, and receiver gain from 3.2 to 5 × 105. Low-intensity signals were recorded in the accumulation mode. The measurements were performed at room temperature using foil samples that were simultaneously prepared for all studies. The portion utilized in the EPR measurements was exposed to sunlight. The catalytic and EPR measurements were conducted independently, approximately at the same time.

2.10. Antimicrobial Activity of PMMA + TOCs Composite Films

The antimicrobial activity of the samples was assessed against Gram-negative bacteria (*Escherichia coli* ATCC 25922, *Escherichia coli* ATCC 8739), Gram-positive bacteria (*Staphylococcus aureus* ATCC 25923, *Staphylococcus aureus* ATCC 6538), and *Candida albicans* ATCC 10231. Prior to the antimicrobial study, the tested PMMA + TOCs foils (20 × 20 mm) were sterilized using UVC for 15 min on both sides and then exposed to visible indoor light. The foils were placed in 12-well plates with 1 mL of microbial inoculum (1.0–3.3 × 10^6 c.f.u. mL^{-1}) in sterile deionized water. The plates were incubated for 24 h at 37 °C under humid conditions with gentle shaking at 80 rpm. The microbial density was adjusted to 0.5 on the McFarland scale using a densitometer (Biosan, Latvia). The inoculum was diluted 100 times with sterile deionized water to achieve the final concentration, which was determined by colony counts after spreading 100 µL of the inoculum on the surface of Tryptic Soy Agar (TSA; Becton Dickinson, Franklin Lakes, NJ, USA for bacteria) or Sabouraud Dextrose Agar (SDA; Becton-Dickinson for *C. albicans*) in Petri plates. The control consisted of the suspension of test microorganisms in a well without the test sample. After incubation, the inoculum was collected from the wells, and serial ten-fold dilutions were prepared. Then, 100 µL of the dilutions were spread on the appropriate medium in Petri dishes. The inoculated plates were further incubated for 24 h at 37 °C, and the colony-forming units (c.f.u) were counted. To express the antimicrobial activity of the tested samples, the reduction (R) index was calculated. The R index was determined using the formula: $R = U_t - A_t$, where U_t represents the common logarithm of the number of microbes in the microbial inoculum and A_t represents the common logarithm of the number of microbes in the treated microbial inoculum. An R-value of $\geq$2 indicates the biocidal activity of the sample.

3. Results

*3.1. Structures of (**1**)–(**5**) Oxo Complexes*

The reaction of the titanium(IV) isobutoxide with the 9-fluorene-carboxylic acid in a 1:1 molar ratio ($Ti(^iOBu)_4$/organic acid) in acetone as a solvent at room temperature in the argon atmosphere leads to the co-crystallization of three types of crystals (which differ in size and shape), after 6–7 days. The use of the optical microscope allowed for the separation of crystals and their isolation from the mother liquor (microscopy images are presented in Figures 1c and 2b,c. The molecular structure of isolated crystals (Figures 1a,b and 2a,d,e) was solved using the single-crystal X-ray diffraction method. The results of this investigation have been summarized in Table 1. The selected bond lengths and angles are presented in Table S1. CCDC 2224562, 2224563, and 2224564 contain the supplementary crystallographic data for (1), (2), and (3), respectively.These data can be obtained free of

charge from The Cambridge Crystallographic Data Centre via www.ccdc.cam.ac.uk.data_request/cif (accessed on 1 May 2023).

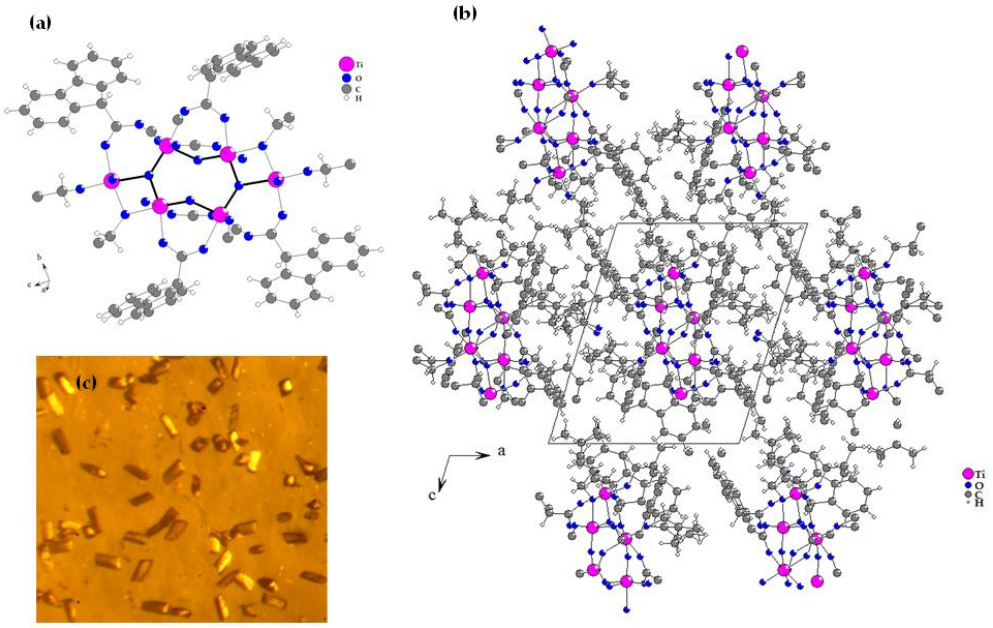


Figure 1. The structure of $[Ti_6O_4(O^iBu)_8(O_2C_{13}H_9)_8] \cdot \mathbf{2}\ (CH_3)_2CO$ (**1**) complex (crystallographic ball-stick scheme). (**a**) The $\{Ti_6O_4\}$ core with labeled titanium and oxygen atoms. For clarity of the picture, all hydrogen atoms and most of carbon atoms are omitted. (**b**) The packing of TOCs in the crystal network of (**1**) along the *b* axis. (**c**) The optical microscope image of (**1**) crystals.

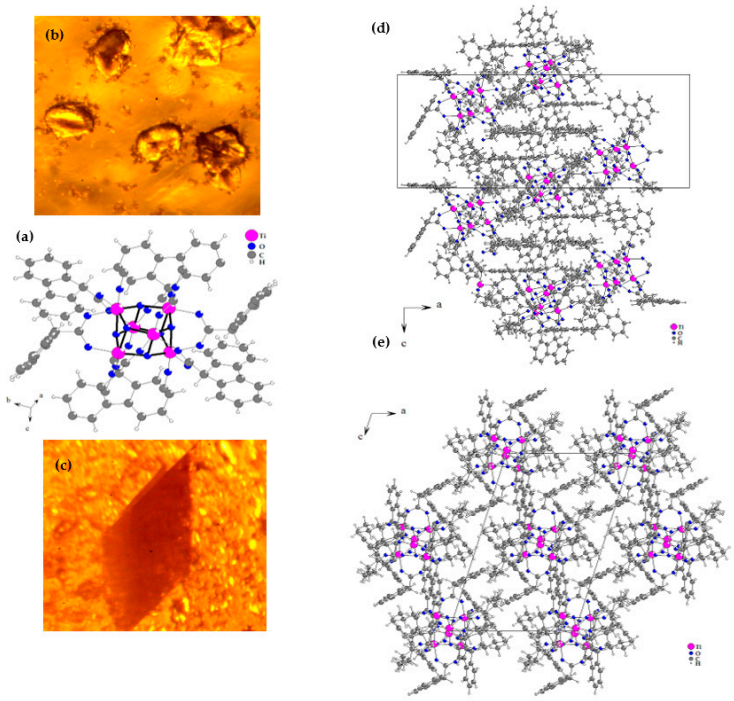


Figure 2. Two polymorphous forms of $[Ti_6O_6(O^iBu)_6(O_2C_{13}H_9)_6]$—(**2**) and (**3**) structures. The $\{Ti_6O_6\}$ core with labeled titanium and oxygen atoms—(**a**). For clarity of the picture, all hydrogen atoms and most carbon atoms are omitted. The optical microscope images of (**2**) and (**3**) crystals—(**b**) and (**c**), respectively. The differences in TOCs packing in the crystal network of (**2**) and (**3**) along b axis—(**d**) and (**e**), respectively.

Table 1. Crystal data and structure refinement for (**1**)–(**3**).

Empirical Formula	**$C_{116}H_{138}O_{26}Ti_6$ (1)**	**$C_{108}H_{108}O_{24}Ti_6$ (2)**	**$C_{108}H_{108}O_{24}Ti_6$ (3)**
Formula weight	2726.14	2077.34	2077.34
Temperature (K)	100 (2)	100 (2)	100 (2)
Wavelength (Å)	1.54184	1.54184	1.54184
Crystal system	Triclinic	Monoclinic	Tetragonal
Space group	P-1	$P2_1/n$	$I4_1/1$
Unit cell dimensions [Å] and [°]	a = 13.7398 (5) α = 103.877 (4) b = 15.6157 (6) β =106.420 (4) c =17.1768 (7) γ = 91.043 (3)	a = 14.2526 (9) α = 90 b = 16.1562 (9) β = 106.427 (6) c = 22.7794 (11) γ = 90	a = 36.8090 (4) α = 90 b = 36.8090 (4) β = 90 c = 15.4415 (4) γ = 90
Volume [$Å^3$]	3417.2 (2)	5031.3 (5)	20,921.7 (7)
Z, calculated density [Mg/m^3]	1, 1.325	2, 1.371	8, 1.319
Absorption coefficient [mm^{-1}]	3.456	4.371	1.301
F(000)	1428	2160	8640
Crystal size [mm^3]	0.060 × 0.050 × 0.040	0.410 × 0.270 × 0.110	0.120 × 0.080 × 0.030
Theta range for data collection	2.774 to 74.497°	3.293 to 74.496°	3.104 to 74.499°
Index ranges	$-17 \leq h \leq 16$ $-19 \leq k \leq 19$ $-20 \leq l \leq 21$	$-17 \leq h \leq 17$ $-20 \leq k \leq 19$ $-22 \leq l \leq 28$	$-43 \leq h \leq 44$ $-41 \leq k \leq 46$ $-17 \leq l \leq 18$
Reflections collected/unique	49,804	33,498	71,517
Completeness to theta = 30.866°	99.8%	98.9%	99.7%
Absorption correction	Gaussian	Gaussian	Analytical
Max. and min. transmission	0.973 and 0.861	1.000 and 0.149	0.888 and 0.729
Refinement method	Full-matrix least-square on F^2	Full-matrix least-square on F^2	Full-matrix least-square on F^2
Data/restraints/parameters	13,516/76/887	9803/10/669	10,156/24/643
Goodness-of-fit on F^2	1.030	1.051	1.035
Final R indices [I > 2sigma(I)]	$R1^a$ = 0.0654, $wR2^b$ = 0.1678	$R1^a$ = 0.0710, $wR2^b$ = 0.1987	$R1^a$ = 0.0678, $wR2^b$ = 0.1097
R indices (all data)	$R1^a$ = 0.1055, $wR2^b$ = 0.1926	$R1^{aa}$ = 0.0816, $wR2^b$ = 0.2103	$R1^a$ = 0.1113, $wR2^b$ = 0.2214
Largest diff. peak and hole	0.554 and −0.507 e.$Å^{-3}$	0.759 and −0.7530 e.$Å^{-3}$	0.961 and −0.483 e.$Å^{-3}$

[a] $R1 = \Sigma||F_0| - |F_c||/\Sigma|F_0|$. [b] $wR2 = [\Sigma w(F_0^2 - F_c^2)^2/\Sigma(w(F_0^2)^2)]^{1/2}$.

Upon analyzing the collected data, it was found that the structure of the (**1**) cluster can be described by the following summary formula: $[Ti_6O_4(O^iBu)_8(O_2CC_{13}H_9)_8] \cdot 2(CH_3)_2CO$. This cluster features a titanium-oxo core composed of flat {Ti_3-(μ_3-O)} motifs, with each motif being stabilized by two carboxylates and one alkoxide bridge (Figure 1a). The units mentioned earlier are interconnected through two {Ti_2-(μ-O)} bridges and four carboxylate bridges. The coordination number 6 of the Ti(IV) central atoms is supplemented by six terminal alkoxide ligands. Figure 1b illustrates the densely packed arrangement of oxo clusters within the crystal lattice, which adopts a triclinic crystal system.

Analysis of crystal data of larger crystals isolated from the mother liquor (Figure 2b,c) proved the formation of hexanuclearTi(IV)-oxo clusters (**2**) and (**3**) with the general formula $[Ti_6O_6(O^iBu)_6(O_2CC_{13}H_9)_6]$. The differences in cluster packing in the crystal lattice of (**2**) and (**3**) are presented in Figure 2d,e. Selected interatomic distances and angles are shown in Table S1.

Crystals (4) and (5) were isolated from reaction mixtures, which composition was earlier described [34,35]. The structures of these complexes were confirmed using single-crystal X-ray diffraction.

3.2. Preparation of the PMMA + TOCs Composite Films and the Estimation of Their Properties

Composite materials were produced by dispersing 10 or 20 wt.% of micro grains of (**1**), (**2**), (**4**), and (**5**) in the PMMA matrix. The structure and distribution of TOCs micro grains within the polymeric matrix were assessed through the analysis of SEM images (Figure 3). The average grain size of composite materials containing 10% and 20% of TOCs (**1**) ranged from 30 to 70 μm. The blurry shape of (**1**) grains dispersed in the PMMA matrix sets them apart from the microcrystalline grains (**2**), (**4**), and (**5**) found in other composite samples. SEM image analysis indicated that the grain size of PMMA + (**2**), (**4**), and (**5**) composites (at both 10 and 20 wt.%) ranged from 3 to 15 μm.

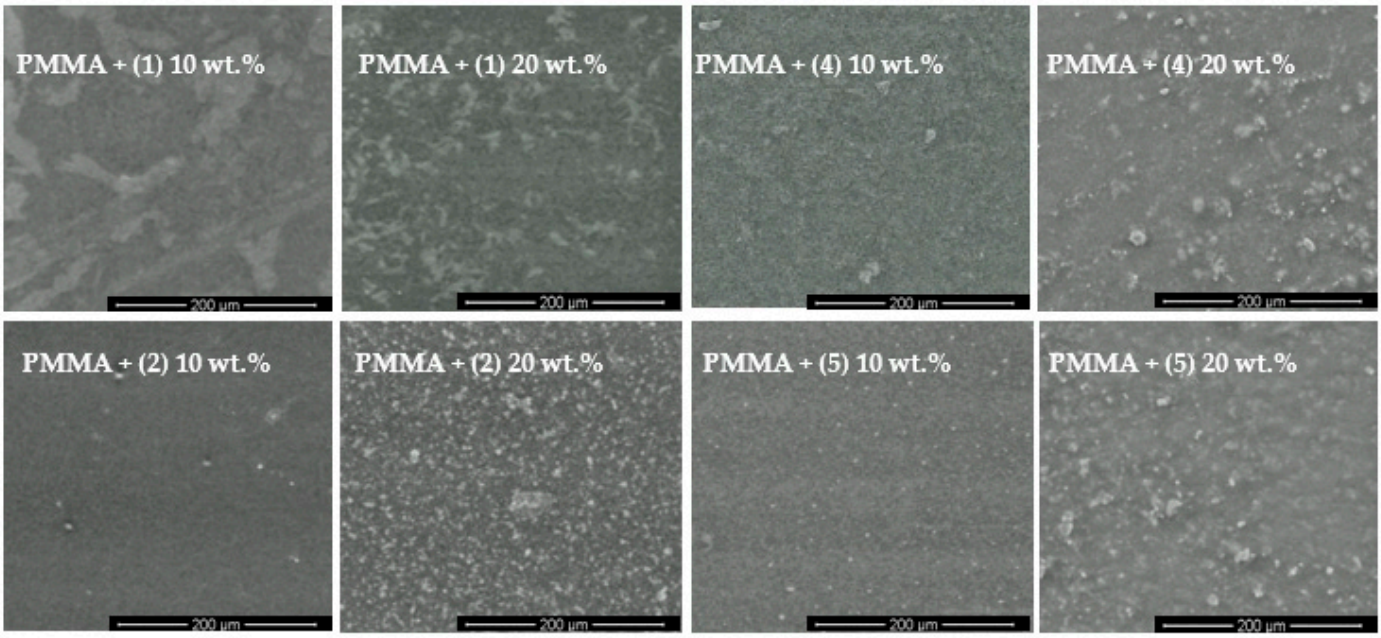


Figure 3. SEM images of PMMA + TOCs (TOCs = (**1**), (**2**), (**4**) and (**5**) composites.

To confirm the presence of (**1**) and (**2**) compounds in composite materials, the SEM/EDX method was used (Table 2, Figure S1). Elements, such as Ti, O, C, were found in composites compared to pure PMMA, where only O and C were found. An additional peak of Al comes from microscope equipment.

Table 2. SEM EDX quantities data. All values are given in mass percent (%).

Composite	C	O	Al	Ti
PMMA	26.10	72.23	1.67	-
PMMA + (1) 10 wt.%	53.02	40.81	1.03	6.12
PMMA + (1) 20 wt.%	53.15	37.90	1.00	7.95
PMMA + (2) 10 wt.%	51.77	42.26	1.49	4.48
PMMA + (2) 20 wt.%	52.45	41.12	0.81	5.62

Another method used to confirm the presence of TOCs grains in the produced composites was the registration of Raman microscope maps (Figure 4). The use of an ultrasonic bath to achieve a uniform dispersion of TOCs grains in the PMMA solution can lead to a slight temperature increase, up to 50 °C. Under these conditions, the formation of a new system through the interaction of TOCs and PMMA is possible. The analysis of Raman maps confirmed that the grains of $\{Ti_6O_4\}$ or $\{Ti_6O_6\}$ dispersed in the PMMA matrix do not undergo structural changes upon introduction into the polymer. The analysis of Raman spectra recorded at selected sample points revealed the presence of regions with varying degrees of TOCs dominance. This phenomenon can be attributed to differences in the dispersion of TOCs grains within the PMMA matrix and/or aggregation processes. In the case of composites containing 10 wt.% addition of TOCs with $\{Ti_6O_4\}$ and $\{Ti_6O_6\}$ cores, the bands derived from the oxo-complexes are barely visible. This suggests that the oxo complex is highly fragmented and dispersed in the polymer matrix. However, when the TOCs concentration increases to 20 wt.%, areas dominated by TOCs grains can be observed, indicating a possible aggregation effect.

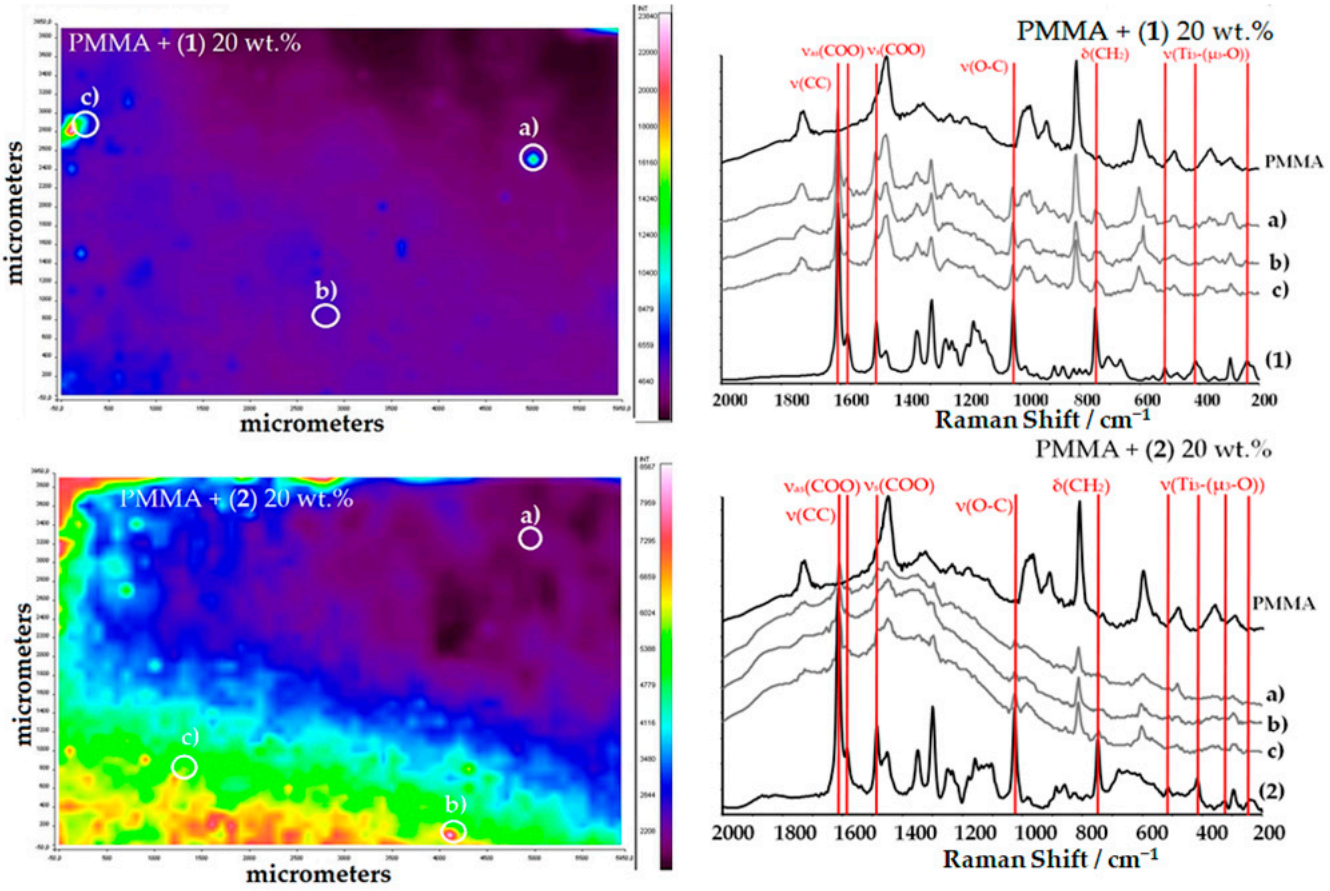


Figure 4. Raman maps and spectra of composites consist of PMMA + TOCs (TOCs = (**1**) 20 wt.% and (**2**) 20 wt.%.

3.3. The Analysis of Thermal Properties of PMMA + TOCs Composites

Thermal properties of TOCs/PMMA composites were characterized by thermogravimetric analysis and differential scanning calorimetry. Measurements were carried out in the temperature range of 20–550 °C in an inert atmosphere. The results of both analyses are presented in Table 3 and Figure S2. As mentioned in our previous research [31], samples consisting of PMMA are characterized by a two-stage decomposition. Stage I results from the solvent evaporation needed to obtain the foil or from the decomposition of the PMMA monomer. This stage is characterized by a slight weight loss (5–15%) and occurs below 270 °C. In contrast, stage II is directly related to the thermal decomposition of the sample. This stage occurs in the temperature range of 270–450 °C and is characterized by a large weight loss (75–85%).

Differential scanning calorimetry (DSC) analysis of (**1**) and (**2**) revealed differences in the glass transition temperature (T_g) of these oxo complexes. In the case of (**1**) (Ti_6O_4 core), the glass transition temperature decreased from 99.6 °C for PMMA up to c.a. 71 °C, while for (**2**) (Ti_6O_6 core), this decrease was only slight, i.e., 90–91 °C. As mentioned earlier [31], in the case of pure PMMA, there is an exothermic peak (150 °C) due to an unreacted monomer. The composite's DSC data analysis revealed that this transition was not found. Comparing temperatures associated with the decomposition transition onset of PMMA and composites exhibited that independently to TOCs type and its concentration in composite samples, significant changes in the decomposition temperature were not noticed.

Table 3. Thermal parameters received from thermogravimetric analysis (TGA) and differential scanning calorimetry (DSC) of the composites (T_g = glass transition temperature, T = evaporation temperature of an unreacted monomer, $T_{d/max}$ = decomposition temperature (transition onset), T_{max} = temperature in the thermal transition maximum, Δm = thermal transition weight loss).

	DSC			TGA		
Sample	**T_g/°C**	**T/°C**	**T_d/°C**	**Stage I T_{max}/°C/Δm/%**	**Stage II T_{max}/°C/Δm/%**	**Solid Residue %**
PMMA	99.6	150.8	315.8	199.9/12	365.1/85	3
(PMMA + (**1**) 10 wt.%)	71.3	-	311.3	200.2/15	372.3/80	5
(PMMA + (**1**) 20 wt.%)	71.5		315.3	200.2/15	375.2/75	10
(PMMA + (**2**) 10 wt.%)	90.3		316.2	190.4/7	375.3/84	9
(PMMA + (**2**) 20 wt.%)	90.8		316.1	219.3/5	376.1/85	10

3.4. UV–Vis Diffuse Reflectance Spectra (UV–Vis-DRS) of the Studied Samples

Solid-state UV-Vis DRS spectra of isolated compounds ((**1**), and (**2**)) were registered using magnesium oxide as a standard reference (Figure 5). The Kubelka-Munk (K-M) function versus light energy (i.e., K = f(hν), where $K = (1-R)^2/2R$ and R is the reflectance), was used for HOMO-LUMO gap determination. Synthesized TOCs exhibit absorption at λ_{max} = 326 nm, which extends further into the high energy visible range with an absorption edge at 395–400 nm (Figure 5a). The HOMO-LUMO gaps (E_a) are almost the same in the case of (**1**) {Ti_6O_4} and (**2**) {Ti_6O_6} core and have values of 2.98 and 2.99 eV, respectively (Figures 5b and S3). For comparison, the UV-Vis-DRS spectra were also registered for previously studied oxo-clusters (**4**) {Ti_3O} and (**5**) {Ti_4O_2} (Figure S3). Analysis of these data exhibited that λmax amounted to 380 and 395 nm while E_a= 2.17 and 2.55 eV for (**4**) and (**5**), respectively.

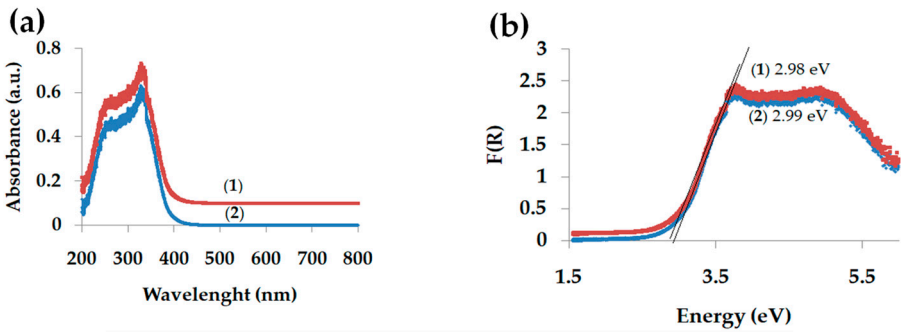


Figure 5. Solid-state UV-Vis-diffuse reflectance spectra (DRS) of the (**1**), (**2**) micro-grains (**a**), Kubelka-Munk function versus light energy plot for the HOMO-LUMO gap determination (**b**).

3.5. Photocatalytic Activity Studies of PMMA + TOCs Composite Films

The photocatalytic activity of PMMA + TOC 20 wt.% composite samples were assessed based on a decolorizing process of the methylene blue (MB) solution in which they were immersed and irradiated with UV or Vis radiation. The results for samples enriched with (**1**) ({Ti_6O_4}) and (**2**) ({Ti_6O_6}) cores have been compared with the previously characterized oxo complexes, i.e., {Ti_3O} TOCs (**4**) and {Ti_4O_2} TOCs (**5**) [34,35]. The changes in MB decolorization versus the time of irradiation are presented in Figure 6. Analysis of this data revealed that the decolorization for studied composite samples proceeds faster in the UV range than in Vis one. The photocatalytic activity of PMMA + TOCs foils was higher than for pure PMMA. According to the results presented in Figure 6, Table 4, the PMMA + 20 wt.% of (**2**) ({Ti_6O_6} core) is the most active both in UV and Vis radiation.

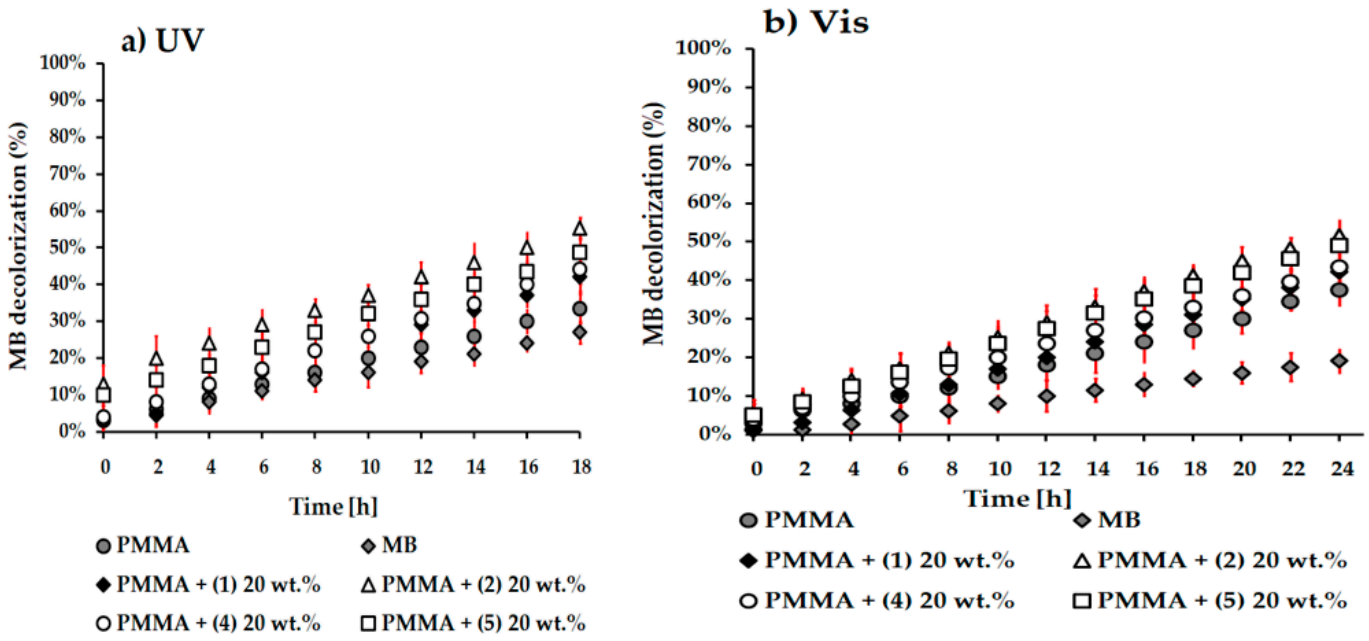


Figure 6. Changes in the concentrations of the methylene blue (MB) solution as a function of time for composite materials PMMA + (**1**), (**2**), (**4**), (**5**) 20 wt.% irradiated with UV and Vis light.

Table 4. MB solution decolorization percentages and ΔA18 or ΔA24 parameters for the studied reactions in relation to the composites irradiated by UV or VIS light.

Composite	MB Decolorization (%)	ΔA 18	ΔA 18 in Reference to PMMA	10^2 Rate Constant, h-1	10^2 Rate Constant in Reference to PMMA, h-1
MB irradiated	27.1 ± 3.1	0.270	−0.063	1.35 ± 0.03	−0.34
PMMA	33.3 ± 3.8	0.333	-	1.69 ± 0.03	-
PMMA + (1) 20 wt.%	42.0 ± 3.4	0.421	0.088	2.14 ± 0.04	0.45
PMMA+ (2) 20 wt.%	55.2 ± 4.4	0.551	0.218	2.25 ± 0.06	0.56
PMMA+ (4) 20 wt.%	44.2 ± 4.1	0.442	0.109	2.19 ± 0.05	0.50
PMMA+ (5) 20 wt.%	48.6 ± 4.2	0.485	0.152	2.23 ± 0.06	0.54
Composite	**MB Decolorization (%)**	**ΔA 24**	**ΔA 24 in Reference to PMMA**	**10^2 Rate Constant, h-1**	**10^2 Rate Constant in Reference to PMMA, h-1**
MB irradiated	19.1 ± 2.9	0.191	−0.182	0.79 ± 0.02	−0.63
PMMA	37.4 ± 3.5	0.373	-	1.42 ± 0.03	-
PMMA + (1) 20 wt.%	42.1 ± 3.1	0.423	0.05	1.63 ± 0.03	0.21
PMMA+ (2) 20 wt.%	51.6 ± 4.2	0.519	0.146	1.96 ± 0.05	0.54
PMMA+ (4) 20 wt.%	43.4 ± 3.2	0.435	0.062	1.74 ± 0.04	0.32
PMMA+ (5) 20 wt.%	49.1 ± 3.9	0.490	0.117	1.85 ± 0.05	0.43

The stability of photocatalytic activity in PMMA + TOCs composite samples (TOCs = (**1**), (**2**), (**4**), and (**5**)) was assessed over three measurement cycles under visible light irradiation (Figure 7). The results indicated that the photocatalytic activity of the tested systems remained consistent, as evidenced by a similar degree of MB discoloration observed in each cycle. By analyzing the data presented in Figures 6 and 7, as well as Table 4, the influence of the $\{Ti_aO_b\}$ core structure on the photocatalytic activity of TOCs-enriched composites can be observed. The trend in the change of photocatalytic activity follows the sequence: $\{Ti_6O_6\}$ (**2**) > $\{Ti_4O_2\}$ (**5**) > $\{Ti_3O\}$ (**4**) > $\{Ti_6O_4\}$ (**1**).

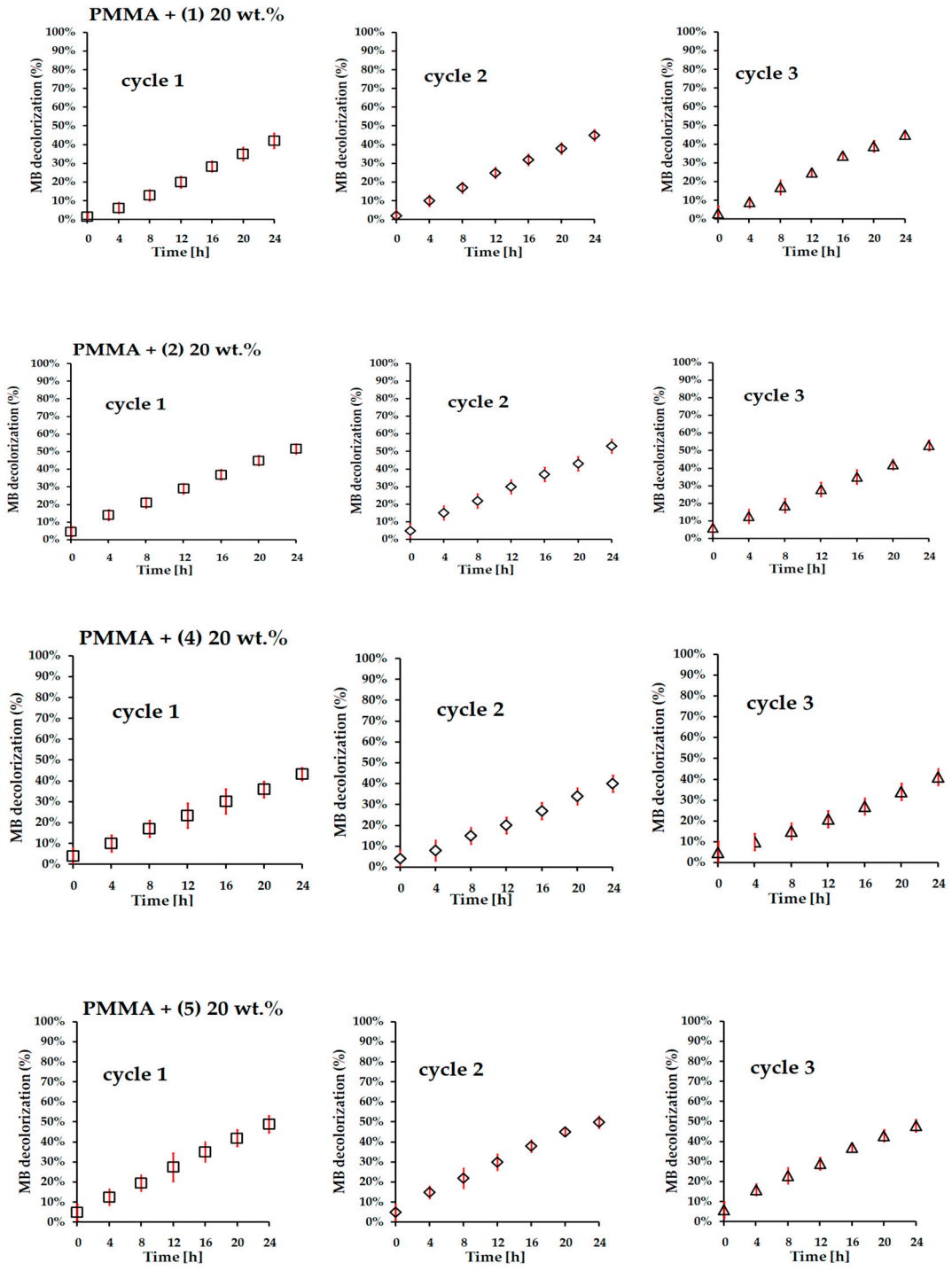


Figure 7. Recycling MB decolorization tests of composite materials PMMA + TOCs 20 wt.% (TOCs = (**1**), (**2**), (**4**), and (**5**)) irradiated with visible light.

3.6. Electron Paramagnetic Resonance (EPR) Studies of PMMA + TOCs Composite Films

EPR spectroscopy was used to detect paramagnetic species on the surface of the synthesized materials. Pure PMMA polymer shows no EPR signal. However, paramagnetic centers are found in all samples of PMMA + TOCs (Figure 8).

Generally, the signals in the EPR spectra are weak, especially for composites with a 10 wt.% admixture of oxo-titanium(IV) complexes. However, the lines in the spectra of the samples with 20 wt.% TOCs addition are more difficult for analysis due to greater line overlap. Therefore, only the EPR spectra of the samples with 10 wt.% admixture of

oxo-titanium(IV) complexes were analyzed in detail. Spectra registered for composites of PMMA + (**1**) 10 wt.% and PMMA + (**2**) 10 wt.% are presented in Figure 8. The EPR parameters and postulated types of observed paramagnetic species, especially ROS, are summarized in Table 5. Some EPR signals are marked with a question mark (Table 5. EPR) due to two different reasons (see Discussion). The first one concerns the g_2-factor for O^- species in PMMA + (**1**) 10 wt.% sample, as the signals from both oxygen species may overlap. Further, concerns the g_2-factor for Ti(III) in both PMMA + TOCs 10 wt.% samples, because the signals are almost on the noise level.

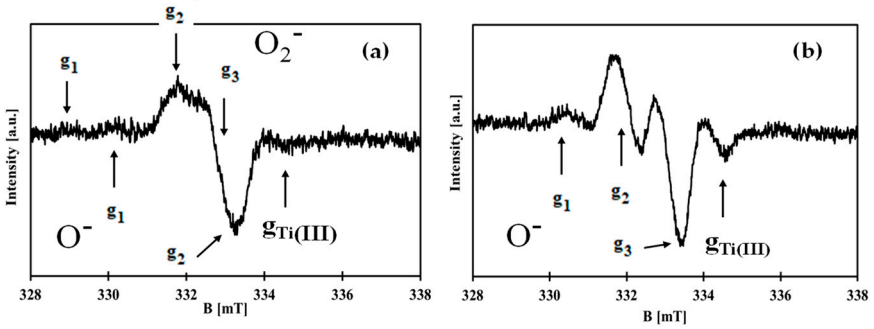


Figure 8. EPR spectra of PMMA + (**1**) 10 wt.% (**a**) and PMMA + (**2**) 10 wt.% (**b**). The experimental conditions: cut foil, room temperature, microwave frequency: 9.32851 (**a**), 9.32908 (**b**) GHz; microwave power: 40 (**a**), 58 (**b**) mW; modulation amplitude: 1 mT; sweep: 20 mT; sweep time: 4 min.; time constant: 0.1 s; receiver gain: 4 (**a**), 5 (**b**) $\times 10^5$.

Table 5. EPR data for PMMA + 10% TOCs (TOCs = (**1**) and (**2**)) composite samples. The samples were exposed to visible light prior to measurement.

Sample	g-Factors	Species	Ref.
PMMA + (**1**) 10 wt.%	2.025, 2.009, 2.003 2.018, ca. 2.008(?), 2.000 1.993, 1.986(?)	O_2^- O^- Ti(III)	-
PMMA + (**2**) 10 wt.%	2.017, 2.008, 1.999 1.993, 1.984(?)	O^- Ti(III)	-
PMMA + (**4**) 20 wt.%	2.025, 2.017, 2.007, 2.000, 1.993, 1.989(?)	O_2^- Ti(III)?	-
PMMA + (**5**) 20 wt.%	2.024, 2.0095, 2.0034 2.003, −1.997 1.967, 1.957, 1.938	O_2^- O^- Ti(III)	[32]

3.7. The Estimation of the Antimicrobial Activity of PMMA + TOCs Composite Folis

The studied PMMA + TOC composite foils showed superior biocidal activity (R index 5.3–5.4) against Gram-positive strains while their activity against Gram-negative strains was variable (R index 1.3–3.2). Although PMMA foils showed at least static activity (reduction index > 1–1.99) against *E. coli* reference strains, the PMMA + (**5**) 20 wt.% and PMMA + (**1**) 20 wt.% displayed biocidal activity (reduction index $\geq$ 2–3.2) against both these strains. None of the tested PMMA + TOC foils showed activity against yeasts of *C. albicans* (Table 6).

Table 6. Antimicrobial activity of PMMA + TOCs (TOCs = (**1**), (**2**), (**4**), and (**5**)) irradiated by visible light.

No.	Composite Sample	Microorganisms				
		Escherichia coli ATCC 8739	*Escherichia coli* ATCC 5922	*Staphylococcus aureus* ATCC 6538	*Staphylococcus aureus* ATCC 25923	*Candida albicans* ATCC 10231
1	PMMA	none	none	none	none	none
2	PMMA + (**1**) 20 wt.%	2.6	2.0	5.3	5.4	0.45
3	PMMA + (**2**) 20 wt.%	1.6	1.3	5.3	5.4	0.5
4	PMMA + (**4**) 20 wt.%	1.3	3.2	5.3	5.4	0.6
5	PMMA + (**5**) 20 wt.%	2.0	3.2	5.3	5.4	0.1

4. Discussion

The reaction between titanium isobutoxide and fluorene-9-carboxylic acid in a 1:1 molar ratio at room temperature, with acetone as the solvent, resulted in the co-crystallization of three complexes with the following summary formulas: $[Ti_6O_4(O^iBu)_8(O_2C_{13}H_9)_8] \cdot 2(CH_3)_2CO$ (**1**), $[Ti_6O_6(O^iBu)_6(O_2C_{13}H_9)_6]$ (**2**), and $[Ti_6O_6(O^iBu)_6(O_2C_{13}H_9)_6]$ (**3**). Single crystals, varying in shape and size (Figures 1c and 2b,c), were manually isolated from the reaction mixture (optical microscope). Their structures were solved using the single-crystal X-ray diffraction method.

Analysis of the structural data revealed that $[Ti_6O_4(O^iBu)_8(O_2C_{13}H_9)_8] \cdot 2(CH_3)_2CO$ (**1**) crystallizes in the triclinic P-1 space group. Six titanium(IV) cations are almost coplanar, with the biggest shift reaching 0.106 Å. The core can be described as two coplanar titanium triangles (Figure 1a). In each triangle, the titanium(IV) cations are bridged by a μ_3-O1 atom shifted by 0.389 Å from the Ti plane, while both triangles are joined by two μ-O_2 bridges. In the former case, the Ti-O1 distances are 1.902 (3), 1.906 (3), and 2.066 (2) Å, with the longest one for the lateral Ti_3 cation clearly indicating that this bridge is asymmetric. The Ti1-O_2-Ti_2 bridge is also asymmetric, with very short Ti-(μ-O_2) bonds (1.755–1.869 (2) Å). In the reported compound, all titanium(IV) cations are found in a distorted octahedral environment, but the coordination sphere content is different. Ti1 and Ti2 are coordinated by two (O1 and O2) oxo anions, three oxygen atoms from carboxylate anions, and one bridging O26 (for Ti1) or terminal O86 (for Ti2) Bu^iO^- anion, whereas lateral Ti_3 is found in an environment of O1 oxo anion, two carboxylates, and three Bu^iO^- anions (one bridging and two terminal). Carboxylate anions also form asymmetric bridges with distances differing by 0.03, 0.06, 0.13, and 0.04 for O11, O31, O51, and O71 carboxylate anions, respectively. Ti-ORCOO bonds introduce differences between Ti1 (three short bonds) and Ti_2 (three long). Based on previous studies [14,17,18,31,32,41–44], it can be assumed that this structure is formed by the connection of two {Ti_3O} subunits [14,43–46] through two μ-O bridges. Previous research has shown that a Ti(IV) complex (**4**) containing {Ti_3O} cores can be isolated from a 4:1 mixture of isopropoxide and fluorene-9-carboxylic acid under similar reaction conditions [35].

It should be noted that the reaction conditions described for the 1:1 mixture also favor the formation of dense structures ((**2**), (**3**)) with a {Ti_6O_6} core stabilized by iso butoxide and fluorene-9-carboxylate ligands (Figure 2a) and are similar to previously studied hexanuclearTi(IV)-oxo complexes [14,43–47]. Analysis of the crystallographic data revealed that $[Ti_6O_6(O^iBu)_6(O_2C_{13}H_9)_6]$ (**2**) (Figure 2d) and $[Ti_6O_6(O^iBu)_6(O_2C_{13}H_9)_6]$ (**3**) (Figure 2e) are polymorphs crystallizing in monoclinic and tetragonal system, respectively (Table 1). Hence, only (**2**) will be described in detail. This oxo complex crystallizes in the P21/n space group with all atoms found in the general positions and half of the molecule given by the formula in the asymmetric unit. The common {$Ti_6(\mu_3$-$O)_6$} core is found in this structure, with Ti-Ti distances ranging from 3.1009 (9) Å to 3.1156 (9) Å for titanium

located in different Ti_3O_3 hexagonal bases, and 3.4859 (9) Å to 3.5087 (9) Å for titanium from the same Ti_3O_3 hexagonal base. A Ti_6O_4 core is formed by two Ti_3O_3 hexagonal bases cross-linked by six carboxylates (Table S1). The coordination spheres of all titanium(IV) cations are composed of six oxygen atoms—three coming from oxo bridges arranged in a fac mode, two from two carboxylate anions, and one from terminal isobutanolate. O11 and O51 are coordinated in an asymmetric mode with two Ti-O distances differing by approximately 0.04 Å, whereas for the O31 anion, both Ti-O bonds were found to be identical within the experimental error. The terminal iso butoxide anions form the shortest bonds in the titanium coordination sphere. In this core, oxo anions connect three titanium atoms with distances falling into two ranges—1.880 (2) Å to 1.916 (3) Å and 2.142 (3) Å to 2.172 (3) Å. In the former case, they correspond to {Ti-(μ_3-O)} distances for titanium and oxygen atoms from the same {Ti_3O_3} base, whereas the longest bond in Ti(IV) coordination occurs for Ti and O atoms from different bases. In the packing of (**2**), we observe densely packed $[Ti_6O_6(O^iBu)_6(O_2C_{13}H_9)_6]$ clusters without any significant cavities, whereas in (**3**), significant voids were found, accounting for 1924.6 $Å^3$ (9.2% of the cell volume). However, the model is complete as the highest peaks on the difference electron map do not exceed $1e/A^3$. In (**2**), the clusters interact via bulk ring moieties, forming both π-π interactions between strongly inclined $C_{13}H_9$ units and C-H . . . π interactions. Hence, intermolecular hydrogen bonds were not found, and isobutanolate was not involved in the crystal network formation. According to our previous results, when titanium isobutoxide and fluorene-9-carboxylic acid were reacted in a 4:1 molar ratio at room temperature, using acetone as the solvent, oxo complexes with the summary formula $[Ti_4O_2(O^iBu)_{10}(O_2C_{13}H_9)_2]$ (**5**) were isolated [35].

One of the research directions exploring oxo-titanium(IV) complexes (TOCs) involves the evaluation of their physicochemical properties, particularly their photoinduced activity [31,34,35,48]. Liu et al. conducted a study where they introduced various carboxylate ligands (e.g.,propionic acid, pivalic acid, bromoacetic acid, trifluoroacetic acid, 2-naphthalenecarboxylic acid, 4-bromo-benzene carboxylic acid, pentafluorobenzoic acid) to the reactive coordination sites of the complex $[Ti_6O_4(O^iPr)_{10}(O_3P\text{-}Phen)_2(OAc)_2]$, resulting in successful modifications of the bandgap size (E_a) within the range of 3.6–3.0 eV [49]. In our earlier investigations, we also demonstrated the ability to modify the energy gap size within the range of E_a = 2.98–2.55 eV for complexes $[Ti_4O_2(O^iBu)_{10}(O_2CR'')_2]$ through the functionalization of carboxylic ligands (R″ = $PhNO_2$, PhCl, $PhNH_2$, $C_{13}H_9$) [35,41]. Moreover, the results of these studies revealed that the complex stabilized by fluorene-9-carboxylate ligands (-$O_2CC_{13}H_9$) exhibited photocatalytic activity both in the UV and visible range [35].

In this paper, we have focused on investigating the impact of the {Ti_aO_b} core structure (while maintaining the same type of stabilized ligands) on the physicochemical properties and photocatalytic activity of oxo complexes. Previous research by Cui et al. explored these dependencies using a group of titanium-oxo complexes with different core architectures ((Ti_4ClSal_4), ($Ti_{11}ClSal_8$), and ($Ti_{14}ClSal_8$)), which were stabilized by isopropoxide and 4-chlorosalicylate (ClSal) ligands [50]. Analysis of the solid-state diffuse reflectance spectra (UV-Vis-DRS) of these oxo clusters revealed that the absorption maximum was observed in the UV range, with absorption edges at 450, 480, and 500 nm, respectively. The resulting optical band gaps exhibited a small range of variation, specifically between 2.8 and 3.0 eV. The photocatalytic activity of these compounds, evaluated through the photodecolorization of a methylene blue solution (MB) under sunlight irradiation, showed changes of approximately 78%, 73%, and 97% (after 32 min) for the (Ti_4ClSal_4), ($Ti_{11}ClSal_8$), and ($Ti_{14}ClSal_8$) clusters, respectively [50]. It is important to note that in all of these photocatalytic experiments, 30 mg of the oxo-cluster grains were added to 50 mL of MB solution. Our experiments focused on investigating the properties of oxo complexes containing {Ti_3O} (**4**) [34], {Ti_4O_2} (**5**) [35], {Ti_6O_4} (**1**), and {Ti_6O_6} (**2**) cores, stabilized by fluorene-9-carboxylate ligands. Due to the potential hydrolysis of these compounds in water solutions, their photocatalytic and antimicrobial activities were evaluated for the composite systems, where 10 or 20 wt.%

of TOCs were dispersed in the PMMA matrix. Examination of the SEM images of the composite films presented in Figure 3 revealed the presence of blurry-shaped (**1**) grains. This effect could be attributed to the interactions between polymer chains and molecules of this oxo complex. The evidence supporting this hypothesis is the noticeable difference in the glass transition temperature between the composite containing (**1**) and PMMA or PMMA + (**2**) (Table 3). SEM images of PMMA composites enriched with the (**2**), (**4**), and (**5**) complexes showed no blurry effect on the dispersed grains within the PMMA matrix (Figure 3). Analysis of the UV-Vis-DRS spectra for compounds (**1**)–(**5**) demonstrated a significant shift in the maximum absorption from the ultraviolet (UV) to the visible range, following this order: λ_{max} = 365 nm for {Ti_6O_4} (**1**) and {Ti_6O_6} (**2**), λ_{max} = 380 nm for {Ti_3O} (4), and λ_{max} = 395 nm for {Ti_4O_2} (5), with corresponding absorption edges at 400 nm (**1**) and (**2**), 420 nm (**4**), and 500 nm (**5**). These results indicate that the absorption of hexanuclear core structures ({Ti_6O_4} and {Ti_6O_6}) tends to shift towards the UV range, while in the case of oxo complexes consisting of simple units ({Ti_3O} and {Ti_4O_2}), the shift occurs towards the visible range. The band gap values for the studied clusters exhibited the following changes: E_a= 2.17 eV for (**4**), 2.55 eV for (**5**), 2.98 eV for (**1**), and 2.99 eV for (**2**) (Figure S3). It is worth noting that these changes differ from the findings reported by Cui et al. [50], where the band gap values remained within a narrow range (E_a = 2.8–3.0 eV) and were highest for the smallest cluster (Ti_4ClSal_4).

The photocatalytic activity of the investigated titanium oxo clusters (TOCs) (1, 2, 4, and 5) incorporated into the PMMA matrix (PMMA + TOCs 20 wt.% systems) was evaluated by measuring the decolorization of a methylene blue (MB) solution. The aforementioned samples were immersed in the MB solution and exposed to UV (340–395 nm) and visible (395–420 nm) light. The analysis of the data presented in Figures 4 and 6 revealed that the photocatalytic activity of the composite samples was more pronounced in the UV range. Specifically, composites containing TOCs with structurally dense cores, such as {Ti_6O_6} (**2**) and {Ti_4O_2} (**5**), exhibited higher activity compared to systems enriched with flat cores, namely {Ti_3O} (**4**) and {Ti_6O_4} (**1**). For composite (**1**), it is important to consider potential interactions between the polymer chains and TOC molecules, which could potentially diminish the photocatalytic activity of the PMMA + composite (**1**). These photoinduced activities observed across all the studied composite samples were found to be reproducible processes (Figure 7). Notably, our samples demonstrated longer MB photodegradation times in comparison to previous studies on the photocatalytic activity of Ti(IV)-oxo clusters [21,23,24,50]. Analyzing the presented experimental data should consider that the photocatalytic activity is assessed for PMMA + TOCs systems in which only 20 wt.% of TOCs are dispersed in the polymer matrix [32,34,35].

Based on previous findings, we made the assumption that the photocatalytic activity of PMMA + TOCs samples is a result of their photoexcitation, leading to the generation of reactive oxygen species (ROS) [51–55]. Additionally, this effect is combined with the photoactivated reduction of Ti(IV) to Ti(III) [52–54]. To confirm the aforementioned phenomenon, we recorded EPR spectra of PMMA + TOCs (TOCs = (**1**) and (**2**)) samples (Figure 8). In the EPR spectrum of PMMA + (1), we observed anisotropic signals corresponding to O_2^- and O^- radicals, as well as Ti(III) (Figure 8a and Table 5). It is worth noting that some lines, particularly g_2 for both oxygen species, may overlap. The formation of O_2^- and O^- paramagnetic centers involves electron removal and stabilization of the resulting radical through the reduction of Ti(IV) to Ti(III) [51,52]. According to the literature, the maximum g-factor for O_2^- is higher compared to O^- species [53]. For the PMMA + (**2**) composite, we obtained an EPR spectrum with improved resolution (Figure 8b), revealing the characteristic signal attributed to O^- paramagnetic species. However, the presence of O_2^- radicals cannot be entirely ruled out; their content on the sample surface is likely much lower. The electron transfer between Ti(IV) and Ti(III) was also confirmed in this sample. Similar spectral patterns were observed for the PMMA + (**5**) 20 wt.% composite in previous studies (Table 5) [35]. In the case of the PMMA + (**4**) 20 wt.% sample, the EPR spectrum indicated the presence of O_2^-, O^-, and possibly Ti(III) forms, consistent with

the results obtained for a composite containing a $\{Ti_6O_4\}$ core built by Ti_3O subunits. The signals observed in the PMMA + (**4**) 20 wt.% sample was relatively weak and exhibited a rapid decrease in intensity over time, indicating lower stability of the $\{Ti_3O\}$ core compared to other cores. It is important to note that other oxygen-based radicals, such as peroxy-type radicals (RCOO•) and organic-type adducts of O_2^-, could potentially be indistinguishable from the superoxide radical anion (O_2^-) using CW-EPR spectroscopy. However, this scenario is unlikely as the first two forms are unstable at room temperature and can only be detected at lower temperatures [55].

The antimicrobial activity of TiO_2-based materials, specifically TiO_2 coatings, is an important but relatively poorly understood issue. Research on TiO_2-based materials with photocatalytic activity has shown their remarkable effectiveness in killing microorganisms on various surfaces [56]. Our previous investigations on the modification of titanium or Ti6Al4V alloy implants [57–59] revealed that the antimicrobial efficiency of TiO_2 coatings is mainly influenced by factors such as surface structure and morphology, hydrophilicity, exposure to light (especially UV), and the presence of oxygen. Kumaravel et al. [56] suggest that antimicrobial activity depends on the interaction between microorganisms and the surface characteristics of the coating material, such as electrostatic interaction, pH, and morphology. They observed that after exposure to light, TiO_2 coatings prevented the reactivation or regrowth of microbes, which may be associated with the generation of reactive oxygen species (ROS). Therefore, while researching the photocatalytic properties of Ti(IV)-oxo clusters, we also drew attention to their antimicrobial activity [31,32]. The significant advantage of using oxo complexes is their ability to reduce the energy gap from 2.9–3.2 eV for TiO_2 to 2.2–3.0 eV for the studied group of TOCs, allowing them to absorb visible light. The core structure and type of carboxylate ligand significantly influences the band gap value in this context. Analysis of electron paramagnetic resonance (EPR) spectra indicated that stable ROS species formed on the surface of the composite film were oxygen radicals (O^-) for PMMA + TOCs (TOCs = (**1**), (**2**), and (**5**)) samples and superoxide radicals (O_2^-) for PMMA + TOCs (TOCs = (**1**), (**4**), and (**5**)) samples. Previous studies on TiO_2 materials have reported that the generation of ROS species can damage cells, hinder microbial growth and migration, and directly interact with the cell membrane [56,60]. This mechanism is also applicable to our PMMA + TOC samples. Based on the data presented in Table 6, we can conclude that all the PMMA + TOCs samples exhibited biocidal activity against *S. aureus* reference strains, and most of them also showed activity against *E. coli* strains. However, the antibacterial activity varied among different strains of *Escherichia coli*. The composite samples enriched with TOCs grains containing $\{Ti_4O_2\}$ cores (**5**) and $\{Ti_6O_4\}$ (**1**) demonstrated the highest antibacterial activity. It is worth noting that, similar to PMMA + (**1**) 10 wt%, the composite PMMA + (**5**) 20 wt.% also released both oxygen anion species (O_2^- and O^-), confirming the crucial role of reactive oxygen species (ROS) as antibacterial agents. The effects of O^- on microorganism cells have been poorly investigated. It is known that O^- reacts with the hydrocarbon bonds of microorganisms [60]. Singlet oxygen or other ROS can damage bacterial cells or other microbes through various mechanisms, including lipid peroxidation, oxidation of amino acids in proteins, protein cross-linking, and oxidative damage to nucleic acids. This damage disrupts the normal functioning of microbial cells [60,61]. ROS can severely impair cell walls and intrinsic structures, leading to rapid and irreversible inactivation. However, the effectiveness of microorganism inactivation depends on the intensity of ROS, the initial population of microorganisms, the exposed area, the environment, and the type of microorganism. In our case, the PMMA + (**2**) 20 wt.% system, which only generated O^- species on its surfaces, exhibited weaker activity against *E. coli* strains compared to PMMA + (**1**) 20 wt.%. [60].

5. Conclusions

The aim of this research was to evaluate the influence of the $\{Ti_aO_b\}$ core structure on the photocatalytic and antimicrobial activity of titanium(IV)-oxo clusters (TOCs). The clusters, denoted by the general formulas $[Ti_6O_4(O^iBu)_8(O_2C_{13}H_9)_8] \cdot 2(CH_3)_2CO$ (**1**),

$[Ti_6O_6(O^iBu)_6(O_2C_{13}H_9)_6]$ (**2**), $[TiO_3(O^iPr)_8(O_2C_{13}H_9)_2]$ (**4**), and $[Ti_4O_2(O^iBu)_{10}(O_2C_{13}H_9)_2]$ (**5**), were used to investigate these effects.

Analysis of UV-Vis-DRS spectra revealed that the core structure of $\{Ti_aO_b\}$ influences the band gap energy of the isolated crystalline powders. The energy values varied as follows: 2.17 eV for $\{Ti_3O\}$ (**4**), 2.55 eV for $\{Ti_4O_2\}$ (**5**), 2.98 eV for $\{Ti_6O_4\}$ (**1**), and 2.99 eV for $\{Ti_6O_6\}$ (**2**). The absorption maximum for the studied TOCs was detected in the UV range (360–395 nm), with an absorption edge at 400 nm ($\{Ti_6O_4\}$ (**1**) and $\{Ti_6O_6\}$ (**2**)), 420 nm ($\{Ti_3O\}$ (**4**)), and 500 nm ($\{Ti_4O_2\}$ (**5**)). According to these data, the investigated oxo complexes can exhibit photocatalytic activity in both UV and visible light.

The photocatalytic and antimicrobial activity of the studied group of Ti(IV)-oxo complexes (TOCs), has been estimated for PMMA + TOCs composite systems. The assumption was the protection of TOCs before possible hydrolysis processes. Analysis of EPR spectra of the samples mentioned above proved the presence of natural photoexcitation of all PMMA + TOCs surface and the generation of ROS species. In the presence of composite samples, the photoinduced de-colorization of methylene blue solution processes revealed that oxo clusters stabilized by 9-fluorene carboxylate ligands are photocatalytic active both in the UV and Vis range. However, this activity was higher in the UV range. The results of conducted experiments revealed that photocatalytic activity of investigated TOCs decreases in the row: $\{Ti_6O_6\}$ (**2**) > $\{Ti_4O_2\}$ (**5**) > $\{Ti_3O\}$ (**4**) > $\{Ti_6O_4\}$ (**1**). It should be noted that the low photocatalytic activity of PMMA + (**1**) could also be attributed to potential interactions between TOCs grains and polymer chains, which is supported by SEM images and DSC data.

In general, PMMA + TOCs composites exhibited greater antibacterial activity against Gram-positive *Staphylococcus aureus* strains compared to Gram-negative *Escherichia coli* strains. However, it is important to mention that the antibacterial activity against *E. coli* strains of PMMA samples enriched with TOCs increased in the following order: $\{Ti_3O\}$ (**4**) <$\{Ti_6O_6\}$ (**2**) <$\{Ti_4O_2\}$ (**5**) <$\{Ti_6O_4\}$ (**1**). It is worth noting that on the surface samples demonstrating the highest antimicrobial activity, namely PMMA + (**1**) and PMMA + (**5**), were generated by both O_2^- and O^- oxygen anion species.

One of the key advantages of PMMA + TOCs composite materials enriched with oxo-Ti(IV) clusters featuring a defined $\{Ti_aO_b\}$ core structure is their antimicrobial activity in the visible range. This characteristic renders this type of composite suitable for preventing the spread of bacteria in high-risk public areas (e.g., hospitals, supermarkets, or malls) without relying on harmful UV light, which is currently widely utilized.

Supplementary Materials: The following supporting information can be downloaded at: https://www.mdpi.com/article/10.3390/cryst13070998/s1, Figure S1: SEM images and EDX patterns of pure PMMA and PMMA + 20(**1**)) and PMMA + 20(**2**)) composites; Figure S2: Thermogravimetric curves (TGA) (a,c) and the differential scanning calorimetry curves of (DSC) (b,d) of the TOCs (**1**),(**2**) and produced composite materials; Figure S3: Structures of $\{T_aO_b\}$ cores in molecules (**1**), (**2**), (**4**), and (**5**) oxo complexes, and values of HOMO-LUMO gap; Figure S3: The results of the photocatalytic process repeatability studies of PMMA + TOCs 20 wt.% composite samples (TOCs = (**1**), (**2**), (**4**) and (**5**)) in the visible light; Table S1: Selected distances and angles in (**1**), (**2**), and (**3**) oxo complexes.

Author Contributions: Conceptualization, P.P. and A.R.; methodology, B.K., P.P. and A.R.; formal analysis, B.K., P.P., A.R., T.M., P.G. and G.W.; investigation, B.K., T.M., P.G. and G.W.; data curation, B.K.; writing—original draft preparation, B.K., P.P., T.M. and P.G.; writing—review and editing, A.R. and P.P.; supervision, P.P. and A.R. All authors have read and agreed to the published version of the manuscript.

Funding: This research received no external funding.

Data Availability Statement: Crystallographic data has been deposited at the Cambridge Crystallographic Data Centre with Deposit Nos. 2224562–2224564 as detailed in Tables 1 and S1.

Conflicts of Interest: The authors declare no conflict of interest.

References

1. Zaky, A.M.; Chaplin, B.P. Porous Substoichiometric TiO_2 Anodes as Reactive Electrochemical Membranes for Water Treatment. *Environ. Sci. Technol.* **2013**, *47*, 6554–6563. [CrossRef]
2. Jandam, N.; Serivalsatit, K.; Hunsom, M.; Pruksathorn, K. Ultrasound-Assisted Synthesis of Nonmetal-Doped Titanium Dioxide Photocatalysts for Simultaneous H_2 Production and Chemical Oxygen Demand Removal from Industrial Wastewater. *ACS Omega* **2021**, *6*, 24709–24719. [CrossRef]
3. Li, A.; Chen, S.; Yang, F.; Gao, H.; Dong, C.; Wang, G. Metalloporphyrin-Decorated Titanium Dioxide Nanosheets for Efficient Photocatalytic Carbon Dioxide Reduction. *Inorg. Chem.* **2021**, *60*, 18337–18346. [CrossRef]
4. Trivedi, M.; Murase, J. Titanium Dioxide in Sunscreen. In *Application of Titanium Dioxide*; Janus, M., Ed.; InTech: London, UK, 2017; ISBN 978-953-51-3429-9.
5. He, Z.; Wu, H.; Shi, Z.; Gao, X.; Sun, Y.; Liu, X. Mussel-Inspired Durable TiO_2/PDA-Based Superhydrophobic Paper with Excellent Self-Cleaning, High Chemical Stability, and Efficient Oil/Water Separation Properties. *Langmuir* **2022**, *38*, 6086–6098. [CrossRef]
6. Radtke, J.; Wiedey, R.; Kleinebudde, P. Alternatives to Titanium Dioxide in Tablet Coating. *Pharm. Dev. Technol.* **2021**, *26*, 989–999. [CrossRef]
7. Younes, M.; Aquilina, G.; Castle, L.; Engel, K.; Fowler, P.; Frutos Fernandez, M.J.; Fürst, P.; Gundert-Remy, U.; Gürtler, R. Safety Assessment of Titanium Dioxide(E171) as Food Additive. *EFS2* **2021**, *19*, e06585.
8. Kitagawa, I.L.; Miyazaki, C.M.; Pitol-Palin, L.; Okamoto, R.; de Vasconcellos, L.M.R.; Constantino, C.J.L.; Lisboa-Filho, P.N. Titanium-Based Alloy Surface Modification with TiO_2 and Poly(Sodium4-Styrenesulfonate) Multilayers for Dental Implants. *ACS Appl. Bio Mater.* **2021**, *4*, 3055–3066. [CrossRef] [PubMed]
9. Kaur, R.; Thakur, N.S.; Chandna, S.; Bhaumik, J. Sustainable Lignin-Based Coatings Doped with Titanium Dioxide Nanocomposites Exhibit Synergistic Microbicidal and UV-Blocking Performance toward Personal Protective Equipment. *ACS Sustain. Chem. Eng.* **2021**, *9*, 11223–11237. [CrossRef]
10. Ganguly, P.; Mathew, S.; Clarizia, L.; Kumar, R.S.; Akande, A.; Hinder, S.; Breen, A.; Pillai, S.C. Theoretical and Experimental Investigation of Visible Light Responsive $AgBiS_2$-TiO_2 Heterojunctions for Enhanced Photocatalytic Applications. *Appl. Catal. B Environ.* **2019**, *253*, 401–418. [CrossRef]
11. Cao, L.; Li, Y.-F.; Tong, Y.; Yang, R.; Sun, L.; Cao, Q.; Chen, R. A Novel $Bi_{12}TiO_{20}$/g-C_3N_4 Hybrid Catalyst with a Bionic Granum Configuration for Enhanced Photocatalytic Degradation of Organic Pollutants. *J. Hazard. Mater.* **2019**, *379*, 120808. [CrossRef] [PubMed]
12. Li, S.; Wang, C.; Liu, Y.; Cai, M.; Wang, Y.; Zhang, H.; Guo, Y.; Zhao, W.; Wang, Z.; Chen, X. Photocatalytic Degradation of Tetracycline Antibiotic by a Novel $Bi_2Sn_2O_7$/Bi_2MoO_6S-Scheme Heterojunction: Performance, Mechanism Insightand Toxicity Assessment. *Chem. Eng. J.* **2022**, *429*, 132519. [CrossRef]
13. Cheng, K.; Chhor, K.; Kanaev, A. Solvent Effect on Nucleation-Growth of Titanium-Oxo-Alkoxy Nanoparticles. *Chem. Phys. Lett.* **2017**, *672*, 119–123. [CrossRef]
14. Schubert, U. Chemical Modification of Titanium Alkoxides for Sol–Gel Processing. *J. Mater. Chem.* **2005**, *15*, 3701. [CrossRef]
15. Liu, X.-X.; Chen, S.; Fang, W.-H.; Zhang, L.; Zhang, J. Amino-Polyalcohol-Solvothermal Synthesis of Titanium-Oxo Clusters: From Ti_6 to Ti_{19} with Structural Diversity. *Inorg. Chem.* **2019**, *58*, 7267–7273. [CrossRef]
16. Sanchez, C.; Rozes, L.; Ribot, F.; Laberty-Robert, C.; Grosso, D.; Sassoye, C.; Boissiere, C.; Nicole, L. "Chimie Douce": A Land of Opportunities for the Designed Construction of Functional Inorganic and Hybrid Organic-Inorganic Nanomaterials. *Comptes Rendus Chim.* **2010**, *13*, 3–39. [CrossRef]
17. Piszczek, P.; Radtke, A.; Muzioł, T.; Richert, M.; Chojnacki, J. The Conversion of Multinuclear μ-OxoTitanium (IV) Species in the Reaction of $Ti(OiBu)_4$ with Branched Organic Acids; Results of Structural and Spectroscopic Studies. *Dalton Trans.* **2012**, *41*, 8261–8269. [CrossRef] [PubMed]
18. Radtke, A.; Piszczek, P.; Muzioł, T.; Wojtczak, A. The Structural Conversion of Multinuclear Titanium(IV)μ-Oxo-Complexes. *Inorg. Chem.* **2014**, *53*, 10803–10810. [CrossRef]
19. Papiernik, R.; Hubert-Pfalzgraf, L.G.; Vaissermann, J.; Goncalves, M.C.H.B. Synthesis and Characterization of New Titanium Hexanuclear Oxo Carboxylato Alkoxides. Molecular Structure of $[Ti_6(\mu_3\text{-}O)_6(\mu\text{-}O_2CC_6H_4OPh)_6(OEt)_6]$. *J. Chem. Soc. Dalton Trans.* **1998**, *14*, 2285–2288. [CrossRef]
20. Lv, H.-T.; Li, H.-M.; Zou, G.-D.; Cui, Y.; Huang, Y.; Fan, Y. Titanium-Oxo Clusters Functionalized with Catecholate-Type Ligands: Modulating the Optical Properties through Charge-Transfer Transitions. *Dalton Trans.* **2018**, *47*, 8158–8163. [CrossRef]
21. Wang, C.; Wang, S.-J.; Kong, F.-G. Calixarene-Protected Titanium-Oxo Clusters and Their Photocurrent Responses and Photocatalytic Performances. *Inorg. Chem.* **2021**, *60*, 5034–5041. [CrossRef]
22. Liu, J.-J.; Li, N.; Sun, J.-W.; Liu, J.; Dong, L.-Z.; Yao, S.-J.; Zhang, L.; Xin, Z.-F.; Shi, J.-W.; Wang, J.-X. Ferrocene-Functionalized Polyoxo-Titanium Cluster for CO_2 Photoreduction. *ACS Catal.* **2021**, *11*, 4510–4519. [CrossRef]
23. Wang, J.-F.; Fang, W.-H.; Li, D.-S.; Zhang, L.; Zhang, J. Cocrystal of $\{Ti_4\}$ and $\{Ti_6\}$ Clusters with Enhanced Photochemical Properties. *Inorg. Chem.* **2017**, *56*, 2367–2370. [CrossRef] [PubMed]
24. Gao, M.-Y.; Fang, W.-H.; Wen, T.; Zhang, L.; Zhang, J. Connecting Titanium-Oxo Clusters by Nitrogen Heterocyclic Ligands to Produce Multiple Cluster Series with Photocatalytic H_2 Evolution Activities. *Cryst. Growth Des.* **2017**, *17*, 3592–3595. [CrossRef]

25. Wang, C.; Liu, C.; Li, L.-J.; Sun, Z.-M. Synthesis, Crystal Structures, and Photochemical Properties of a Family of Heterometallic Titanium Oxo Clusters. *Inorg. Chem.* **2019**, *58*, 6312–6319. [CrossRef] [PubMed]
26. Svenson, F.G.; Sensenbaeva, G.A.; Keesler, V.G. Mixed-Ligand Titanium "Oxo-Clusters": Structural Insights into the Formation and Binding of Organic Molecules and Transformation into Oxide Nanostructures on Hydrolysis and Thermolysis. *Eur. J. Inorg. Chem.* **2017**, *35*, 4117–4122. [CrossRef]
27. Khalil, A.T.; Ovais, M.; Ullah, I.; Ali, M.; Shinwari, Z.K.; Khamlich, S.; Maaza, M. *Sageretia Thea* (Osbeck.) Mediated Synthesis of Zinc Oxide Nanoparticles and Its Biological Applications. *Nanomedicine* **2017**, *12*, 1767–1789. [CrossRef] [PubMed]
28. Wang, G.; Feng, H.; Hu, L.; Jin, W.; Hao, Q.; Gao, A.; Peng, X.; Li, W.; Wong, K.-Y.; Wang, H.; et al. An Antibacterial Platform Based on Capacitive Carbon-Doped TiO_2 Nanotubes after Direct or Alternating Current Charging. *Nat. Commun.* **2018**, *9*, 2055. [CrossRef]
29. Mutalik, C.; Lin, I.-H.; Krisnawati, D.I.; Khaerunnisa, S.; Khafid, M.; Widodo; Hsiao, Y.C.; Kuo, Y.-R. Antibacterial Pathways in Transition Metal-Based Nanocomposites: A Mechanistic Overview. *Int. J. Nanomed.* **2022**, *7*, 6821–6842. [CrossRef]
30. Gupta, A.; Mumtaz, S.; Li, C.-H.; Hussain, I.; Rotello, V.M. Combatting Antibiotic-Resistant Bacteria Using Nanomaterials. *Chem. Soc. Rev.* **2019**, *48*, 415–427. [CrossRef]
31. Piszczek, P.; Kubiak, B.; Golińska, P.; Radtke, A. Oxo-Titanium(IV) Complex/Polymer Composites—Synthesis, Spectroscopic Characterization and Antimicrobial Activity Test. *IJMS* **2020**, *21*, 9663. [CrossRef]
32. Kubiak, B.; Radtke, A.; Topolski, A.; Wrzeszcz, G.; Golińska, P.; Kaszkowiak, E.; Sobota, M.; Włodarczyk, J.; Stojko, M.; Piszczek, P. The Composites of PCL and Tetranuclear Titanium(IV)-Oxo Complexes as Materials Exhibiting the Photocatalytic and the Antimicrobial Activity. *IJMS* **2021**, *22*, 7021. [CrossRef] [PubMed]
33. Meth-Cohn, O.; Thorpe, D.; Twitchett, H.J. Insertion Reactions of Titanium Alkoxides with Isocyanates and Carbodiimides. *J. Chem. Soc. C* **1970**, 132–135. [CrossRef]
34. Janek, M.; Muzioł, T.M.; Piszczek, P. Trinuclear Oxo-Titanium Clusters: Synthesis, Structure, and Photocatalytic Activity. *Materials* **2019**, *12*, 3195. [CrossRef]
35. Janek, M.; Radtke, A.; Muzioł, T.; Jerzykiewicz, M.; Piszczek, P. Tetranuclear Oxo-Titanium Clusters with Different Carboxylate Aromatic Ligands: Optical Properties, DFT Calculations, and Photoactivity. *Materials* **2018**, *11*, 1661. [CrossRef] [PubMed]
36. *E. CrysAlis Red and CrysAlis CCD*; Oxford Diffraction Ltd.: Abingdon, UK, 2000.
37. Sheldrick, G.M. Crystal Structure Refinement with *SHELXL*. *Acta Crystallogr. C Struct. Chem.* **2015**, *71*, 3–8. [CrossRef]
38. Brandenburg, K.; Berndt, M. *Diamond, Release 2.1e, Crystal Impact GbR*; Scientific Research: Bonn, Germany, 2001.
39. Farrugia, L.J. WinGX and ORTEP for Windows: An Update. *J. Appl. Crystallogr.* **2012**, *45*, 849–854. [CrossRef]
40. Xu, H.; Ouyang, S.; Liu, L.; Reunchan, P.; Umezawa, N.; Ye, J. Recent Advances in TiO_2-Based Photocatalysis. *J. Mater. Chem. A* **2014**, *2*, 12642–12661. [CrossRef]
41. Janek, M.; Muzioł, T.M.; Piszczek, P. The Structure and Photocatalytic Activity of the Tetranuclear Titanium(IV) Oxo-Complex with 4-Aminobenzoate Ligands. *Polyhedron* **2018**, *141*, 110–117. [CrossRef]
42. Piszczek, P.; Grodzicki, A.; Richert, M.; Wojtczak, A. Structural and Thermal Stability Studies of Ti(IV) Hexanuclear Oxo Trimethylacetato Isopropoxide Complex. *Inorganica Chim. Acta* **2004**, *357*, 2769–2775. [CrossRef]
43. Schubert, U. Titanium-Oxo Clusters with Bi- and Tridentate Organic Ligands: Gradual Evolution of the Structures from Small to Big. *Chem. Eur. J.* **2021**, *27*, 11239–11256. [CrossRef]
44. Schubert, U. En Route from Metal Alkoxides to Metal Oxides: Metal Oxo/Alkoxo Clusters. *J. Sol.-Gel. Sci. Technol.* **2023**, *105*, 587–595. [CrossRef]
45. Fang, W.-H.; Zhang, L.; Zhang, J. Synthetic Strategies, Diverse Structures and Tuneable Properties of Polyoxo-Titanium Clusters. *Chem. Soc. Rev.* **2018**, *47*, 404–421. [CrossRef] [PubMed]
46. Piszczek, P. Thermal Behaviour of Hexanuclear Titanium(IV) Oxo Isopropoxide Carboxylates, and Their Usability as a Single-Source TiO_2 CVD Precursors. *Polyhedron* **2007**, *26*, 93–100. [CrossRef]
47. Piszczek, P.; Richert, M.; Wojtczak, A. Crystal Structure and Spectral Characterization of Hexanuclear Oxo Titanium(IV) Clusters: $[Ti_6O_6(OSi(CH_3)_3)_6(OOCR)_6]$ (R = Bu^t, CH2Bu^t, C(CH3)2Et). *Polyhedron* **2008**, *27*, 602–608. [CrossRef]
48. Nguyen, H.L.; Vu, T.T.; Le, D.; Doan, T.L.H.; Nguyen, V.Q.; Phan, N.T.S. A Titanium Organic Framework: Engineering of the Band-Gap Energy for Photocatalytic Property Enhancement. *ACS Catal.* **2017**, *7*, 338–342. [CrossRef]
49. Liu, J.-X.; Gao, M.-Y.; Fang, W.-H.; Zhang, L.; Zhang, J. Bandgap Engineering of Titanium-Oxo Clusters: Labile Surface Sites Used for Ligand Substitution and Metal Incorporation. *Angew. Chem. Int. Ed. Engl.* **2016**, *55*, 5160–5165. [CrossRef]
50. Cui, Y.; Zou, G.-D.; Li, H.-M.; Huang, Y.; Fan, Y. 4-Chlorosalicylate-Stabilized Titanium-Oxo Clusters with Structures Mediated by Tetrazole and Their Photophysical Properties. *Polyhedron* **2019**, *157*, 177–182. [CrossRef]
51. He, W.; Liu, Y.; Wamer, W.G.; Yin, J.-J. Electron Spin Resonance Spectroscopy for the Study of Nanomaterial-Mediated Generation of Reactive Oxygen Species. *J. Food Drug Anal.* **2014**, *22*, 49–63. [CrossRef]
52. Xiong, L.-B.; Li, J.-L.; Yang, B.; Yu, Y. Ti^{3+} in the Surface of Titanium Dioxide: Generation, Properties and Photocatalytic Application. *J. Nanomater.* **2012**, *2012*, 831524. [CrossRef]
53. Suriye, K.; Lobo-Lapidus, R.J.; Yeagle, G.J.; Praserthdam, P.; Britt, R.D.; Gates, B.C. Probing Defect Sites on TiO_2 with $[Re_3(CO)_{12}H_3]$: Spectroscopic Characterization of the Surface Species. *Chem. Eur. J.* **2008**, *14*, 1402–1414. [CrossRef]
54. Dan-Hardi, M.; Serre, C.; Frot, T.; Rozes, L.; Maurin, G.; Sanchez, C.; Férey, G. A New Photoactive Crystalline Highly Porous Titanium(IV) Dicarboxylate. *J. Am. Chem. Soc.* **2009**, *131*, 10857–10859. [CrossRef] [PubMed]

55. Richards, E.; Murphy, D.M.; Che, M. An EPR Characterization of Stable and Transient Reactive Oxygen Species Formed under Radiative and Non-Radiative Conditions. *Res. Chem. Intermed.* **2019**, *45*, 5763–5779. [CrossRef]
56. Kumaravel, V.; Nair, K.M.; Mathew, S.; Bartlett, J.; Kennedy, J.E.; Manning, H.G.; Whelan, B.J.; Leyland, N.S.; Pillai, S.C. Antimicrobial TiO_2 nanocomposite coatings for surfaces, dental and orthopedic implants. *Chem. Eng. J.* **2021**, *416*, 129071. [CrossRef]
57. Radtke, A.; Topolski, A.; Jedrzejewski, T.; Kozak, W.; Sadowska, B.; Wieckowska-Szakiel, M.; Piszczek, P. Bioactivity Studies on Titania Coatings and the Estimation of Their Usefulness in the Modification of Implant Surfaces. *Nanomaterials* **2017**, *4*, 90. [CrossRef] [PubMed]
58. Piszczek, P.; Radtke, A.; Ehlert, M.; Jędrzejewski, M.; Sznarkowska, A.; Sadowska, B.; Bartmański, M.; Kemal Erdoğan, Y.K.; Ercan, B.; Jedrzejczyk, W. Comprehensive Evaluation of the Biological Properties of Surface-Modified Titanium Alloy Implants. *J. Clin. Med.* **2020**, *9*, 342. [CrossRef]
59. Ehlert, M.; Radtke, A.; Forbot, N.; Jędrzejewski, T.; Roszek, K.; Golińska, P.; Trykowski, G.; Piszczek, P. TiO_2/HA and Titanate/HA Double Layer Coatings on Ti6Al4V Surface and Their Influence on In Vitro Cell Growth and Osteogenic Potential. *J. Funct. Biomater.* **2022**, *13*, 271. [CrossRef]
60. Li, L.; Wu, F.; Chen, Y.; Xu, L.; Hao, X.; Chen, Y.; Sun, Y.; Xiong, G. Reactions of Microorganisms with Atomic Oxygen Radical Anions: Damage of Cells and Irreversible Inactivation. *J. Nanomater.* **2019**, *2019*, 2483060. [CrossRef]
61. Luksiene, Z. Photodynamic therapy: Mechanism of action and ways to improve the efficiency of treatment. *Medicina* **2003**, *9*, 1137–1150.

Disclaimer/Publisher's Note: The statements, opinions and data contained in all publications are solely those of the individual author(s) and contributor(s) and not of MDPI and/or the editor(s). MDPI and/or the editor(s) disclaim responsibility for any injury to people or property resulting from any ideas, methods, instructions or products referred to in the content.

Materiały uzupełniające

Distances [Å]	(**1**)		(**2**)		(**3**)	
Ti-Ti	Ti(1)-Ti(3)	3.0824(11)	Ti(1)-Ti(3)#1	3.1009(9)	Ti(1)-Ti(2)#1	3.1081(11)
	Ti(1)-Ti(2)	3.3574(10)	Ti(1)-Ti(2)#1	3.1185(9)	Ti(1)-Ti(3)#1	3.1093(12)
			Ti(2)-Ti(3)#1	3.1156(9)		
Ti-O	Ti(1)-O(2)	1.755(3)	Ti(1)-O(71)	1.769(3)	Ti(1)-O(71)	1.759(3)
	Ti(1)-O(1)#1	1.902(3)	Ti(1)-O(3)	1.881(3)	Ti(1)-O(1)	1.896(3)
	Ti(1)-O(51)	2.024(3)	Ti(1)-O(1)	1.904(3)	Ti(1)-O(3)	1.899(3)
	Ti(1)-O(11)	2.039(3)	Ti(1)-O(11)	2.035(2)	Ti(1)-O(11)	2.050(3)
	Ti(1)-O(26)	2.044(3)	Ti(1)-O(32)#1	2.071(3)	Ti(1)-O(32)#1	2.066(3)
	Ti(1)-Ti(2)	3.3574(10)	Ti(1)-O(2)#1	2.148(3)	Ti(1)-O(2)#1	2.151(3)
	Ti(2)-O(86)	1.751(4)	Ti(2)-O(91)	1.755(3)	Ti(3)-O(81)	1.766(3)
	Ti(2)-O(2)	1.869(2)	Ti(2)-O(3)	1.896(2)	Ti(3)-O(2)	1.887(3)
	Ti(2)-O(1)	1.906(2)	Ti(2)-O(2)	1.916(3)	Ti(3)-O(1)	1.895(3)
	Ti(2)-O(72)#1	2.056(3)	Ti(2)-O(51)	2.046(3)	Ti(3)-O(12)#1	2.069(3)
	Ti(2)-O(12)	2.072(3)	Ti(2)-O(12)#1	2.073(2)	Ti(3)-O(52)#1	2.074(3)
	Ti(2)-O(32)	2.101(3)	Ti(2)-O(1)#1	2.142(3)	Ti(3)-O(3)#1	2.142(3)
	Ti(3)-O(66)	1.786(3)	Ti(3)-O(81)	1.773(3)	Ti(2)-O(91)	1.769(3)
	Ti(3)-O(46)	1.793(3)	Ti(3)-O(2)	1.880(2)	Ti(2)-O(3)	1.886(3)
	Ti(3)-O(26)	1.978(3)	Ti(3)-O(1)	1.899(3)	Ti(2)-O(2)	1.911(3)
	Ti(3)-O(71)	2.017(3)	Ti(3)-O(31)	2.073(3)	Ti(2)-O(51)	2.043(3)
	Ti(3)-O(1)#1	2.066(2)	Ti(3)-O(52)#1	2.081(3)	Ti(2)-O(31)	2.072(3)
	Ti(3)-O(52)	2.157(3)	Ti(3)-O(3)#1	2.172(3)	Ti(2)-O(1)#1	2.144(3)
Angles [°]	(**1**)		(**2**)		(**3**)	
Ti-O-Ti	Ti(1)#1-O(1)-Ti(2)	128.79(13)	O(2)-Ti(1)-O(1)#1	104.53(11)	Ti(3)#1-Ti(2)-Ti(1)#1	68.84(2)
	Ti(1)#1-O(1)-Ti(3)#1	101.84(11)	O(2)-Ti(1)-O(51)	92.97(11)	Ti(3)-O(1)-Ti(1)	135.43(17)
	Ti(2)-O(1)-Ti(3)#1	129.36(14)	O(1)#1-Ti(1)-O(51)	92.98(11)	Ti(3)-O(1)-Ti(2)#1	99.98(13)
	Ti(1)-O(2)-Ti(2)	135.75(14)	O(2)-Ti(1)-O(11)	93.65(11)	Ti(1)-O(1)-Ti(2)#1	100.43(13)
			O(1)#1-Ti(1)-O(11)	90.26(11)	Ti(3)-O(2)-Ti(2)	133.69(16)
			O(51)-Ti(1)-O(11)	171.67(10)	Ti(3)-O(2)-Ti(1)#1	100.50(13)
			O(2)-Ti(1)-O(26)	176.25(12)	Ti(2)-O(2)-Ti(1)#1	99.66(13)
			O(1)#1-Ti(1)-O(26)	79.07(11)	Ti(2)-O(3)-Ti(1)	132.25(16)
			O(51)-Ti(1)-O(26)	85.78(11)	Ti(2)-O(3)-Ti(3)#1	100.33(13)
O-Ti-O	O(2)-Ti(1)-O(1)#1	104.53(11)	O(71)-Ti(1)-O(3)	104.95(12)	O(71)-Ti(1)-O(1)	100.75(14)
	O(2)-Ti(1)-O(51)	92.97(11)	O(71)-Ti(1)-O(1)	100.59(12)	O(71)-Ti(1)-O(3)	99.04(14)
	O(1)#1-Ti(1)-O(51)	92.98(11)	O(3)-Ti(1)-O(1)	101.69(11)	O(1)-Ti(1)-O(3)	102.74(13)
	O(2)-Ti(1)-O(11)	93.65(11)	O(71)-Ti(1)-O(11)	91.56(11)	O(71)-Ti(1)-O(11)	96.10(13)

O(1)#1-Ti(1)-O(11)	90.26(11)	O(3)-Ti(1)-O(11)	157.82(12)	O(1)-Ti(1)-O(11)	157.46(13)
O(51)-Ti(1)-O(11)	171.67(10)	O(1)-Ti(1)-O(11)	89.40(11)	O(3)-Ti(1)-O(11)	89.17(13)
O(2)-Ti(1)-O(26)	176.25(12)	O(71)-Ti(1)-O(32)#1	92.51(12)	O(71)-Ti(1)-O(32)#1	95.21(14)
O(1)#1-Ti(1)-O(26)	79.07(11)	O(3)-Ti(1)-O(32)#1	85.77(11)	O(1)-Ti(1)-O(32)#1	86.55(13)
O(51)-Ti(1)-O(26)	85.78(11)	O(1)-Ti(1)-O(32)#1	162.56(11)	O(3)-Ti(1)-O(32)#1	161.14(13)
O(11)-Ti(1)-O(26)	87.30(10)	O(11)-Ti(1)-O(32)#1	78.70(11)	O(11)-Ti(1)-O(32)#1	77.04(13)
O(2)-Ti(1)-O(31)	91.76(12)	O(3)-Ti(1)-O(2)#1	78.27(10)	O(71)-Ti(1)-O(2)#1	175.77(14)
O(1)#1-Ti(1)-O(31)	163.58(11)	O(1)-Ti(1)-O(2)#1	77.60(11)	O(1)-Ti(1)-O(2)#1	78.00(12)
O(51)-Ti(1)-O(31)	88.14(12)	O(11)-Ti(1)-O(2)#1	85.59(10)	O(3)-Ti(1)-O(2)#1	77.41(12)
O(11)-Ti(1)-O(31)	86.60(11)	O(32)#1-Ti(1)-O(2)#1	88.71(11)	O(11)-Ti(1)-O(2)#1	86.20(11)
O(26)-Ti(1)-O(31)	84.68(11)				

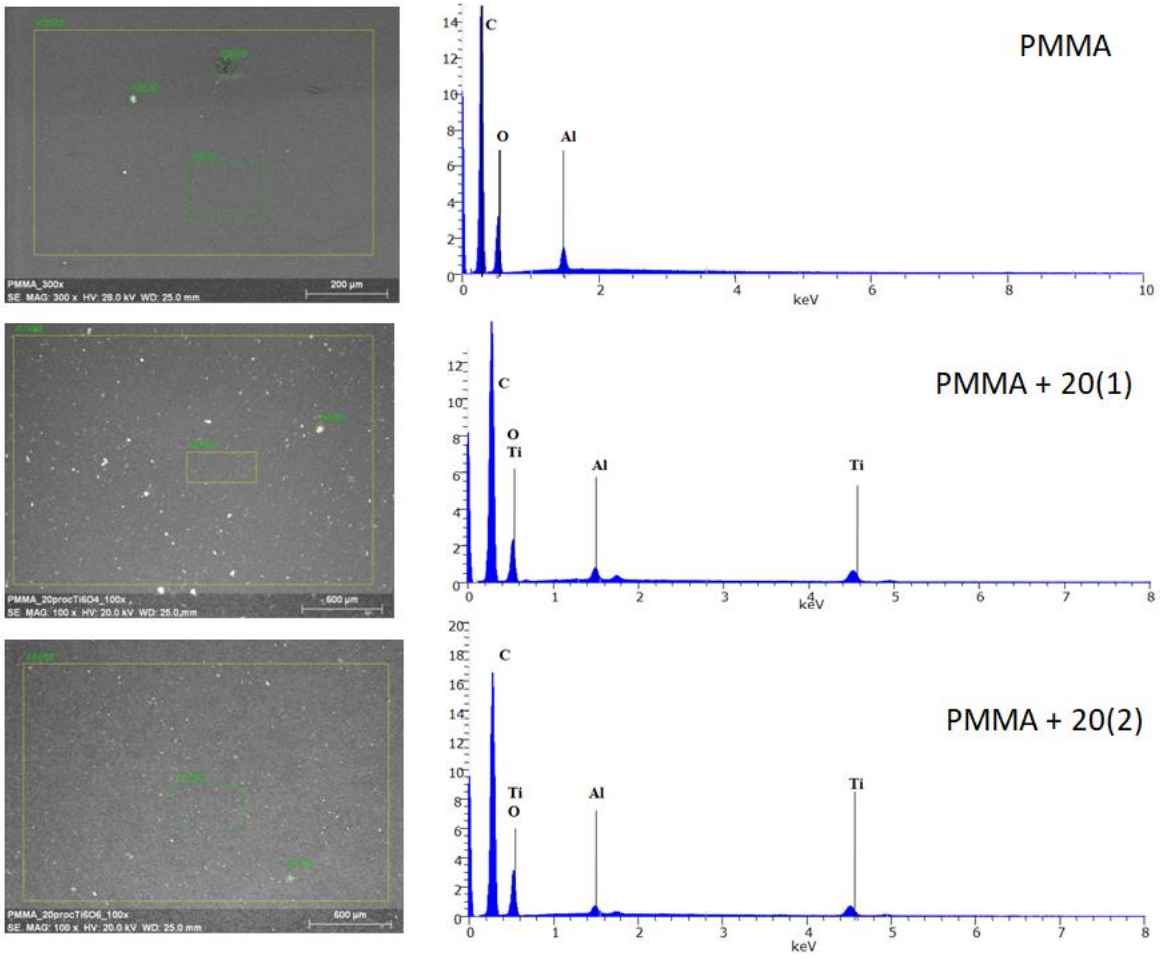


Figure S1: SEM images and EDX patterns of pure PMMA and PMMA + 20(**1**)) and PMMA + 20(**2**)) composites.

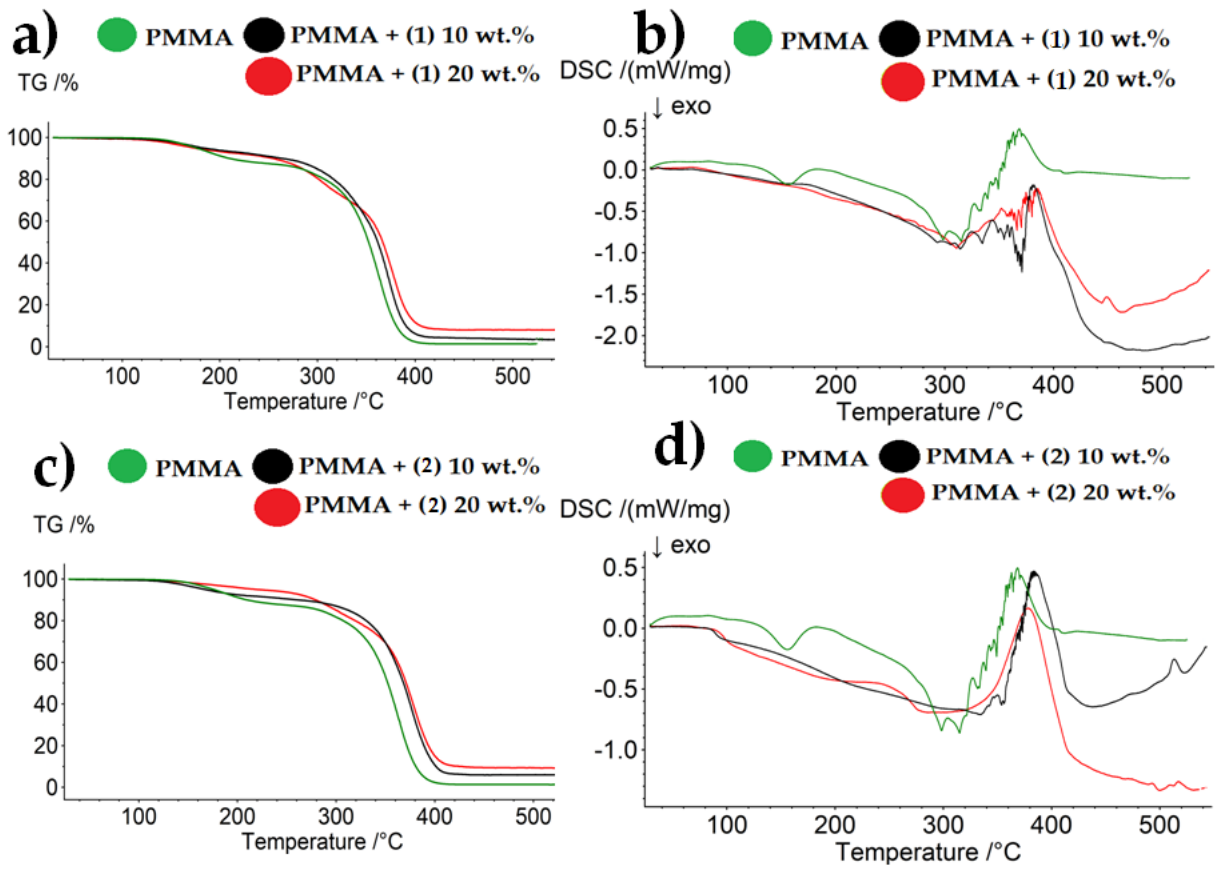


Figure S2: Thermogravimetric curves (TGA) (a,c) and the differential scanning calorimetry curves of (DSC) (b,d) of the TOCs (**1**),(**2**) and produced composite materials.

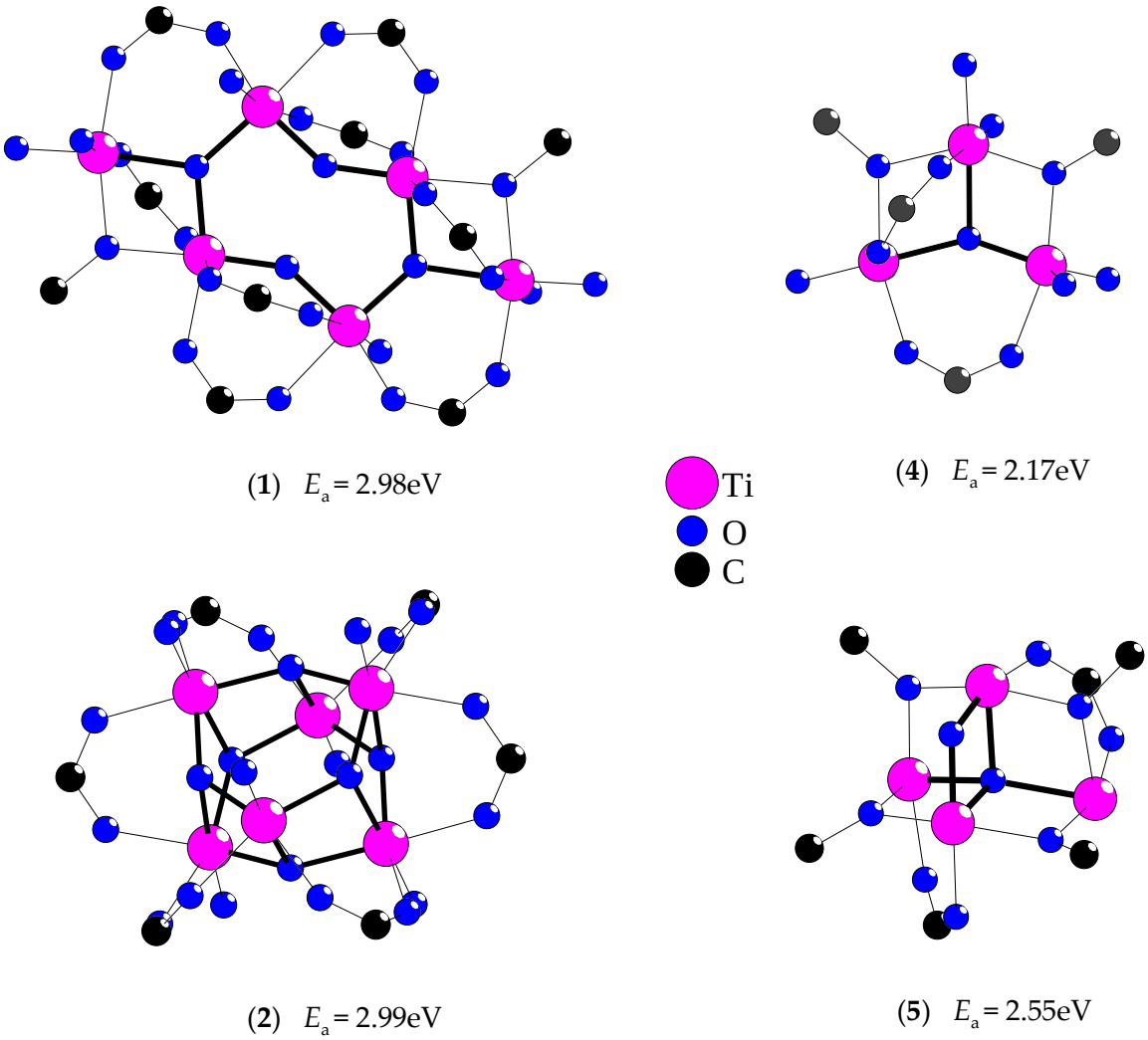


Figure S3: Structures of $\{T_aO_b\}$ cores in molecules (**1**), (**2**), (**4**), and (**5**) oxo complexes, and values of HOMO-LUMO gap; Figure S3: The results of the photocatalytic process repeatability studies of PMMA + TOCs 20 wt.% composite samples (TOCs = (**1**), (**2**), (**4**) and (**5**)) in the visible light.

P3. *The Composites of PCL and Tetranuclear Titanium(IV) – Oxo Complexes as Materials Exhibiting the Photocatalytic and the Antimicrobial Activity.*

International Journal of
Molecular Sciences

MDPI

Article

The Composites of PCL and Tetranuclear Titanium(IV)-oxo Complexes as Materials Exhibiting the Photocatalytic and the Antimicrobial Activity

Barbara Kubiak [1], Aleksandra Radtke [1,*], Adrian Topolski [1], Grzegorz Wrzeszcz [1], Patrycja Golińska [2], Ewelina Kaszkowiak [1], Michał Sobota [3], Jakub Włodarczyk [3], Mateusz Stojko [3] and Piotr Piszczek [1,*]

1 Faculty of Chemistry, Nicolaus Copernicus University in Toruń, Gagarina 7, 87-100 Toruń, Poland; basiak0809@gmail.com (B.K.); topolski@umk.pl (A.T.); wrzeszcz@umk.pl (G.W.); kaszkowiake@gmail.com (E.K.)
2 Faculty of Biological and Veterinary Sciences, Nicolaus Copernicus University, Lwowska 1, 87-100 Toruń, Poland; golinska@umk.pl
3 Centre of Polymer and Carbon Materials, Polish Academy of Sciences, M. Curie-Skłodowskiej 34, 41-819 Zabrze, Poland; msobota@cmpw-pan.edu.pl (M.S.); jwlodarczyk@cmpw-pan.edu.pl (J.W.); mstojko@cmpw-pan.edu.pl (M.S.)
* Correspondence: aradtke@umk.pl (A.R.); piszczek@umk.pl (P.P.); Tel.: +48-611-43-16 (A.R.); +48-611-45-92 (P.P.)

check for updates

Citation: Kubiak, B.; Radtke, A.; Topolski, A.; Wrzeszcz, G.; Golińska, P.; Kaszkowiak, E.; Sobota, M.; Włodarczyk, J.; Stojko, M.; Piszczek, P. The Composites of PCL and Tetranuclear Titanium(IV)-oxo Complexes as Materials Exhibiting the Photocatalytic and the Antimicrobial Activity. *Int. J. Mol. Sci.* **2021**, *22*, 7021. https://doi.org/10.3390/ijms22137021

Academic Editor: Ilaria Armentano

Received: 25 May 2021
Accepted: 27 June 2021
Published: 29 June 2021

Publisher's Note: MDPI stays neutral with regard to jurisdictional claims in published maps and institutional affiliations.

Copyright: © 2021 by the authors. Licensee MDPI, Basel, Switzerland. This article is an open access article distributed under the terms and conditions of the Creative Commons Attribution (CC BY) license (https://creativecommons.org/licenses/by/4.0/).

Abstract: Excessive misuse of antibiotics and antimicrobials has led to a spread of microorganisms resistant to most currently used agents. The resulting global threats has driven the search for new materials with optimal antimicrobial activity and their application in various areas of our lives. In our research, we focused on the formation of composite materials produced by the dispersion of titanium(IV)-oxo complexes (TOCs) in poly(ε-caprolactone) (PCL) matrix, which exhibit optimal antimicrobial activity. TOCs, of the general formula $[Ti_4O_2(O^iBu)_{10}(O_2CR')_2]$ (R′ = $PhNH_2$ (**1**), $C_{13}H_9$ (**2**)) were synthesized as a result of the direct reaction of titanium(IV) isobutoxide and 4-aminobenzoic acid or 9-fluorenecarboxylic acid. The microcrystalline powders of (**1**) and (**2**), whose structures were confirmed by infrared (IR) and Raman spectroscopy, were dispersed in PCL matrixes. In this way, the composites PCL + *n*TOCs (*n* = 5 and 20 wt.%) were produced. The structure and physicochemical properties were determined on the basis of Raman microscopy, thermogravimetric analysis (TGA), differential scanning calorimetry (DSC), electron paramagnetic resonance spectroscopy (EPR), and UV–Vis diffuse reflectance spectroscopy (DRS). The degree of TOCs distribution in the polymer matrix was monitored by scanning electron microscopy (SEM). The addition of TOCs micro grains into the PCL matrix only slightly changed the thermal and mechanical properties of the composite compared to the pure PCL. Among the investigated PCL + TOCs systems, promising antibacterial properties were confirmed for samples of PCL + *n*(**2**) (*n* = 5, 20 wt.%) composites, which simultaneously revealed the best photocatalytic activity in the visible range.

Keywords: PCL; titanium(IV)-oxo complex; composite; physicochemical properties; photocatalytic activity; reactive oxygen species; antimicrobial activity

1. Introduction

The interest in titanium(IV)-oxo complexes (TOCs) is inter alia due to their physicochemical and optical properties (e.g., luminescent, photochromic, and photocatalytic properties), which can be compared to titanium dioxide particles (TiO_2) [1–5]. From a practical point of view, photocatalytic activity of TOCs is important; for example, their application in the photodegradation of organic water pollutants or the formation of self-cleaning materials [6–10]. However, the systems mentioned above differ in the mechanism responsible for the course of photocatalytic processes. Titanium dioxide is a cheap, non-toxic semiconductor of high-value bandgap energy (E_g of rutile and anatase, the two most

known polymorphic forms of titania are equal to 3.02 eV, and 3.20 eV, respectively), which corresponds to the radiation energy in the UV range [11]. The characteristic feature of semiconductor nanoparticles (SNP) is their ability to transfer electrons from the valence band to the conduction band as a result of photon absorption, which leads to the formation of the electron (*e*-) and hole (*h*+) pair (exciton) [12,13]. Excitons exhibit strong redox properties and can react with water and oxygen molecules adsorbed on the SNP surface and lead to the generation of reactive oxygen species (ROS) [14,15]. The following factors influence the photocatalytic activity of TiO_2-based nanomaterials: particle size, surface morphology, structure, radiation intensity, and exposure time [15,16]. Friehs et al. drew attention to the fact that the photoinduced toxicity of TiO_2 P25 powder is stronger than other TiO_2 nanoparticles. Moreover, the rutile form revealed lower toxicity than the anatase particles [11]. The presence of organic ligands stabilizing the $\{Ti_aO_b\}$ cores in the structures of oxo-complexes can work as a photosensitizer and lead to the absorption range widening towards the visible light [16–18]. Due to this effect, the electrons transfer distance decrease between HOMO–LUMO orbitals of the ligands and the $\{Ti_aO_b\}$ core, and the energy of the absorption band is lower [16,19,20]. Analysis of the literature data shows that photocatalytic activity of TOCs can be controlled by way of ligand functionalization, especially of carboxylate groups [21]. The results of our previous research on the photocatalytic activity estimation of composites, which contained PMMA and TOCs consisting of $\{Ti_4O_2\}$ cores, confirmed this [17,18]. According to these reports, systems stabilized with 9-fluorenocarboxylate and 4-aminobenzonate ligands exhibited the best properties. The results obtained r were so promising that we decided to continue the work on the above-mentioned TOCs group.

In searching for new, more effective agents/materials with bactericidal effect, attention has been drawn to metal oxides exhibiting photocatalytic properties [22,23]. The direct contact of the microorganism with the photocatalyst surface leads to the damage of the integral cell membrane due to the action of the ROS, mainly hydroxyl radicals (•OH) and hydrogen peroxide (H_2O_2) [24,25]. According to Foster et al., in the first stage, the bacterial cell contents leak, followed by cell lysis, up to the full mineralization of the microorganism [24,26]. Photocatalytic activity of TOCs suggests that also, in this case, that ROS can be generated on their surface. The hydrophobicity of TOCs grains/powders and their sensitivity on hydrolysis processes caused the previous interest of this group of compounds as potential antimicrobial agents to be limited. Although studies of the hydrolyzed form of the complexes consisted of $\{Ti_4O_2\}$ cores stabilized by two triclosan ligands, they revealed antibacterial activity against *Staphylococcus aureus* [27]. However, it should be noted that the triclosan ligand, which was used for oxo-complex stabilization, is a potent antibacterial and antifungal agent [28]. Therefore, in this case, the presence of the triclosan (as a hydrolysis product) can be seen as a main bactericidal factor. The results of our earlier investigations on $[Ti_4O_2(O^iBu)_{10}(O_2CR')_2]$ and $[Ti_3O(O^iPr)_8(O2CR')_2]$ (R′ = $C_{13}H_9$, PhCl, $PhNO_2$, $PhNH_2$, PhOH) complexes, dispersed in PMMA matrix, proved their resistance on the hydrolysis processes and made it possible to evaluate their photocatalytic activity [17,18,29,30]. Moreover, studies of (PMMA + TOCs) composites (TOCs = $[Ti_3O(O^iPr)_8(O_2CPhR')_2]$ and $[Ti_4O_2(O^iBu)_{10}(O_2CPhR')_2]$ (R′ = NH_2 and OH)) confirmed their phototoxicity against *Staphylococcus aureus*, *Escherichia coli*, and *Candida albicans*, their effectiveness was 85–99% [18]. According to earlier reports, it should be noted that in order to produce a composite material with suitable microbicidal properties, the TOCs of a specific core structure $\{Ti_aO_b\}$ and/or functionalized carboxylate ligands must be introduced to the polymer matrix.

In our studies, we have focused on studying the microbicidal activity of tetranuclear titanium(IV)-oxo complexes with high photocatalytic activity [17,18]. Synthesized compounds were dispersed in the poly(ε-caprolactone) (PCL) matrix. PCL is a biodegradable (degradation time from 2 to 3 years) thermoplastic polymer, which is increasingly used in the production of medical devices, e.g., catchers, stents, intrauterine devices [31–37], as well as environmentally friendly packaging for food products [38]. The analysis of

the previous reports shows the growing interest in modifying PCL films/coatings to obtain biodegradable materials, which can be antimicrobial agent release carriers, e.g., antimicrobial peptides [39] or antibiotics [37]. Moreover, work is underway on composite materials with appropriate antimicrobial activity, which are obtained by introducing an inorganic agent, such as ZnO and CuO, into the PCL matrix [40]. The use of the PCL/TiO_2 system is especially interesting in the production of composite fibers using the electrospinning method [41–46]. It was noticed that the addition of TiO_2 particles to PCL matrix influences the reduction of its water absorption and improves the mechanical properties (e.g., compressive strength) [41]. Moreover, Kiran et al., investigating the antimicrobial activity of PCL/TiO_2 coatings and irradiated by UV light produced on the titanium implants surface, exhibited improvement of their biological properties and antibacterial activity [42]. For this reason, in our investigations, we have focused on PCL + TOCs systems (TOCs = $[Ti_4O_2(O^iBu)_{10}(O_2CR')_2]$) containing R′ = 9-fluorenocarboxylic groups and 4-aminobenzoic ones as the stabilized ligands. The novelty of the research carried out was the use of the PCL + *n*TOCs system (*n* = 5 and 20 wt.% TOCs) to obtain extruded fittings, which reveal the antimicrobial properties. The research results could be used for the production of composite coatings with self-disinfecting surfaces.

2. Results

The TOCs, of the general formula $[Ti_4O_2(O^iBu)_{10}(O_2CR')_2]$ (R′ = $PhNH_2$(**1**) and $C_{13}H_9$ (**2**)), were isolated from a 4:1 molar ratio mother liquor of $Ti(O^iBu)_4$ and organic acids (HO_2CR'; R′ = $C_{13}H_9$, $PhNH_2$) according to the procedure described earlier [17,30]. Analysis of spectra registered using diffuse reflectance infrared Fourier transformation (DRIFT) and Raman spectroscopy allowed for their structure to be confirmed [17,30]. SEM images of (1) and (2) oxo-complexes micro-powders isolated from the mother liquor are presented in Figure 1 (moreover, the SEM EDX data concerning (1) and (2) are shown in Figure S1).

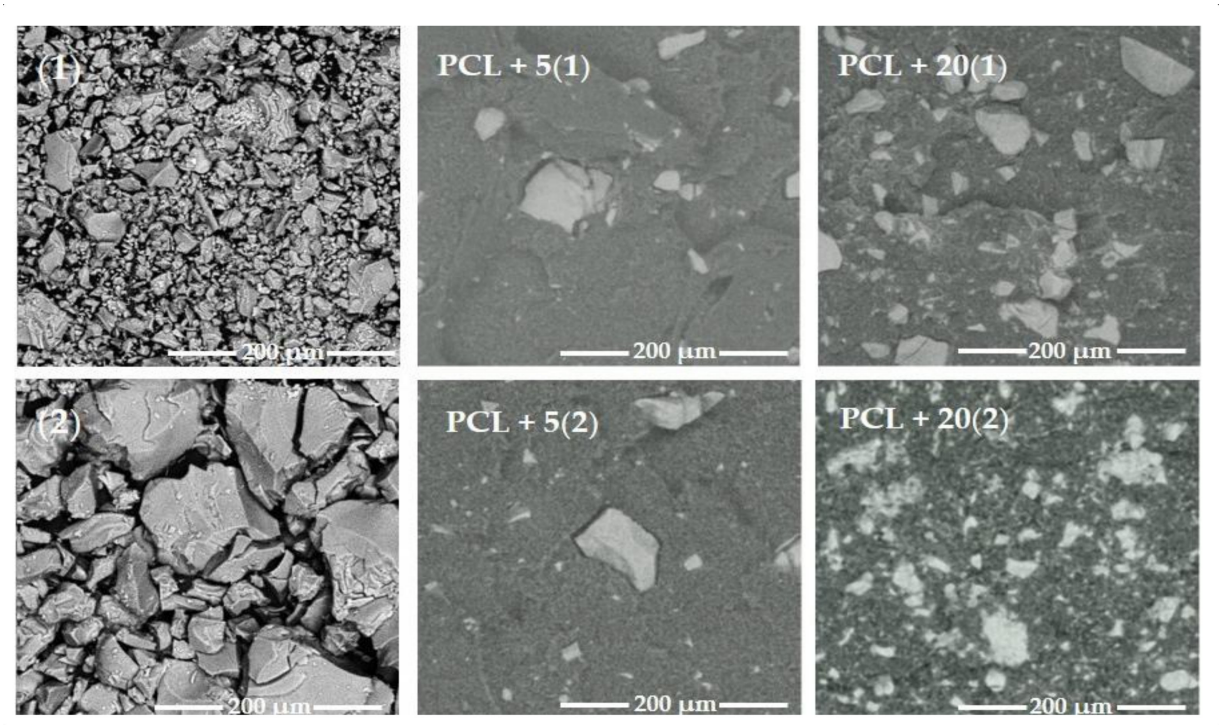


Figure 1. SEM images of isolated micro-powders of oxo-complexes (**1**) and (**2**) and cross sections of the produced PCL + *n*TOCs (TOCs = (**1**) and (**2**)) composite fittings.

2.1. The Production of Polymer + TOCs Composites and Studies of Their Physicochemical and Thermal Properties

The produced (**1**) and (**2**) microcrystalline powders were dispersed in the poly(ε-caprolactone) (PCL) matrix and then, applying the injection molding method, produced the fittings containing n = 5 and 20 wt.% of TOCs (PCL + n(TOCs composite). The size of TOCs grains and their distribution in the produced fittings are shown in Figure 1. Analysis of SEM images exhibited the relatively homogeneous distribution of TOCs grains in the PCL matrix. In samples that contain the 5 wt.% TOCs, grains of sizes from 3 to 15 μm predominated, however, larger grains (size 30–90 μm) were also found. The increasing of TOCs content up to 20 wt.% resulted in a uniform distribution of larger grains (ca. 20–70 μm) in the entire volume of the fittings, regardless of the oxo-complex type (Figure 1 and Figure S2).

The presence of TOCs in all studied samples and their structural stability during the fabrication of composite fittings has been confirmed by the registration of Raman microscope maps (Figures 2 and 3). The structural stability confirmation of (**1**) and (**2**) was especially important, as the sample was heated up to 70 °C during injection molding, which could change their structure in dispersed compounds. For comparison, the Raman spectra of (**1**) and (**2**) dispersed in PMMA at room temperature are presented.

Moreover, the presence of TOCs grains in the PCL matrix was confirmed by the SEM EDX method (Table 1, Figure 4). Analysis of these data confirms the presence of peaks assigned to Ti, O, and C in EDX patterns of the samples containing TOCs micro grains, while in the case of the pure PCL sample, the Ti peaks were not found (the Al peak is derived from microscope equipment).

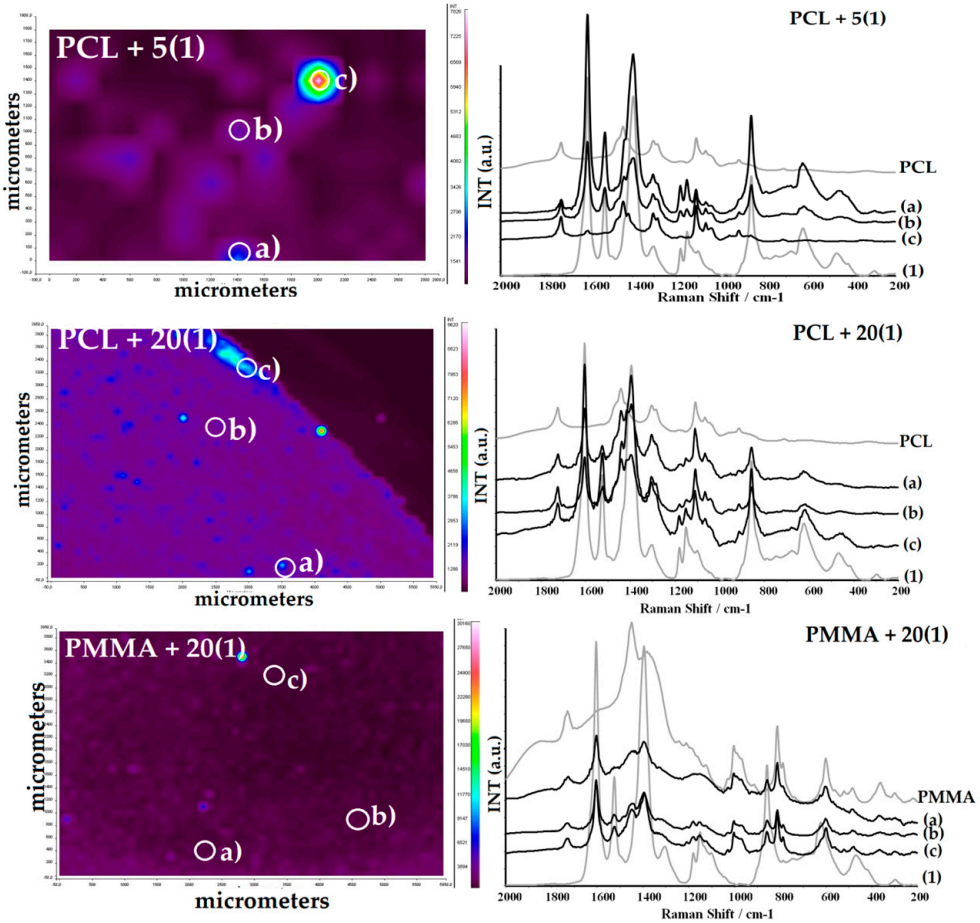


Figure 2. Raman microscopy maps and spectra of PCL + 5(**1**), PCL + 20(**1**), and PMMA + 20(**1**) composites.

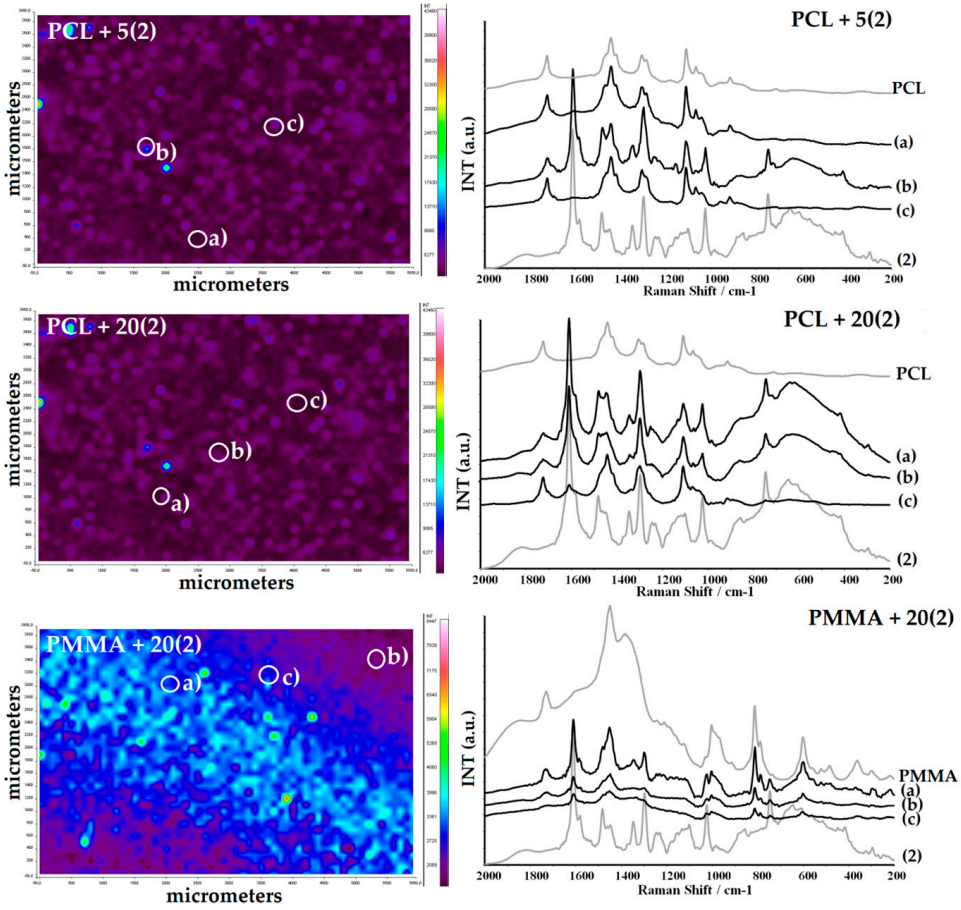


Figure 3. Raman microscopy maps and spectra of PCL + 5(**2**), PCL + 20(**2**), and PMMA + 20(**2**) composites.

Possible changes in thermal properties of the studied composites, caused by the addition of TOCs, were estimated using thermogravimetric analysis (TGA) and differential scanning calorimetry (DSC). The measurements were carried out in the temperature range 30–550 °C, at nitrogen atmosphere, and obtained results are presented in Table 2 and Figure 5a,c). Thermal decomposition of PCL proceeded in one stage between 20 and 460 °C (Figure 5a). In general, the dispersion of (**1**) and (**2**) grains in PCL matrix slightly reduces the decomposition temperature of most investigated composites (2–5 °C), which can be associated with the decomposition of TOCs below 320 °C (in thermograms, the weak decomposition stage below 320 °C was found (Figure 5a). The exception was the PCL + 20(**2**), for which the decomposition temperature was decreased and their one-stage thermal decomposition proceeded between 260 and 420 °C. For PMMA composites, it can be seen that the decomposition process takes place in two stages, as described in the publication [18]. For comparison, TGA studies of PMMA and PMMA + 20TOCs (TOCs = (**1**) and (**2**)) samples revealed that addition TOCs grains decreased the first stage of thermolysis temperature and increased the second one (Figure 5c, Table 2).

Table 1. SEM EDX quantitative data; mean value of mass percent (%).

Composite	C	O	Al	Ti
PCL	28.35	70.98	0.67	-
(PCL + 5%(**1**))	26.15	66.53	0.32	7.00
(PCL + 20%(**1**))	25.23	65.73	0.21	8.83
(PCL + 5%(**2**))	26.06	66.15	0.37	7.42
(PCL + 20%(**2**))	22.79	65.39	0.20	11.62

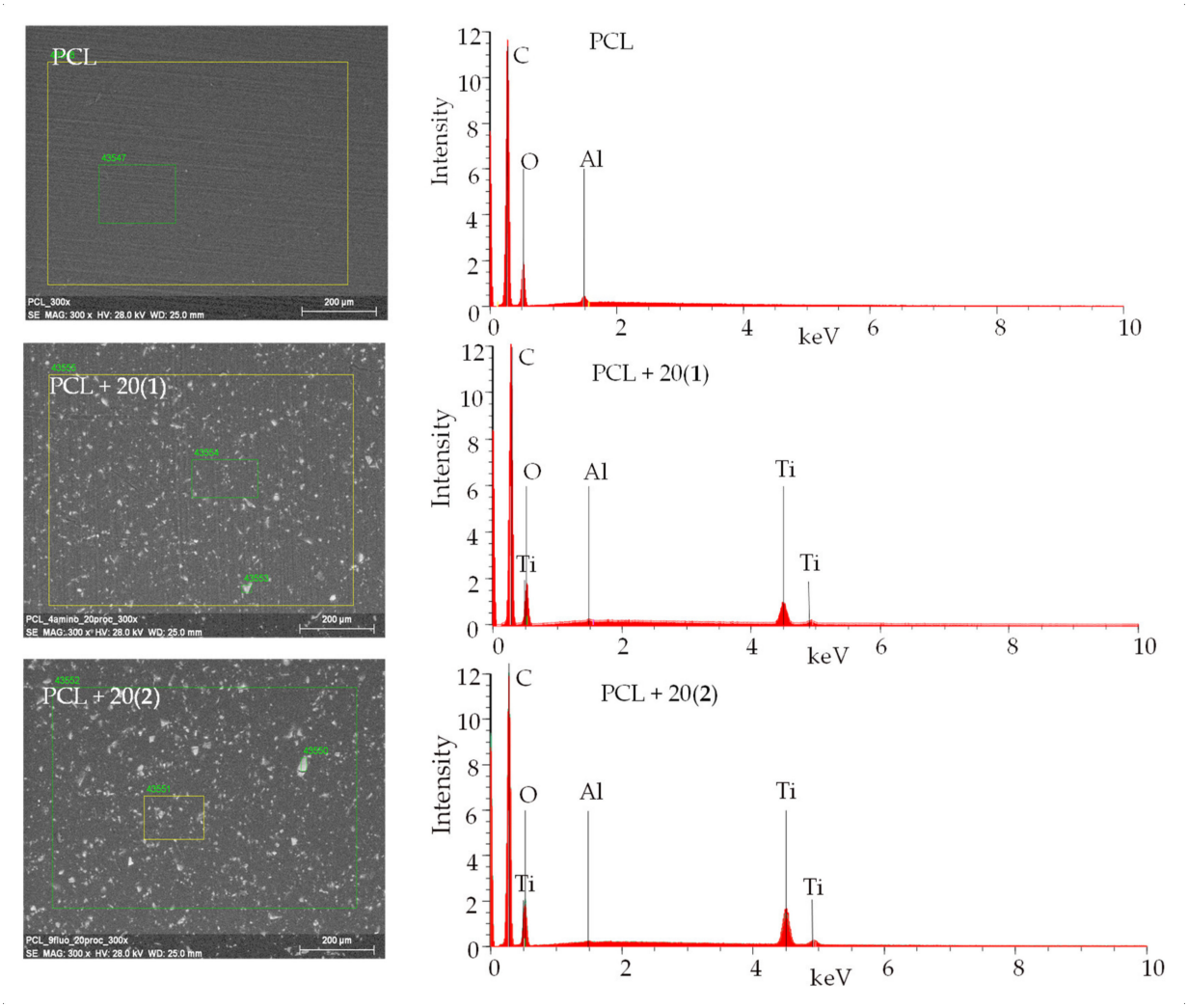


Figure 4. SEM images and EDX patterns of (PCL + 20(**1**)) and (PCL + 20(**2**)) composites, the pure PCL spectra are given for comparison.

Table 2. Thermal parameters received from thermogravimetric analysis (TGA) and differential scanning calorimetry (DSC) of the composites (T_g = glass transition temperature, T = evaporation temperature of an unreacted monomer, T_m = melting temperature, $T_{d/max}$ = decomposition temperature (transition maximum), T_{max} = temperature in the thermal transition maximum, Δm = thermal transition weight loss).

	DSC					TGA		
Composite	**T_g/°C**	**T_m/°C**	**T/°C**	**T_d °C**	**$T_{d/mx}$/°C**	**Stage I T_{max}/°C/Δm/%**	**Stage II T_{max}/°C/Δm/%**	**Solid Residue %**
PCL	-	66.1	-	-	402.3	400.1/100	-	0
(PCL + 5(**1**))	-	66.7	-	-	398.3	397.9/97	-	3
(PCL + 20(**1**))	-	65.5	-	-	394.9	394.7/89	-	11
(PCL + 5(**2**))	-	66.7	-	353.6	395.5	396.3/96	-	4
(PCL + 20(**2**))	-	67.2	-	328.0	373.6	366.2/89	-	11
PMMA	99.6	-	150.8	-	368.6	199.9/12	365.1/85	3
(PMMA + 20(**1**))	99.0	-	-	-	377.8	159.9/15	372.7/76	9
(PMMA + 20(**2**))	100.9	-	-	-	381.3	189.8/12	371.0/76	12

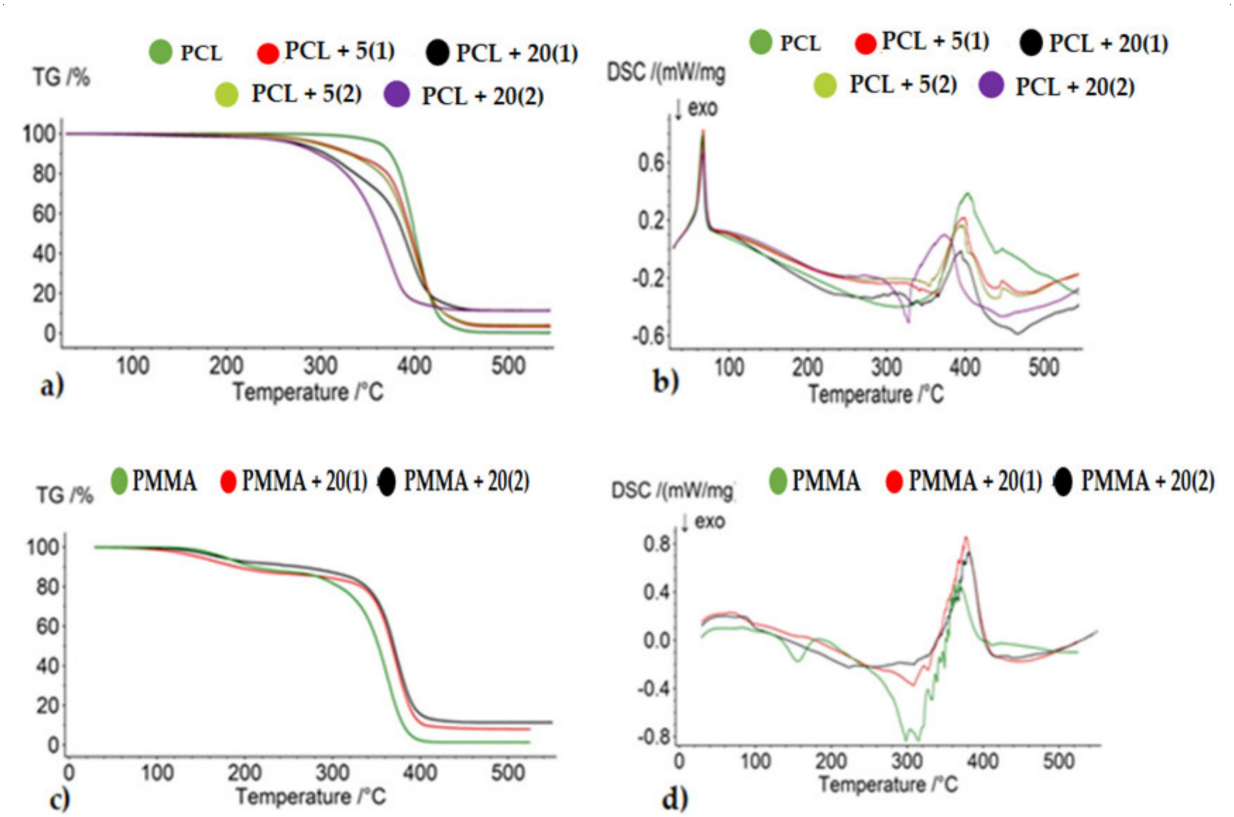


Figure 5. Thermogravimetric curves (TGA) (**a**,**c**) and the differential scanning calorimetry curves of (DSC) (**b**,**d**) of the produced composite materials.

The results of DSC thermal analysis of pure polymers (PCL, PMMA) and composites containing (**1**) and (**2**) powders are presented in Figure 5b,d and Table 2. The thermogram of pure PCL showed a single endothermic peak at around 66 °C (Tm), which was attributed to the polymer melting. Since DSC measurements were carried out between 30 and 550 °C, the glass transition temperature (T_g) of PCL (T_g = −61 °C [44]) could not be observed. The dispersion of TOCs grains in the PCL matrix practically does not influence the melting temperature (Table 2). The second endothermic peak at ca. $T_{d/max}$ = 402 °C, which was found in the PCL thermogram was assigned to the polymer decomposition (the polymer thermal decomposition starts at 344.9 °C). In the case of composites containing 5 wt.% of TOCs grains, a slight reduction of $T_{d/max}$, i.e., 4 °C for PCL + 5(**1**) and 6 °C PCL + 5(**2**) was observed (Table 2). The beginning of the decomposition was registered at ca. 342 °C (**1**) and 354 °C (**2**), respectively (Table 2). In the thermogram of PCL + 20(**1**) sample, the additional weak peak was found at $T_{d/max}$ = 332 °C (Figure 5b). This transition can result from the thermal decomposition of (**1**), whose start was found at c.a 290 °C. Endo–exo transitions, which were noticed at 328 and 374 °C, respectively in the thermogram of PCL + 20(**2**), were also attributed to composite decomposition (Table 2, Figure 5b). Analysis of DSC thermograms of PMMA and PMMA + 20TOCs (TOCs = (**1**) and (**2**)) showed that the addition of TOCs eliminated the thermal effect occurring at ca. 151 °C for pure PMMA (Table 2, Figure 5b) [18]. Furthermore, in these cases, exo–endo transitions between 200 and 440 °C, resulted from the composite thermal decomposition, however, the increase of T_d of both composites versus the pure PMMA was observed (Table 2, Figure 5d).

The mechanical strength studies of the polymer and composite fittings subjected to the static tensile test allowed us to determine the effect of introducing micro grains of complexes (**1**) and (**2**) into the PCL matrix. Samples containing 20 wt.% TOCs were subjected to these measurements, and obtained results are presented in Table 3. In general, it should be noted that the introduction TOCs grains to the PCL matrix increased the Young's modulus value (E) in comparison to pure PCL, wherein this increase was greater

after the introduction of (**1**) than (**2**). Simultaneously, tensile strength and strain at break decreased their values independently according to the type of added oxo-complex (Table 3). In the case of the compressive test of the samples, the analogous change in Young's modulus value (E) of the composite compared to pure PCL was observed, but the differences were not visible. These results show that the elastomeric character of the samples was kept even with 20 wt.% of addition TOCs grains.

Table 3. The results of composite fittings mechanical strength and compressive strength studies in the static tensile test.

Sample	$E_{tensile}$ [MPa]	σ_{max} [MPa]	ε_{max} [%]	σ_{BR} [MPa]	ε_{BR} [%]	$E_{compressive}$ [MPa]	σ_{yield} [MPa]	ε_{yield} [%]
PCL	422 + 13	21.0 + 1.4	6.6 + 0.9	20.7 + 1.3	6.8 + 0.9	100 + 4	8.4 + 0.1	20.0 + 0.6
PCL + 20(**1**)	504 + 21	15.9 + 0.6	4.2 + 0.1	15.9 + 0.6	4.2 + 0.2	107 + 3	8.4 + 0.1	20.1 + 0.3
PCL + 20(**2**)	480 + 3	15.8 + 0.5	4.5 + 0.1	15.7 + 0.5	4.5 + 0.1	115 + 1	8.5 + 0.1	19.1 + 0.5

E,Young's modulus (MPa); $\sigma_{max,}$ maximum stress (tensile strength) (MPa); ε_{max}, strain at the maximum stress (%); σ_{BR}, stress at break (MPa); ε_{BR}, strain at break (%); $E_{compressive}$, compressive strength (MPa); σ_{yield}, stress at the yield (MPa); ε_{yield}, strain at the yield (%).

2.2. Estimation of Photocatalytic Activity of the Oxo-Complexes

The UV–Vis–DRS spectra of produced PCL + TOCs composites were recorded to determine of the PCL absorption maximum position before and after the introduction of 5 and 20 wt.% (**1**) and (**2**) (Figure 6). Analysis of these data revealed the clear shifting of absorption maximum towards visible range from 236 nm for PCL up to 375–400 nm for produced composites. Therefore, in all our photocatalytic experiments samples were irradiated by visible light (λ = 350–2200 nm).

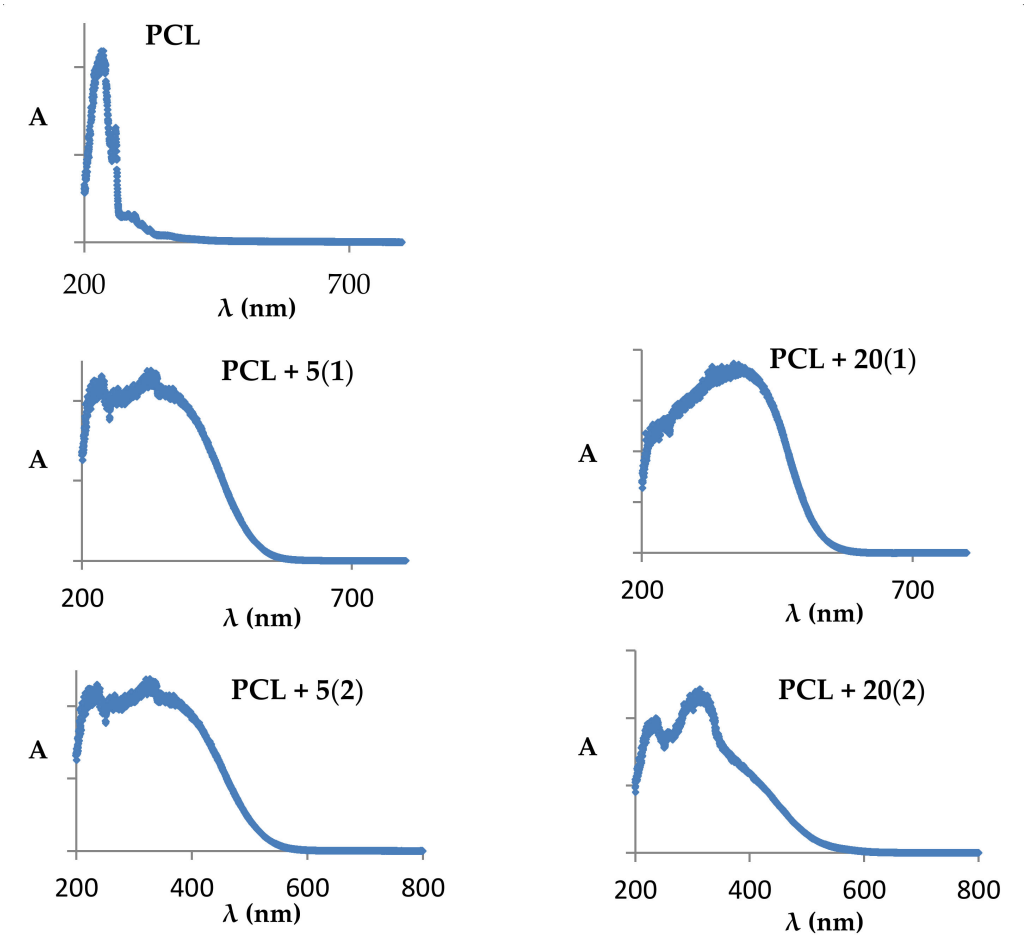


Figure 6. UV–Vis–DRS spectra of PCL and studied PCL + nTOCs composites.

The photocatalytic activity was estimated on the basis of methylene blue solution (MB) decolorization during irradiation with visible light by 30 h. Changes in MB concentration in the presence of PCL + *n*TOCs (TOCs = (**1**) or (**2**)) composites are presented in Figure 7 and Table 4. The results of these investigations were compared with the studies of photocatalytic activity of PMMA + 20TOCs (TOCs = (**1**) or (**2**)) also irradiated by visible light (these studies were not carried out in our earlier works). According to the data presented in Figure 7a,b and Table 4, it should be noted that a 5 wt.% addition of the oxo-complexes (TOCs = (**1**) or (**2**)) to the PCL matrix increases photocatalytic activity of PCL + 5TOCs in comparison to the pure polymer, especially in the case of PCL + 5(**2**) (the reference rate constants were 00029 h^{-1} and 0.0078 h^{-1} for PCL + 5(**1**) and PCL + 5(**2**), respectively. According to presented data, a pure PCL showed no photocatalytic activity in the visible range; its activity was generally the same as for irradiated MB solution. The increase of TOCs content up to 20 wt.%, significantly improved the activity of studied materials, especially for the PCL + 20(**2**) system. Comparative studies carried out for the composites PMMA + 20TOCs (TOCs = (**1**) or (**2**)) revealed that photocatalytic activity of the PMMA + 20(**2**) composite was also clearly greater than the activity of (PMMA + 20(**1**) one (Figure 7c,d and Table 4).

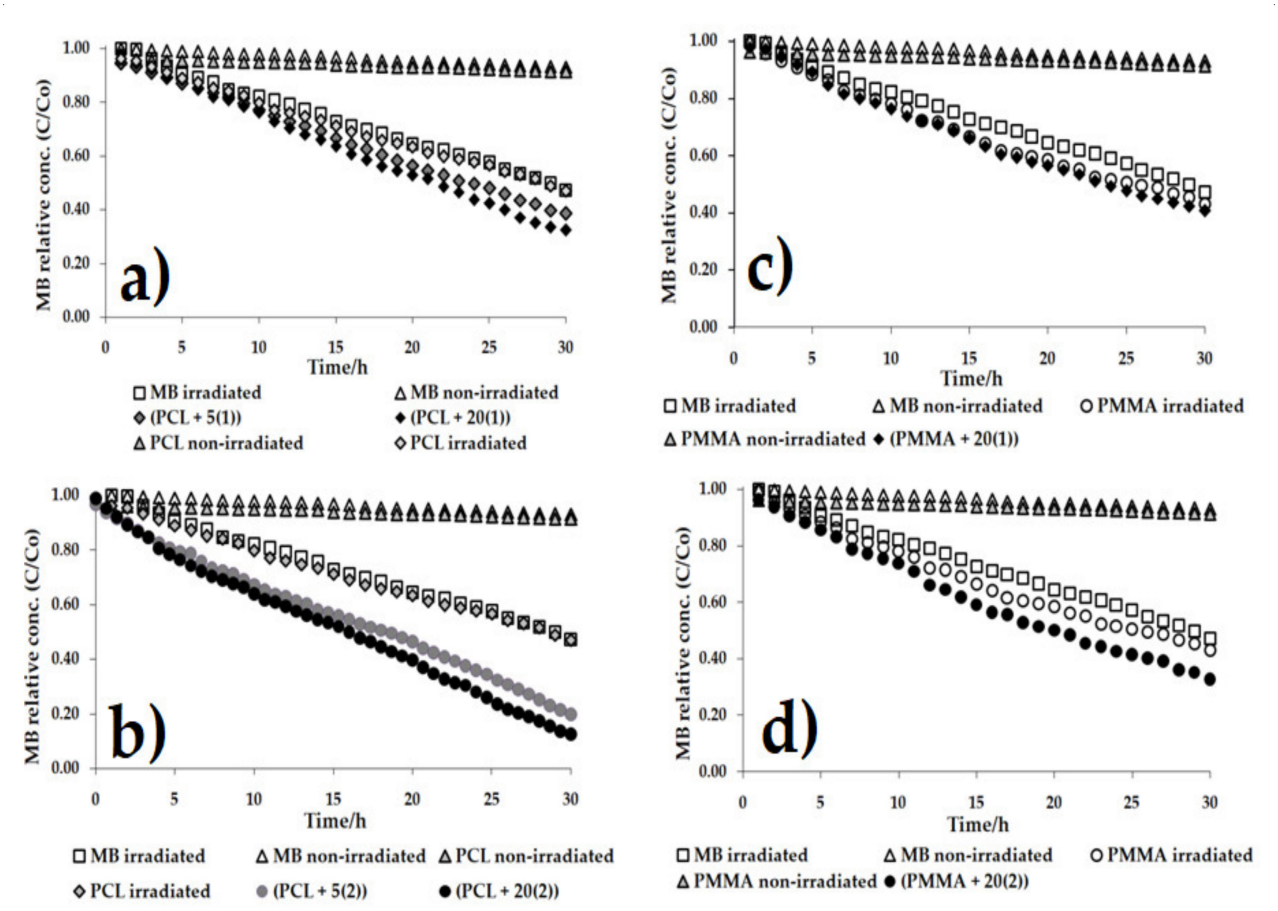


Figure 7. Changes in the concentrations of the methylene blue (MB) solution as a function of time for the respective composite materials irradiated with VIS radiation ((**a**) PCl + *n*(**1**), (**b**) PCL + *n*(**2**) (*n* = 5, 20 wt.%), (**c**) PMMA + 20(**1**), (**d**) PMMA + 20(**2**) (*n* = 20 wt.%).

Table 4. MB solution decolorization percentages and ΔA_{180} parameters for the studied reactions in relation to the composites.

Composite	MB Decolorization [a] (%)	ΔA 30	ΔA 30 in Reference to MB	10^2 Rate Constant h^{-1}	10^2 Rate Constant in Reference to MB, h^{-1}
MB irradiated	76.35	0.749	-	2.50 + 0.02	-
PCL	76.91	0.726	−0.023	2.51 ± 0.03	0.01
PCL + 5(**1**)	75.54	0.701	−0.048	2.79 ± 0.04	0.29
PCL + 20(**1**)	81.46	0.782	0.033	2.96 ± 0.05	0.46
PCL + 5(**2**)	79.56	0.755	0.006	3.28 ± 0.04	0.78
PCL + 20(**2**)	87.32	0.847	0.980	3.40 ± 0.06	0.90
Composite	**MB Decolorization [a] (%)**	**ΔA 30**	**ΔA 30 in Reference to MB**	**10^2 Rate Constant h^{-1}**	**10^2 Rate Constant in Reference to MB, h^{-1}**
MB irradiated	76.35	0.749	-	2.50 ± 0.02	-
PMMA	75.18	0.751	0.002	2.60 ± 0.03	0.10
PMMA + 20(**1**)	83.75	0.804	0.055	2.63 ± 0.04	0.13
PMMA + 20(**2**)	85.20	0.787	0.038	2.74 ± 0.07	0.24

Methylene blue (MB) decolorization at the end of the measurements (t = 30 h).

2.3. Results of EPR Studies

EPR spectroscopy was used to detect paramagnetic species on the surface of the synthesized materials. Pure PCL polymer shows no EPR signal. However, paramagnetic centers were found in all samples of PCL + TOCs. Generally, the signals in the EPR spectra were very weak, especially for composites with a 5 wt.% admixture of oxo-titanium(IV) complexes. Therefore, only the EPR spectra of the samples with 20 wt.% addition of oxo-titanium(IV) complexes were analyzed in detail. Spectra registered for composites of PCL + 20(**1**) and PCL + 20(**2**) are presented in Figure 8. The EPR parameters and types of observed paramagnetic species (ROS) are summarized in Table 5.

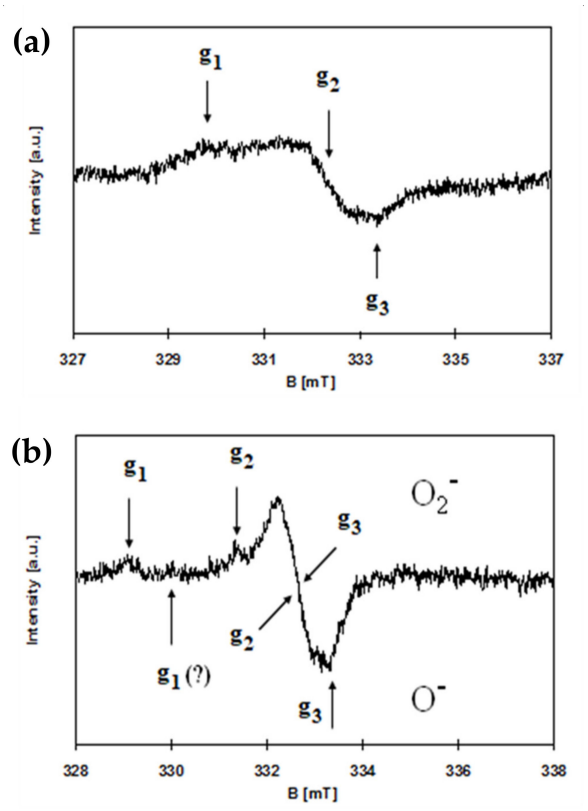


Figure 8. EPR spectra of PCL + 20(**1**) (**a**) and PCL + 20(**2**) (**b**).

Table 5. EPR data for PCL + 20TOCs (TOCs = (**1**) and (**2**)) composite samples. The samples were exposed to visible light prior to measurement.

Sample	g-Factors	Species
PCL + 20(**1**)	2.020, 2.005, 1.999	O^-
PCL + 20(**2**)	2.025, 2.010, 2.003(?), 2.019, 2.003, 1.999	O_2^- O^-

Some EPR signals are marked with a question mark (Table 5 and Figure 8b) for two reasons. The first one (Table 5) concerns the value of the lowest g-factor for O_2^- species, as the signals from both oxygen species overlapped. Another reason (Figure 8b) concerns the very weak and very broad signal for O^- species, which during accumulation disappeared probably due to slight fluctuations in the magnetic field.

2.4. Antimicrobial Activity of PCL + TOC Composites

Antibacterial and antifungal activities of PCL and PCL + *n*TOCs (*n* = 5 and 20 wt.%) are presented in Table 6. Generally, these studies revealed that enrichment of the polymer with TOCs grains decreased the number of microorganisms when compared with pure polymer (PCL). However, the biocidal effect of PCL + TOCs composites (R $\geq$ 2) was observed against bacteria, and when PCL was enriched with 5 wt.% TOCs containing 9-fluorenocarboxylic stabilized ligand (2), with one exception (*Staphylococcus aureus* ATCC 6538), or with 20 wt.% TOCs containing 4-aminobenzoic stabilize ligand (1) and 9-fluorenocarboxylic stabilize ligand (2). Gram-negative bacteria showed higher sensitivity to PCL + TOCs than Gram-positive bacteria, especially in the presence of 20 wt.% TOCs (2). In these cases, the reduction indexes were found to be between 3.5-4.5 and 2.0-2.6, respectively. In general should be noted the weak antimicrobial activity of studied samples against yeasts, i.e., Candida albicans. The PCL + 20(2) showed the best antifungal properties among studied systems (Table 6).

Table 6. Antimicrobial activity of PCL and PCL + *n*TOCs.

Sample	Microorganisms				
	Escherichia coli **ATCC 8739**	***Escherichia coli*** **ATCC 25922**	***Staphylococcus aureus*** **ATCC 6538**	***Staphylococcus aureus*** **ATCC 25923**	***Candida albicans*** **ATCC 10231**
	R	R	R	R	R
PCL	0.9	0.9	0.1	0.6	0.0
PCL + 5(**1**)	1.6	0.7	0.2	0.7	0.3
PCL + 5(**2**)	2.0	2.6	1.1	2.3	0.3
PCL + 20(**1**)	2.0	2.0	2.0	2.5	0.7
PCL + 20(**2**)	4.5	3.5	2.0	2.6	0.9

R, reduction index. R $\geq$2 is a biocidal effect when the microbial growth is reduced at least 100 times (99.0%).

3. Discussion

The previous studies on films based on poly(methyl methacrylate) (PMMA) enriched with 20 wt.% TOCs (TOCs = $[Ti_4O_2(O^iBu)_{10}(O_2CR')_2]$; R′ = $PhNH_2$ and PhOH) revealed their photocatalytic activity in the UVA/Visible range, and also, their clear bactericidal properties [17,18]. The studies were carried out on PMMA + TOCs composite films of 25–50 μm thickness, containing TOCs grains, with sizes ca. 3–5 μm (R′ = NH_2) or ca. 100–300 μm (R′ = OH) [18]. Analysis of Raman spectra of the composites mentioned above confirmed structural stability of TOCs introduced to the polymer matrix and their low sensibility on hydrolysis processes. This prompted us to continue our research on the possibility of using multinuclear Ti(IV)-oxo complexes as an antimicrobial agent. This paper presents the research results on PCL + *n*TOCs (*n* = 5 and 20 wt.%) composite fittings of 1.5 mm thickness, produced with the use of equipment for plastics processing consisting of

a twin-screw extruder and a pneumatic mini-injection molding machine. The tetranuclear oxo-complexes $[Ti_4O_2(O^iBu)_{10}(O_2CR')_2]$ (R' = $PhNH_2$ (**1**) and $C_{13}H_9$ (**2**)) were used in the fabrication of test samples, which were irradiated with the visible light during all photocatalytic and microbiological experiments. Analysis of Raman microscopy data and SEM-EDX ones confirmed the uniform dispersion of TOCs grains (both (**1**) and (**2**)) in the whole volume of fittings and their structural stability during the production process. The size of dispersed TOCs grains depended on their content and, in the case of 5 wt.% amounted 3–90 µm while for 20 wt.% 20–70 µm. The TGA and DSC data analysis revealed that depending on the type of used polymer (PCL, PMMA), the thermolysis temperature was slightly lower for PCL + 20TOCs composites and increased for PMMA + 20TOCs ones, in comparison to the pure polymers. This effect can be related to the thermal decomposition of TOCs, for which T_{dmax} were ca. 310 and 291, 393 °C for (**1**) and (**2**), respectively (thermal decomposition of (**2**) proceeds in two stages), which dependently to decomposition temperature of the pure polymer (ca. 402 °C for PCL and ca. 365 °C for PMMA) can accelerate or decelerate composite thermal decomposition processes.

The photocatalytic activity studies of PCL + *n*TOCs composites were preceded by the determination of their absorption maximum, which was carried out using the UV-Vis-DRS technique. Analyzing the registered data (Figure 6), it was noticed that the dispersion of TOCs grains into the PCL matrix results in a clear shift of their absorption maximum from the UV range (236 nm for pure polymer) towards the visible range (375–400 nm). Earlier studies of Ti(IV)-oxo complexes (**1**) and (**2**) showed that the bandgap magnitudes were 2.57 and 2.55 eV [17,18], respectively. The narrowing of the bandgap of TOCs compared to TiO_2 (ca. 3.0–3.2 eV [11]) results from the photosensitizing effect of functionalized carboxylate ligands bonded to the $\{Ti_4O_2\}$ core [47]. As a result, electrons excited under the influence of visible light can be transferred between the HOMO–LUMO of ligands with energy bands of the titanium-oxo core. Accordingly, the photocatalytic activity of studied PCL + *n*TOCs composites has been evaluated based on the MB decolorization for samples exposed to visible light. Analysis of data presented in Figure 7a,b, and Table 4 revealed the clear photocatalytic activity of PCL samples containing grains of TOCs (TOCs = (**1**) and (**2**)), in contrast to the pure PCL, which is inactive in this range of the light. The content of TOCs in the composite samples (*n* = 5 and 20 wt.%) and the type of carboxylic stabilization ligand ($-O_2CPhNH_2$ (**1**) and $-O_2CC_{13}H_9$ (**2**)) are the main factors that influenced the photodecolorization of the MB solution. Moreover, the data provided in Table 4 suggests the possible relationship between the polymer matrix type and the composite photocatalytic activity. According to these data, the PMMA exhibits a weak ability to MB photodecolorization during exposure to visible light, unlike PCL, which is inactive. Comparing both studied composites, it should be noted that the photocatalytic activity of PMMA + 20TOCs composites was significantly lower than PCL + 20TOCs ones (Table 4).

Considering the relatively well-known mechanism of the photocatalytic action of TiO_2 based materials, it can be assumed that after visible light photoexcitation of studied samples, the ROS can be generated on their surface [48]. Therefore, the microbiocidal activity estimation of the produced composites (containing 20 wt.% of TOCs) were preceded by an analysis of their EPR spectra, which allowed for the detection of ROS formation and their identification. In the EPR spectrum of PCL + 20(**1**), the characteristic anisotropic signals for O^- radical were found (Figure 8, Table 5). The formation of O^- type paramagnetic centers consists of removing the electron and stabilizing the radical formed by reduction of titanium(IV) to titanium(III) [49]. So, although the presence of titanium(III) is not excluded, the respective signals are not visible due to their much greater width compared to the signals of radicals and, consequently, their lower intensity. The EPR spectra of PCL + (**2**) are more complex and contain more lines. The literature data shows that the maximum g-factor (g_{zz}) for O_2^- is greater than for O^- species. [50]. On the other hand, titanium(III), due to a positive spin-orbit coupling constant, shows EPR signals at even lower g-values, below 1.99 [48–52]. This approach makes it possible to identify the presence of ROS of the type O_2^- and O^- in PCL + (**2**) samples (Table 5). The above analysis does not exclude the presence of other

oxygen-based radicals because the superoxide radical anion, O_2^-, the peroxy-type radicals (RCOO·) and O_2^- of organic-type adducts could be indistinguishable by the CW-EPR spectroscopy [52]. The role of oxidative stress in titanium dioxide-induced antimicrobial activity was confirmed by several previously published reports [24,25,41,53,54]. The promote photo-oxidation and photo-reduction processes, which can lead to ROS generation, were also observed for TOCs systems [14,18,55]. The formation of such radicals as oxide (O^-), superoxide (O_2^-) or hydroxyl (•OH), and non-radicals, e.g., hydrogen peroxide (H_2O_2) or hydroxyl (OH^-) ions, has been confirmed [14,56]. The generation of ROS is considered as the main mechanism of antimicrobial activity. ROS are effective in vitro against Gram-positive, and Gram-negative organisms, including multidrug-resistant (MDR) isolates and fungi, as they cause several types of oxidative damage intracellularly. They are also highly active against viruses [57–59]; for example, H_2O_2 causes its antimicrobial action by a reaction with thiol groups in proteins, including enzymes, DNA, and bacterial cell membranes, while hydroxyl radical, which is a strong and nonselective oxidant, breaks DNA, peroxidates lipids, and carbonylates proteins [59,60]. Moreover, ROS oxidize the deoxyguanosine triphosphate (dGTP) and deoxycytidine triphosphate (dCTP) pools causing incorrect incorporation of bases into DNA. They also cause double-stranded breaks in DNA through disrupted repair intermediates [61–63]. The free radicals affect bacterial lipopolysaccharide (LPS) in outer membrane, peptidoglycan, and the phospholipid bilayer by causing peroxidation [54]. The relationship of photocatalytic activity and antimicrobial activity of PMMA + TOCs containing Ti_3O or Ti_4O_2 cores (20 wt.%) and 4-hydroxybenzoic or 4-aminobenzoic ligands, against Gram-positive and Gram-negative bacteria, and yeasts was revealed in our previous studies [18]. All of the studied PMMA + TOC foils strongly (>99%) inhibited the growth of tested bacteria (*E. coli* and *S. aureus*). Both PMMA + TOCs with Ti_4O_2 core and 4-hydroxybenzoic or 4-aminobenzoic ligands also significantly inhibited the growth of yeasts of *C. albicans* not the complex of PMMA with a $\{Ti_3O\}$ core and stabilized by the $-O_2C$-4-$PhNH_2$ ligand [18]. In the presented paper, the antimicrobial activity of PCL + *n*TOCs (*n* = 5 and 20 wt.%., TOCs = (**1**) and (**2**)) composite samples were assessed, which were activated by visible light. Strong antibacterial activity for PCL containing 20 wt.% of the TOCs was found, like during the previous studies. However, in the case of 5 wt.% content of (**2**) in the composite sample such activity was recorded.

When the bactericidal activity of TOCs is studied, attention should be paid to the role of photocatalytically assisted antimicrobial processes activated by light. The importance of UV-assisted TiO_2 photocatalysis for the inactivation of bacteria has been widely described in the existing literature [54,64–66]. However, in the case of PCL + *n*TOCs composites, the absorption maximum was shifted towards the visible range, which suggests that visible light plays a decisive role in microbicidal processes. The role of visible light as an antibacterial agent was pointed out by Angarano et al. [67]. They revealed that visible light in the high-energy range (400–420 nm) could inactivate biofilms formed by both Gram-negative *Pseudo-monas fluorescens* and Gram-positive *Staphylococcus epidermidisbacteria* [67]. It is hypothesized that the reactive oxygen species are involved in the antimicrobial effect of high-energy visible light [68]. Liou et al. assumed that the photocatalytic processes occurring on the surfaces of TiO_2-based materials are the most important factors, which can facilitate the prevention of diseases caused by microorganisms [69]. These authors investigated the microbicidal activity of modified TiO_2 systems (the modification consisted in shifting the absorption towards the visible light spectrum) against model bacteria *E. coli* and human pathogens showed that irradiation with visible light significantly decreased the number of test bacteria [69]. The results of the carried out and described here investigations showed that the PCL + *n*TOCs ((**1**), (**2**)) composites exhibit photocatalytic activity in the visible range by generating the reactive oxygen species (as was proved by EPR spectroscopy). Taking into account the received results we can assume that the ROS generated on the surface of the manufactured composite fittings under their influence of exposition on the visible light are the main antimicrobial factor.

4. Materials and Methods

4.1. Materials

Titanium(IV) isobutoxide (Aldrich, St. Louis, MO, USA), 4-aminobenzoic acid (Aldrich, St. Louis, MO, USA), 9-fluorenecarboxylic acid (Organic Acros, Geel, Belgium) were purchased commercially and were used without further purification. All solvents used in synthesis, i.e., acetone and toluene were distilled before their use and stored in an argon atmosphere. The processes of Ti(IV) oxo-complexes synthesis were carried out using the standard Schlenk technique in the inert gas atmosphere (Ar) and at room temperature (RT).

4.2. Synthesis of Ti(IV) oxo-Complexes(TOCs) and Polymer/TOCs Composites

4.2.1. The Synthesis of $[Ti_4O_2(O^iBu)_{10}(O_2CPhNH_2)_2]$ (1)

The complex was synthesized, as reported [17]. 0.12 g of 4-aminobenzoic acid (0.875 mmol) was added to the solution of 1.19 g of titanium(IV) isobutoxide (3.5 mmol) in 2 ml of toluene, leading to clear yellow solution. The solution was left for crystallization. The yield basing on acid: 41% (0.22 g). Anal. Calc. for $C_{54}H_{102}O_{14}Ti_4N_2$:C, 52.86; H, 8.38; N, 2.28; Ti, 15.61. Found: C, 53.14; H, 7.83; N, 2.05; Ti, 15.56. ^{13}C NMR (solid state, 295 K, δ[ppm]): 14.3, 19.5 (CH_3), 31.5, 34.7 (CH), 64.8, 78.6 (CH_2), 113.6, 133.1 (C(Ph)), 152.4 (C-NH_2), 175.4 (COO).

4.2.2. The Synthesis of $[Ti_4O_2(O^iBu)_{10}(O_2CC_{13}H_9)_2]$ (2)

Complex was synthesized, as reported [17]. 0.184 g of 9-fluorenecarboxylic acid (0.875 mmol) was added to the solution of 1.19 g of titanium(IV) isobutoxide (3.5 mmol) in 2 ml of acetone, leading to clear yellow solution. The solution was left for crystallization. The yield basing on acid: 62% (0.36 g). Anal. Calc. for $C_{68}H_{108}O_{16}Ti_4$:C, 59.28; H, 7.93; Ti, 13.94. Found: C, 58.17; H, 7.86; Ti, 13.64. ^{13}C NMR (solid state, 295 K, δ[ppm]): 14.6, 19.5 (CH_3), 35.4 (CH), 55.6, 77.7 (CH_2), 119.3, 127.5, 142.3 (C(Ph)), 178.4 (COO).

4.2.3. The Composite Fittings Production

The poly(ε-caprolactone) (PCL) fittings and the PCL composite ones, containing 5 and 20 wt.% of TOCs (Figure 9), were produced by using equipment for plastics processing consisting of a twin-screw extruder (Haake MiniLab II, Thermo Scientific, Waltham, MA, USA) and a pneumatic mini-injection molding machine (Haake MiniJet II, Thermo Scientific, Waltham, MA, USA). The following injection parameters were used: temperature of the plasticizing system: 70 °C; injection cylinder temperature: 80 °C; mold temperature: 25 °C; injection pressure: 400 bar; holding pressure: 300 bar; holding time: 3 s. The mechanical strength studies of the manufactured fittings in the static tensile test were carried out in the following conditions: tensile speed: 20 mm/min; jaw opening: 50 mm; length of the measuring section of the fittings: 40 mm; fittings thickness: 1.5 mm; measurement temperature: 25 °C.

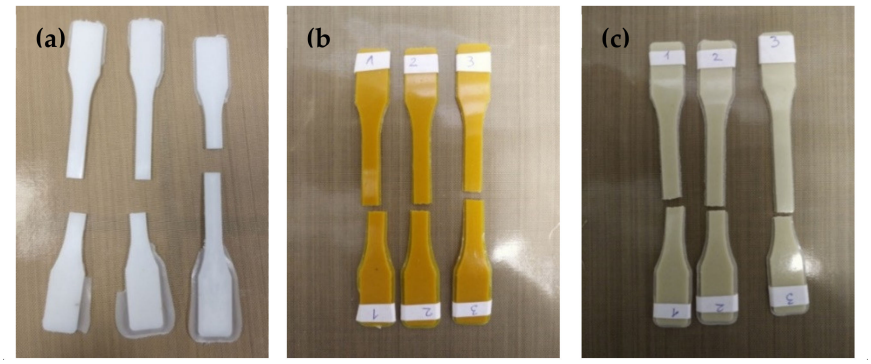


Figure 9. Fittings produced by injection molding method, samples after breaking on a testing machine: (**a**) PCL, (**b**) PCL + 20(1), and (**c**) PCL + 20(2).

The compressive strength was determined using the same equipment. The rectangular samples' dimensions were: width, 10 mm; thickness, 10 mm; and specimen gauge length, 3 mm. The condition of the test was: temperature, 25 °C; and compressive speed, 1.2 mm/min.

4.2.4. The Composite Foils Production

Foils of composites based on poly(methyl methacrylate) (PMMA), i.e., PMMA + 20TOCs (TOCs = (**1**), (**2**)), have been prepared for comparison [17]. The TOCs powder portion (acting the 20 wt.% of the reaction mixture) was dispersed (with the use of ultrasonic bath) in the solution, which was received by dissolving 1 g PMMA in 5 cm^3 of toluene. The composite films were produced by slow solvent evaporation in a glove box at room temperature.

4.3. Analytical Procedures

The structure of isolated solid synthesis products was confirmed using vibrational spectroscopy methods, i.e., IR spectrophotometry (Perkin Elmer Spectrum 2000 FT-IR spectrometer (400–4000 cm^{-1} range, KBr pellets)) and Raman microscopy (RamanMicro 200 spectrometer (PerkinElmer, Waltham, MA, USA)). Raman spectra were registered using a laser of wavelength 785 nm, with maximum power 350 mW, in the range 200–3200 cm^{-1}, using a 20 × 0.40/FN22 objective lens and an exposure time of 15 s each time. Solid-state ^{13}C NMR spectra were registered at 22 °C on Bruker AMX 300 (Cambridge Scientific Corp. Watertown, MA, USA). Elemental analyses were performed on an Elemental Analyser vario Macro CHN Elementar Analysensysteme GmbH (Hanau, Germany).

The cross-sections of manufactured fittings were studied using a scanning electron microscope (SEM) with field emission and backscattered electron detector (BSE) (Quanta 3D FEG, Huston, TX, USA). The diffuse reflectance UV-Vis (UV-VIS-DRS) spectra registered between 200 and 800 nm were used for the absorption maximum determination. The Jasco V-750 spectrophotometer was used in our works (JASCO Deutschland GmbH, Pfungstadt, Germany). The electron paramagnetic resonance (EPR) spectroscopy was used in order to confirm the presence of reactive oxygen species on the surface of the investigated samples. Measurements were carried out using an X band EPR SE/X-2541M spectrometer (Radiopan, Poznań, Poland) with a 100 kHz modulation. The microwave frequency was monitored with a frequency meter. The magnetic field was measured with an automatic NMR-type JTM-147 magnetometer (Radiopan, Poznań, Poland). Measurement conditions: microwave frequency: ca. 9.33 GHz; microwave power: 20–40 mW; modulation amplitude: 0.2–1 mT; sweep: 10-50 mT; sweep time: 1–8 min.; time constant: 0.03–0.3 s; receiver gain: 3.2–5 × 10^5. Low intensity signals were recorded in the accumulation mode. The measurements were performed for cut films of PCL + TOCs composites at room temperature. The thermal gravimetric analysis (TGA) and the differential scanning calorimetry (DSC) were performed using Thermal Analyzer STA 449 F5 Jupiter (Netzsch, Selb, Germany), the In, Bi, Zn, Al, and Au were used as the references. The analysis was carried out in the range 30–550 °C at a rate 5 °C/min in the nitrogen atmosphere. The mechanical strength studies of the polymer and composite fittings, subjected to the static tensile test (Model 4204, Instron, USA) were carried out in the following conditions: tensile speed: 20 mm/min; grip distance, 50 mm; length of the measuring section of the fittings, 40 mm; fittings thickness, 1.5 mm; measurement temperature, 25 °C.

4.4. The Photocatalytic Activity Evaluation of Produced (Polymer + nTOCs) Composites

The photocalatytic activity of PMMA + 20TOCs composites (TOCs = (1)–(2)) and PCL + *n*TOCs composites (TOCs = (1)–(2), *n* = 5, 20 wt.%) was studied by monitoring of MB aqueous solution decolorization. Samples of a 10 × 10 mm size were preconditioned by exposition to Vis light for 28 h. In the next steps, composites were placed in quartz cuvettes with dye solution (V = 3.5 cm^3, $c = 2.0 \times 10^{-5}$ M). After 12 h in the dark, the solution was replaced by the final MB solution (V = 3.5 cm^3, $c = 1.0 \times 10^{-5}$ M) intended for the kinetic measurements. The prepared samples were exposed to Vis light (77 W

tungsten halogen lamp, range of 350–1200 nm). All cuvettes were covered with Teflon lid during irradiation. MB absorbance at 660 nm was registered (Metertech SP-830 PLUS, Metertech, Inc., Taipei, Taiwan) every 40 minutes for 30 hours of irradiation. Percentage of MB decolorization was calculated using the Equation (1):

$$\%\ \text{of dye decolorization} = [(c_0 - c_t)/c_0]\ \frac{c_o - c_t}{c_o} \times 100 \quad (1)$$

where c_0 is an initial concentration of dye and c_t is a dye concentration at a given time t [42].

4.5. The Estimation of Antimicrobial Activity of Studied (Polymer + TOCs) Composites

Antibacterial and antifungal activities of PCL and PCL + TOCs composites (20 × 10 × 1 mm) was studied against Gram-positive (*Staphylococcus aureus* ATCC 6538 and *S. aureus* ATCC 25923) and Gram-negative (*Escherichia coli* ATCC 8739 and *E. coli* ATCC 25922) bacteria and yeasts of *Candida albicans* ATCC 10231. All strains were purchased from the American Type Culture Collection (Manassas, VA 20110 USA). Tested samples were sterilized in 70% ethanol for 15 minutes and then using a UVC lamp for 15 min in the laminar hood (Bioquell, Hampshire, UK) each side. Specimens were subsequently treated with indoor light (visible light). The earlier investigations revealed that the absorption maximum of PCL + TOCs samples was found at the UVA-Vis border, which enables the use of UVC radiation for their sterilization. Sterile samples were placed in sterile 25 ml screw-cap tubes (Sarstedt) with 2 ml of tested microorganism suspension (1.0–5.8 × 10^6 colony forming units (c.f.u) $cm^3/^{-1}$) prepared in sterile deionized water and incubated for 24 h at 37 °C in a humid atmosphere and gently shaken (80 rpm) conditions. Samples were then vortexed and specimens removed from the tubes. Microbial suspensions were then serially ten-fold diluted and aliquots (100 µl) of each dilution were aseptically spread over the surface of Triptic Soy Agar (TSA, Becton Dickinson, USA) for bacteria and Sabouraud Dextrose Agar (SDA, Becton Dickinson) for yeasts poured into Petri plates. Inoculated plates were incubated at 37 °C for 24 h. Assays were performed in triplicate. After incubation, colony-forming units (cfu) were counted on the agar plates. Control was the suspension of test microorganisms in the tube.

The antimicrobial activity was determined on the basis of the reduction factor (R) calculated according to the Equation (2):

$$R = U_t - A_t \quad (2)$$

where U_t is the average of the common logarithm of the number of viable bacteria on Petri plate, recovered from the untreated microbial suspension after 24 h, A_t is the average of the common logarithm of the number of viable bacteria, on Petri plate, recovered from the treated microbial suspension with PCL or PCL + TOCs after 24 h. $R \geq 2$ determines biocidal activity (at least 99% reduction of microbial growth).

5. Conclusions

The studies carried out lead to the production of PCL + *n*TOCs (*n* = 5 and 20 wt%) composites and to the determination of their physicochemical properties. Using the equipment for plastics processing, the tetranuclear Ti(IV)-oxo complexes (TOCs), of the general formula $[Ti_4O_2(O^iBu)_{10}(O_2CR')_2]$ (R′ = $PhNH_2$ (**1**) and $C_{13}H_9$ (**2**)), were dispersed in the poly(ε-caprolactone) (PCL) matrix. The enrichment of the polymer with micro-grains of TOCs slightly affects PCL thermal and mechanical properties while significantly shifting the absorption maximum towards the visible range.

The photocatalytic activity of produced (polymer + TOCs) composites were assessed using the methylene blue (MB) photoinduced decolorization process in the visible range. The obtained results revealed the clear photocatalytic activity of composites containing 20 wt.% of (**1**) and (**2**). Analysis of EPR spectra of the above-mentioned samples proved that photo-excitation of their surface by visible light leads to ROS generation. According to

EPR data, the paramagnetic species of O^- were generated on the surface of PCL + 20(**1**) composite sample while both O^- and O_2^- ones on the surface of PCL + 20(**2**). The obtained results suggest that the type of carboxylic ligands can influence the type of appearing ROS specimens.

From the studied composite samples, the strong antibacterial activity (against *E. coli* and *S. aureus* strains) and weak inhibition of yeasts (*C. albicans*) growth was found for composites PCL + 20 TOCs (TOCs = (**1**) and (**2**)). However, good antibacterial properties also revealed the PCL + 5(**2**) system. The obtained results indicate that the composite containing the $[Ti_4O_2(O^iBu)_{10}(O_2CC_{13}H_9)_2]$ micro grains exhibit better bactericidal activity, which can be associated with the ability to generate more differentiated forms of ROS (O^-, O_2^-) during exposure to visible light, suggesting that the produced materials can be considered as the materials with self-disinfecting activity. It should be noted that this paper includes the preliminary results of studies on the antimicrobial potential of TOCs dispersed in the PCL matrix. A detailed analysis determining the mechanisms of antimicrobial action of polymer + TOCs composites will be carried out during the next step of our works and will form the basis of another publication.

Supplementary Materials: The following are available online at https://www.mdpi.com/article/10.3390/ijms22137021/s1.

Author Contributions: Conceptualization, P.P.; methodology, B.K., A.R., A.T., G.W., P.G., J.W., M.S. (Michał Sobota), and P.P.; formal analysis, B.K., A.R., A.T., G.W., P.G., M.S. (Mateusz Stojko), M.S. (Michał Sobota), and J.W.; investigation, B.K., G.W., P.G., E.K., J.W., and M.S. (Mateusz Stojko); data curation, P.P.; writing—original draft preparation, P.P., A.R., and P.G.; writing—review and editing, P.P. and A.R.; supervision, P.P. and A.R.; project administration, P.P. and A.R.; funding acquisition, P.P., B.K., A.R., and A.T. All authors have read and agreed to the published version of the manuscript.

Funding: This research received no external funding.

Institutional Review Board Statement: Not applicable.

Informed Consent Statement: Not applicable.

Data Availability Statement: Data is contained within the article or Supplementary Materials.

Acknowledgments: The authors would like to thank Piotr Dobrzyński from Centre of Polymer and Carbon Materials, Polish Academy of Sciences at Zabrze, Poland, for his support and assistance in the research carried out.

Conflicts of Interest: The authors declare no conflict of interest.

References

1. Lin, Y.; Zhou, Y.-F.; Chen, Z.-H.; Lui, F.-H.; Zhao, L.; Su, Z.-M. Synthesis, structure, and photo catalytic hydrogen of three environmentally friendly titanium oxo-clusters. *Inorg. Chem. Commun.* **2014**, *40*, 22–25. [CrossRef]
2. Wu, Y.-Y.; Luo, W.; Wang, Y.-H.; Pu, Y.-Y.; Zhang, X.; You, L.-S.; Zhu, Q.-Y.; Dai, J. Titanium–oxo–Clusters with Dicarboxylates: Single-Crystal Structure and Photochromic Effect. *Inorg. Chem.* **2012**, *51*, 8982–8988. [CrossRef] [PubMed]
3. Wu, Y.-Y.; Lu, X.-W.; Qi, M.; Su, H.-C.; Zhao, X.-W.; Zhu, Q.-Y.; Dai, J. Titanium–Oxo cluster with 9-anthracenecarboxylate antennae: A fluorescent and photocurrent transfer material. *Inorg. Chem.* **2014**, *53*, 7233–7240. [CrossRef]
4. Yin, P.; Huo, S.; Wang, J.; Wu, Q.-Y.; Zhu, J.; Dai, J. A tetrathiafulvalene-grafted titanium-oxo-cluster material: Self-catalyzed crystal exfoliation and photocurrent response properties. *J. Mater. Chem. C* **2015**, *3*, 409–415. [CrossRef]
5. Coppens, P.; Chen, Y.; Trzop, E. Crystallography and Properties of Polyoxotitanate Nanoclusters. *Chem. Rev.* **2014**, *114*, 9645–9661. [CrossRef]
6. Lu, D.F.; Kong, X.J.; Lu, T.B.; Long, L.-S.; Zheng, L.S. Heterometallic Lanthanide–Titanium Oxo Clusters: A New Family of Water Oxidation Catalysts. *Inorg. Chem.* **2017**, *56*, 1057–1060. [CrossRef]
7. Nunes, D.; Pimentel, A.; Gonçalves, A.; Pereira, S.; Branquinho, R.; Barquinha, P.; Fortunato, E.; Martins, R. Metal Oxide Nanostructures for Sensor Applications. *Semicond. Sci. Technol.* **2019**, *34*, 043001. [CrossRef]
8. Yates, J.T., Jr. Photochemistry on TiO_2: Mechanisms behind the surface chemistry. *Surf. Sci.* **2009**, *603*, 1605–1612. [CrossRef]
9. Josset, S.; Keller, N.; Lett, M.C.; Ledoux, M.J.; Keller, V. Numeration methods for targeting photoactive materials in the UV-A photocatalytic removal of microorganisms. *Chem. Soc. Rev.* **2008**, *37*, 744–755. [CrossRef] [PubMed]

10. Joost, U.; Juganson, K.; Visnapuu, M.; Mortimer, M.; Kahru, A.; Nõmmiste, E.; Joost, U.; Kisand, V.; Ivask, A. Photocatalytic antibacterial activity of nano-TiO_2(anatase)-based thin films: Effects on Escherichia coli cells and fatty acids. *J. Photochem. Photobiol. B Biol.* **2015**, *142*, 178–185. [CrossRef] [PubMed]
11. Friehs, E.; AlSalkaa, Y.; Jonczyk, R.; Lavrentieva, A.; Jochums, A.; Walter, J.-G.; Stahl, F.; Scheper, T.; Bahnemann, D. Toxicity, phototoxicity and biocidal activity of nanoparticles employed in photocatalysis. *J. Photochem. Photobiol. C Photochem. Rev.* **2016**, *29*, 1–28. [CrossRef]
12. Subramanian, Y.; Ramasamy, V.; Karthikeyan, R.J.; Srinivasan, G.R.; Arulmozhi, D.; Gubendiran, R.K.; Sriramalu, M. Investigations on the enhanced dye degradation activity of heterogeneous $BiFeO_3$-$GdFeO_3$ nanocomposite photocatalyst. *Heliyon* **2019**, *5*, e01831. [CrossRef] [PubMed]
13. Smith, A.M.; Nie, S. Semiconductor nanocrystals: Structure, properties, and band gap engineering. *Acc. Chem. Res.* **2010**, *43*, 190–200. [CrossRef]
14. Abdal Dayem, A.; Hossain, M.K.; Lee, S.B.; Kim, K.; Saha, S.K.; Yang, G.M.; Choi, H.Y.; Cho, S.G. The Role of Reactive Oxygen Species (ROS) in the Biological Activities of Metallic Nanoparticles. *Int. J. Mol. Sci.* **2017**, *18*, 120. [CrossRef] [PubMed]
15. Li, D.; Song, H.; Meng, X.; Shen, T.; Sun, J.; Han, W.; Wang, X. Effects of Particle Size on the Structure and Photocatalytic Performance by Alkali-Treated TiO_2. *Nanomaterials* **2020**, *10*, 546. [CrossRef]
16. Chaumont, C.; Chaumont, A.; Kyritsakas, N.; Mobiant, P.; Henry, M. Titanium oxo-clusters dervitatized form the $Ti_{10}O_{12}(cat)_8(py)_8$ complex: Structural investigation and spectroscopic studies of light absorption. *Dalton Trans.* **2016**, *45*, 8760–8769. [CrossRef]
17. Janek, M.; Radtke, A.; Muzioł, T.M.; Jerzykiewicz, M.; Piszczek, P. Tetranuclear Oxo-Titanium Clusters with Different Carboxylate Aromatic Ligands: Optical Properties, DFT Calculations, and Photoactivity. *Materials* **2018**, *11*, 1661. [CrossRef] [PubMed]
18. Piszczek, P.; Kubiak, B.; Golińska, P.; Radtke, A. Oxo-Titanium(IV) Complex/Polymer Composites—Synthesis, Spectroscopic Characterization and Antimicrobial Activity Test. *Int. J. Mol. Sci.* **2020**, *21*, 9663. [CrossRef]
19. Hong, Z.-F.; Xu, S.-H.; Yan, Z.-H.; Lu, D.-F.; Kong, X.-J.; Long, L.-S.; Zheng, L.-S. A Large Titanium Oxo Cluster Featuring a Well-Defined Structural Unit of Rutile. *Cryst. Growth Des.* **2018**, *18*, 4864–4868. [CrossRef]
20. Su, M.K.; Wu, Y.; Tan, W.; Wang, D.; Yuan, M.H. A monomeric bowl-like pyrogallol[4]arene Ti_{12} coordination complex. *Chem. Commun.* **2017**, *53*, 9598–9601. [CrossRef]
21. Kim, S.; Sarkar, D.; Kim, Y.; Park, M.H.; Yoon, M.; Kim, Y.; Kim, M. Synthesis of functionalizedtitanium-carboxylate molecular clusters and their catalytic activity. *J. Ind. Eng. Chem.* **2017**, *53*, 171–176. [CrossRef]
22. Qi, K.; Cheng, B.; Yu, J.; Ho, W. Review on the improvement of the photocatalytic and antibacterial activities of ZnO. *J. Alloy. Compd.* **2017**, *727*, 792–820. [CrossRef]
23. Yemmireddy, V.K.; Hung, Y.C. Using Photocatalyst Metal Oxides as Antimicrobial Surface Coatings to Ensure Food Safety-Opportunities and Challenges. *Compr. Rev. Food Sci. Food Saf.* **2017**, *16*, 617–631. [CrossRef]
24. Foster, H.A.; Ditta, I.B.; Varghese, S.; Steele, A. Photocatalytic disinfection using titanium dioxide: Spectrum and mechanism of antimicrobial activity. *Appl. Microbiol. Biotechnol.* **2011**, *90*, 1847–1868. [CrossRef]
25. Park, S.; Lee, S.; Kim, B.; Lee, S.; Lee, J.; Sangjun, S.; Gu, M.; Yi, J.; Lee, J. Toxic effects of titanium dioxide nanoparticles on microbial activity and metabolic flux. *Biotechnol. Bioprocess Eng.* **2012**, *17*, 276–282. [CrossRef]
26. Raut, A.V.; Yadav, H.M.; Gnanamani, A.; Pushpavanam, S.; Pawar, S.H. Synthesis and characterization of chitosan-TiO_2:Cu nanocomposite and their enhanced antimicrobial activity with visible light. *Colloids Surf. B Biointerfaces* **2016**, *148*, 566–575. [CrossRef]
27. Svensson, F.G.; Seisenbaeva, G.A.; Kessler, V.G. Mixed-Ligand Titanium "Oxo Clusters": Structural Insights into the Formation and Binding of Organic Molecules and Transformation into Oxide Nanostructures on Hydrolysis and Thermolysis. *Eur. J. Inorg. Chem.* **2017**, *35*, 4117–4122. [CrossRef]
28. Siamak, P.; Yazdankhah, S.P.; Scheie, A.A.; Høiby, E.A.; Lunestad, B.-T.; Heir, E.; Fotland, T.Ø.; Naterstad, K.; Kruse, H. Triclosan and antimicrobial resistance in bacteria: An overview. *Microb. Drug Resist.* **2006**, *12*, 83–90.
29. Janek, M.; Muzioł, T.M.; Piszczek, P. Trinuclear Oxo-Titanium Clusters: Synthesis, Structure, and Photocatalytic Activity. *Materials* **2019**, *12*, 3195. [CrossRef] [PubMed]
30. Janek, M.; Muzioł, T.; Piszczek, P. The structure and photocatalytic activity of the tetranuclear titanium(IV)oxo-complex with 4-aminobenzoate ligands. *Polyhedron* **2018**, *141*, 110–117. [CrossRef]
31. Malikmammadov, E.; Tanir, T.E.; Kiziltay, A.; Hasirci, V.; Hasirci, N. PCL and PCL-based materials in biomedical applications. *J. Biomater. Sci. Polym. Ed.* **2017**, *29*, 863–893. [CrossRef]
32. Azimi, B.; Nourpanah, P.; Rabiee, M.; Arbab, S. Poly (ε-caprolactone) fiber: An overview. *J. Eng. Fiber Fabr.* **2014**, *9*, 74–90.
33. Woodruff, M.A.; Hutmacher, D.W. The return of a forgotten polymer—Polycaprolactone in the 21st century. *Prog. Polym. Sci.* **2010**, *35*, 1217–1256. [CrossRef]
34. Chiari, C.; Koller, U.; Dorotka, R. A tissue engineering approach to meniscus regeneration in a sheep model. *Osteoarthr. Cartil.* **2006**, *14*, 1056–1065. [CrossRef] [PubMed]
35. Mondrinos, M.; Dembzynski, R.; Lu, L. Porogen-based solid freeform fabrication of polycaprolactone-calcium phosphate scaffolds for tissue engineering. *Biomaterials* **2006**, *27*, 4399–4408. [CrossRef] [PubMed]
36. Nair, L.; Laurencin, C. Polymers as Biomaterials for Tissue Engineering and Controlled Drug Delivery. *Adv. Biochem. Eng./Biotech.* **2006**, *102*, 47–90.

37. Dave, R.N.; Joshi, H.M.; Venugopalan, V.P. Novel Biocatalytic Polymer-Based Antimicrobial Coatings as Potenetial Ureeral Biomaterial: Preparation and In Vitro Performance Evaluation. *Antimicrob. Agents Chemother.* **2011**, *55*, 845–853. [CrossRef]
38. de Vasconcelos Pina, H.; de Farias, A.J.A.; Barbosa, F.C.; de Lima Souza, J.W.; de Sousa Barros, A.B.; Cardoso, M.J.B.; Fook, M.V.L.; Wellen, R.M.R. Microbiological and cytotoxic perspectives of active PCL/ZnO film for food packing. *Mater. Res. Express.* **2020**, *7*, 025312. [CrossRef]
39. Le Low, J.; Kao, P.H.-N.; Tambyah, P.A.; Koh, G.E.K.; Ling, H.; Kline, K.A.; Cheow, W.S.; Leong, S.S.J. Development of a polymer-based antimicrobial coating for efficacious urinary catheter protection. *Biotechnol. Notes* **2021**, *2*, 1–10. [CrossRef]
40. Balcucho, J.; Narváez, D.M.; Castro-Mayorga, J.L. Antimicrobial and Biocompatible Polycaprolactone and Copper Oxide Nanoparticle Wound Dressings against Methicillin-Resistant Staphylococcus aureus. *Nanomaterials* **2020**, *10*, 1692. [CrossRef]
41. del Ángel-Sánchez, K.; Borbolla-Torres, C.I.; Palacios-Pineda, L.M.; Nicolás, A.; Ulloa-Castillo, N.A.; Elías-Zúñiga, A. Development, Fabrication, and Characterization of Composite Polycaprolactone Membranes Reinforced with TiO_2 Nanoparticles. *Polymers* **2019**, *11*, 1955. [CrossRef] [PubMed]
42. Kiran, A.S.K.; Kumar, T.S.S.; Sanghavi, R.; Doble, M.; Ramakrishna, S. Antibacterial and Bioactive Surface Modifications of Titanium Implants by PCL/TiO_2 Nanocomposite Coatings. *Nanomatrials* **2018**, *8*, 860. [CrossRef]
43. Abdellah, M.H.; Nosier, S.A.; El-Shazly, A.H.; Mubarak, A.A. Photocatalytic decolorization of methylene blue using TiO_2/UV system enhanced by air sparging. *Alex. Eng. J.* **2018**, *57*, 3727–3735. [CrossRef]
44. Rusu, M.; Ursu, M.; Rusu, D. Poly(vinyl chloride) and Poly(e-caprolactone) Blends for Medical Use. *J. Thermoplast. Compos. Mater.* **2006**, *19*, 173–190. [CrossRef]
45. Shkarina, S.; Surmeneva, M.; Surmenev, R. Fabrication and characterization of polycaprolactone cross-linked and highly-aligned 3-D artificial scaffolds for bone tissue regeneration via electrospinning technology. *IOP Conf. Ser. Mater. Sci. Eng.* **2015**, *98*, 012024.
46. Kotula, A.P.; Snyder, C.R.; Migler, K.B. Determining conformational order and crystallinity in polycaprolactone via Raman spectroscopy. *Polymer* **2017**, *117*, 1–10. [CrossRef]
47. Li, N.; Matthews, P.D.; Luo, H.-K.; Wright, D.S. Novel properties and potential applications of functional ligand-modified polyoxotitanate cages. *Chem. Commun.* **2016**, *52*, 11180–11190. [CrossRef]
48. He, W.; Liu, Y.; Wamer, W.G.; Yin, J.-J. Electron spin resonance spectroscopy for the study of nanomaterial-mediated generation of reactive oxygen species. *J. Food Drug Anal.* **2014**, *22*, 49–63. [CrossRef]
49. Xiong, L.B.; Li, J.L.; Yang, B.; Yu, Y. Ti^{3+} in the Surface of Titanium Dioxide: Generation, Properties and Photocatalytic Application. *J. Nanomater.* **2012**, *2012*, 831524. [CrossRef]
50. Suriye, K.; Lobo-Lapidus, R.J.; Yeagle, G.J.; Praserthdam, P.; Britt, D.; Gates, B.C. Probing Defect Sites on TiO_2 with $[Re_3(CO)_{12}H_3]$: Spectroscopic Characterization of the Surface Species. *Chem. Eur. J.* **2008**, *14*, 1402–1414. [CrossRef] [PubMed]
51. Dan-Hardi, M.; Serre, C.; Frot, T.; Rozes, L.; Maurin, G.; Sanchez, C.; Fe'rey, G. A New Photoactive Crystalline Highly Porous Titanium(IV) Dicarboxylate. *J. Am. Chem. Soc.* **2009**, *131*, 10857–10859. [CrossRef]
52. Richards, E.; Murphy, D.E.; Che, M. An EPR characterisation of stable and transient reactive oxygen species formed under radiative and non-radiative conditions. *Res. Chem. Intermed.* **2019**, *45*, 5763–5779. [CrossRef]
53. Maness, P.-C.; Smolinski, S.; Blake, D.M.; Huang, Z.; Wolfrum, E.J.; Jacoby, W.A. Bactericidal activity of photocatalytic TiO_2 reaction: Toward an understanding of its killing mechanism. *Appl. Environ. Microbiol.* **1999**, *65*, 4094–4098. [CrossRef]
54. Shaikh, S.; Nazam, N.; Rizvi, S.M.D.; Ahmad, K.; Baig, M.H.; Lee, E.J.; Choi, I. Mechanistic insights into the antimicrobial actions of metallic nanoparticles and their implications for multidrug resistance. *Int. J. Mol. Sci.* **2019**, *20*, 2468. [CrossRef]
55. De Pasquale, I.; Lo Porto, C.; Dell'Edera, M.; Petronella, F.; Agostiano, A.; Curri, M.L.; Comparelli, R. Photocatalytic TiO_2-Based Nanostructured Materials for Microbial Inactivation. *Catalysts* **2020**, *10*, 1382. [CrossRef]
56. Memar, M.Y.; Ghotaslou, R.; Samiei, M.; Adibkia, K. Antimicrobial use of reactive oxygen therapy: Current insights. *Infect. Drug Resist.* **2018**, *11*, 567–576. [CrossRef] [PubMed]
57. Su, W.; Wang, S.; Wang, X.; Fu, X.; Weng, J. Plasma pre-treatment and TiO_2 coating of PMMA for the improvement of antibacterial properties. *Surf. Coat. Technol.* **2010**, *205*, 465–469. [CrossRef]
58. Ramesh, T.; Nayak, B.; Amirbahman, A.; Tripp, C.P.; Mukhopadhyay, S. Application of ultraviolet light assisted titanium dioxide photocatalysis for food safety: A review. *Innov. Food Sci. Emerg. Technol.* **2016**, *38*, 105–115. [CrossRef]
59. Dryden, M. Reactive oxygen species: A novel antimicrobial. *Int. J. Antimicrob. Agents* **2018**, *51*, 299–303. [CrossRef] [PubMed]
60. Dwyer, D.J.; Belenky, P.A.; Yang, J.H.; MacDonald, I.C.; Martell, J.D.; Takahashi, N.; Chan, C.T.Y.; Lobritz, M.A.; Braff, D.; Schwarz, E.G.; et al. Antibiotics induce redox-related physiological alterations as part of their lethality. *Proc. Natl. Acad. Sci. USA* **2014**, *111*, E2100–E2109. [CrossRef]
61. Foti, J.J.; Devadoss, B.; Winkler, J.A.; Collins, J.J.; Walker, G.C. Oxidation of the guanine nucleotide pool underlies cell death by bactericidal antibiotics. *Science* **2012**, *336*, 315–319. [CrossRef] [PubMed]
62. Fan, X.Y.; Tang, B.-K.; Xu, Y.-Y.; Han, A.-X.; Shi, K.-X.; Wu, Y.-K.; Ye, Y.; Wei, M.-L.; Niu, C.; Wong, K.-W.; et al. Oxidation of dCTP contributes to antibiotic lethality in stationary-phase mycobacteria. *Proc. Natl. Acad. Sci. USA* **2018**, *115*, 2210–2215. [CrossRef] [PubMed]
63. Gruber, C.C.; Walker, G.C. Incomplete base excision repair contributes to cell death from antibiotics and other stresses. *DNA Repair* **2018**, *71*, 108–117. [CrossRef]
64. Wang, G.; Jin, W.; Qasim, A.M.; Gao, A.; Peng, X.; Li, W.; Feng, H.; Chu, P.K. Antibacterial effects of titanium embedded with silver nanoparticles based on electron-transfer-induced reactive oxygen species. *Biomaterials* **2017**, *124*, 25–34. [CrossRef] [PubMed]

65. Pan, R.; Liu, Y.; Chen, W.; Dawson, G.; Wang, X.; Li, W.; Dong, B.; Zhu, Y. The toxicity evaluation of nano-trititanate with bactericidal properties in vitro. *Nanotoxicology* **2012**, *6*, 327–337. [CrossRef] [PubMed]
66. Liu, P.; Duan, W.; Wang, Q.; Li, X. The damage of outer membrane of escherichia coli in the presence of TiO_2 combined with UV light. *Colloids Surf. B Biointerfaces* **2010**, *78*, 171–176. [CrossRef]
67. Angarano, V.; Smet, C.; Akkermans, S.; Watt, C.; Chieffi, A.; Van Impe, J.F.M. Visible Light as an Antimicrobial Strategy for Inactivation of Pseudomonas fluorescens and Staphylococcus epidermidis Biofilms. *Antibiotics* **2020**, *9*, 171. [CrossRef]
68. Lubart, R.; Lipovski, A.; Nitzan, Y.; Friedmann, H. A possible mechanism for the bactericidal effect of visible light. *Laser Ther.* **2011**, *20*, 17–22. [CrossRef]
69. Liou, J.W.; Chang, H.H. Bactericidal Effects and Mechanisms of Visible Light-Responsive Titanium Dioxide Photocatalysts on Pathogenic Bacteria. *Arch. Immunol. Ther. Exp.* **2012**, *60*, 267–275. [CrossRef]

Materiały uzupełniające

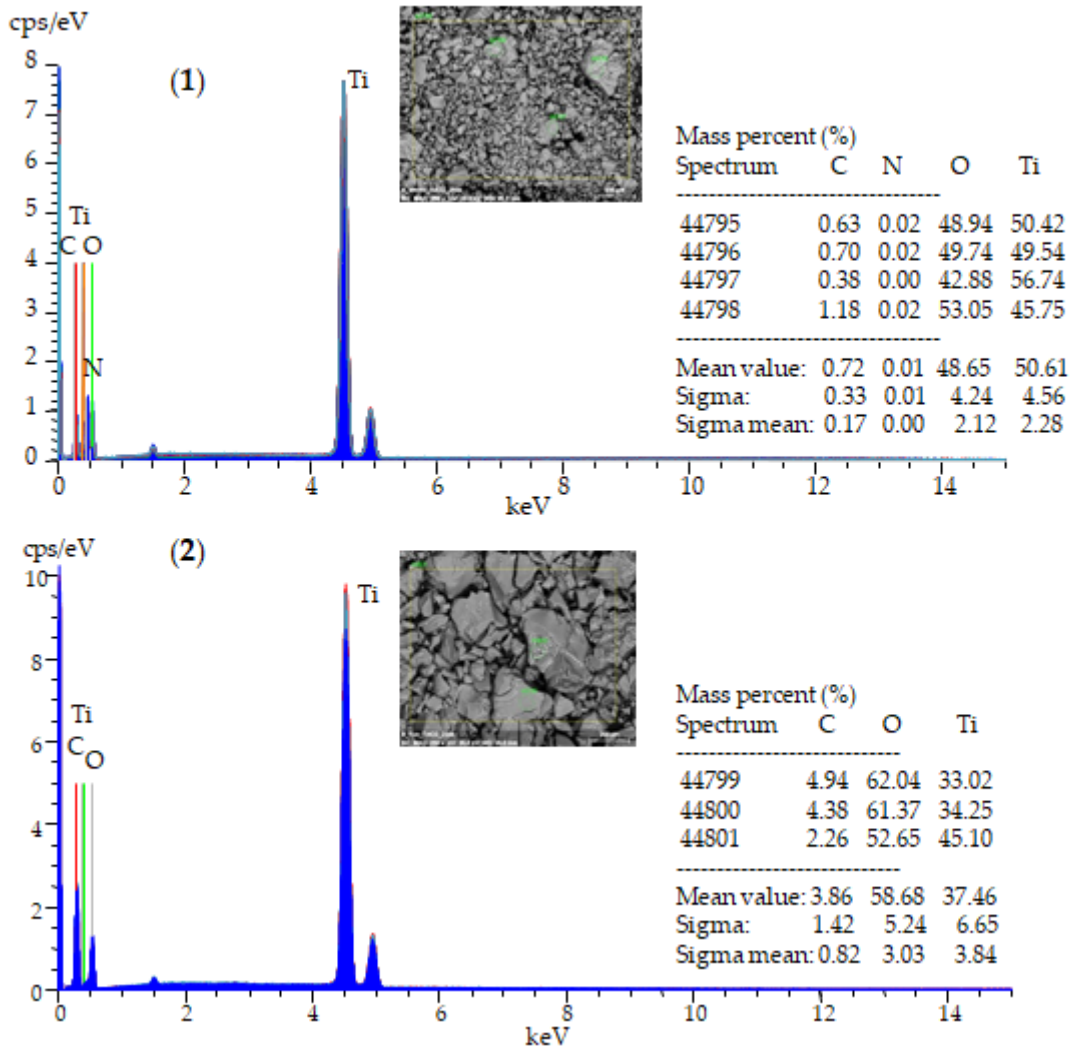


Figure S1: SEM EDX data for (1) and (2).

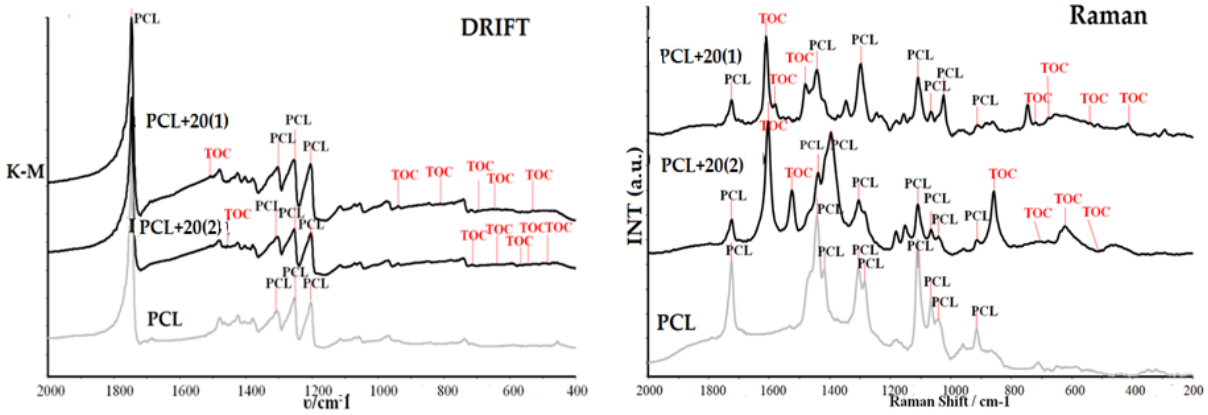


Figure S2: DRIFT and Raman spectrum for samples: PCL, PCL + 20(1) and PCL + 20(2).

P4. *Structural Characterization and Bioactivity of a Titanium(IV) – Oxo Complex Stabilized by Mandelate Ligands.*

molecules

MDPI

Article

Structural Characterization and Bioactivity of a Titanium(IV)-Oxo Complex Stabilized by Mandelate Ligands

Barbara Kubiak [1,*], Tadeusz Muzioł [1], Grzegorz Wrzeszcz [1], Aleksandra Radtke [1], Patrycja Golińska [2], Tomasz Jędrzejewski [3], Sylwia Wrotek [3] and Piotr Piszczek [1,*]

[1] Department of Inorganic and Coordination Chemistry, Faculty of Chemistry, Nicolaus Copernicus University in Toruń, Gagarina 7, 87-100 Toruń, Poland; tadeuszmuziol@wp.pl (T.M.); wrzeszcz@umk.pl (G.W.); aleksandra.radtke@umk.pl (A.R.)

[2] Department of Microbiology, Faculty of Biological and Veterinary Sciences, Nicolaus Copernicus University in Toruń, Lwowska 1, 87-100 Toruń, Poland; golinska@umk.pl

[3] Department of Immunology, Faculty of Biological and Veterinary Sciences, Nicolaus Copernicus University in Toruń, Lwowska 1, 87-100 Toruń, Poland; tomaszj@umk.pl (T.J.); wrotek@umk.pl (S.W.)

* Correspondence: basiak0809@gmail.com (B.K.); piszczek@umk.pl (P.P.)

Abstract: Research on titanium-oxo complexes (TOCs) is usually focused on their structure and photocatalytic properties. Findings from these investigations further sparked our interest in exploring their potential biological activities. In this study, we focused on the synthesis and structure of a compound with the general formula $[Ti_8O_2(O^iPr)_{20}(man)_4]$ (**1**), which was isolated from the reaction mixture of titanium(IV) isopropoxide with mandelic acid (Hman) in a molar ratio of 4:1. The structure (**1**) was determined using single-crystal X-ray diffraction, while spectroscopic studies provided insights into its physicochemical properties. To assess the potential practical applications of (**1**), its microcrystals were incorporated into a polymethyl methacrylate (PMMA) matrix, yielding composite materials of the type PMMA + (**1**) (2 wt.%, 5 wt.%, 10 wt.%, and 20 wt.%). The next stage of our research involved the evaluation of the antimicrobial activity of the obtained materials. The investigations performed demonstrated the antimicrobial activity of pure (**1**) and its composites (PMMA + (**1**)) against both Gram-positive and Gram-negative strains. Furthermore, MTT tests conducted on the L929 murine fibroblast cell line confirmed the lack of cytotoxicity of these composites. Our study identified (**1**) as a promising antimicrobial agent, which is also may be use for producing composite coatings.

Keywords: titanium(IV)-oxo complex; α-hydroxyacid; mandelic acid; crystal structure; antimicrobial activity; cytotoxicity

check for updates

Citation: Kubiak, B.; Muzioł, T.; Wrzeszcz, G.; Radtke, A.; Golińska, P.; Jędrzejewski, T.; Wrotek, S.; Piszczek, P. Structural Characterization and Bioactivity of a Titanium(IV)-Oxo Complex Stabilized by Mandelate Ligands. *Molecules* **2024**, *29*, 1736. https://doi.org/10.3390/molecules29081736

Academic Editor: Teodorico C. Ramalho

Received: 18 March 2024
Revised: 4 April 2024
Accepted: 9 April 2024
Published: 11 April 2024

Copyright: © 2024 by the authors. Licensee MDPI, Basel, Switzerland. This article is an open access article distributed under the terms and conditions of the Creative Commons Attribution (CC BY) license (https://creativecommons.org/licenses/by/4.0/).

1. Introduction

The wide interest in titanium(IV)-oxo complexes (TOCs) is associated with their structural diversity and photocatalytic activity [1,2]. These compounds have found applications in diverse technologies, including hydrogen production or water purification [3,4]. Previous research led to the synthesis of TOCs with cores containing from 2 to 44 titanium atoms [5–12], with the largest group consisting of compounds with four- and six-nuclear cores [13–17]. The cores $\{Ti_aO_b\}$ of TOCs can be stabilized by alkoxide groups, as well as carboxylate or phosphonate ligands, although β-diketonate, β-ketoester, and sulfonate ligands have also been employed [5,18,19]. The varied possibilities of carboxylate ligand coordination with titanium atoms [20] explain the fact that most of the works focus on investigations of Ti(IV)-oxo complexes stabilized with alkoxide and carboxylate ligands. Notably, the type of carboxylate ligand has a significant influence both on the $\{Ti_aO_b\}$ core structure and the oxo complex photocatalytic activity [5,7,21–26].

Interest in Ti(IV)-oxo complexes also stems from their potential biomedical applications. Studies on the utilization of TOCs in photodynamic therapy [27] and as antimicrobial

agents [5,13,24,28–30] are particularly significant. With the ongoing search for materials possessing bactericidal properties and the ability to prevent microbial growth, our research has concentrated on the latter aspect. The analysis of literature reports suggests that research on this issue is developing in three main directions. The first involves the introduction of a heteroatom into the core structure, resulting in the synthesis of compounds containing {AgTi-oxo} or {AgTi} cores, which demonstrate favorable optical, antibacterial, and photothermal properties [29,30]. Luo et al., in their study on a complex featuring a $\{Ag_9Ti_4\}$ core stabilized by salicylate ligands, proved that its bacteriostatic efficacy against strains of *Staphylococcus aureus* and *Escherichia coli* was 94.51% and 95.42%, respectively, surpassing that of a comparable complex with a $\{Ag_2Ti\}$ core [30]. The improvement in the biocidal properties of the complex with the $\{Ag_9Ti_4\}$ core was achieved by the formation of a hydrogel $\{Ag_9Ti_4$-gel$\}$.

Another approach to leveraging the antibacterial properties of Ti(IV)-oxo complexes was introduced in the research of Svensson et al. [13]. In their study of the tetranuclear Ti(IV)-oxo complex ($\{Ti_4O_2\}$ core) stabilized with triclosan ligands, they capitalized on the compound's high susceptibility to hydrolysis processes, facilitating the release of an antibacterial agent (triclosan). According to this theory, Ti(IV)-oxo complexes are considered as carriers of bactericidal agents. The third strategy involves harnessing the photocatalytic activity of TOCs and their capability to generate reactive oxygen species (ROS) [25,31]. In this case, the mechanism of biocidal action is associated with oxidative stress induced by the generated ROS. Our previous investigations confirmed the biocidal activity of $\{Ti_4O_2\}$ clusters stabilized with carboxylate ligands (such as 4-aminobenzoic acid, 4-hydroxybenzoic acid, and 9-fluorene carboxylate) [5,24,25]. The analysis of the electron paramagnetic resonance (EPR) spectra of these compounds confirmed the generation of O_2^- and O^- oxygen anions on the surface of both pure oxo complexes and composites prepared by dispersing the complexes in a poly(methyl methacrylate) (PMMA) matrix. It is worth noting that the $\{Ti_aO_b\}$ core structure also influenced the antimicrobial activity of composites containing Ti(IV)-oxo complexes. Studying oxo complexes with different core structures stabilized by 9-fluorene carboxylate ligands allowed for the observation of this effect. It was found that the biocidal activity of samples with $\{Ti_6O_4\}$ and $\{Ti_4O_2\}$ cores was higher than that of $\{Ti_6O_6\}$ and $\{Ti_3O\}$ systems, when irradiated with visible light [5].

To enhance the biocidal properties of synthesized TOCs, we decided to incorporate α-hydroxy carboxylate ligands, known for their antimicrobial and anti-inflammatory properties [32–34], into their structure. Our goal was to develop a new, durable material with antimicrobial traits which were responsive to light exposure in the UVA and visible range. The introduction of carboxylate ligands possessing α-hydroxy groups to the structure of TOCs increases their possibilities of coordinating with Ti(IV), resulting in the formation of more structurally stable systems in comparison to those of compounds stabilized by carboxylate groups [5,26,35]. Previous investigations have proven that the photocatalytic properties of TOCs may be stabilized with the addition of α-hydroxy carboxylate ligands such as salicylate, 4-chlorosalicylate, 1-hydroxynaphthoate, citrate, and 2,5-dihydroxybenzoate [14,26,35–38]. Therefore, incorporating such ligands into the structure of oxo complexes is also expected to yield systems with biocidal activity.

Considering the widespread application of mandelic acid (Hman) as a bactericidal agent in the cosmetic industry, its introduction to the structure of TOCs was intriguing [39,40]. Previous research regarding mandelic acid properties showed that prolonged skin exposure to Hman absorption may lead to redness, dryness, and excessive skin exfoliation [41,42]. Hence, investigations carried out in recent years has focused on the synthesis and evaluation of the biocidal action of Hman salts and their complex compounds [43,44]. The compounds synthesized in the reaction of titanium isopropoxide with mixtures of mandelic and benzohydroxamic acid [45] or mandelic and phenylphosphonic acid [46] typically form dimeric structures, wherein two titanium atoms ($\{Ti_2\}$) are connected solely by mandelic ligands (man). Schetter et al. synthesized titanium complexes with multinuclear cores, particularly $\{Ti_2\}$, $\{Ti_6\}$, $\{Ti_9\}$, stabilized by mandelic and tert-butoxide ligands [47].

Mandelic ligands play a crucial role in the formation of $\{Ti_2\}$ dimer units by binding to metal atoms via carboxyl and hydroxyl groups. This mode of coordination also facilitates the construction of larger $\{Ti_6\}$ and $\{Ti_9\}$ systems. It is worth noting that the described compounds have no $\{Ti_aO_b\}$ cores, so the oxo complex we have synthesized is completely new, from a structural point of view.

In this paper, we present the results concerning the synthesis of a structurally stable Ti(IV)-oxo complex with the general formula $[Ti_8O_2(O^iPr)_{20}(man)_4]$ (**1**). The novel $\{Ti_8O_2\}$ core exhibits a unique topology characterized by a plethora of labile isopropoxide ligands and a limited number of oxo bridges. Our objective was to evaluate the biocidal activity of the synthesized compound (**1**) and the composite films formed by dispersing (**1**) in the PMMA matrix (PMMA + (**1**)).

2. Results

*2.1. Structure of (**1**) Oxo Complex*

The octanuclear cluster $\{Ti_8O_2\}$ of the oxo complex (**1**) is formed around a central tetranuclear $\{Ti_4O_2\}$ unit, in an unprecedented manner, with two lateral dimers $\{Ti_2\}$ attached to it via O1 and O11 mandelate ligand bridges (Figure 1). In these lateral dimers, the Ti3 and Ti4 cations are connected by an O61 isopropionate anion and an O13 hydroxyl group from the O11 mandelate anion, resulting in a very short intermetalic distance between them, measuring 3.2486(15) Å (Table S1). The central $\{Ti_4O_2\}$ core consists of two Ti1 and two Ti2 cations, forming a slightly distorted rhombus, with Ti1-Ti2 distances of 3.1036(10) and 3.1940(10) Å, respectively. This arrangement is stabilized by two O10 μ_3-oxo bridges connecting two Ti1 cations and one Ti2 cation, along with two O31 isopropionate anions and two O3 hydroxyl groups from the O1 mandelate anion. The O10 oxo group forms one short bond and two much longer bonds, leading to a topology distinct from those of the previously reported $\{Ti_4O_2\}$ cores, in which titanium cations are coupled by one μ_4-oxo and one μ-oxo bridge [7] (Figure S1). Ti(IV) titanium cations exhibit significant differences in coordination number and coordination sphere content (refer to Table S2). Ti1, Ti2, and Ti3 are found in an octahedral environment, whereas the outermost Ti4 cation is found in pentacoordinated, significantly distorted, trigonal bipyramid coordination sphere ($\tau5 = 0.60$) [48]. Mandelate ligands are invovled in bridging titanium cations. Moreover, they also form chelate rings, with Ti1 and Ti3 cations. In those rings, an enhanced charge concentration is observed (Figure S2).

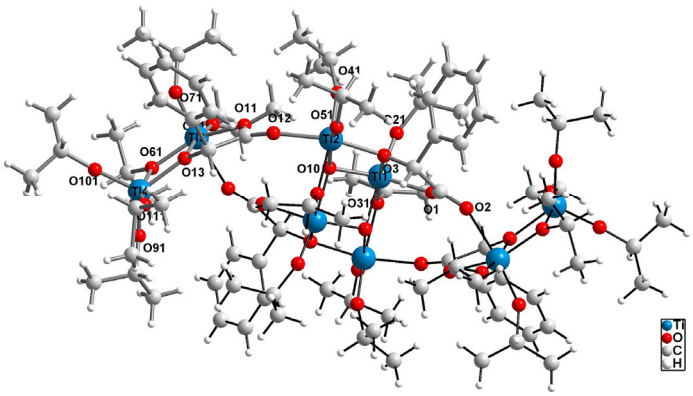


Figure 1. Structure of $[Ti_8(\mu_3\text{-}O)_2(\mu\text{-}O^iPr)_4(O^iPr)_{16}(man)_4]$ (**1**) as a ball and stick model, with hydrogen atoms omitted for the clarity of the figure. The structure presents only the main conformations. Atom labels for the titanium and oxygen atoms are provided. The asymmetric area is presented with bonds shown in medium grey, and the area related to the inversion center is shown in black.

The crystal network does not exhibit any cavities containing uniformly distributed octanuclear clusters (Figure 2). Hirshfeld surface analysis reveals that weak interactions dominate the landscape of the formed interactions (Figure 3). Specifically, H. . .H interactions constitute 96.8% of the intermolecular contacts, with the remaining 3.2% attributed to

H. . .C contacts. Despite careful analysis, no intermolecular hydrogen bonds were observed, while several intramolecular C-H. . .O hydrogen bonds were identified.

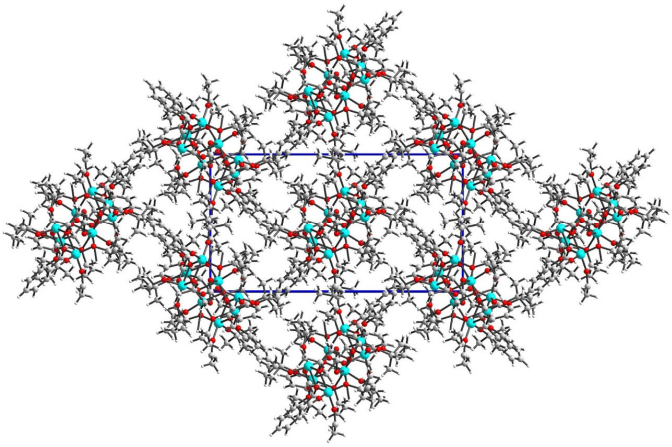


Figure 2. Crystal network of (**1**) along the c axis shows ab layers.

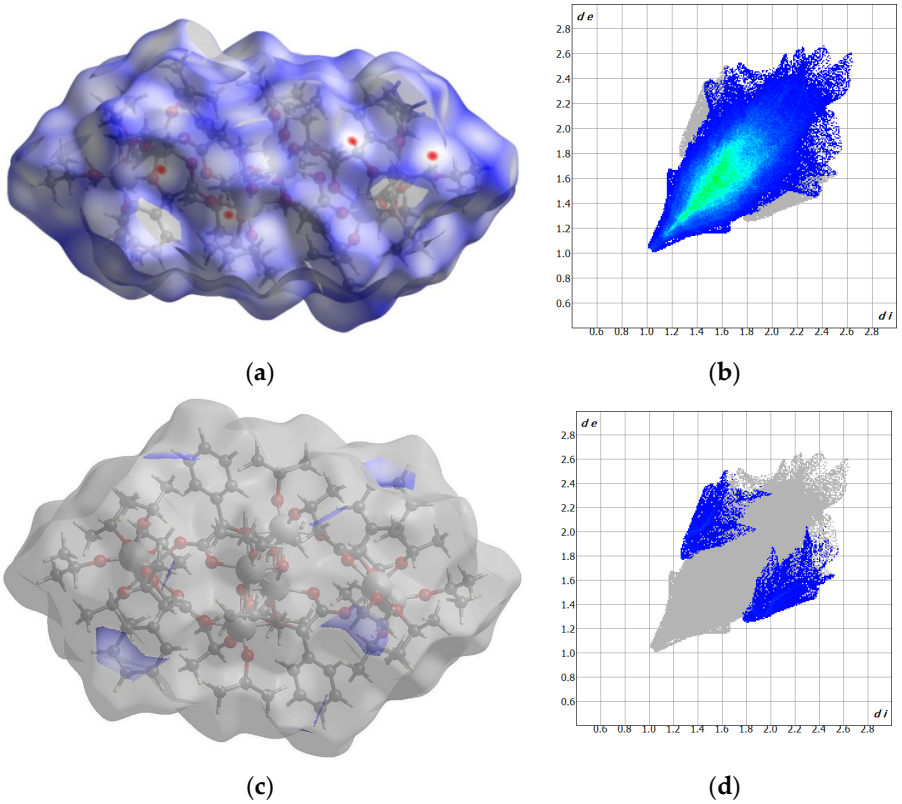


Figure 3. Hirshfeld surfaces and fingerprints of selected interactions created in the crystal network of (**1**): Hirshfeld surface (**a**) and fingerprint (**b**) for H. . .H (96.8%); Hirshfeld surface (**c**) and fingerprint (**d**) for H. . .C (3.2%). In brackets, the surface area is included as a percentage of the total surface area.

These results suggest that the oxygen atoms are buried and inaccessible to the hydrogen atoms from the adjacent clusters. Moreover, the high propanalate/mandelate ratio (5:1) results in only one π–π interaction, occurring between the strongly inclined C14 phenol ring and the Ti3O11 five-membered chelate ring. In summary, we synthesized a stable complex with the unprecedented core structure $\{Ti_8O_2\}$, which may interact with biomolecules in the cell via external and easily accessed unsaturated Ti4 cation, as well as through weak non-covalent van der Waals forces.

2.2. Spectral Characterization of (**1**) and its Composite with Poly(methyl methacrylate)

The objective of the spectral studies was to determine the structural stability, including susceptibility to hydrolysis processes, and the physicochemical properties of both the complex and its composite formed by dispersing micrograins of this compound in a non-toxic poly(methyl methacrylate) matrix (PMMA + (**1**)). Research on composite systems has aimed to assess their practical potential as antimicrobial coatings. To this end, PMMA + (**1**) composite samples were prepared, with 2 wt.%, 5 wt.%, 10 wt.%, and 20 wt.%. Figure 4 illustrates the XRD patterns of the (**1**) sample, recorded before and after immersion in distilled water for 72 h. Both diffractograms were compared to the pattern calculated in Ref. [49]. Analysis of the XRD data revealed no significant differences in the patterns, before and after immersion in water. The resemblance between these diffractograms indicates that the core structure was preserved, and no significant transformation towards crystalline TiO_2, amorphous forms, or other crystalline species related to rearrangement of the titanium co-ordination spheres and topology, was detected. The structural stability of (**1**) was further confirmed using IR spectroscopy (Figure 5). The comparison of the IR spectra of samples, before and after immersion in water, showed no changes. There were no alterations in the intensity and position of the bands within the ranges of (a) 1624–1450 cm^{-1}, which are associated with the vibrations ν(CC), ν_{as}(COO), and ν_{s}(COO), (b) 900–1200 cm^{-1}, assigned to the ν(O-CR) vibrations, and (c) bands appearing below 900 cm^{-1}, indicated titanium-oxo bridges.

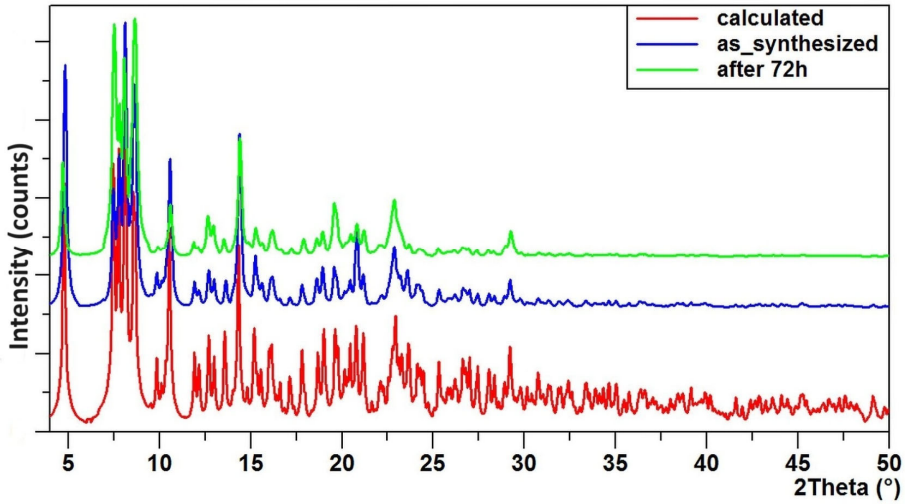


Figure 4. The powder diffractograms, calculated using our model (red), the synthesized complex (blue), and the sample after being immersed in distilled water for 72 h (green), in the range of 4–50° 2θ.

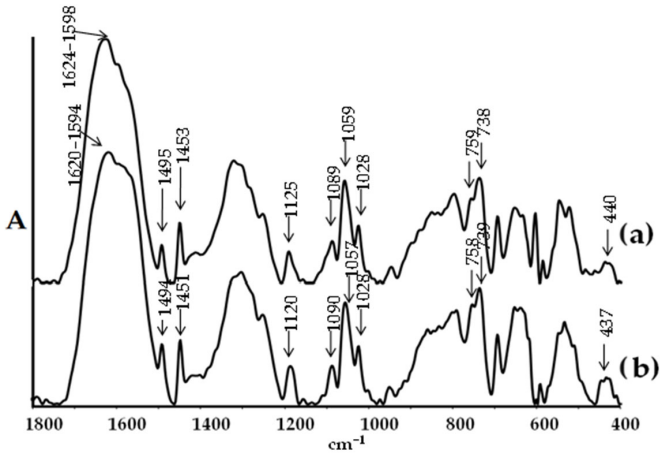


Figure 5. IR spectrum of structure (**1**) before (**a**) and after (**b**) 72 h contact with water.

The presence of (**1**) in the polymer matrix was confirmed using SEM EDX (Table 1). Titanium peaks are observed in each composite sample, and the percentage of titanium increases with the (**1**) sample concentration. To verify the absence of structural changes in (**1**) upon incorporation into the PMMA matrix, we compared the Raman spectra of the oxo complex (**1**), the composite of PMMA + (**1**) 20 wt.%, and pure PMMA polymer (Figure 6). The results obtained suggest that the structure of the compound remains unchanged upon its introduction into the matrix.

Table 1. SEM EDX data for composites PMMA + (**1**). All values are given in mass percent (%).

Composite	C	O	Al	Ti
PMMA	26.10	72.23	1.67	-
PMMA + (**1**) 2 wt.%	28.27	71.00	0.45	0.27
PMMA + (**1**) 5 wt.%	24.75	66.45	0.59	8.21
PMMA + (**1**) 10 wt.%	19.02	67.24	0.52	13.22
PMMA + (**1**) 20 wt.%	18.77	58.68	0.48	22.07

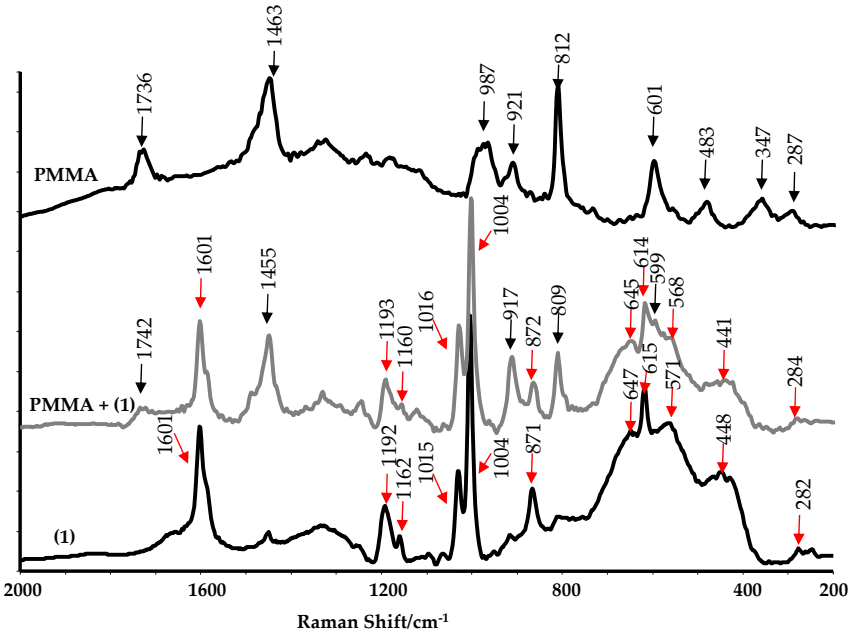


Figure 6. Raman spectra of (**1**), PMMA + (**1**) 20 wt.%, and pure PMMA.

The EPR spectra of (**1**) powders and cut composite foil were recorded to identify paramagnetic species on the surface of the synthesized materials (Table 2 and Figure S2). The pure PMMA polymer exhibited no EPR signal. Paramagnetic centers were detected in all the samples of the PMMA + TOCs composites, as well as in the spectrum of pure (**1**). Generally, the signals in the EPR spectra were weak, particularly for composites with a low (2,5,10 wt.%) admixture of titanium(IV)-oxo complexes (although ROS signals were detected, see Table 2). Consequently, only the EPR spectra of the pure (**1**) sample and the composite sample containing 20 wt.% of titanium(IV)-oxo complex grains were analyzed in detail. The spectra registered for pure (**1**) and the composite of PMMA + (**1**) 20 wt.% are presented in Figure S3. The analysis of the EPR spectra of the aforementioned samples demonstrated that natural photoexcitation of their surfaces, i.e., generated without additional UV–Vis lamp radiation, led to the formation of ROS. Additionally, it is worth noting that both O^- and O_2^- paramagnetic species were generated by the PMMA + TOCs composite. Interestingly, the O_2^- radical was also generated in the pure substrate.

Table 2. EPR data for powdered TOC and PMMA + (**1**) composite samples. The samples were exposed to visible light prior to measurement.

Sample	g-Factor	Species
(**1**)	2.025, 2.011, 2.003 1.992	O_2^- Ti(III)
PMMA	-	-
PMMA + (**1**) 5 wt.%	2.010, 2.002 2.005, 2.000 1.992	O_2^- O^- Ti(III)
PMMA + (**1**) 10 wt.%	2.025, 2.010, 2.000 2.016 1.992	O_2^- O^- Ti(III)
PMMA + (**1**) 20 wt.%	2.025, 2.010, 2.002 2.016, 2.005, 2.000 1.992, 1.972	O_2^- O^- Ti(III)

*2.3. Antimicrobial Activity of (**1**) and its Composites*

The subsequent phase of our research involved evaluating the biocidal activity of both (**1**) and the PMMA + (**1**) composite. These assessments were conducted against Staphylococcus aureus and Escherichia coli bacteria, as well as *Candida albicans fungi*. The results, as depicted in Table 3, reveal that the complex (**1**) exhibited significant antimicrobial activity, even at low concentrations. According to the ISO 22196:2011 standard [50], the suspensions exhibit a biocidal effect when the R value is $\geq$3. In the case of (**1**) suspensions, the R value for Gram-negative bacteria ranged from 5.7 to 6.0, while for Gram-positive bacteria, it varied from 4.2 to 6.2. Microbiological activity against *Candida albicans* was only apparent with a 20% (*w*/*v*) addition of (**1**). Non-porous surfaces are considered bactericidal when R $\geq$ 2. Microbiological tests of composite samples (PMMA + (**1**)) exhibited outstanding activity against both *E. coli* and *S. aureus* bacteria across all tested concentrations of TOCs (2 wt.%, 5 wt.%, 10 wt.%, and 20 wt.%), as detailed in Table 3. Even at a modest (**1**) content of 2 wt.%, the composite displays effective activity against E. *coli* bacteria (R $\geq$ 2). In terms of *S. aureus* bacteria, the R values ranged from 4.7 to 5.1. It is noteworthy that the tested composites do not diminish the count of *C. albicans* cells.

Table 3. Antimicrobial activity of TOC and PMMA + n(**1**) composites; value R $\geq$ 2 determines biocidal activity for the composites and R $\geq$ 3 for the (**1**) suspension.

No.	Samples	Microorganisms				
		E. coli **ATCC 8739**	***E. coli*** **ATCC 25922**	***S. aureus*** **ATCC 6538**	***S. aureus*** **ATCC 25923**	***C. albicans*** **ATCC 10231**
1	(**1**) 2 wt.%	6.0 (>99.99%)	6.0 (>99.99%)	4.2 (>99.99%)	5.4 (>99.99%)	0 (0%)
2	(**1**) 5 wt.%	6.0 (>99.99%)	5.7 (>99.99%)	5.9 (>99.99%)	6.0 (>99.99%)	0.3 (53.20%)
3	(**1**) 10 wt.%	6.0 (>99.99%)	6.0 (>99.99%)	6.2 (>99.99%)	6.0 (>99.99%)	0.9 (87.45%)
4	(**1**) 20 wt.%	6.0 (>99.99%)	6.0 (>99.99%)	6.5 (>99.99%)	5.7 (>99.99%)	6.7 (>99.99%)
5	PMMA	none (0%)	none (0%)	none (0%)	none (0%)	none (0%)
6	PMMA + (**1**) 2 wt.%	2.0 (99.00%)	3.1 (>99.90%)	4.7 (>99.99%)	5.1 (>99.99%)	+0.9 (+87.41%)
7	PMMA + (**1**) 5 wt.%	3.1 (>99.90%)	4.9 (>99.99%)	4.7 (>99.99%)	5.1 (>99.99%)	+0.82 (+84.86%)
8	PMMA + (**1**) 10 wt.%	4.9 (>99.99%)	3.9 (>99.90%)	4.7 (>99.99%)	5.1 (>99.99%)	+0.8 (+84.20%)
9	PMMA + (**1**) 20 wt.%	4.9 (>99.99%)	4.7 (>99.99%)	4.7 (>99.99%)	5.1 (>99.99%)	+0.7 (+80.05%)

*2.4. Cytotoxicity of PMMA + (**1**) Composites*

The potential cytotoxicity of the tested specimens was assessed using MTT assays and analysis of the SEM images. The purpose of this study is to determine whether compound (**1**) can damage mammalian cells. A material is considered non-cytotoxic if

cell viability is greater than 70%. The results of the MTT assays showed that the level of cell viability measured for the reference PMMA samples was comparable to the values received for specimens containing mandelic ligands in all tested concentrations. This effect was observed for both 24 and 72 h of incubation time. Importantly, these results also demonstrated that with an increase in the incubation time, more L929 fibroblasts proliferated on all the tested specimens (Figure 7).

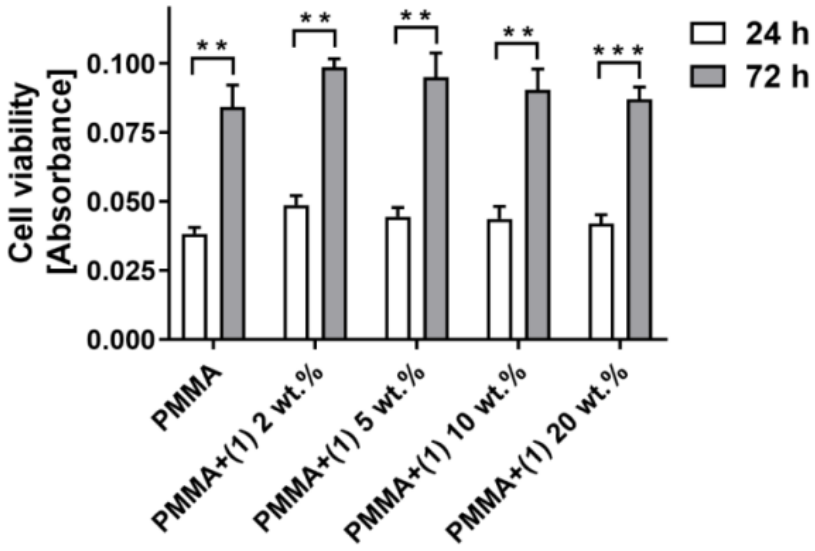


Figure 7. The viability of L929 fibroblasts growing on the surfaces of the PMMA reference samples and the PMMA specimens containing mandelic ligands at a concentration of 2 wt.%, 5 wt.%, 10 wt.%, and 20 wt.%. The cells were cultured on the samples for 24 and 72 h. The absorbance values are expressed as means ± S.E.M of four independent experiments. Asterisks indicate significant statistical differences in the cell viability between 24 and 72 h (*** $p < 0.001$; ** $p < 0.01$).

Figure 8 presents selected images of L929 cells cultured on the PMMA specimens containing mandelic ligands at a concentration of 2 (A, B, J), 5 (C, D), 10 (E, F), and 20 wt.% (G, H, I). Firstly, the analysis of these micrographs confirmed the results from the MTT assays, indicating that L929 fibroblasts effectively attached to the surfaces, and the number of the growing cells increased over time. After 72 h, the fibroblasts covered the sample surface area at a significantly higher density, which is especially visible in different magnifications of electron microscopy photos (compared Figure 8E,F).

Importantly, the elongated shape of the cells was already observed after 24 h of culturing, indicating their normal adhesion, with few cytoplasmic projections at the cell edges, which also allowed cells to attach to the surface of the specimens (Figure 8J). After 72 h, the number of cytoplasmic projections at the cell periphery had increased, and after entering into closer proximity to the neighboring cells, they started forming cell–cell contacts (Figure 8I). The cytoplasmic projections, called filopodia, play a fundamental role in cell attachment, migration, proliferation, and cell–cell interaction [51,52]. The results from the MTT assays and the SEM analysis showed that the tested specimens containing MA did not affect the morphology of the L929 fibroblasts and did not reduce their viability.

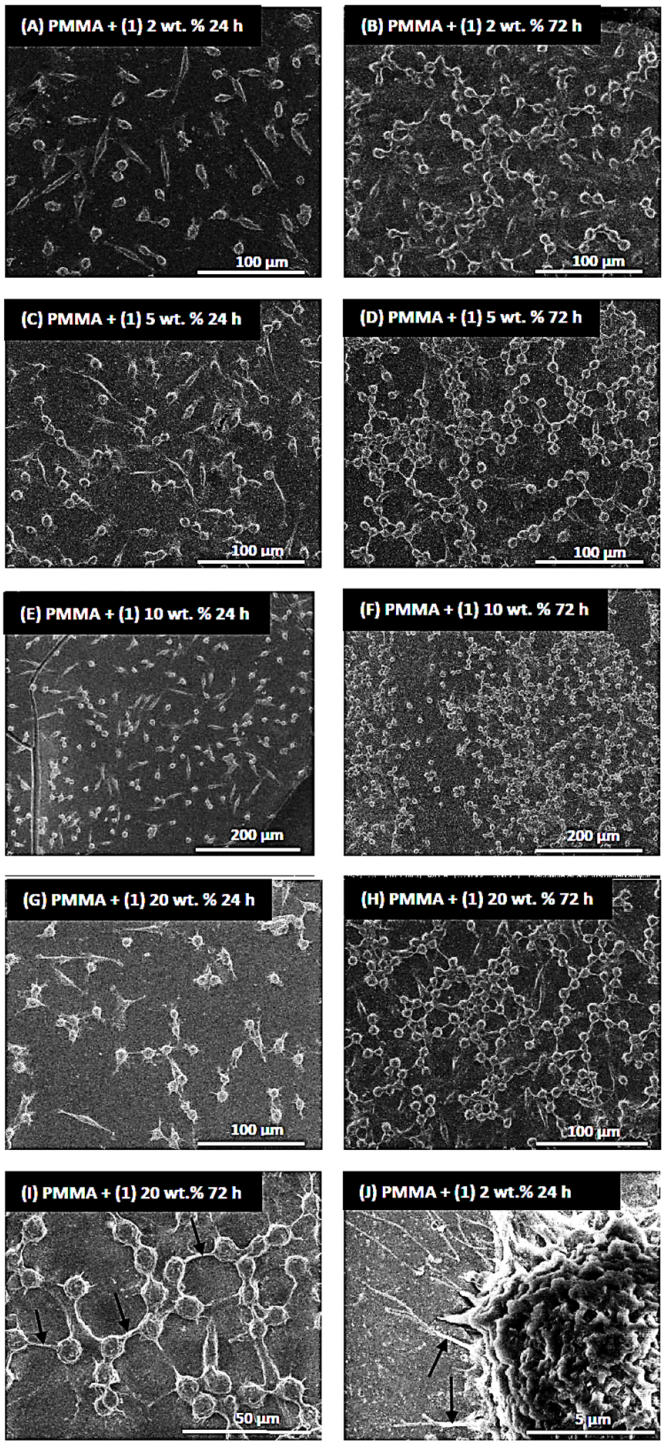


Figure 8. Scanning electron microscopy images of L929 cells cultured on the surfaces of PMMA specimens containing mandelic ligands at a concentration 2 (**A**,**B**,**J**), 5 (**C**,**D**), 10 (**E**,**F**), and 20 wt.% (**G**,**H**,**I**). The type of samples, incubation time, and scales of the images are presented in the figures. Black arrows in (**I**) indicate cytoplasmic projections spread between the cells, whereas those in (**J**) present cytoplasmic projections attaching the cells to the surface.

3. Discussion

*3.1. Structure and Physicochemical Properties of (**1**) and its Composite PMMA + (**1**)*

The crystals with the general formula $[Ti_8O_2(O^iPr)_{20}(man)_4]$ (**1**) were obtained at room temperature from a reaction mixture containing titanium isopropoxide and mandelic acid in

a 4:1 molar ratio, using tetrahydrofuran as a solvent. Single crystal X-ray diffraction analysis confirmed that the structure of (**1**) consists of a $\{Ti_8O_2\}$ core stabilized by isopropoxide and mandelate ligands (Figure 1). Previous studies have reported the occurrence of $\{Ti_8O_8\}$ cores in octanuclear Ti(IV)-oxo complexes, composed of eight-membered rings, where Ti atoms are surrounded by μ-O and μ-carboxyl bridges [53–57]. Czakler et al. synthesized a compound with a $\{Ti_8O_2\}$ core consisting of two $\{Ti_4O\}$ units bridged by two μ_3-O atoms [58].

The structure of (**1**) is more intricate, as its core comprises a central $\{Ti_4O_2\}$ unit and two lateral dimers ($\{Ti_2\}$). This reported structure presents a novel, unprecedented core among titanium-oxo complexes (TOCs), stabilized by two μ_3-O bridges and mandelate anions forming bridges, and for Ti1 and Ti3, a five-membered chelate ring. To verify the structural stability of (**1**), both in aqueous solutions and after its integration into the polymer matrix, spectroscopic analyses were conducted on powder samples after contact with water (employing XRD and IR methods) and samples of the PMMA + 20 composite (**1**) (with Raman spectra recorded).

TOCs are recognized for their vulnerability to structural destabilization and hydrolysis. Compounds prone to hydrolysis find limited utility, particularly in applications involving exposure to aqueous environments. The existing literature suggests that incorporating carboxylates, phenols, phosphonates, and catechols into the coordination sphere can bolster the stability of such structures [12,59–61]. Our research affirms that the obtained compound maintained its structure when exposed to an aqueous environment. This result is supported by the absence of notable alterations in the X-ray diffraction patterns and IR spectra, before and after exposure to water. Examination of the Raman spectra of PMMA + (**1**) 20 wt.% composite samples revealed that the compound (**1**) maintained its structure subsequent to its integration into the polymer matrix.

The pivotal focus of this stage of the research centered on evaluating the photoactivity of both the pure oxo complex and its composites. Utilizing electron paramagnetic resonance (EPR) facilitated the detection of reactive oxygen species (ROS) generated on the surface of samples previously exposed to visible light. Considering the literature data, it is reasonable to assume that upon photoexcitation of the samples, Ti(III) and ROS would be initially generated on their surfaces [62–66].

The formation of O_2^- and O^- type paramagnetic centers involves electron removal and stabilization of the radical formed by reducing Ti(IV) to Ti(III) [62,63]. The maximum g-factor for O_2^- exceeds that of O^- species [64]. In the EPR spectrum of (**1**), characteristic anisotropic signals for the O_2^- radical were identified (Table 2, Figure S2a). Detecting titanium(III) is not straightforward; in this case, a weak and broad signal, nearly at the noise level, may be present (Figure S2a, Table 2). The EPR spectra of PMMA + (**1**) composites are more intricate and contain numerous overlapping lines (Figure S2). The spectra of all the composites are akin, except for variations in intensity. Weaker lines are indiscernible for samples containing minor admixtures (2 and 5%) of the titanium(IV) complex. In the spectrum of PMMA + (**1**) 20% wt.%, distinct signals of both ROS, i.e., O_2^- and O^-, as well as Ti(III), are evident (Table 2, Figure S2b). Some lines, particularly for g_2 and g_3 of both oxygen species, may overlap. Individual lines are relatively broad due to the high content of (**1**) and potentially high paramagnetic center concentrations, resulting in line broadening via exchange interactions. In contrast to similar TOCs composites with PCL [25,67], Ti(III) was discerned on the surface of the investigated composite material (Table 2, Figure S2b). Due to a positive spin–orbit coupling constant, Ti(III) exhibits EPR signals at g-values below 2.0 [25,62–67]. The first signal, with a g-factor of 1.992, is clearly visible, while the second, with a lower g-factor of approximately 1.972, is very weak and broad.

*3.2. Antimicrobial Activity of (**1**) and its Composite PMMA + (**1**)*

Elucidating the biocidal attributes of the synthesized oxo complex (**1**) and its composite PMMA + (**1**) involves considering two factors: (i) the photocatalytic capability of the oxo complex, and (ii) the structural factors, particularly the formation of chelate rings. The

photocatalytic prowess of (**1**) is associated with the generation of reactive oxygen species (ROS) upon exposure to visible light, as confirmed by EPR tests. Introducing ROS to a bacterial cell induces oxidative stress, leading to the impairment of cellular lipids, proteins, and nucleic acids, ultimately resulting in the demise of the microorganism [68–71].

The antimicrobial efficacy can also be linked to the compound's structure, especially the formation of chelate rings and surface hydrophobicity (as observed in the Hirshfeld surface). According to Tweedy's chelation theory and Overtone's concept, coordination diminishes the metal ion's polarity by overlapping the ligand orbitals and partially sharing the positive charge with the donor groups [72]. The enhanced delocalization of π-electrons in the chelate ring augments the compound's lipophilic nature. This increased lipophilicity promotes the solubility of lipids in the cell membrane upon contact with the oxo complex grains, leading to irreversible damage to the membrane and cell functions [72].

Literature reports suggest a correlation between electron density and antimicrobial activity, with chelation increasing the electron density of the central ion [73]. It should be emphasized that the synergy of mechanisms involving the generation of ROS and effects related to the presence of a chelating ring can only be considered as the primary mechanism in the case of the antimicrobial action of (**1**), where the entire surface of the oxo complex grain comes into contact with the microbial suspension. However, in composite materials, the grains are surrounded by a polymeric matrix exhibiting weaker biocidal activity, solely due to ROS generation on their surface. This is confirmed by the data analysis presented in Table 3, indicating that the activity of the PMMA + (**1**) composite is weaker compared to that of the pure compound.

Studies on the antimicrobial activity of mandelic acid (Hman) revealed that the minimum inhibitory concentration (MIC) required to inhibit the growth of *S. aureus* and *E. coli* strains fell within the range of 0.18–0.23% [43,74]. In the case of crystalline powder tests of (**1**), the mandelic ligand content in the suspension of the studied sample was 0.013%, 0.034%, 0.069%, and 0.14% for concentrations of 2%, 5%, 10%, and 20% (*w*/*v*), respectively. This suggests that the antibacterial activity of (**1**) against *S. aureus* and *E. coli* strains is superior to that of mandelic acid.

When evaluating the biocidal properties of the tested samples, it is essential to consider that, according to ISO standards, a suspension is deemed bactericidal when 99.90% or more of the microorganisms are inhibited (reduction index (R) $\geq$ 3), while for non-porous surfaces, the reduction index is $\geq$2. It seems that the incorporation of (**1**) grains into a polymer matrix resulted in a decrease in antimicrobial activity when compared with that of suspensions, but biocidal activity was still achieved at the required level, according to ISO 22196:2011 standard (Table 3).

An interesting comparison can be made with the results obtained by Luo et al. for compounds containing $\{Ag_9Ti_4\}$ cores, as well as type $\{Ag_9Ti_4\}$-gel hydrogel samples. Antimicrobial activity assessments showed that $\{Ag_9Ti_4\}$ crystals exhibited antibacterial activity on the level of 94.51% for *S. aureus* and 95.42% for *E. coli*, respectively [30]. For comparison, our oxo complex (**1**) showed an inhibitory effect of >99.99% for both strains of the tested samples containing 2% (*w*/*v*) in the studied suspension. The hydrogel of $\{Ag_9Ti_4\}$-gel exhibited bactericidal effects of 99.6% against *S. aureus* and 99.95% against *E. coli* [30]. The authors suggest that the increase in antimicrobial activity is a result of the synergistic effect of the $\{Ag_9Ti_4\}$ cluster and polydopamine, added as a cross-linking agent in hydrogel formation. In the case of our composites, even a 2% addition of TOCs reduced the presence of *S. aureus* by 99.00% and *E. coli* by 99.99%. This is in line with the ISO standard for bactericidal properties, which states that the number of microorganisms must be reduced by $\geq$99% (R $\geq$ 2).

*3.3. Cytotixity of PMMA + (**1**) Composites*

Testing the cytotoxicity of the obtained materials was a very important aspect of our study, from the application point of view. In addition to antimicrobial properties, the obtained surfaces should not exhibit cytotoxicity towards fibroblast cells. This guarantees

safety in case of contact with skin. We presume that the topology affects the cytotoxic activity. The exact mechanism of titanium cluster cytotoxicity is not known, and it is not clear if it is related to DNA intercalation [75]. Studies show that the cytotoxic effect is related to the stability of the compound. Hydrolyzed molecules are characterized by strong cytotoxic activity. L(OEt)Ti-O-Ti(OEt)L, as a product of the partial hydrolysis of $[L(OEt)_2Ti]$, shows strong cytotoxicity, despite bulky substituents [76]. The compound we obtained is characterized by high stability and low cytotoxicity, which confirms this theory.

4. Materials and Methods

4.1. Materials

Titanium(IV) isopropoxide was acquired from Sigma-Aldrich, Inc. (St. Louis, MO, USA), while mandelic acid was purchased from Warchem LLC (Warsaw, Poland). Both compounds were used without further purification. Before application, tetrahydrofuran (THF) underwent distillation and was then stored in an argon atmosphere. The synthesis of Ti(IV)-oxo complexes was conducted under an inert gas atmosphere (Ar) at room temperature (RT).

4.2. Synthesis of Ti(IV) Oxo-Complex (α-TOCs) and Preparation of PMMA/TOC Composites

4.2.1. The Synthesis of $[Ti_8O_2(O^iPr)_{20}(man)_4]$ (**1**)

A total of 0.13 g of mandelic acid (0.875 mmol), 1 mL of titanium(IV) isopropoxide (3.5 mmol), and 2 mL of THF were mixed, yielding a clear yellow solution. Crystals of (**1**) appeared after 3 days. The yield based on acid was 66% (0.62 g). Anal. Calc. for $C_{92}H_{168}O_{34}Ti_8$:C, 50.18; H, 7.63; Ti,17.45. Found: C, 50.09; H, 7.58; Ti, 17.54. ^{13}C NMR (solid state, 295 K, δ[ppm]): 9.75 (CH3), 25.4, 30.1 (CH), 60.1, 71.3 ((Ph)C(Ph)), 90.7, 130.7, 139.6, 182.3, (C(Ph)), 198.3, 209.4 (COO).

4.2.2. PMMA/TOCs Composites Preparation

PMMA/TOCs composites were prepared by adding an appropriate amount of the TOC (ca. 0.025, 0.062, 0.12, or 0.25 g of (**1**) dispersed in 5 mL of THF) to the poly(methyl methacrylate) (PMMA) solution (1.0 g of PMMA per 10 mL of THF). After 150 min in an ultrasonic bath, the dispersions were poured into a glass Petri dish and held at RT in a glove box to evaporate the THF. As a result, materials containing 2, 5, 10, and 20% of TOC were obtained.

4.3. Analytical Methods

4.3.1. Structural and Spectroscopic Characterization of TOCs

The vibrational spectra of the synthesized compounds (crystals) were registered using: (a) IR spectrophotometry (Perkin Elmer Spectrum 2000 FTIR spectrophotometer (PerkinElmer Inc., Waltham, MA, USA) (400–4000 cm^{-1} range, KBr pellets)), and (b) Raman spectroscopy (RamanMicro 200 spectrometer (PerkinElmer Inc., Waltham, MA, USA)). The Raman spectra were recorded using a laser with the wavelength 785 nm, with a maximum power of 350 mW, in the range 200–3200 cm^{-1}, with a 20 × 0.40/FN22 objective lens and an exposure time of 15 s each time. The ^{13}C NMR spectra in the solid phase were recorded on a Bruker Advance 700 (Madison, WI, USA) 700 MHz spectrometer, with a spectral width of 76,923.08 Hz and 4096 complex points. Elemental analyses were performed on an Elemental AnalyserVario Macro CHN (ElementarAnalysensysteme GmbH, Langenselbold, Germany).

4.3.2. Single Crystal X-ray Diffraction Measurement

The diffraction data were collected at 100 K on a Rigaku XtaLAB Synergy (Dualflex) diffractometer (Rigaku Inc., Wilmington, MA, USA) with a HyPix detector with a monochromated CuKα X-ray source (λ = 1.54184 Å). The data processing and the numerical absorption correction were performed using CrysAlis Pro [77]. The structure was using direct methods and refined by employing the full-matrix least-squares procedure on F^2 (SHELX-

97 [78]). Heavy atoms were refined with anisotropic displacement parameters, whereas hydrogen atoms were assigned at calculated positions, with thermal displacement parameters fixed to a value of 20% or 50% higher than those of the corresponding carbon atoms. A disorder was observed for the O31 (0.5:0.5) and O111 (0.6:0.4) isopropionate anions. Some restraints on geometry (DFIX) and thermal parameters (ISOR) of those disordered anions were applied to assure a stable refinement process. All figures were prepared in DIAMOND [79]. The results of the data collections and refinement have been summarized in Table 4; selected bond lengths and angles are presented in Table S1. CCDC 2310326 contains the supplementary crystallographic data for (**1**). These data can be obtained free of charge from The Cambridge Crystallographic Data Center via www.ccdc.cam.ac.uk.data_request/cif (accessed on 25 November 2023).

Table 4. Crystal data and structure refinement for (**1**).

Empirical formula	$C_{92}H_{164}O_{34}Ti_8$ (**1**)
Formula weight	2197.42
Temperature	100(2) K
Wavelength [Å]	1.54184
Crystal system	Monoclinic
Space group	$P2_1/c$
Unit cell dimensions [Å] and [°]	a = 19.9172(6) b = 12.3935(3) c = 24.4651(8) α = 90 β = 111.483(4) γ = 90
Volume [$Å^3$]	5619.5(3)
Z, calculated density [Mg/m^3]	2, 1.299
Absorption coefficient [mm^{-1}]	5.193
F(000)	2328
Crystalsize [mm^3]	0.220 × 0.180 × 0.080
Theta range for data collection [°]	2.384 to 74.492
Index ranges	$-24 \leq h \leq 24$ $-15 \leq k \leq 14$ $-30 \leq l \leq 21$
Reflections collected/unique	44,138/11,218 [R(int) = 0.0943
Completeness to theta	67.684° 99.9%
Absorption correction	Gaussian
Max. and min. transmission	1.000 and 0.414
Refinement method	Full-matrix least-squares on F2
Data/restraints/parameters	11,218/35/654
Goodness-of-fit on F2	1.054
Final R indices [I > 2sigma(I)]	R1 [a] = 0.0865, wR2 [b] = 0.2451
R indices (all data)	R1 [a] = 0.1092, wR2 [b] = 0.2674
Largest diff. peak and hole	0.766 and −0.915 e·$Å^{-3}$

[a] $R1 = \sum||F_0| - |F_c|/\sum|F_0|$, [b] $wR2 = [\sum w(F_0^2 - F_c^2)^2/\sum(w(F_0^2)^2)]^{1/2}$.

4.3.3. X-ray Diffraction of Powders

Powder experiments were performed using a Rigaku XtaLAB Synergy (Dualflex) diffractometer with a HyPix detector and a monochromated CuKα X-ray source (λ = 1.54184 Å), working in the powder diffraction mode. The data were collected in the range 4–50° 2θ, with an exposure time 240 s per frame.

4.3.4. Characterization of PMMA + TOCs Composite Materials

The chemical composition of the produced composite films was determined using an energy-dispersive X-ray spectrometer (EDS, Quantax 200 XFlash 4010, Bruker AXS, Karlsruhe, Germany). The maximum of absorption for the PMMA + (**1**) samples was

also registered using the UV–Vis DRS method. The resulting composite materials had a thickness of approximately 50 μm and were characterized using Raman.

4.3.5. The Electron Paramagnetic Resonance (EPR) Spectroscopy

Formation of reactive oxygen species on the surface of the obtained samples was confirmed using EPR. The spectra were recorded using an X band EPR SE/X-2541M spectrometer (Radiopan, Poznań, Poland) with a 100 kHz modulation. The microwave frequency was monitored with a frequency meter. The magnetic field was measured with an automatic NMR-type JTM-147 magnetometer (Radiopan, Poznań, Poland). Measurement conditions: microwave frequency: ca. 9.33 GHz; modulation amplitude: 0.25–1 mT; sweep: 20–50 mT; sweep time: 4 min.; time constant: 0.1 s; receiver gain: 4×10^5. The measurements were performed for the powder of the substrate and the cut films of PMMA + TOCs composites, at room temperature.

4.4. Studies of the Biological Activity of Synthesized Materials

4.4.1. Antimicrobial Activity of PMMA + (**1**) Composites and Powder (**1**)

The antimicrobial activity of the samples was determined against Gram-negative (*Escherichia coli* ATCC 25922, *Escherichia coli* ATCC 8739) and Gram-positive (*Staphylococcus aureus* ATCC 25923, *Staphylococcus aureus* ATCC 6538) bacteria and *Candida albicans* ATCC 10231. Prior to antimicrobial study, the tested PMMA + TOCs foils (20 × 20 mm) were sterilized using UVC for 15 min on both sides, subsequently treated with visible indoor light, placed in the 12-well plates with 1 mL of microbial inoculum (1.0–4.7 $\times 10^6$ c.f.u. mL^{-1}) in sterile deionized water, and incubated for 24 h at 37 °C in a humid atmosphere under gently shaking (80 r.p.m.) conditions.

Microbial inoculum with a density of 0.5 McFarland (approximately 1.5×10^8 c.f.u. mL^{-1}) were prepared in sterile distilled water from cultures of bacterial strains and *C. albicans* grown in tryptic soy broth (TSB, Becton Dickinson, Heidelberg, Germany) and Sabouraud dextrose broth (SDB, Becton Dickinson), respectively, for 24 h at 37 °C, under shaking conditions (120 rpm). Each of the microbial inoculum were diluted 100 times prior to use.

The control was the suspension of test microorganisms in the well, without test samples. After incubation, inoculum was collected from the wells, diluted ten-fold, and spread (100 μL) on appropriate medium in Petri dishes. The plates were incubated for 24 h at 37 °C, and colony forming units (c.f.u) were counted on the inoculated plates. The concentration of microorganisms was calculated per one mL.

The antimicrobial activity of the samples of (**1**) were determined by suspending them in microbial inoculum in sterile deionized water to obtain suspensions with concentrations of 2, 5, 10, and 20% (*w*/*v*) and gently (20 r.p.m) mixing them using the rotary shaker (Biosan, Riga, Latvia) for 24 h at 37 °C.

The microbial inoculum after treatment with (**1**) samples was diluted ten-fold in sterile deionized water, and each dilution (1000 μL) was aseptically mixed with 20 mL of appropriate medium in Petri plates and incubated at 37 °C for 24 h. The colony forming units (c.f.u) were counted and the final concentration of the microorganisms was calculated per one mL.

The antimicrobial activity of the powder and the composites was determined based on the reduction (R) index, calculated according to the formula: R = Ut − At, where Ut is the common logarithm of the number of microorganisms in the inoculum, and At is the common logarithm of the number of microorganisms in the treated inoculum. $R \geq 2$ and $R \geq 4$ determine the biocidal activity of (**1**) in the studied form of the composite (antimicrobial activity of the surface) and suspension samples, respectively.

4.4.2. Assessment of Material Cytotoxicity

The L929 murine fibroblast cell line (NCTC clone 929) was purchased from American Type Culture Collection (Manassas, VA, USA). The cells were cultured in Dulbecco's Modified Eagle's Medium (DMEM) supplemented with 10% heat-inactivated fetus bovine

serum and antibiotics (100 μg/mL of streptomycin and 100 IU/mL of penicillin) at 37 °C in an atmosphere of 5% CO_2. All reagents used for cell culture were purchased from VWR International (Radnor, PA, USA).

The specimens were cut into squares measuring 6 mm × 6 mm and were sterilized using UV irradiation for 30 min for each side of the samples before testing.

For evaluation of potential cytotoxicity of the tested materials, the samples were placed in individual wells of 24-well plates, followed by seeding of the cell suspension (1×10^4 cells suspended in a 25 μL of culture medium). Then, the cells were incubated for 4 h at 37 °C and 5% CO_2 to allow the cells to attach to the surface of the materials before flooding with 1 mL of DMEM medium. The L929 cells were incubated on the specimens for 24 and 72 h at 37 °C and 5% CO_2.

After incubation, the samples were transferred to new wells of 24-well plates, and 500 μL of the MTT (tetrazolium salt 3-[4,5-dimethylthiazol-2-yl]-2,5-diphenyltetrazolium bromide purchased from Merck KGaA (Darmstadt, Germany)) solution, prepared in culture medium without phenol red at a final concentration 0.5 mg/mL, was added to each well and kept in an incubator for 3 h. Then, the MTT solution was aspirated, and 500 μL of dimethyl sulfoxide was added to each well, followed by measurement of the absorbance at 570 nm with the subtraction of the 630 nm background, using a Synergy HT microplate reader (BioTek Instruments, Winooski, VT, USA). The MTT assays were repeated in four separate experiments. All values are reported as means ± standard error (SEM). Statistical analysis of the data was performed using two-way analysis of variance (ANOVA) and a Duncan test to determine differences in cytotoxicity, with the level of significance set at $p < 0.05$.

The analysis of cell numbers growing on the sample surfaces, as well as cell morphology, was conducted using scanning electron microscopy (SEM; Quanta 3D FEG; Carl Zeiss, Göttingen, Germany). After 24 or 72 h, the cells were washed in PBS and fixed in 2.5% *w*/*v* glutaraldehyde for 4 h at 4 °C. Subsequently, the specimens were dehydrated in ethanol at increasing concentrations (50%, 75%, 90%, and 100%) for 10 min for each concentration at room temperature. Finally, the specimens were dried and stored at room temperature until the SEM analysis was performed.

5. Conclusions

Crystals of an oxo complex with the general formula $[Ti_8O_2(O^iPr)_{20}(man)_4]$ (**1**) were successfully isolated from the reaction mixture of titanium isopropoxide and mandelic acid, mixed in a molar ratio of 4:1 at room temperature, using tetrahydrofuran as a solvent. Structural analysis revealed that the $\{Ti_8O_2\}$ core comprises a central $\{Ti_4O_2\}$ unit and two side dimers ($\{Ti_2\}$), stabilized by two μ_3-O bridges, bridge-forming anions, and a five-membered chelate ring.

Spectral tests, including XRD, IR, and Raman spectroscopy, confirmed the structural stability of compound (**1**) in both aqueous environments and after incorporation into a polymer matrix. EPR spectroscopy facilitated the detection of reactive oxygen species (ROS) on the surface of the grains (**1**) (in O_2^- form), as well as in the PMMA + (**1**) composite film (in O^- and O_2^- forms).

Biocidal assessments of compound (**1**) and the PMMA + (**1**) composite were conducted against *E. coli* and *S. aureus* bacteria strains, as well as *Candida albicans fungi*. The antibacterial effect was observed for a suspension containing as little as 2% of (**1**). A suspension containing 20% of (**1**) exhibited biocidal activity against both bacteria and fungi. The bactericidal activity of the composite PMMA + (**1**) systems was slightly weaker; moreover, they did not show a biocidal effect against fungi.

The observed significant antimicrobial activity of oxo complex (**1**) could stem from the synergetic effects associated with ROS generation and the existence of a chelating ring within its structure. Incorporating (**1**) into the polymer matrix restricted its direct interaction with microorganisms, consequently diminishing its antimicrobial efficacy. However, in such

instances, the mechanisms linked to ROS generation remain operational. All PMMA + (**1**) materials demonstrated non-cytotoxic characteristic towards L929 fibroblasts.

In summary, the test results from our investigations affirm that compound (**1**) fulfills its intended objectives, namely, possessing antibacterial properties, while being non-cytotoxic. This compound can be utilized as an antibacterial coating in public facilities or hospitals to mitigate the risk of bacterial infections.

Supplementary Materials: The following supporting information can be downloaded at: https://www.mdpi.com/article/10.3390/molecules29081736/s1, Figure S1: The topological analysis of the cluster with a $\{Ti_4O_2\}$ core (left) [7] (a), and $\{Ti_8O_2\}$ (**1**) (right) (b), performed in TOPS; Figure S2: A 3D-deformation density map for (**1**) showing the presence of charge depletion regions (in red) and charge concentration regions (in blue), mapped using Crystal Explorer 21.5. The isosurfaces are drawn at 0.008 eau−3. The green circles show two of four chelate rings present in this molecule. In all of them, the same feature occurs—the blue color prevails, pointing at charge concentration in this region. The wavefunction was calculated at the level B3LYP/6-31G(d,p) References [80–83]; Figure S3: EPR spectra obtained for the powdered sample of (**1**) (a) and a cut foil of PMMA + (**1**) 20 wt.% (b). The experimental conditions were as follows: room temperature, microwave frequencies of 9.31648 (a) and 9.32357 (b) GHz; modulation amplitude of 1 mT; sweep width of 20 mT; sweep time of 4 min; time constant of 0.1 s; receiver gain of 4×10^5; Table S1: Selected bond lengths [Å] and bond angles [°] in (**1**); Table S2. Coordination modes in (**1**).

Author Contributions: Conceptualization, P.P. and B.K.; methodology, P.P., T.M., S.W. and B.K.; validation, P.P.; formal analysis, P.P., B.K., G.W., T.M., P.G. and T.J. ; investigation, B.K., G.W., T.M., P.G. and T.J.; resources, B.K.; data curation, P.P. and A.R.; writing—original draft preparation, P.P. and B.K.; writing—review and editing, P.P., A.R. and B.K.; supervision, P.P., A.R. and S.W.; project administration, P.P.; funding acquisition, P.P., A.R. and B.K. All authors have read and agreed to the published version of the manuscript.

Funding: The studies have been carried out within the Project 4101.00000085 IDUB/IDUB Biomaterials and Cosmetics Research Group, Nicolaus Copernicus University in Toruń, Poland.

Institutional Review Board Statement: Not applicable.

Informed Consent Statement: Not applicable.

Data Availability Statement: Crystallographic data have been deposited at The Cambridge Crystallographic Data Center via www.ccdc.cam.ac.uk.data_request/cif accessed on 25 November 2023. Other data are unavailable due to their potential application meaning.

Conflicts of Interest: The authors declare no conflicts of interest.

References

1. Zhuang, G.; Yan, J.; Wen, Y.; Zhuang, Z.; Yu, Y. Two-Dimensional Transition Metal Oxides and Chalcogenides for Advanced Photocatalysis: Progress, Challenges, and Opportunities. *Sol. RRL* **2021**, *5*, 2000403. [CrossRef]
2. Wang, C.; Wang, S.-J.; Kong, F.-G. Calixarene-Protected Titanium-Oxo Clusters and Their Photocurrent Responses and Photocatalytic Performances. *Inorg. Chem.* **2021**, *60*, 5034–5041. [CrossRef] [PubMed]
3. Ni, L.; Liang, D.; Cai, Y.; Diao, G.; Zhou, Z. A Novel Hexanuclear Titanium(IV)-Oxo-Iminodiacetate Cluster with a Ti_6O_9 Core: Single-Crystal Structure and Photocatalytic Activities. *Dalton Trans.* **2016**, *45*, 7581–7588. [CrossRef] [PubMed]
4. Lin, Y.; Zhu, Y.-F.; Chen, Z.-H.; Liu, F.-H.; Zhao, L.; Su, Z.-M. Synthesis, Structure, and Photocatalytic Hydrogen of Three Environmentally Friendly Titanium Oxo-Clusters. *Inorg. Chem. Commun.* **2014**, *40*, 22–25. [CrossRef]
5. Kubiak, B.; Piszczek, P.; Radtke, A.; Muzioł, T.; Wrzeszcz, G.; Golińska, P. Photocatalytic and Antimicrobial Activity of Titanium(IV)-Oxo Clusters of Different Core Structure. *Crystals* **2023**, *13*, 998. [CrossRef]
6. Janek, M.; Muzioł, T.M.; Piszczek, P. Trinuclear Oxo-Titanium Clusters: Synthesis, Structure, and Photocatalytic Activity. *Materials* **2019**, *12*, 3195. [CrossRef] [PubMed]
7. Janek, M.; Radtke, A.; Muzioł, T.; Jerzykiewicz, M.; Piszczek, P. Tetranuclear Oxo-Titanium Clusters with Different Carboxylate Aromatic Ligands: Optical Properties, DFT Calculations, and Photoactivity. *Materials* **2018**, *11*, 1661. [CrossRef] [PubMed]
8. Fenton, J.L.; Laaroussi, A.; Mobian, P.; Chaumont, C.; Khalil, G.; Huguenard, C.; Henry, M. Structural Investigation of Pyridinecarboxylato Titanium(IV) Complexes: An Uncommon Monomeric Octacoordinated Complex vs. a Hexaprismatic Architecture. *Eur. J. Inorg. Chem.* **2014**, *2014*, 357–363. [CrossRef]

9. Seisenbaeva, G.A.; Ilina, E.; Håkansson, S.; Kessler, V.G. A New Concept for Titanium Oxo-Alkoxo-Carboxylates' Encapsulated Biocompatible Time Temperature Food Indicators Based on Arising, Not Fading Color. *J. Sol.-Gel Sci. Technol.* **2010**, *55*, 1–8. [CrossRef]
10. Benedict, J.B.; Freindorf, R.; Trzop, E.; Cogswell, J.; Coppens, P. Large Polyoxotitanate Clusters: Well-Defined Models for Pure-Phase TiO_2 Structures and Surfaces. *J. Am. Chem. Soc.* **2010**, *132*, 13669–13671. [CrossRef] [PubMed]
11. Sokolow, J.D.; Trzop, E.; Chen, Y.; Tang, J.; Allen, L.J.; Crabtree, R.H.; Benedict, J.B.; Coppens, P. Binding Modes of Carboxylate- and Acetylacetonate-Linked Chromophores to Homodisperse Polyoxotitanate Nanoclusters. *J. Am. Chem. Soc.* **2012**, *134*, 11695–11700. [CrossRef]
12. Zhang, L.; Fan, X.; Yi, X.; Lin, X.; Zhang, J. Coordination-Delayed-Hydrolysis Method for the Synthesis and Structural Modulation of Titanium-Oxo Clusters. *Acc. Chem. Res.* **2022**, *55*, 3150–3161. [CrossRef] [PubMed]
13. Svensson, F.G.; Seisenbaeva, G.A.; Kessler, V.G. Mixed-Ligand Titanium "Oxo Clusters": Structural Insights into the Formation and Binding of Organic Molecules and Transformation into Oxide Nanostructures on Hydrolysis and Thermolysis. *Eur. J. Inorg. Chem.* **2017**, *2017*, 4117–4122. [CrossRef]
14. Wu, R.-H.; Guo, M.; Yu, M.-X.; Zhu, L.-G. Two Titanium(IV)-Oxo-Clusters: Synthesis, Structures, Characterization and Recycling Catalytic Activity in the Oxygenation of Sulfides. *Dalton Trans.* **2017**, *46*, 14348–14355. [CrossRef] [PubMed]
15. Czakler, M.; Artner, C.; Schubert, U. Two New Hexanuclear Titanium Oxo Cluster Types and Their Structural Connection to Known Clusters. *New J. Chem.* **2018**, *42*, 12098–12103. [CrossRef]
16. Yu, Y.-Z.; Zhang, Y.-R.; Geng, C.-H.; Sun, L.; Guo, Y.; Feng, Y.-R.; Wang, Y.-X.; Zhang, X.-M. Precise and Wide-Ranged Band-Gap Tuning of Ti_6-Core-Based Titanium Oxo Clusters by the Type and Number of Chromophore Ligands. *Inorg. Chem.* **2019**, *58*, 16785–16791. [CrossRef] [PubMed]
17. Guo, Y.-H.; Yu, Y.-Z.; Shen, Y.-H.; Yang, L.-G.; Liu, N.-N.; Zhou, Z.-Y.; Niu, Y.-S. "Three-in-One" Structural-Building-Mode-Based Ti_{16}-Type Titanium Oxo Cluster Entirely Protected by the Ligands Benzoate and Salicylhydroxamate. *Inorg. Chem.* **2022**, *61*, 8685–8693. [CrossRef] [PubMed]
18. Schubert, U. Titanium-Oxo Clusters with Bi- and Tridentate Organic Ligands: Gradual Evolution of the Structures from Small to Big. *Chem. Eur. J.* **2021**, *27*, 11239–11256. [CrossRef] [PubMed]
19. Radtke, A.; Piszczek, P.; Muzioł, T.; Wojtczak, A. The Structural Conversion of Multinuclear Titanium(IV) μ-Oxo-Complexes. *Inorg. Chem.* **2014**, *53*, 10803–10810. [CrossRef] [PubMed]
20. Zheng, Y.-Z.; Zheng, Z.; Chen, X.-M. A Symbol Approach for Classification of Molecule-Based Magnetic Materials Exemplified by Coordination Polymers of Metal Carboxylates. *Coord. Chem. Rev.* **2014**, *258–259*, 1–15. [CrossRef]
21. Rozes, L.; Sanchez, C. Titanium Oxo-Clusters: Precursors for a Lego-like Construction of Nanostructured Hybrid Materials. *Chem. Soc. Rev.* **2011**, *40*, 1006–1030. [CrossRef] [PubMed]
22. Schubert, U. Chemical Modification of Titanium Alkoxides for Sol–Gel Processing. *J. Mater. Chem.* **2005**, *15*, 3701–3715. [CrossRef]
23. Wang, J.-F.; Fang, W.-H.; Li, D.-S.; Zhang, L.; Zhang, J. Cocrystal of $\{Ti_4\}$ and $\{Ti_6\}$ Clusters with Enhanced Photochemical Properties. *Inorg. Chem.* **2017**, *56*, 2367–2370. [CrossRef]
24. Piszczek, P.; Kubiak, B.; Golińska, P.; Radtke, A. Oxo-Titanium(IV) Complex/Polymer Composites—Synthesis, Spectroscopic Characterization and Antimicrobial Activity Test. *Int. J. Mol. Sci.* **2020**, *21*, 9663. [CrossRef] [PubMed]
25. Kubiak, B.; Radtke, A.; Topolski, A.; Wrzeszcz, G.; Golińska, P.; Kaszkowiak, E.; Sobota, M.; Włodarczyk, J.; Stojko, M.; Piszczek, P. The Composites of PCL and Tetranuclear Titanium(IV)-Oxo Complexes as Materials Exhibiting the Photocatalytic and the Antimicrobial Activity. *Int. J. Mol. Sci.* **2021**, *22*, 7021. [CrossRef]
26. Cui, Y.; Zou, G.-D.; Li, H.-M.; Huang, Y.; Fan, Y. 4-Chlorosalicylate-Stabilized Titanium-Oxo Clusters with Structures Mediated by Tetrazole and Their Photophysical Properties. *Polyhedron* **2019**, *157*, 177–182. [CrossRef]
27. Luo, W.; Shu, X.-P.; Liu, P.-Y.; Yu, S.-K.; Zhu, Q.-Y.; Dai, J. Lanthanide-Titanium Oxo-Clusters, New Precursors of Multifunctional Colloids for Effective Imaging and Photodynamic Therapy. *J. Mol. Liq.* **2020**, *317*, 113946. [CrossRef]
28. Li, N.; Pranantyo, D.; Kang, E.-T.; Wright, D.S.; Luo, H.-K. A Simple Drop-and-Dry Approach to Grass-Like Multifunctional Nanocoating on Flexible Cotton Fabrics Using In Situ-Generated Coating Solution Comprising Titanium-Oxo Clusters and Silver Nanoparticles. *ACS Appl. Mater. Interfaces* **2020**, *12*, 12093–12100. [CrossRef] [PubMed]
29. Chen, S.; Fang, W.; Zhang, L.; Zhang, J. Atomically Precise Multimetallic Semiconductive Nanoclusters with Optical Limiting Effects. *Angew. Chem. Int. Ed.* **2018**, *57*, 11252–11256. [CrossRef] [PubMed]
30. Luo, W.; Hu, B.; Zhang, H.-L.; Li, C.; Shi, Y.; Li, X.; Jin, L. Antibacterial, Photothermal and Stable Ag-Titanium-Oxo-Clusters Hydrogel Designed for Wound Healing. *Mater. Des.* **2023**, *226*, 111674. [CrossRef]
31. De Pasquale, I.; Lo Porto, C.; Dell'Edera, M.; Petronella, F.; Agostiano, A.; Curri, M.L.; Comparelli, R. Photocatalytic TiO_2-Based Nanostructured Materials for Microbial Inactivation. *Catalysts* **2020**, *10*, 1382. [CrossRef]
32. Parcheta, M.; Świsłocka, R.; Świderski, G.; Matejczyk, M.; Lewandowski, W. Spectroscopic Characterization and Antioxidant Properties of Mandelic Acid and Its Derivatives in a Theoretical and Experimental Approach. *Materials* **2022**, *15*, 5413. [CrossRef] [PubMed]
33. Egner, P.; Pavlačková, J.; Sedlaříková, J.; Pleva, P.; Mokrejš, P.; Janalíková, M. Non-Alcohol Hand Sanitiser Gels with Mandelic Acid and Essential Oils. *Int. J. Mol. Sci.* **2023**, *24*, 3855. [CrossRef] [PubMed]
34. Tang, S.-C.; Yang, J.-H. Dual Effects of Alpha-Hydroxy Acids on the Skin. *Molecules* **2018**, *23*, 863. [CrossRef] [PubMed]

35. Hou, J.-L.; Luo, W.; Wu, Y.-Y.; Su, H.-C.; Zhang, G.-L.; Zhu, Q.-Y.; Dai, J. Two Ti_{13}-Oxo-Clusters Showing Non-Compact Structures, Film Electrode Preparation and Photocurrent Properties. *Dalton Trans.* **2015**, *44*, 19829–19835. [CrossRef]
36. Ding, Q.-R.; Liu, J.-X.; Narayanam, N.; Zhang, L.; Zhang, J. Construction of Molecular Rectangles with Titanium–Oxo Clusters and Rigid Aromatic Carboxylate Ligands. *Dalton Trans.* **2017**, *46*, 16000–16003. [CrossRef] [PubMed]
37. Huang, Y.; Zou, G.-D.; Li, H.-M.; Cui, Y.; Fan, Y. A Photoactive $\{Ti_{16}\}$ Metal–Organic Capsule: Structural, Photoelectrochemical and Photocatalytic Properties. *New J. Chem.* **2018**, *42*, 14079–14082. [CrossRef]
38. Kemmitt, T.; Al-Salim, N.I.; Gainsford, G.J.; Bubendorfer, A.; Waterland, M. Unprecedented Oxo-Titanium Citrate Complex Precipitated from Aqueous Citrate Solutions, Exhibiting a Novel Bilayered Ti_8O_{10} Structural Core. *Inorg. Chem.* **2004**, *43*, 6300–6306. [CrossRef] [PubMed]
39. Salam, A.; Dadzie, O.E.; Galadari, H. Chemical Peeling in Ethnic Skin: An Update. *Br. J. Dermatol.* **2013**, *169* (Suppl. S3), 82–90. [CrossRef] [PubMed]
40. Gentili, G.; Perugini, P.; Bugliaro, S.; D'Antonio, C. Efficacy and Safety of a New Peeling Formulated with a Pool of PHAs for the Treatment of All Skin Types, Even Sensitive. *J. Cosmet. Dermatol.* **2023**, *22*, 517–528. [CrossRef] [PubMed]
41. Dębowska, R.M.; Kaszuba, A.; Michalak, I.; Dzwigałowska, A.; Cieścińska, C.; Jakimiuk, E.; Zielińska, J.; Kaszuba, A. Evaluation of the Efficacy and Tolerability of Mandelic Acid-Containing Cosmetic Formulations for Acne Skin Care. *Dermatol. Rev./Przegląd Dermatol.* **2015**, *4*, 316–321. [CrossRef]
42. Greive, K.; Tran, D.; Townley, J.; Barnes, T. An Antiaging Skin Care System Containing Alpha Hydroxy Acids and Vitamins Improves the Biomechanical Parameters of Facial Skin. *CCID* **2014**, *8*, 9–17. [CrossRef] [PubMed]
43. Świsłocka, R.; Świderski, G.; Nasiłowska, J.; Sokołowska, B.; Wojtczak, A.; Lewandowski, W. Research on the Electron Structure and Antimicrobial Properties of Mandelic Acid and Its Alkali Metal Salts. *Int. J. Mol. Sci.* **2023**, *24*, 3078. [CrossRef] [PubMed]
44. Masoud, M.S.; Ali, A.E.; Shokry, A.A.; Kolkaila, S.A. Chelation and Molecular Structure of Mandelic Acid Complexes. *J. Chem. Res. Adv.* **2021**, *2*, 1–9.
45. Youzhu, Y.; Hui, W.; Leilei, L.; Yuhua, G.; Jing, F.; Yichao, L. Crystal Structure of Bis(μ_2-2-Oxido-2-Phenylacetato-κ^3 *O*,*O*′:*O*′)-Bis(*N*-Oxido-Benzamide-κ^2 *O*,*O*′)-Bis(Propan-2-Olato-κ^1 *O*)Dititanium(IV), $C_{36}H_{38}N_2O_{12}Ti_2$. *Z. Krist. New Cryst. Struct.* **2022**, *237*, 957–959. [CrossRef]
46. Youzhu, Y.; Yuhua, G.; Yongsheng, N.; Nana, L.; Hongfei, Z. Crystal Structure of Bis(μ_2-2-Oxido-2-Phenylacetate-κ^3 *O*:*O*,*O*′)-Bis(1-Isopropoxy-2-Oxo-2-Phenylethan-1-Olato-κ^2 O,O′)-Bis(Propan-2-Olato-κ^1 O)Dititanium(IV), $C_{44}H_{52}O_{14}Ti_2$. *Z. Krist. New Cryst. Struct.* **2021**, *236*, 467–469. [CrossRef]
47. Schetter, B.; Stosiek, C.; Ziemer, B.; Mahrwald, R. Multinuclear Enantiopure Titanium Self-Assembly Complexes—Synthesis, Characterization and Application to Organic Synthesis. *Appl. Organometal. Chem.* **2007**, *21*, 139–145. [CrossRef]
48. Addison, A.W.; Rao, T.N.; Reedijk, J.; Van Rijn, J.; Verschoor, G.C. Synthesis, Structure, and Spectroscopic Properties of Copper(II) Compounds Containing Nitrogen–Sulphur Donor Ligands; the Crystal and Molecular Structure of Aqua[1,7-Bis(N-Methylbenzimidazol-2′-Yl)-2,6-Dithiaheptane]Copper(II) Perchlorate. *J. Chem. Soc. Dalton Trans.* **1984**, *7*, 1349–1356. [CrossRef]
49. Macrae, C.F.; Sovago, I.; Cottrell, S.J.; Galek, P.T.A.; McCabe, P.; Pidcock, E.; Platings, M.; Shields, G.P.; Stevens, J.S.; Towler, M.; et al. Mercury 4.0: From Visualization to Analysis, Design and Prediction. *J. Appl. Crystallogr.* **2020**, *53*, 226–235. [CrossRef] [PubMed]
50. *ISO 22196:2011 Standard*; Measurement of Antibacterial Activity on Plastics and Other Non-Porous Surfaces. ISO: Geneva, Switzerland, 2021. Available online: https://www.iso.org/standard/54431.html (accessed on 25 November 2023).
51. Cicco, S.; Vona, D.; Gristina, R.; Sardella, E.; Ragni, R.; Lo Presti, M.; Farinola, G. Biosilica from Living Diatoms: Investigations on Biocompatibility of Bare and Chemically Modified Thalassiosira Weissflogii Silica Shells. *Bioengineering* **2016**, *3*, 35. [CrossRef]
52. Xue, F.; Janzen, D.M.; Knecht, D.A. Contribution of Filopodia to Cell Migration: A Mechanical Link between Protrusion and Contraction. *Int. J. Cell Biol.* **2010**, *2010*, 507821. [CrossRef] [PubMed]
53. Piszczek, P.; Richert, M.; Grodzicki, A.; Głowiak, T.; Wojtczak, A. Synthesis, Crystal Structures and Spectroscopic Characterization of $[Ti_8O_8(OOCR)_{16}]$ (Where R = But, CH_2But, $C(CH_3)_2$Et). *Polyhedron* **2005**, *24*, 663–670. [CrossRef]
54. Frot, T.; Cochet, S.; Laurent, G.; Sassoye, C.; Popall, M.; Sanchez, C.; Rozes, L. $Ti_8O_8(OOCR)_{16}$, a New Family of Titanium–Oxo Clusters: Potential NBUs for Reticular Chemistry. *Eur. J. Inorg. Chem.* **2010**, *2010*, 5650–5659. [CrossRef]
55. Fan, X.; Yuan, F.; Li, D.; Chen, S.; Cheng, Z.; Zhang, Z.; Xiang, S.; Zang, S.; Zhang, J.; Zhang, L. Threefold Collaborative Stabilization of Ag_{14}-Nanorods by Hydrophobic Ti_{16}-Oxo Clusters and Alkynes: Designable Assembly and Solid-State Optical-Limiting Application. *Angew. Chem. Int. Ed.* **2021**, *60*, 12949–12954. [CrossRef] [PubMed]
56. Wang, S.; Reinsch, H.; Heymans, N.; Wahiduzzaman, M.; Martineau-Corcos, C.; De Weireld, G.; Maurin, G.; Serre, C. Toward a Rational Design of Titanium Metal-Organic Frameworks. *Matter* **2020**, *2*, 440–450. [CrossRef]
57. Kim, B.; Keum, Y.; Chen, Y.-P.; Oh, H.S.; Lee, J.Y.; Park, J. Stimuli-Responsive Ti-Organic Gels and Aerogels Derived from Ti-Oxo Clusters: Hierarchical Porosity and Photocatalytic Activity. *Inorg. Chem.* **2019**, *58*, 15936–15941. [CrossRef] [PubMed]
58. Czakler, M.; Artner, C.; Schubert, U. Influence of the Phosphonate Ligand on the Structure of Phosphonate-Substituted Titanium Oxo Clusters. *Eur. J. Inorg. Chem.* **2013**, *2013*, 5790–5796. [CrossRef]
59. Fan, X.; Fu, H.; Gao, M.-Y.; Zhang, L.; Zhang, J. One-Pot and Postsynthetic Phenol-Thermal Synthesis toward Highly Stable Titanium-Oxo Clusters. *Inorg. Chem.* **2019**, *58*, 13353–13359. [CrossRef] [PubMed]
60. Liu, J.-X.; Gao, M.-Y.; Fang, W.-H.; Zhang, L.; Zhang, J. Bandgap Engineering of Titanium-Oxo Clusters: Labile Surface Sites Used for Ligand Substitution and Metal Incorporation. *Angew. Chem. Int. Ed.* **2016**, *55*, 5160–5165. [CrossRef] [PubMed]

61. Wu, Y.-Y.; Luo, W.; Wang, Y.-H.; Pu, Y.-Y.; Zhang, X.; You, L.-S.; Zhu, Q.-Y.; Dai, J. Titanium–Oxo–Clusters with Dicarboxylates: Single-Crystal Structure and Photochromic Effect. *Inorg. Chem.* **2012**, *51*, 8982–8988. [CrossRef] [PubMed]
62. He, W.; Liu, Y.; Wamer, W.G.; Yin, J.-J. Electron Spin Resonance Spectroscopy for the Study of Nanomaterial-Mediated Generation of Reactive Oxygen Species. *J. Food Drug Anal.* **2014**, *22*, 49–63. [CrossRef]
63. Xiong, L.-B.; Li, J.-L.; Yang, B.; Yu, Y. Ti^{3+} in the Surface of Titanium Dioxide: Generation, Properties and Photocatalytic Application. *J. Nanomater.* **2012**, *2012*, 831524. [CrossRef]
64. Suriye, K.; Lobo-Lapidus, R.J.; Yeagle, G.J.; Praserthdam, P.; Britt, R.D.; Gates, B.C. Probing Defect Sites on TiO2 with [Re3(CO)12H3]: Spectroscopic Characterization of the Surface Species. *Chem. Eur. J.* **2008**, *14*, 1402–1414. [CrossRef] [PubMed]
65. Dan-Hardi, M.; Serre, C.; Frot, T.; Rozes, L.; Maurin, G.; Sanchez, C.; Férey, G. A New Photoactive Crystalline Highly Porous Titanium(IV) Dicarboxylate. *J. Am. Chem. Soc.* **2009**, *131*, 10857–10859. [CrossRef] [PubMed]
66. Richards, E.; Murphy, D.M.; Che, M. An EPR Characterisation of Stable and Transient Reactive Oxygen Species Formed under Radiative and Non-Radiative Conditions. *Res. Chem. Intermed.* **2019**, *45*, 5763–5779. [CrossRef]
67. Śmigiel, J.; Piszczek, P.; Wrzeszcz, G.; Jędrzejewski, T.; Golińska, P.; Radtke, A. The Composites of PCL and Tetranuclear Titanium(IV)–Oxo Complex with Acetylsalicylate Ligands—Assessment of Their Biocompatibility and Antimicrobial Activity with the Correlation to EPR Spectroscopy. *Materials* **2023**, *16*, 297. [CrossRef] [PubMed]
68. Vaishampayan, A.; Grohmann, E. Antimicrobials Functioning through ROS-Mediated Mechanisms: Current Insights. *Microorganisms* **2021**, *10*, 61. [CrossRef] [PubMed]
69. Mazur, P.; Skiba-Kurek, I.; Mrowiec, P.; Karczewska, E.; Drożdż, R. Synergistic ROS-Associated Antimicrobial Activity of Silver Nanoparticles and Gentamicin against *Staphylococcus epidermidis*. *Int. J. Nanomed.* **2020**, *15*, 3551–3562. [CrossRef] [PubMed]
70. Lam, P.-L.; Wong, R.S.-M.; Lam, K.-H.; Hung, L.-K.; Wong, M.-M.; Yung, L.-H.; Ho, Y.-W.; Wong, W.-Y.; Hau, D.K.-P.; Gambari, R.; et al. The Role of Reactive Oxygen Species in the Biological Activity of Antimicrobial Agents: An Updated Mini Review. *Chem.-Biol. Interact.* **2020**, *320*, 109023. [CrossRef]
71. Joe, A.; Park, S.-H.; Kim, D.-J.; Lee, Y.-J.; Jhee, K.-H.; Sohn, Y.; Jang, E.-S. Antimicrobial Activity of ZnO Nanoplates and Its Ag Nanocomposites: Insight into an ROS-Mediated Antibacterial Mechanism under UV Light. *J. Solid. State Chem.* **2018**, *267*, 124–133. [CrossRef]
72. Beyene, B.B.; Mihirteu, A.M.; Ayana, M.T.; Yibeltal, A.W. Synthesis, Characterization and Antibacterial Activity of Metalloporphyrins: Role of Central Metal Ion. *Results Chem.* **2020**, *2*, 100073. [CrossRef]
73. Chen, S.; Wu, G.; Zeng, H. Preparation of High Antimicrobial Activity Thiourea Chitosan–Ag^{+} Complex. *Carbohydr. Polym.* **2005**, *60*, 33–38. [CrossRef]
74. Burns, J.; McCoy, C.P.; Irwin, N.J. Synergistic Activity of Weak Organic Acids against Uropathogens. *J. Hosp. Infect.* **2021**, *111*, 78–88. [CrossRef]
75. Tshuva, E.Y.; Peri, D. Modern Cytotoxic Titanium(IV) Complexes; Insights on the Enigmatic Involvement of Hydrolysis. *Coord. Chem. Rev.* **2009**, *253*, 2098–2115. [CrossRef]
76. Immel, T.A.; Grützke, M.; Batroff, E.; Groth, U.; Huhn, T. Cytotoxic Dinuclear Titanium-Salan Complexes: Structural and Biological Characterization. *J. Inorg. Biochem.* **2012**, *106*, 68–75. [CrossRef] [PubMed]
77. CrysAlis CCD. *CrysAlis Red and CrysAlis CCD*; Oxford Diffraction Ltd.: Oxfordshire, UK, 2000.
78. Sheldrick, G.M. Crystal Structure Refinement with *SHELXL*. *Acta Crystallogr. C Struct. Chem.* **2015**, *71*, 3–8. [CrossRef] [PubMed]
79. Brandenburg, K.; Berndt, M. *Diamond, Release 2.1e*; Crystal Impact GbR: Bonn, Germany, 2001.
80. Becke, A.D. Density-functional thermochemistry. III. The role of exact exchange. *J. Chem. Phys.* **1993**, *98*, 5648–5652. [CrossRef]
81. Stephens, P.J.; Devlin, F.J.; Chabalowski, C.F.; Frisch, M.J. Ab Initio Calculation of Vibrational Absorption and Circular Dichroism Spectra Using Density Functional Force Fields. *J. Phys. Chem.* **1994**, *98*, 11623–11627. [CrossRef]
82. Becke, A.D. Density-functional exchange-energy approximation with correct asymptotic behavior. *Phys. Rev. A* **1988**, *38*, 3098–3100. [CrossRef] [PubMed]
83. Lee, C.; Yang, W.; Parr, R.G. Development of the Colle-Salvetti correlation-energy formula into a functional of the electron density. *Phys. Rev. B* **1988**, *37*, 785–789. [CrossRef] [PubMed]

Disclaimer/Publisher's Note: The statements, opinions and data contained in all publications are solely those of the individual author(s) and contributor(s) and not of MDPI and/or the editor(s). MDPI and/or the editor(s) disclaim responsibility for any injury to people or property resulting from any ideas, methods, instructions or products referred to in the content.

Materiały uzupełniające

Supplementary Information

Structural Characterization and Bioactivity of a Titanium(IV)-Oxo Complex Stabilized by Mandelate Ligands

Barbara Kubiak 1,*, Tadeusz Muzioł 1, Grzegorz Wrzeszcz 1, Aleksandra Radtke 1, Patrycja Golińska 2, Tomasz Jędrzejewski 3, Sylwia Wrotek 3 and Piotr Piszczek 1,*

1 Department of Inorganic and Coordination Chemistry, Faculty of Chemistry, Nicolaus Copernicus University in Toruń, Gagarina 7, 87-100 Toruń, Poland; tadeuszmuziol@wp.pl (T.M.); wrzeszcz@umk.pl (G.W.); aleksandra.radtke@umk.pl (A.R.)
2 Department of Microbiology, Faculty of Biological and Veterinary Sciences, Nicolaus Copernicus University in Toruń, Lwowska 1, 87-100 Toruń, Poland; golinska@umk.pl
3 Department of Immunology, Faculty of Biological and Veterinary Sciences, Nicolaus Copernicus University in Toruń, Lwowska 1, 87-100 Toruń, Poland; tomaszj@umk.pl (T.J.); wrotek@umk.pl (S.W.)
* Correspondence: basiak0809@gmail.com (B.K.); piszczek@umk.pl (P.P.)

Table S1. Selected bond lengths [Å] and bond angles [°] in (**1**).

	Distance [Å]		Angles [°]		Angles [°]
Ti1-O21	1.798(3)	O21-Ti1-O10	106.35(13)	O3-Ti2-O31^{i}	88.97(12)
Ti1-O10	1.867(3)	O21-Ti1-O31	95.00(13)	O10-Ti2-O31^{i}	75.77(11)
Ti1-O31	1.952(3)	O10-Ti1-O31	104.11(12)	O12-Ti2-O31^{i}	82.35(12)
Ti1-O1	2.055(3)	O21-Ti1-O1	93.57(13)	O81-Ti3-O71	93.59(19)
Ti1-O3	2.058(3)	O10-Ti1-O1	147.75(13)	O81-Ti3-O61	108.5(2)
Ti1-O10^{i}	2.074(3)	O31-Ti1-O1	98.98(12)	O71-Ti3-O61	99.92(18)
Ti1-Ti1^{i}	3.0086(13)	O21-Ti1-O3	92.88(13)	O81-Ti3-O13	171.30(16)
Ti1-Ti2	3.1036(10)	O10-Ti1-O3	78.25(11)	O71-Ti3-O13	94.42(16)
Ti1-Ti2^{i}	3.1940(10)	O31-Ti1-O3	170.73(13)	O61-Ti3-O13	73.42(15)
Ti2-O41	1.769(3)	O1-Ti1-O3	75.62(11)	O81-Ti3-O11	100.03(18)
Ti2-O51	1.807(3)	O21-Ti1-O10^{i}	171.33(13)	O71-Ti3-O11	93.70(16)
Ti2-O3	2.006(3)	O10-Ti1-O10^{i}	80.61(12)	O61-Ti3-O11	147.34(15)
Ti2-O10	2.040(3)	O31-Ti1-O10^{i}	78.06(12)	O13-Ti3-O11	76.06(13)
Ti2-O12	2.054(3)	O1-Ti1-O10^{i}	82.53(11)	O81-Ti3-O2^{i}	82.89(16)
Ti2-O31^{i}	2.091(3)	O3-Ti1-O10^{i}	93.64(11)	O71-Ti3-O2^{i}	173.50(17)
Ti3-O81	1.784(4)	O41-Ti2-O51	97.93(16)	O61-Ti3-O2^{i}	86.41(14)
Ti3-O71	1.795(4)	O41-Ti2-O3	95.43(15)	O13-Ti3-O2^{i}	88.81(13)
Ti3-O61	1.933(4)	O51-Ti2-O3	95.79(13)	O11-Ti3-O2^{i}	81.59(12)
Ti3-O13	2.038(4)	O41-Ti2-O10	98.47(14)	O101-Ti4-O111	101.9(3)
Ti3-O11	2.070(3)	O51-Ti2-O10	162.13(14)	O101-Ti4-O91	111.3(3)
Ti3-O2^{i}	2.172(3)	O3-Ti2-O10	75.65(11)	O111-Ti4-O91	100.0(3)
Ti3-Ti4	3.2486(15)	O41-Ti2-O12	91.80(15)	O101-Ti4-O13	118.1(3)
Ti4-O101	1.773(5)	O51-Ti2-O12	96.26(14)	O111-Ti4-O13	91.02(19)
Ti4-O111	1.787(5)	O3-Ti2-O12	164.96(12)	O91-Ti4-O13	125.55(19)
Ti4-O91	1.801(5)	O10-Ti2-O12	90.27(12)	O101-Ti4-O61	90.6(3)
Ti4-O13	1.979(3)	O41-Ti2-O31^{i}	171.70(14)	O111-Ti4-O61	161.70(19)
Ti4-O61	2.098(4)	O51-Ti2-O31^{i}	88.60(14)	O91-Ti4-O61	87.5(2)
				O13-Ti4-O61	71.20(14)

Table S2. Coordination modes in (**1**).

	Coordination sphere content – number of atoms involved in Ti(IV) binding					
Central atom	Coordination number	mandelate		$iPrO^-$ anion		Oxo anion
		$RCOO^-$	RO^-	terminal	bridging	
Ti1	6	1	**1**	1	1	2
Ti2	6	1	1	2	1	1
Ti3	6	2	**1**	2	1	-
Ti4	5	-	1	3	1	-

In bold are marked hydroxyl groups involved in five-membered chelate ring with one oxygen atom from carboxylic group

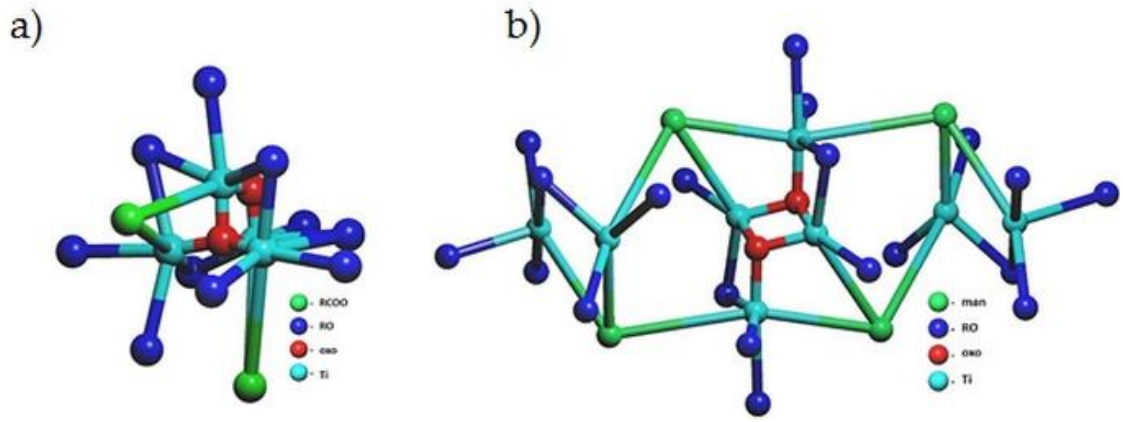


Figure S1. The topological analysis of the cluster with $\{Ti_4O_2\}$ core ([7] left) (a), and $\{Ti_8O_2\}$ (**1**) (this paper, right) cores performed in TOPOS with titanium cations in cyan, oxo anions in red, mandelate (carboxylate) anions in green and propionate anions in blue.

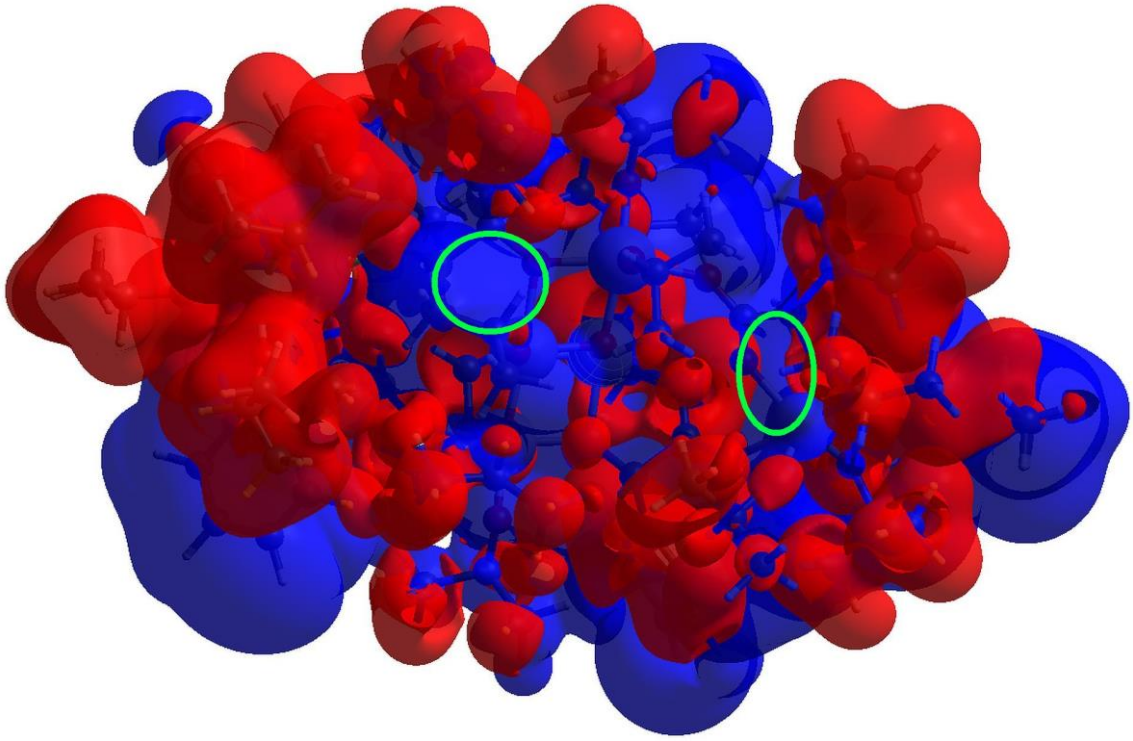


Figure S2. 3D-deformation density map for (**1**) showing the presence of charge depletion regions (in red) and charge concentration regions (in blue), mapped using Crystal Explorer 21.5. The isosurfaces are drawn at 0.008 eau−3. The green circles show two of four chelate rings present in this molecule. In all of them the same feature occurs – the blue color prevails pointing at charge concentration in this region. The wavefunction was calculated at the level B3LYP/6-31G(d,p) [80-83].

Reference:

[80] Becke, A.D. Density-functional thermochemistry. III. The role of exact exchange. J. Chem. Phys. 1993, 98, 5648–5652.
[81] Stephens, P.J.; Devlin, F.J.; Chabalowski, C.F.; Frisch, M.J. Ab Initio Calculation of Vibrational Absorption and Circular Dichroism Spectra Using Density Functional Force Fields. J. Phys. Chem. 1994, 98, 11623–11627.
[82] Becke, A.D. Density-functional exchange-energy approximation with correct asymptotic behavior. Phys. Rev. A 1988, 38, 3098–3100.
[83] Lee, C.; Yang, W.; Parr, R.G. Development of the Colle-Salvetti correlation-energy formula into a functional of the electron density. Phys. Rev. B 1988, 37, 785–789.

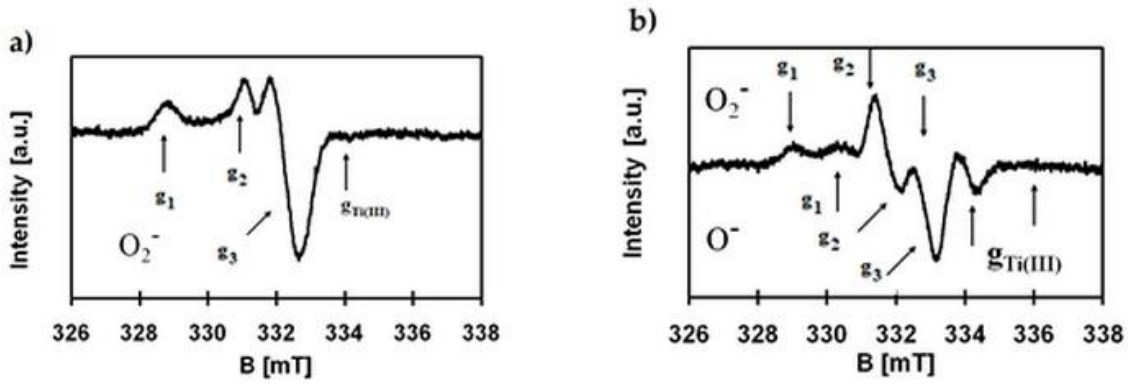


Figure S3. EPR spectra of powdered TOCs (a) and PMMA + (**1**) wt.20% composite (b) of TOCs. Some experimental conditions: room temperature, microwave frequency: 9.31648 GHz (a) 9.32357 GHz (b); modulation amplitude: 1 mT; sweep: 20 mT; sweep time: 4 min.; time constant: 0.1 s; receiver gain: 4 $x10^5$.

P5. *Investigation of Titanium(IV) – Oxo Complexes Stabilized with α-Hydroxy Carboxylate Ligands: Structural Analysis and DFT Studies.*

Dalton Transactions

ROYAL SOCIETY OF CHEMISTRY

PAPER

View Article Online
View Journal

Published on 02 August 2024. Downloaded by Uniwersytet Mikolaja Kopernika on 8/19/2024 9:35:51 AM.

Check for updates

Cite this: DOI: 10.1039/d4dt01710b

Investigation of titanium(IV)-oxo complexes stabilized with α-hydroxy carboxylate ligands: structural analysis and DFT studies†

Barbara Kubiak, *[a] Tadeusz Muzioł, [a] Mirosław Jabłoński,[b] Aleksandra Radtke[a] and Piotr Piszczek *[a]

Received 12th June 2024,
Accepted 25th July 2024

DOI: 10.1039/d4dt01710b

rsc.li/dalton

This paper explores the findings on the structures and physicochemical properties of titanium-oxo complexes (TOCs) stabilized by 9-hydroxy-9-fluorenecarboxylate ligands. Two complexes, with the overall formulas $[Ti_4O(O^iPr)_{10}(O_3C_{14}H_8)_2]$ (**1**) and $[Ti_6O_4(O^iPr)_2(O_3C_{14}H_8)_4(O_2CEt)_6]$ (**2**), have been synthesized. The structures of the isolated crystals (**1** and **2**) were determined using single-crystal X-ray diffraction. Molecular structure analysis of the crystals also employed vibrational spectroscopic techniques (IR and Raman), UV–Vis diffuse reflectance spectroscopy (UV–Vis–DRS), and powder X-ray diffraction (XRD). Density functional theory (DFT) was utilized to elucidate the electronic structures of these complexes. Furthermore, the theoretical charge distribution in **1** and **2** and their reactivity were calculated. The results of these investigations suggest that the reactivity of **2** is significantly greater than that of **1**.

Introduction

The exceptional properties of titanium dioxide (TiO_2) have led to widespread applications of TiO_2-based materials in various aspects of daily life. Due to their non-toxic nature, limited chemical reactivity, and notable photocatalytic and antimicrobial capabilities[1–4] these materials play a crucial role in decomposing organic pollutants through photocatalytic processes. This makes them highly effective in water purification, air cleansing, surface decontamination, and even in antibiotic elimination technologies.[5–8] Beyond their photocatalytic prowess, TiO_2-based materials are attracting significant attention for their bioactivity.[9–12] A factor hindering broader utilization of these materials in modern technologies is their activity being confined to ultraviolet light,[1,3] which is associated with relatively large bandgap values of 2.9 and 3.2 eV for rutile and anatase, respectively.[13] Consequently, current research focuses on modifying TiO_2-based materials to increase their photocatalytic and bactericidal activity in visible light.[2,4,12,14,15] One proposed solution to address this issue involves the utilization of multinuclear titanium(IV)-oxo complexes (TOCs).[16–26] These compounds are mainly synthesized by reacting Ti(IV) alkoxides with organic or phosphonic acids using either traditional or solvothermal methods.[27,28] The formation of the $\{Ti_aO_b\}$ core is influenced by factors such as the type of titanium alkoxide, stabilizing ligands, reactant ratios, reaction temperature, and solvent choice.[27–29] Research has shown that the type of stabilizing ligand (mainly carboxylate or phosphonate) significantly impacts the HOMO–LUMO energy gap and photocatalytic properties.[30–32] Our previous studies on TOCs with $\{Ti_4O_2\}$ cores highlighted the effectiveness of 9-fluorenecarboxylate ligands. Among complexes stabilized with 3-chlorobenzoic, 3-nitrobenzoic, 9-fluorenecarboxylate, 4-aminobenzoic, and 4-hydroxybenzoic ligands, the cluster stabilized by 9-fluorenecarboxylate ligands had the narrowest HOMO–LUMO gap (2.55 eV), making it photocatalytically active in visible light.[33] Studies of TOC structures with $\{Ti_aO_b\}$ cores (a = 3, 4, 6; b = 1, 2, 4, 6) stabilized with the aforementioned ligand showed photocatalytic activity under both UV and visible light. The activity varied depending on the core structure as follows: $\{Ti_6O_6\} > \{Ti_4O_2\} > \{Ti_3O\} > \{Ti_6O_4\}$.[34]

In this study, we focused on synthesizing crystals of oxo complexes resulting from the reaction between titanium isopropoxide and 9-hydroxy-9-fluorenecarboxylic acid. We characterized their structural properties and stability, particularly in an aqueous environment. We investigated the structural and electronic properties, as well as potential reactivity, using density functional theory (DFT).

[a]Department of Inorganic and Coordination Chemistry, Faculty of Chemistry, Nicolaus Copernicus University in Toruń, Gagarina 7, 87-100 Toruń, Poland. E-mail: basiak0809@gmail.com
[b]Department of Quantum Chemistry and Atomic Spectroscopy, Faculty of Chemistry, Nicolaus Copernicus University in Toruń, Gagarina 7, 87-100 Toruń, Poland

†Electronic supplementary information (ESI) available. CCDC 2284906 and 2284900. For ESI and crystallographic data in CIF or other electronic format see DOI: https://doi.org/10.1039/d4dt01710b

Published on 02 August 2024. Downloaded by Uniwersytet Mikolaja Kopernika on 8/19/2024 9:35:51 AM.

Experimental section

Materials

Titanium(IV) isopropoxide (Aldrich, St Louis, MO, USA), 9-hydroxy-9-fluorenecarboxylic acid (Aldrich, St Louis, MO, USA), and propionic acid (PA) (Warchem, Warsaw, Poland) were purchased commercially and used without further purification. All solvents (tetrahydrofuran and isopropanol) used in our experiments were distilled before use and stored under an argon atmosphere.

Methods

The crystalline powders of compounds **1** and **2** were characterized using infrared spectrophotometry, specifically with the FT-IR Vertex 70V infrared spectrophotometer (Bruker Optik GmbH, Ettlingen, Baden-Württemberg, Germany). The analysis primarily focused on the spectra within the 400–2000 cm^{-1} range, where vibrational bands of coordinated functional groups such as –OOC, –OR, –OC, and Ti–O–Ti are observed. Spectra were recorded for KBr pellets of the tested compounds. Furthermore, samples of compounds **1** and **2** were subjected to examination using the Raman microscopy method, utilizing the RamanMicro 200 microscope (PerkinElmer, Waltham, MA, USA). Raman spectra were recorded employing a laser with a wavelength of 785 nm and a maximum power of 350 mW within the range of 200–2200 cm^{-1}. This was achieved using a 20× 0.40/FN22 objective with an exposure time of 15 seconds for each recording. The ^{13}C NMR spectra in the solid phase were recorded on a Bruker Avance 700 MHz spectrometer (Madison, WI, USA), with a spectral width of 76 923.08 Hz and 4096 complex points. Elemental analyses were performed on a Vario Macro CHN Elemental Analyser (Elementar Analysensysteme GmbH, Langenselbold, Germany). Diffuse reflectance UV-Vis (UV-VIS-DRS) spectroscopy was used to determine the absorption maximum and the HOMO–LUMO gap between 200 and 800 nm. For this purpose, the Jasco V-750 spectrophotometer (JASCO Deutschland GmbH, Pfungstadt, Germany) was used.

Synthesis of $[Ti_4O(O^iPr)_{10}(O_3C_{14}H_8)_2]$ (1)

0.20 g of 9-OH-9-fluorenecarboxylic acid (0.875 mmol) was dissolved in 1 ml of a mixture of tetrahydrofuran/isopropanol (THF/HO^{i}Pr) (1 : 1) and mixed with 1 mL of a solution of titanium(IV) isopropoxide (3.5 mmol) in 1 mL of THF/HO^{i}Pr (1 : 1), leading to a clear yellow solution. The reaction was carried out at room-temperature (RT), using a glovebox under an argon atmosphere. The solution was left for crystallization (1 day). The yield calculated based on Ti was 26%. The titanium content was determined as that of TiO_2, according to the Meth-Cohn *et al.* method.[35] Anal. Calc. for $C_{58}H_{86}O_{17}Ti_4$: C, 55.86; H, 6.90; Ti, 15.41. Found: C, 56.07; H, 7.01; Ti, 15.64. ^{13}C NMR (solid state, 295 K, δ [ppm]): 10.4, 22.3 (CH_3), 30.5 (CH), 52.9 61.0, 72.7, 78.9 ((Ph)C(Ph)), 97.4, 119.8, 129.7, 140.6, 148.3, 188.2, 197.7 (C(Ph)), 208.4, 215.8 (COO). FT IR (KBr pallet, 295 K, ν [cm^{-1}]): ν_{as}(COO) 1632 (s), 1609 (s), ν(CC), ν_s(COO) 1498 (m), 1474 (w), δ(CH_2), δ(CH_3) 1449 (m), 1364 (w), 1281 (m), ν(CO) 1204 (m), ν(COR) 1156 (w), 1107 (m), 1051 (m), 1004 (w), ν(Ti–O–Ti) 782 (m), 771 (w), δ(CCC) 737 (s), δ(COO) 529 (m); Raman (solid state, 295 K, Raman shift [cm^{-1}]): ν_{as}(COO) 1600 (s), 1498 (m), 1450 (m), (ν(CC)) 1595 (w), (ν_s(COO)) 1485 (m), (δ(CH_2, δ(CH_3) 1407 (m), 1358 (m), 1292 (m), ν(CO) 1216 (m), 1200 (m), ν(COR)) 1178 (m) 1158 (m), 1117 (m), 1020 (s), ν(Ti–O–Ti)) 550 (m).

Synthesis of $[Ti_6O_4(O^iPr)_2(O_3C_{14}H_8)_4(O_2CEt)_6]$ (2)

0.20 g of 9-OH-9-fluorenecarboxylic acid (0.875 mmol) and 0.33 mL of propionic acid (4.38 mmol) were dissolved in 1 mL of THF and mixed with a solution of 1.24 mL of titanium(IV) isopropoxide (4.38 mmol) in 1 mL of THF, leading to a clear brown solution. The reaction was carried out at 70 °C, using a glovebox under an argon atmosphere. The solution was left for crystallization (5 days). The yield calculated based on Ti was 22%. The titanium content was determined as that of TiO_2, according to the Meth-Cohn *et al.* method.[35] Anal. Calc. for $C_{80}H_{76}O_{30}Ti_6$: C, 53.22; H, 4.21; Ti, 15.96. Found: C, 53.19; H, 4.36; Ti, 15.77. ^{13}C NMR (solid state, 295 K, δ [ppm]): 9.4, 21.3, 29.5 (CH_3), 51.6 (CH_2) 57.1 (CH), 58.4, 62.3, 72.1, 78.2 ((Ph)C(Ph)), 88.1, 98.3 (COO), 119.8, 125.2, 129.3, 140.1, 143.3, 177.6, 185.3, 193.1, 198.0 (C(Ph)), 208.4, 214.2 (COO). FT IR (KBr pallet, 295 K, ν [cm^{-1}]): ν_{as}(COO), 1711 (m), ν_{as}(COO) 1510 (s), (ν(CC), ν_s(COO)) 1465 (m), 1450 (m), δ(CH_2, δ(CH_3)), 1434 (s), 1378 (m), ν_s(COO) 1298 (m), ν(CO) 1216 (s), 1200 (m), ν(COR) 1165 (w), 1115 (m), 1105 (m), 1083 (m), 1023 (s), (ν_s(Ti–O–Ti)) 778 (m), 764 (m), δ(CCC) 738 (s), 724 (s), δ(COO) 560 (m), 536 (m); Raman (solid state, 295 K, Raman shift [cm^{-1}]): ν_{as}(COO) 1715 (w), ν_{as}(COO) 1606 (s), (ν(CC)) 1596 (w), (ν_s(COO)) 1495 (m), δ(CH_2), δ(CH_3) 1450 (m), 1350 (m), 1328 (w), (ν(CO), ν(COR)) 1175 (m) 1154 (m), 1113 (m), 1022 (m), ν(Ti–O–Ti) 475 (w), 447(w).

Crystallography

The diffraction data for both compounds were collected at 100 K on a Rigaku XtaLAB Synergy (Dualflex) diffractometer with a HyPix detector with a monochromated CuKα X-ray source (λ = 1.54184 Å). Data processing and absorption correction were performed using CrysAlisPro.[36] For **1** the extinction parameter was also refined. The direct methods were used and refinement was carried out with the full-matrix least-squares procedure on F^2 (SHELX-97).[37] Heavy atoms were refined with anisotropic displacement parameters. In contrast, hydrogen atoms were assigned at calculated positions with thermal displacement parameters fixed to a value of 20% or 50% higher than those of the corresponding carbon atoms. Positional disorder was observed for O61 $^-$O^{i}Pr anions in **1** with two sets equally populated (0.5 : 0.5) and the methyl group of the O61 propionate anion in **2** also with identical (0.5) occupancies for both atom sets. In **2**, some restraints were applied for thermal parameters (DELU) of the disordered O61 propionate. In **2**, the BYPASS procedure implemented in Olex2 [38] was used for the poorly defined electron density in the solvent region. All figures were prepared in DIAMOND.[39] The data collection and refinement results have been summarized in Table S1, and

 This journal is © The Royal Society of Chemistry 2024

Published on 02 August 2024. Downloaded by Uniwersytet Mikolaja Kopernika on 8/19/2024 9:35:51 AM.

selected bond lengths and angles are presented in Table S2.† CCDC 2284906 and 2284900 contain supplementary crystallographic data for **1** and **2**, respectively.

XRD measurements

Powder XRD experiments were performed on a Rigaku XtaLab Synergy (Dualflex) diffractometer equipped with a HyPix detector and using monochromated CuKα X-ray radiation (λ = 1.54184 Å). The diffractometer worked in powder diffraction mode and data were collected in the 2θ range of 4–50° with an exposure time of 240 s per frame.

Theoretical research methodology

The crystallographically determined structures of complexes **1** and **2** were used as preliminary ones in the optimization procedure carried out at the B3LYP/6-31G(d,p) level of theory, *i.e.* using the B3LYP exchange–correlation functional[40,41] of density functional theory (DFT)[42,43] and the 6-31G(d,p) basis set.[44] Then, a frequency analysis was performed to verify that the minima were found indeed. The obtained geometries were then used to determine the theoretical IR, Raman, and UV-VIS spectra, as well as the HOMO and LUMO, Hirshfeld atomic charges[45] and molecular electrostatic potential (MEP) maps. The UV-VIS spectra were determined using TD-DFT (*i.e.* the time-dependent DFT) utilizing diffuse functions needed in excited state calculations. To quantify the reactivity of compounds **1** and **2**, various reactivity indices derived from the so-called conceptual DFT[46–48] were also computed at the (B3LYP)/6-31+G(d,p)//B3LYP/6-31G(d,p) level of theory. Instead of the less reliable calculations based on the HOMO and LUMO energies, these calculations were made using cation and anion total energies within the vertical approximation.[49] Having the values of the ionization potential (I) and electron affinity (A), one can then calculate the electronic chemical potential ($\mu = -1/2(I + A)$), which describes the tendency of a system to gain or lose electrons.[50,51] This quantity with a minus sign gives the absolute electronegativity χ. From the difference of I and A, one can obtain chemical hardness (η), describing the rate of change of μ with electron density, and therefore the resistance towards electron cloud polarization.[50,51] Thus, it is a good measure of molecular reactivity. In turn, its inverse gives the chemical softness σ. Finally, the ratio $(I + A)^2/8(I - A)$ defines the electrophilicity index (ω), which determines the capacity of an electrophile to receive electrons from a nucleophile.[52,53] Its reciprocal is the nucleophilicity index (ε). All calculations were performed using the Gaussian 16 program package,[54] and the GaussView 6 program[55] was used to visualize some of the results.

Results and discussion

Synthesis and structural studies of oxo complexes

The synthesis of compound **1** involved the reaction between titanium(IV) isopropoxide and 9-OH-9-fluorenecarboxylic acid ($HO_3C_{14}H_9$) as the primary reagents. $Ti(O^iPr)_4/HO_3C_{14}H_9$ with a molar ratio of 4 : 1 and a solvent mixture of THF/HO^iPr (1 : 1) were used. Compound **2** was isolated from the reaction mixture containing 9-OH-9-fluorenecarboxylic acid, propionic acid, and titanium(IV) isopropoxide. The molar ratio of Ti $(O^iPr)_4$ to organic acids was 1 : 1.2. THF was the solvent employed, and the reaction occurred at 70 °C. The molecular structure of the isolated crystals was determined through single-crystal X-ray diffraction. Detailed results are presented in Fig. 1–4.

The structure of $[Ti_4O(O^iPr)_{10}(O_3C_{14}H_8)_2]$ (1)

The analysis of X-ray diffraction data revealed that $[Ti_4O(O^iPr)_{10}(O_3C_{14}H_8)_2]$ (**1**) crystallizes in the monoclinic $C2/c$ space group. As given by the formula above, half of the molecule is present in the asymmetric unit, and the O16 oxo anion is located at the twofold axis. Four Ti(IV) cations form a torsion angle of −60.25° with Ti1–Ti2, and the Ti1–Ti1 [$1 - x$, y, $1.5 - z$] distances are 3.3510(5) and 3.4643(7) Å, respectively. The Ti1 ions form the central part, while Ti2 is lateral. They differ significantly because Ti1 is found in an octahedral environment, whereas for Ti2, a pentacoordinate geometry was detected (Fig. 1).

In the latter case, a square pyramidal environment was detected (τ_5 = 0.02)[56] with Ti2 shifting by 0.531 Å from the base toward the apical O61 atom, forming the shortest bond (1.778(2) Å). The Ti2 coordination sphere consists of three oxygen atoms from isopropylate anions (two terminal and one bridging) and two oxygen atoms from α-hydroxycarboxylate ligands. The basal Ti2–O distances range from 1.7819(19) Å to 2.0651(15) Å (Table S2†). For Ti1, the coordination sphere consists of three oxygen atoms from isopropylate anions (two terminal and one bridging), two oxygen atoms from α-hydroxycarboxylate ligands, and an oxygen atom from the oxo anion, with Ti1–O bond lengths ranging from 1.7921(15) to 2.2274(15) Å. Ti1 and Ti2 cations, separated by 3.3510(5) Å, are connected by asymmetric O21 isopropylate bridges and α-hydroxycarboxylate ligands, whereas central Ti1 cations, sep-

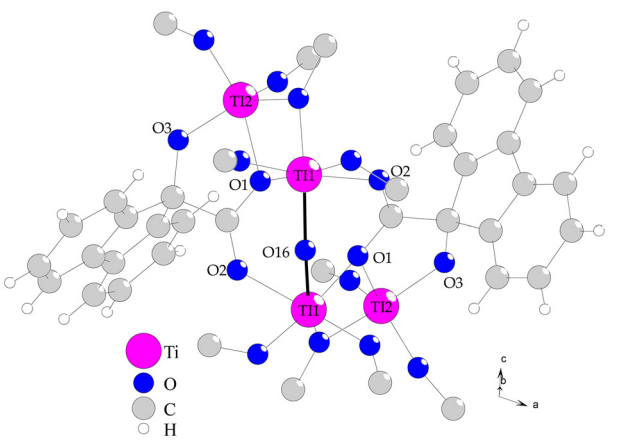


Fig. 1 Structure of $[Ti_4O(O^iPr)_{10}(O_3C_{14}H_8)_2]$ (**1**) (a) as a ball and stick model. For clarity of the figure for the $^iPrO^-$ anions, carbon chains are not shown. Atom labels for titanium and oxygen atoms are given.

Published on 02 August 2024. Downloaded by Uniwersytet Mikolaja Kopernika on 8/19/2024 9:35:51 AM.

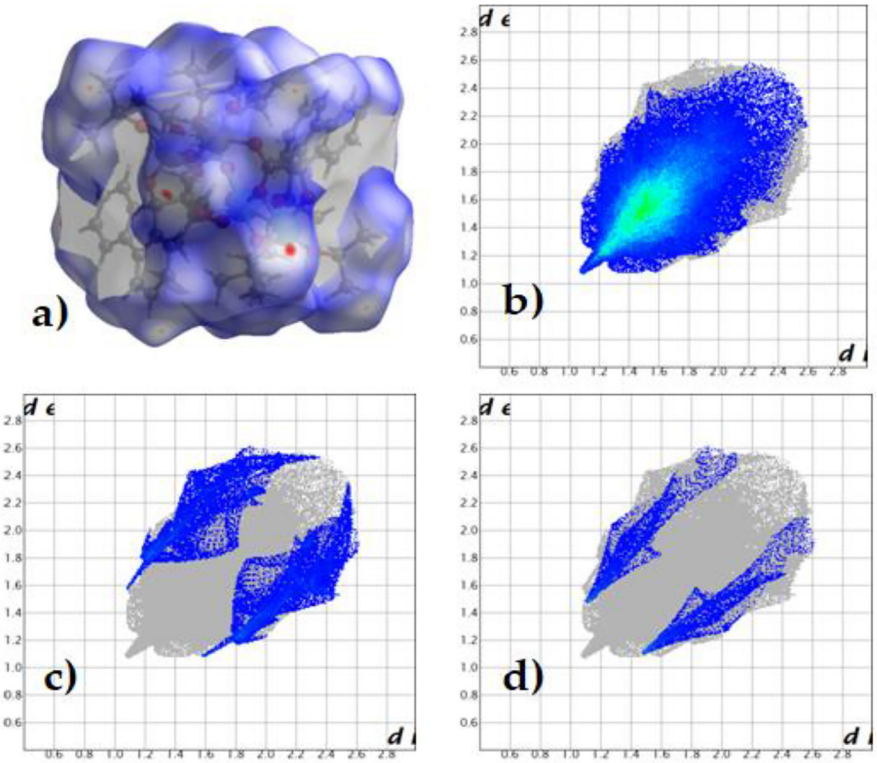


Fig. 2 (a) Hirshfeld surface of **1** with all projected interactions, the fingerprints for (b) H···H (83.9%), (c) for C···H (11.5%), and (d) for O···H (4.6%).

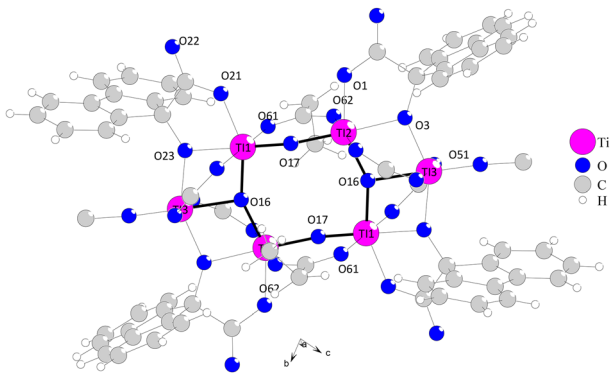


Fig. 3 Structure of $[Ti_6O_4(O^iPr)_2(O_3C_{14}H_8)_4(O_2CEt)_6]$ (**2**) (a) as a ball and stick model. For clarity of the figure for the $^iPrO^-$ anions, carbon chains are not shown. The structure presents only the main conformations. Atom labels for titanium and oxygen atoms are given.

arated by 3.4643(7) Å, are connected by carboxylic groups of two α-hydroxy acid anions and the only O16 oxo anion, forming a Ti1–O16–Ti1 $[1 - x, y, 1.5 - z]$ angle of 142.49(12)°.

Hence, in this structure, the oxo anion couples two titanium(IV) cations, while the α-hydroxycarboxylate (its carboxylic group) forms μ_3 bridges with two aromatic systems inclined by 59.0°. The packing is dense and shows *ab* layers (Fig. S1†). Hirshfeld surface analysis shows weak interactions dominating the landscape of the formed interactions (Fig. 2). However, no significant O···H interactions were detected, which could be considered an intermolecular hydrogen bond. It is notable that the reaction between $Ti(O^iPr)_4$ and 9-OH-9-fluorenecarbocylic acid yielded a Ti(IV)-oxo complex containing the $\{Ti_4O\}$ core.

What sets this complex apart is its unique core structure compared to those of previously documented oxo complexes with a similar configuration (Scheme 1(a) and (b)).[28,57,58] These types of cores mainly consisted of tetrahedral oxo bridges of the Ti_4-(μ_4-O) type (Scheme 1(a)).[28,58,59] They were stabilized not only by phosphonate ligands but also by other ligands, *e.g.* alkoxides ($[Ti_4O(O^iPr)_6(DTBC)_4]$ (DTBC = 3,5-di-*tert*-butylcatechol)[60]), azides ($[Ti_4O(O^iPr)_{10}(\mu\text{-}N_3)_4]$[61]), and oximes ($Ti_4O(OMe)_6(L1)_4$ (L1 = salicylaldoxime)[62]). Another method of creating the $\{Ti_4O\}$ core was noted by Czakler *et al.* (Scheme 1(b)), where the core is formed by Ti_3-(μ_3-O) bridges connected to the fourth Ti(IV) ion by a phosphonate ligand.[67] In the structure of **1**, the $\{Ti_2O\}$ core is connected to the other two Ti(IV) ions through the oxygen atoms of the 9-OH-9-fluorenecarboxylate ligands (Fig. 1).

According to previous results, the coordination number of all Ti(IV) ions forming the $\{Ti_4O\}$ core was six. However, in the structure of **1**, the coordination number of Ti(IV) forming the Ti_2-(μ-O) bridge is six, while the remaining two have a coordination number of five. Moreover, it should be noted that the 9-OH-9-fluorenecarboxylate ligands are involved in the formation of chelate bridges with titanium ions.

This journal is © The Royal Society of Chemistry 2024

Published on 02 August 2024. Downloaded by Uniwersytet Mikolaja Kopernika on 8/19/2024 9:35:51 AM.

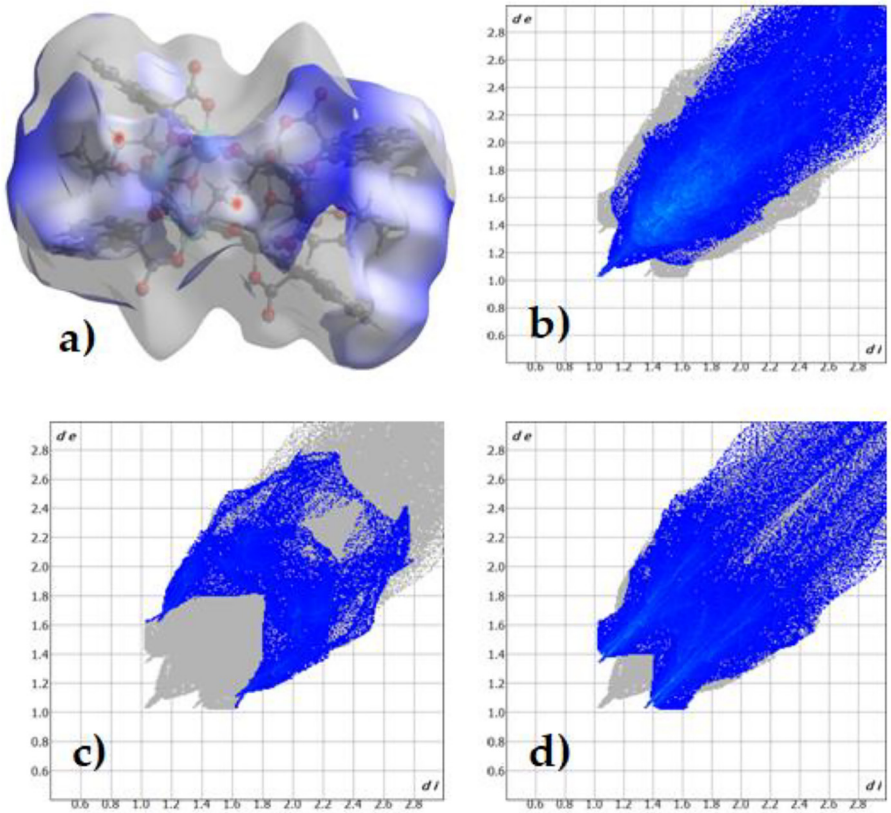
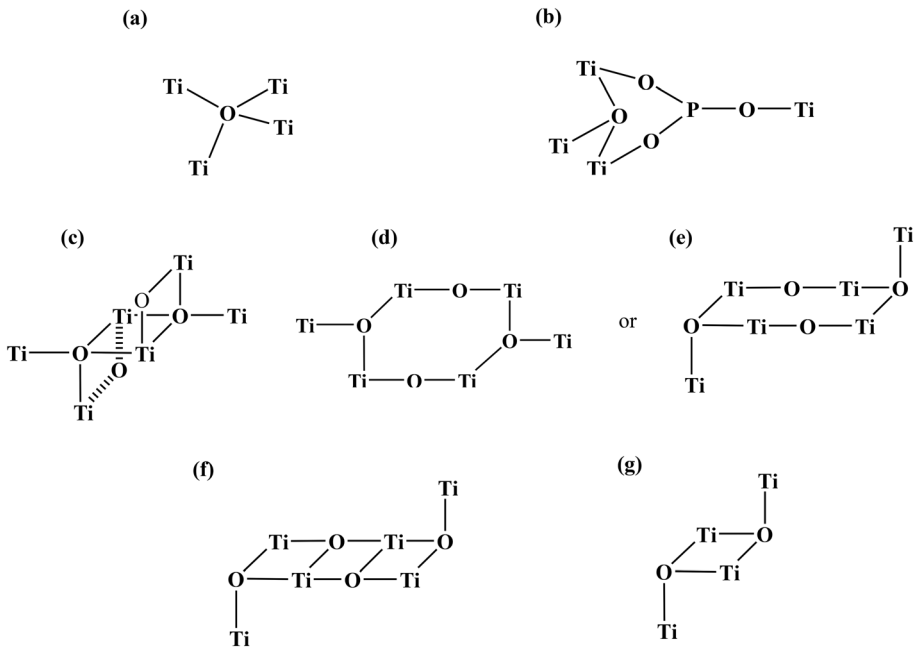


Fig. 4 (a) Hirshfeld surface of **2** with all projected interactions shows a prevailing blue color. The fingerprints for (b) H···H (55.2%), (c) C···H (10.8%), and (d) O···H (30.2%).



Scheme 1 The different types of oxygen interactions in $\{Ti_aO_b\}$ cores: (a) $\{Ti_4O\}$ $[Ti_4O(OEt)_{12}(O_3PR'')]$ (R'' = ^{t}Bu, Ph) and $[Ti_{10}O_2(OR)_{32}(O_3PR'')_2]$,[28] (b) $[Ti_4O(O^iPr)_8(O_3P\text{-allyl})_3(dmso)]$;[57] (c) $\{Ti_6O_4\}$ $[Ti_6O_4(OR)_{14}(O_2R'')_2]$,[28] (d) $[Ti_6O_4(OR)_{12}(O_2R'')_4]$,[28] $[Ti_6O_4(OR)_{10}(O_2R')_2(O_3PR'')_2]$,[63] (e) $[Ti_6O_4(OR)_8(O_2R'')_8]$,[28] (f) $[Ti_6O_4(OR)_{12}(O_2R'')_4]$, $[Ti_6O_4(OR)_{10}(O_2R'')_6]$;[28] and (g) $\{Ti_4O_2\}$ $[Ti_8O_2(OR)_{20}(O_3R'')_4]$.[64] For the clarity of the figure alkoxide and carboxylate ligands are not shown.

Published on 02 August 2024. Downloaded by Uniwersytet Mikolaja Kopernika on 8/19/2024 9:35:51 AM.

The structure of $[Ti_6O_4(O^iPr)_2(O_3C_{14}H_8)_4(O_2CEt)_6]$ (2)

Due to the significantly lower quality of the crystals (despite repeated attempts to synthesize and adjust reaction conditions) than that of compound (**1**), the structural quality of $[Ti_6O_4(O^iPr)_2(O_3C_{14}H_8)_4(O_2CEt)_6]$ (**2**) is much worse, leading to the loss of clear diffraction patterns. This is likely caused by disordered solvent molecules (see the Experimental section). As a result, we will not focus on detailed measurements of bond lengths and valence angles (these values are also listed in Table S1†). Nonetheless, the primary characteristics of compound **2** can still be identified and discussed. This complex crystallizes in the triclinic $P\bar{1}$ space group, with half of the molecule represented by the aforementioned formula in the asymmetric unit. The metallic core comprises six titanium(IV) cations arranged in two nearly coplanar triangles. In the Ti_3 motif, the titanium(IV) cations are interconnected by a μ_3-oxo bridge, two α-hydroxycarboxylate groups, and two carboxylate groups from propionate anions (Fig. 3). Both triangles are linked by two μ-oxo bridges and two propionate anions. As a result, all carboxylate anions contribute to coupling adjacent Ti(IV) cations in this structure. The Ti–Ti distances measure 3.1182(18) Å (Ti1–Ti3), 3.1185(15) Å (Ti2–Ti3), and 3.6723(17) Å (Ti1–Ti2) within the triangle, with a distance of 3.4246(16) Å between triangles (Ti2–Ti1 [$1 - x$, $2 - y$, $1 - z$]). The effect of $\{Ti_6O_4\}$ core formation is frequently observed in TOC structures, and potential variations in the Ti–O bond arrangement are depicted in Scheme 1(c)–(f).[28,65–68] It should be noted that this type of system can be formed by both Ti(IV) complexes and mixed-metal oxo clusters.[69] In addition to alkoxide ligands, $\{Ti_6O_4\}$ cores were also stabilized with carboxylate, silicate, or sulphate ligands.[59] Our previous studies showed that a similar type of core was formed for the $[Ti_6O_4(BuiO)_8(O_2CC_{13}H_9)_8]\cdot Me_2CO$ ($O_2CC_{13}H_9$ = 9-fluorenecarboxylate ligands) complex, but its structure was different from that of complex **2** (Fig. S3†).[34] These discrepancies are noticeable in the Ti(IV) connections within the triangles. The described structure of the oxo complex stabilized with 9-fluorenecarboxylate ligands contains only two terminal isopropoxy ligands, while the –OR groups can serve as bridges. Modification of the synthesis conditions and the introduction of two different carboxylic acids into the reaction mixture led to changes in the structure of the $\{Ti_6O_4\}$ core and its interactions with the immediate environment (Fig. S3†). It is notable that in the structure of compound **2**, the 9-OH-9-fluorenecarboxylate ligands form a chelate ring but one –C═O group in every carboxylate remains uncoordinated and can be exposed to the solvent. Moreover, the coordination number for all titanium atoms remains at six. This allows us to distinguish the structure of **2** from that of **1** and also from that of the previously synthesized oxo complex stabilized with mandelate ligands (Scheme 1(g)). In the last case, the central unit is formed by a $\{Ti_4O_2\}$ core connected by mandelate anions to two side $\{Ti_2\}$ dimers.[64]

The packing of $[Ti_6O_4(O^iPr)_2(O_3C_{14}H_8)_4(O_2CEt)_6]$ (**2**) molecules in the crystal network shows some voids accounting for 395.8 $Å^3$ (17.5% of the cell volume) related to the BYPASS procedure applied for this region (Fig. S2†). In **2**, the crystal network is maintained by multiple π–π interactions, particularly stacking interactions usually formed by C23 rings. These weak interactions dominate the landscape of the contacts formed (Fig. 4). The most numerous and relatively short interactions are H···H interactions, indicated by red spots on the surface. Additionally, the molecules form intermolecular C–H···O hydrogen bonds, utilizing the oxygen atoms of the hydroxycarboxylate group (O1, O2, O21, and O22 atoms). In contrast, in **1**, the oxygen atoms are buried and do not form numerous contacts. In **2**, these contacts are more abundant, as indicated by the tiny spikes on the fingerprint (Fig. 4d).

The spectral characterization of 1 and 2

Structural differences between the tested oxo complexes were also confirmed through analysis of their IR and Raman spectra. The formation of carboxylate bridges coordinated with Ti(IV) atoms in the structure of **1** is confirmed by the appearance of bands at 1632, 1609, and 1449 cm^{-1}, which originate from the asymmetric and symmetric stretching vibrations of –COO groups (ν_{as}(COO) and ν_s(COO)). The IR spectrum of complex **2** (Fig. S4†) indicates the presence of two different carboxyl groups with distinct coordination modes. This is evidenced by the bands at 1711 and 1298 cm^{-1} for unidentate 9-OH-9-fluorenecarboxylate ligands, and at 1510 and 1434 cm^{-1} for bridging propionate ligands (for ν_{as}(COO) and ν_s(COO), respectively).[70] Assigning vibration bands for the Ti–O–Ti bridge is challenging due to overlaps with bands from organic ligand functional groups below 1000 cm^{-1} in the IR and Raman spectra. DFT calculations were used to predict the frequencies of normal vibrations for the Ti–O–Ti bridges in the $\{Ti_4O\}$ (**1**) and $\{Ti_6O_4\}$ (**2**) cores, with geometries optimized using Gaussian16, employing the B3LYP exchange–correlation functional and the 6-31G(d,p) basis set. The experimental data are compared with computational results in Table 1. Vibrations for Ti_2-(μ-O) bridges (C_{2v} symmetry) in the structures of **1** and **2**, and Ti_3-(μ_3-O) bridges (C_{2v} symmetry) in the structure of **2**, are active in both IR and Raman spectra. Nonlinear M–O–M bridges have bands at 730–772 cm^{-1} (stronger in IR) and 497–540 cm^{-1} (stronger in Raman).[70] DFT calculations suggest that Ti–O–Ti vibrations appear at 740 and 795 cm^{-1}, and 538 and 434 cm^{-1}, in the IR and Raman spectra for (**1**) and (**2**), respectively. Therefore, the bands at 782 cm^{-1} (IR) and 550 cm^{-1} (Raman) in the spectrum of **1** were assigned

Table 1 Experimental and calculated frequencies of stretching modes of Ti–O–Ti bridges

	(1) (C_{2v})				(2) (C_{2v})			
	IR		Raman		IR		Raman	
Modes	Exp.	Calc.	Exp.	Calc.	Exp.	Calc.	Exp.	Calc.
ν(Ti–O–Ti)	782 (m)	740	550 (m)	538	778 (m) 764 (m)	795	475 (w) 447 (w)	434

This journal is © The Royal Society of Chemistry 2024

Published on 02 August 2024. Downloaded by Uniwersytet Mikolaja Kopernika on 8/19/2024 9:35:51 AM.

to Ti–O–Ti stretching modes. In the spectrum of **2**, the bands at 778 and 764 cm^{-1} (IR), and 475 and 447 cm^{-1} (Raman), correspond to the stretching vibrations of Ti_2-(μ-O) and Ti_3-(μ_3-O) bridges.

The solid-state UV-Vis DRS spectra of **1** and **2** were analysed using magnesium oxide as the reference sample. The Kubelka–Munk (K–M) function, plotted against light energy ($K = f(h\upsilon)$, where $K = (1 - R)^2/2R$ and R represents reflectance), was utilized to determine the HOMO–LUMO gap. The results of these investigations are depicted in Fig. 5. Absorption maxima were observed at 306 nm for **1** and at 330 and 395 nm for **2** (Table 2). This result is in qualitative agreement with the calculated λ_{max} values, which are 283 nm for **1** and 420 nm for **2**. Moreover, calculations have shown that in the case of **1** the most intense transition at λ = 283 nm is mainly associated with the following excitation: H → L+6 (18.0%), H−1 → L+8 (14.4%), and H−1 → L+7 (12.4%).

In the case of **2**, in addition to the presence of two excited states in the closest vicinity of the maximum (*i.e.* 418 nm with the dominant H−3 → L+2 transition (38.4%) and 420 nm with the main contribution H → L+2 (38.3%)) the theoretical spectrum also shows other excited states at longer wavelengths. The most intense of them are located at 427 nm (with dominant excitation of the types H−3 → L (47.6%) and H−2 → L+1 (33.6%)) and at 442 nm (H−2 → L+1 (46.5%) and H−3 → L (39.3%)). Although shifted, they may correspond to the lower experimental band at 395 nm. The designated HOMO–LUMO gap values were 2.96 eV for **1** and 2.39 eV for **2** (Fig. 5(b)). Although the theoretical HOMO–LUMO gap values are larger (4.31 eV for **1** and 3.21 eV for **2**), they qualitatively agree with the experimental results, indicating that this gap is evidently smaller for **2**. The results of these investigations show that in the case of **2** the absorption edge is shifted towards visible light (up to approximately 395 nm) compared to that of compound **1** (around 306 nm). This effect aligns with the research conducted by Liu *et al.* where functionalization of TOCs with ferrocene led to a shift in the absorption maximum from 330 nm to 500 nm, accompanied by a reduction in the HOMO–LUMO gap from E_a = 3.14 eV to E_a = 1.83 eV.[71] Based on these results, it can be assumed that complex **2** should be more active, *e.g.*, photocatalytically during irradiation with visible light.

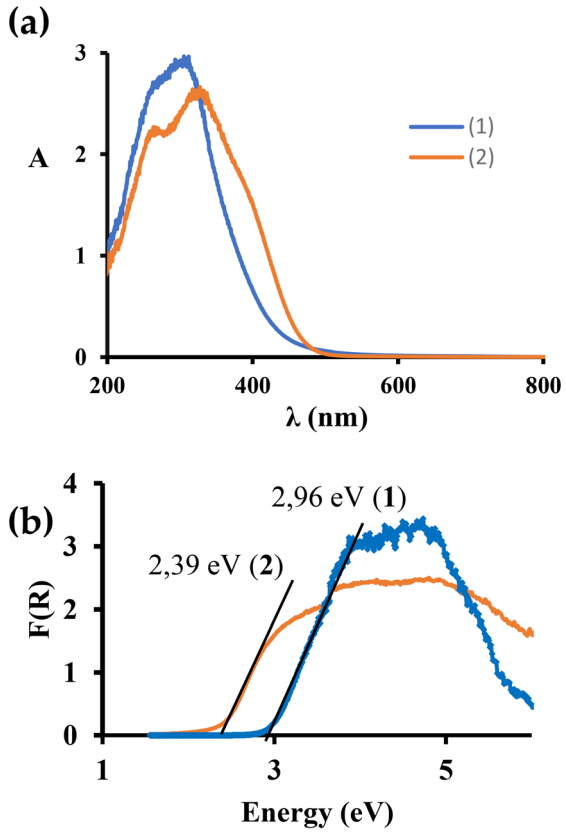


Fig. 5 Solid-state UV-Vis-diffuse reflectance spectra (DRS) of the **1** and **2** micro-grains (a) and Kubelka–Munk function *versus* light energy plot for HOMO–LUMO gap determination (b).

Table 2 The experimental and calculated (B3LYP/6-31++G(d,p)) UV-Vis spectra of **1** and **2**

	(1)		(2)	
	UV-Vis-DRS			
	Exp.	Calc.	Exp.	Calc.
λ_{max} (nm)	306	283	330 395	420

The powder XRD investigations aimed to determine the susceptibility of compounds **1** and **2** to hydrolysis. Fig. 6 presents the XRD patterns of the synthesized compounds, recorded before and after immersion in distilled water for 72 hours. Both diffractograms were compared with the standard calculated in ref. 72. The results showed no significant differences in the patterns before and after water immersion. The similarity between these diffractograms indicates that the core structure is preserved, and no significant transformation towards crystalline TiO_2, amorphous species, or other crystalline forms related to the rearrangement of titanium coordination spheres and topologies is detected.

The results of theoretical calculations

The theoretical analysis revealed that in both systems, the HOMOs are primarily localized on aromatic fragments, whereas the LUMOs are predominantly associated with titanium atoms (Fig. 7). Specifically, in system **1**, approximately 97% of the contribution to the HOMO arises from two fluorene fragments. Within these fragments, the largest contributions (7.6–7.7% each) originate from the outer carbon atoms (*i.e.*, C12, C24, C94, and C106), as well as all non-apical carbon atoms from the inner five-membered ring (approximately 5–6% each). Conversely, the LUMO is notably dominated (with a contribution of 38.6% each) by the d orbitals of two titanium atoms forming the Ti–O–Ti bridge (*i.e.*, Ti1 and Ti84). Interestingly, in the case of **2**, the HOMO is predominantly

Published on 02 August 2024. Downloaded by Uniwersytet Mikolaja Kopernika on 8/19/2024 9:35:51 AM.

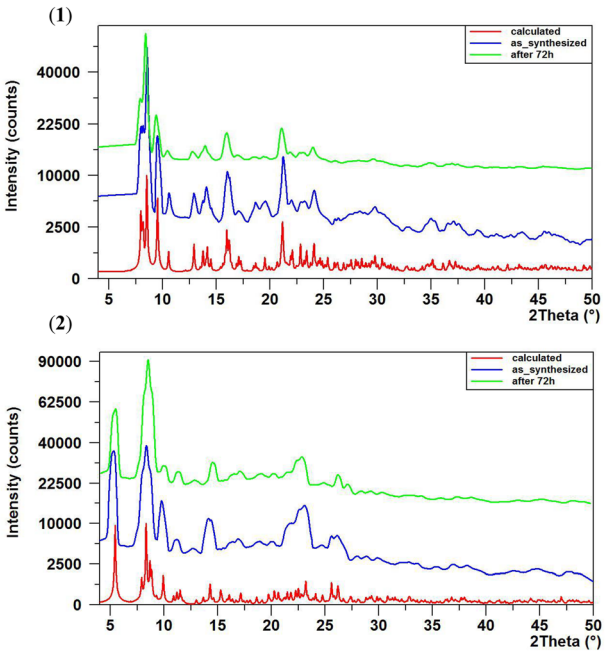


Fig. 6 The XRD patterns for **1** and **2** exhibit calculated diffractograms using our models (red line), diffractograms of samples post-compound synthesis (blue line), and diffractograms of samples after immersion in distilled water for 72 hours (green line) within the 4–50° 2θ range.

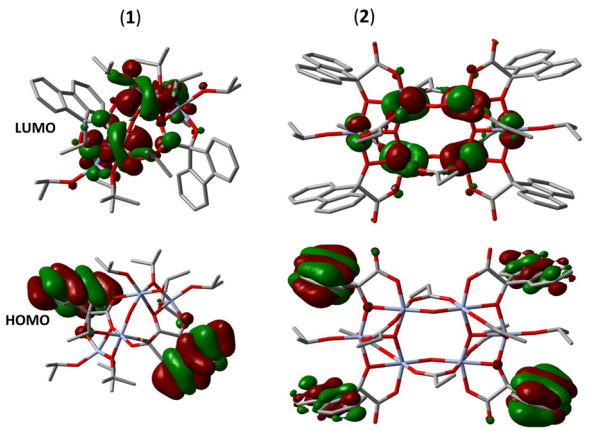


Fig. 7 HOMO (bottom) and LUMO (top) for **1** (left) and **2** (right).

contributed by only two fluorene fragments (81%), rather than four, which are related to each other by an inversion centre. The remaining two fragments contribute much less, accounting for only 10%. Similar to the case of system **1**, this contribution mainly stems from the outer carbon atoms of the benzene rings (*i.e.*, C14, C26, C110, and C122), as well as the inner five-membered ring (excluding the apical atom). The largest contributions to the LUMO originate from the d orbitals of the central titanium atoms (20% each), while contributions from the outer titanium atoms are considerably smaller, amounting to 6.4%.

Theoretical charge distribution in 1 and 2

To compare the charge distribution in **1** and **2**, maps of the molecular electrostatic potential (MEP) were generated. Additionally, Hirshfeld atomic charges[45] were calculated, known for their practical independence on the basis set used (unlike popular Mulliken atomic charges).[73,74] The MEP maps for systems **1** and **2** are depicted in Fig. 8. Using the same scale of values, these maps primarily illustrate that **2** exhibits significantly larger areas of relatively large positive and negative electrostatic potentials compared to **1**. In the latter system, the negative region is confined to the fluorene rings and nearby oxygen atoms, whereas in the former, this region visibly extends along the bridge chains containing oxygen atoms. Furthermore, the area with high positive potential values (dark blue) practically encompasses the entire molecule in **2**. The analysis of atomic charges (values in ESI, Table S3†) shows that in the case of **1** the highest negative atomic charge (−0.389 au) is located on the bridge oxygen atom O16. The situation is similar in system **2**, in which the bridge atoms O16 and O17 have charges of −0.369 and −0.349 au, respectively, and are larger than the negative charges on the carbonyl atoms O2 and O22 (−0.265 au.).

Reactivity of 1 and 2

The MEP distribution suggests that system **2** is more reactive than **1**. In order to even better describe the reactivity of the considered systems **1** and **2**, and more importantly quantitatively, various reactivity indices were determined based on conceptual DFT. These indices are presented in Table 3. As seen, the value of electron affinity (A) itself suggests that system **2**

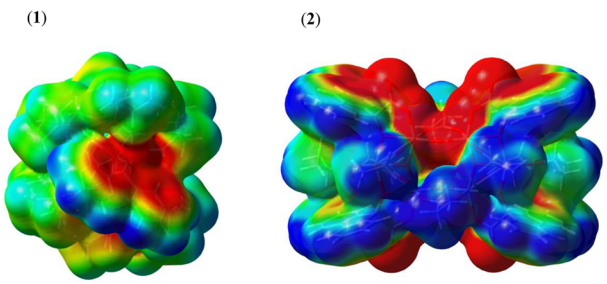


Fig. 8 Electrostatic potential maps (from −0.02 (red) to +0.02 (dark blue)) of systems **1** and **2**.

Table 3 Reactivity indices for **1** and **2** systems

Parameter	1	2
I (ionization potential)	7.06 eV	7.04 eV
A (electron affinity)	0.76 eV	2.19 eV
μ (electronic chemical potential)	−3.91 eV	−4.62 eV
χ (absolute electronegativity)	3.91 eV	4.62 eV
η (chemical hardness)	6.30 eV	4.85 eV
σ (chemical softness)	0.16 eV^{-1}	0.21 eV^{-1}
ω (electrophilicity index)	1.21 eV	2.20 eV
ε (nucleophilicity index)	0.83 eV^{-1}	0.45 eV^{-1}

This journal is © The Royal Society of Chemistry 2024

Published on 02 August 2024. Downloaded by Uniwersytet Mikolaja Kopernika on 8/19/2024 9:35:51 AM.

should accept electrons more willingly than system **1** (2.19 and 0.76 eV, respectively). This is also confirmed by the higher value of the electrophilicity index ω (2.20 and 1.21 eV for **2** and **1**, respectively), which is a better parameter for describing the electrophilic properties of chemical compounds. Additionally, the lower chemical hardness of **2** (4.85 eV) compared to that of **1** (6.30 eV) also confirms that the former should be more susceptible to changes in the electronic structure and therefore more reactive.

Conclusions

Two Ti(IV)-oxo complexes, designated as **1** and **2**, were synthesized *via* a 4 : 1 reaction of titanium isopropoxide and 9-OH-9-fluorenecarboxylic acid, and subsequently structurally characterized with an unprecedented core topology. The results of these investigations revealed that complex **1** contains $\{Ti_4O\}$ cores, with the centre formed by a Ti_2-(μ-O) bridge connected to two Ti(IV) ions through 9-OH-9-fluorenecarboxylate ligands and alkoxide bridges. In the structure of both compounds, chelate rings are formed. These ligands act also as bridges – μ_3 in **1** and μ in **2** – due to different oxygen atoms involved in bridging and coordination. Importantly, it should be emphasized that only in structure **2** do the –C═O groups of the carboxylate ligands remain uncoordinated.

The DFT calculations unveiled that complex **2** displays the highest tendency to release its most energetic electrons, suggesting its heightened reactivity compared to that of **1**. To further validate the reactivity disparity between the studied systems **1** and **2**, and crucially, to quantify it, diverse reactivity indices were determined using conceptual DFT. These indices corroborate that the oxo complex **2** is more prone to alterations in the electronic structure and consequently exhibits greater reactivity.

Author contributions

The manuscript was written with the contributions of all authors. All authors have given approval to the final version of the manuscript.

Data availability

CCDC 2284906 and 2284900† contain supplementary crystallographic data for **1** and **2**, respectively.

The authors declare that the data supporting the findings of this study are available within the paper and its ESI.†

Conflicts of interest

There are no conflicts to declare.

Acknowledgements

The studies have been carried out within the project 4101.00000070 IDUB, Grants4NCUStudents, Nicolaus Copernicus University in Toruń, Poland.

References

1 C. Byrne, G. Subramanian and S. C. Pillai, Recent advances in photocatalysis for environmental applications, *J. Environ. Chem. Eng.*, 2018, **6**, 3531–3555.
2 F. He, W. Jeon and W. Choi, Photocatalytic air purification mimicking the self-cleaning process of the atmosphere, *Nat. Commun.*, 2021, **12**, 2528.
3 A. Hojjati-Najafabadi, M. Mansoorianfar, T. Liang, K. Shahin, Y. Wen, A. Bahrami, C. Karaman, N. Zare, H. Karimi-Maleh and Y. Vasseghian, Magnetic-MXene-based nanocomposites for water and wastewater treatment: A review, *J. Water Process Eng.*, 2022, **47**, 102696.
4 M. Irshad, Q. T. Ain, M. Zaman, M. Z. Aslam, N. Kousar, M. Asim, M. Rafique, K. Siraj, A. N. Tabish, M. Usman, M. U. Hassan Farooq, M. A. Assiri and M. Imran, Photocatalysis and perovskite oxide-based materials: a remedy for a clean and sustainable future, *RSC Adv.*, 2022, **12**, 7009–7039.
5 H. Hao, L. Zhang, W. Wang and S. Zeng, Modification of heterogeneous photocatalysts for selective organic synthesis, *Catal. Sci. Technol.*, 2018, **8**, 1229–1250.
6 P. Ganguly, S. Mathew, L. Clarizia, S. R. Kumar, A. Akande, S. Hinder, A. Breen and S. C. Pillai, Theoretical and experimental investigation of visible light responsive AgBiS2-TiO2 heterojunctions for enhanced photocatalytic applications, *Appl. Catal., B*, 2019, **253**, 401–418.
7 L. Zhang, J. Ran, S.-Z. Qiao and M. Jaroniec, Characterization of semiconductor photocatalysts, *Chem. Soc. Rev.*, 2019, **48**, 5184–5206.
8 G. Zhuang, J. Yan, Y. Wen, Z. Zhuang and Y. Yu, Two–Dimensional Transition Metal Oxides and Chalcogenides for Advanced Photocatalysis: Progress, Challenges, and Opportunities, *Sol. RRL*, 2021, **5**, 2000403.
9 X. Fan, H. Fu, M.-Y. Gao, L. Zhang and J. Zhang, One-Pot and Postsynthetic Phenol-Thermal Synthesis toward Highly Stable Titanium-Oxo Clusters, *Inorg. Chem.*, 2019, **58**, 13353–13359.
10 A. J. Haider, Z. N. Jameel and I. H. M. Al-Hussaini, Review on: Titanium Dioxide Applications, *Energy Procedia*, 2019, **157**, 17–29.
11 D. Ziental, B. Czarczynska-Goslinska, D. T. Mlynarczyk, A. Glowacka-Sobotta, B. Stanisz, T. Goslinski and L. Sobotta, Titanium Dioxide Nanoparticles: Prospects and Applications in Medicine, *Nanomaterials*, 2020, **10**, 387.
12 C. Wang, S.-J. Wang and F.-G. Kong, Calixarene-Protected Titanium-Oxo Clusters and Their Photocurrent Responses and Photocatalytic Performances, *Inorg. Chem.*, 2021, **60**, 5034–5041.

Published on 02 August 2024. Downloaded by Uniwersytet Mikolaja Kopernika on 8/19/2024 9:35:51 AM.

13 V. Pfeifer, P. Erhart, S. Li, K. Rachut, J. Morasch, J. Brötz, P. Reckers, T. Mayer, S. Rühle, A. Zaban, I. Mora Seró, J. Bisquert, W. Jaegermann and A. Klein, Energy Band Alignment between Anatase and Rutile TiO_2, *J. Phys. Chem. Lett.*, 2013, **4**, 4182–4187.

14 S. Al Jitan, G. Palmisano and C. Garlisi, Synthesis and Surface Modification of TiO2-Based Photocatalysts for the Conversion of CO2, *Catalysts*, 2020, **10**, 227.

15 Y. Yamaguchi and A. Kudo, Visible light responsive photocatalysts developed by substitution with metal cations aiming at artificial photosynthesis, *Front. Energy*, 2021, **15**, 568–576.

16 B. Sambandam, A. Surenjan, L. Philip and T. Pradeep, Rapid Synthesis of C-TiO_2 : Tuning the Shape from Spherical to Rice Grain Morphology for Visible Light Photocatalytic Application, *ACS Sustainable Chem. Eng.*, 2015, **3**, 1321–1329.

17 L. Ni, D. Liang, Y. Cai, G. Diao and Z. Zhou, A novel hexanuclear titanium(IV)-oxo-iminodiacetate cluster with a Ti_6O_9 core: single-crystal structure and photocatalytic activities, *Dalton Trans.*, 2016, **45**, 7581–7588.

18 A. Šuligoj, I. Arčon, M. Mazaj, G. Dražić, D. Arčon, P. Cool, U. L. Štangar and N. N. Tušar, Surface modified titanium dioxide using transition metals: nickel as a winning transition metal for solar light photocatalysis, *J. Mater. Chem. A*, 2018, **6**, 9882–9892.

19 M.-Y. Gao, Z. Wang, Q.-H. Li, D. Li, Y. Sun, Y. H. Andaloussi, C. Ma, C. Deng, J. Zhang and L. Zhang, Black Titanium-Oxo Clusters with Ultralow Band Gaps and Enhanced Nonlinear Optical Performance, *J. Am. Chem. Soc.*, 2022, **144**, 8153–8161.

20 Y.-H. Guo, Y.-Z. Yu, Y.-H. Shen, L.-G. Yang, N.-N. Liu, Z.-Y. Zhou and Y.-S. Niu, "Three-in-One" Structural-Building-Mode-Based Ti_{16} -Type Titanium Oxo Cluster Entirely Protected by the Ligands Benzoate and Salicylhydroxamate, *Inorg. Chem.*, 2022, **61**, 8685–8693.

21 X.-X. Liu, G.-H. Chen, J. Tao, J. Zhang and L. Zhang, Synthesis, Structure, and Light Absorption Behaviors of Prismatic Titanium-Oxo Clusters Containing Lacunary Lindqvist-like Species, *Inorg. Chem.*, 2022, **61**, 1385–1390.

22 M. Roškarič, G. Žerjav, J. Zavašnik and A. Pintar, The influence of synthesis conditions on the visible-light triggered photocatalytic activity of g-C3N4/TiO2 composites used in AOPs, *J. Environ. Chem. Eng.*, 2022, **10**, 107656.

23 A. Said, C. Gao, C. Liu, H. Niu, D. Wang, Y. Liu, L. Du, C.-H. Tung and Y. Wang, A Mesoporous Lead-Doped Titanium Oxide Compound with High Performance and Recyclability in I_2 Uptake and Photocatalysis, *Inorg. Chem.*, 2022, **61**, 586–596.

24 S. E. Brown, I. Mantaloufa, R. T. Andrews, T. J. Barnes, M. R. Lees, F. De Proft, A. V. Cunha and S. D. Pike, Photoactivation of titanium-oxo cluster $[Ti_6O_6(OR)_6(O_2C^tBu)_6]$: mechanism, photoactivated structures, and onward reactivity with O_2 to a peroxide complex, *Chem. Sci.*, 2023, **14**, 675–683.

25 I. S. Hwang, V. Manikandan, R. P. Patil, M. A. Mahadik, W.-S. Chae, H.-S. Chung, S. H. Choi and J. S. Jang, Hydrogen-Treated TiO_2 Nanorods Decorated with Bimetallic Pd–Co Nanoparticles for Photocatalytic Degradation of Organic Pollutants and Bacterial Inactivation, *ACS Appl. Nano Mater.*, 2023, **6**, 1562–1572.

26 W. Luo, B. Hu, H.-L. Zhang, C. Li, Y. Shi, X. Li and L. Jin, Antibacterial, photothermal and stable Ag-titanium-oxo-clusters hydrogel designed for wound healing, *Mater. Des.*, 2023, **226**, 111674.

27 U. Schubert, Chemical modification of titanium alkoxides for sol–gel processing, *J. Mater. Chem.*, 2005, **15**, 3701.

28 U. Schubert, Titanium–Oxo Clusters with Bi– and Tridentate Organic Ligands: Gradual Evolution of the Structures from Small to Big, *Chem. – Eur. J.*, 2021, **27**, 11239–11256.

29 A. Radtke, P. Piszczek, T. Muzioł and A. Wojtczak, The Structural Conversion of Multinuclear Titanium(IV) μ-Oxo-complexes, *Inorg. Chem.*, 2014, **53**, 10803–10810.

30 J.-F. Wang, W.-H. Fang, D.-S. Li, L. Zhang and J. Zhang, Cocrystal of $\{Ti_4\}$ and $\{Ti_6\}$ Clusters with Enhanced Photochemical Properties, *Inorg. Chem.*, 2017, **56**, 2367–2370.

31 H.-T. Lv, H.-M. Li, G.-D. Zou, Y. Cui, Y. Huang and Y. Fan, Titanium-oxo clusters functionalized with catecholate-type ligands: modulating the optical properties through charge-transfer transitions, *Dalton Trans.*, 2018, **47**, 8158–8163.

32 M. Janek, T. M. Muzioł and P. Piszczek, Trinuclear Oxo-Titanium Clusters: Synthesis, Structure, and Photocatalytic Activity, *Materials*, 2019, **12**, 3195.

33 M. Janek, A. Radtke, T. Muzioł, M. Jerzykiewicz and P. Piszczek, Tetranuclear Oxo-Titanium Clusters with Different Carboxylate Aromatic Ligands: Optical Properties, DFT Calculations, and Photoactivity, *Materials*, 2018, **11**, 1661.

34 B. Kubiak, P. Piszczek, A. Radtke, T. Muzioł, G. Wrzeszcz and P. Golińska, Photocatalytic and Antimicrobial Activity of Titanium(IV)-Oxo Clusters of Different Core Structure, *Crystals*, 2023, **13**, 998.

35 O. Meth-Cohn, D. Thorpe and H. J. Twitchett, Insertion reactions of titanium alkoxides with isocyanates and carbodiimides, *J. Chem. Soc. C*, 1970, 132.

36 *E. CrysAlis Red and CrysAlis CCD*, Oxford Diffraction Ltd., Abingdon, Oxfordshire, 2000.

37 G. M. Sheldrick, Crystal structure refinement with *SHELXL*, *Acta Crystallogr., Sect. C: Struct. Chem.*, 2015, **71**, 3–8.

38 O. V. Dolomanov, L. J. Bourhis, R. J. Gildea, J. A. K. Howard and H. Puschmann, *OLEX2*: a complete structure solution, refinement and analysis program, *J. Appl. Crystallogr.*, 2009, **42**, 339–341.

39 K. Brandenburg and M. Berndt, *Diamond, Release 2.1e*, Crystal Impact, Bonn, Germany, 2001.

40 A. D. Becke, Density-functional exchange-energy approximation with correct asymptotic behavior, *Phys. Rev. A*, 1988, **38**, 3098–3100.

 This journal is © The Royal Society of Chemistry 2024

Published on 02 August 2024. Downloaded by Uniwersytet Mikolaja Kopernika on 8/19/2024 9:35:51 AM.

41 C. Lee, W. Yang and R. G. Parr, Development of the Colle-Salvetti correlation-energy formula into a functional of the electron density, *Phys. Rev. B: Condens. Matter Mater. Phys.*, 1988, **37**, 785–789.
42 P. Hohenberg and W. Kohn, Inhomogeneous Electron Gas, *Phys. Rev.*, 1964, **136**, B864–B871.
43 W. Kohn and L. J. Sham, Self-Consistent Equations Including Exchange and Correlation Effects, *Phys. Rev.*, 1965, **140**, A1133–A1138.
44 B. P. Pritchard, D. Altarawy, B. Didier, T. D. Gibson and T. L. Windus, New Basis Set Exchange: An Open, Up-to-Date Resource for the Molecular Sciences Community, *J. Chem. Inf. Model.*, 2019, **59**, 4814–4820.
45 F. L. Hirshfeld, Bonded-atom fragments for describing molecular charge densities, *Theor. Chim. Acta*, 1977, **44**, 129–138.
46 P. Geerlings, F. De Proft and W. Langenaeker, Conceptual Density Functional Theory, *Chem. Rev.*, 2003, **103**, 1793–1874.
47 D. Chakraborty and P. K. Chattaraj, Conceptual density functional theory based electronic structure principles, *Chem. Sci.*, 2021, **12**, 6264–6279.
48 S. Liu, *Conceptual density functional theory: towards a new chemical reactivity theory*, Wiley-VCH, Weinheim, Germany, 2022.
49 P. Politzer and J. S. Murray, Electronegativity—a perspective, *J. Mol. Model*, 2018, **24**, 214.
50 R. G. Pearson, Chemical hardness and the electronic chemical potential, *Inorg. Chim. Acta*, 1992, **198–200**, 781–786.
51 R. G. Pearson, The electronic chemical potential and chemical hardness, *J. Mol. Struct.: THEOCHEM*, 1992, **255**, 261–270.
52 A. T. Maynard, M. Huang, W. G. Rice and D. G. Covell, Reactivity of the HIV-1 nucleocapsid protein p7 zinc finger domains from the perspective of density-functional theory, *Proc. Natl. Acad. Sci. U. S. A.*, 1998, **95**, 11578–11583.
53 R. G. Parr, L. V. Szentpály and S. Liu, Electrophilicity Index, *J. Am. Chem. Soc.*, 1999, **121**, 1922–1924.
54 M. J. Frisch, G. W. Trucks, H. B. Schlegel, G. E. Scuseria, M. A. Robb, J. R. Cheeseman, G. Scalmani, V. Barone, G. A. Petersson, H. Nakatsuji, X. Li, M. Caricato, A. V. Marenich, J. Bloino, B. G. Janesko, R. Gomperts, B. Mennucci, H. P. Hratchian, J. V. Ortiz, A. F. Izmaylov, J. L. Sonnenberg, D. Williams-Young, F. Ding, F. Lipparini, F. Egidi, J. Goings, B. Peng, A. Petrone, T. Henderson, D. Ranasinghe, V. G. Zakrzewski, J. Gao, N. Rega, G. Zheng, W. Liang, M. Hada, M. Ehara, K. Toyota, R. Fukuda, J. Hasegawa, M. Ishida, T. Nakajima, Y. Honda, O. Kitao, H. Nakai, T. Vreven, K. Throssell, J. A. Montgomery Jr., J. E. Peralta, F. Ogliaro, M. J. Bearpark, J. J. Heyd, E. N. Brothers, K. N. Kudin, V. N. Staroverov, T. A. Keith, R. Kobayashi, J. Normand, K. Raghavachari, A. P. Rendell, J. C. Burant, S. S. Iyengar, J. Tomasi, M. Cossi, J. M. Millam, M. Klene, C. Adamo, R. Cammi, J. W. Ochterski, R. L. Martin, K. Morokuma, O. Farkas, J. B. Foresman and D. J. Fox, *Gaussian 16, Revision C.01*, Gaussian, Inc., Wallingford CT, 2019.
55 R. Dennington, T. Keith and J. Millam, *GaussView, Version 6*, Semichem Inc., Shawnee Mission, KS, USA, 2019.
56 A. W. Addison, T. N. Rao, J. Reedijk, J. Van Rijn and G. C. Verschoor, Synthesis, structure, and spectroscopic properties of copper(II) compounds containing nitrogen–sulphur donor ligands; the crystal and molecular structure of aqua[1,7-bis(N-methylbenzimidazol-2′-yl)-2,6-dithiaheptane]copper(II) perchlorate, *J. Chem. Soc., Dalton Trans.*, 1984, 1349–1356.
57 M. Czakler, C. Artner and U. Schubert, Influence of the Phosphonate Ligand on the Structure of Phosphonate–Substituted Titanium Oxo Clusters, *Eur. J. Inorg. Chem.*, 2013, **2013**, 5790–5796.
58 F. G. Svensson, G. Daniel, C.-W. Tai, G. A. Seisenbaeva and V. G. Kessler, Titanium phosphonate oxo-alkoxide "clusters": solution stability and facile hydrolytic transformation into nano titania, *RSC Adv.*, 2020, **10**, 6873–6883.
59 U. Schubert and B. Stöger, Structural Chemistry of Titanium(IV) Oxo Clusters, Part 2: Clusters without Carboxylate or Phosphonate Ligands, *Chem. – Eur. J.*, 2024, **30**, e202400744.
60 J. Hou, Q. Zhang, Y. Wu, Y. Liu, L. Du, C.-H. Tung and Y. Wang, Interfacial charge transfer in a functionalized polyoxotitanate cluster, *Inorg. Chim. Acta*, 2016, **443**, 279–283.
61 S. Shekar, B. Twamley and R. J. Wehmschulte, Facile Synthesis of Monoazidotitanium Isopropoxides, *Inorg. Chem.*, 2008, **47**, 10804–10806.
62 S. Chen, W.-H. Fang, L. Zhang and J. Zhang, Synthesis, Structures, and Photocurrent Responses of Polyoxo-Titanium Clusters with Oxime Ligands: From Ti_4 to Ti_{18}, *Inorg. Chem.*, 2018, **57**, 8850–8856.
63 M. Czakler, C. Artner and U. Schubert, Titanium oxo/alkoxo clusters with both phosphonate and methacrylate ligands, *Monatsh. Chem. – Chem. Mon.*, 2015, **146**, 1249–1256.
64 B. Kubiak, T. Muzioł, G. Wrzeszcz, A. Radtke, P. Golińska, T. Jędrzejewski, S. Wrotek and P. Piszczek, Structural Characterization and Bioactivity of a Titanium(IV)-Oxo Complex Stabilized by Mandelate Ligands, *Molecules*, 2024, **29**, 1736.
65 G. Kickelbick, D. Holzinger, C. Brick, G. Trimmel and E. Moons, Hybrid Inorganic–Organic Core–Shell Nanoparticles from Surface-Functionalized Titanium, Zirconium, and Vanadium Oxo Clusters, *Chem. Mater.*, 2002, **14**, 4382–4389.
66 Y. Gao, F. R. Kogler, H. Peterlik and U. Schubert, Ring-opening metathesis polymerizations with norbornene carboxylate-substituted metal oxo clusters, *J. Mater. Chem.*, 2006, **16**, 3268.
67 M. Czakler, C. Artner and U. Schubert, Two new hexanuclear titanium oxo cluster types and their structural connection to known clusters, *New J. Chem.*, 2018, **42**, 12098–12103.

Published on 02 August 2024. Downloaded by Uniwersytet Mikolaja Kopernika on 8/19/2024 9:35:51 AM.

68 Y.-Z. Yu, Y.-R. Zhang, C.-H. Geng, L. Sun, Y. Guo, Y.-R. Feng, Y.-X. Wang and X.-M. Zhang, Precise and Wide-Ranged Band-Gap Tuning of Ti_6 -Core-Based Titanium Oxo Clusters by the Type and Number of Chromophore Ligands, *Inorg. Chem.*, 2019, **58**, 16785–16791.

69 C. Artner, A. Koyun, M. Czakler and U. Schubert, Mixed–Metal Oxo Clusters Structurally Derived from $Ti_6O_4(OR)_8(OOCR')_8$, *Eur. J. Inorg. Chem.*, 2014, **2014**, 5008–5014.

70 K. Nakamoto, *Infrared and Raman Spectra of Inorganic and Coordination Compounds: Part A: Theory and Applications in Inorganic Chemistry*, Wiley, 1st edn, 2008.

71 J.-J. Liu, N. Li, J.-W. Sun, J. Liu, L.-Z. Dong, S.-J. Yao, L. Zhang, Z.-F. Xin, J.-W. Shi, J.-X. Wang, S.-L. Li and Y.-Q. Lan, Ferrocene-Functionalized Polyoxo-Titanium Cluster for CO_2 Photoreduction, *ACS Catal.*, 2021, **11**, 4510–4519.

72 C. F. Macrae, I. Sovago, S. J. Cottrell, P. T. A. Galek, P. McCabe, E. Pidcock, M. Platings, G. P. Shields, J. S. Stevens, M. Towler and P. A. Wood, *Mercury* 4.0 : from visualization to analysis, design and prediction, *J. Appl. Crystallogr.*, 2020, **53**, 226–235.

73 K. B. Wiberg and P. R. Rablen, Atomic Charges, *J. Org. Chem.*, 2018, **83**, 15463–15469.

74 M. Jabłoński and T. M. Krygowski, Study of the influence of intermolecular interaction on classical and reverse substituent effects in *para*-substituted phenylboranes, *New J. Chem.*, 2020, **44**, 9656–9670.

This journal is © The Royal Society of Chemistry 2024

Materiały uzupełniające

Supplementary Information (SI) for Dalton Transactions.
This journal is © The Royal Society of Chemistry 2024

Supplementary Information

Investigation of Titanium(IV)-Oxo Complexes Stabilized with α-Hydroxy Carboxylate Ligands: Structural Analysis And DFT Studies

Barbara Kubiak[1*], Tadeusz Muziol[1], Mirosław Jabłoński[2], Aleksandra Radtke[1], Piotr Piszczek[1*]

[1] Department of Inorganic and Coordination Chemistry, Faculty of Chemistry, Nicolaus Copernicus University in Toruń, Gagarina 7, 87-100 Toruń, Poland

[2] Department of Quantum Chemistry and Atomic Spectroscopy, Faculty of Chemistry, Nicolaus Copernicus University in Toruń, Gagarina 7, 87-100 Toruń, Poland

* Correspondence: piszczek@umk.pl, basiak0809@gmail.com

Table S1. Crystal data and structure refinement for (**1**) and (**2**).

Empirical formula	$C_{58}H_{86}O_{17}Ti_4$ (**1**)	$C_{80}H_{76}O_{30}Ti_6$ (**2**)
Formula weight	1246.86	1804.80
Temperature	100(2) K	100(2) K
Wavelength [Å]	1.54184	1.54184
Crystal system	Monoclinic	Triclinic
Space group	C2/c	P-1
Unit cell dimensions [Å] and [°]	a = 22.4667(4)	a = 12.4059(10)
	b = 12.6262(2)	b = 12.5243(11)
	c = 23.0730(5)	c = 17.3816(13)
	α = 90	α = 77.520(7)
	β = 106.0037(19)	β = 69.528(8)
	γ = 90	γ = 63.331(9)
Volume [$Å^3$]	6291.4(2)	2255.3(4)
Z, calculated density [Mg/m^3]	4, 1.316	1, 1.329
Absorption coefficient [mm^{-1}]	4.707	4.956
F(000)	2632	928
Crystal size [mm^3]	0.080 × 0.040 × 0.020	0.120 × 0.060 × 0.040
Theta range for data collection [°]	3.986 to 74.492	3.960 to 74.443
Index ranges	-26<=h<=27	-14<=h<=15
	-15<=k<=15	-12<=k<=15
	-27<=l<=28	-21<=l<=21
Reflections collected/unique	29621/ 6404 [R(int) = 0.0474]	27429/ 8652 [R(int) = 0.0968]
Completeness to theta	67.684° 99.9 %	67.684° 97.8 %
Absorption correction	Numerical	Semi-empirical from equivalents
Max. and min. transmission	1.000 and 0.746	1.00000 and 0.65108
Refinement method	Full-matrix least-squares on F2	Full-matrix least-squares on F2
Data / restraints / parameters	6404 / 0 / 397	8652 / 3 / 531
Goodness-of-fit on F2	1.095	1.019
Final R indices [I>2sigma(I)]	$R1^a$ = 0.0428, $wR2^b$ = 0.1131	$R1^a$ = 0.0941, $wR2^b$ = 0.2558

R indices (all data)	R1[a] = 0.0498, wR2[b] = 0.1169	R1[a] = 0.1461, wR2[b] = 0.2977
Extinction coefficient	0.00009(2)	nd
Largest diff. peak and hole	0.470 and -0.630 e·Å^{-3}	0.851 and -0.953 e·Å^{-3}

[a] $R1 = \Sigma \| |F_0| - |F_c| \| / \Sigma |F_0|$ [b] $wR2 = \left[\Sigma w(F_0^2 - F^2)^2 / \Sigma (w(F_0^2)^2)\right]^{1/2}$

Table S2. Experimental and theoretical (B3LYP/6-31G(d,p)) values of bond lengths [Å] and angles [º] for **1** and **2**.

$[Ti_4O(O^iPr)_{10}(O_3C_{14}H_8)_2]$ (**1**)			$[Ti_6O_4(O^iPr)_2(O_3C_{14}H_8)_4(O_2CEt)_6]$ (**2**)		
Parameter	Distances [Å]		Parameter	Distances [Å]	
	Exp.	Calc.		Exp.	Calc.
Ti(1)-O(31)	1.7921(15)	1.793	Ti(1)-O(17)	1.794(5)	1.800
Ti(1)-O(41)	1.8195(16)	1.821	Ti(1)-O(16)	1.884(4)	1.901
Ti(1)-O(16)	1.8293(7)	1.824	Ti(1)-O(21)	1.929(4)	1.884
Ti(1)-O(21)	2.0940(15)	2.139	Ti(1)-O(61)	2.008(5)	2.055
Ti(1)-O(1)	2.1801(15)	2.212	Ti(1)-O(52)	2.028(4)	2.036
Ti(1)-O(2)#1	2.2274(15)	2.283	Ti(1)-O(23)	2.093(5)	2.147
Ti(1)-Ti(2)	3.3510(5)	3.419	Ti(1)-Ti(3)	3.1182(18)	3.163
Ti(2)-O(61)	1.778(2)	1.788	Ti(2)-O(17)#1	1.800(4)	1.802
Ti(2)-O(51)	1.7819(19)	1.796	Ti(2)-O(16)	1.894(4)	1.895
Ti(2)-O(3)	1.8773(16)	1.873	Ti(2)-O(1)	1.936(5)	1.881
Ti(2)-O(21)	1.9695(16)	1.973	Ti(2)-O(41)	2.010(5)	2.042
Ti(2)-O(1)	2.0651(15)	2.106	Ti(2)-O(62)#1	2.022(5)	2.052
O(1)-C(2)	1.299(2)	1.301	Ti(2)-O(3)	2.094(4)	2.169
O(2)-C(2)	1.226(3)	1.234	Ti(2)-Ti(3)	3.1185(15)	3.164
C(3)-O(3)	1.393(3)	1.401	Ti(3)-O(71)	1.728(5)	1.740
			Ti(3)-O(3)	1.940(4)	1.962
			Ti(3)-O(23)	1.953(4)	1.972
			Ti(3)-O(42)	2.002(6)	2.040
			Ti(3)-O(51)	2.006(6)	2.050
			Ti(3)-O(16)	2.077(4)	2.070
			O(1)-C(2)	1.323(9)	1.331
			O(2)-C(2)	1.205(8)	1.207
			C(3)-O(3)	1.435(8)	1.423
	Angles [º]			Angles [º]	
	Exp.	Calc.		Exp.	Calc.
O(31)-Ti(1)-O(41)	98.34(7)	98.6	O(17)-Ti(1)-O(16)	105.82(19)	104.9
O(31)-Ti(1)-O(16)	100.86(7)	102.0	O(17)-Ti(1)-O(21)	101.6(2)	104.1
O(41)-Ti(1)-O(16)	101.60(6)	100.1	O(16)-Ti(1)-O(21)	152.6(2)	150.8
O(31)-Ti(1)-O(21)	103.26(7)	102.6	O(17)-Ti(1)-O(61)	90.4(2)	89.9
O(41)-Ti(1)-O(21)	91.45(7)	91.9	O(16)-Ti(1)-O(61)	89.64(19)	88.9
O(16)-Ti(1)-O(21)	150.51(8)	150.6	O(21)-Ti(1)-O(61)	89.14(19)	88.0
O(31)-Ti(1)-O(1)	166.71(7)	165.2	O(17)-Ti(1)-O(52)	90.5(2)	93.5
O(41)-Ti(1)-O(1)	91.67(6)	92.9	O(16)-Ti(1)-O(52)	89.70(19)	89.1
O(16)-Ti(1)-O(1)	85.54(6)	85.1	O(21)-Ti(1)-O(52)	91.11(19)	92.4
O(21)-Ti(1)-O(1)	67.58(6)	67.4	O(61)-Ti(1)-O(52)	179.0(2)	176.4
O(31)-Ti(1)-O(2)#1	84.84(7)	85.3	O(17)-Ti(1)-O(23)	175.8(2)	178.5
O(41)-Ti(1)-O(2)#1	171.77(7)	172.5	O(16)-Ti(1)-O(23)	76.33(18)	75.1
O(16)-Ti(1)-O(2)#1	85.16(5)	85.2	O(21)-Ti(1)-O(23)	76.37(19)	75.9
O(21)-Ti(1)-O(2)#1	80.41(6)	81.1	O(61)-Ti(1)-O(23)	93.29(19)	91.6
O(1)-Ti(1)-O(2#1)	84.12(6)	82.3	O(52)-Ti(1)-O(23)	85.85(18)	85.0
O(31)-Ti(1)-Ti(2)	136.14(5)	134.8	O(17)-Ti(1)-Ti(3)	142.97(14)	141.8
O(41)-Ti(1)-Ti(2)	82.29(5)	85.5	O(16)-Ti(1)-Ti(3)	40.32(13)	39.1
O(16)-Ti(1)-Ti(2)	122.13(5)	121.7	O(21)-Ti(1)-Ti(3)	113.44(14)	113.1
O(21)-Ti(1)-Ti(2)	33.26(4)	32.2	O(61)-Ti(1)-Ti(3)	101.36(15)	99.3
O(1)-Ti(1)-Ti(2)	36.68(4)	36.6	O(52)-Ti(1)-Ti(3)	77.67(14)	77.2
O(2)#-Ti(1)-Ti(2)	90.15(4)	87.2	O(23)-Ti(1)-Ti(3)	37.97(12)	37.8
O(61)-Ti(2)-O(51)	107.54(10)	108.2	O(17)#1-Ti(2)-O(16)	106.52(19)	106.7
O(61)-Ti(2)-O(3)	106.21(8)	106.0	O(17)#1-Ti(2)-O(1)	100.76(19)	103.2

O(51)-Ti(2)-O(3)	95.72(8)	93.6	O(16)-Ti(2)-O(1)	152.5(2)	150.1
O(61)-Ti(2)-O(21)	102.92(8)	104.6	O(17)#1-Ti(2)-O(41)	91.5(2)	90.7
O(51)-Ti(2)-O(21)	97.16(8)	99.1	O(16)-Ti(2)-O(41)	89.34(19)	88.6
O(3)-Ti(2)-O(21)	142.74(7)	141.1	O(1)-Ti(2)-O(41)	93.4(2)	93.1
O(61)-Ti(2)-O(1)	108.26(9)	107.6	O(17)#1-Ti(2)-O(62)#1	90.7(2)	90.2
O(51)-Ti(2)-O(1)	144.09(8)	144.2	O(16)-Ti(2)-O(62)#1	88.01(18)	89.2
O(3)-Ti(2)-O(1)	76.93(6)	75.8	O(1)-Ti(2)-O(62)#1	88.3(2)	88.6
O(21)-Ti(2)-O(1)	72.19(6)	72.5	O(41)-Ti(2)-O(62)#1	176.96(19)	177.8
O(61)-Ti(2)-Ti(1)	119.65(7)	118.1	O(17)#1-Ti(2)-O(3)	176.2(2)	175.3
O(51)-Ti(2)-Ti(1)	116.53(7)	119.8	O(16)-Ti(2)-O(3)	76.00(18)	74.8
O(3)-Ti(2)-Ti(1)	108.03(5)	107.5	O(1)-Ti(2)-O(3)	76.94(18)	75.6
O(21)-Ti(2)-Ti(1)	35.67(4)	35.3	O(41)-Ti(2)-O(3)	85.6(2)	84.8
O(1)-Ti(2)-Ti(1)	39.10(4)	38.7	O(62)#1-Ti(2)-O(3)	92.33(18)	94.4
Ti(1)#1-O(16)-Ti(1)	142.49(12)	144.9	O(17)#1-Ti(2)-Ti(3)	143.93(14)	142.4
			O(16)-Ti(2)-Ti(3)	40.38(13)	39.0
			O(1)-Ti(2)-Ti(3)	113.89(15)	112.6
			O(41)-Ti(2)-Ti(3)	77.24(14)	76.7
			O(62)#1-Ti(2)-Ti(3)	99.76(13)	101.4
			O(3)-Ti(2)-Ti(3)	37.60(11)	37.6
			O(71)-Ti(3)-O(3)	105.8(2)	106.4
			O(71)-Ti(3)-O(23)	103.5(2)	102.4
			O(3)-Ti(3)-O(23)	150.71(19)	151.2
			O(71)-Ti(3)-O(42)	94.6(3)	94.1
			O(3)-Ti(3)-O(42)	88.0(2)	88.4
			O(23)-Ti(3)-O(42)	88.81(19)	89.5
			O(71)-Ti(3)-O(51)	92.6(3)	93.4
			O(3)-Ti(3)-O(51)	90.9(2)	91.0
			O(23)-Ti(3)-O(51)	88.6(2)	87.4
			O(42)-Ti(3)-O(51)	172.8(2)	172.3
			O(71)-Ti(3)-O(16)	177.9(3)	177.8
			O(3)-Ti(3)-O(16)	75.47(17)	75.8
			O(23)-Ti(3)-O(16)	75.29(17)	75.4
			O(42)-Ti(3)-O(16)	87.09(19)	86.3
			O(51)-Ti(3)-O(16)	85.71(19)	86.1
			O(71)-Ti(3)-Ti(1)	142.43(19)	142.5
			O(3)-Ti(3)-Ti(1)	110.37(14)	109.9
			O(23)-Ti(3)-Ti(1)	41.27(13)	41.9
			O(42)-Ti(3)-Ti(1)	96.57(15)	96.2
			O(51)-Ti(3)-Ti(1)	77.09	76.8
			O(16)-Ti(3)-Ti(1)	35.94(12)	35.4
			O(71)-Ti(3)-Ti(2)	145.41(19)	147.0
			O(3)-Ti(3)-Ti(2)	41.21(13)	42.5
			O(23)-Ti(3)-Ti(2)	109.84(13)	109.3
			O(42)-Ti(3)-Ti(2)	77.49(14)	77.3
			O(51)-Ti(3)-Ti(2)	97.02(13)	97.1
			O(16)-Ti(3)-Ti(2)	36.21(12)	35.2
			Ti(1)-Ti(3)-Ti(2)	72.15(4)	70.6
			Ti(1)-O(16)-Ti(2)	152.8(2)	148.7
			Ti(1)-O(16)-Ti(3)	103.74(18)	105.6
			Ti(2)-O(16)-Ti(3)	103.4(2)	105.8
			Ti(1)-O(17)-Ti(2)#1	144.6(3)	146.1

Symmetry transformations used to generate equivalent atoms:

(**1**) #1 -x+1, y, -z+3/2
(**2**) #1 -x+1, -y+2, -z+1

Table S3. Hirshfeld atomic charges (in au.) obtained at the B3LYP/6-31G(d,p) level of theory for **1** and **2.**

$[Ti_4O(O^iPr)_{10}(O_3C_{14}H_8)_2]$ (**1**)		$[Ti_6O_4(O^iPr)_2(O_3C_{14}H_8)_4(O_2CEt)_6]$ (**2**)	
Atom	Charge	Atom	Charge
Ti1	0.581	Ti1	0.622
Ti2	0.601	Ti2	0.623
O16	–0.389	Ti3	0.595
O1	–0.197	O16	–0.369
O2	–0.193	O17	–0.349
O3	–0.287	O1	–0.238
O21	–0.254	O3	–0.249
O31	–0.253	O21	–0.239
O41	–0.273	O23	–0.250
O51	–0.266	O41	–0.217
O61	–0.272	O42	–0.208
		O51	–0.208
		O52	–0.218
		O61	–0.210
		O62	–0.212
		O2	–0.265
		O22	–0.266
		O71	–0.222

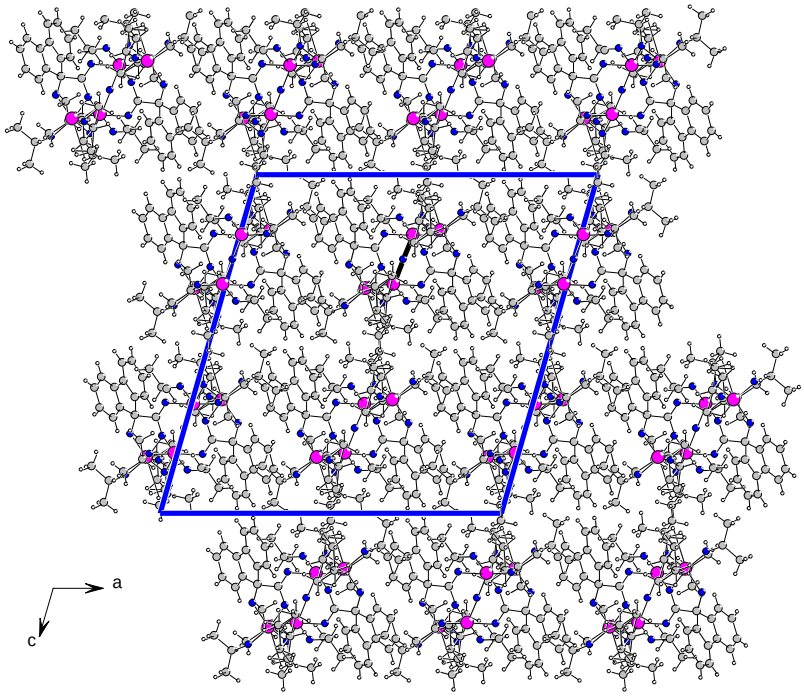


Figure S1. The TOCs packing in the crystal network of (**1**) along *b* axis.

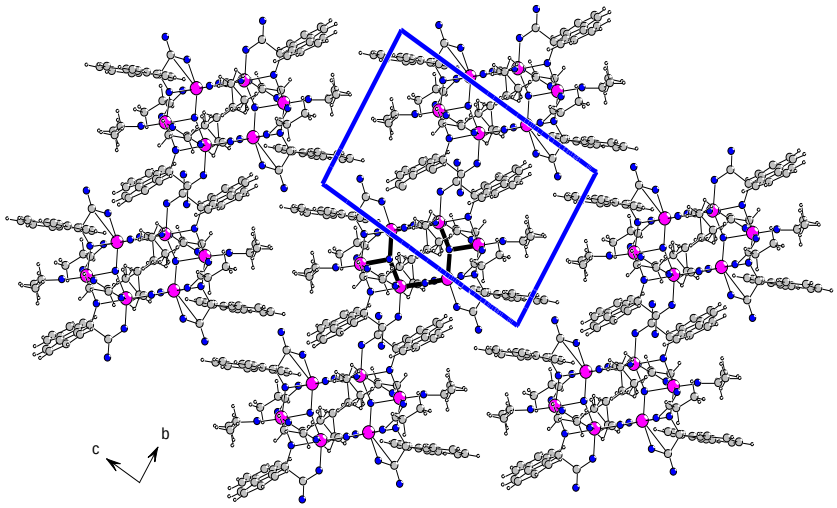


Figure S2. The differences in TOCs packing in the crystal network of (**2**) along *a* axis (b).

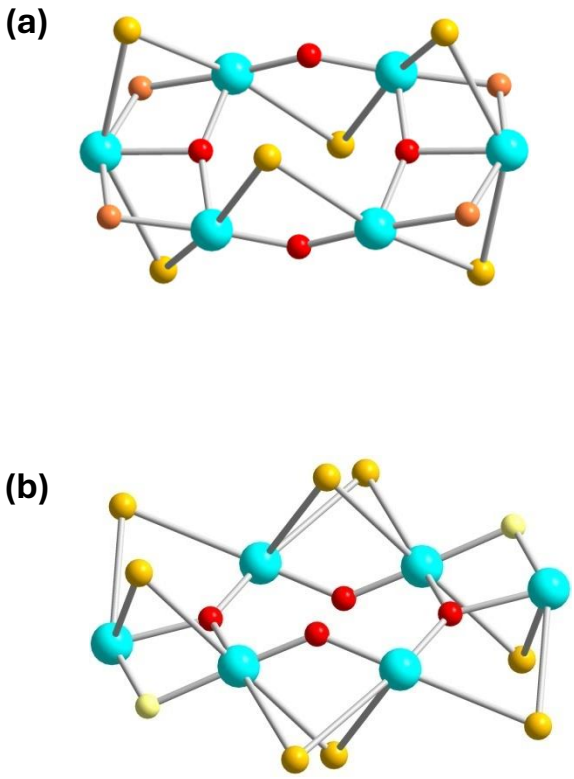


Figure S3. Cages of [[$Ti_6O_4(O^iPr)_2(O_3C_{14}H_8)_4(O_2C_3H_5)_6$] (**2**) (a) and [$Ti_6O_4(O^iBu)_8(O_2CC_{13}H_9)_8$]·$Me_2CO$ (b) [1]. Titanium atoms in cyan, oxo bridges in red, orange – 9-hydroxy-9-fluorenecarboxylate ligand, dark yellow – propionate, yellow – 9-fluorenecarboxylate ligand, light yellow – bridging isobutanolate. The central part - [$Ti_6(\mu_3\text{-}O)_2(\mu\text{-}O)_2$] is common but due to different complex content the connectivity of lateral ligands is distinct.

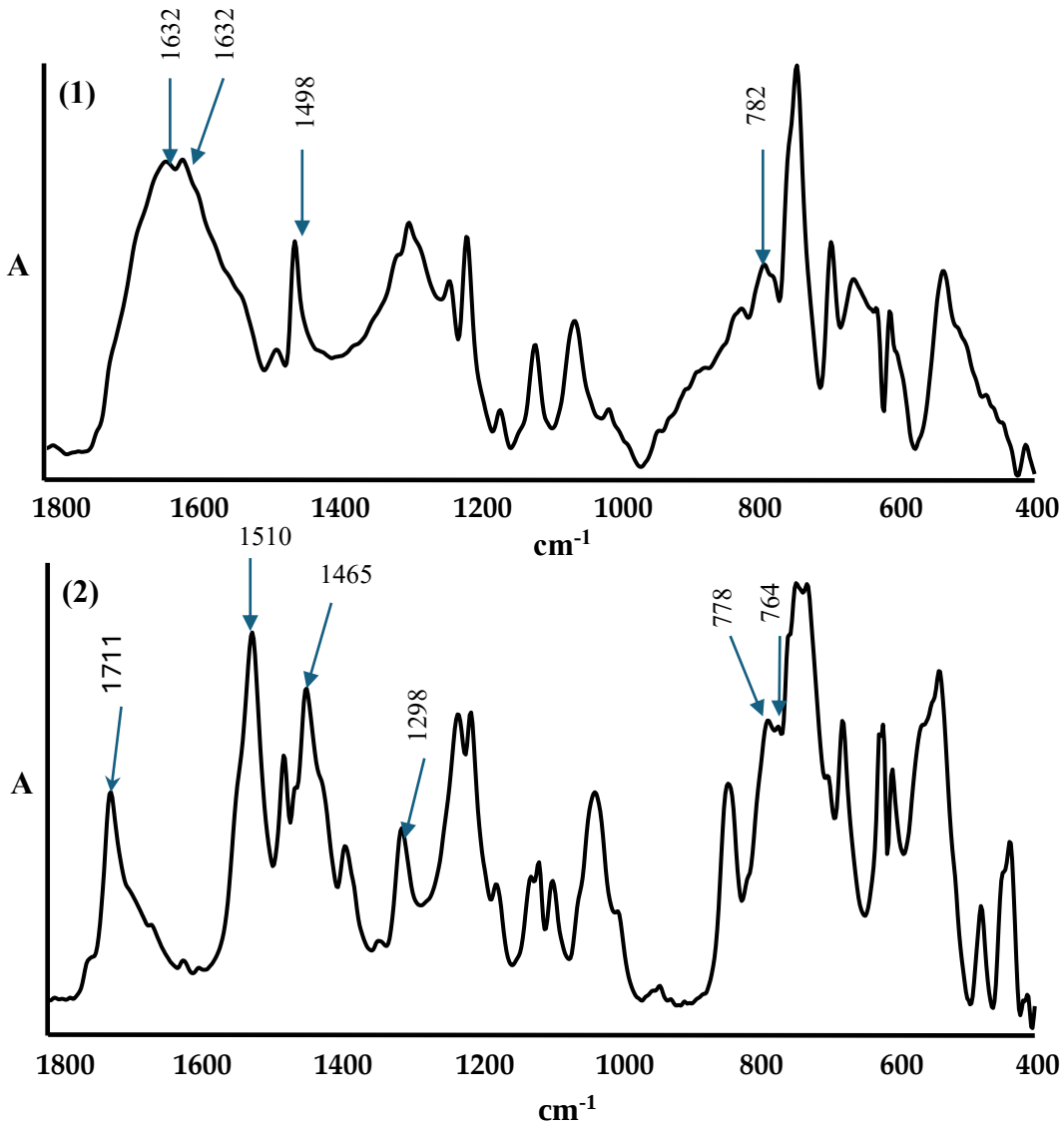


Figure S4. IR spectra of (**1**) and (**2**)

References

1 B. Kubiak, P. Piszczek, A. Radtke, T. Muzioł, G. Wrzeszcz and P. Golińska, *Crystals*, 2023, **13**, 998.

P6. *Analysis of Photocatalytic Properties of Poly(Methyl Methacrylate) Composites with Titanium(IV) and Ruthenium(III) Complexes*

applied sciences

MDPI

Article

Analysis of Photocatalytic Properties of Poly(Methyl Methacrylate) Composites with Titanium(IV) and Ruthenium(III) Complexes

Barbara Kubiak [1,*], Adrian Topolski [1], Aleksandra Radtke [1,*], Tadeusz Muzioł [1], Olga Impert [1], Anna Katafias [1], Rudi van Eldik [1,2] and Piotr Piszczek [1]

[1] Department of Inorganic and Coordination Chemistry, Faculty of Chemistry, Nicolaus Copernicus University in Toruń, Gagarina 7, 87-100 Toruń, Poland; topolski@umk.pl (A.T.); tadeuszmuziol@wp.pl (T.M.); oimpert@umk.pl (O.I.); katafias@umk.pl (A.K.); rudi.vaneldik@fau.de (R.v.E.); piszczek@umk.pl (P.P.)

[2] Department of Chemistry and Pharmacy, University of Erlangen-Nuremberg, Egerlandstrasse 1, 91058 Erlangen, Germany

* Correspondence: basiak0809@gmail.com (B.K.); aradtke@umk.pl (A.R.)

Abstract: This study explores poly(methyl methacrylate) (PMMA)-based composites as potential alternatives to conventional TiO_2-based photocatalysts. Specifically, it examines PMMA composites enriched with oxo–titanium(IV) complexes, $[Ti_8O_2(O^iPr)_{20}(man)_4]$ (**1**), $[Ti_4O(O^iPr)_{10}(O_3C_{14}H_8)_2]$ (**2**), and $[Ti_6O_4(O^iPr)_2(O_3C_{14}H_8)_4(O_2CEt)_6]$ (**3**), alongside ruthenium(III) complexes, $K[Ru(Hedta)Cl]\cdot 2H_2O$ (**4**) and $[Ru(pic)_3]\cdot H_2O$ (**5**). We assessed the physicochemical, adsorption, and photocatalytic properties of these composites with structural analyses (Raman spectroscopy, X-ray absorption (XAS), and SEM-EDX), confirming the stability of complexes within the PMMA matrix. Composites containing titanium(IV) compounds demonstrated notably higher photocatalytic efficiency than those with ruthenium(III) complexes. Based on activity profiles, composites were categorized into three types: (i) UV-light active (complexes (**1**) and (**2**)), (ii) visible-light active (complexes (**4**) and (**5**)), and (iii) dual-range active (complex (**3**)). The results highlight the strong potential of titanium(IV)–PMMA composites for UV-driven photocatalysis. Moreover, their activity can be extended to the visible range after structural modifications. Ruthenium(III)–PMMA composites, in turn, showed superior performance under visible light. Overall, PMMA composites with titanium(IV) or ruthenium(III) complexes demonstrate promising photocatalytic properties for applications using both UV and visible light ranges.

Keywords: titanium(IV)–oxo complexes; ruthenium(III) complexes; PMMA-based composites; photocatalytic activity; adsorptive properties; physicochemical properties

check for updates

Academic Editor: Antonio Miotello

Received: 16 January 2025
Revised: 31 January 2025
Accepted: 3 February 2025
Published: 7 February 2025

Citation: Kubiak, B.; Topolski, A.; Radtke, A.; Muzioł, T.; Impert, O.; Katafias, A.; van Eldik, R.; Piszczek, P. Analysis of Photocatalytic Properties of Poly(Methyl Methacrylate) Composites with Titanium(IV) and Ruthenium(III) Complexes. *Appl. Sci.* **2025**, *15*, 1679. https://doi.org/10.3390/app15041679

Copyright: © 2025 by the authors. Licensee MDPI, Basel, Switzerland. This article is an open access article distributed under the terms and conditions of the Creative Commons Attribution (CC BY) license (https://creativecommons.org/licenses/by/4.0/).

1. Introduction

Rapid industrial growth has increased the need for more efficient methods to address water and air pollution [1–4]. Organic dyes, such as methylene blue and rhodamine B, pose significant health risks due to their toxic effects, including skin and respiratory irritation [5,6]. Traditional methods, like adsorption and filtration, are effective, but they come with limited capacity and high energy requirements, diminishing their efficiency [7,8]. Photocatalysis offers significant advantages, particularly in environmental applications. It effectively degrades organic pollutants, neutralizes harmful substances, and eliminates microorganisms, making it a key water and air purification method [9–11]. Among photocatalysts, titanium dioxide (TiO_2) is the most widely used due to its stability and effectiveness [12–14]. However, its practical application is constrained by its ability to absorb

light mainly in the UV range, which constitutes just 5% of sunlight [15–17]. To overcome this limitation, current research focuses on modifying TiO_2 or the creation of TiO_2-based materials capable of absorbing visible light, thereby enhancing their efficiency and applicability [18–20].

Titanium–oxo complexes (TOCs) are an important research direction for modifying TiO_2-based materials. These compounds are characterized by stable structures in which the $\{Ti_aO_b\}$ core can be stabilized by various organic ligands, e.g., alkoxide and carboxylate [21–26]. Coordination of appropriate ligands reduces the HOMO–LUMO gap, causing radiation absorption in a wider range. An example is the study by Pei et al., who investigated TOCs with $\{Ti_{10}O_{12}\}$ cores stabilized by benzoic acid derivatives. They exhibited that using 4-methoxybenzoate ligands significantly enhanced the photocatalytic efficiency of these complexes against rhodamine B [27]. This effect was attributed to a reduction in the gap from 3.34 eV to 2.47 eV. The proposed mechanism of photocatalytic activity was related to the ligand-to-metal charge transfer (LMCT), which facilitated the generation of reactive oxygen species (ROS) responsible for degrading the dyes into H_2O and CO_2 [28,29]. The structure of the $\{Ti_aO_b\}$ core can also influence the photocatalytic activity of TOCs. Results of our work on oxo complexes with core structures $\{Ti_6O_6\}$, $\{Ti_4O_2\}$, $\{Ti_3O\}$, and $\{Ti_6O_4\}$, stabilized by 9-fluorenecarboxylate ligands, confirm this effect. Systems containing $\{Ti_6O_4\}$ and $\{Ti_6O_6\}$ cores tended to shift the absorption maximum toward the UV range, whereas simpler units ($\{Ti_3O\}$ and $\{Ti_4O_2\}$) shifted it toward visible light [30]. Continuing this line of research, we replaced carboxylate ligands with α-hydroxy carboxylate ligands (i.e., with 9-OH-9-fluorenecarboxylate [31] and mandelate ligands [32]). Our aim was to stabilize the structures of oxo complexes using new ligands, synthesize complexes with novel core structures, and evaluate the impact of these factors on their photocatalytic activity.

While analyzing the possibilities of modifying TiO_2-based materials, we became interested in a method to enhance their photocatalytic activity through doping with ruthenium complexes [33–38]. In recent years, the electrocatalytic and photocatalytic activity of single Ru atoms was investigated [39]. However, ruthenium(II) tris(bipyridine) complexes are regarded as benchmark photocatalysts due to their strong light absorption and long excited-state lifetimes [40–42]. Relatively few reports address the photocatalytic activity of Ru(III) complexes, although they have gained attention in recent years [43–45]. This led us to investigate the effects of ruthenium(III) complexes on organic dye degradation and compare their performance with oxo–Ti(IV) complexes. The photocatalytic mechanism of Ru(III) complexes involves metal-to-ligand charge transfer (MLCT) upon light irradiation, generating an excited [RuIII]* complex, which can act as an oxidant or a reductant, depending on the presence of electron acceptors or donors [46].

Studies on ruthenium complexes conducted by Fleming et al. showed that incorporating them into a poly(methyl methacrylate) (PMMA) matrix to enhance the stability of the complex enabled electron transfer measurements based on MLCT [47]. Moreover, it reduced the tendency for grain aggregation, thereby improving the practical applicability of such systems. A similar challenge arises with titanium–oxo complexes (TOCs), which are commonly used in photocatalytic experiments in powder form. This form makes them prone to hydrolysis, significantly complicating their practical application. To overcome this limitation, the stability of TOCs can be enhanced by coordinating suitable ligands [48,49] or embedding them into a polymer matrix [30,50,51]. In our previous studies, we introduced oxo complexes into the PMMA matrix and evaluated the photocatalytic performance of the resulting composites, achieving promising results [30,42,50–52]. PMMA was chosen as the polymer matrix due to its transparency to visible light, excellent mechanical properties, and environmental stability. Furthermore, incorporating TiO_2 into the PMMA matrix has been shown to improve the thermal stability and electrical conductivity of the composites [53,54].

Despite these advantages, PMMA + TOC composites have not been widely investigated in photocatalytic applications, which provided additional motivation for our research. Incorporating the complex into a polymer matrix also addresses important environmental considerations. Hydrolysis products can contribute to additional contaminants that require removal, and their elevated concentrations, along with potential interactions with other substances, may present significant environmental risks.

2. Materials and Methods

2.1. Materials

Titanium–oxo complexes (**1**)–(**3**) were synthesized as reported in [31,32], while ruthenium complexes (**4**) and (**5**) were prepared following the procedures previously outlined [55,56]. Detailed information regarding the preparation of the studied compounds is provided in the Supplementary Information.

2.2. Analytical Procedures

The structures of the synthesized compounds (**1**)–(**5**) were characterized using IR spectrophotometry performed on a Perkin Elmer Spectrum 2000 FT-IR spectrometer (operating in the 400–4000 cm^{-1} range with KBr pellets) and Raman microscopy using a RamanMicro 200 spectrometer (PerkinElmer, Waltham, MA, USA). Raman spectra were recorded with a 785 nm laser (maximum power: 350 mW) across the 200–3200 cm^{-1} range, employing a 20× 0.40/FN22 objective lens and an exposure time of 15 s for each measurement. Solid-state 13C13C NMR spectra were obtained at 22 °C using a Bruker AMX 300 spectrometer (Cambridge Scientific Corp., Watertown, MA, USA). Elemental analyses were conducted with an Elementar vario Macro CHN analyzer (Elementar Analysensysteme GmbH, Hanau, Germany). Titanium content was determined as TiO_2, according to the method of Meth-Cohn et al. [57]. According to [58], ruthenium content was determined as RuO_2. Diffuse reflectance UV-Vis (UV-VIS-DRS) spectra, recorded between 200 and 800 nm on a Jasco V-750 spectrophotometer (JASCO Deutschland GmbH, Pfungstadt, Germany), were used to determine the absorption maxima.

2.3. Composite Film Preparation

The composite films were prepared through compound (**1**)–(**5**) dispersion (approximately 0.025, 0.062, 0.12, or 0.25 g in 5 mL of THF) into poly(methyl methacrylate) (PMMA). For this purpose, 1.0 g of PMMA was dissolved in 10 mL of THF, and the powdered samples of the complexes were added to the resulting solution to achieve concentrations of 2%, 5%, 10%, and 20%, respectively. After mixing for 120 min in an ultrasonic bath, the solution containing the dispersed complex powders was poured into a glass Petri dish and left at room temperature (in a glove box) to allow the solvent to evaporate slowly. The composite films, with a thickness of approximately 50 μm, were characterized using Raman spectroscopy. The complexes' size and dispersion pattern in the composite samples were analyzed using a Quanta scanning electron microscope with field emission (SEM, Quanta 3D FEG, Houston, TX, USA). X-ray absorption spectra were recorded at the National Synchrotron Radiation Centre SOLARIS on the PIRX beamline with a bending magnet, focusing on the Ti $L_{2,3}$-edge (440–510 eV). Finely ground powder samples were mounted on double-sided adhesive conductive graphite tape, while composite materials were similarly secured. Measurements for both sample types were conducted with a step size of 0.2 eV in the pre-edge region, 0.1 eV in the edge regions, and 0.5 eV in the high-energy range. Data acquisition was performed at room temperature under ultra-high vacuum (UHV) conditions, using total electron yield (TEY) and fluorescence yield (FY) detection modes. Each measurement was

repeated at least three times. The collected data were processed and deconvoluted using ATHENA software (v3) from the Demeter package [53].

2.4. Estimation of the Adsorption Capacity

The adsorption capacity of PMMA + TOCs films (TOCs = (**1**)–(**5**)) was determined by measuring changes in the absorbance of the dye solution (methylene blue (MB), rhodamine B (RhB) and crystal violet (CV)) (C = 1.0 × 10^{-5} M). The composites (26 × 26 mm) and 30 mL of the dye solution were placed in a laboratory bottle in a dark place. Spectra were recorded (JASCO Deutschland GmbH, Pfungstadt, Germany) in the range of 400–700 nm at 0, 1, 3, 5, 9, and 24 h by taking 3.5 mL of the solution into a quartz cuvette. The absorption maxima were recorded at 664, 590, and 554 nm for MB, RhB, and CV, respectively. The percentage of MB decolorization was calculated using the following equation:

$$\% \text{ dye decolourization} = \frac{(C_0 - C_t)}{C_0} \cdot 100\% \quad (1)$$

where C_0 is an initial dye concentration and C_t is a dye concentration at a given time t [54].

2.5. Estimation of the Photocatalytic Activity

The photocatalytic activity of PMMA + TOCs foils (TOCs = (**1**)–(**5**)) was estimated by monitoring the concentration changes of methylene blue (MB) and crystal violet (CV) in aqueous solution. Sample preparation included irradiating the samples with UVA or Vis radiation for 28 h and placing them in quartz cuvettes with dye solution (V = 3.5 mL and C = 2.0 × 10^{-5} M). After 12 h in the dark, the solution was replaced by MB solution (C = 1.0 × 10^{-5} M). Samples with dye solution were exposed to UVA irradiation (18 W lamp, 340–395 nm range) and Vis light (77 W tungsten halogen lamp, range of 350–2200 nm). Absorbance was measured at 664 nm for MB and 590 nm for CV (Metertech SP-830 PLUS, Metertech, Inc., Taipei, Taiwan) every 7 h during 38 h of irradiation. The percentage of MB decolorization caused during photodegradation was calculated using the same equation as the adsorption capacity [54]. Linear changes of the studied dyes' concentration in time (zero-order kinetics) allowed for the assumption that the dye concentration does not affect the monitored process in the studied reaction time, as the process rate reached its maximum in the applied conditions. Thus, calculation of the observed rate constants can be performed with a simple equation after the following mathematical transformations:

$$-\frac{dc_{dye}}{dt} = k \quad (2)$$

$$dc_{dye} = -kdt \quad (3)$$

$$c_t - c_0 = -kt \quad (4)$$

$$c_0 - c_t = kt \quad (5)$$

Taking into account the definition of the dye decolorization percentage, the above equation can be transformed as follows:

$$\% \text{ dye decolourization} = \frac{c_0 - c_t}{c_0} 100\% = \frac{kt}{c_0} 100\% = \frac{100\%k}{c_0} t = k_{obs} t \quad (6)$$

Application of the same starting concentration of the used dyes (c_0) allows for estimation of the relative photoactivity of the studied materials and their mutual comparison.

2.6. Electron Paramagnetic Resonance (EPR) Spectroscopy

EPR measurements were performed on an X band EPR SE/X-2541M spectrometer (Radiopan, Poznań, Poland) with 100 kHz modulation. The microwave frequency was monitored with a frequency meter. The magnetic field was observed with an automatic NMR-type JTM-147 magnetometer (Radiopan, Poznań, Poland). Measurement conditions were as follows: microwave frequency: ca. 9.33 GHz (X-band); microwave power: 2–58 mW; modulation amplitude: 0.12–1 mT; sweep: 10–100 mT; sweep time: 4 min; time constant: 0.1 s; receiver gain: 0.3–8.0 × 10^5. Spectra of complexes (**2**)–(**5**) were registered for powdered samples and composites.

3. Results

The structural compatibility and purity of the synthesized complexes (**1**)–(**5**) were verified using spectroscopic methods. However, it should be noted that ^{13}C NMR spectra for complexes (**4**) and (**5**) were not recorded, as Ru(III) compounds are paramagnetic, which limits the applicability of this technique [59]. The obtained powdered samples of the studied compounds were introduced in a poly(methyl methacrylate) (PMMA) matrix to create composite systems that were subsequently subjected to further investigations.

3.1. Characterization of PMMA + Complex Composites

The obtained compounds and their composites were analyzed using solid-state UV-Vis diffuse reflectance spectroscopy (UV-Vis DRS). The HOMO–LUMO energy gap of powders (**1**)–(**5**) was determined using the Kubelka–Munk (K-M) function plotted against light energy (i.e., K = f(hν), where K = $(1-R)^2/2R$ and R is the reflection). In the case of TOCs, the HOMO–LUMO gap is 3.12 eV, 2.96 eV, and 2.39 eV for (**1**) (Figure 1a), (**2**) [31], and (**3**) [31], respectively. In turn, for ruthenium complexes, it is 2.75 eV and 2.78 eV for (**4**) and (**5**), respectively (Figure 1b). Analysis of spectral data revealed that λ_{max} was 308 nm (**1**) (Figure 1c), 306 nm (**2**) [31], 330 nm, 395 nm (**3**) [31], and 334 nm (**4**), (**5**) (Figure 1d). The maximum absorption was also determined for the composite materials.

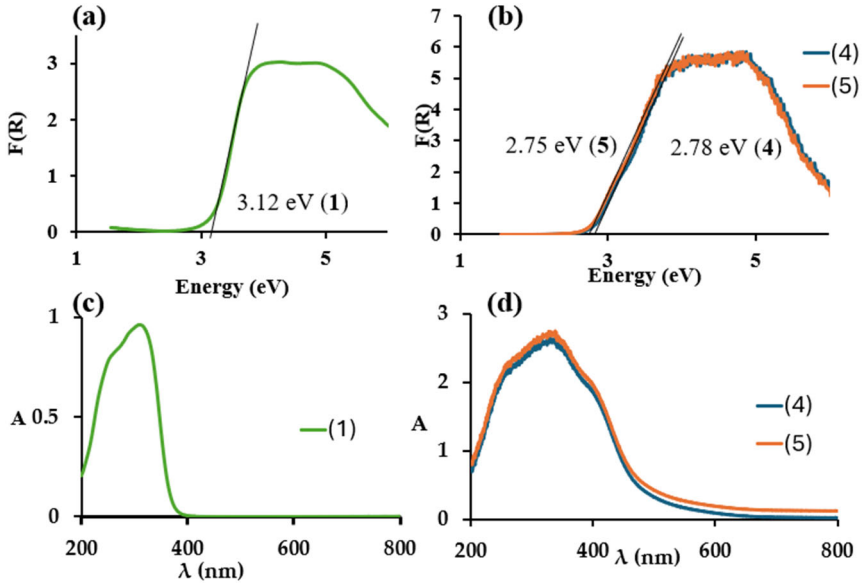


Figure 1. The results of studies on micro-grains (**1**), (**4**), and (**5**), carried out using UV-Vis diffuse reflectance spectroscopy (DRS) to investigate their optical properties (**a**,**b**), are presented together with the determination of the HOMO–LUMO gap for these compounds, derived from Kubelka–Munk function plots versus light energy (**c**,**d**).

Samples containing complex (**1**) (2% and 5% by weight) exhibited two maxima at 236 nm and 281 nm (Figure 2a), corresponding to the absorption maxima of PMMA. The PMMA + (1) 20 wt.% composite showed a broad absorption range (200–450 nm) with a low-intensity band peaking at approximately 330 nm. In the case of the PMMA + (**2**) series, the absorption edge is slightly shifted toward the visible light range (400 nm for PMMA + (**2**) 2% and 5%, and 480 nm for PMMA + (**2**) 10% and 20%) (Figure 2b). However, for the PMMA + (**3**) composites, the absorption edge is positioned at 480 nm for PMMA + (**3**) 2% and 5% samples and 500 nm for PMMA + (**3**) 10% and 20%. The absorption maximum remains in the ultraviolet range (Figure 2c).

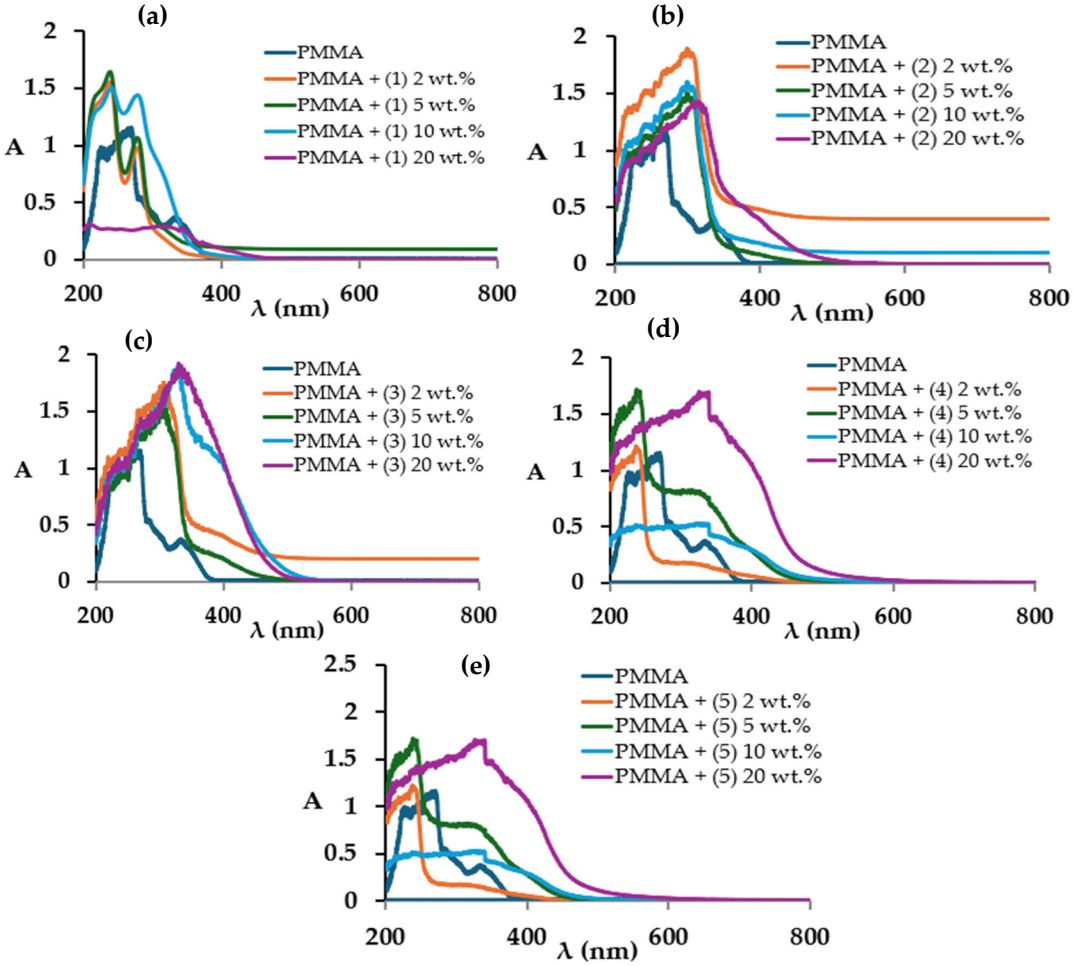


Figure 2. Solid-state UV-Vis-diffuse reflectance spectra (DRS) of the composites PMMA + (**1**)–(**5**) (**a**–**e**).

Composite materials made of PMMA and ruthenium complexes are characterized by an absorption edge in the 400–450 nm range. Almost all samples have two maximum absorptions in the 238–336 nm range (λ = 236–281 nm PMMA range). The exception is the PMMA + (**5**) 20 wt.% sample, where the absorption edge is located around 550 nm and one of the maximum absorptions was found at 420 nm (Figure 2d,e).

Composite materials based on poly(methyl methacrylate) containing 2%, 5%, 10% and 20% of complexes (**1**)–(**5**) were spectrally characterized to confirm the presence of the complex and that the structure of the compound does not change after introduction into the polymer matrix (Figure 3). Previously, our research exhibited that the structures of titanium–oxo complexes (**1**)–(**3**) are stable in contact with water. IR spectra and XRD diffractograms did not register significant differences [31,32].

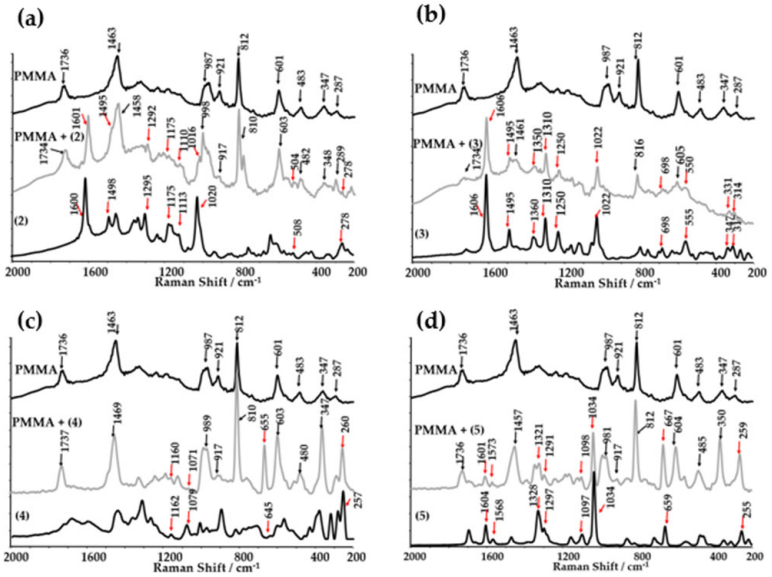


Figure 3. Raman spectra of powders (**2**) (**a**), (**3**) (**b**), (**4**) (**c**), and (**5**) (**d**), their composites containing 20 wt.% of the complex, and pure PMMA.

The analysis of scanning electron microscope (SEM) images provided insights into the dispersion of complexes (**1**)–(**5**) within the polymer matrix (Figures S1 and S2). The PMMA + (**1**) and PMMA + (**2**) composite samples are comparable, containing grains with diameters between 60 and 200 nm. Their high surface energy promotes aggregation, forming 30 to 250 μm grains. The packing density of these aggregates increases with the wt.% concentration of the complexes in the PMMA matrix. In the PMMA + (**3**) sample, densely packed crystalline grains are observed, with sizes dependent on the complex concentration in the matrix. At lower concentrations (2 wt.% and 5 wt.%), the sample primarily comprises grains with diameters between 145 and 355 nm and occasional larger grains measuring 200 to 500 μm. At higher concentrations (10 and 20 wt.%), the samples contain microcrystals of the oxo complex ranging from 900 nm to 5 μm in size (Figure S1).

The morphology of composite samples enriched with complexes (**4**) and (**5**) resembles that of the composites containing complexes (**1**) and (**2**). These composites are formed by dispersed grains with diameters of 40–200 nm, which, depending on concentration, may form larger micrometric aggregates (Figure S2). Additionally, SEM-EDX analysis confirms the presence of complexes (**2**)–(**5**) in the composite samples (Figures S3 and S4, Table S1), while the presence of complex (**1**) grains in the PMMA composites was verified in a previous SEM-EDX study [32].

A crucial aspect of our study was confirming that the investigated complexes retained their structure after being incorporated into the polymer matrix. To this end, we recorded Raman spectra of pure PMMA, complexes (**2**)–(**5**), and PMMA + ((**2**)–(**5**)) composites. Analysis of the spectra confirmed that the introduction of the studied complexes into the PMMA matrix did not significantly alter their structure (Figure 3). Key to this identification were the bands observed around 1600 cm^{-1} (ν_{as}(COO)), which confirm the coordination of the carboxylate group within the α-hydroxycarboxylate ligand. Additionally, the detection of ν(O-CR) bands between 1200 and 1000 cm^{-1} indicates the presence of coordinated alkoxide groups characteristic of the TOCs' structure. Weak bands appearing below 900 cm^{-1} further suggest the presence of titanium–oxo bridges. The structural stability of complex (**1**) in the PMMA + (**1**) composite had been previously confirmed [37]. In the Raman spectra of composites containing ruthenium(III) complexes, bands around 1600 cm^{-1} were observed, confirming the coordination of ligands. Moreover, bands in the range of 1320–650 cm^{-1}

were attributed to (CN) group vibrations, while the band near 260 cm^{-1} corresponds to ν(Ru-O) vibrations.

X-ray Absorption Near-Edge Structure (XANES) spectroscopy, utilizing synchrotron radiation, was employed to confirm the structure of complexes (**1**)–(**3**) in the composite samples. This technique involves photon absorption, where core-level electrons are excited to unoccupied states when the photon energy meets or exceeds the binding energy. The absorption edge, corresponding to the core-level energy specific to each element, makes XANES an element-selective method. Titanium L-edges are rarely studied in complex titanium clusters. The discussion of electronic structures is difficult because the observed pattern depends on crystal field splitting, spin–orbit coupling, and charge transfer effects. Also, in a theoretical approach, multiplet interactions affect the Ti L-edge spectrum [60]. However, it is known that peak numbers and their positions and profiles depend strongly on the local environment. Lätsch et al. discussed in detail XAS spectra of several Ti(IV) complexes, among them $[Ti_2O_2(acac)_4]$ with bridging oxo ligands. They showed that it significantly differs from tetrahedral mononuclear complexes, and four main features are observed.

Nevertheless, the described complexes did not exceed the dimer. We decided to apply the XANES method for Ti L-edges for the complicated cores observed in our structures. The energy range for titanium was carefully selected to avoid the edge regions of other elements, which is crucial for proper spectra normalization. Two detection modes were also used, differing in penetration depth; the TEY detector reaches tens of nanometers, whereas the fluorescence yield (FY) detector can go up to several hundred nanometers [61]. Signals of a powder from TEY and FY detectors are comparable, and only TEY results will be presented. For composites, the TEY detector cannot provide any signal, and so results from the FY detector will be given. The L-edges of 3*d* transition metals have been relatively underexplored, partly due to their significant surface sensitivity. These edges are highly responsive to variations in coordination and oxidation states and, owing to their reduced intrinsic broadening, provide more detailed insights into the electronic structure of transition metal ions.

The spectra for titanium significantly differ in peak position. For powders, two additional tiny features in the pre-edge region were identified (at. ca. 456.4 and 457.3 eV), resulting from dipole forbidden transitions (Figure 4).

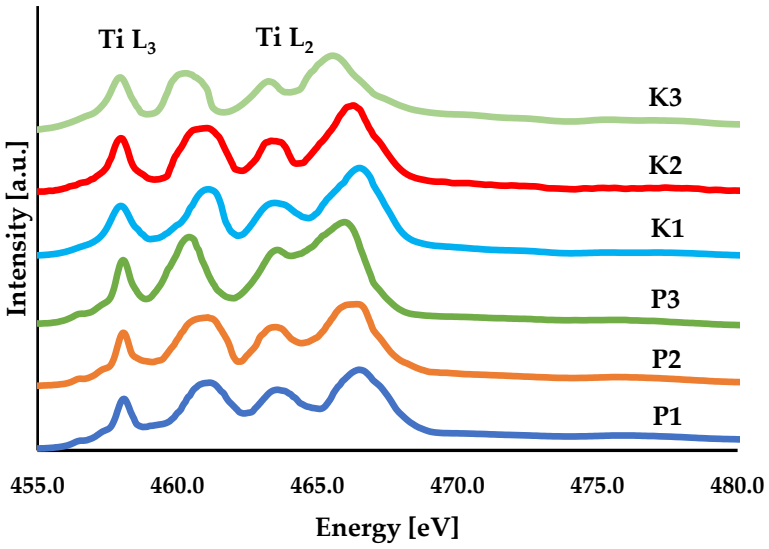


Figure 4. Normalized XANES spectra of titanium(IV) $L_{2,3}$-edge for powdered samples (P1, P2, P3) collected using the TEY detector and composite materials (K1, K2, K3) with 20% admixture of the studied titanium complexes using an FY detector.

Such signals in the range of 456.5–457.5 eV were also observed for TiO_2 [62,63]. They are not visible for our composites registered in FY mode. It should be noted that the spectra were successfully measured only for the composites with the highest admixture of the studied titanium complex (20%). After dispersing our complexes in a polymeric matrix, those spectra underwent no significant changes, and the shifts are within 0.3 eV. This might indicate the stability of the obtained cores. In all cases, titanium spectra show more intense bands corresponding to the L_2 edge than for the L_3 peaks. In general, there are four main features (Table S2). Peaks at ca. 458 and 461 eV correspond to $2p_{3/2} \rightarrow t_{2g}$ and $2p_{3/2} \rightarrow e_g$ transitions, whereas at ca. 463 and 466 eV they correspond to $2p_{1/2} \rightarrow t_{2g}$ and $2p_{1/2} \rightarrow e_g$, respectively. It should be noted that we cannot distinguish any significant profile change or band splitting for e_g levels. This effect is quite common, even for TiO_2, and it is ascribed to the splitting of e_g levels into d_{z^2} and $d_{x^2-y^2}$, and the profile change is considered a fingerprint between rutile and anatase [63]. In the reported spectra, a deconvolution was performed in Athena using Gaussian functions, and the results are presented in Table S2. In the case of FY detection mode, the spectra were much noisier, and hence they were smoothed. Nevertheless, no obvious pre-peak was observed, and smoothing did not exclude any peak. The profound structural and topological differences concerning even coordination numbers for the studied titanium complexes resulted in peak position shifts. The separation between t_{2g} and e_g levels is called crystal field splitting (Δ parameter). Hence, we can calculate this parameter from L_3 and L_2 edges. In our case, this difference is similar for both edges, being 3.0 and 3.0 for P1, 2.9 and 2.8 eV for P2, 2.3 and 2.4 eV for P3, 3.1 and 3.1 for K1, 3.0 and 3.0 for K2, and 2.3 and 2.2 eV for K3. Hence, we can suppose that both core holes ($2p_{3/2}$ and $2p_{3/2}$) are screened similarly. These data also show that Δ_{oct} (almost all titanium atoms were found in an octahedral environment, except for Ti4 in (**1**) and Ti2 in (**2**) [31,32]) for powders and composites are almost identical, and the changes are tiny (up to 0.2 eV). It also proves that the polymeric matrix did not affect the structure of titanium clusters. Moreover, these data agree well with those determined using the Kubelka–Munk method and theoretical calculations, which were 3.12, 2.96, and 2.39 eV for (**1**), (**2**), and (**3**), respectively [32].

Unfortunately, XANES experiments have only been conducted on titanium complexes, which is primarily due to sample availability and the characteristics of the beamline. Our spectra were measured using soft X-ray radiation, with 2000 eV as the maximum available energy at the PIRX beamline. This setup is ideal for probing 3d transition metals at their L-edges but is far less effective for 4d metals; for ruthenium, only the M-edge would be accessible. This limitation is supported by numerous studies on L-edges of first-row transition metals, with far fewer publications addressing the M-edges of ruthenium.

*3.2. Cationic Dyes' Adsorption on Composites PMMA + ((**1**)–(**5**))*

The adsorption capacity of the tested composites was evaluated to measure their effectiveness in removing dye contaminants from water. Cationic dyes—methylene blue (MB), rhodamine B (RhB), and crystal violet (CV)—were selected as model contaminants. The results in Figure 5 and Table S3 reflect 24 h of interaction between the composites and the dye solutions without light. In interpreting the received results, we considered (i) the effect of the complex type on the adsorption of model dyes and (ii) the impact of varying complex concentrations within the composite samples. Generally, it was noted that the oxo–Ti(IV) complexes showed superior adsorption of MB compared to the other dyes, while the Ru(III) complexes more effectively adsorbed CV. Both types of complexes demonstrated low adsorption of RhB (Figure 5). The amount of adsorbed dye increased with rising complex concentration (Table S3). The composite enriched with complex (**3**) exhibited the highest adsorption, while the dye adsorption levels of composites containing

the remaining complexes were relatively similar, remaining below 11% even at 20 wt% complex content.

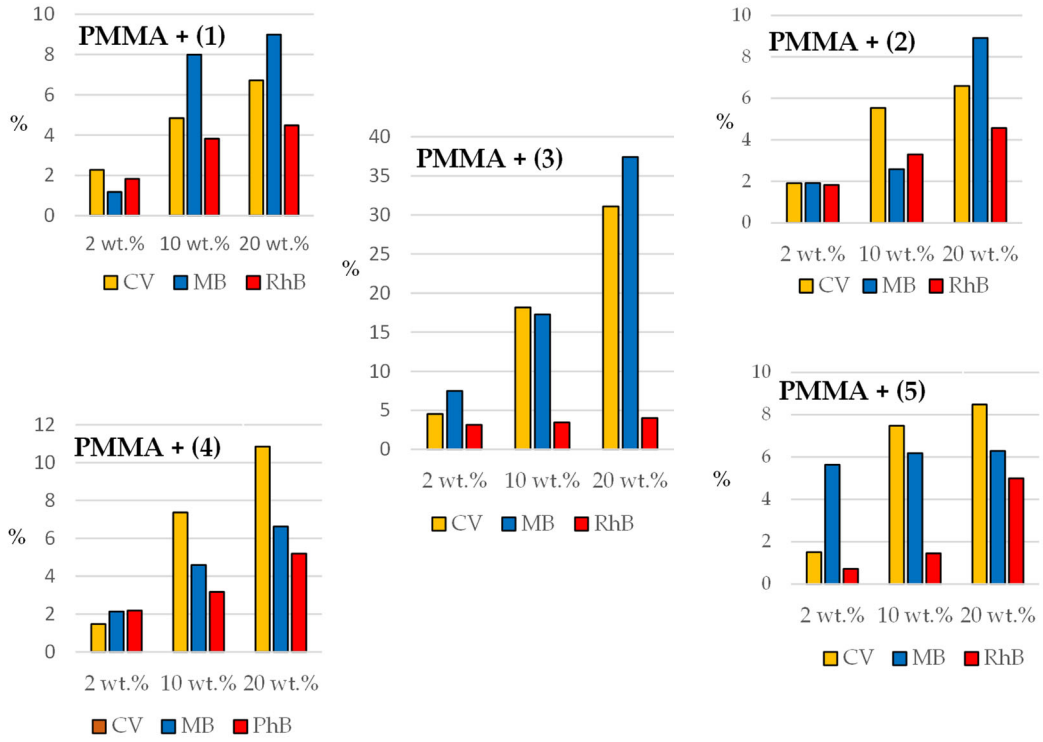


Figure 5. Percentage reduction of the concentration of the studied group of dyes by PMMA composites with complexes (**1**)–(**5**). For clarity, results are shown for systems containing 2, 10, and 20 wt.% of complexes; complete data are provided in Table S3.

*3.3. Estimation of Photocatalytic Activity of Composites PMMA + ((**1**)–(**5**))*

The photocatalytic activity of composites containing titanium(IV)–oxo complexes and ruthenium(III) complexes was assessed by monitoring changes in the decolorization of MB and CV solutions under UV irradiation and MB under visible light (Vis) (Figures S5–S7 and Tables S4–S6). The study focused on MB and CV dyes, as these were the most readily absorbed by the tested composites. Figure 6 presents representative changes in the decolorization percentages of MB (Vis and UV) and CV (UV) using the PMMA + (**3**) composite.

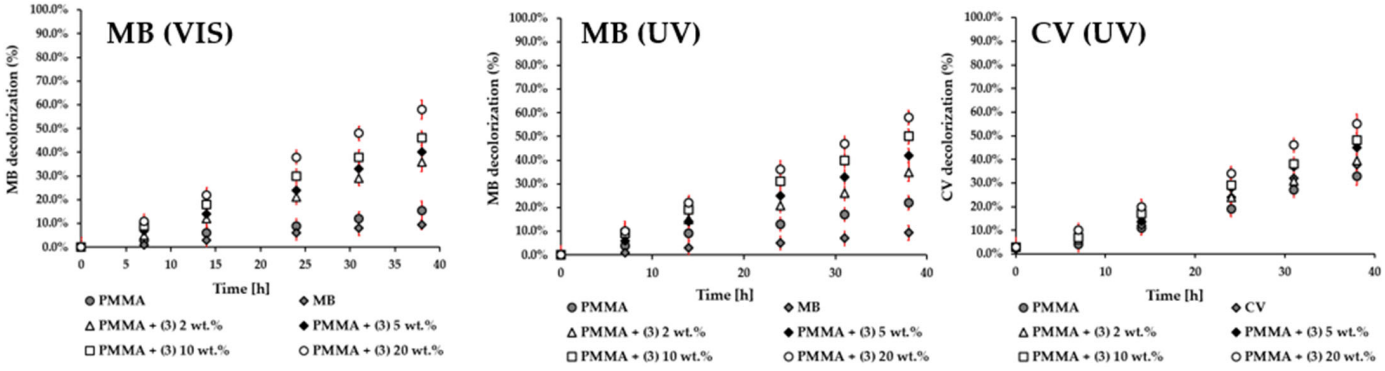


Figure 6. Changes in the percentage of dye decolorization over time for MB (VIS and UV) and CV (UV) with PMMA + (**3**) composite, as an example.

Figure 7 illustrates the changes in the observed rate constants (h^{-1}) for MB solution decolorization relative to PMMA for PMMA + (**1**)–(**5**) composites exposed to Vis and UV light (measurement data provided in Figures S5 and S7 and Tables S4 and S6). Meanwhile,

Figure 8 presents the results of the study of changes in the rate constants (h^{-1}) for CV solution decolorization under UV light for the tested group of composites (measurement data provided in Figure S6 and Table S5). The decrease in the concentration of both dyes during irradiation follows a linear trend consistent with zero-order kinetics, indicating that the photodecomposition rate of each dye remains constant throughout the measurement period. The analysis of the results indicates that the composites enriched with oxo–Ti(IV) complexes (**1**) and (**2**) exhibited the highest photocatalytic activity under UV light. Among these, the PMMA + (**2**) composites stand out for their exceptional performance, achieving the highest percentage of MB solution decolorization across all tested concentrations (2–20 wt.%), with values ranging from 45.3% to 73.1%, significantly outperforming the PMMA control (17.4%) (Table S4).

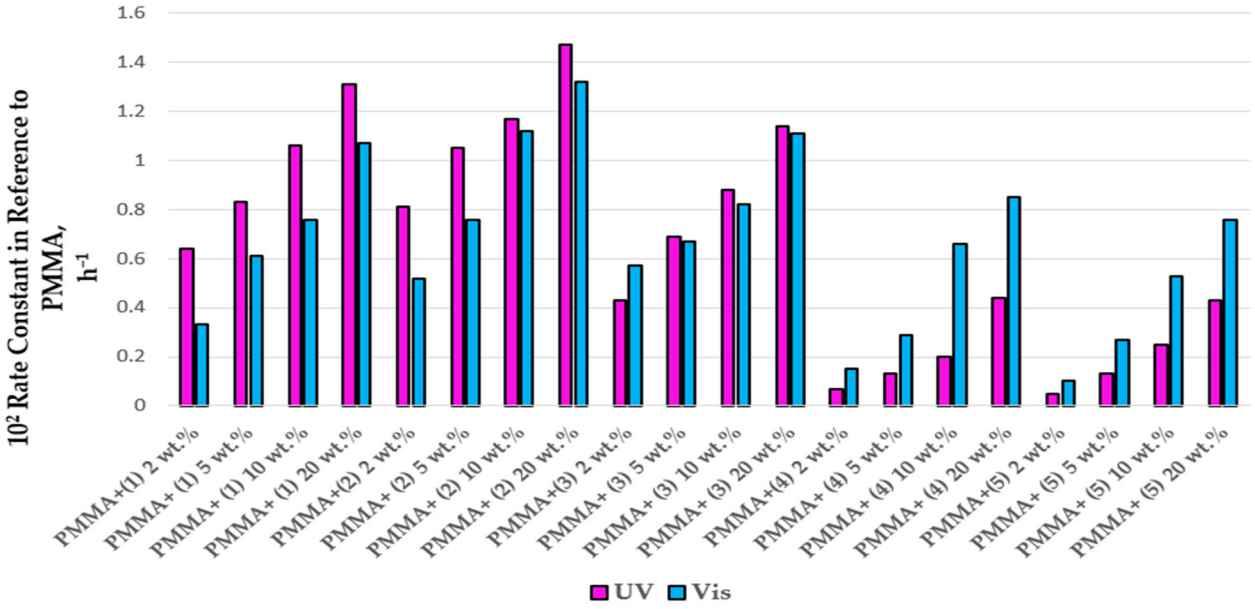


Figure 7. Changes in the observed rate constants (h^{-1}) of MB solution decolorization processes relative to PMMA for composites PMMA + (**1**)–(**5**) exposed to UV and visible (Vis) light.

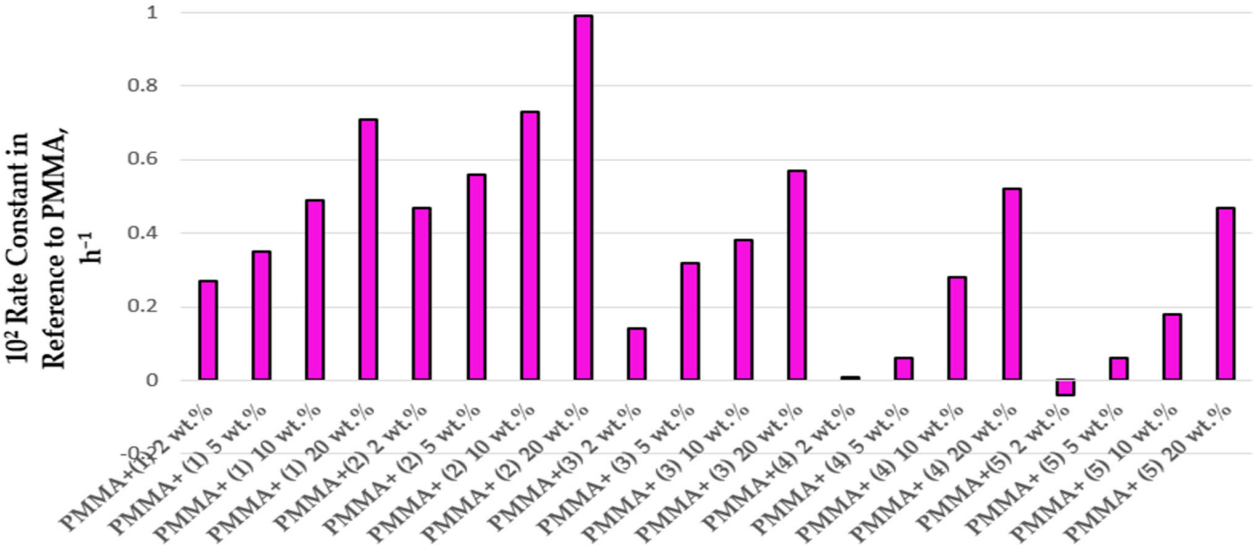


Figure 8. Changes in the observed rate constants (h^{-1}) of CV solution decolorization processes relative to PMMA for composites PMMA + (**1**)–(**5**) exposed to UV light.

This superior activity is further corroborated by the decolorization studies on CV solutions, where the PMMA + (**2**) samples with 2–20 wt.% of the complex achieved a decolorization degree between 51.1% and 70.9%, compared to 37.5% for pure PMMA. In contrast, the oxo complex (**3**) and Ru(III) complexes (**4**) and (**5**) showed markedly lower photocatalytic efficiencies. Notably, for all composites, the photocatalytic activity was consistently improved with increasing concentrations of the complexes in the PMMA matrix. However, it should be emphasized that the composites containing Ru(III) complexes did not exhibit any photocatalytic activity at the lowest concentration tested (2 wt.%) in the decolorization of CV solutions (Figures 8 and S6).

The studied samples were also irradiated with visible light (Vis) to assess their effect on the decolorization of MB solutions. The results of these measurements are presented in Figure 7 and Figure S7, as well as Table S6. Subsequently, these experiments were repeated over three cycles to verify the stability of the photocatalytic activity of the tested systems. The findings demonstrated that the photocatalytic activity of the studied samples remained consistent across all measured cycles (Figure 9). The results of our investigations revealed that composites containing complexes (**1**) and (**2**) exhibited lower photocatalytic activity under visible light compared to their activity under UV radiation (Figure 7). However, the composite containing complex (**3**) as a filler showed a significant increase in activity under visible light, nearing the activity observed under UV exposure (Figure 7 and Table S6). In contrast, both composites containing Ru(III) complexes (PMMA + (**4**) and PMMA + (**5**)) displayed notable activity under visible light. Additionally, it is worth emphasizing that in all samples, the concentration of the complex within the polymer matrix played a crucial role in determining their photocatalytic activity.

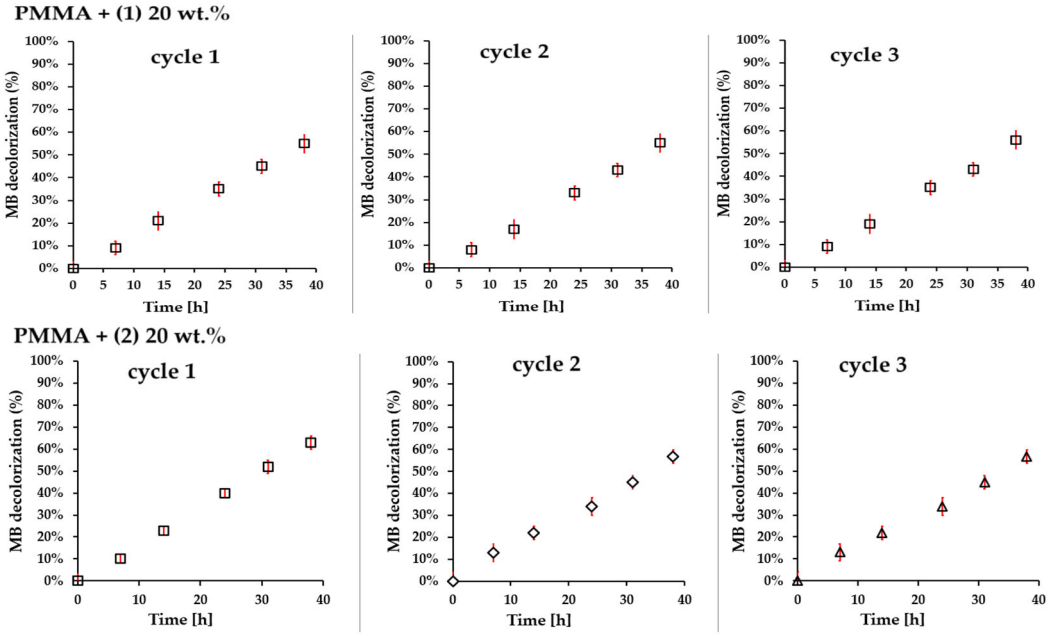


Figure 9. *Cont.*

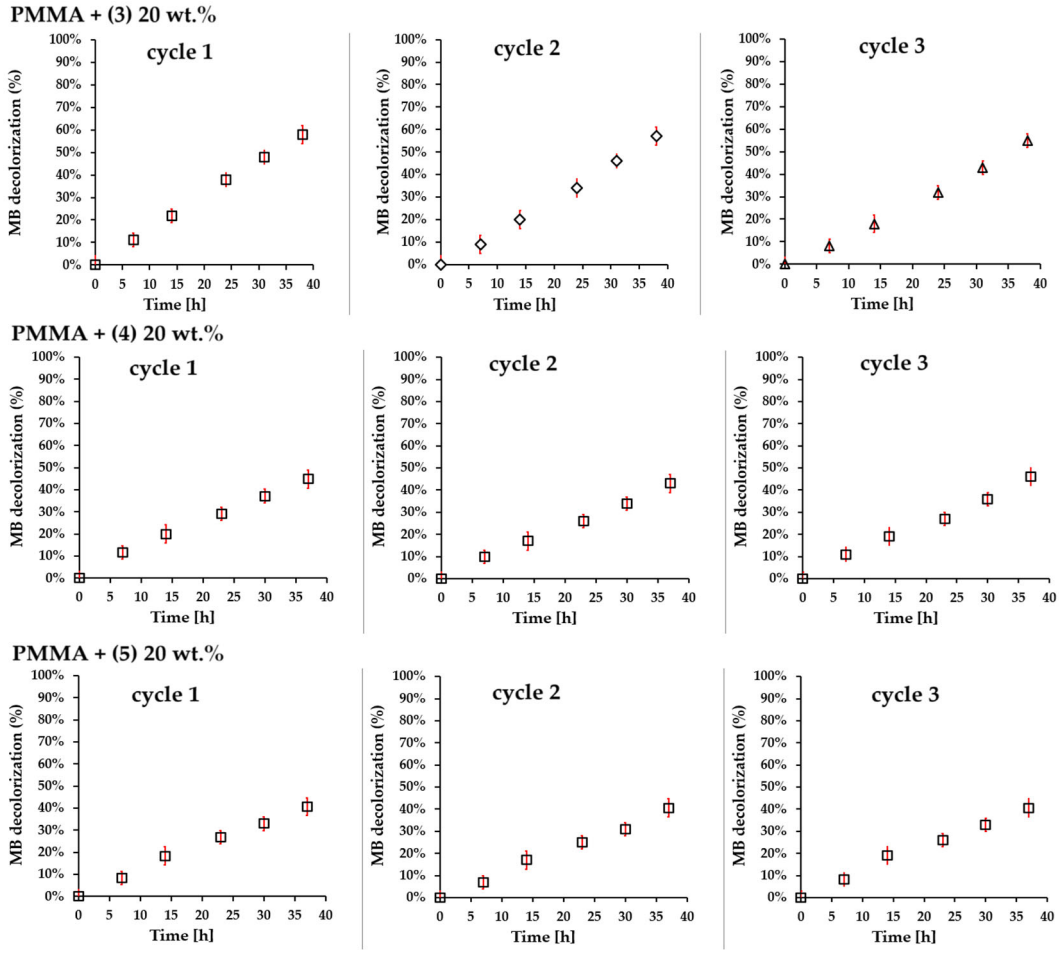


Figure 9. Recycling MB decolorization tests of composite materials PMMA + Comp. 20 wt.% (Comp. = (**1**), (**2**), (**3**), (**4**), and (**5**)) irradiated with visible light.

3.4. Electron Paramagnetic Resonance (EPR) Spectroscopy

EPR spectroscopy confirmed the presence of paramagnetic species in all tested complexes and their composites, while no signals were detected in the spectra of pure PMMA. Upon daylight activation, complex (**1**) generated O_2^- and Ti(III) species, while its PMMA composite also contained O^- [32]. Complexes (**2**) and (**3**) exhibited different behaviors, as (**2**) showed a free electron signal, whereas (**3**) produced O^-, O_2^-, and Ti^{3+} species, which were also present in samples of both composites (Table S7, Figures S8 and S9). Analysis of ruthenium(III) complexes' spectra revealed that (**5**) generates a significantly more intensive signal than complex (**4**). In the case of both powders and composites, signals from Ru(III) were recorded, but in the case of composites, they are much weaker (Table S7, Figures S10 and S11). These results support the proposed photocatalytic mechanisms by confirming that photoactivation generates reactive paramagnetic species, which play a crucial role in catalytic processes.

4. Discussion

The conducted studies focused on evaluating the photocatalytic activity of Ti(IV)–oxo complexes stabilized with α-hydroxycarboxylic ligands, which were incorporated into a PMMA matrix. The compounds studied included $[Ti_8O_2(O^iPr_{)20}(man)_4]$ (**1**), $[Ti_4O(O^iPr)_{10}(O_3C_{14}H_8)_2]$ (**2**), and $[Ti_6O_4(O^iPr)_2(O_3C_{14}H_8)_4(O_2CEt)_6]$ (**3**), which had been structurally and spectroscopically characterized in our earlier research [31,32]. Additionally, composites containing K[Ru(Hedta)Cl]·$2H_2O$ (**4**) and $[Ru(pic)_3]\cdot H_2O$ (**5**) were investigated.

These Ru(III) complexes were synthesized via reactions of aquapentachlororuthenate(III) hydrate or ruthenium(III) chloride with EDTA or picolinic acid [38,64].

One of the aims of this research was to determine the possibility for the fabrication of surface-active composite coatings of the PMMA + Comp. type (Comp. = TOCs or Ru(III) complexes). The formation of such systems was crucial to protecting the structure of the studied compounds from hydrolysis or dissolution processes and minimizing nanograin aggregation. It is noteworthy that previous studies on the photocatalytic activity of TOCs primarily involved powdered forms. Thus, a significant stage of the research was confirming the structure of complexes (**1**)–(**5**) after their incorporation into the PMMA matrix. A comparison of the Raman spectra for complexes (**1**)–(**5**) and the PMMA + (**1**)–(**5**) composites revealed that embedding these complexes into the PMMA matrix did not induce significant structural changes. For multinuclear oxo-Ti(IV) complexes (**1**)–(**3**), the stability of their structure within the composite was further confirmed through XAS studies.

In the initial stage of the study, we aimed to determine how the introduction of Ti(IV) or Ru(III) complexes into a polymer matrix influences the adsorption of organic dyes. Most of the insights into the sorption properties of Ti(IV) and Ru(III) compounds come from studies on metal–organic frameworks (MOFs) [65–70], which are valued for their high porosity, structural diversity, and highly active dye adsorption sites [71–73]. The amount of dye adsorbed depends on the dye's structure and is influenced by the electron density of the adsorbents [74]. For example, MB and CV molecules are smaller than RhB, allowing more of them to interact with TOCs or Ru(III) complexes.

In our previous work, we demonstrated that introducing an additional ligand into the structure of compound (**3**) increases the electron density due to chelate rings and free carboxyl groups [31]. In contrast, compound (**2**) contains significantly fewer electron-dense areas. We hypothesize that electron-dense regions attract dye molecules, as the positively charged nitrogen in the dye structure is generally inclined to interact with electron-rich surface groups [75]. Molecular electrostatic maps of mandelic acid suggest that the hydroxyl group is most susceptible to nucleophilic attack [76,77]. However, in compound (**1**), this hydroxyl group is coordinated, potentially reducing the electron density. For Ru(III) complexes containing EDTA and picolinate ligands, the highest electron density is expected in the C=O groups [78,79]. This effect aligns with studies on EDTA-containing copper complexes, where the C=O groups exhibit high electronegativity, while the rest of the molecule remains neutral [78]. The reduced adsorption efficiency of Ru(III) complexes, especially compared to titanium compounds, such as (**3**), may be attributed to their smaller size, which limits the electron-dense surface area available for interactions with dye molecules.

Basing on the obtained results, the next stage of our study focused on the use of methylene blue (MB) and crystal violet (CV) solutions. To evaluate the photocatalytic activity of the studied complexes (1)–(5), it was crucial to determine their maximum absorption within the composite materials as well as their HOMO–LUMO gap values. These parameters can be tailored to achieve desired properties, for instance, through structural modifications of the complexes, such as functionalizing the stabilizing ligands. Liu et al. demonstrated that introducing salicylate ligands can reduce the Ep values of complexes from 2.24 to 1.88 eV [80], while chromophore ligands broaden this range from 3.41 to 1.98 eV [81]. For ruthenium compounds, the existing literature suggests that modifications to the HOMO–LUMO gap are primarily focused on Ru(II) complexes, particularly those containing bipyridine ligands. Adjusting the position of the bipyridine substituent or altering the halide coordination can result in either an increase or decrease in the HOMO–LUMO gap [82,83]. Similar trends are expected to apply to Ru(III) complexes; however, these compounds have been studied less extensively. Among the tested Ru(III) compounds, complexes (**4**) and (**5**) exhibit comparable Ep values of 2.75 and 2.78 eV, respectively, placing

them between studied complexes (**2**) (Ep = 2.96 eV) and (**3**) (Ep = 2.39 eV). This suggests that these complexes are also likely to exhibit photocatalytic activity [84,85].

The photocatalytic activity of the studied composites containing 2, 5, 10, and 20 wt.% of complexes (**1**)–(**5**) was assessed by analyzing the decolorization of MB solution samples irradiated with UV and visible (Vis) light, following the ISO 10678 standards [86]. Additionally, tests in UV was carried out using CV solutions.

The performed tests confirmed that some percentage of each studied dye is adsorbed on the composite surface (Table S3). To maintain the same concentration condition in each kinetic run, during photodegradation tests, the "old" dye solution was replaced after the adsorption process with a fresh one. Thus, the starting dye concentration during each kinetic run was the same. This is important considering the equation used for calculation of the observed rate constants (Equation (6)), where k_{obs} is defined as

$$k_{obs} = \frac{100\%k}{c_0} \quad (7)$$

As a measure of a dye concentration, the percentage of dye decolorization was used. Because both of these parameters are inversely proportional to each other, the observed linear dependencies for decolorization vs. time increase, although the dye undergoes decomposition. Application of the change in the solution color during the photodegradation of MB and CV is based on the mechanism of their photodecomposition, studied earlier [5,87,88].

Paths of MB photodegradation have been studied for years [5,87–89]. The process can be studied spectrophotometrically because a blue, oxidized form of MB in a reaction with reactive oxygen species, mainly $^{\bullet}OH$, generated on a photocatalyst surface forms colorless photodegradation intermediates [87]. The decolorization is caused by breaking of the MB central aromatic ring [5]. The further decomposition of the intermediates continues until CO_2, H_2O, and other inorganic ions are formed as final photodegradation products [5,87]. Moreover, spectrophotometric MB photodegradation is a kind of reference process, being involved in the norm ISO 10678:2024 (formerly ISO 10678: 2010) [86,90].

Photodegradation of CV proceeds similarly. A free electron generated during composite irradiation reacts with water molecules on the composite surface, producing different ROS. This process, i.e., the water splitting reaction, in fact, is crucial for the whole photodegradation process here and in other, similar photodegradation reactions [91]. One of the most common ROS in aqueous systems is hydroxyl radical [87,91,92]. It reacts with CV molecules, making it fragment into colorless species [92], and it finally produces simple inorganic molecules [93]. Processes of N-demethylation and oxidative degradation are placed among the first steps of CV photodegradation [93,94].

The monitored decolorization of MB and CV aqueous solutions is related to the first step of a particular dye's photodecomposition. This procedure is commonly used in the photoactivity tests [5,86–94] because of its simplicity (spectrophotometric studies, the zero-order or first-order kinetic equations) and sensitivity (e.g., significant changes of absorption). Among the tested dyes, MB solutions showed the highest photocatalytic degradation efficiency, as well as MB's susceptibility to light-induced breakdown under both UV and visible light irradiation [95]. The highest rate constant for the photoinduced decolorization process was observed in UV-irradiated PMMA + (**2**) samples, where the per cent of MB decolorization increased from 33.6% to 63.6% as the complex concentration dose rose from 2 to 20 wt.% (Figure 7, Table S4). The tested composites can be classified by their activity profile as follows: (i) composites mainly active in the UV range, enriched with complexes (**1**) and (**2**); (ii) composites active under visible light, containing complexes (**4**) and (**5**); and (iii) a composite showing activity in both UV and visible light ranges, incorporating complex (**3**). In the systems evaluated, oxo–Ti(IV) complexes demonstrated the greatest photocatalytic

activity. Findings from previous structural studies of complexes (**1**)–(**3**) [31,32] and their physicochemical properties suggest that the stabilizing carboxylate ligand type is the primary factor impacting their photocatalytic activity. Complexes (**1**) and (**2**), stabilized by α-hydroxycarboxylic ligands (mandelate or 9-hydroxy-9-fluorenecarboxylate), exhibited relatively large HOMO-LUMO energy gaps of 3.12 eV and 2.96 eV, respectively, accounting for their strong UV activity, which is confirmed by the rate constants of the photoinduced decolorization of MB and CV solutions. In contrast, complex (**3**), stabilized by 9-hydroxy-9-fluorenecarboxylate and propionate ligands, has a reduced E_p value of 2.39 eV, resulting in lower UV activity but increased visible light activity. The PMMA + (**3**) composite (2 wt.%) showed superior activity in the visible light range compared to the UV range. It slightly decreased with the complex concentration increase (Figure 6).

Ruthenium(III) complexes (**4**) and (**5**) exhibited generally lower photocatalytic activity compared to the Ti(IV)-based complexes (**1**)–(**3**). They were primarily active under visible light, likely due to their HOMO–LUMO energy gap values of 2.75 and 2.78 eV for (**4**) and (**5**), respectively. The reduced activity of the Ru(III) complexes may be attributed to their photocatalytic mechanism, which involves the reduction of Ru(III) to Ru(II). In aqueous solutions, this reduction produces H_2O_2 molecules that subsequently form hydroxyl radicals [96,97]. The lower reactivity of Ru(III) complexes suggests that they generate fewer hydroxyl radicals compared to the number of reactive oxygen species (ROS) produced by Ti(IV)–oxo complexes stabilized with α-hydroxycarboxylate ligands. These results indicate that, in this case, the type of ligand also affects the activity differences observed between complexes (**4**) and (**5**).

The photocatalytic mechanism involves the excitation of electrons from the valence band to the conduction band upon irradiation with light of an appropriate wavelength, leading to the formation of electron–hole pairs. These species interact with oxygen or water, generating reactive oxygen species (ROS), which drive photocatalytic reactions [84]. In metal complexes, electron transfer occurs between the HOMO (ligand) and LUMO (metal center, Ti or Ru) [29]. EPR spectroscopy was used to identify the ROS generated on the surface of the tested materials, helping to understand their photocatalytic behavior. The results indicate that the most effective material is the PMMA + (2) composite, as its EPR spectrum shows the least distortion, suggesting efficient charge transfer. Composites containing titanium oxo-clusters (TOCs) exhibit similar EPR patterns, with signals corresponding to O^-, $O_2{}^-$ radicals, and Ti^{3+} species, which are key contributors to photocatalysis [30]. Among the studied TOCs, (2) shows a distinct free electron signal, while (**1**) and (**3**) display typical features of Ti^{3+} and superoxide radicals, confirming their role in ROS generation [32,98]. For ruthenium(III) complexes, the EPR spectra indicate that Ru(III) centers are the only paramagnetic species present, with no ROS signals detected. This suggests that photocatalysis in these materials follows a different mechanism, likely involving Ru(III) reduction to Ru(II) upon irradiation. Because Ru(II) is diamagnetic, it does not produce an EPR signal, supporting the idea that electron transfer occurs within the ruthenium center rather than through ROS formation [85]. Notably, only the composite containing 20 wt.% of (5) exhibits a relatively intense signal, indicating a higher concentration of Ru(III) centers (Table S7 and Figures S9 and S10) [99]. These findings align with the observed photocatalytic activity trends, confirming that titanium-based composites primarily operate through ROS-mediated processes, while ruthenium-based materials rely on direct electron transfer mechanisms.

5. Conclusions

This study assessed the adsorption properties and photocatalytic activity of composite materials created by incorporating Ti(IV)–oxo complexes stabilized with α-hydroxy

carboxylate ligands ((**1**)–(**3**)) and Ru(III) complexes ((**4**) and (**5**)) into a PMMA matrix. Spectroscopic analyses (Raman and XAS) confirmed that introducing these complexes into the polymer matrix did not lead to significant alterations in their structures. Notably, the absorption maximum of the composites shifted toward the visible light range (from 221 and 281 nm for pure PMMA to 336 and 420 nm in the case of sample PMMA + (**5**) 20 wt.%), especially in samples containing 10 and 20 wt.% of the complexes, enhancing their potential responsiveness under visible light.

The adsorption properties were evaluated using three cationic dyes: methylene blue (MB), crystal violet (CV), and rhodamine B (RhB). The composites demonstrated the highest adsorption with MB (max 37%) and the lowest with RhB (max 5%), with PMMA + (**3**) exhibiting the greatest adsorption capacity, likely due to the high electron density of complex (**3**) (Table 1).

Table 1. Comparative table of PMMA composites with Ti(IV) and Ru(III) complexes (the presented data refer to composites containing 2 wt.% and 20 wt.% of the tested complexes).

Composite	Maximum Dye Adsorption (%) MB	Photocatalytic Activity MB (%)	EPR Signals	Light Activation Range
TOCs				
PMMA + (**1**)	2.27–8.99	38–69 (UV) 27–55 (Vis)	Moderate (O_2^-, Ti^{3+})	UV
PMMA + (**2**)	1.92–8.91	45–73 (UV) 34–64 (Vis)	Strong (O^-, O_2^-, Ti^{3+})	UV
PMMA + (**3**)	7.48–37.40	35–58 (UV) 36–59 (Vis)	Moderate (O^-, O_2^-, Ti^{3+})	UV + Vis
Ru(III) complexes				
PMMA + (**4**)	2.14–6.62	19–33 (UV) 18–45 (Vis)	Weak (Ru^{3+})	Vis
PMMA + (**5**)	5.63–6.69	17–32 (UV) 16–41 (Vis)	Weak (Ru^{3+})	Vis

The photocatalytic activity was assessed under both UV and visible light. The results showed that composites containing titanium complexes had higher photocatalytic activity (58–73% degradation of MB in UV light, 55–71% degradation of CV in UV light, and 55–63% degradation of MB in visible light) than those containing ruthenium complexes (32–33% degradation of MB in UV light, 49–52% degradation of CV in UV light, and 40–45% degradation of MB in visible light). Based on photocatalytic performance, the composites could be classified as (i) UV-active composites ((**1**) and (**2**)), (ii) composites active under visible light ((**4**) and (**5**)), and (iii) a composite active under both UV and visible light ((**3**)). The photocatalytic activity was directly influenced by the type of central ion and the stabilizing ligand (Table 1). Ti(IV)-based composites exhibited superior photocatalytic performance due to the ability of Ti(IV) to generate reactive oxygen species (ROS), which are essential for efficient photocatalysis. In contrast, Ru(III)-based complexes rely on redox cycling between Ru(III) and Ru(II) rather than ROS generation, resulting in lower photocatalytic efficiency. Additionally, the stabilizing ligands affected the electronic structure of the complexes, with certain ligands widening the HOMO–LUMO gap and enhancing UV activity, while others extended the activity into the visible range. Therefore, the type of central ion and the stabilizing ligand both play crucial roles in determining the photocatalytic behavior of the composites.

Future research should focus on investigating the use of alternative polymer matrices to better understand how the properties of the host material influence photocatalytic

performance. Additionally, evaluating the composites under real-world conditions, such as in wastewater treatment applications, will help assess their long-term stability and efficiency in handling complex pollutant mixtures. Further studies on the recyclability and reusability of the composites are also crucial for improving their practical applicability and ensuring their sustainability in industrial processes.

Supplementary Materials: The following supporting information can be downloaded at https://www.mdpi.com/article/10.3390/app15041679/s1, Materials: Synthesis procedures of complexes (**1**)–(**5**). Figure S1. SEM images of the composite films enriched with titanium(IV)–oxo complexes (yellow rings mark TOCs' grains); Figure S2. SEM images of the composite films enriched with ruthenium(III) complexes (yellow rings mark Ru(III) complexes' grains); Table S1. SEM EDX quantity data. All values are given in mass per cent (%); Figure S3. SEM EDX spectra of pure PMMA and composites containing titanium(IV)–oxo complexes (**2**) and (**3**); Figure S4. SEM EDX spectra of composites containing ruthenium(III) complexes (**4**) and (**5**); Table S2. Ti $L_{2,3}$ edge (two first features correspond to L_3 and two latter features correspond to L_2 edges). Pre-edge features were visible at ca. 456.4 457.3 eV for powdered samples and experiments performed in TEY mode; Table S3. Percentage reduction of dyes by composites PMMA + ((**1**)–(**5**)); Figure S5. Changes in the concentrations of the methylene blue (MB) solution as a function of time for composite materials PMMA + (**1**)–(**5**) 2–20 wt.% irradiated with UV light; Table S4. Decolorization percentages of MB solutions for the studied reactions relative to the composites irradiated by UV light; Figure S6. Changes in the concentrations of the crystal violet (CV) solution as a function of time for composite materials PMMA + (**1**)–(**5**) 2–20 wt.% irradiated with UV light; Table S5. Decolorization percentages of CV solutions for the studied reactions relative to the composites irradiated by UV light. Figure S7. Changes in the concentrations of the methylene blue (MB) solution as a function of time for composite materials PMMA + (**1**)–(**5**) 2–20 wt.% irradiated with Vis light; Table S6. Decolorization percentages of MB solutions for the studied reactions relative to the composites irradiated by VIS light. Figure S8. EPR spectra of the PMMA composites with (**2**) and of powdered TOC. Conditions: room temperature; microwave frequencies: 9.324675 GHz (PMMA+ (**2**) 2 wt.%), 9.324486 GHz (PMMA+ (**2**) 5 wt.%), 9.323992 GHz (PMMA+ (**2**) 10 wt.%), 9.323746 GHz (PMMA+ (**2**) 20 wt.%), and 9.317209 GHz ((**2**)); modulation amplitude: 1 mT; sweep: 20 mT; sweep time: 4 min; time constant: 0.1 s; receiver gain: 2×10^5 (composites) and 0.5×10^5 ((**2**)). Table S7. EPR data for the studied PMMA composites and powdered complexes. Figure S9. EPR spectra of the PMMA composites with (**3**) and of powdered TOC. Conditions: room temperature; microwave frequencies: 9.324157 GHz (PMMA+ (**3**) 2 wt.%), 9.324280 GHz (PMMA+ (**3**) 5 wt.%), 9.323349 GHz (PMMA+ (**3**) 10 wt.%), 9.322974 GHz (PMMA+ (**3**) 20 wt.%), and 9.324018 GHz ((**3**)); modulation amplitude: 1 mT; sweep: 20 mT; sweep time: 8 min (composites) and 4 min ((**3**)); time constant: 0.1 s; receiver gain: 4×10^5 (composites) and 5×10^5 ((**3**)). Figure S10. EPR spectra of the PMMA composites with (**4**) and of powdered complex. Conditions: room temperature; microwave frequencies: 9.325410 GHz (PMMA+ (**4**) 2 wt.%), 9.324910 GHz (PMMA+ (**4**) 5 wt.%), 9.325450 GHz (PMMA+ (**4**) 10 wt.%), 9.325550 GHz (PMMA+ (**4**) 20 wt.%), and 9.322220 GHz (**4**); modulation amplitude: 1 mT; sweep: 400 mT (composites) and 200 mT (**4**); sweep time: 8 min (composites) and 4 min (**4**); time constant: 0.1 s; receiver gain: 6.3×10^5 (composites) and 4×10^5 (**4**). Figure S11. EPR spectra of the PMMA composites with (**5**) and of powdered complex. Conditions: room temperature; microwave frequencies: 9.325300 GHz (PMMA+ (**5**) 2 wt.%), 9.325630 GHz (PMMA+ (**5**) 5 wt.%), 9.325390 GHz (PMMA+ (**5**) 10 wt.%), 9.325470 GHz (PMMA+ (**5**) 20 wt.%), and 9.323610 GHz (**5**); modulation amplitude: 1 mT; sweep: 500 mT; sweep time: 2 min (**5**) and 4 min (composites); time constant: 0.1 s; receiver gain: 3.2×10^5 (composites and (**5**)).

Author Contributions: Conceptualization, A.R., O.I. and B.K.; methodology, B.K, P.P., T.M., O.I., A.T. and A.K.; validation, R.v.E., P.P. and A.R.; formal analysis, P.P., A.K. and O.I.; investigation, B.K., T.M. and A.T.; resources, B.K.; data curation, B.K., A.T., O.I., T.M and P.P.; writing—original draft preparation, B.K. and P.P.; writing—review and editing, P.P., A.R., A.T., T.M., R.v.E. and A.K.; visualization, P.P., B.K., A.T. and T.M.; supervision, P.P. and R.v.E.; project administration, P.P.; funding acquisition, R.v.E. All authors have read and agreed to the published version of the manuscript.

Funding: This research was funded by the National Science Center (Grant No. 2020/37/B/ST4/01082).

Institutional Review Board Statement: Not applicable.

Informed Consent Statement: Not applicable.

Data Availability Statement: The raw data supporting the conclusions of this article will be made available by the authors upon request.

Conflicts of Interest: The authors declare no conflicts of interest.

References

1. Yan, X.; Feng, J.; Li, P.; Li, J.; Ren, B.; Gao, S.; Cao, R. Fast and Efficient Removal of Mercury Ions Using Zirconium-Based Metal–Organic Framework Filter Membranes. *Inorg. Chem. Commun.* **2021**, *131*, 108796. [CrossRef]
2. Al-Tohamy, R.; Ali, S.S.; Li, F.; Okasha, K.M.; Mahmoud, Y.A.-G.; Elsamahy, T.; Jiao, H.; Fu, Y.; Sun, J. A Critical Review on the Treatment of Dye-Containing Wastewater: Ecotoxicological and Health Concerns of Textile Dyes and Possible Remediation Approaches for Environmental Safety. *Ecotoxicol. Environ. Saf.* **2022**, *231*, 113160. [CrossRef]
3. Olisah, C.; Adams, J.B.; Rubidge, G. The State of Persistent Organic Pollutants in South African Estuaries: A Review of Environmental Exposure and Sources. *Ecotoxicol. Environ. Saf.* **2021**, *219*, 112316. [CrossRef]
4. Lellis, B.; Fávaro-Polonio, C.Z.; Pamphile, J.A.; Polonio, J.C. Effects of Textile Dyes on Health and the Environment and Bioremediation Potential of Living Organisms. *Biotechnol. Res. Innov.* **2019**, *3*, 275–290. [CrossRef]
5. Khan, I.; Saeed, K.; Zekker, I.; Zhang, B.; Hendi, A.H.; Ahmad, A.; Ahmad, S.; Zada, N.; Ahmad, H.; Shah, L.A.; et al. Review on Methylene Blue: Its Properties, Uses, Toxicity and Photodegradation. *Water* **2022**, *14*, 242. [CrossRef]
6. Zada, N.; Saeed, K.; Khan, I. Decolorization of Rhodamine B Dye by Using Multiwalled Carbon Nanotubes/Co–Ti Oxides Nanocomposite and Co–Ti Oxides as Photocatalysts. *Appl. Water Sci.* **2020**, *10*, 40. [CrossRef]
7. Li, J.; Huang, L.; Jiang, X.; Zhang, L.; Sun, X. Preparation and Characterization of Ternary Cu/Cu2O/C Composite: An Extraordinary Adsorbent for Removing Anionic Organic Dyes from Water. *Chem. Eng. J.* **2021**, *404*, 127091. [CrossRef]
8. Suman; Chahal, S.; Kumar, A.; Kumar, P. Zn Doped α-Fe_2O_3: An Efficient Material for UV Driven Photocatalysis and Electrical Conductivity. *Crystals* **2020**, *10*, 273. [CrossRef]
9. Khan, I.; Shah, T.; Tariq, M.R.; Ahmad, M.; Zhang, B. Understanding the Toxicity of Trinitrophenol and Promising Decontamination Strategies for Its Neutralization: Challenges and Future Perspectives. *J. Environ. Chem. Eng.* **2024**, *12*, 112720. [CrossRef]
10. Shan, Z.; Yang, Y.; Shi, H.; Zhu, J.; Tan, X.; Luan, Y.; Jiang, Z.; Wang, P.; Qin, J. Hollow Dodecahedra Graphene Oxide- Cuprous Oxide Nanocomposites With Effective Photocatalytic and Bactericidal Activity. *Front. Chem.* **2021**, *9*, 755836. [CrossRef]
11. Khan, I.; Rizwan Tariq, M.; Ahmad, M.; Khan, I.; Zhang, B. Strategically Coupled Tungsten Oxide-Zinc Oxide Photosystems for Solar-Driven Nerve Agent Simulant Degradation and Hydrogen Evolution. *Sep. Purif. Technol.* **2025**, *354*, 129078. [CrossRef]
12. He, X.; Yang, D.-P.; Zhang, X.; Liu, M.; Kang, Z.; Lin, C.; Jia, N.; Luque, R. Waste Eggshell Membrane-Templated CuO-ZnO Nanocomposites with Enhanced Adsorption, Catalysis and Antibacterial Properties for Water Purification. *Chem. Eng. J.* **2019**, *369*, 621–633. [CrossRef]
13. Xiao, M.; Wang, Z.; Lyu, M.; Luo, B.; Wang, S.; Liu, G.; Cheng, H.; Wang, L. Hollow Nanostructures for Photocatalysis: Advantages and Challenges. *Adv. Mater.* **2019**, *31*, 1801369. [CrossRef] [PubMed]
14. Saravanan, R.; Gracia, F.; Stephen, A. Basic Principles, Mechanism, and Challenges of Photocatalysis. In *Nanocomposites for Visible Light-Induced Photocatalysis*; Khan, M.M., Pradhan, D., Sohn, Y., Eds.; Springer Series on Polymer and Composite Materials; Springer International Publishing: Cham, Switzerland, 2017; pp. 19–40, ISBN 978-3-319-62445-7.
15. Krakowiak, R.; Musial, J.; Bakun, P.; Spychała, M.; Czarczynska-Goslinska, B.; Mlynarczyk, D.T.; Koczorowski, T.; Sobotta, L.; Stanisz, B.; Goslinski, T. Titanium Dioxide-Based Photocatalysts for Degradation of Emerging Contaminants Including Pharmaceutical Pollutants. *Appl. Sci.* **2021**, *11*, 8674. [CrossRef]
16. Schneider, J.; Matsuoka, M.; Takeuchi, M.; Zhang, J.; Horiuchi, Y.; Anpo, M.; Bahnemann, D.W. Understanding TiO_2 Photocatalysis: Mechanisms and Materials. *Chem. Rev.* **2014**, *114*, 9919–9986. [CrossRef]
17. Armaković, S.J.; Savanović, M.M.; Armaković, S. Titanium Dioxide as the Most Used Photocatalyst for Water Purification: An Overview. *Catalysts* **2022**, *13*, 26. [CrossRef]
18. Fang, W.; Xing, M.; Zhang, J. Modifications on Reduced Titanium Dioxide Photocatalysts: A Review. *J. Photochem. Photobiol. C Photochem. Rev.* **2017**, *32*, 21–39. [CrossRef]
19. Pawar, T.J.; Contreras López, D.; Olivares Romero, J.L.; Vallejo Montesinos, J. Surface Modification of Titanium Dioxide. *J. Mater. Sci.* **2023**, *58*, 6887–6930. [CrossRef]
20. Li, R.; Li, T.; Zhou, Q. Impact of Titanium Dioxide (TiO_2) Modification on Its Application to Pollution Treatment—A Review. *Catalysts* **2020**, *10*, 804. [CrossRef]

21. Pajot, N.; Papiernik, R.; Hubert-Pfalzgraf, L.G.; Vaissermann, J.; Parraud, S. Metal-Assisted Activation of the C–O Bond of 2-Hydroxyethylmethacrylate. Synthesis and Molecular Structure of $Ti_5(OPr^i)_9(\mu\text{-}OPr^i)(\mu,\eta^2\text{-}OC_2H_4O)(\mu_3,\eta^2\text{-}OC_2H_4O)_3(\mu_4,\eta^2\text{-}OC_2H_4O)$. *J. Chem. Soc. Chem. Commun.* **1995**, *17*, 1817–1819. [CrossRef]
22. Czakler, M.; Artner, C.; Schubert, U. Influence of the Phosphonate Ligand on the Structure of Phosphonate-Substituted Titanium Oxo Clusters. *Eur. J. Inorg. Chem.* **2013**, *2013*, 5790–5796. [CrossRef]
23. Czakler, M.; Artner, C.; Schubert, U. Titanium Oxo/Alkoxo Clusters with Both Phosphonate and Methacrylate Ligands. *Monatshefte Für Chem. Chem. Mon.* **2015**, *146*, 1249–1256. [CrossRef] [PubMed]
24. Mou, W.-Y.; Xie, B.; Li, X.-L.; Lai, C.; Li, T.; Chen, L.; Feng, J.-S.; Bai, X.-X.; Wu, Y.; Wu, W.-P.; et al. Tartrate-Stabilized Titanium–Oxo Clusters Containing Sulfonate Chromophore Ligands: Synthesis, Crystal Structures and Photochemical Properties. *New J. Chem.* **2021**, *45*, 10930–10939. [CrossRef]
25. Radtke, A.; Piszczek, P.; Muzioł, T.; Wojtczak, A. The Structural Conversion of Multinuclear Titanium(IV) μ-Oxo-Complexes. *Inorg. Chem.* **2014**, *53*, 10803–10810. [CrossRef] [PubMed]
26. Guo, Y.-H.; Yu, Y.-Z.; Shen, Y.-H.; Yang, L.-G.; Liu, N.-N.; Zhou, Z.-Y.; Niu, Y.-S. "Three-in-One" Structural-Building-Mode-Based Ti_{16}-Type Titanium Oxo Cluster Entirely Protected by the Ligands Benzoate and Salicylhydroxamate. *Inorg. Chem.* **2022**, *61*, 8685–8693. [CrossRef]
27. Pei, X.-Y.; He, Y.; Wang, J.-Y.; Wang, H.-Y.; Bo, Q.-B. Substituted Benzoate-Anchored Decanuclear Titanium-Oxo Clusters Featuring an Unprecedented Defective Double-Cubane Geometry. *CrystEngComm* **2023**, *25*, 1617–1625. [CrossRef]
28. Nasikhudin; Diantoro, M.; Kusumaatmaja, A.; Triyana, K. Study on Photocatalytic Properties of TiO_2 Nanoparticle in Various pH Condition. *J. Phys. Conf. Ser.* **2018**, *1011*, 012069. [CrossRef]
29. Hong, Z.-F.; Xu, S.-H.; Yan, Z.-H.; Lu, D.-F.; Kong, X.-J.; Long, L.-S.; Zheng, L.-S. A Large Titanium Oxo Cluster Featuring a Well-Defined Structural Unit of Rutile. *Cryst. Growth Des.* **2018**, *18*, 4864–4868. [CrossRef]
30. Kubiak, B.; Piszczek, P.; Radtke, A.; Muzioł, T.; Wrzeszcz, G.; Golińska, P. Photocatalytic and Antimicrobial Activity of Titanium(IV)-Oxo Clusters of Different Core Structure. *Crystals* **2023**, *13*, 998. [CrossRef]
31. Kubiak, B.; Muziol, T.M.; Jabłoński, M.; Radtke, A.; Piszczek, P. Investigation of Titanium(IV)-Oxo Complexes Stabilized with α-Hydroxy Carboxylate Ligands: Structural Analysis and DFT Studies. *Dalton Trans.* **2024**, *53*, 14457–14468. [CrossRef] [PubMed]
32. Kubiak, B.; Muzioł, T.; Wrzeszcz, G.; Radtke, A.; Golińska, P.; Jędrzejewski, T.; Wrotek, S.; Piszczek, P. Structural Characterization and Bioactivity of a Titanium(IV)-Oxo Complex Stabilized by Mandelate Ligands. *Molecules* **2024**, *29*, 1736. [CrossRef]
33. Bossmann, S.H.; Wörner, M.; Pokhrel, M.R.; Baumeister, B.; Göb, S.; Braun, A.M. Ruthenium(II)-Tris-Bipyridine/Titanium Dioxide Codoped Zeolite Y Photocatalyst: Performance Optimization Using 2,4-Xylidine (1-Amino-2,4-Dimethyl-Benzene). *Sep. Purif. Technol.* **2009**, *67*, 201–207. [CrossRef]
34. Gajardo, F.; Leiva, A.M.; Loeb, B.; Delgadillo, A.; Stromberg, J.R.; Meyer, G.J. Interfacial Electron Transfer on TiO2 Sensitized with an Axially Anchored Trans Tetradentate Ru(II) Compound. *Inorganica Chim. Acta* **2008**, *361*, 613–619. [CrossRef]
35. Ni, J.-S.; Hung, C.-Y.; Liu, K.-Y.; Chang, Y.-H.; Ho, K.-C.; Lin, K.-F. Effects of Tethering Alkyl Chains for Amphiphilic Ruthenium Complex Dyes on Their Adsorption to Titanium Oxide and Photovoltaic Properties. *J. Colloid Interface Sci.* **2012**, *386*, 359–365. [CrossRef] [PubMed]
36. Góngora, J.F.; Elizondo, P.; Hernández-Ramírez, A. Photocatalytic Degradation of Ibuprofen Using TiO2 Sensitized by Ru(II) Polyaza Complexes. *Photochem. Photobiol. Sci.* **2017**, *16*, 31–37. [CrossRef] [PubMed]
37. Sastre, F.; Bouizi, Y.; Fornés, V.; Garcia, H. Visible-Light Hydrogen Generation Using as Photocatalysts Layered Titanates Incorporating in the Intergallery Space Ruthenium Tris(Bipyridyl) and Methyl Viologen. *J. Colloid Interface Sci.* **2010**, *346*, 172–177. [CrossRef]
38. Chatterjee, D.; Edik, R.V. Prospect of Ru^{III} (Edta) in Catalysis of Bicarbonate Reduction. *CCAT* **2020**, *9*, 23–31. [CrossRef]
39. Yu, Z.; Li, Y.; Torres-Pinto, A.; LaGrow, A.P.; Diaconescu, V.M.; Simonelli, L.; Sampaio, M.J.; Bondarchuk, O.; Amorim, I.; Araujo, A.; et al. Single-Atom Ir and Ru Anchored on Graphitic Carbon Nitride for Efficient and Stable Electrocatalytic/Photocatalytic Hydrogen Evolution. *Appl. Catal. B Environ.* **2022**, *310*, 121318. [CrossRef]
40. Singha, K.; Laha, P.; Chandra, F.; Dehury, N.; Koner, A.L.; Patra, S. Long-Lived Polypyridyl Based Mononuclear Ruthenium Complexes: Synthesis, Structure, and Azo Dye Decomposition. *Inorg. Chem.* **2017**, *56*, 6489–6498. [CrossRef] [PubMed]
41. Rupp, M.; Auvray, T.; Rousset, E.; Mercier, G.M.; Marvaud, V.; Kurth, D.G.; Hanan, G.S. Photocatalytic Hydrogen Evolution Driven by a Heteroleptic Ruthenium(II) Bis(Terpyridine) Complex. *Inorg. Chem.* **2019**, *58*, 9127–9134. [CrossRef] [PubMed]
42. Li, C.-X.; Liu, Y.; Guo, Z.; Wang, Y.-J.; Guo, Z.-Y.; Lau, T.-C.; Li, W.-W. Efficient Pollutant Degradation via Non-Radical Dominated Pathway by Self-Regenerative Ru(Bpy)32+/Peroxydisulfate under Visible Light. *Chem. Eng. J.* **2020**, *400*, 125993. [CrossRef]
43. Dhanaraj, C.J.; Raj, S.S.S.; Synthesis, S.S.S.R. Structural Elucidation and Photocatalytic Studies of Some 4-Aminoantipyrine Based Ruthenium (III) Complexes. *J. Environ. Nanotechnol.* **2019**, *8*, 21–22. [CrossRef]
44. Gao, Y.; Qian, B.-F.; Wang, J.-L.; Jia, A.-Q.; Mei, Q.; Zhang, Q.-F. μ-Disulfido Complexes of Ruthenium(III) 1,1′-Dithiolate [{(Me3tacn)Ru}2(K2-S2COR)(K2-S2C = O)(μ-S2)]PF6 (Me3tacn = 1,4,7-Trimethyl-1,4,7-Triazacyclononane; R = Alkyl). *Inorganica Chim. Acta* **2023**, *548*, 121374. [CrossRef]

45. Ghosh, D.; Takeda, H.; Fabry, D.C.; Tamaki, Y.; Ishitani, O. Supramolecular Photocatalyst with a Rh(III)-Complex Catalyst Unit for CO_2 Reduction. *ACS Sustain. Chem. Eng.* **2019**, *7*, 2648–2657. [CrossRef]
46. Mongal, B.N.; Tiwari, A.; Malapaka, C.; Pal, U. Ruthenium(III)-Bis(Phenolato)Bipyridine/TiO_2 Hybrids: Unprecedented Photocatalytic Hydrogen Evolution. *Dalton Trans.* **2019**, *48*, 10070–10077. [CrossRef] [PubMed]
47. Fleming, C.N.; Dattelbaum, D.M.; Thompson, D.W.; Ershov, A.Y.; Meyer, T.J. Excited State Intervalence Transfer in a Rigid Polymeric Film. *J. Am. Chem. Soc.* **2007**, *129*, 9622–9630. [CrossRef] [PubMed]
48. Piszczek, P.; Kubiak, B.; Golińska, P.; Radtke, A. Oxo-Titanium(IV) Complex/Polymer Composites—Synthesis, Spectroscopic Characterization and Antimicrobial Activity Test. *IJMS* **2020**, *21*, 9663. [CrossRef] [PubMed]
49. Kubiak, B.; Radtke, A.; Topolski, A.; Wrzeszcz, G.; Golińska, P.; Kaszkowiak, E.; Sobota, M.; Włodarczyk, J.; Stojko, M.; Piszczek, P. The Composites of PCL and Tetranuclear Titanium(IV)-Oxo Complexes as Materials Exhibiting the Photocatalytic and the Antimicrobial Activity. *IJMS* **2021**, *22*, 7021. [CrossRef] [PubMed]
50. Aloui, F.; Jabli, M.; Hassine, B.B. Synthesis and Characterization of a New Racemic Helically Chiral Ru(II) Complex and Its Catalytic Degradation of Eriochrome Blue Black B. *Synth. Commun.* **2012**, *42*, 3620–3631. [CrossRef]
51. Motaung, T.E.; Luyt, A.S.; Bondioli, F.; Messori, M.; Saladino, M.L.; Spinella, A.; Nasillo, G.; Caponetti, E. PMMA–Titania Nanocomposites: Properties and Thermal Degradation Behaviour. *Polym. Degrad. Stab.* **2012**, *97*, 1325–1333. [CrossRef]
52. Raheem, G. Kadhim Study the Electrical and Structural Properties of (PMMA-TiO_2) Nanocomposites. *Chem. Mater. Res.* **2015**, *7*, 37–48.
53. Ravel, B.; Newville, M. *ATHENA*, *ARTEMIS*, *HEPHAESTUS*: Data Analysis for X-Ray Absorption Spectroscopy Using *IFEFFIT*. *J. Synchrotron Radiat.* **2005**, *12*, 537–541. [CrossRef] [PubMed]
54. Xu, H.; Ouyang, S.; Liu, L.; Reunchan, P.; Umezawa, N.; Ye, J. Recent Advances in TiO_2-Based Photocatalysis. *J. Mater. Chem. A* **2014**, *2*, 12642. [CrossRef]
55. Diamantis, A.A.; Dubrawski, J.V. Preparation and Structure of Ethylenediaminetetraacetate Complexes of Ruthenium(II) with Dinitrogen, Carbon Monoxide, and Other .Pi.-Acceptor Ligands. *Inorg. Chem.* **1981**, *20*, 1142–1150. [CrossRef]
56. Impert, O.; Katafias, A.; Kita, P.; Wrzeszcz, G.; Fenska, J.; Lente, G.; Fábián, I. Base Hydrolysis of Mer-Trispicolinatoruthenium(III): Kinetics and Mechanism. *Transition Met Chem* **2011**, *36*, 761–766. [CrossRef]
57. Meth-Cohn, O.; Thorpe, D.; Twitchett, H.J. Insertion Reactions of Titanium Alkoxides with Isocyanates and Carbodiimides. *J. Chem. Soc. C* **1970**, 132. [CrossRef]
58. Badea, M.; Olar, R.; Marinescu, D.; Uivarosi, V.; Nicolescu, T.O.; Iacob, D. Thermal Study of Some New Quinolone Ruthenium(III) Complexes with Potential Cytostatic Activity. *J Therm Anal Calorim* **2010**, *99*, 829–834. [CrossRef]
59. Chyba, J.; Hruzíková, A.; Knor, M.; Pikulová, P.; Marková, K.; Novotný, J.; Marek, R. Nature of NMR Shifts in Paramagnetic Octahedral Ru(III) Complexes with Axial Pyridine-Based Ligands. *Inorg. Chem.* **2023**, *62*, 3381–3394. [CrossRef]
60. Lätsch, L.; Guda, S.A.; Romankov, V.; Wartmann, C.; Neudörfl, J.-M.; Dreiser, J.; Berkessel, A.; Guda, A.A.; Copéret, C. Tracking Coordination Environment and Reaction Intermediates in Homo- and Heterogeneous Epoxidation Catalysts via Ti L2,3-Edge NEXAFS 2024. *J. Am. Chem. Soc.* **2024**, *146*, 7456. [CrossRef] [PubMed]
61. Fioretti, A.N.; Schwartz, C.P.; Vinson, J.; Nordlund, D.; Prendergast, D.; Tamboli, A.C.; Caskey, C.M.; Tuomisto, F.; Linez, F.; Christensen, S.T.; et al. Understanding and Control of Bipolar Self-Doping in Copper Nitride. *J. Appl. Phys.* **2016**, *119*, 181508. [CrossRef] [PubMed]
62. Ye, Y.; Kapilashrami, M.; Chuang, C.-H.; Liu, Y.; Glans, P.-A.; Guo, J. X-Ray Spectroscopies Studies of the 3d Transition Metal Oxides and Applications of Photocatalysis. *MRS Commun.* **2017**, *7*, 53–66. [CrossRef]
63. Wojtaszek, K.; Błachucki, W.; Tyrała, K.; Nowakowski, M.; Zając, M.; Stępień, J.; Jagodziński, P.; Banaś, D.; Stańczyk, W.; Czapla-Masztafiak, J.; et al. Determination of Crystal-Field Splitting Induced by Thermal Oxidation of Titanium. *J. Phys. Chem. A* **2021**, *125*, 50–56. [CrossRef] [PubMed]
64. Impert, O.; Pryshchepa, O.; Pomastowski, P.; Rafińska, K.; Chatterjeec, D. Redox Reaction of a RuIII(Pic)3 Complex with Cysteine: Spectral, Kinetic and Biological Studies. *Inorganica Chim. Acta* **2025**, *574*, 122401. [CrossRef]
65. Nguyen, H.L. The Chemistry of Titanium-Based Metal–Organic Frameworks. *New J. Chem.* **2017**, *41*, 14030–14043. [CrossRef]
66. Chen, X.; Peng, X.; Jiang, L.; Yuan, X.; Yu, H.; Wang, H.; Zhang, J.; Xia, Q. Recent Advances in Titanium Metal–Organic Frameworks and Their Derived Materials: Features, Fabrication, and Photocatalytic Applications. *Chem. Eng. J.* **2020**, *395*, 125080. [CrossRef]
67. Wang, J.; Cherevan, A.S.; Hannecart, C.; Naghdi, S.; Nandan, S.P.; Gupta, T.; Eder, D. Ti-Based MOFs: New Insights on the Impact of Ligand Composition and Hole Scavengers on Stability, Charge Separation and Photocatalytic Hydrogen Evolution. *Appl. Catal. B Environ.* **2021**, *283*, 119626. [CrossRef]
68. Ho, J.; Nord, M.T.; Stafford, J.P.; Stylianou, K.C. Ruthenium-Based Metal–Organic Framework Catalyst for CO_2 Fixation onto Epoxides. *Catal. Sci. Technol.* **2022**, *12*, 6998–7002. [CrossRef]

69. Liu, J.; Shi, L.; Wang, Y.; Li, M.; Zhou, C.; Zhang, L.; Yao, C.; Yuan, Y.; Fu, D.; Deng, Y.; et al. Ruthenium-Based Metal-Organic Framework with Reactive Oxygen and Nitrogen Species Scavenging Activities for Alleviating Inflammation Diseases. *Nano Today* **2022**, *47*, 101627. [CrossRef]
70. Al-Ahmed, Z.A.; Aljohani, M.M.; Sallam, S.; Alkhatib, F.M.; Alaysuy, O.; Alsharief, H.H.; Shah, R.; El-Metwaly, N.M. Synthesis of Magnetic Ruthenium Metal-Organic Frameworks for Efficient Removal of 2,4-Dichlorophenylacetic Pesticide from Aqueous Solutions: Batch Adsorption, Box-Behnken Design Optimization and Reusability. *J. Water Process Eng.* **2023**, *56*, 104444. [CrossRef]
71. Petit, C. Present and Future of MOF Research in the Field of Adsorption and Molecular Separation. *Curr. Opin. Chem. Eng.* **2018**, *20*, 132–142. [CrossRef]
72. Ghanbari, T.; Abnisa, F.; Wan Daud, W.M.A. A Review on Production of Metal Organic Frameworks (MOF) for CO_2 Adsorption. *Sci. Total Environ.* **2020**, *707*, 135090. [CrossRef] [PubMed]
73. Wang, C.; Xiong, C.; He, Y.; Yang, C.; Li, X.; Zheng, J.; Wang, S. Facile Preparation of Magnetic Zr-MOF for Adsorption of Pb(II) and Cr(VI) from Water: Adsorption Characteristics and Mechanisms. *Chem. Eng. J.* **2021**, *415*, 128923. [CrossRef]
74. Minitha, C.R.; Lalitha, M.; Jeyachandran, Y.L.; Senthilkumar, L.; RT, R.K. Adsorption Behaviour of Reduced Graphene Oxide towards Cationic and Anionic Dyes: Co-Action of Electrostatic and π–π Interactions. *Mater. Chem. Phys.* **2017**, *194*, 243–252. [CrossRef]
75. Pijović, M.; Manić, N.; Anićijević, D.V.; Krstić, A.; Mitrić, M.; Matić, T.; Janković, B. Simple and Effective One-Step Production of High-Quality Mesoporous Pyrolytic Char from Waste Tires: Rhodamine B Adsorption Kinetics and Density Functional Theory (DFT) Study. *Diam. Relat. Mater.* **2022**, *121*, 108768. [CrossRef]
76. Parcheta, M.; Świsłocka, R.; Świderski, G.; Matejczyk, M.; Lewandowski, W. Spectroscopic Characterization and Antioxidant Properties of Mandelic Acid and Its Derivatives in a Theoretical and Experimental Approach. *Materials* **2022**, *15*, 5413. [CrossRef]
77. Świsłocka, R.; Świderski, G.; Nasiłowska, J.; Sokołowska, B.; Wojtczak, A.; Lewandowski, W. Research on the Electron Structure and Antimicrobial Properties of Mandelic Acid and Its Alkali Metal Salts. *IJMS* **2023**, *24*, 3078. [CrossRef] [PubMed]
78. García-Rubiño, M.E.; Matilla-Hernández, A.; Frontera, A.; Lezama, L.; Niclós-Gutiérrez, J.; Choquesillo-Lazarte, D. Dicopper(II)-EDTA Chelate as a Bicephalic Receptor Model for a Synthetic Adenine Nucleoside. *Pharmaceuticals* **2021**, *14*, 426. [CrossRef]
79. Barbas, R.; Font-Bardia, M.; Frontera, A.; Prohens, R. Polymorphism in the 1/1 Pterostilbene/Picolinic Acid Cocrystal. *Cryst. Growth Des.* **2022**, *22*, 590–597. [CrossRef] [PubMed]
80. Liu, C.; Hu, J.; Liu, W.; Zhu, F.; Wang, G.; Tung, C.; Wang, Y. Binding Modes of Salicylic Acids to Titanium Oxide Molecular Surfaces. *Chem. A Eur. J.* **2020**, *26*, 2666–2674. [CrossRef] [PubMed]
81. Yu, Y.-Z.; Zhang, Y.-R.; Geng, C.-H.; Sun, L.; Guo, Y.; Feng, Y.-R.; Wang, Y.-X.; Zhang, X.-M. Precise and Wide-Ranged Band-Gap Tuning of Ti_6 -Core-Based Titanium Oxo Clusters by the Type and Number of Chromophore Ligands. *Inorg. Chem.* **2019**, *58*, 16785–16791. [CrossRef] [PubMed]
82. Kinnunen, T.-J.J.; Haukka, M.; Pakkanen, T.A. Alkoxycarbonyl Substituted Ruthenium Mono(Bipyridine) Complexes: Steric Effects of the Bipyridine Substituents. *J. Organomet. Chem.* **2002**, *654*, 8–15. [CrossRef]
83. Kinnunen, T.-J.J.; Haukka, M.; Pesonen, E.; Pakkanen, T.A. Ruthenium Complexes with 2,2′-, 2,4′- and 4,4′-Bipyridine Ligands: The Role of Bipyridine Coordination Modes and Halide Ligands. *J. Organomet. Chem.* **2002**, *655*, 31–38. [CrossRef]
84. Cruz-Ortiz, B.R.; Hamilton, J.W.J.; Pablos, C.; Díaz-Jiménez, L.; Cortés-Hernández, D.A.; Sharma, P.K.; Castro-Alférez, M.; Fernández-Ibañez, P.; Dunlop, P.S.M.; Byrne, J.A. Mechanism of Photocatalytic Disinfection Using Titania-Graphene Composites under UV and Visible Irradiation. *Chem. Eng. J.* **2017**, *316*, 179–186. [CrossRef]
85. Webb, M.I.; Walsby, C.J. EPR as a Probe of the Intracellular Speciation of Ruthenium(Iii) Anticancer Compounds. *Metallomics* **2013**, *5*, 1624. [CrossRef] [PubMed]
86. *ISO 10678:2010*; Fine Ceramics (Advanced Ceramics, Advanced Technical Ceramics)—Determination of Photocatalytic Activity of Surfaces in an Aqueous Medium by Degradation of Methylene Blue 2010. ISO: Geneva, Switzerland, 2010.
87. Ali, M.A.; Maafa, I.M.; Qudsieh, I.Y. Photodegradation of Methylene Blue Using a UV/H_2O_2 Irradiation System. *Water* **2024**, *16*, 453. [CrossRef]
88. Mouele, E.S.M.; Tijani, J.O.; Masikini, M.; Fatoba, O.O.; Eze, C.P.; Onwordi, C.T.; Myint, M.T.Z.; Kyaw, H.H.; Al-Sabahi, J.; Al-Abri, M.; et al. Spectroscopic Measurements of Dissolved O3, H2O2 and OH Radicals in Double Cylindrical Dielectric Barrier Discharge Technology: Treatment of Methylene Blue Dye Simulated Wastewater. *Plasma* **2020**, *3*, 59–91. [CrossRef]
89. Zuo, R.; Du, G.; Zhang, W.; Liu, L.; Liu, Y.; Mei, L.; Li, Z. Photocatalytic Degradation of Methylene Blue Using TiO_2 Impregnated Diatomite. *Adv. Mater. Sci. Eng.* **2014**, *2014*, 1–7. [CrossRef]
90. Ehlert, M.; Radtke, A.; Topolski, A.; Śmigiel, J.; Piszczek, P. The Photocatalytic Activity of Titania Coatings Produced by Electrochemical and Chemical Oxidation of Ti6Al4V Substrate, Estimated According to ISO 10678:2010. *Materials* **2020**, *13*, 2649. [CrossRef] [PubMed]
91. Sifat, M.; Shin, E.; Schevon, A.; Ramos, H.; Pophali, A.; Jung, H.-J.; Halada, G.; Meng, Y.; Olynik, N.; Sprouster, D.J.; et al. Photocatalytic Degradation of Crystal Violet (CV) Dye over Metal Oxide (MOx) Catalysts. *Catalysts* **2024**, *14*, 377. [CrossRef]

92. Sanakousar, M.F.; Vidyasagar, C.C.; Jiménez-Pérez, V.M.; Jayanna, B.K.; Mounesh; Shridhar, A.H.; Prakash, K. Efficient Photocatalytic Degradation of Crystal Violet Dye and Electrochemical Performance of Modified MWCNTs/Cd-ZnO Nanoparticles with Quantum Chemical Calculations. *J. Hazard. Mater. Adv.* **2021**, *2*, 100004. [CrossRef]
93. Hunge, Y.M.; Uchida, A.; Tominaga, Y.; Fujii, Y.; Yadav, A.A.; Kang, S.-W.; Suzuki, N.; Shitanda, I.; Kondo, T.; Itagaki, M.; et al. Visible Light-Assisted Photocatalysis Using Spherical-Shaped $BiVO_4$ Photocatalyst. *Catalysts* **2021**, *11*, 460. [CrossRef]
94. Som, I.; Roy, M.; Saha, R. Advances in Nanomaterial-based Water Treatment Approaches for Photocatalytic Degradation of Water Pollutants. *ChemCatChem* **2020**, *12*, 3409–3433. [CrossRef]
95. Štrbac, D.; Aggelopoulos, C.A.; Štrbac, G.; Dimitropoulos, M.; Novaković, M.; Ivetić, T.; Yannopoulos, S.N. Photocatalytic Degradation of Naproxen and Methylene Blue: Comparison between ZnO, TiO_2 and Their Mixture. *Process Saf. Environ. Prot.* **2018**, *113*, 174–183. [CrossRef]
96. AlHamedi, F.H.; Rauf, M.A.; Ashraf, S.S. Degradation Studies of Rhodamine B in the Presence of UV/H_2O_2. *Desalination* **2009**, *239*, 159–166. [CrossRef]
97. Zuorro, A.; Lavecchia, R. Evaluation of UV/H_2O_2 Advanced Oxidation Process (AOP) for the Degradation of Diazo Dye Reactive Green 19 in Aqueous Solution. *Desalination Water Treat.* **2014**, *52*, 1571–1577. [CrossRef]
98. Suriye, K.; Lobo-Lapidus, R.J.; Yeagle, G.J.; Praserthdam, P.; Britt, R.D.; Gates, B.C. Probing Defect Sites on TiO_2 with $[Re_3(CO)_{12}H_3]$: Spectroscopic Characterization of the Surface Species. *Chem. Eur. J.* **2008**, *14*, 1402–1414. [CrossRef] [PubMed]
99. Canevali, C.; Chiodini, N.; Morazzoni, F.; Scotti, R. Electron Paramagnetic Resonance Characterization of Ruthenium-Dispersed Tin Oxide Obtained by Sol–Gel and Impregnation Methods. *J. Mater. Chem.* **2000**, *10*, 773–778. [CrossRef]

Disclaimer/Publisher's Note: The statements, opinions and data contained in all publications are solely those of the individual author(s) and contributor(s) and not of MDPI and/or the editor(s). MDPI and/or the editor(s) disclaim responsibility for any injury to people or property resulting from any ideas, methods, instructions or products referred to in the content.

Materiały uzupełniające

Supplementary Information

Analysis of Photocatalytic Properties of Poly(Methyl Methacrylate) Composites with Titanium(IV) and Ruthenium(III) Complexes

Barbara Kubiak [1,*], Adrian Topolski [1], Aleksandra Radtke [1,*], Tadeusz Muzioł [1], Olga Impert [1], Anna Katafias [1], Rudi van Eldik [1,2] and Piotr Piszczek [1]

[1] Department of Inorganic and Coordination Chemistry, Faculty of Chemistry, Nicolaus Copernicus University in Toruń, Gagarina 7, 87-100 Toruń, Poland; topolski@umk.pl (A.T.); tadeuszmuziol@wp.pl (T.M.); oimpert@umk.pl (O.I.); katafias@umk.pl (A.K.); rudi.vaneldik@fau.de (R.v.E.); piszczek@umk.pl (P.P.)

[2] Department of Chemistry and Pharmacy, University of Erlangen-Nuremberg, Egerlandstrasse 1, 91058 Erlangen, Germany

* Correspondence: basiak0809@gmail.com (B.K.); aradtke@umk.pl (A.R.)

1. Synthesis of titanium oxo clusters (TOCs)

1.1. $[Ti_8O_2(O^iPr)_{20}(man)_4]$ (1)

The complex was synthesized as reported [1]. 0.13 g of mandelic acid (0.875 mmol), 1 mL of titanium(IV) isopropoxide (3.5 mmol), and 2 mL of THF were mixed, yielding a clear yellow solution. Crystals of (**1**) appeared after 3 days. The yield based on acid was 66% (0.62 g). Titanium content was determined as TiO_2, according to the method of Meth-Cohn et al. [2]. Anal. Calc. for $C_{92}H_{168}O_{34}Ti_8$:C, 50.18; H, 7.63; Ti,17.45. Found: C, 50.09; H, 7.58; Ti, 17.54. ^{13}C NMR (solid state, 295 K, δ[ppm]): 9.75 (CH_3), 25.4, 30.1 (CH), 60.1, 71.3 ((Ph)C(Ph)), 90.7, 130.7, 139.6, 182.3, (C(Ph)), 198.3, 209.4 (COO). FT IR (KBr pellet, 295 K, ν [cm^{-1}]: ν_{as}(COO) 1624 (s), 1598 (s), ν(CC), ν_s(COO) 1495 (m), 1453 (w), δ(CH_2), δ(CH_3) 1337 (s), ν_s(COO) 1298 (s), ν(CO) 1284 (s), 1263 (m), 1198 (m), ν(COR) 1125 (m), 1089 (m), 1059 (s), 1028 (m), ν(Ti-O-Ti) 759 (w), δ(CCC) 738 (m); Raman (solid state, 295 K, Raman Shift [cm^{-1}]: ν_{as}(COO) 1601 (s), 1457 (m), ν(CO) 1192 (m), ν(COR)) 1162 (m), 1015 (m), 1004 (s), ν(Ti-O-Ti)) 571 (m), 448 (m).

1.2. $[Ti_4O(O^iPr)_{10}(O_3C_{14}H_8)_2]$ (2)

The complex was synthesized as reported [3]. 0.20 g of 9-OH-9-fluorenecarboxylic acid (0.875 mmol), 1 mL of titanium(IV) isopropoxide (3.5 mmol) and 2 mL of mixture tetrahydrofuran/isopropanol (THF/ HO^iPr) (1:1), were mixed leading to clear yellow solution. Crystals appeared after 1 day. The yield was based on acid: 53% (0.29 g). Titanium content was determined as TiO_2, according to the method of Meth-Cohn et al. [2]. Anal. Calc. for $C_{58}H_{86}O_{17}Ti_4$: C, 55.86; H, 6.90; Ti,15.41. Found: C, 56.07; H, 7.01; Ti, 15.64. ^{13}C NMR (solid state, 295 K, δ[ppm]): 10.4, 22.3 (CH_3), 30.5 (CH), 52.9 61.0, 72.7, 78.9 ((Ph)C(Ph)), 97.4, 119.8, 129.7, 140.6, 148.3, 188.2, 197.7 (C(Ph)), 208.4, 215.8 (COO). FT IR (KBr pellet, 295 K, ν [cm^{-1}]: ν_{as}(COO) 1632 (s), 1609 (s), ν(CC), ν_s(COO) 1498 (m), 1474 (w), δ(CH_2), δ(CH_3) 1449 (m), 1364 (w), 1281 (m), ν(CO) 1204 (m), ν(COR) 1156 (w), 1107 (m), 1051 (m), 1004 (w), ν(Ti-O-Ti) 782 (m), 771 (w), δ(CCC) 737 (s), δ(COO) 529 (m); Raman (solid state, 295 K, Raman Shift [cm^{-1}]: ν_{as}(COO) 1600 (s), 1498 (m), 1450 (m), (ν(CC)) 1595 (w), (ν_s(COO)) 1485 (m), (δ(CH_2, δ(CH_3) 1407 (m), 1358 (m), 1292 (m), ν(CO) 1216 (m), 1200 (m), ν(COR)) 1178 (m) 1158 (m), 1117 (m), 1020 (s), ν(Ti-O-Ti)) 550 (m).

1.3. $[Ti_6O_4(O^iPr)_2(O_3C_{14}H_8)_4(O_2CEt)_6]$ (3)

The complex was synthesized as reported [3]. 0.20 g of 9-OH-9-fluorenecarboxylic acid (0.875 mmol), 0.33 mL of propionic acid (4.38 mmol), 1.24 mL of titanium(IV) isopropoxide (4.38 mmol) were dissolved in 2 mL of THF, leading to a clear brown solution. Crystals appeared after 5 days. The yield was based on 9-OH-9-fluorenecarboxylic acid: 20% (0.08 g). Titanium content was determined as TiO_2, according to the method of Meth-Cohn et al. [2]. Anal. Calc. for $C_{80}H_{76}O_{30}Ti_6$: C, 53.22; H, 4.21; Ti, 15.96. Found: C, 53.19; H, 4.36; Ti, 15.77. 13C NMR (solid state, 295 K, δ[ppm]): 9.4, 21.3, 29.5(CH3), 51.6 (CH2) 57.1 (CH), 58.4, 62.3, 72.1, 78.2 ((Ph)C(Ph)), 88.1, 98.3 (COO), 119.8, 125.2, 129.3, 140.1, 143.3, 177.6, 185.3, 193.1, 198.0 (C(Ph)), 208.4, 214.2 (COO). FT IR (KBr pellet, 295 K, ν [cm^{-1}]: ν_{as}(COO), 1711 (m), ν_{as}(COO) 1510 (s), (ν(CC), ν_s(COO)) 1465 (m), 1450 (m), δ(CH_2, δ(CH_3)), 1434 (s), 1378 (m), ν_s(COO) 1298 (m), ν(CO) 1216 (s), 1200 (m), ν(COR) 1165 (w), 1115 (m), 1105 (m), 1083 (m), 1023 (s), (ν_s(Ti-O-Ti)) 778 (m), 764 (m), δ(CCC) 738 (s), 724 (s), δ(COO) 560 (m), 536 (m); Raman (solid state, 295 K, Raman Shift [cm^{-1}]: ν_{as}(COO) 1715 (w), ν_{as}(COO) 1606 (s), (ν(CC)) 1596 (w), (ν_s(COO)) 1495 (m), (δ(CH_2, δ(CH_3) 1450 (m), 1350 (m), 1328 (w), (ν(CO), ν(COR)) 1175 (m) 1154 (m), 1113 (m), 1022 (m), ν(Ti-O-Ti) 475 (w), 447(w).

2. Synthesis of ruthenium(III) complexes

2.1. $K[Ru^{III}(Hedta)Cl]\cdot 2H_2O$ (4)

The complex was synthesized as reported [4]. 3.0 g (8.0 mmol) of $K_2[RuCl_5(H_2O)]$ was dissolved in 60 mL of 0.001M $HClO_4$ and heated under reflux for 3h. Then the solution of 3.0 g (5.7 mmol) of $Na_2(edta)\cdot 2H_2O$ dissolved in 60 mL of 0.001M $HClO_4$ was added. After heating for 30 min, the solution was filtered, and the brown filtrate was heated for 2 h. The solution was left for crystallization (14 days). Yield: 42% (1.8 g). According to [5],

ruthenium content was determined as RuO_2. Anal. calculated for $K[Ru^{III}(Hedta)Cl]\cdot 2H_2O$: C, 24.0, H, 3.42, N, 5.59; Ru, 20.9. Found: C, 23.60; H, 3.38; N, 5.57; Ru, 21.6. FT IR (KBr pellet, 295 K, ν [cm^{-1}]: ν_{as}(COOH) 1723 (m), ν_{as}(COO) 1635 (s), 1595 (s), ν_s(COO) 1437 (m), δ(CH), δ(CH_2) 1437 (m), 1356 (m), ν(CN) 1318 (s), 1303 (s), 1242 (s), ν(CO) 1217 (s), ν(CN), ν(CO) 1083 (m), ν(CC) 1010 (m), 915 (m), ν(OH) 822 (m), ν(CH_2) 766 (m), ν(Ru-Cl) 693 (m), ν(Ru-O) 643 (m), ν(Ru-N) 594 (m), 557 (w), ν(Ru-O) 461 (w). Raman (solid state, 295 K, Raman Shift [cm^{-1}]: ν_{as}(COOH) 1683 (s), ν_{as}(COO) 1602 (s), ν_s(COO) 1442 (s), δ(CH_2) 1365 (m), 1314 (s), 1269 (s), ν(CO), ν(CN) 1162 (w), 1079 (m), ν(CN) 1038 (w), ν(CC) 1010 (m), 975 (m), 897 (s), ν(OH) 822 (m), ν(CH_2) 753 (m), 711 (m), ν(CN) 603 (m), ν(Ru-N) 568 (s), 460 (m), 382 (s), ν(Ru-O) 527 (s), 432 (m), 322 (s), 257 (s).

2.2. $[Ru(pic)_3]\cdot H_2O$ (5)

The complex was synthesized as reported [6]. 1.45 g (7.0 mmol) $RuCl_3\cdot nH_2O$ was dissolved in 50 mL anhydrous ethanol and refluxed for 3 hours. Then, the solution was filtered. 8.61 g (70.0 mmol) of picolinic acid dissolved in 50 mL of distilled water was added to the filtrate. The solution was stirred to evaporate the ethanol. The yellow powder was filtered and recrystallized from hot water. Yield: 60% (2.04 g). According to [5], ruthenium content was determined as RuO_2. Anal. calculated for $[Ru(pic)_3]\cdot H_2O$: C, 44.0; H, 2.9; N, 8.4; Ru, 20.8. Found: C, 43.8; H, 2.8; N, 8.5; Ru, 21.3. FT IR (KBr pellet, 295 K, ν [cm^{-1}]: ν_{as}(COO) 1669 (s), 1601 (s), 1565 (m), ν_s(COO), ν(CC), δ(CH), 1465 (m), 1451 (m), ν(CN) 1308 (s), δ(CH), ν(CO), ν(CC) 1278 (s), ν(CN) 1255 (s), 1232 (m), 1099 (m), δ(CH), ν(CC) 1136 (s), ν(CO) 1049 (m), 1031 (m), ν(CC) 1008 (w), 978 (w), 913 (w), ν(CC), 761 (s), ν(Ru-N) 451 (s), ν(Ru-O) 416 (m). Raman (solid state, 295 K, Raman Shift [cm^{-1}]: ν_{as}(COO) 1694 (s), 1659 (m), 1604 (s), 1568 (m), ν_s(COO) 1469 (m), δ(CH_2) 1328 (s), 1297 (m), ν(CO), ν(CN) 1156 (m), 1097 (m), ν(CN) 1034 (s), ν(CC) 860 (m), 820 (m), 716 (m), ν(CH) 659 (s), ν(Ru-N) 473 (m), 452 (m), ν(Ru-O) 349 (m), 312 (m), 255 (m).

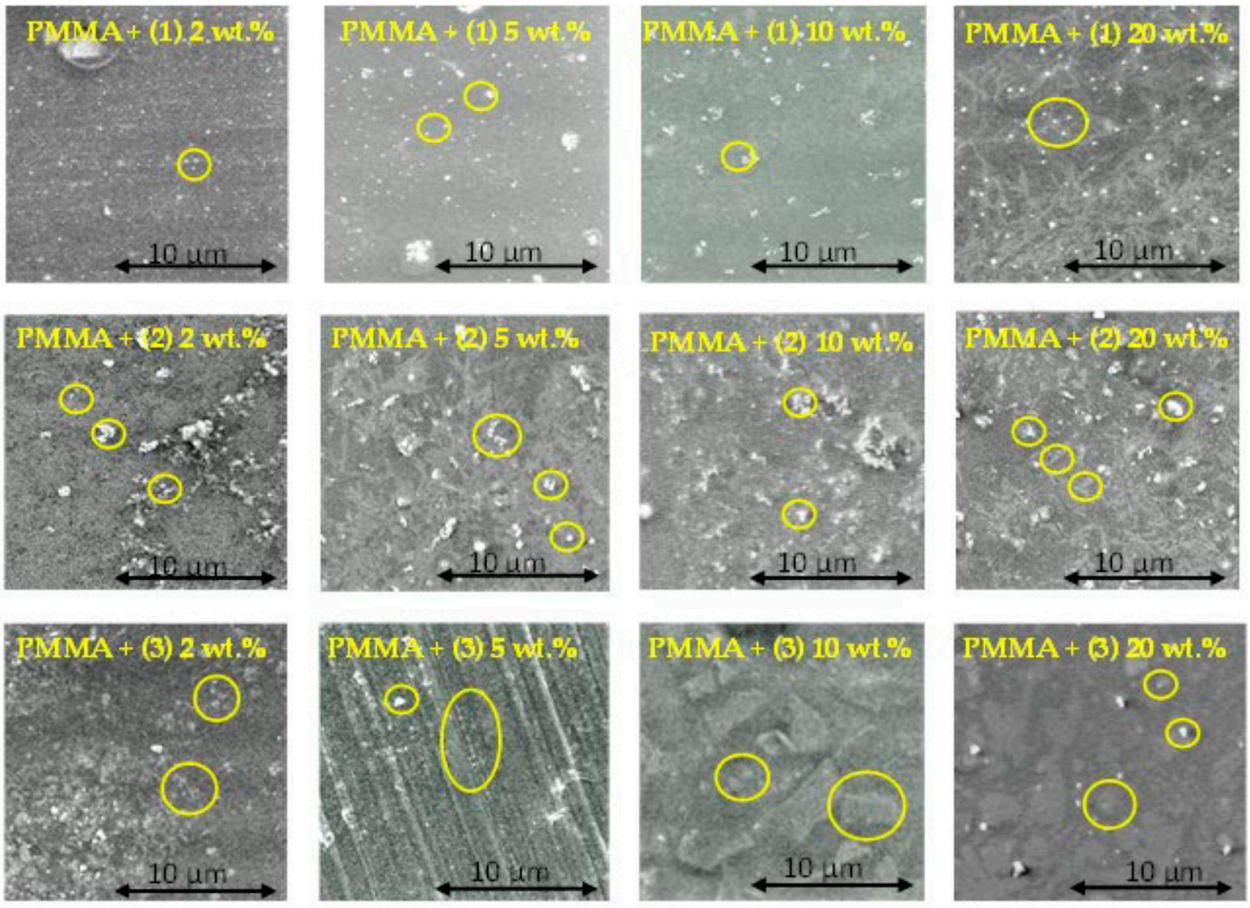


Figure S1. SEM images of the composite films enriched with titanium(IV)-oxo complexes (yellow rings mark TOCs grains).

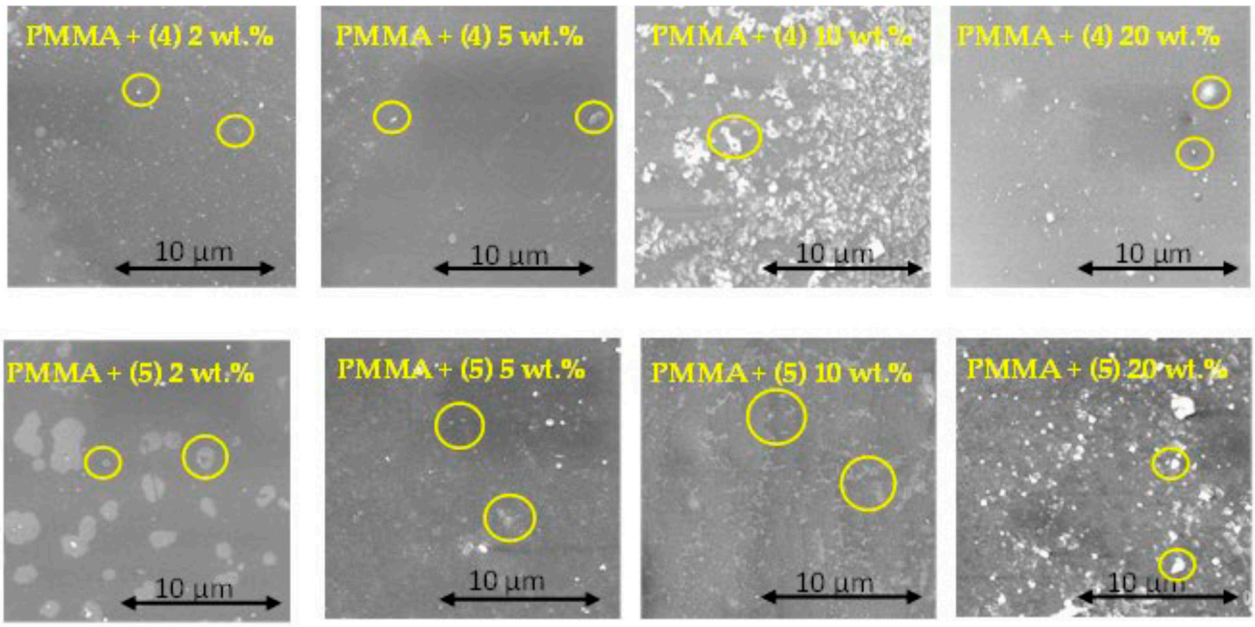


Figure S2. SEM images of the composite films enriched with ruthenium(III) complexes (yellow rings mark Ru(III) complexes grains).

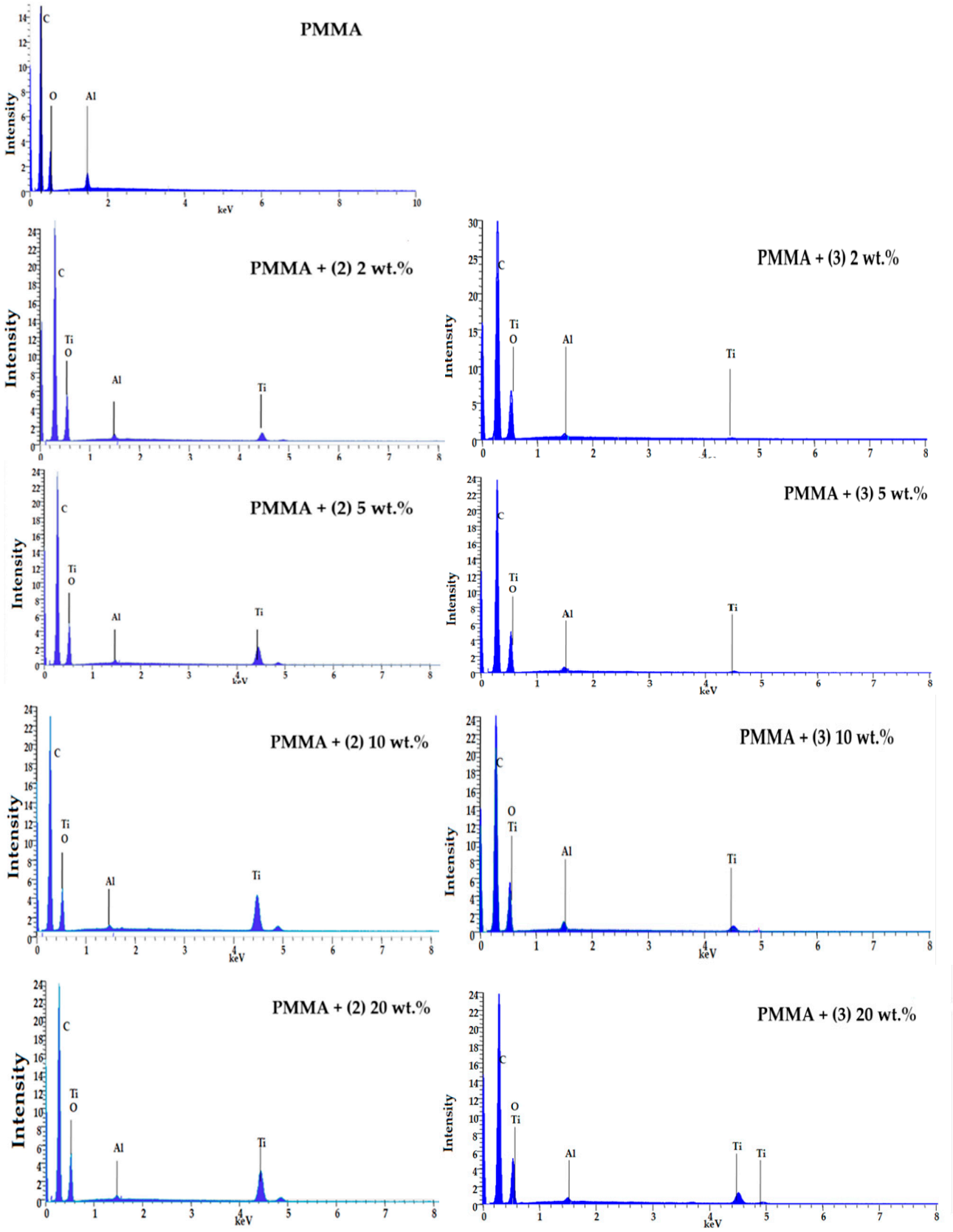


Figure S3. SEM EDX spectra of pure PMMA and composites containing titanium(IV) oxo-complexes (**2**) and (**3**).

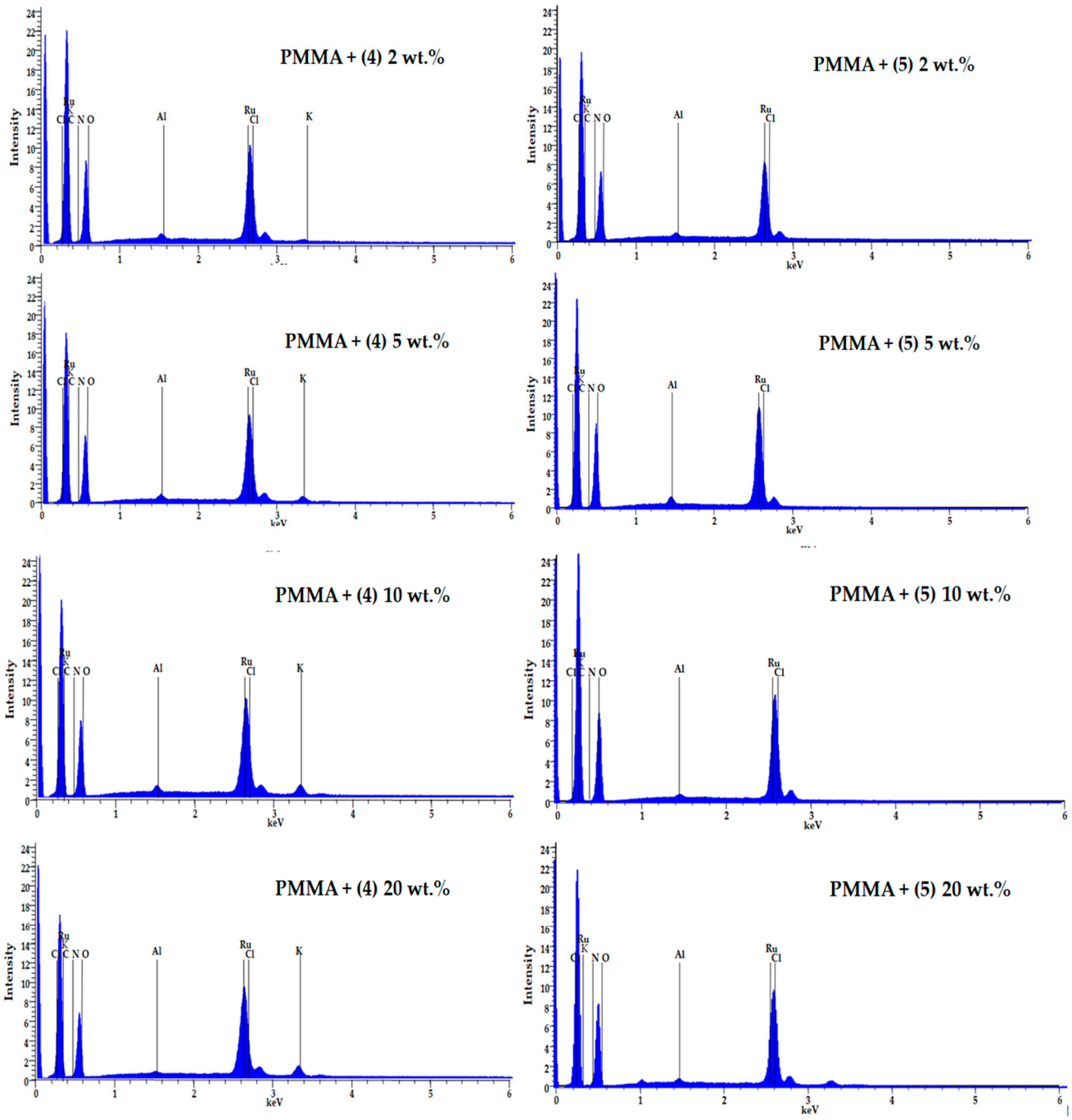


Figure S4. SEM EDX spectra of composites containing ruthenium(III) complexes (**4**) and (**5**).

Table S1. SEM EDX quantities data. All values are given in mass percent (%).

Composite	C	O	Al	Ti	Ru	N	Cl	K
PMMA	26.10	72.23	1.67	—	—	—	—	—
PMMA + (**2**) 2 wt.%	47.98	43.05	0.36	8.62	—	—	—	—
PMMA + (**2**) 5 wt.%	47.65	42.34	0.54	9.49	—	—	—	—
PMMA + (**2**) 10 wt.%	43.91	45.33	0.35	10.40	—	—	—	—
PMMA + (**2**) 20 wt.%	46.36	42.06	0.37	11.20	—	—	—	—
PMMA + (**3**) 2 wt.%	54.58	44.53	0.39	0.50	—	—	—	—
PMMA + (**3**) 5 wt.%	54.41	44.36	0.39	0.84	—	—	—	—
PMMA + (**3**) 10 wt.%	52.45	42.99	1.02	3.54	—	—	—	—
PMMA + (**3**) 20 wt.%	50.37	40.05	0.45	9.13	—	—	—	—
PMMA + (**4**) 2 wt.%	38.01	47.83	0.29	—	1.45	5.05	6.46	0.34
PMMA + (**4**) 5 wt.%	35.53	45.30	0.38	—	3.84	5.65	6.74	1.98
PMMA + (**4**) 10 wt.%	36.95	45.78	0.41	—	4.47	4.62	6.36	1.41
PMMA + (**4**) 20 wt.%	35.84	44.70	0.15	—	6.57	4.75	6.02	1.98
PMMA + (**5**) 2 wt.%	42.37	49.25	0.30	—	2.29	5.78	—	—
PMMA + (**5**) 5 wt.%	41.30	49.56	0.43	—	3.32	5.39	—	—
PMMA + (**5**) 10 wt.%	40.73	49.90	0.19	—	3.77	5.42	—	—
PMMA + (**5**) 20 wt.%	39.81	48.64	0.37	—	5.09	6.08	—	—

Table S2. Ti $L_{2,3}$ edge (two first features correspond to L_3 and two latter features to L_2 edges). Pre-edge features were visible at ca. 458.1 - 466.6 eV for powdered samples and experiments performed in TEY mode.

file	Energy peak for L_3 and L_2 [eV]	Intensity (area) for L_3 and L_2	transitions
P1-TEY	458.1	3.369	$2p_{3/2} \rightarrow t_{2g}$
	461.1	9.757	$2p_{3/2} \rightarrow e_g$
	463.5	3.515	$2p_{1/2} \rightarrow t_{2g}$
	466.5	14.611	$2p_{1/2} \rightarrow e_g$
P2-TEY	458.1	4.552	$2p_{3/2} \rightarrow t_{2g}$
	461.0	10.250	$2p_{3/2} \rightarrow e_g$
	463.5	5.568	$2p_{1/2} \rightarrow t_{2g}$
	466.3	15.437	$2p_{1/2} \rightarrow e_g$
P3-TEY	458.1	15.323	$2p_{3/2} \rightarrow t_{2g}$
	460.4	31.041	$2p_{3/2} \rightarrow e_g$
	463.5	36.007	$2p_{1/2} \rightarrow t_{2g}$
	465.9	48.348	$2p_{1/2} \rightarrow e_g$
K1-20-FY	458.1	9.873	$2p_{3/2} \rightarrow t_{2g}$
	461.2	11.708	$2p_{3/2} \rightarrow e_g$
	463.5	9.043	$2p_{1/2} \rightarrow t_{2g}$
	466.6	25.960	$2p_{1/2} \rightarrow e_g$
K2-20-FY	458.1	6,450	$2p_{3/2} \rightarrow t_{2g}$
	461.1	13.184	$2p_{3/2} \rightarrow e_g$
	463.4	6.176	$2p_{1/2} \rightarrow t_{2g}$
	466.4	22.405	$2p_{1/2} \rightarrow e_g$
K3-20-FY	458.1	3.684	$2p_{3/2} \rightarrow t_{2g}$
	460.4	5.525	$2p_{3/2} \rightarrow e_g$
	463.4	2.899	$2p_{1/2} \rightarrow t_{2g}$
	465.6	9.945	$2p_{1/2} \rightarrow e_g$

Table S3. Percentage reduction of dyes concentration in the solution by composites PMMA + ((**1**) – (**5**)).

Material	[CV] reduction [%]	[MB] reduction [%]	[RhB] reduction [%]
PMMA + (**1**) 2 wt.%	1.18	2.27	1.83
PMMA + (**1**) 5 wt.%	2.67	3.39	1.95
PMMA + (**1**) 10 wt.%	4.84	7.99	3.82
PMMA + (**1**) 20 wt.%	6.72	8.99	4.48
PMMA + (**2**) 2 wt.%	1.91	1.92	1.83
PMMA + (**2**) 5 wt.%	2.56	4.91	2.82
PMMA + (**2**) 10 wt.%	2.59	5.54	3.30
PMMA + (**2**) 20 wt.%	6.60	8.91	4.57
PMMA + (**3**) 2 wt.%	4.53	7.48	3.14
PMMA + (**3**) 5 wt.%	7.57	15.43	3.52
PMMA + (**3**) 10 wt.%	17.26	18.17	3.46
PMMA + (**3**) 20 wt.%	31.08	37.40	4.02
PMMA + (**4**) 2 wt.%	1.47	2.14	2.19
PMMA + (**4**) 5 wt.%	2.00	3.34	2.93
PMMA + (**4**) 10 wt.%	7.37	4.59	3.18
PMMA + (**4**) 20 wt.%	10.84	6.62	5.20
PMMA + (**5**) 2 wt.%	1.51	5.63	0.71
PMMA + (**5**) 5 wt.%	7.46	5.84	1.27
PMMA + (**5**) 10 wt.%	7.48	6.19	1.45
PMMA + (**5**) 20 wt.%	8.48	6.29	5.0

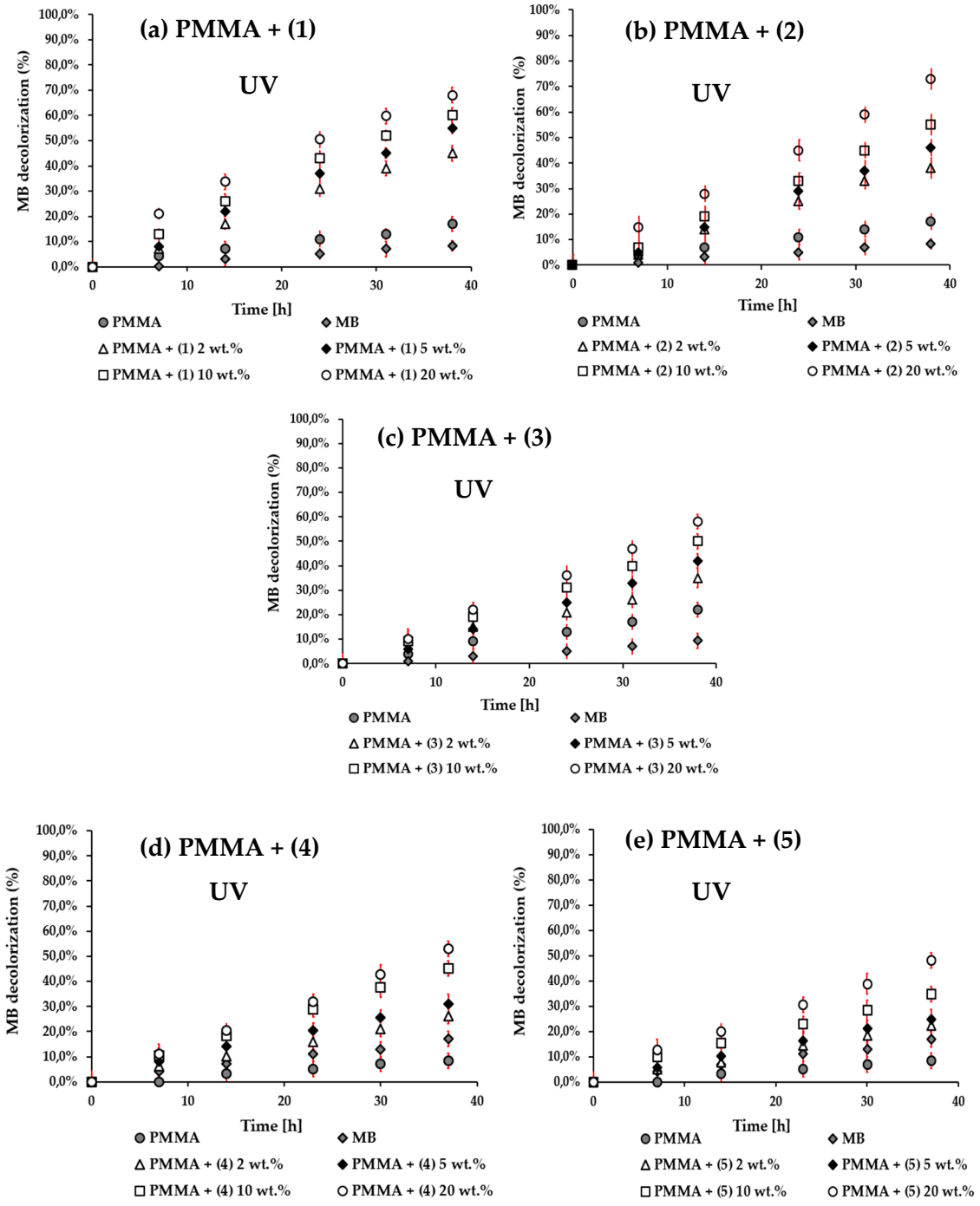


Figure S5. Changes in the concentrations of the methylene blue (MB) solution as a function of time for composite materials PMMA + (**1**) - (**5**) 2-20 wt.% irradiated with UV light.

Table S4. Decolorization percentages of MB solutions and calculated observed rate constants for the studied reactions relative to the composites irradiated by UV light.

Composite	MB Decolourisation (%)	ΔA 38	ΔA 38 in Reference to PMMA	10^2 Observed Rate Constant, h^{-1}	10^2 Observed Rate Constant in Reference to PMMA, h^{-1}
MB	9.4 ± 2.1	0.094	-0.081	0.24 ± 0.01	-0.18
PMMA	17.4 ± 2.4	0.175	-	0.42 ± 0.01	-
PMMA+(1) 2 wt.%	38.2 ± 3.2	0.383	0.129	1.06 ± 0.03	0.64
PMMA+ (1) 5 wt.%	46.4 ± 3.4	0.464	0.210	1.25 ± 0.02	0.83
PMMA+ (1) 10 wt.%	55.8 ± 3.8	0.558	0.304	1.48 ± 0.02	1.06
PMMA+ (1) 20 wt.%	68.6 ± 3.8	0.687	0.512	1.73 ± 0.04	1.31
PMMA+(2) 2 wt.%	45.3 ± 3.1	0.454	0.264	1.23 ± 0.02	0.81
PMMA+ (2) 5 wt.%	55.7 ± 2.9	0.556	0.381	1.47 ± 0.04	1.05
PMMA+ (2) 10 wt.%	60.4 ± 3.4	0.604	0.429	1.59 ± 0.03	1.17
PMMA+ (2) 20 wt.%	73.1 ± 4.2	0.731	0.477	1.89 ± 0.03	1.47
PMMA+(3) 2 wt.%	35.2 ± 2.2	0.351	0.176	0.85 ± 0.01	0.43
PMMA+ (3) 5 wt.%	42.8 ± 2.8	0.421	0.246	1.11 ± 0.01	0.69
PMMA+ (3) 10 wt.%	50.4 ± 3.3	0.504	0.329	1.30 ± 0.02	0.88
PMMA+ (3) 20 wt.%	58.4 ± 3.4	0.584	0.428	1.53 ± 0.01	1.14
PMMA+(4) 2 wt.%	19.1 ± 3.1	0.191	0.016	0.49 ± 0.03	0.07
PMMA+ (4) 5 wt.%	21.8 ± 2.0	0.212	0.037	0.55 ± 0.02	0.13
PMMA+ (4) 10 wt.%	24.2 ± 2.3	0.238	0.063	0.62 ± 0.03	0.20
PMMA+ (4) 20 wt.%	32.9 ± 2.4	0.321	0.146	0.86 ± 0.03	0.44
PMMA+(5) 2 wt.%	17.5 ± 2.8	0.168	0.007	0.47 ± 0.02	0.05
PMMA+ (5) 5 wt.%	20.7 ± 2.1	0.249	0.074	0.55 ± 0.03	0.13
PMMA+ (5) 10 wt.%	25.9 ± 2.1	0.320	0.145	0.67 ± 0.03	0.25
PMMA+ (5) 20 wt.%	32.3 ± 2.5	0.320	0.145	0.85 ± 0.03	0.43

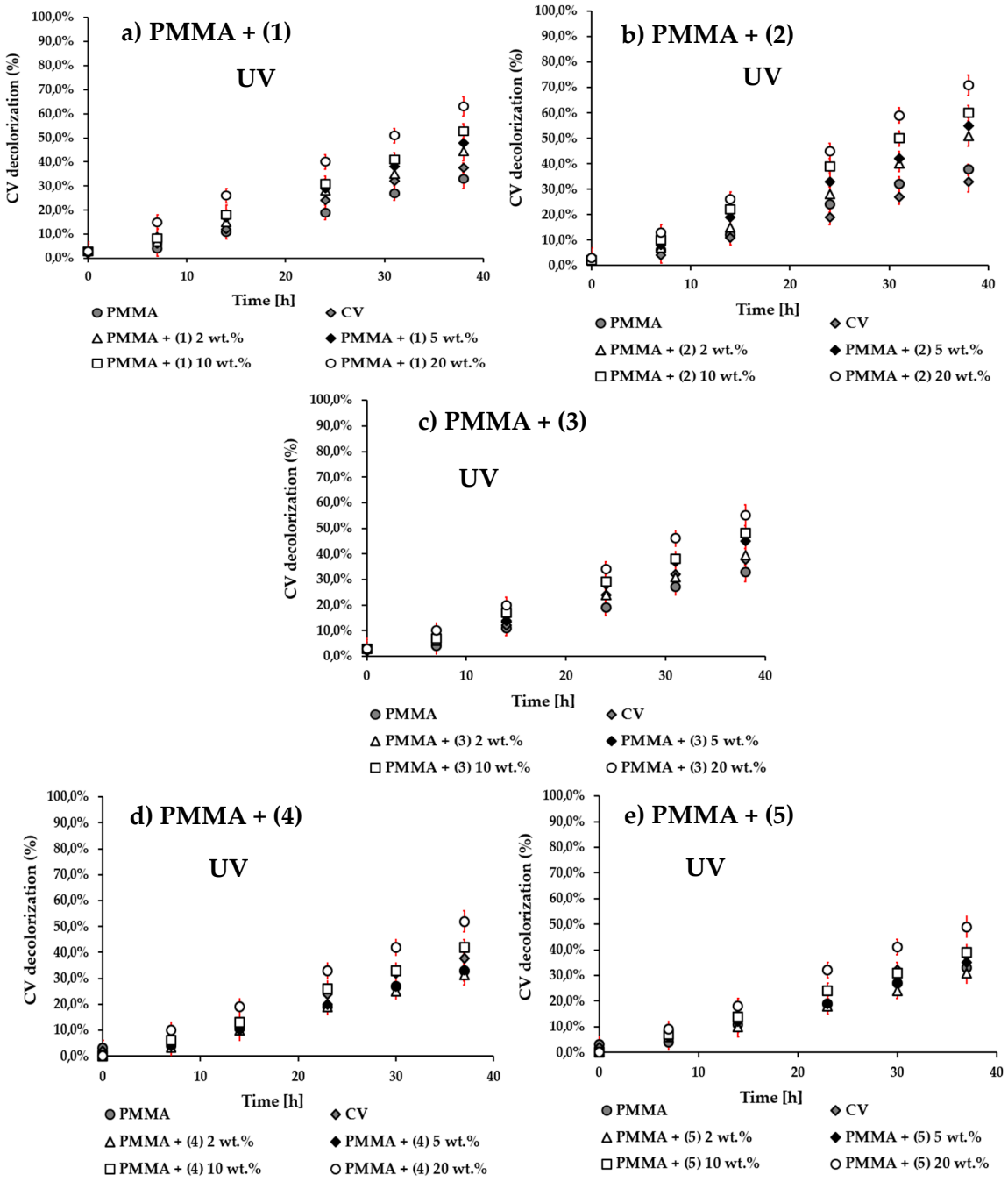


Figure S6. Changes in the concentrations of the crystal violet (CV) solution as a function of time for composite materials PMMA + (**1**) - (**5**) 2-20 wt.% irradiated with UV light.

Table S5. Decolorization percentages of CV solutions and calculated observed rate constants for the studied reactions relative to the composites irradiated by UV light.

Composite	CV Decolourisation (%)	ΔA 38	ΔA 38 in Reference to PMMA	10^2 Observed Rate Constant, h^{-1}	10^2 Observed Rate Constant in Reference to PMMA, h^{-1}
CV	33.2 ± 2.3	0.332	-0.043	0.99 ± 0.01	-0.15
PMMA	37.5 ± 2.1	0.375	-	0.84 ± 0.01	-
PMMA+(1) 2 wt.%	44.3 ± 2.6	0.443	0.068	1.11 ± 0.01	0.27
PMMA+ (1) 5 wt.%	48.4 ± 2.8	0.485	0.110	1.19 ± 0.03	0.35
PMMA+ (1) 10 wt.%	52.9 ± 3.2	0.527	0.152	1.33 ± 0.02	0.49
PMMA+ (1) 20 wt.%	63.9 ± 3.1	0.638	0.263	1.55 ± 0.01	0.71
PMMA+(2) 2 wt.%	51.1 ± 2.9	0.512	0.137	1.31 ± 0.01	0.47
PMMA+ (2) 5 wt.%	55.3 ± 3.1	0.549	0.174	1.40 ± 0.03	0.56
PMMA+ (2) 10 wt.%	60.4 ± 3.5	0.602	0.227	1.57 ± 0.02	0.73
PMMA+ (2) 20 wt.%	70.9 ± 3.3	0.709	0.334	1.83 ± 0.01	0.99
PMMA+(3) 2 wt.%	39.4 ± 2.7	0.393	0.018	0.98 ± 0.01	0.14
PMMA+ (3) 5 wt.%	45.1 ± 2.6	0.452	0.077	1.16 ± 0.03	0.32
PMMA+ (3) 10 wt.%	48.1 ± 3.0	0.480	0.105	1.22 ± 0.02	0.38
PMMA+ (3) 20 wt.%	55.1 ± 3.2	0.552	0.177	1.41 ± 0.01	0.57
PMMA+(4) 2 wt.%	31.4 ± 2.3	0.313	-0.019	0.85 ± 0.02	0.01
PMMA+ (4) 5 wt.%	33.3 ± 1.9	0.332	0.00	0.90 ± 0.03	0.06
PMMA+ (4) 10 wt.%	42.4 ± 4.5	0.425	0.093	1.12 ± 0.02	0.28
PMMA+ (4) 20 wt.%	52.1 ± 4.4	0.520	0.188	1.36 ± 0.01	0.52
PMMA+(5) 2 wt.%	31.0 ± 2.5	0.308	-0.023	0.80 ± 0.01	-0.04
PMMA+ (5) 5 wt.%	35.0 ± 2.1	0.347	0.016	0.90 ± 0.02	0.06
PMMA+ (5) 10 wt.%	39.9 ± 3.2	0.391	0.059	1.02 ± 0.02	0.18
PMMA+ (5) 20 wt.%	49.0 ± 3.8	0.490	0.158	1.31 ± 0.02	0.47

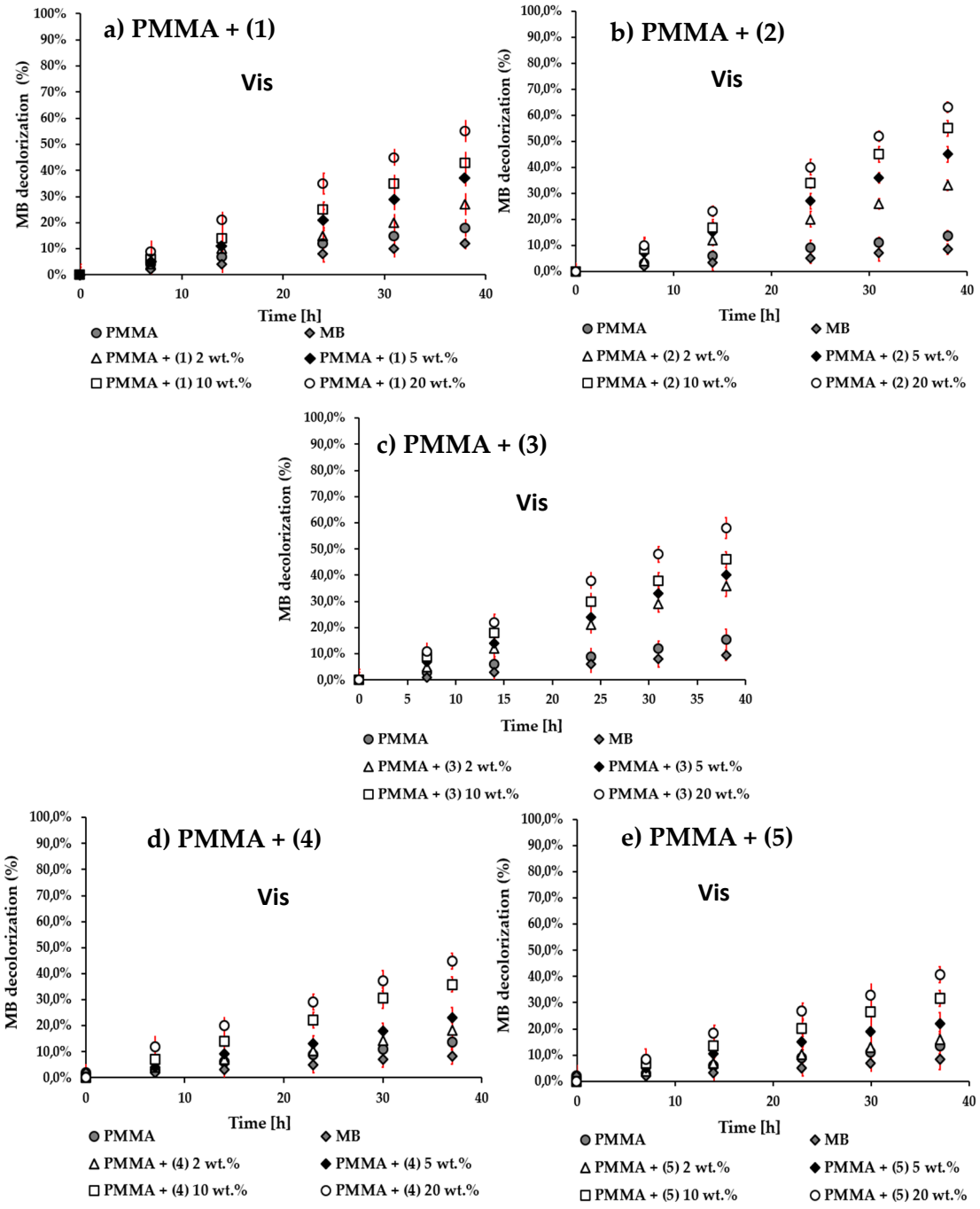


Figure S7. Changes in the concentrations of the methylene blue (MB) solution as a function of time for composite materials PMMA + (**1**) - (**5**) 2-20 wt.% irradiated with Vis light.

Table S6. Decolorization percentages of MB solutions and calculated observed rate constants for the studied reactions relative to the composites irradiated by VIS light.

Composite	MB Decolourisation (%)	ΔA 38	ΔA 38 in Reference to PMMA	10^2 Observed Rate Constant, h^{-1}	10^2 Observed Rate Constant in Reference to PMMA, h^{-1}
MB	8.4 ± 1.7	0.084	-0.062	0.23 ± 0.01	-0.13
PMMA	14.6 ±1.9	0.146	-	0.36 ± 0.02	-
PMMA+(1) 2 wt.%	27.3 ± 3.1	0.274	0.128	0.69 ± 0.03	0.33
PMMA+ (1) 5 wt.%	37.2 ± 2.4	0.372	0.226	0.97 ± 0.02	0.61
PMMA+ (1) 10 wt.%	43.6 ± 2.6	0.435	0.289	1.12 ± 0.02	0.76
PMMA+ (1) 20 wt.%	55.3 ± 3.2	0.552	0.406	1.43 ± 0.03	1.07
PMMA+(2) 2 wt.%	33.6 ± 2.2	0.336	0.190	0.88 ± 0.01	0.52
PMMA+ (2) 5 wt.%	45.7 ± 3.4	0.457	0.311	1.12 ± 0.01	0.76
PMMA+ (2) 10 wt.%	55.1 ± 3.3	0.550	0.404	1.48 ± 0.02	1.12
PMMA+ (2) 20 wt.%	63.6 ± 3.6	0.635	0.489	1.68 ± 0.03	1.32
PMMA+(3) 2 wt.%	36.2 ± 3.3	0.361	0.205	0.96 ± 0.02	0.57
PMMA+ (3) 5 wt.%	40.6 ± 3.5	0.405	0.249	1.06 ± 0.03	0.67
PMMA+ (3) 10 wt.%	46.1 ± 4.2	0.461	0.305	1.21 ± 0.02	0.82
PMMA+ (3) 20 wt.%	58.7 ± 3.1	0.587	0.412	1.53 ± 0.03	1.11
PMMA+(4) 2 wt.%	18.1 ± 2.4	0.180	0.044	0.47 ± 0.02	0.15
PMMA+ (4) 5 wt.%	23.2 ± 2.2	0.232	0.096	0.61 ± 0.02	0.29
PMMA+ (4) 10 wt.%	35.9 ± 2.1	0.358	0.222	0.98 ± 0.02	0.66
PMMA+ (4) 20 wt.%	44.8 ± 2.5	0.449	0.313	1.17 ± 0.03	0.85
PMMA+(5) 2 wt.%	16.1 ± 2.2	0.160	0.024	0.42 ± 0.02	0.1
PMMA+ (5) 5 wt.%	22.1 ± 2.1	0.221	0.085	0.59 ± 0.03	0.27
PMMA+ (5) 10 wt.%	31.7 ± 4.1	0.316	0.180	0.85 ± 0.02	0.53
PMMA+ (5) 20 wt.%	40.6 ± 2.5	0.405	0.269	1.08 ± 0.03	0.76

Table S7. EPR data for the studied PMMA composites and powdered complexes.

Sample	g-Factor	Species [7,8]
PMMA	—	—
PMMA + (**2**) 2 wt.%	2.025; 2.011	O_2^-
	2.008; 2.003	O^-
	1.992	Ti(III)
PMMA + (**2**) 5 wt.%	2.025; 2.011	O_2^-
	2.007; 2.003	O^-
	1.992	Ti(III)
PMMA + (**2**) 10 wt.%	2.024; 2.011	O_2^-
	2.016; 2.006; 2.000	O^-
	1.993	Ti(III)
PMMA + (**2**) 20 wt.%	2,024; 2.010; 2.002	O_2^-
	2.016; 2.006; 1.999	O^-
	1.993	Ti(III)
Powder of (**2**)	2.003	e^-
PMMA + (**3**) 2 wt.%	2.010; 2.003	O_2^-
	2.017; 2.006; 1.999	O^-
	1.992	Ti(III)
PMMA + (**3**) 5 wt.%	2.010; 2.002	O_2^-
	2.017; 2.006; 1.999	O^-
	1.993	Ti(III)
PMMA + (**3**) 10 wt.%	2.010; 2.003	O_2^-
	2.017; 2.006; 1.999	O^-
	1.993	Ti(III)
PMMA + (**3**) 20 wt.%	2.024; 2.010; 2.002	O_2^-
	2.017; 2.006; 1.999	O^-
	1.993	Ti(III)
Powder of (**3**)	2.023; 2.011; 2.005	O_2^-
	2.016; 2.007; 2.002	O^-
	1.993	Ti(III)
PMMA + (**4**) 2 wt.%	2.42	Ru(III)
PMMA + (**4**) 5 wt.%	2.40	Ru(III)
PMMA + (**4**) 10 wt.%	2.42; 2.30	Ru(III)
PMMA + (**4**) 20 wt.%	2.42; 2.28	Ru(III)
Powder of **(4)**	2.40; 2.25; 1.79	Ru(III)
PMMA + (**5**) 2 wt.%	2.57	Ru(III)
PMMA + (**5**) 5 wt.%	2.65; 2.31	Ru(III)
PMMA + (**5**) 10 wt.%	2.53; 2.25	Ru(III)
PMMA + (**5**) 20 wt.%	2.65; 2.29; 1.76	Ru(III)
Powder of **(5)**	2.65; 2.30; 1.78	Ru(III)

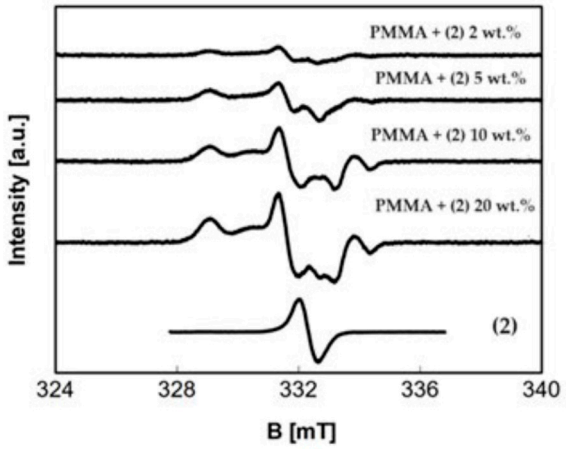


Figure S8. EPR spectra of the PMMA composites with (**2**) and of powdered TOC. Conditions: room temperature; microwave frequencies: 9.324675 GHz (PMMA+ (**2**) 2 wt.%), 9.324486 GHz (PMMA+ (**2**) 5 wt.%), 9.323992 GHz (PMMA+ (**2**) 10 wt.%), 9.323746 GHz (PMMA+ (**2**) 20 wt.%), and 9.317209 GHz ((**2**)); modulation amplitude: 1 mT; sweep: 20 mT; sweep time: 4 min; time constant: 0.1 s; receiver gain: 2×10^5 (composites) and 0.5×10^5 ((**2**)).

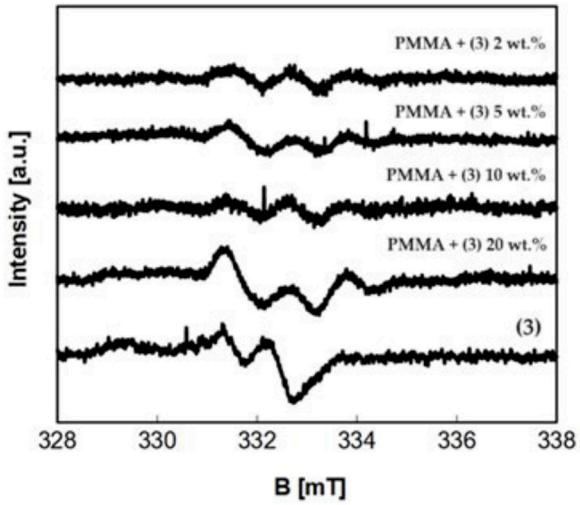


Figure S9. EPR spectra of the PMMA composites with (**3**) and of powdered TOC. Conditions: room temperature; microwave frequencies: 9.324157 GHz (PMMA+ (**3**) 2 wt.%), 9.324280 GHz (PMMA+ (**3**) 5 wt.%), 9.323349 GHz (PMMA+ (**3**) 10 wt.%), 9.322974 GHz (PMMA+ (**3**) 20 wt.%), and 9.324018 GHz ((**3**)); modulation amplitude: 1 mT; sweep: 20 mT; sweep time: 8 min (composites) and 4 min ((**3**)); time constant: 0.1 s; receiver gain: 4×10^5 (composites) and 5×10^5 ((**3**)).

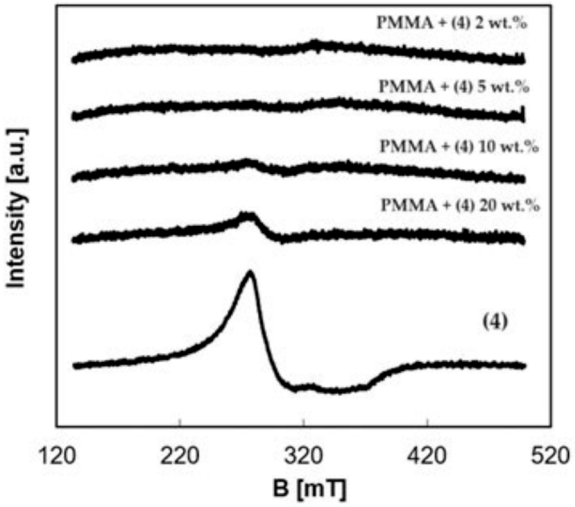


Figure S10. EPR spectra of the PMMA composites with (**4**) and of powdered complex. Conditions: room temperature; microwave frequencies: 9.325410 GHz (PMMA+ (**4**) 2 wt.%), 9.324910 GHz (PMMA+ (**4**) 5 wt.%), 9.325450 GHz (PMMA+ (**4**) 10 wt.%), 9.325550 GHz (PMMA+ (**4**) 20 wt.%), and 9.322220 GHz (**4**); modulation amplitude: 1 mT; sweep: 400 mT (composites) and 200 mT (**4**); sweep time: 8 min (composites) and 4 min (**4**); time constant: 0.1 s; receiver gain: 6.3×10^5 (composites) and 4×10^5 (**4**).

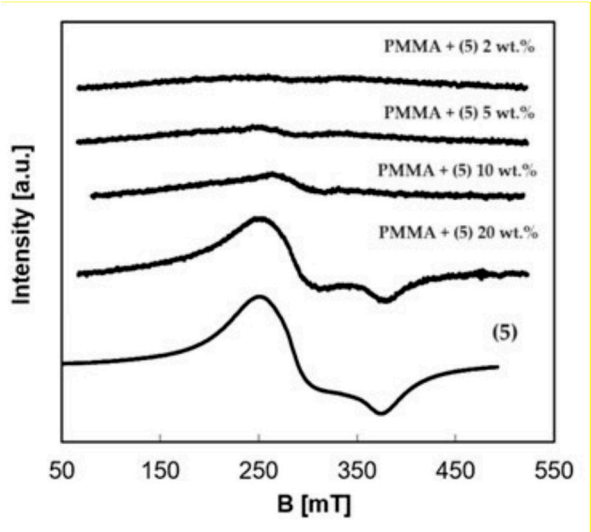


Figure S11. EPR spectra of the PMMA composites with (**5**) and of powdered complex. Conditions: room temperature; microwave frequencies: 9.325300 GHz (PMMA+ (**5**) 2 wt.%), 9.325630 GHz (PMMA+ (**5**) 5 wt.%), 9.325390 GHz (PMMA+ (**5**) 10 wt.%), 9.325470 GHz (PMMA+ (**5**) 20 wt.%), and 9.323610 GHz (**5**); modulation amplitude: 1 mT; sweep: 500 mT; sweep time: 2 min (**5**) and 4 min (composites); time constant: 0.1 s; receiver gain: 3.2×10^5 (composites and (**5**)).

References

1. Kubiak, B.; Muzioł, T.; Wrzeszcz, G.; Radtke, A.; Golińska, P.; Jędrzejewski, T.; Wrotek, S.; Piszczek, P. Structural Characterization and Bioactivity of a Titanium(IV)-Oxo Complex Stabilized by Mandelate Ligands. *Molecules* **2024**, *29*, 1736, doi:10.3390/molecules29081736.
2. Meth-Cohn, O.; Thorpe, D.; Twitchett, H.J. Insertion Reactions of Titanium Alkoxides with Isocyanates and Carbodiimides. *J. Chem. Soc., C* **1970**, 132, doi:10.1039/j39700000132.
3. Kubiak, B.; Muziol, T.M.; Jabłoński, M.; Radtke, A.; Piszczek, P. Investigation of Titanium(IV)-Oxo Complexes Stabilized with α-Hydroxy Carboxylate Ligands: Structural Analysis and DFT Studies. *Dalton Trans.* **2024**, 10.1039.D4DT01710B, doi:10.1039/D4DT01710B.
4. Diamantis, A.A.; Dubrawski, J.V. Preparation and Structure of Ethylenediaminetetraacetate Complexes of Ruthenium(II) with Dinitrogen, Carbon Monoxide, and Other .Pi.-Acceptor Ligands. *Inorg. Chem.* **1981**, *20*, 1142–1150, doi:10.1021/ic50218a037.
5. Badea, M.; Olar, R.; Marinescu, D.; Uivarosi, V.; Nicolescu, T.O.; Iacob, D. Thermal Study of Some New Quinolone Ruthenium(III) Complexes with Potential Cytostatic Activity. *J Therm Anal Calorim* **2010**, *99*, 829–834, doi:10.1007/s10973-009-0479-4.
6. Impert, O.; Katafias, A.; Kita, P.; Wrzeszcz, G.; Fenska, J.; Lente, G.; Fábián, I. Base Hydrolysis of Mer-Trispicolinatoruthenium(III): Kinetics and Mechanism. *Transition Met Chem* **2011**, *36*, 761–766, doi:10.1007/s11243-011-9530-y.
7. Suriye, K.; Lobo-Lapidus, R.J.; Yeagle, G.J.; Praserthdam, P.; Britt, R.D.; Gates, B.C. Probing Defect Sites on TiO2 with [Re3(CO)12H3]: Spectroscopic Characterization of the Surface Species. *Chem. Eur. J.* **2008**, *14*, 1402–1414, doi:10.1002/chem.200701514.
8. Canevali, C.; Chiodini, N.; Morazzoni, F.; Scotti, R. Electron Paramagnetic Resonance Characterization of Ruthenium-Dispersed Tin Oxide Obtained by Sol–Gel and Impregnation Methods. *J. Mater. Chem.* **2000**, *10*, 773–778, doi:10.1039/a907947e.

Oświadczenia współautorów

UNIWERSYTET
MIKOŁAJA KOPERNIKA
W TORUNIU
Wydział Chemii

Mgr Barbara Kubiak
Wydział Chemii
Uniwersytet Mikołaja Kopernika w Toruniu
ul. Gagarina 7
87 – 100 Toruń

Toruń, 07.02.2025

OŚWIADCZENIE

Jako autorka przedłożonej rozprawy doktorskiej oświadczam, że mój wkład naukowy w powstanie poniższych artykułów polegał na:

P1. P. Piszczek*, **B. Kubiak,** P. Golińska, A. Radtke*, Oxo-Titanium(IV) Complex/Polymer Composites—Synthesis, Spectroscopic Characterization and Antimicrobial Activity Test. *IJMS* **2020**, *21*, 9663

Byłam odpowiedzialna za syntezę kompleksów okso-tytanu(IV) (TOCs) oraz wytwarzanie materiałów kompozytowych. Do moich zadań należało także przeprowadzanie mapowania Ramana, pomiarów spektroskopowych IR, Ramana oraz UV-Vis DRS, a także badanie aktywności fotokatalitycznej. Dodatkowo uczestniczyłam w przygotowywaniu rysunków, tworzeniu wprowadzenia do artykułu i opisywaniu rezultatów badań.

P2. **B. Kubiak*,** P. Piszczek*, A. Radtke, T. Muzioł, G. Wrzeszcz, P. Golińska, Photocatalytic and Antimicrobial Activity of Titanium(IV)-Oxo Clusters of Different Core Structure. *Crystals* **2023**, *13*, 998

Byłam odpowiedzialna za zaplanowanie i syntezę kompleksów okso-tytanu(IV) (TOCs) oraz wytwarzanie materiałów kompozytowych. Do moich zadań należało także przeprowadzanie mapowania Ramana oraz rejestracja widm UV-Vis DRS, a także badanie aktywności fotokatalitycznej. Zinterpretowałam także otrzymane wyniki (SEM, SEM EDX, analiza termiczna, mapy Ramana, widma UV – Vis DRS, aktywność fotokatalityczna). Dodatkowo uczestniczyłam w określeniu celu i kształtowaniu zakresu pracy i wniosłam przeważający wkład w treść manuskryptu (wstępu, części fizykochemicznej, dyskusji i wniosków). Odpowiadałam także za przygotowanie części rysunków.

P3. **B. Kubiak,** A. Radtke*, A. Topolski, G. Wrzeszcz, P. Golińska, E. Kaszkowiak, M. Sobota, J. Włodarczyk, M. Stojko, P. Piszczek*, The Composites of PCL and Tetranuclear Titanium(IV) – Oxo Complexes as Materials Exhibiting the Photocatalytic and the Antimicrobial Activity. *IJMS* **2021**, *22*, 7021

Byłam odpowiedzialna za syntezę kompleksów okso-tytanu(IV) (TOCs). Do moich zadań należało także rejestracja map Ramana, rejestracja widm IR - DRIFT, Ramana oraz UV-Vis

DRS, a także badanie aktywności fotokatalitycznej. Zinterpretowałam także otrzymane wyniki (SEM, SEM EDX, analiza termiczna, mapy Ramana, widma UV – Vis DRS, aktywność fotokatalityczna). Dodatkowo uczestniczyłam w przygotowywaniu rysunków, tworzeniu wprowadzenia do artykułu i opisywaniu rezultatów badań.

P4. **B. Kubiak*, T.** Muzioł, G. Wrzeszcz, A. Radtke, P. Golińska, T. Jędrzejewski, S. Wrotek, P. Piszczek*, Structural Characterization and Bioactivity of a Titanium(IV) – Oxo Complex Stabilized by Mandelate Ligands. *Molecules* **2024**, *29*, 1736

Byłam odpowiedzialna za zaplanowanie i syntezę kompleksów okso-tytanu(IV) (TOCs) oraz wytwarzanie materiałów kompozytowych. Do moich zadań należała także rejestracja widm IR i Ramana. Zinterpretowałam także otrzymane wyniki (SEM EDX, widma IR i Ramana, aktywność przeciwdrobnoustrojowa). Dodatkowo uczestniczyłam w określeniu celu i kształtowaniu zakresu pracy i wniosłam przeważający wkład w treść manuskryptu (wstępu, części fizykochemicznej, dyskusji (również badań przeciwdrobnoustrojowych) i wniosków). Odpowiadałam także za przygotowanie części rysunków.

P5. **B. Kubiak***, T. M. Muzioł, M. Jabłoński, A. Radtke, P. Piszczek*, Investigation of Titanium(IV) – Oxo Complexes Stabilized with α-Hydroxy Carboxylate Ligands: Structural Analysis and DFT Studies. *Dalton Trans.* **2024**, 53, 14457-14468

Byłam odpowiedzialna za zaplanowanie i syntezę kompleksów okso-tytanu(IV) (TOCs). Do moich zadań należała także rejestracja widm UV – Vis DRS, IR i Ramana. Zinterpretowałam także otrzymane wyniki (widma IR i Ramana). Dodatkowo uczestniczyłam w określeniu celu i kształtowaniu zakresu pracy i wniosłam przeważający wkład w treść manuskryptu (wstępu, części fizykochemicznej, dyskusji, wniosków i odpowiedzi na recenzje). Odpowiadałam także za przygotowanie części rysunków.

P6. **B. Kubiak*,** A. Topolski, A. Radtke*, T. Muzioł, O. Impert, A. Katafias, R. van Eldik, P. Piszczek, Analysis of Photocatalytic Properties of Poly(Methyl Methacrylate) Composites with Titanium(IV) and Ruthenium(III) Complexes. Applied Sciences, 2025, 15(4), 1679

Byłam odpowiedzialna za syntezę kompleksów okso-tytanu(IV) (TOCs), kompleksów rutenu(III) oraz wytwarzanie materiałów kompozytowych. Do moich zadań należała także rejestracja widm UV – Vis DRS, Ramana, map Ramana, badanie zdolności adsorpcyjnych oraz fotokatalitycznych kompozytów zawierających kompleksy tytanu(IV) lub rutenu(III). Zinterpretowałam także otrzymane wyniki (SEM, SEM EDX, widma UV – Vis DRS, Ramana, mapy Ramana, badanie zdolności adsorpcyjnych oraz fotokatalitycznych kompozytów zawierających kompleksy tytanu(IV) lub rutenu(III). Dodatkowo uczestniczyłam w określeniu celu i kształtowaniu zakresu pracy i wniosłam przeważający wkład w treść manuskryptu (wstępu, części fizykochemicznej, dyskusji, wniosków i odpowiedzi na recenzje).

Barbara Kubiak

Podpis

UNIWERSYTET
MIKOŁAJA KOPERNIKA
W TORUNIU
Wydział Chemii

Dr hab. Piotr Piszczek, prof. UMK
Wydział Chemii
Uniwersytet Mikołaja Kopernika w Toruniu
ul. Gagarina 7
87 – 100 Toruń

Toruń, 07.02.2025

OŚWIADCZENIE

Dotyczy publikacji:

P1. P. Piszczek*, **B. Kubiak,** P. Golińska, A. Radtke*, Oxo-Titanium(IV) Complex/Polymer Composites—Synthesis, Spectroscopic Characterization and Antimicrobial Activity Test. *IJMS* **2020**, *21*, 9663

P2. **B. Kubiak*,** P. Piszczek*, A. Radtke, T. Muzioł, G. Wrzeszcz, P. Golińska, Photocatalytic and Antimicrobial Activity of Titanium(IV)-Oxo Clusters of Different Core Structure. *Crystals* **2023**, *13*, 998

P3. **B. Kubiak,** A. Radtke*, A. Topolski, G. Wrzeszcz, P. Golińska, E. Kaszkowiak, M. Sobota, J. Włodarczyk, M. Stojko, P. Piszczek*, The Composites of PCL and Tetranuclear Titanium(IV) – Oxo Complexes as Materials Exhibiting the Photocatalytic and the Antimicrobial Activity. *IJMS* **2021**, *22*, 7021

P4. **B. Kubiak*, T.** Muzioł, G. Wrzeszcz, A. Radtke, P. Golińska, T. Jędrzejewski, S. Wrotek, P. Piszczek*, Structural Characterization and Bioactivity of a Titanium(IV) – Oxo Complex Stabilized by Mandelate Ligands. *Molecules* **2024**, *29*, 1736

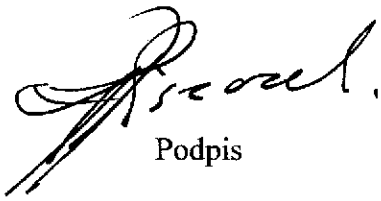
P5. **B. Kubiak***, T. M. Muzioł, M. Jabłoński, A. Radtke, P. Piszczek*, Investigation of Titanium(IV) – Oxo Complexes Stabilized with α-Hydroxy Carboxylate Ligands: Structural Analysis and DFT Studies. *Dalton Trans.* **2024**, 53, 14457-14468

P6. **B. Kubiak***, A. Topolski, A. Radtke*, T. Muzioł, O. Impert, A. Katafias, R. van Eldik, P. Piszczek, Analysis of Photocatalytic Properties of Poly(Methyl Methacrylate) Composites with Titanium(IV) and Ruthenium(III) Complexes. Applied Sciences, 2025, 15(4), 1679

1. Oświadczam, że mój udział w artykule **P1** obejmował opracowanie założeń badawczych oraz metodologii badań, analizę otrzymanych wyników, przygotowywanie i edycję tekstu oraz koordynację prac związanych z publikacją otrzymanych wyników.
2. Oświadczam, że mój udział w artykule **P2** obejmował opracowanie założeń badawczych oraz metodologii badań i analizę otrzymanych wyników. Odpowiadałem także za edycję tekstu oraz koordynację prac związanych z publikacją otrzymanych wyników.
3. Oświadczam, że mój udział w artykule **P3** obejmował opracowanie założeń badawczych oraz metodologii badań i analizę otrzymanych wyników. Odpowiadałem także za

przygotowywanie i edycję tekstu, koordynację prac związanych z publikacją otrzymanych wyników oraz pozyskanie środków finansowych.

4. Oświadczam, że mój udział w artykule **P4** obejmował opracowanie założeń badawczych oraz metodologii badań i analizę otrzymanych wyników. Odpowiadałem także za edycję tekstu, koordynację prac związanych z publikacją otrzymanych wyników oraz pozyskanie środków finansowych.
5. Oświadczam, że mój udział w artykule **P5** obejmował opracowanie założeń badawczych oraz metodologii badań i analizę otrzymanych wyników. Odpowiadałem także za edycję tekstu oraz koordynację prac związanych z publikacją otrzymanych wyników.
6. Oświadczam, że mój udział w artykule **P6** obejmował opracowanie metodologii badań i analizę otrzymanych wyników. Odpowiadałem także za edycję tekstu oraz koordynację prac związanych z publikacją otrzymanych wyników.



Podpis

UNIWERSYTET
MIKOŁAJA KOPERNIKA
W TORUNIU
Wydział Chemii

Dr hab. Aleksandra Radtke, prof. UMK
Wydział Chemii
Uniwersytet Mikołaja Kopernika w Toruniu
ul. Gagarina 7
87 – 100 Toruń

Toruń, 07.02.2025

OŚWIADCZENIE

Dotyczy publikacji:

P1. P. Piszczek*, **B. Kubiak,** P. Golińska, A. Radtke*, Oxo-Titanium(IV) Complex/Polymer Composites—Synthesis, Spectroscopic Characterization and Antimicrobial Activity Test. *IJMS* **2020**, *21*, 9663

P2. **B. Kubiak*,** P. Piszczek*, A. Radtke, T. Muzioł, G. Wrzeszcz, P. Golińska, Photocatalytic and Antimicrobial Activity of Titanium(IV)-Oxo Clusters of Different Core Structure. *Crystals* **2023**, *13*, 998

P3. **B. Kubiak,** A. Radtke*, A. Topolski, G. Wrzeszcz, P. Golińska, E. Kaszkowiak, M. Sobota, J. Włodarczyk, M. Stojko, P. Piszczek*, The Composites of PCL and Tetranuclear Titanium(IV) – Oxo Complexes as Materials Exhibiting the Photocatalytic and the Antimicrobial Activity. *IJMS* **2021**, *22*, 7021

P4. **B. Kubiak*, T.** Muzioł, G. Wrzeszcz, A. Radtke, P. Golińska, T. Jędrzejewski, S. Wrotek, P. Piszczek*, Structural Characterization and Bioactivity of a Titanium(IV) – Oxo Complex Stabilized by Mandelate Ligands. *Molecules* **2024**, *29*, 1736

P5. **B. Kubiak***, T. M. Muzioł, M. Jabłoński, A. Radtke, P. Piszczek*, Investigation of Titanium(IV) – Oxo Complexes Stabilized with α-Hydroxy Carboxylate Ligands: Structural Analysis and DFT Studies. *Dalton Trans.* **2024**, 53, 14457-14468

P6. **B. Kubiak*,** A. Topolski, A. Radtke*, T. Muzioł, O. Impert, A. Katafias, R. van Eldik, P. Piszczek, Analysis of Photocatalytic Properties of Poly(Methyl Methacrylate) Composites with Titanium(IV) and Ruthenium(III) Complexes. Applied Sciences, 2025, 15(4), 1679

1. Oświadczam, że mój udział w artykule **P1** obejmował opracowanie metodologii badań, analizę otrzymanych wyników, edycję tekstu oraz koordynację prac związanych z publikacją otrzymanych wyników.
2. Oświadczam, że mój udział w artykule **P2** obejmował opracowanie założeń badawczych oraz metodologii badań, analizę otrzymanych wyników. Odpowiadałam także za edycję tekstu oraz koordynację prac związanych z publikacją otrzymanych wyników.

3. Oświadczam, że mój udział w artykule **P3** obejmował opracowanie metodologii badań, analizę otrzymanych wyników, edycję tekstu oraz koordynację prac związanych z publikacją otrzymanych wyników.
4. Oświadczam, że mój udział w artykule **P4** obejmował edycję tekstu, koordynację prac związanych z publikacją otrzymanych wyników oraz pozyskanie środków finansowych.
5. Oświadczam, że mój udział w artykule **P5** obejmował opracowanie metodologii badań, analizę otrzymanych wyników, edycję tekstu oraz koordynację prac związanych z publikacją otrzymanych wyników.
6. Oświadczam, że mój udział w artykule **P6** obejmował opracowanie założeń badawczych oraz metodologii badań, analizę otrzymanych wyników. Odpowiadałam także za edycję tekstu.

Podpis



UNIWERSYTET
MIKOŁAJA KOPERNIKA
W TORUNIU
Wydział Chemii

Dr Tadeusz Muzioł

Wydział Chemii

Uniwersytet Mikołaja Kopernika w Toruniu

ul. Gagarina 7

87 – 100 Toruń

Toruń, 07.02.2025

OŚWIADCZENIE

Dotyczy publikacji:

P2. **B. Kubiak*,** P. Piszczek*, A. Radtke, T. Muzioł, G. Wrzeszcz, P. Golińska, Photocatalytic and Antimicrobial Activity of Titanium(IV)-Oxo Clusters of Different Core Structure. *Crystals* **2023**, *13*, 998

P4. **B. Kubiak*, T.** Muzioł, G. Wrzeszcz, A. Radtke, P. Golińska, T. Jędrzejewski, S. Wrotek, P. Piszczek*, Structural Characterization and Bioactivity of a Titanium(IV) – Oxo Complex Stabilized by Mandelate Ligands. *Molecules* **2024**, *29*, 1736

P5. **B. Kubiak***, T. M. Muzioł, M. Jabłoński, A. Radtke, P. Piszczek*, Investigation of Titanium(IV) – Oxo Complexes Stabilized with α-Hydroxy Carboxylate Ligands: Structural Analysis and DFT Studies. *Dalton Trans.* **2024**, 53, 14457-14468

P6. **B. Kubiak*,** A. Topolski, A. Radtke*, T. Muzioł, O. Impert, A. Katafias, R. van Eldik, P. Piszczek, Analysis of Photocatalytic Properties of Poly(Methyl Methacrylate) Composites with Titanium(IV) and Ruthenium(III) Complexes. Applied Sciences, 2025, 15(4), 1679

1. Oświadczam, że mój udział w artykule **P2** obejmował pomiary dyfrakcji rentgenowskiej pojedynczego kryształu i określenie struktury dla trzech związków, ogólną dyskusję na temat danych krystalograficznych i udział w przygotowaniu rękopisu.
2. Oświadczam, że mój udział w artykule **P4** obejmował pomiary dyfrakcji rentgenowskiej pojedynczego kryształu i określenie struktury dla jednego związku, pomiar dyfrakcji rentgenowskiej proszku, ogólną dyskusję na temat danych krystalograficznych i udział w przygotowaniu rękopisu.
3. Oświadczam, że mój udział w artykule **P5** obejmował pomiary dyfrakcji rentgenowskiej pojedynczego kryształu i określenie struktury dla dwóch związków, pomiar dyfrakcji rentgenowskiej proszków, ogólną dyskusję na temat danych krystalograficznych i udział w przygotowaniu rękopisu.
4. Oświadczam, że mój udział w artykule **P6** obejmował zaplanowanie i przeprowadzenie pomiarów techniką XAS kompleksów okso-tytanu(IV) i ich kompozytów. Odpowiadałem także za dyskusję otrzymanych wyników i udział w przygotowaniu rękopisu.

Tadeusz Muzioł

UNIWERSYTET
MIKOŁAJA KOPERNIKA
W TORUNIU
Wydział Chemii

Prof. dr hab. Patrycja Golińska
Wydział Nauk Biologicznych i Weterynaryjnych
Uniwersytet Mikołaja Kopernika w Toruniu
ul. Lwowska 1
87 – 100 Toruń

Toruń, 12.11.2024

OŚWIADCZENIE

Dotyczy publikacji:

P1. P. Piszczek*, **B. Kubiak,** P. Golińska, A. Radtke*, Oxo-Titanium(IV) Complex/Polymer Composites—Synthesis, Spectroscopic Characterization and Antimicrobial Activity Test. *IJMS* **2020**, *21*, 9663

P2. **B. Kubiak*,** P. Piszczek*, A. Radtke, T. Muzioł, G. Wrzeszcz, P. Golińska, Photocatalytic and Antimicrobial Activity of Titanium(IV)-Oxo Clusters of Different Core Structure. *Crystals* **2023**, *13*, 998

P3. **B. Kubiak,** A. Radtke*, A. Topolski, G. Wrzeszcz, P. Golińska, E. Kaszkowiak, M. Sobota, J. Włodarczyk, M. Stojko, P. Piszczek*, The Composites of PCL and Tetranuclear Titanium(IV) – Oxo Complexes as Materials Exhibiting the Photocatalytic and the Antimicrobial Activity. *IJMS* **2021**, *22*, 7021

P4. **B. Kubiak*, T.** Muzioł, G. Wrzeszcz, A. Radtke, P. Golińska, T. Jędrzejewski, S. Wrotek, P. Piszczek*, Structural Characterization and Bioactivity of a Titanium(IV) – Oxo Complex Stabilized by Mandelate Ligands. *Molecules* **2024**, *29*, 1736

1. Oświadczam, że mój udział w artykule **P1** dotyczył prac związanych z badaniem aktywności przeciwdrobnoustrojowej próbek: PMMA, PMMA + (**1**), PMMA + (**2**), PMMA + (**3**), PMMA + (**4**). Odpowiadałam także za analizę oraz dyskusję otrzymanych wyników.
2. Oświadczam, że mój udział w artykule **P2** dotyczył prac związanych z badaniem aktywności przeciwdrobnoustrojowej próbek: PMMA + (**1**) 20 wt.%, PMMA + (**2**) 20 wt.%, PMMA + (**4**) 20 wt.%, PMMA + (**5**) 20 wt.%. Odpowiadałam także za analizę oraz dyskusję otrzymanych wyników.
3. Oświadczam, że mój udział w artykule **P3** dotyczył prac związanych z badaniem aktywności przeciwdrobnoustrojowej próbek: PCL, PCL + 5(**1**), PCL + 20(**1**), PCL + 5(**2**), PCL + 20(**2**). Odpowiadałam także za analizę oraz dyskusję otrzymanych wyników.
4. Oświadczam, że mój udział w artykule **P4** dotyczył prac związanych z badaniem aktywności przeciwdrobnoustrojowej próbek: PMMA, PMMA + (**1**) 2 – 20 wt.% oraz (**1**) 2 – 20 wt.%. Odpowiadałam także za analizę otrzymanych wyników.

Patrycja Golińska

Podpis

UNIWERSYTET
MIKOŁAJA KOPERNIKA
W TORUNIU
Wydział Chemii

Dr Adrian Topolski
Wydział Chemii
Uniwersytet Mikołaja Kopernika w Toruniu
ul. Gagarina 7
87 – 100 Toruń

Toruń, 07.02.2025

OŚWIADCZENIE

Dotyczy publikacji:

P3. **B. Kubiak,** A. Radtke*, A. Topolski, G. Wrzeszcz, P. Golińska, E. Kaszkowiak, M. Sobota, J. Włodarczyk, M. Stojko, P. Piszczek*, The Composites of PCL and Tetranuclear Titanium(IV) – Oxo Complexes as Materials Exhibiting the Photocatalytic and the Antimicrobial Activity. *IJMS* **2021**, *22*, 7021

P6. **B. Kubiak*,** A. Topolski, A. Radtke*, T. Muzioł, O. Impert, A. Katafias, R. van Eldik, P. Piszczek, Analysis of Photocatalytic Properties of Poly(Methyl Methacrylate) Composites with Titanium(IV) and Ruthenium(III) Complexes. *Applied Sciences*, **2025**, 15(4), 1679

1. Oświadczam, że mój udział w artykule **P3** dotyczył zaplanowania badań aktywności fotokatalitycznej próbek: PCL, PCL + 5(**1**), PCL + 5(**2**), PCL + 20(**1**) i PCL + 20(**2**).
2. Oświadczam, że mój udział w artykule **P6** dotyczył sprawdzenia poprawności prac związanych z badaniem aktywności fotokatalitycznej próbek: PMMA + (**2**) 2- 20 wt.%, PMMA + (**3**) 2- 20 wt.%, PMMA + (**4**) 2- 20 wt.%, PMMA + (**5**) 2- 20 wt.% oraz przeprowadzenia pomiarów EPR i ich interpretacji. Odpowiadałem także za weryfikację treści i edycję manuskryptu.

Podpis

UNIWERSYTET
MIKOŁAJA KOPERNIKA
W TORUNIU
Wydział Chemii

Dr hab. Mirosław Jabłoński, prof. UMK
Wydział Chemii
Uniwersytet Mikołaja Kopernika w Toruniu
ul. Gagarina 7
87 – 100 Toruń

Toruń, 08.11.2024

OŚWIADCZENIE

Dotyczy publikacji:

P5. **B. Kubiak***, T. M. Muzioł, M. Jabłoński, A. Radtke, P. Piszczek*, Investigation of Titanium(IV) – Oxo Complexes Stabilized with α-Hydroxy Carboxylate Ligands: Structural Analysis and DFT Studies. *Dalton Trans.* **2024**, 53, 14457-14468

1. Oświadczam, że mój udział w artykule **P5** dotyczył prac związanych z zaplanowaniem i wykonaniem obliczeń DFT związków (**1**) i (**2**): teoretycznych geometrii, widm IR, Ramana i UV-VIS, wyznaczeniem orbitali HOMO i LUMO, obliczeniem indeksów reaktywności oraz otrzymaniem map potencjału elektrostatycznego. Odpowiadałem także za przygotowanie niektórych rysunków, analizę oraz dyskusję otrzymanych wyników teoretycznych. Napisałem też część artykułu dotyczącą wyników teortetycznych.

Podpis

UNIWERSYTET
MIKOŁAJA KOPERNIKA
W TORUNIU
Wydział Chemii

Dr Tomasz Jędrzejewski

Wydział Nauk Biologicznych i Weterynaryjnych

Uniwersytet Mikołaja Kopernika w Toruniu

ul. Lwowska 1

87 – 100 Toruń

Toruń, 12.11.2024

OŚWIADCZENIE

Dotyczy publikacji:

P4. **B. Kubiak*, T.** Muzioł, G. Wrzeszcz, A. Radtke, P. Golińska, T. Jędrzejewski, S. Wrotek, P. Piszczek*, Structural Characterization and Bioactivity of a Titanium(IV) – Oxo Complex Stabilized by Mandelate Ligands. *Molecules* **2024**, *29*, 1736

1. Oświadczam, że mój udział w artykule **P4** dotyczył prac związanych z zaplanowaniem i wykonaniem badań cytotoksyczności próbek: PMMA, PMMA + (**1**) 2 – 20 wt.% względem fibroblastów linii L929. Oprócz tego, brałem udział w analizie i dyskusji wyników biologicznych oraz analizie obrazów SEM, komórek rosnących na badanych kompozytach.

Jędrzejewski Tomasz

Podpis

UNIWERSYTET
MIKOŁAJA KOPERNIKA
W TORUNIU
Wydział Chemii

Dr hab. Anna Katafias, prof. UMK
Wydział Chemii
Uniwersytet Mikołaja Kopernika w Toruniu
ul. Gagarina 7
87 – 100 Toruń

Toruń, 07.02.2025

OŚWIADCZENIE

Dotyczy publikacji:

P6. **B. Kubiak*,** A. Topolski, A. Radtke*, T. Muzioł, O. Impert, A. Katafias, R. van Eldik, P. Piszczek, Analysis of Photocatalytic Properties of Poly(Methyl Methacrylate) Composites with Titanium(IV) and Ruthenium(III) Complexes. Applied Sciences, 2025, 15(4), 1679

1. Oświadczam, że mój udział w artykule **P6** dotyczył zaplanowania badań spektroskopowych próbek: (**4**), (**5**), PMMA + (**4**) 2- 20 wt.%, PMMA + (**5**) 2- 20 wt.%. Odpowiadałam także za weryfikację treści i edycję manuskryptu.

UNIWERSYTET
MIKOŁAJA KOPERNIKA
W TORUNIU
Wydział Chemii

Dr Mateusz Stojko

Centrum Materiałów Polimerowych i Węglowych

Polska Akademia Nauk

ul. Marii Curie – Skłodowskiej 34

41 – 819 Zabrze

Toruń, 31.10.2024

OŚWIADCZENIE

Dotyczy publikacji:

P3. **B. Kubiak,** A. Radtke*, A. Topolski, G. Wrzeszcz, P. Golińska, E. Kaszkowiak, M. Sobota, J. Włodarczyk, M. Stojko, P. Piszczek*, The Composites of PCL and Tetranuclear Titanium(IV) – Oxo Complexes as Materials Exhibiting the Photocatalytic and the Antimicrobial Activity. *IJMS* **2021**, *22*, 7021

1. Oświadczam, że mój udział w artykule **P3** dotyczył prac związanych z otrzymywaniem materiałów kompozytowych przy użyciu wytłaczarki dwuślimakowej i pneumatycznej miniwtryskarki. Ponadto uczestniczyłem w wykonaniu badań mechanicznych, tzn. wytrzymałość na rozciąganie i ściskanie, próbek: PCL, PCL + 20(1), PCL + 20(2). Przygotowałem także opisy przeprowadzonych badań.

Podpis

UNIWERSYTET
MIKOŁAJA KOPERNIKA
W TORUNIU
Wydział Chemii

Dr hab. Michał Sobota

Centrum Materiałów Polimerowych i Węglowych

Polska Akademia Nauk

ul. Marii Curie – Skłodowskiej 34

41 – 819 Zabrze

Toruń, 31.10.2024

OŚWIADCZENIE

Dotyczy publikacji:

P3. **B. Kubiak,** A. Radtke*, A. Topolski, G. Wrzeszcz, P. Golińska, E. Kaszkowiak, M. Sobota, J. Włodarczyk, M. Stojko, P. Piszczek*, The Composites of PCL and Tetranuclear Titanium(IV) – Oxo Complexes as Materials Exhibiting the Photocatalytic and the Antimicrobial Activity. *IJMS* **2021**, *22*, 7021

1. Oświadczam, że mój udział w artykule **P3** dotyczył prac związanych z otrzymywaniem materiałów kompozytowych przy użyciu wytłaczarki dwuślimakowej i pneumatycznej miniwtryskarki. Ponadto uczestniczyłem w planowaniu i wykonaniu badań mechanicznych, tzn. wytrzymałość na rozciąganie i ściskanie, próbek: PCL, PCL + 20(1), PCL + 20(2). Przygotowałem także opisy przeprowadzonych badań.

Podpis

UNIWERSYTET
MIKOŁAJA KOPERNIKA
W TORUNIU
Wydział Chemii

Prof. Dr. Dr. h. c. mult. em. Rudi van Eldik
Faculty of Chemistry
Nicolaus Copernicus University in Toruń
Gagarina Street 7
87 – 100 Toruń

Toruń, 07.02.2025

DECLARATION

P6. **B. Kubiak*,** A. Topolski, A. Radtke*, T. Muzioł, O. Impert, A. Katafias, R. van Eldik, P. Piszczek, Analysis of Photocatalytic Properties of Poly(Methyl Methacrylate) Composites with Titanium(IV) and Ruthenium(III) Complexes. Applied Sciences, 2025, 15(4), 1679

1. I declare that my participation in the article **P6** concerned funding acquisition, supervision, review and editing of manuscript.

UNIWERSYTET
MIKOŁAJA KOPERNIKA
W TORUNIU
Wydział Chemii

Toruń, 31.10.2024

Dr inż. Jakub Włodarczyk
Centrum Materiałów Polimerowych i Węglowych
Polska Akademia Nauk
ul. Marii Curie – Skłodowskiej 34
41 – 819 Zabrze

OŚWIADCZENIE

Dotyczy publikacji:

P3. **B. Kubiak,** A. Radtke*, A. Topolski, G. Wrzeszcz, P. Golińska, E. Kaszkowiak, M. Sobota, J. Włodarczyk, M. Stojko, P. Piszczek*, The Composites of PCL and Tetranuclear Titanium(IV) – Oxo Complexes as Materials Exhibiting the Photocatalytic and the Antimicrobial Activity. *IJMS* **2021**, *22*, 7021

1. Oświadczam, że mój udział w artykule **P3** dotyczył prac związanych z otrzymywaniem materiałów kompozytowych przy użyciu wytłaczarki dwuślimakowej i pneumatycznej miniwtryskarki. Ponadto uczestniczyłem w wykonaniu badań mechanicznych, tzn. wytrzymałość na rozciąganie i ściskanie, próbek: PCL, PCL + 20(1), PCL + 20(2). Przygotowałem także opisy przeprowadzonych badań.

UNIWERSYTET
MIKOŁAJA KOPERNIKA
W TORUNIU
Wydział Chemii

Dr hab. Sylwia Wrotek, prof. UMK
Wydział Nauk Biologicznych i Weterynaryjnych
Uniwersytet Mikołaja Kopernika w Toruniu
ul. Lwowska 1
87 – 100 Toruń

Toruń, 12.11.2024

OŚWIADCZENIE

Dotyczy publikacji:

P4. **B. Kubiak*, T.** Muzioł, G. Wrzeszcz, A. Radtke, P. Golińska, T. Jędrzejewski, S. Wrotek, P. Piszczek*, Structural Characterization and Bioactivity of a Titanium(IV) – Oxo Complex Stabilized by Mandelate Ligands. *Molecules* **2024**, *29*, 1736

1. Oświadczam, że mój udział w artykule **P4** dotyczył prac związanych z zaplanowaniem badań cytotoksyczności próbek: PMMA, PMMA + (**1**) 2 – 20 wt.% względem fibroblastów linii L929.

Podpis

S. Wrotek

UNIWERSYTET
MIKOŁAJA KOPERNIKA
W TORUNIU
Wydział Chemii

Toruń, 08.11.2024

Dr hab. Grzegorz Wrzeszcz, prof. UMK
Wydział Chemii
Uniwersytet Mikołaja Kopernika w Toruniu
ul. Gagarina 7
87 – 100 Toruń

OŚWIADCZENIE

Dotyczy publikacji:

P2. **B. Kubiak*,** P. Piszczek*, A. Radtke, T. Muzioł, G. Wrzeszcz, P. Golińska, Photocatalytic and Antimicrobial Activity of Titanium(IV)-Oxo Clusters of Different Core Structure. *Crystals* **2023**, *13*, 998

P3. **B. Kubiak,** A. Radtke*, A. Topolski, G. Wrzeszcz, P. Golińska, E. Kaszkowiak, M. Sobota, J. Włodarczyk, M. Stojko, P. Piszczek*, The Composites of PCL and Tetranuclear Titanium(IV) – Oxo Complexes as Materials Exhibiting the Photocatalytic and the Antimicrobial Activity. *IJMS* **2021**, *22*, 7021

P4. **B. Kubiak*, T.** Muzioł, G. Wrzeszcz, A. Radtke, P. Golińska, T. Jędrzejewski, S. Wrotek, P. Piszczek*, Structural Characterization and Bioactivity of a Titanium(IV) – Oxo Complex Stabilized by Mandelate Ligands. *Molecules* **2024**, *29*, 1736

1. Oświadczam, że mój udział w artykule **P2** dotyczył prac związanych z zaplanowaniem i wykonaniem badań spektroskopii EPR próbek: PMMA + (**1**) 10 wt.%, PMMA + (**2**) 10 wt.%, PMMA + (**3**) 20 wt.%, PMMA + (**4**) 20 wt.%. Odpowiadałem także za przygotowanie rysunków, analizę oraz dyskusję otrzymanych wyników.
2. Oświadczam, że mój udział w artykule **P3** dotyczył prac związanych z zaplanowaniem i wykonaniem badań spektroskopii EPR próbek: PCL + 20(**1**), PCL + 20(**2**). Odpowiadałem także za przygotowanie rysunków, analizę oraz dyskusję otrzymanych wyników.
3. Oświadczam, że mój udział w artykule **P4** dotyczył prac związanych z zaplanowaniem i wykonaniem badań spektroskopii EPR próbek: PMMA, PMMA + (**1**) 2 – 20 wt.%, proszek (**1**). Odpowiadałem także za przygotowanie rysunków, analizę oraz dyskusję otrzymanych wyników.

Grzegorz Wrzeszcz

Podpis

UNIWERSYTET
MIKOŁAJA KOPERNIKA
W TORUNIU
Wydział Chemii

Dr Olga Impert
Wydział Chemii
Uniwersytet Mikołaja Kopernika w Toruniu
ul. Gagarina 7
87 – 100 Toruń

Toruń, 07.02.2025

OŚWIADCZENIE

Dotyczy publikacji:

P6. **B. Kubiak***, A. Topolski, A. Radtke*, T. Muzioł, O. Impert, A. Katafias, R. van Eldik, P. Piszczek, Analysis of Photocatalytic Properties of Poly(Methyl Methacrylate) Composites with Titanium(IV) and Ruthenium(III) Complexes. Applied Sciences, 2025, 15(4), 1679

1. Oświadczam, że mój udział w artykule **P6** dotyczył zaplanowania badań spektroskopowych próbek: (**4**), (**5**), PMMA + (**4**) 2- 20 wt.%, PMMA + (**5**) 2- 20 wt.%. Odpowiadałam także za weryfikację treści i edycję manuskryptu.

Impert Olga
Podpis

UNIWERSYTET
MIKOŁAJA KOPERNIKA
W TORUNIU
Wydział Chemii

Mgr Ewelina Kaszkowiak

Wydział Chemii

Uniwersytet Mikołaja Kopernika w Toruniu

ul. Gagarina 7

87 – 100 Toruń

Toruń, 31.10.2024

OŚWIADCZENIE

Dotyczy publikacji:

P3. **B. Kubiak,** A. Radtke*, A. Topolski, G. Wrzeszcz, P. Golińska, E. Kaszkowiak, M. Sobota, J. Włodarczyk, M. Stojko, P. Piszczek*, The Composites of PCL and Tetranuclear Titanium(IV) – Oxo Complexes as Materials Exhibiting the Photocatalytic and the Antimicrobial Activity. *IJMS* **2021**, *22*, 7021

1. Oświadczam, że mój udział w artykule **P3** dotyczył współpracy przy badaniu aktywności fotokatalitycznej próbek: PCL, PCL + 5(1), PCL + 5(2), PCL + 20(1) i PCL + 20(2).

Podpis